

Opportunities and Risks of Nanomaterials

Swiss National Research Programme 64

Journal of Nanobiotechnology

Opportunities and Risks of Nanomaterials

Swiss National Research Programme 64

Journal of Nanobiotechnology

Editorial Board

Editors-in-Chief

Prof Ueli Aebi (University of Basel, Switzerland)
Prof Fernando Patolsky (University of Tel Aviv, Israel)

Commissioning Editor

Prof Peter Gehr (University of Bern, Switzerland)

Associate Editors

Dr Martin Clift (Swansea University Medical School, UK)
Prof Martin Hegner (Trinity College Dublin, Ireland)
Prof Ningping Huang (Southeast University, China)
Dr Pablo del Pino (University of Santiago de Compostela, Spain)
Prof Kuan Wang (Academia Sinica, Taiwan)
Dr Meni Wanunu (Northeastern University, USA)

Editorial Board

Prof Dario D Anselmetti (University of Bielefeld, Germany)
Prof Vasudevanpillai Biju (National Institute of Advanced Industrial Science and Technology, Japan)
Prof Derek J Blake (University of Oxford, UK)
Dr Michel Bottlaender (Service Hospitalier Frédéric Joliot, France)
Prof Peter Burkhard (University of Connecticut, USA)
Prof Wah Chiu (Baylor College of Medicine, USA)
Dr Francisco Ciruela (University of Barcelona, Spain)
Prof Matthew Cooper (The University of Queensland, Australia)
Dr Simon M Cutting (Royal Holloway University of London, UK)
Prof Philip Demokritou (Harvard University, USA)
Prof Alain L Fymat (International Institute of Medicine and Science, USA)
Prof Hermann Gaub (Ludwig-Maximilian University Munich, Germany)
Prof Andreas Hoenger (University of Colorado at Boulder, USA)
Prof Twan Lammers (RWTH Aachen University, Germany)
Prof Chwee T Lim (National University Singapore, Singapore)
Prof Christopher R R Lowe (University of Cambridge, UK)
Prof Paul Matsudaira (National University of Singapore, Singapore)
Dr Piero Morandini (University of Milan, Italy)
Prof Daniel J Müller (ETH Zürich, Switzerland)
Prof Wolfgang Parak (Philipps University Marburg, Germany)
Dr Oleg Salata (Arborescent Ltd, UK)
Prof Simon Scheuring (UMR-CNRS / Institut Curie - Research, France)
Prof Youqing Shen (Zhejiang University, China)
Prof Francesco Stellacci (Ecole Polytechnique Fédérale de Lausanne (EPFL), Switzerland)
Prof Kenji Yasuda (Tokyo Medical and Dental University, Japan)

Contents

- 1 **Swiss National Research Programme “Opportunities and Risks of Nanomaterials” (NRP 64): key findings**
Ueli Aebi and Peter Gehr
Journal of Nanobiotechnology 2017 **15**:47
- 3 **Magnetic separation-based blood purification: a promising new approach for the removal of disease-causing compounds?**
IK Herrmann, AA Schlegel, R Graf, WJ Stark and Beatrice Beck-Schimmer
Journal of Nanobiotechnology 2015 **13**:49
- 7 **Probabilistic modelling of prospective environmental concentrations of gold nanoparticles from medical applications as a basis for risk assessment**
Indrani Mahapatra, Tian Yin Sun, Julian RA Clark, Peter J Dobson, Konrad Hungerbuehler, Richard Owen, Bernd Nowack and Jamie Lead
Journal of Nanobiotechnology 2015 **13**:93
- 21 **Effect of nanoparticles on red clover and its symbiotic microorganisms**
Janine Moll, Alexander Gogos, Thomas D Bucheli, Franco Widmer and Marcel GA van der Heijden
Journal of Nanobiotechnology 2016 **14**:36
- 29 **Vertical transport and plant uptake of nanoparticles in a soil mesocosm experiment**
Alexander Gogos, Janine Moll, Florian Klingenfuss, Marcel van der Heijden, Fahmida Irin, Micah J Green, Renato Zenobi and Thomas D Bucheli
Journal of Nanobiotechnology 2016 **14**:40
- 40 **Critical review of the safety assessment of nano-structured silica additives in food**
Hans Christian Winkler, Mark Suter and Hanspeter Naegeli
Journal of Nanobiotechnology 2016 **14**:44
- 49 **Photoinduced effects of m-tetrahydroxyphenylchlorin loaded lipid nanoemulsions on multicellular tumor spheroids**
Doris Hinger, Fabrice Navarro, Andres Käch, Jean-Sébastien Thomann, Frédérique Mittler, Anne-Claude Couffin and Caroline Maake
Journal of Nanobiotechnology 2016 **14**:68
- 63 **Lipid nanoemulsions and liposomes improve photodynamic treatment efficacy and tolerance in CAL-33 tumor bearing nude mice**
Doris Hinger, Susanna Gräfe, Fabrice Navarro, Bernhard Spingler, Devaraj Pandiarajan, Heinrich Walt, Anne-Claude Couffin and Caroline Maake
Journal of Nanobiotechnology 2016 **14**:71
- 77 **Release of copper-amended particles from micronized copper-pressure-treated wood during mechanical abrasion**
Chiara Civardi, Lukas Schlagenhauf, Jean-Pierre Kaiser, Cordula Hirsch, Claudio Mucchino, Adrian Wichser, Peter Wick and Francis WMR Schwarze
Journal of Nanobiotechnology 2016 **14**:77
- 87 **A critical review of the current knowledge regarding the biological impact of nanocellulose**
C Endes, S Camarero-Espinosa, S Mueller, EJ Foster, A Petri-Fink, B Rothen-Rutishauser, C Weder and MJD Clift
Journal of Nanobiotechnology 2016 **14**:78
- 101 **Interaction of biomedical nanoparticles with the pulmonary immune system**
Fabian Blank, Kleanthis Fytianos, Emilie Seydoux, Laura Rodriguez-Lorenzo, Alke Petri-Fink, Christophe von Garnier and Barbara Rothen-Rutishauser
Journal of Nanobiotechnology 2017 **15**:6
- 110 **Transformation of the released asbestos, carbon fibers and carbon nanotubes from composite materials and the changes of their potential health impacts**
Jing Wang, Lukas Schlagenhauf and Ari Setyan
Journal of Nanobiotechnology 2017 **15**:15
- 126 **Interaction of silver nanoparticles with algae and fish cells: a side by side comparison**
Yang Yue, Xiaomei Li, Laura Sigg, Marc J-F Suter, Smitha Pillai, Renata Behra and Kristin Schirmer
Journal of Nanobiotechnology 2017 **15**:16
- 137 **Non-invasive continuous monitoring of pro-oxidant effects of engineered nanoparticles on aquatic microorganisms**
Christian Santschi, Nadia Von Moos, Volodymyr B Koman, Vera I Slaveykova, Paul Bowen and Olivier JF Martin
Journal of Nanobiotechnology 2017 **15**:19
- 155 **Effects of silica nanoparticle exposure on mitochondrial function during neuronal differentiation**
Angélique D. Ducray, Andrea Felser, Jana Zielinski, Annela Bittner, Julia V. Bürgi, Jean-Marc Nuoffer, Martin Frenz and Meike Mevissen
Journal of Nanobiotechnology 2017 **15**:49
- 169 **Characteristics and properties of nano-LiCoO₂ synthesized by pre-organized single source precursors: Li-ion diffusivity, electrochemistry and biological assessment**
Jean-Pierre Brog, Aurélien Crochet, Joël Seydoux, Martin JD Clift, Benoît Baichette, Sivarajakumar Maharajan, Hana Barosova, Pierre Brodard, Mariana Spodaryk, Andreas Züttel, Barbara Rothen-Rutishauser, Nam Hee Kwon and Katharina M Fromm
Journal of Nanobiotechnology 2017 **15**:58

Journal of Nanobiotechnology

Journal information

Journal of Nanobiotechnology is published by:

BioMed Central Ltd
Floor 6, 236 Gray's Inn Road
London WC1X 8HB, UK
T: +44 (0) 20 3192 2009
F: +44 (0) 20 3192 2010
E: info@biomedcentral.com

Journal of Nanobiotechnology is an open access peer-reviewed journal communicating scientific and technological advances in the fields of medicine and biology, with an emphasis in their interface with nanoscale sciences. The journal provides biomedical scientists and the international biotechnology business community with the latest developments in the growing field of Nanobiotechnology.

The journal consists of the following sections:

- Nanomaterials in Biology, Medicine, Food, Environment and Agriculture
- Nanoparticles in Biology, Medicine, Food, Environment and Agriculture
- Nanosensors in Biology, Medicine, Food, Environment and Agriculture
- Nanomedicine: Diagnostics, Imaging, Therapy and Drug Development
- Micro- and Nanofluidics; Micro- & NanoElectroMechanical Systems (MEMS & NEMS)
- Nanotoxicology.

The journal can be found at
<https://jnanobiotechnology.biomedcentral.com/>
(ISSN 1477-3155). Access to *Journal of Nanobiotechnology* is free and available to all.

Open Access

All articles published in *Journal of Nanobiotechnology* are open access, which means they are universally and freely accessible via the Internet and deposited in at least one widely and internationally recognized open access repository (such as PubMed Central). Open access also means that the authors or copyright owners grant any third party the right to use, reproduce and disseminate the research article. BioMed Central is committed to maintaining open access for all research articles that it publishes, both retrospectively and prospectively, in all eventualities, including any future changes in ownership. For more information please refer to the BioMed Central Open Access Charter and permanency of articles webpages accessible from <http://www.biomedcentral.com/about>

Indexing/abstracting

Journal of Nanobiotechnology is indexed/ tracked/covered by:

- Biological Abstracts
- BIOSIS
- CABI
- CAS
- Citebase
- Compendex
- DOAJ
- Embase
- EmBiology
- Global Health
- MEDLINE
- OALster
- PubMed
- PubMed Central
- Science Citation Index Expanded
- SCImago
- Scopus
- SOCOLAR
- Zetoc

Supplements

Journal of Nanobiotechnology accepts supplements (which may be meeting abstracts, thematic reviews or proceedings) subject to the approval of the journal's Editor-in-Chief. Articles submitted to supplements are subject to peer review and BioMed Central's standard editorial policies apply. For further information please email supplements@biomedcentral.com

Advertising

For information about advertising in *Journal of Nanobiotechnology*, including the rate card and specifications, contact the Advertising Department at the above address. Alternatively send an email to: advertising@biomedcentral.com

Reprints

BioMed Central can provide high quality reprints and offers a rapid delivery service. For further information and prices, contact the above address, or send an email to: reprints@biomedcentral.com

Disclaimer

Whilst every effort is made by the publishers, editor and editorial board to see that no inaccurate or misleading data, opinion, or statement appear in this publication, they wish to make it clear that the data and opinions appearing in the articles and advertisements herein are the responsibility of the contributor or advertiser concerned. Accordingly, the publishers, the editor and editorial board, and their respective employees, officers, and agents accept no liability whatsoever for the consequences of any such inaccurate or misleading data, opinion or statement.

EDITORIAL

Open Access



Swiss National Research Programme “Opportunities and Risks of Nanomaterials” (NRP 64): key findings

Ueli Aebi^{1*}  and Peter Gehr²

This *Special Issue* is devoted to the outcome of a 5-year Swiss *National Research Programme* on the “Opportunities and Risks of Nanomaterials” (NRP 64). Nanotechnology is an enabling technology that explores the structure and function of naturally occurring nanomaterials, as a basis for engineering synthetic nanomaterials inspired by nature. Nanomaterials have rapidly come to play an important role in healthcare, the consumer industry, energy storage and other areas. NRP 64 comprised 23 mostly interdisciplinary research projects that studied the impact of engineered nanomaterials on the environment and on human health. The outcome of the programme has been highly satisfying, as all projects yielded new and in some cases unexpected results [1]. In this special issue, we present the key findings of 15 projects, some in the form of reviews rather than original research articles to put things into a broader perspective.

As the title of NRP 64 “Opportunities and Risks of Nanomaterials” implies, the programme’s primary goal was to investigate potential applications of existing nanomaterials in healthcare, the consumer industry and in the environment, and to identify, characterise and minimise the possible risks associated with their use. Several projects dealt with the development and/or testing of tools and measurement protocols to track the fate, effect or biodegradation of nanoparticles in cells, tissues, soil and aquatic environments. Highlights of the programme included: single cell surgery by metal nanomagnets; biomedical nanoparticles as immune modulators [2]; novel nanoparticles for efficient and safe drug delivery; nanofiber-reinforced bone substitute materials; aerogels and new tissue engineering scaffolds (e.g. artificial cartilage) made of cellulose nanocrystals; nanoparticle

transport across the human placenta; transport of nanoparticles after release from biodegradable implants; non-invasive monitoring of the interaction between nanoparticles and aquatic microorganisms [3]; evaluation platforms for safety and environmental risks of carbon nanotube reinforced nanocomposites [4]; development of a “lab-on-a-chip” tool to rapidly assess the safety of novel nanoscale active materials for next-generation battery systems.

NRP 64 has undeniably generated a large amount of new knowledge about the use, application and risk assessment of nanomaterials. This will enable Switzerland to remain at the cutting edge of efforts to develop smart and novel nanomaterials that are inspired by nature, and to look for new applications that minimise their health and environmental risks. In addition, when it comes to a more physiological or pathological understanding of how nanomaterials interact with cells, tissues and the environment, we have definitely made significant progress. What is still lacking are long-term studies that clearly document how exposure to nanoparticles over a longer period affects our bodies and the environment. By the same token, we still know very little about the effects of indirect exposure to nanoparticles, e.g. through the accumulation of nanoparticles in plants or animals that will eventually end up in our food chain.

One of the general conclusions drawn from NRP 64 is the following: whenever a new nanomaterial is identified or a new application of an established nanomaterial pursued, carrying out a risk re-assessment is essential to guarantee safety. Overall, the programme has clearly shown that, for the nanomaterials investigated, the opportunities outweigh the risks. Not only has NRP 64 taken the research field a big step forward, its results have made it evident where more basic research and/or a more detailed risk assessment are necessary before researchers can start exploiting the application potential of individual nanomaterials.

*Correspondence: ueli.aebi@unibas.ch

¹ Steering Committee of the Swiss National Research Programme NRP 64 and Prof. Emeritus, Biozentrum University of Basel, Basel, Switzerland
Full list of author information is available at the end of the article

Authors' contributions

UA and PG prepared the manuscript. Both authors read and approved the final manuscript.

Author details

¹ Steering Committee of the Swiss National Research Programme NRP 64 and Prof. Emeritus, Biozentrum University of Basel, Basel, Switzerland. ² Steering Committee of the Swiss National Research Programme NRP 64 and Prof. Emeritus, University of Bern, Bern, Switzerland.

Competing interests

The authors declare that they have no competing interests.

Publisher's Note

Springer Nature remains neutral with regard to jurisdictional claims in published maps and institutional affiliations.

Received: 28 April 2017 Accepted: 13 June 2017

Published online: 24 June 2017

References

1. The SNSF P3 Grant Search Database. P3.snf.ch. 2017. <http://p3.snf.ch/?QueryID=278b9f22-b8a3-49da-8ce3-6fc79416900a>. Accessed 19 June 2017.
2. Blank F, Fytianos K, Seydoux E, Rodriguez-Lorenzo L, Petri-Fink A, von Garnier C, Rothen-Rutishauser B. Interaction of biomedical nanoparticles with the pulmonary immune system. *J Nanobiotechnol*. 2017;15:6.
3. Santschi C, Von Moos N, Koman VB, Slaveykova VI, Bowen P, Martin OJF. Non-invasive continuous monitoring of pro-oxidant effects of engineered nanoparticles on aquatic microorganisms. *J Nanobiotechnol*. 2017;15:19.
4. Wang J, Schlagenhauf L, Setyan A. Transformation of the released asbestos, carbon fibers and carbon nanotubes from composite materials and the changes of their potential health impacts. *J Nanobiotechnol*. 2017;15:15.

Submit your next manuscript to BioMed Central and we will help you at every step:

- We accept pre-submission inquiries
- Our selector tool helps you to find the most relevant journal
- We provide round the clock customer support
- Convenient online submission
- Thorough peer review
- Inclusion in PubMed and all major indexing services
- Maximum visibility for your research

Submit your manuscript at
www.biomedcentral.com/submit



REVIEW

Open Access



Magnetic separation-based blood purification: a promising new approach for the removal of disease-causing compounds?

I K Herrmann^{1,2}, A A Schlegel³, R Graf³, W J Stark⁴ and Beatrice Beck-Schimmer^{1,2*}

Abstract

Recent studies report promising results regarding extracorporeal magnetic separation-based blood purification for the rapid and selective removal of disease-causing compounds from whole blood. High molecular weight compounds, bacteria and cells can be eliminated from blood within minutes, hence offering novel treatment strategies for the management of intoxications and blood stream infections. However, risks associated with incomplete particle separation and the biological consequences of particles entering circulation remain largely unclear. This article discusses the promising future of magnetic separation-based purification while keeping important safety considerations in mind.

Keywords: Blood purification, Intoxication, Magnetic separation, Magnetic nanoparticles, Sepsis

Background

The direct removal of disease-causing compounds is an inherently attractive treatment modality for a range of pathological conditions, including intoxications and blood stream infections [1]. While low molecular weight compounds (potassium, urea, etc.) are routinely removed from blood circulation by membrane-based processes, such as hemodialysis and hemofiltration [2], high molecular weight targets are only accessible by sorption-based processes e.g. hemoadsorption and hemoperfusion, where blood is pushed at high flow rates through adsorbent cartridges. In spite of promising initial findings, the practical use of hemoperfusion is still controversial and concerns have been raised due to potential side effects such as unspecific protein adsorption, loss of blood cells (e.g. platelets) and possible activation of coagulation and inflammation pathways during operation. Compared to porous membranes, the use of free-floating nano-sized particles exhibits significant benefits in terms of surface accessibility (no pore diffusion, shorter contact

times), but this comes at a price: the pathogen-loaded particles need to be removed from the blood. Recently, it has been demonstrated that magnetic (nano-)particles can be employed to bind pathogenic substances on their surface, followed by a re-collection by magnetic separation. In magnetic separation-based blood purification, capturing agents attached to tiny magnetic nanoparticles are injected into an extracorporeal blood circuit (Fig. 1). They then form a complex consisting of the target compounds attached to the magnetic particle which can be rapidly removed from blood by magnetic separation. The performance of such blood cleansing processes is essentially determined by the target-ligand binding (binding site accessibility, specificity, contact time), the throughput and, most critically, the efficiency of the magnetic separation process.

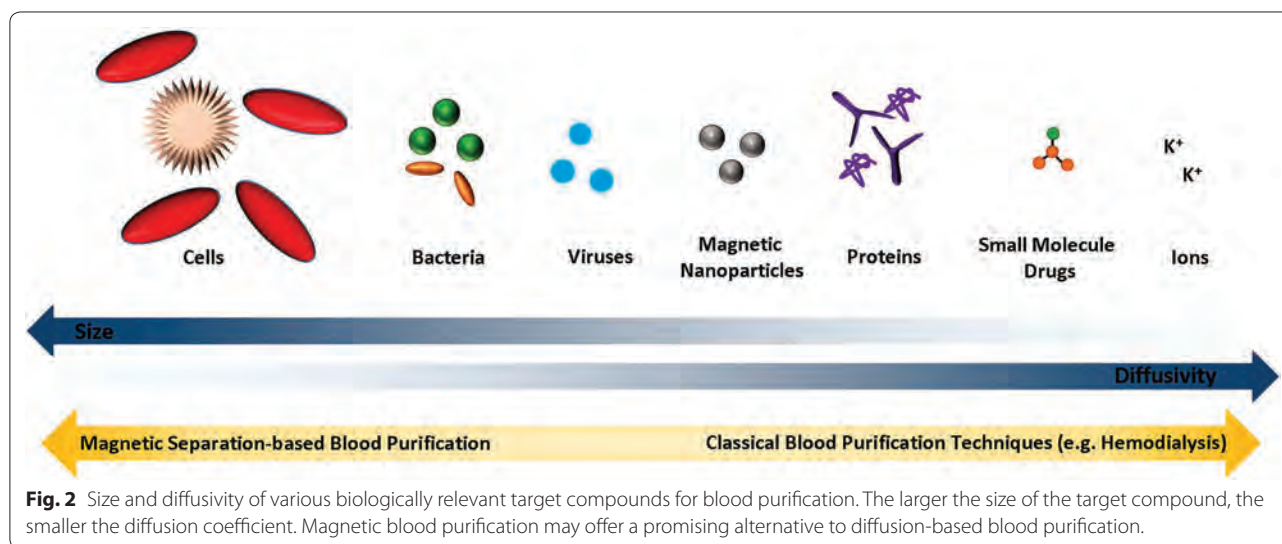
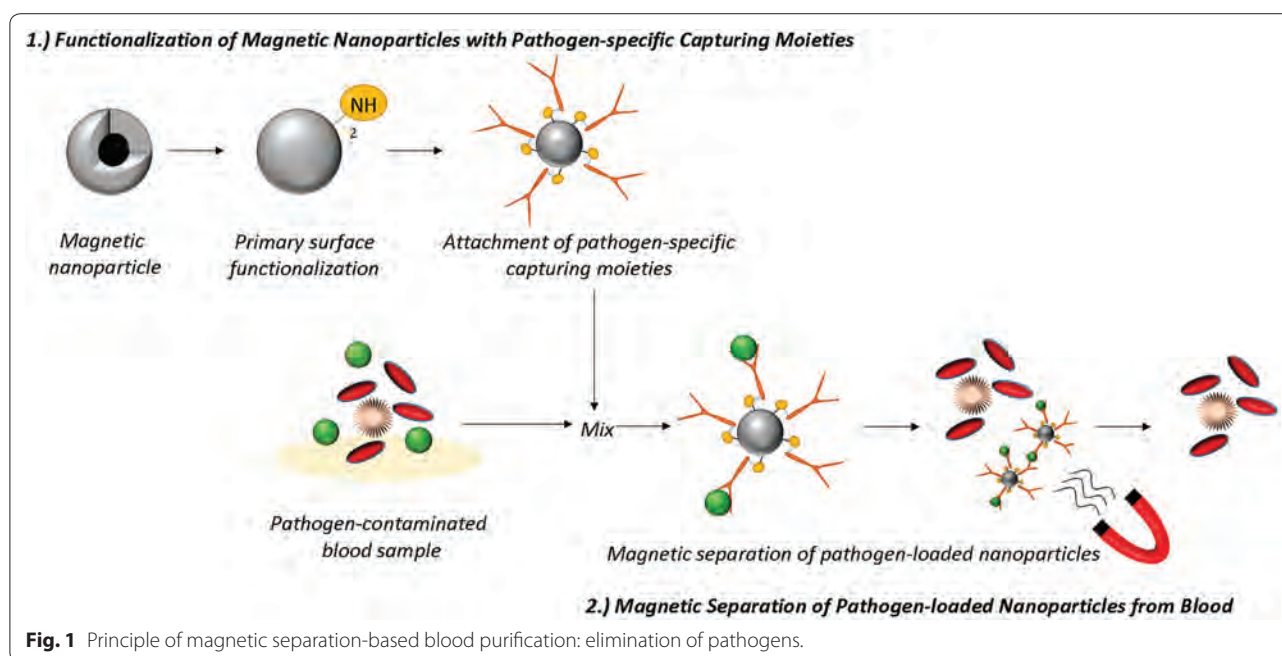
Review

Magnetic separation-based blood purification is especially attractive for the removal of high molecular weight compounds, which are poorly removed by conventional (diffusion-based) blood purifications systems (e.g. dialysis, hemoadsorption) (Fig. 2) [2]. The small size, the high surface-to-volume ratio and the high mobility of nanoparticles allow short diffusion distances and hence

*Correspondence: beatrice.beckschimmer@uzh.ch

¹ Institute of Anesthesiology, University Hospital Zurich, Rämistrasse 100, 8091 Zurich, Switzerland

Full list of author information is available at the end of the article



increased binding efficiencies even for high molecular weight compounds. A range of chemically diverse target compounds, including heavy metal ions (uranyl [3], lead [4–6] and cadmium ions [7], small molecule drugs (digoxin [5, 6, 8], diazepam [9]), proteins (cytokines [5, 8]), bacteria and bacterial compounds [10] have been successfully removed ex vivo from whole blood in the past decade (Table 1). However, such targeted compound removal generally requires the use of magnetic beads with a pathogen-specific capturing agent and thus has been significantly limiting the future applicability of

magnetic blood purification. Particularly, urgent medical situations, such as acute intoxications or blood stream infections where the disease-causing factor is unknown, remain challenging. In their recent study, Kang et al. [1] present a very promising capturing agent in scenarios of systemic infections that omits the necessity of first identifying the disease-causing factor. The mannose binding lectin (MBL) captures a wide range of pathogens (gram-negative, gram-positive bacteria, and fungi) and allows rapid therapeutic intervention. This is particularly relevant in sepsis patients, where identification of the causing

Table 1 Compound removed from whole blood by magnetic separation-based blood purification

Compound removed from whole blood	Model	Publication
Uranyl ions	In vitro	Wang et al. [3]
Lead ions	In vitro	Lee et al. [4]
		Herrmann et al. [5]
	In vivo (rat)	Herrmann et al. [6]
Cadmium ions	In vitro	Jin et al. [7]
Digoxin	In vitro	Herrmann et al. [5]
		Herrmann et al. [8]
	In vivo (rat)	Herrmann et al. [6]
Diazepam	In vitro	Cai et al. [9]
Interleukin-6 (IL-6)	In vitro	Herrmann et al. [5]
Interleukin-1 β (IL-1 β)	In vitro	Herrmann et al. [8]
Lipopolysaccharide (LPS), <i>Escherichia coli</i>	In vitro	Herrmann et al. [10]
Endotoxins, gram-negative and gram-positive bacteria, fungi	In vitro and in vivo (rat)	Kang et al. [1]

microbe based on blood cultures typically takes 24–48 h (with a high rate of false negatives). As every hour in delayed treatment onset leads to an increased patient mortality of up to 9% [11], broad spectrum antibiotics are generally administered early. However, such overuse of antibiotics leads to antibiotic-resistant strains, increased costs and other important side effects. While magnetic capturing of circulating bacterial pathogens is very promising in the experimental setting [1], the impact on survival in human sepsis where bacterial loads in the blood are variable, and generally much lower than in animal models, remains to be investigated.

When bringing magnetic blood purification processes closer to clinical evaluation, safety of operation becomes pivotal. Extracorporeal blood purification has been suggested previously to provide a possible alternative to direct in vivo application (injection) of magnetic nanoparticles and to prevent off-target accumulation of magnetic capturing agents (e.g. in the liver or lung). Recent studies have shown that the capturing efficiency of magnetic iron oxide nanoparticles is significantly decreased under clinically desirable blood flow rates, thereby potentially compromising the procedure's efficiency and safety [12]. Blood flow partition in front of the magnetic separator has been suggested as a valid method to decrease the perfusion flow in the magnetic separator while keeping the throughput at an acceptably high rate [1, 8]. We recently showed that ferromagnetic iron nanoparticles were retained at high efficiency under high flow rates and that magnetic bead concentration after the separator was below detection limit after a single pass [12]. However, ultra-sensitive particle detection in samples with high matrix complexity (e.g., blood, tissue) are urgently warranted as even state-of-the-art elemental analytical measurements (e.g., Inductively Coupled Plasma

Mass Spectrometry) encounter significant limitations and reach detection limits in the order of $>1 \mu\text{g}$ particles per gram of sample (where 1 g of particles corresponds to $\sim 10^{18}$ single particles). Magnetic measurements for ultrasensitive magnetic nanoparticle detection are now increasingly being explored, which would allow detection of off-target accumulation of nanomaterial and biodegradation of nanomaterials, which in turn could initiate acute and long-term effects such as tumorigenesis, fibrosis and toxic effects.

Other important safety aspects include non-specific adsorption of blood constituents (coagulation and complement factors, cells, etc.) as well as activation of inflammatory reactions in the blood compartment [13]. Such possible side effects have to be evaluated in detail and ruled out before this new operation is translated into a clinical scenario.

Unfortunately, there is an ever growing disequilibrium between manuscripts reporting on the synthesis of new nanomaterials and their promising applications and studies actually performing comprehensive risk evaluation of the synthesized materials [14]. At present, risk analysis using relevant exposure conditions remains to be the bottle neck when translating promising nanomaterial-based approaches. Hence, it is of major importance to establish strategies to gain insight into the potential risks—both short-term and long-term—associated with magnetic blood purification and, to balance risks adequately with therapeutic benefits.

Conclusions

In summary, extracorporeal magnetic separation-based blood purification is a promising strategy to rapidly and selectively remove high molecular weight compounds from blood. The technique has been successfully

evaluated *in vivo* in experimental settings investigating the clinically relevant scenarios of intoxication and sepsis in rat models [1]. However, for translation, ultra-sensitive particle detection systems and risk evaluation strategies are needed in order to better understand relevant exposure scenarios and the therewith associated benefit-risk ratio. Once safety issues have been ruled out, magnetic separation-based blood purification may become an attractive treatment modality enabling rapid removal of poorly accessible high molecular weight disease-causing compounds from blood, potentially bridging the time to run diagnostic tests and establish a suitable therapy.

Abbreviation

MBL: mannose binding lectin.

Authors' contributions

IKH, AAS, RG, WJS and BBS participated in discussions and were involved in the manuscript writing and/or editing. All authors read and approved the final manuscript.

Author details

¹ Institute of Anesthesiology, University Hospital Zurich, Rämistrasse 100, 8091 Zurich, Switzerland. ² Institute of Physiology and Zurich Center for Integrative Human Physiology, University of Zurich, Winterthurerstrasse 190, 8057 Zurich, Switzerland. ³ Department of Surgery, Swiss HPB and Transplant Center, University Hospital Zurich, Rämistrasse 100, 8091 Zurich, Switzerland. ⁴ Institute for Chemical and Bioengineering, ETH Zurich, Vladimir-Prelog-Weg 1-5/10, 8093 Zurich, Switzerland.

Compliance with ethical guidelines

Competing interests

IKH: None. AAS: None. RG: None. WJS: declares ownership of shares of the company Turbobeads GmbH, a manufacturer of magnetic particles. BBS: None.

Received: 9 June 2015 Accepted: 29 July 2015

Published online: 08 August 2015

References

- Kang JH, Super M, Yung CW, Cooper RM, Domansky K, Graveline AR et al (2014) An extracorporeal blood-cleansing device for sepsis therapy. *Nat Med* 20:1211–1216

- Vanholder R, Baurmeister U, Brunet P, Cohen G, Glorieux G, Jankowski J (2008) European Uremic Toxin Work G: a bench to bedside view of uremic toxins. *J Am Soc Nephrol* 19:863–870
- Wang L, Yang Z, Gao J, Xu K, Gu H, Zhang B et al (2006) A biocompatible method of decorporation: bisphosphonate-modified magnetite nanoparticles to remove uranyl ions from blood. *J Am Chem Soc* 128:13358–13359
- Lee HY, Bae DR, Park JC, Song H, Han WS, Jung JH (2009) A selective fluoroionophore based on BODIPY-functionalized magnetic silica nanoparticles: removal of Pb²⁺ from human blood. *Angew Chem Int Ed Engl* 48:1239–1243
- Herrmann I, Urner M, Koehler F, Hasler M, Roth Z'graggen B, Grass RN et al (2010) Blood purification using functionalized core/shell nanomagnets. *Small* 6:1388–1392
- Herrmann IK, Schlegel A, Graf R, Schumacher CM, Senn N, Hasler M et al (2013) Nanomagnet-based removal of lead and digoxin from living rats. *Nanoscale* 5:8718–8723
- Jin J, Yang F, Zhang F, Hu W, Sun SB, Ma J (2012) 2, 2'-(Phenylazanediy) diacetic acid modified Fe₃O₄@PEI for selective removal of cadmium ions from blood. *Nanoscale* 4:733–736
- Herrmann IK, Bernabei RE, Urner M, Grass RN, Beck-Schimmer B, Stark WJ (2011) Device for continuous extracorporeal blood purification using target-specific metal nanomagnets. *Nephrol Dial Transpl* 26:2948–2954
- Cai K, Li J, Luo Z, Hu Y, Hou Y, Ding X (2011) Beta-cyclodextrin conjugated magnetic nanoparticles for diazepam removal from blood. *Chem Commun (Camb)* 47:7719–7721
- Herrmann IK, Urner M, Graf S, Schumacher CM, Roth-Z'graggen B, Hasler M et al (2013) Endotoxin removal by magnetic separation-based blood purification. *Adv Healthc Mater* 2:829–835
- Dellinger RP, Carlet JM, Masur H, Gerlach H, Calandra T, Cohen J et al (2004) Surviving Sepsis Campaign guidelines for management of severe sepsis and septic shock. *Crit Care Med* 32:858–873
- Schumacher CM, Herrmann IK, Bubenhofer SB, Gschwind S, Hirt AM, Beck-Schimmer B et al (2013) Quantitative recovery of magnetic nanoparticles from flowing blood: trace analysis and the role of magnetization. *Adv Funct Mater* 23:4888–4896
- Bircher L, Theusinger OM, Locher S, Eugster P, Roth Z'graggen B, Schumacher CM et al (2014) Characterization of carbon-coated magnetic nanoparticles using clinical blood coagulation assays: effect of PEG-functionalization and comparison to silica nanoparticles. *J Mater Chem B* 2:3753–3758
- Weissleder R, Nahrendorf M, Pittet MJ (2014) Imaging macrophages with nanoparticles. *Nat Mater* 13:125–138

Submit your next manuscript to BioMed Central and take full advantage of:

- Convenient online submission
- Thorough peer review
- No space constraints or color figure charges
- Immediate publication on acceptance
- Inclusion in PubMed, CAS, Scopus and Google Scholar
- Research which is freely available for redistribution

Submit your manuscript at
www.biomedcentral.com/submit




RESEARCH

Open Access



Probabilistic modelling of prospective environmental concentrations of gold nanoparticles from medical applications as a basis for risk assessment

Indrani Mahapatra¹, Tian Yin Sun^{2,3}, Julian R. A. Clark¹, Peter J. Dobson^{4,5}, Konrad Hungerbuehler³, Richard Owen⁶, Bernd Nowack^{2*}  and Jamie Lead^{1,7*}

Abstract

Background: The use of gold nanoparticles (Au-NP) based medical applications is rising due to their unique physical and chemical properties. Diagnostic devices based on Au-NP are already available in the market or are in clinical trials and Au-NP based therapeutics and theranostics (combined diagnostic and treatment modality) are in the research and development phase. Currently, no information on Au-NP consumption, material flows to and concentrations in the environment are available. Therefore, we estimated prospective maximal consumption of Au-NP from medical applications in the UK and US. We then modelled the Au-NP flows post-use and predicted their environmental concentrations. Furthermore, we assessed the environmental risks of Au-NP by comparing the predicted environmental concentrations (PECs) with ecological threshold (PNEC) values.

Results: The mean annual estimated consumption of Au-NP from medical applications is 540 kg for the UK and 2700 kg for the US. Among the modelled concentrations of Au-NP in environmental compartments, the mean annual PEC of Au-NP in sludge for both the UK and US was estimated at 124 and 145 $\mu\text{g kg}^{-1}$, respectively. The mean PEC in surface water was estimated at 468 and 4.7 pg L^{-1} , respectively for the UK and US. The NOEC value for the water compartment ranged from 0.12 up to 26,800 $\mu\text{g L}^{-1}$, with most values in the range of 1000 $\mu\text{g L}^{-1}$.

Conclusion: The results using the current set of data indicate that the environmental risk from Au-NP used in nanomedicine in surface waters and from agricultural use of biosolids is minimal in the near future, especially because we have used a worst-case use assessment. More Au-NP toxicity studies are needed for the soil compartment.

Keywords: Gold nanoparticles, Nanomedicine, Probabilistic modelling, Species sensitivity distribution, PEC, PNEC

Background

There has been an increased focus on developing gold nanoparticles (Au-NP) based applications in fields

ranging from electronics to medicine. Between 2000 and 2013, gold nanotechnology related patents increased exponentially, with about 1600 patents published in 2013 [1]. The number of publications related to Au-NP in the health sector in Thomson Reuters' Web of Science data base also show an exponential increase from 54 to 9083 publications between 2004 and 2014, of which 2150 articles were published in 2014 alone (search conducted on 28 Dec 2014) [2]. The unique chemical and physical properties of Au-NP [3–5] make them excellent candidates for exploitation in the medical field to help in disease diagnosis and treatment. Furthermore, their ease of

*Correspondence: nowack@empa.ch; jlead@mailbox.sc.edu

² Empa–Swiss Federal Laboratories for Materials Science and Technology, Technology and Society Laboratory, Lerchenfeldstrasse 5, 9014 St. Gallen, Switzerland

⁷ Department of Environmental Health Sciences, Center for Environmental Nanoscience and Risk, Arnold School of Public Health, University of South Carolina, Columbia, SC 29208, USA
Full list of author information is available at the end of the article

Indrani Mahapatra and Tian Yin Sun are joint first authors.

synthesis in a variety of sizes and shapes and their amenability towards surface functionalization creates the possibility for multi-functionality including imaging and targeted drug delivery [6–10].

Drug delivery applications based on Au-NP are forecast to have a 21 % share of the USD 136 billion total market of nano-drug delivery applications by 2021 [11]. The enormous range of potential applications of Au-NP and their increased future use could result in greater risk of environmental release and exposure at low concentrations, as is the case with many pharmaceutical products [12–15]. Proliferation and increased application of single use and disposable cheap medical diagnostic devices [16] could add to this environmental burden.

Uptake, biodistribution, accumulation and biomagnification of Au-NP by environmental organisms have been studied by many investigators [17–19], and it has also been shown that Au-NP can be toxic to animals and plants [20–23] thus indicating that these supposedly biocompatible materials could present a significant hazard to plants and wildlife. Au-NP have been shown to have different modes of action for creating toxic effects dependent on their properties and the organism studied [24, 25] and show promise as an antibacterial agent [26].

In terms of environmental risks, studies on potential flows and concentrations of Au-NP in anthropogenic and ecological systems are non-existent. Overall there is limited environmental hazard data and no exposure data, making risk assessment highly problematic. Since there is potential for an exponential increase in use of Au-NP, it is timely to model their environmental flows and concentrations to help frame the risk analysis [27, 28], as has been done also for other nanomaterials [29–32].

In this study we have estimated the environmental concentrations of Au-NP for the United Kingdom (UK) and for the United States of America (US) from selected medical applications that are currently on the market or have potential to be introduced in the near future by developing a conceptual environmental exposure model and by combining this with the hazard data. Since no measured environmental concentration data is available for Au-NP, we have used probabilistic material flow analysis [33] to track the flow and fate of Au-NP during use and disposal as a first step to establish the possible future baseline in a worst case Au-NP release scenario. This approach attempts to address the uncertainty and variability in the data by creating probability distributions for all input data as has been described before [33, 34] Where there is limited toxicity data and where experimental procedures and methodologies have variability, use of probabilistic/stochastic methods to establish and quantify environmental risks can help to increase the robustness of the risk quotients. Thus, probabilistic species sensitivity

distribution (pSSD) for quantifying ecotoxicological risks and comparing the modeled PEC to the predicted no adverse effect concentration (PNEC) based on toxicity data for the corresponding environmental compartment, forms the basis of our approach to derive risk levels for the ecosystem [35].

Results and discussion

Estimation of nano gold consumption from prospective medical applications

Table 1 details the estimated quantity of Au-NP from nano-enabled medical applications. As the table depicts, very small amounts—in the range of milligram to less than a few kilograms—are estimated to originate from in vitro medical devices or devices used for detection of specific disease biomarkers. Larger quantities of Au-NP are estimated to be released from applications used for treating or managing a particular disease, for example, for the treatment of gum infections, cancer and diabetes. The amount of Au-NP per patient was estimated to range from 0.05 mg to 5000 mg for the whole treatment cycle, the higher values corresponding to the treatment modality of photothermal ablation of cancer using gold nanoshells. A study [36] conducted in Northwest England estimated the consumption of anticancer drugs from hospital records and showed total consumption of all the identified anticancer drugs to be around 350 kg. Thus, the annual Au-NP consumption amount in the range <1 kg to 250 kg could be reached in the near future for the UK for treatment of breast, lung, pancreatic and bowel cancer. This is because these diseases have high incidence rates, however, it needs to be kept in mind that we have used high release scenario of 100 % patient access and treatment by the same Au-NP based therapeutic for all patients.

The Au-NP consumption data could be estimated due to the strict regulatory governance framework associated with approval of pharmaceutical products for human use and also because of the availability of disease incidence and prevalence data for widespread diseases, such as cancer, diabetes. In contrast, estimating Au-NP quantities from in vitro diagnostic devices was challenging due to the dependence on the patenting literature, wherein specific details are obscured and also because of the less stringent regulatory pathway for in vitro medical devices. Hence, the estimated data relied on vast number of assumptions and data was extrapolated from various literature sources.

Mass flows of Au-NP

The annual mean prospective Au-NP use estimates for the UK and US are 540 kg and 2700 kg respectively. The yearly disease incidence rates of HIV/AIDS and cancer

Table 1 Prospective amount (per annum) of Gold nanoparticles in selected medical applications (high release scenario)

Application	Consumption		Waste compartment
	UK	US	
Lab based lateral flow assay to detect the presence of Methicillin Resistant and Methicillin Sensitive <i>Staphylococcus aureus</i> in blood	0.34	6	Hazardous Medical/Clinical/ Infectious Waste (HMCIW)
In vitro lab based diagnostic test kit for detection and genotyping warfarin metabolism	0.36	3	HMCIW
In vitro lab based diagnostic test kit for detection of single nucleotide polymorphism to detect risk from venous thrombosis	1	3	HMCIW
OTC pregnancy and ovulation test kits to detect hormones in urine	3–100	20–460	Municipal solid waste
Lab based in vitro rapid test kits for qualitative detection of antibodies to HIV-1 and HIV-2 in human serum, plasma and blood	2–80	20–830	HMCIW
Home based in vitro HIV test kits	20	90	Municipal solid waste
Lab based in vitro tests for detection of CD4 cells and viral loads for HIV patients	60	540	HMCIW
Lab based diagnostic test kits for infectious diseases	70	350	HMCIW
Removal of <i>Staphylococcus aureus</i> from the nasal passage of patients to reduce risks of nosocomial infections	30–53,300	110–164,640	HMCIW
Treatment of periodontitis	270–106,560	940–365,160	Waste water
Sensors for diagnosing diseases from breath samples	0.01–1590	0.03–4620	HMCIW
Treatment for solid tumors (colorectal, pancreas, breast)	70–(480)–1100	310–(2020)–4600	Waste water
Last line treatment for patients with solid tumors (colorectal, pancreatic and breast)	420	1500	Waste water
Treatment for patients diagnosed with head and neck and lung cancer	140,290–233,820	744,750–1,241,260	Waste water
Last line treatment for patients with head and neck and lung cancer	104,710–174,520	468,250–780,410	Waste water
Transbuccal insulin delivery platforms	128,250	841,620	Waste water

The Table presents total gold nanoparticles consumption per annum for the UK and US using a worst case scenario. Data rounded off to 2 significant digits for values below 1 or data rounded off to the nearest integer or ten. Unit: gram. Refer to Additional file 1: Section S2 Estimation of annual Au-NP consumption for details related to assumptions and references

were found to be relatively stable over the last few years [37–41], so the data estimated in this study (which uses incidence and prevalence data compiled in the recent national disease registries and are for the years between 2007 and 2014) can be assumed to remain constant for the next 5 years. By combining the estimated maximal possible consumption of Au-NP with the technical and environmental transfer coefficients, we were able to obtain Au-NP flows from the end user to technical compartments and then further to receiving environmental compartments. Currently this represents an unrealistically high use of Au-NP and therefore our PEC values also represent highest possible concentrations. If Au-NP based applications for the healthcare sector are realised over the coming years, it may result in very high market penetration. For example, seven in vitro diagnostics, based on Au-NP for determining pregnancy and ovulation, were approved by the USFDA between 2009 and 2012. In our current assessment, only two uses dominate

the overall Au-NP flows, a cancer treatment and an insulin delivery platform. The overall flows are therefore to a large extent following the flows of Au-NP used in these two applications, with all other uses having only a minor influence on the mean values but influencing the overall distribution and therefore the extreme values.

Figure 1 shows that the most prominent Au-NP flows arise from consumption, leading to accumulation in the human body for both the UK and US. Based on pre-clinical data, we assumed 35 % [42] and 85 % [43] accumulation of Au-NP in the body for the two cancer therapeutics used as model input data. For other Au-NP based applications we assumed 100 % excretion [44, 45]. Of the total yearly consumption of Au-NP, around 160 and 850 kg of Au-NP respectively for the UK and the US would remain in the body of treated patients.

The second largest flow of Au-NP for both the UK and US is via sewage to sewage treatment plants (STPs). About 230 and 1300 kg of Au-NP from the total

(See figure on next page.)

Fig. 1 Modelled annual prospective mass flows (in kg) of Au-NP in the UK and US. Technical and environmental compartments are expressed as boxes and flows are expressed as arrows. The flow volumes used are mean values from the probability distribution of each flow. Each box (compartment) is given a code. Mean values, mode, quantile 15 (Q_{15}) and Quantile 85 (Q_{85}) values are also given. These are indicated with compartment codes on the right side of the flowchart. The flow volumes are visualised by the thickness of the arrows. The compartments which we assumed to be the final sink are indicated by a *black square box* (body of living patients, crematorium, burial, landfill, soil, sediments and subsurface soils). Complete Au-NP suspension in surface water and complete Au-NP sedimentation from surface water to sediment are assumed in the calculation of mass flow (indicated by *dashed arrow*) and concentrations

consumption for the UK and US, respectively, end up in sewage. In the UK, small amounts of Au-NP are directly transported to surface water due to misconnections and overflows. No data about misconnection for the US could be found, hence we have not modelled this value, but it is a potentially important source of uncertainty. In addition to misconnections, leakages from sewer pipes result in Au-NP mass transfer to subsurface soils. Au-NP reaching the STP might additionally not flow into the STP due to overflow discharges during rainy seasons. Compared to the US, overflows for the UK are more significant; direct discharge to surface waters accounts for nearly one-fifth of the total Au-NP initially reaching STPs; whereas for the US only 0.04 % of the total Au-NP by-passes the STP and reaches the surface waters.

Significant removal of Au-NP into the sludge, for both regions, results in significant quantities of Au-NP entering STPs, ending up in biosolids, which is partially further distributed onto agricultural soils as a fertilizer. Total Au-NP inputs in soil were modeled to be around 150 and 730 kg/year for the UK and US respectively. For the UK, around 32 kg of Au-NP present in the sludge reach the municipal waste incinerators (MWIs) and a negligible quantity pass to the landfill i.e. the majority is applied as sludge to land. For the US, of the 990 kg of Au-NP present in sludge from centralized treatment works, around 280 and 150 kg were estimated to reach the landfill and MWIs compartments respectively. Au-NP from decentralized systems such as septic tanks, cesspools, etc. can be released to land and/or surface water, or underground water, based on the implementation status of relevant regulations. We assumed all Au-NP passing through the decentralized systems end up in sludge treated soils.

The third major flow of Au-NP is to the hazardous waste compartment for both regions. For the UK, 60 % of the 27 kg of hazardous waste was estimated to reach landfill, with the remainder in hazardous medical/clinical/infectious waste (HMCIW) incinerator, whereas for the US, 90 % of the 84 kg of Au-NP in the hazardous waste end up in landfills. These values indicate that clinical waste treatment via incineration is not a prevalent practice for both regions, and hence there is a possibility of Au-NP becoming accumulated in landfills in the future. However, these values need to be treated with

caution because of the scarcity of national scale data with regard to waste management from healthcare facilities. Comprehensive and updated reports for medical waste for the US were not available and we depended on extrapolations from data reported in non-peer reviewed literature sources (details in Additional file 1: Table AFT3.2). For the UK, only one peer reviewed paper [46] containing data for the year 2007 was available. Furthermore, the difference in the healthcare and biological waste (H&B) generation data in the Eurostat database, updated on Dec 6, 2013 [47] and DEFRA [48] report for the years 2004, 2006, 2008 indicate the need for coherent definitions and reporting. H&B generation data in the Eurostat database for the year 2010 was approximately 3 times more than the waste generated in 2008. Since there was no publication from DEFRA for the year 2010, the data reported in the Eurostat database could not be verified/triangulated and the reason for the increase was undecipherable. This indicates the poor state of environmental reporting, monitoring and updating between national scale and regional scale databases and between organizations in the EU.

Au-NP concentrations in technical and environmental compartments

Table 2 shows the predicted Au-NP concentrations in STP effluent, surface water, STP sludge, and yearly concentration in sediments and biosolid treated soils for the UK and US. The values presented are mean values, mode values (the most probable values) and their 15th and 85th percentiles (Q_{15} and Q_{85}) from each distribution. When comparing the two regions, predicted Au-NP concentrations were higher in the UK in nearly all the compartments when compared to those in the US, except for STP sludge which shows similar mean concentrations. The predicted environment concentration (PEC) in surface water in the US is the lowest among all the modeled technical and environmental compartments for UK and US.

In the UK, the predicted Au-NP concentration in surface water is higher than in sewage effluent. This is due to the fact that a significant amount of Au-NP is estimated to be released directly to surface waters via overflows. In contrast, the lower Au-NP concentration in STP effluent and the lower PEC in surface water for the US can be

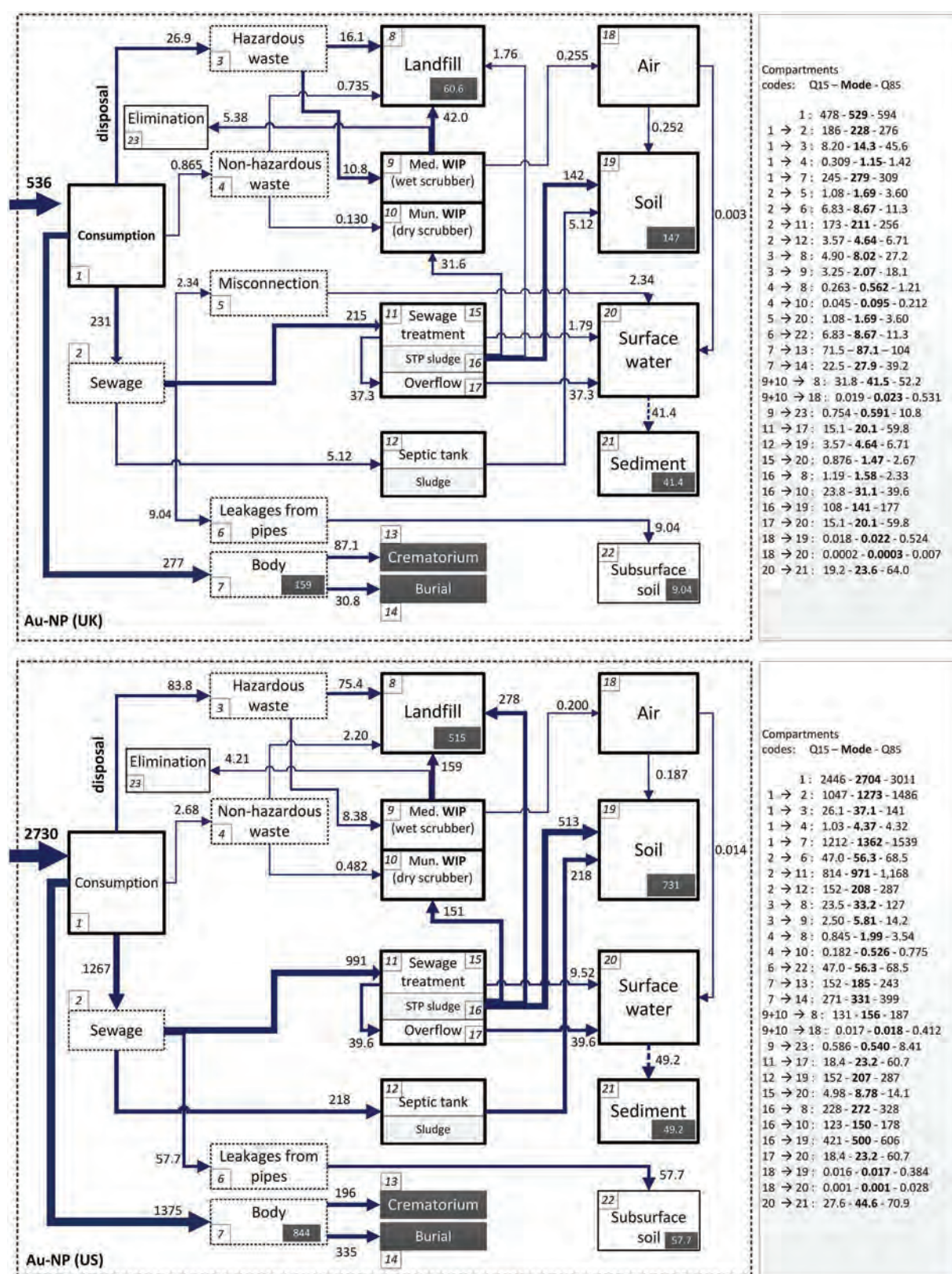


Table 2 Predicted Au-NP concentrations in technical and environmental compartments

	UK				US				Units
	Mean	Mode	Q ₁₅	Q ₈₅	Mean	Mode	Q ₁₅	Q ₈₅	
STP Effluent	440	360	220	670	140	130	71	200	pg/L
Surface water	470	270	210	730	4.7	4.0	2.7	6.8	pg/L
STP sludge	120	130	94	150	150	150	120	170	μg/kg
Sludge treated soil	300	300	230	370	150	150	120	170	ng/kg·years
Sediment	290	170	130	450	5.0	4.5	3.0	8.0	ng/kg·years
Hazardous waste	77	78	23	130	65	69	20	110	μg/kg
Medical WIP									
Fly ash	270	30	36	530	260	32	36	530	μg/kg
Bottom ash	200	25	27	410	200	26	27	400	μg/kg
Municipal WIP									
Fly ash	72	70	53	92	39	38	31	47	μg/kg
Bottom ash	55	52	39	71	30	27	22	37	μg/kg

The mean, mode (most probable values), quantile 15 (Q₁₅) and quantile 85 (Q₈₅) for the predicted concentrations in the technical environmental compartments are provided on the table. Values in italics designate yearly increases in concentrations. Au-NP concentrations in surface water and sediments represent no and complete sedimentation respectively. The results are expressed up to two significant digits

explained by the much larger STP effluent volume produced per capita. According to USEPA, 625 liters of STP effluent is produced per capita per day [49] whereas for the UK, it is 150–180 liters per capita per day [50, 51] (see tables in Additional file 1). The mean modeled Au-NP concentration in surface waters for both regions is in the range of 5–470 pg L⁻¹ which is similar to the background gold concentration reported in freshwaters (reviewed by McHugh [52]). PECs in surface water of Germany for iron oxide nanoparticles based MRI contrast agents were estimated to be 400 and 3140 pg L⁻¹ for the year 2015 for two different scenarios used by author [53]. Measured environmental concentrations in surface waters of various anticancer drugs in use are in the range 500 to 41000 pg L⁻¹ [36], indicating that the results of our model are at a similar level.

Predicted mean concentrations of Au-NP in STP sludge are 124 and 145 μg kg⁻¹ for the UK and US, respectively. The PEC in sludge is considerably less than the measured total gold concentration of 790 μg kg⁻¹ reported in a Swedish study [54]. The second highest concentration of Au-NP is in biosolid treated soils, although yearly concentrations are only in ng kg⁻¹ levels. However, continuous application of biosolids on agricultural land might lead to Au-NP accumulation in soil over years. The lower predicted concentration of Au-NP in US agricultural soils is because of the larger area of the country and hence larger mass of biosolid treated agricultural soils in comparison to the UK.

The Au-NP concentrations for water and sediment concentrations are for worst-case scenarios, i.e., we did

not model any fate in the environment but assumed that for the water compartment no sedimentation and for the sediment compartment complete sedimentation. Only a full environmental fate modelling including a mechanistic modelling of heteroagglomeration, sedimentation and transport will enable to predict the actual concentrations but these models [55–57] will rely heavily on input data to the environmental compartments that are provided by the material flow modelling carried out in this study. The environmental concentrations calculated in this work are valid for a regional assessment and are based on well-mixed compartments and follow as such the ECHA guidance [58]. A next step in the exposure assessment would be to regionalize the emissions which also allow to identify hotspots [59, 60].

Risk assessment with probabilistic species sensitivity distribution (pSSD)

Aquatic species show a wide range of responses to Au-NP, with no observed effect concentrations (NOECs) ranging from 0.12 μg L⁻¹ up to 26,800 μg L⁻¹; a spread of five orders of magnitude, although most values are in the 1000 μg L⁻¹ range. The most sensitive species was the single cell green algae, *Chlamydomonas reinhardtii*, (an acute toxicity study done using 2 nm Au-NP capped with D-manno-pyranoside terminated PAMAM (poly-amidoamine) G0 generation dendrimer) [23]. PAMAM dendrimers of different cores and generations (G2 to G6) have been shown to exert toxic effects in fish, freshwater crustaceans and algae with L(E)C₅₀ values in the range 0.13–194 μM (reviewed in [61]).

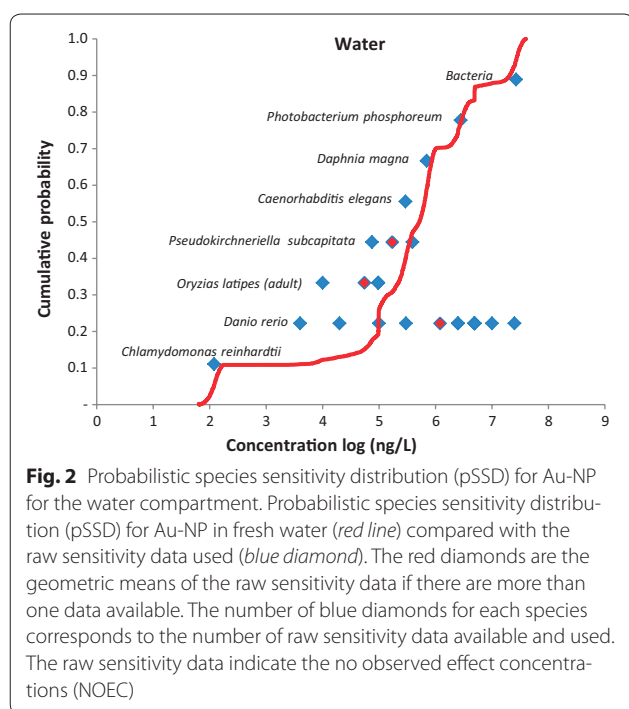


Figure 2 shows the cumulative probabilistic species sensitivity distribution (pSSD) for Au-NP in water. The results lacked sufficient resolution to decipher which taxa are most affected, and what particle properties are related to toxicity, though it seems fish (*Danio rerio*) were the least sensitive species when exposed to Au-NP in an aquatic environment. Publications with properly designed experiments [62, 63] or environmentally relevant exposure concentrations for studying toxic effects of Au-NP on environmental organisms are sparse. Barring a few, the studies selected do not report the $L(E)C_x$ (lethal/toxic effect shown by x % of the organisms at a particular concentration) value, or the statistical method used to arrive at the reported data, do not mention acceptable control performance, and lack characterization of the NPs throughout the exposure duration. These results indicate the high variability of input model data, reflecting the varied toxic potential of Au-NP of different sizes and coating to different species. Therefore, reliable toxicity studies with specific Au-NP used for medical applications are needed for improved environmental risk assessment to influence policy makers for aiding regulatory decision making and responsible innovation [64]. It is also necessary to study the environmental stability and fate of the coatings of the Au-NP once released to wastewater or the environment.

By using probability distributions in place of single values we attempted to address the variability and the uncertainty which is inherent in toxicity studies. The hazard

assessment we performed is for a “generic” Au-NP, considering all different sizes and coatings, representing the full width of currently used Au-NP in toxicity studies. This enables us to compare in a next step this “generic Au-NP SSD” with the modelling of the flows and concentrations which is also for a “generic Au-NP” because data on specific forms of Au-NP is not available.

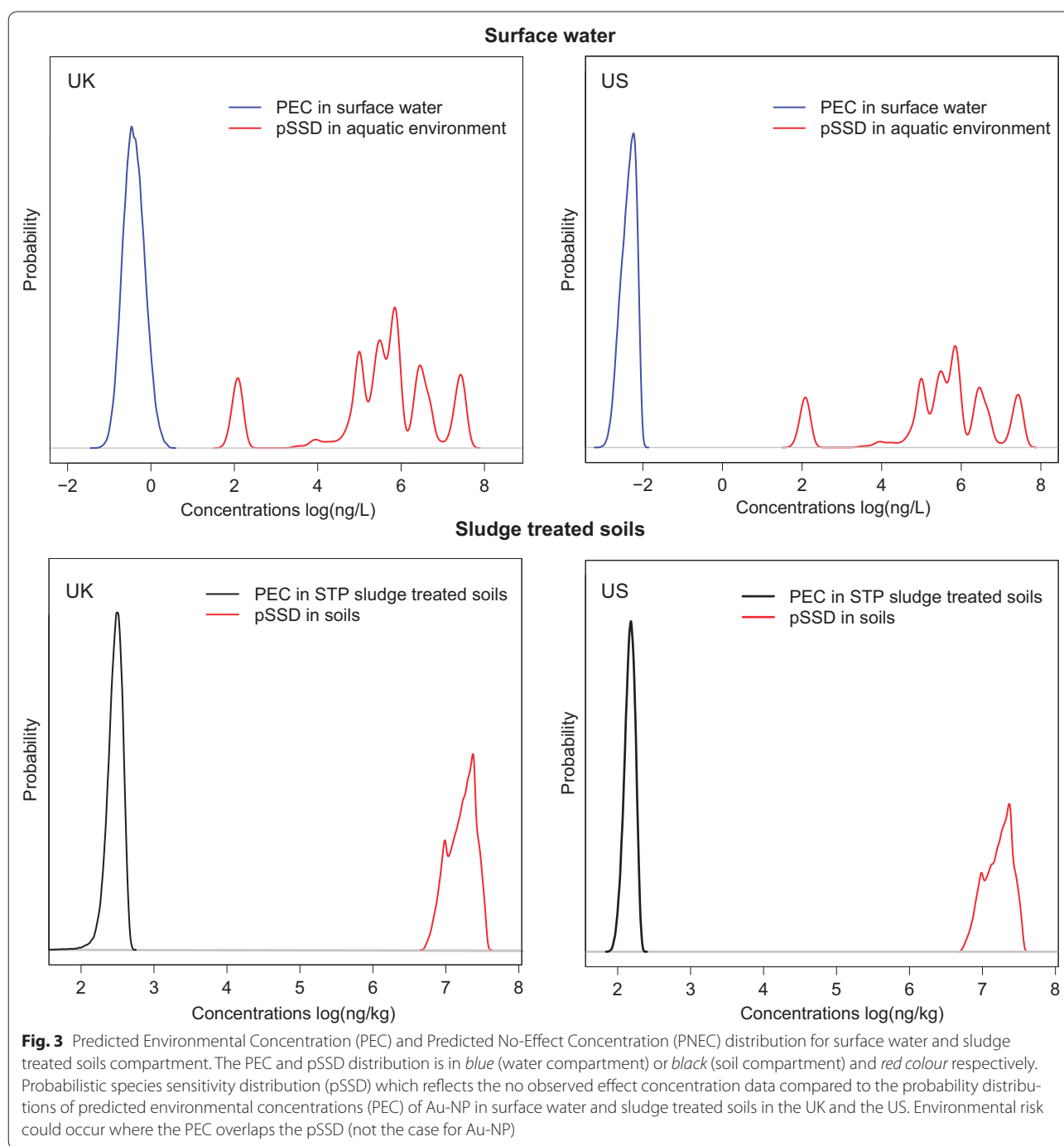
Figure 3 shows the probability distributions of the PECs and the pSSDs for Au-NP in the aquatic and terrestrial environment for both the UK and US. The PEC and pSSD for surface water and soils are compared and risks may arise where the PEC and pSSD overlap. It is clear that there is no overlap between the PEC and pSSD in both environmental compartments considered for the UK and US. The narrowness of the PEC probability density curves is due to the fact that few of the Au-NP application categories dominate the total consumption resulting in a narrow distribution of the total input into the system.

Conclusion

Many human pharmaceuticals occur in the aquatic environment in $ng\ L^{-1}$ concentrations [14, 65, 66] and studies have shown accumulation of these chemicals in aquatic organisms [15, 67, 68] and their adverse effects [13, 69]. The very defining property of nanoparticles—size and surface area—coupled with their ability to interact at subcellular levels to generate subtle biochemical changes [70], their novel properties and gaps in knowledge regarding relationship between chronic and acute toxicity, calls for the inclusion of sub-lethal toxicity endpoints for regulatory decision making. In one scenario we also included selected sub-lethal endpoints in the pSSD (results are provided in the Additional file 1 section S3: Alternate Scenarios) but the risk assessment does not significantly change.

Because nanomaterials have been found to undergo transformation both inside human body as well as the environment [71], their fate can change accordingly in real world situations. However, for Au-NP chemical degradation is rather unlikely due to the inert nature of gold but transformations of surface coatings will strongly affect environmental fate. This will be important when the results from our material flow modelling are used in environmental fate models which include a specific description of fate processes [55–57].

In an ideal situation environmental risk assessment should be based on a full characterization of the material and its transformation products; in the case of nanomaterials such complete risk assessments are not yet available [27]. The complex challenge can currently be addressed in a number of ways, for example by using expert judgment and multi-criteria decision analysis [72, 73] and species sensitivity distributions [74] for different types of



a nanomaterial. The probabilistic risk assessment using both probabilistic species sensitivity distributions and probabilistic mass flow models enables to consider the complete current knowledge in a systematic and comprehensive way and has been applied to other ENM before [75, 76]. Both exposure and hazard data are limited and the model provides a way to deal with this uncertainty.

Extensive literature search combined with communications with experts in the field has helped us to arrive at plausible estimates. The results from the model can be used to provide a baseline for realistic and environmentally relevant exposure/toxicology studies and can help in iterative problem formulation and solution, as more concrete data becomes available. The modelling performed

here suggest that freshwater (and hence sediments) and biosolids treated soils would likely receive highest loads of Au-NP for the UK. Risk from Au-NP to aquatic organisms and soil organisms seems to be unlikely in the near future at a regional scale, although variations will exist temporally and spatially and can also be influenced by the presence of natural Au-NP [77]. The study models for high loading of Au-NP and depends on worst case assumptions with regard to environmental transformation and fate, hence real concentrations in the environment are likely to be much lower. Developing environmental fate models and models addressing temporal and spatial issues can be a possible next step to arrive at more robust estimates of Au-NP concentration in the environment. Hazard assessment data for soil organisms is severely limited and so uncertainty is particularly high indicating that more Au-NP toxicity research is needed for soil organisms. Empirical fate and transformation data of Au-NP for incinerators as well as freshwater systems is non-existent and research is needed for Au-NP transformation in STPs with different treatment processes using Au-NP with surface coatings used in medical applications.

Methodology

General model layout

We have used the geographical regions of the UK and US (excluding dependent areas) as the units of analysis for our study. Similar to the approach proposed by the Guidelines for environmental risk assessment (ERA) of human pharmaceuticals [78, 79], (hereinafter referred to as 'Guidelines') where the consumption data of a drug per year is the key input factor, the model input in this study is based on population based estimates of use and consumption of the selected medical applications in a given year and disregards the manufacturing and processing facilities as a potential source. The model is a step-wise process where the selected application's post usage life cycle has been mapped through the technical compartments of STPs, waste incineration plants (WIPs), landfills and the environmental compartments of soil, water and sediments. In addition to Au-NP based therapeutic agents which are in early stages of clinical trials, we have estimated Au-NP concentrations in medical devices approved by regulatory agencies or in late stages of product development. A deviation from the Guidelines is the use of excretion rates from pre-clinical studies as opposed to assuming 100 % excretion. We have considered possible variable retention of Au-NP in STPs. PECs in various compartments and risk assessment results considering 100 % excretion are provided in the Additional file 1 under section 3: Alternate Scenarios. The

data and values used to arrive at gold amounts per use are based on broad estimates derived from the available literature and the patient population and hence the study is a bottom up, high release scenario study. We have assumed Au-NP to be spherical in shape and have used mass concentrations to estimate consumption amounts.

Transfer coefficients (TC) have been used to model the behaviour of Au-NP in various environmental and technical compartments included within the model (see Fig. 1 for details). The data used in the model have high uncertainty, compounded by large variability and hence we built probability distributions for the majority of input data. Estimated consumption values of products which have the same life-cycle pathway have been summed by adding their individual probability distributions. Additional file 1: Table AFT1 illustrates the probability distributions for all data used in the study.

To estimate the volumes of the environmental compartments, we have used ECHA's guidance on environmental exposure estimation for chemicals for a regional scale model [58]. The mass and volumes along with the assumptions of the transition and final environmental compartments are detailed in Additional file 1: Tables AFT3.1, AFT3.2 and AFT3.3. Seawater is not included in our model. The assumptions of a well-mixed, homogeneous and stationary system have been applied in this study which is a standard approach to arrive at crude estimates of environmental concentrations at a regional level [29]. The model tracks the Au-NP mass and not the total gold mass. Loss of the nano-property (e.g. by vaporization) therefore constitutes an elimination flow.

Methodological approach for input data

An extensive literature search was carried out to identify relevant peer reviewed scientific publications of Au-NP or gold colloids in the medical field, administration doses, distribution, excretion, environmental fate and behaviour and environmental toxicity. Our aim was to identify Au-NP enabled medical applications which are approved, in clinical trials or show promise of translation from pre-clinical models. Reports published by UK and US Government Department and Agencies have been relied upon for estimating population, environment and technical compartment data. The transfer coefficients have been estimated by reviewing literature and/or soliciting expert viewpoints. Triangulations between various publications were performed and the approach of the best available data was adopted to arrive at the estimates used in this study. Details regarding consumption data and assumptions and references therein are included in the Additional file 1 section 2: Estimation of annual Au-NP consumption and Additional file 1: Table AT.T2.

Transfer factors

Therapeutics based on Au-NP, after use, will end up either in solid waste, when the containers with the remnants of the therapeutic and associated procedural implements are disposed of as part of HMCIW and/or in the sewerage system when it is excreted from the body in urine or faeces. In vitro diagnostic devices used in hospitals and other healthcare settings will likely be part of HMCIW. Over-the-counter (OTC) single use medical devices are likely to end up in household waste. Therefore, wastewater (WW)/sewerage, HMCIW and household waste are defined as the key potential sources of entry of Au-NP from medical products to the environment.

Au-NP flow into sewage treatment plants and surface water

Not all houses are served by a centralised STP. The connection rates to STP are 96 % [80] and 74 % [81] for the UK and the US respectively. Untreated sewer overflows, misconnections whereby grey water from households is connected to the storm water drainage systems, and exfiltration from sewerage pipes can result in untreated WW reaching surface waters, groundwater and subsurface soil directly. Au-NP from WW can also enter the environment due to failure of decentralised STPs. Since the connection rate to STPs for the UK is 96 %, we have neglected the contribution of individual septic tanks, cesspools, etc. to the pollution load. However, for the US, nearly 25 % of the total population is served by decentralised systems and the USEPA suggests a failure rate of 6 % annually of these systems [82]. Therefore, for the US we have considered failures of decentralised systems as a source of Au-NP reaching the environment. Additionally, discharge of untreated WW due to the dilapidated state of sewerage infrastructure [83] and polluted outfalls from combined sewers during rains [81] can add to the pollution load of surface waters.

Behaviour of Au-NP in surface water

Data was non-existent with regard to Au-NP fate in surface waters and we have therefore modelled two extreme scenarios to represent worst case conditions for both compartments. We assumed that Au-NP entering the surface freshwater compartment were either 100 % deposited to the sediment to derive sediment concentrations, or remained 100 % in the water phase to derive freshwater concentrations.

Behaviour of Au-NP in Sewage Treatment Plant

Only one published study is available where an estimate of the removal efficiency of Au-NP in STPs has been provided [84]. This study found 99 % removal rate of polymer coated Au-NP of sizes 10 nm and 100 nm in activated sludge batch experiments irrespective of coating, sizes

and treatment. We have therefore used a removal efficiency of 99 % for wastewater treatment. However, we acknowledge that removal efficiencies will differ based on the WW treatment systems used [85, 86].

Au-NP flow into waste compartment

Household waste is non-hazardous in nature and hence in addition to incineration, discarding to landfill is another preferred mode of treatment. OTC disposable in vitro diagnostic devices containing Au-NP will be part of the household and similar waste category as defined in the European Union Waste catalogue [87]. In the UK, the proportion of landfilled and incinerated waste for the category of household and similar waste is 85 and 15 % respectively for the year 2008 [47]. For the US, the proportion of household waste sent to landfill and incinerated is 82 and 18 % respectively of the total waste discarded after the recovered fraction [88].

Wastes from healthcare settings are both hazardous and non-hazardous in type. Hazardous waste from healthcare facilities are generally sent for high temperature treatments like incineration and pyrolysis, or alternatively non-burn low temperature treatments or chemical treatments to disinfect the infectious waste [46]. These alternative treatment technologies use wet or dry steam at temperatures lower than 200 °C and use chemical disinfection methods. We have assumed that Au-NP will not be transformed/destroyed when waste is treated via non-burn alternative treatment technologies and will eventually end up in landfill.

Behaviour of Au-NP during Waste Incineration

No information is available about the fate of Au-NP in incinerators. Depending on the type of waste, type of incinerator and operating temperatures, configuration of the air pollution control devices (APCDs), and the particle size, it is likely that Au-NP will partition into bottom ash, APCD residues and stack emissions from APCDs.

Emissions from incinerators are under strict regulatory control; therefore it has been assumed that all municipal waste and HMCIW incinerators will have associated APCDs. Both the UK and US use dry or semi-dry scrubbing systems with fabric filters or electrostatic precipitators (ESPs) as the main types of APCDs in the municipal waste incinerators [89, 90].

The temperatures in HMCIW incinerators having secondary chambers can reach as high as 1100 °C, which is higher than the melting temperature of bulk gold. Melting temperature depression related to particle size, both for free Au-NP and substrate supported Au-NP, has been proven by many investigators [91–95]. Furthermore, the presence of chlorine generated from Polyvinyl chloride in the incinerator can increase metal volatility and

release into gas phase [96]. The vapour pressure of gold at 1095 °C is about 1×10^{-5} torr (1.33×10^{-3} Pa) [97] and that means typically around one monolayer of gold will be vaporized in 0.1 s. Hence, Au-NP entering the HMCIW incinerators will either melt or vaporize. In both cases the nano-property of the gold is lost and the Au-NP is no longer distinguishable from the other gold forms. We have used both the case of 0 and 100 % elimination of the gold mass. In the case of 0 % elimination, we assume Au-NP to be distributed 81 % in the bottom ash and 19 % in the fly ash using the values found by Walser et al. [98] for removal of Ceria nanoparticles in municipal waste incinerators. Of the 19 % of Au-NP in the fly ash, we assume 50 % of the Au-NP pass through the wet scrubbers and the remaining 50 % through the fabric filter for both the UK and US. This assumption was extrapolated from the type of APCD installed in the HMCIW incinerators in the US [99] since no data was available with regard to APCDs for HMCIW incinerators in the UK.

The operating temperatures in municipal waste incinerators are around 850 °C, so we assume that 81 % of Au-NP mass will be removed in the bottom ash and 19 % in the fly ash [98] of which 99.99 % will be removed by the ESP and fabric filter as APCD residue. These residues are treated as hazardous waste and are finally disposed to secured landfills or abandoned underground mines [100]. Bottom ash from municipal waste combustors can be used in the construction sector [101]. However, due to non-uniformity in available data for the selected regions and to simplify the model, we have neglected bottom ash recycling rate and have presumed that 100 % of the bottom ash from both types of incinerators will be landfilled.

We have not included the leachate from landfill and subsequent contamination of the ground water compartment because studies on the fate of nanoparticles in landfills are not yet available. The technical compartment of cremation has been considered in the model boundary with the assumption that some percentage of Au-NP might remain in the human body post treatment when Au-NP has been administered as a last line treatment. The temperature in crematoria is not high enough to vaporize or melt Au-NP [102] and hence we assume that untransformed Au-NP will form part of the ash.

Therefore, human body, landfills, sediments, subsurface soils and burial grounds have been considered as the final sink of the product life cycle post usage.

Ecological risk assessment

To derive species sensitivity distributions for environmental effects of Au-NP, an extensive search of the ecotoxicological literature was conducted. Fourteen relevant studies were found published between 2008 and Feb

2014. Twenty-six data points across five taxonomically different environmental organisms—bacteria, fish, algae, crustacean and ciliates—were included in the assessment. The endpoints used were mortality and malformations, growth inhibition and reproductive performance. These endpoints were selected to maximize utility of the data points from the available published literature and because these endpoints can impact species survival. We considered all endpoints reported in a study even if they used different particle size and coating with the aim to create a generic Au-NP species sensitivity distribution to compare with the PEC of Au-NP which considers the mass of Au-NP. If in a study only one concentration has been tested on an organism and it had shown no effect for the selected toxicity endpoint, we have used that concentration as no-observed-effect concentration (NOEC), acknowledging that this could in reality be higher. When a range of concentrations were tested [103, 104], the highest concentration at which no statistically significant adverse effect was observed was used as the highest-observed-no-effect-concentration (HONEC). The raw data were converted to species sensitive values below which long-term negative impacts on the species were considered to be excluded using two assessment factors (AF) based on the REACH guidelines [105]. The first AF was used to convert acute toxicity to chronic toxicity (AF time = 1, in the case of chronic and long-term test; AF time = 10, in the case of acute and short-term test). All but two data points represented acute or short-term exposures. The second AF was used to convert the various endpoints to NOEC values (AF no effect = 1 for NOEC, AF no-effect = 2, if $L(E)C_{10} \leq L(E)C_x < L(E)C_{50}$ and AF = 10, if $L(E)_{50} \leq L(E)C_x \leq L(E)C_{100}$). In studies where effect concentrations were reported in terms of molar concentrations, we have converted the values to mass concentration ($\mu\text{g/L}$), because regulatory limits are expressed as such. The studies selected and the associated end points arranged species wise are detailed in Additional file 1: Tables AFT4.1, AFT4.2. Probabilistic species sensitivity distributions were constructed for soil and freshwater as explained in an earlier study [35].

Additional file

[Additional file 1.](#) Supporting Information

Abbreviations

AF: assessment factors; APCDs: air pollution control devices; DEFRA: Department for Environment, Food and Rural Affairs; ECHA: European Chemicals Agency; ERA: environmental risk assessment; ESPs: electrostatic precipitators; EU: European Union; Au-NP: gold nanoparticles; H&B: healthcare and biological; HIV/AIDS: human immunodeficiency virus/acquired immunodeficiency syndrome; HMCIW: hazardous medical/clinical/infectious waste; HONEC: highest-observed-no-effect-concentration; $L(E)C_x$: lethal (adverse effect) concentration, when x % of the test organisms die or are adversely affected; LOEC:

lowest observed effect concentration; MRI: magnetic resonance imaging; MWIs: municipal waste incinerators; NOEC: no-observed-effect concentration; OTC: over-the-counter; PAMAM: polyamidoamine; PEC: predicted environment concentration; PNEC: predicted no-effect concentration; pSSD: probabilistic species sensitivity distribution; REACH: Registration, Evaluation, Authorisation and restriction of Chemicals; SI: supporting information; TC: transfer coefficients; UK: United Kingdom; US: United States of America; USFDA: United States Food and Drug Administration; USEPA: United States Environment Protection Agency; WW: waste water; WIPs: waste incineration plants.

Authors' contributions

IM collected and prepared the input data for the model and drafted the manuscript. TYS wrote the code of the probabilistic model, generated the model output, created the figures and tables for the manuscript, and helped to draft the manuscript. BN supervised and designed the study, gave inputs on the data and helped to draft the manuscript. JRL conceived and supervised the study and helped to draft the manuscript. PJD gave inputs on the data, checked the data and helped to draft the manuscript. JC, KH, RO helped to draft the manuscript. All authors read and approved the final manuscript.

Author details

¹ School of Geography, Earth and Environmental Sciences, University of Birmingham, Edgbaston, Birmingham B15 2TT, UK. ² Empa—Swiss Federal Laboratories for Materials Science and Technology, Technology and Society Laboratory, Lerchenfeldstrasse 5, 9014 St. Gallen, Switzerland. ³ Safety and Environmental Technology Group, Institute for Chemical and Bioengineering, ETH-Hoenggerberg, 8093 Zurich, Switzerland. ⁴ The Queen's College, Oxford OX1 4AW, UK. ⁵ Warwick Manufacturing Group, University of Warwick, Coventry CV4 7AL, UK. ⁶ Business School, University of Exeter, Exeter EX4 4PU, UK. ⁷ Department of Environmental Health Sciences, Center for Environmental Nanoscience and Risk, Arnold School of Public Health, University of South Carolina, Columbia, SC 29208, USA.

Acknowledgements

The authors are grateful for the support of Dr. Claire Packer and Mr. Matthew Fung from the National Institute of Health Research's Horizon Scanning Research & Intelligence Centre, at University of Birmingham, for allowing access to the subscription data base of Citeline and Adis R&D insight. The authors thank the School of Geography, Earth and Environmental Sciences, University of Birmingham which funded the studentship which supported IM. Financial support from the SmartState Center for Environmental Nanoscience and Risk is acknowledged. TYS is supported by the Swiss National Science Foundation within the National Research Programme "Opportunities and Risks of Nanomaterials" (NRP 64).

Competing interests

The authors declare that they have no competing interests.

Received: 1 October 2015 Accepted: 18 November 2015

Published online: 22 December 2015

References

- World Gold Council. Number of published patents including the words 'gold' and 'nanoparticles'. http://www.gold.org/advanced_by_gold/#science#gold-applications-en. Accessed 4 Jan 2015.
- Title search = (health* or medic* or therap* or diseases* or cancer* or HIV or AID*) AND title search = (nano* or ultra small) AND (gold or Au) -Time period: 2004-2014 [database on the Internet]. Accessed: 28 December 2014.
- Eustis S, El-Sayed MA. Why gold nanoparticles are more precious than pretty gold: noble metal surface plasmon resonance and its enhancement of the radiative and nonradiative properties of nanocrystals of different shapes. *Chem Soc Rev*. 2006;35(3):209–17. doi:10.1039/B514191E.
- Masitas RA, Zamborini FP. Oxidation of highly unstable <4 nm diameter gold nanoparticles 850 mV negative of the bulk oxidation potential. *J Am Chem Soc*. 2012;134(11):5014–7. doi:10.1021/ja2108933.
- Trudel S. Unexpected magnetism in gold nanostructures: making gold even more attractive. *Gold Bull*. 2011;44(1):3–13. doi:10.1007/s13404-010-0002-5.
- Lukianova-Hleb EY, Ren X, Sawant RR, Wu X, Torchilin VP, Lapotko DO. On-demand intracellular amplification of chemoradiation with cancer-specific plasmonic nanobubbles. *Nat Med*. 2014;20(7):778–84. doi:10.1038/nm.3484.
- Shilo M, Motiei M, Hana P, Popovtzer R. Transport of nanoparticles through the blood–brain barrier for imaging and therapeutic applications. *Nanoscale*. 2014;6(4):2146–52.
- Setua S, Ouberaï M, Piccirillo SG, Watts C, Welland M. Cisplatin-tethered gold nanospheres for multimodal chemo-radiotherapy of glioblastoma. *Nanoscale*. 2014;6(18):10865–73. doi:10.1039/C4NR03693J.
- Kircher MF, de la Zerda A, Jokerst JV, Zavaleta CL, Kempen PJ, Mittra E et al. A brain tumor molecular imaging strategy using a new triple-modality MRI-photoacoustic-Raman nanoparticle. *Nat Med*. 2012;18(5):829–34. <http://www.nature.com/nm/journal/v18/n5/abs/nm.2721.html#supplementary-information>.
- Arnaiz B, Martinez-Avila O, Falcon-Perez JM, Penades S. Cellular uptake of gold nanoparticles bearing HIV gp120 oligomannosides. *Bioconj Chem*. 2012;23(4):814–25. doi:10.1021/bc200663r.
- Cientifica Ltd. Market opportunities in nanotechnology drug delivery. online. London, UK 2012.
- Ramirez AJ, Brain RA, Usenko S, Mottaleb MA, O'Donnell JG, Stahl LL, et al. Occurrence of pharmaceuticals and personal care products in fish: results of a national pilot study in the United States. *Environ Toxicol Chem*. 2009;28(12):2587–97. doi:10.1897/08-561.1.
- Jobling S, Owen R. Ethinyl oestradiol in the aquatic environment. Copenhagen, Denmark: European Environment Agency 2013. Report No.: No. 1, Vol. 13.
- Roberts PH, Thomas KV. The occurrence of selected pharmaceuticals in wastewater effluent and surface waters of the lower Tyne catchment. *Sci Total Environ*. 2006;356(1–3):143–53. doi:10.1016/j.scitotenv.2005.04.031.
- Miller TH, McEneff GL, Brown RJ, Owen SF, Bury NR, Barron LP. Pharmaceuticals in the freshwater invertebrate, *Gammarus pulex*, determined using pulverised liquid extraction, solid phase extraction and liquid chromatography–tandem mass spectrometry. *Sci Total Environ*. 2015;511:153–60. doi:10.1016/j.scitotenv.2014.12.034.
- Keel T. Gold and diagnostics—some staggering numbers. *Gold Bull*. 2013;46(2):63. doi:10.1007/s13404-013-0097-6.
- Ferry JL, Craig P, Hexel C, Sisco P, Frey R, Pennington PL et al. Transfer of gold nanoparticles from the water column to the estuarine food web. *Nat Nano*. 2009;4(7):441–4. http://www.nature.com/nnano/journal/v4/n7/supinfo/nnano.2009.157_S1.html.
- Judy JD, Unrine JM, Bertsch PM. Evidence for biomagnification of gold nanoparticles within a terrestrial food chain. *Environ Sci Technol*. 2011;45(2):776–81. doi:10.1021/es103031a.
- Sabo-Attwood T, Unrine JM, Stone JW, Murphy CJ, Ghoshroy S, Blom D, et al. Uptake, distribution and toxicity of gold nanoparticles in tobacco (*Nicotiana glauca*) seedlings. *Nanotoxicology*. 2012;6(4):353–60. doi:10.3109/17435390.2011.579631.
- Tsyusko OV, Unrine JM, Spurgeon D, Balock E, Starnes D, Tseng M, et al. Toxicogenomic responses of the model organism *Caenorhabditis elegans* to gold nanoparticles. *Environ Sci Technol*. 2012;46(7):4115–24. doi:10.1021/es2033108.
- Kim KT, Zaikova T, Hutchison JE, Tanguay RL. Gold nanoparticles disrupt zebrafish eye development and pigmentation. *Toxicol Sci Off J Soc Toxicol*. 2013;133(2):275–88. doi:10.1093/toxsci/kft081.
- Geffroy B, Ladhar C, Cambier S, Treguer-Delapierre M, Brethes D, Bourdineau JP. Impact of dietary gold nanoparticles in zebrafish at very low contamination pressure: the role of size, concentration and exposure time. *Nanotoxicology*. 2012;6(2):144–60. doi:10.3109/17435390.2011.562328.
- Perreault F, Bogdan N, Morin M, Claverie J, Popovic R. Interaction of gold nanoglycodendrimers with algal cells (*Chlamydomonas reinhardtii*) and their effect on physiological processes. *Nanotoxicology*. 2012;6(2):109–20. doi:10.3109/17435390.2011.562325.
- Cui Y, Zhao Y, Tian Y, Zhang W, Lu X, Jiang X. The molecular mechanism of action of bactericidal gold nanoparticles on *Escherichia coli*. *Biomaterials*. 2012;33(7):2327–33. doi:10.1016/j.biomaterials.2011.11.057.

25. Coradeghini R, Gioria S, García CP, Nativo P, Franchini F, Gilliland D, et al. Size-dependent toxicity and cell interaction mechanisms of gold nanoparticles on mouse fibroblasts. *Toxicol Lett.* 2013;217(3):205–16. doi:10.1016/j.toxlet.2012.11.022.
26. Zhao Y, Tian Y, Cui Y, Liu W, Ma W, Jiang X. Small molecule-capped gold nanoparticles as potent antibacterial agents that target Gram-negative bacteria. *J Am Chem Soc.* 2010;132(35):12349–56. doi:10.1021/ja1028843.
27. Owen R, Handy RD. Viewpoint: formulating the Problems for Environmental Risk Assessment of Nanomaterials. *Environ Sci Technol.* 2007;41(16):5582–8. doi:10.1021/es072598h.
28. Pastoor TP, Bachman AN, Bell DR, Cohen SM, Dellarco M, Dewhurst IC, et al. A 21st century roadmap for human health risk assessment. *Crit Rev Toxicol.* 2014;44(53):1–5.
29. Gottschalk F, Sonderer T, Scholz RW, Nowack B. Modeled environmental concentrations of engineered nanomaterials (TiO₂, ZnO, Ag, CNT, Fullerenes) for different regions. *Environ Sci Technol.* 2009;43(24):9216–22. doi:10.1021/es9015553.
30. Sun TY, Gottschalk F, Hungerbühler K, Nowack B. Comprehensive probabilistic modelling of environmental emissions of engineered nanomaterials. *Environ Pollut.* 2014;185:69–76. doi:10.1016/j.envpol.2013.10.004.
31. Keller A, McFerran S, Lazareva A, Suh S. Global life cycle releases of engineered nanomaterials. *J Nanopart Res.* 2013;15(6):1–17. doi:10.1007/s11051-013-1692-4.
32. Keller AA, Lazareva A. Predicted releases of engineered nanomaterials: from global to regional to local. *Environ Sci Technol Lett.* 2014;1(1):65–70. doi:10.1021/ez400106t.
33. Gottschalk F, Scholz RW, Nowack B. Probabilistic material flow modeling for assessing the environmental exposure to compounds: methodology and an application to engineered nano-TiO₂ particles. *Environ Model Softw.* 2010;25(3):320–32. doi:10.1016/j.envsoft.2009.08.011.
34. Gottschalk F, Sonderer T, Scholz RW, Nowack B. Possibilities and limitations of modeling environmental exposure to engineered nanomaterials by probabilistic material flow analysis. *Environ Toxicol Chem.* 2010;29(5):1036–48. doi:10.1002/etc.135.
35. Gottschalk F, Nowack B. A probabilistic method for species sensitivity distributions taking into account the inherent uncertainty and variability of effects to estimate environmental risk. *Integr Environ Assess Manag.* 2013;9(1):79–86. doi:10.1002/ieam.1334.
36. Booker V, Halsall C, Llewellyn N, Johnson A, Williams R. Prioritising anticancer drugs for environmental monitoring and risk assessment purposes. *Sci Total Environ.* 2014;473–474:159–70. doi:10.1016/j.scitotenv.2013.11.145.
37. Prejean J, Song R, Hernandez A, Ziebell R, Green T, Walker F, et al. Estimated HIV incidence in the United States, 2006–2009. *PLoS One.* 2011;6(8):e17502.
38. Cancer Research UK. Cancer incidence for all cancers combined. <http://www.cancerresearchuk.org/cancer-info/cancerstats/incidence/all-cancers-combined/#Trends>. Accessed 5 Jan 2015.
39. Yin Z, Brown AE, Hughes G, Nardone A, Gill ON, VC D et al. HIV in the United Kingdom: 2014 Report: data to end 2013. London: Public Health England. 2014.
40. Siegel R, Ma J, Zou Z, Jemal A. Cancer statistics, 2014. *CA Cancer J Clin.* 2014;64(1):9–29.
41. CDC. Estimates of New HIV Infections in the United States, 2006–2009. Atlanta, US: Centres for Disease Control and Prevention. 2011.
42. Goel R, Shah N, Visaria R, Paciotti GF, Bischof JC. Biodistribution of TNF- α -coated gold nanoparticles in an in vivo model system. *Nanomedicine (Lond).* 2009;4(4):401–10. doi:10.2217/nnm.09.21.
43. Gad SC, Sharp KL, Montgomery C, Payne JD, Goodrich GP. Evaluation of the toxicity of intravenous delivery of auroshell particles (gold-silica nanoshells). *Int J Toxicol.* 2012;31(6):584–94. doi:10.1177/1091581812465969.
44. Zhang X-D, Wu D, Shen X, Liu P-X, Fan F-Y, Fan S-J. In vivo renal clearance, biodistribution, toxicity of gold nanoclusters. *Biomaterials.* 2012;33(18):4628–38. doi:10.1016/j.biomaterials.2012.03.020.
45. Longmire M, Choyce PL, Kobayashi H. Clearance properties of nano-sized particles and molecules as imaging agents: considerations and caveats. *Nanomedicine.* 2008;3(5):703–17. doi:10.2217/17435889.3.5.703.
46. Tudor TL, Townend WK, Cheeseman CR, Edgar JE. An overview of arisings and large-scale treatment technologies for healthcare waste in the United Kingdom. *Waste Manage Res.* 2009;27(4):374–83. doi:10.1177/0734242X09336244.
47. Waste Generation and Management [database on the Internet]. European Commission. 2013. Available from: http://epp.eurostat.ec.europa.eu/portal/page/portal/waste/waste_generation_management. Accessed: 5 Nov 2013.
48. DEFRA. Environment Statistics—Key facts. online. London: Department for Environment, Food and Rural Affairs 2013 January 2013. Report No.: PB 13671.
49. USEPA. Progress in Water Quality: An Evaluation of the National Investment in Municipal Wastewater Treatment. online. Washington DC: United States Environmental Protection Agency 2000. Report No.: EPA-832-R-00-008.
50. British Water. Code of Practice—Flows and Loads 4—Sizing criteria, Treatment Capacity for Sewage Treatment Systems. online. London: British Water 2013. Report No.: BW COP: 18.11/13.
51. British Water. Codes of Practice—Flows and Loads 3—Sizing criteria, Treatment Capacity for Small Wastewater Treatment Systems. online 2009. Report No.: BW COP: 7.1/09.
52. McHugh JB. Concentration of gold in natural waters. *J Geochem Explor.* 1988;30(1–3):10.
53. Filser J, Arndt D, Baumann J, Geppert M, Hackmann S, Luther EM, et al. Intrinsically green iron oxide nanoparticles? From synthesis via (eco-) toxicology to scenario modelling. *Nanoscale.* 2013;5(3):1034–46. doi:10.1039/c2nr31652h.
54. Eriksson J. Concentrations of 61 trace elements in sewage sludge, farmyard manure, mineral fertiliser, precipitation and in oil and crops. Stockholm, Sweden: Swedish Environmental Protection Agency 2001. Report No.: 5159.
55. Liu HH, Cohen Y. Multimedia environmental distribution of engineered nanomaterials. *Environ Sci Technol.* 2014;48(6):3281–92. doi:10.1021/es405132z.
56. Praetorius A, Scheringer M, Hungerbühler K. Development of environmental fate models for engineered nanoparticles—A case study of TiO₂ nanoparticles in the Rhine river. *Environ Sci Technol.* 2012;46(12):6705–13. doi:10.1021/es204530n.
57. Meesters JAJ, Koelmans AA, Quik JTK, Hendriks AJ, van de Meent D. Multimedia modeling of engineered nanoparticles with Simple-Box4nano: model definition and evaluation. *Environ Sci Technol.* 2014;48(10):5726–36. doi:10.1021/es500548h.
58. ECHA. Guidance on information requirements and chemical safety assessment: Chapter R.16 Environmental exposure estimation. Helsinki, Finland: European Chemicals Agency, 2012.
59. Dumont E, Johnson AC, Keller VDJ, Williams RJ. Nano silver and nano zinc-oxide in surface waters—Exposure estimation for Europe at high spatial and temporal resolution. *Environ Pollut.* 2015;196:341–9. doi:10.1016/j.envpol.2014.10.022.
60. Gottschalk F, Ort C, Scholz RW, Nowack B. Engineered nanomaterials in rivers—exposure scenarios for Switzerland at high spatial and temporal resolution. *Environ Pollut.* 2011;159(12):3439–45.
61. Suarez IJ, Rosal R, Rodriguez A, Ucles A, Fernandez-Alba AR, Hernandez MD, et al. Chemical and ecotoxicological assessment of poly(amidoamine) dendrimers in the aquatic environment. *TrAC Trends Anal Chem.* 2011;30(3):492–506. doi:10.1016/j.trac.2010.11.009.
62. ICMM. MERAG: Fact Sheet 03 Effects Assessment: Data Compilation, Selection and Derivation of PNEC Values for the Risk Assessment of Different Environmental Compartments (Water, STP, Soil, Sediment). London: International Council on Mining and Metals, 2007.
63. Wheeler JR, Grist EPM, Leung KMY, Morritt D, Crane M. Species sensitivity distributions: data and model choice. *Mar Pollut Bull.* 2002;45(1–12):192–202. doi:10.1016/S0025-326X(01)00327-7.
64. Stilgoe J, Owen R, Macnaghten P. Developing a framework for responsible innovation. *Res Policy.* 2013;42(9):1568–80.
65. Ashton D, Hilton M, Thomas KV. Investigating the environmental transport of human pharmaceuticals to streams in the United Kingdom. *Sci Total Environ.* 2004;333(1–3):167–84. doi:10.1016/j.scitotenv.2004.04.062.

66. Thomas KV, Hilton MJ. The occurrence of selected human pharmaceutical compounds in UK estuaries. *Mar Pollut Bull.* 2004;49(5–6):436–44. doi:10.1016/j.marpolbul.2004.02.028.
67. Liu J, Lu G, Zhang Z, Bao Y, Liu F, Wu D, et al. Biological effects and bioaccumulation of pharmaceutically active compounds in crucian carp caged near the outfall of a sewage treatment plant. *Environ Sci Process Impacts.* 2015;17(1):54–61. doi:10.1039/C4EM00472H.
68. Liu J, Lu G, Xie Z, Zhang Z, Li S, Yan Z. Occurrence, bioaccumulation and risk assessment of lipophilic pharmaceutically active compounds in the downstream rivers of sewage treatment plants. *Sci Total Environ.* 2015;511:54–62. doi:10.1016/j.scitotenv.2014.12.033.
69. Sanchez W, Sremski W, Piccini B, Palluel O, Maillot-Maréchal E, Betoulle S, et al. Adverse effects in wild fish living downstream from pharmaceutical manufacture discharges. *Environ Int.* 2011;37(8):1342–8. doi:10.1016/j.envint.2011.06.002.
70. Shvedova AA, Kagan VE, Fadeel B. Close encounters of the small kind: adverse effects of man-made materials interfacing with the nano-cosmos of biological systems. *Annu Rev Pharmacol Toxicol.* 2010;50(1):63–88. doi:10.1146/annurev.pharmtox.010909.105819.
71. Lowry GV, Gregory KB, Apte SC, Lead JR. Transformations of nanomaterials in the environment. *Environ Sci Technol.* 2012;46(13):6893–9. doi:10.1021/es300839e.
72. Linkov I, Satterstrom FK, Steevens J, Ferguson E, Pleus RC. Multi-criteria decision analysis and environmental risk assessment for nanomaterials. *J Nanopart Res.* 2007;9(4):543–54. doi:10.1007/s11051-007-9211-0.
73. Owen R, Crane M, Grieger K, Handy R, Linkov I, Depledge M. Strategic approaches for the management of environmental risk uncertainties posed by nanomaterials. In: Linkov I, Steevens J (eds) *Nanomaterials: Risks and Benefits*. NATO Science for Peace and Security Series C: Environmental Security: Springer Netherlands; 2009. p 369–84.
74. Garner KL, Suh S, Lenihan HS, Keller AA. Species sensitivity distributions for engineered nanomaterials. *Environ Sci Technol.* 2015; doi:10.1021/acs.est.5b00081.
75. Coll C, Notter D, Gottschalk F, Sun TY, Som C, Nowack B. Probabilistic environmental risk assessment of five nanomaterials (nano-TiO₂, nano-Ag, nano-ZnO, CNT, Fullerenes). *Nanotoxicology.* 2015 (in press).
76. Gottschalk F, Kost E, Nowack B. Engineered nanomaterials in water and soils: a risk quantification based on probabilistic exposure and effect modeling. *Environ Toxicol Chem.* 2013;32(6):1278–87. doi:10.1002/etc.2177.
77. Hough R, Noble R, Hitchen G, Hart R, Reddy S, Saunders M, et al. Naturally occurring gold nanoparticles and nanoplates. *Geology.* 2008;36(7):571–4.
78. US FDA. Guidance for Industry: Environmental Assessment of Human Drug and Biologics Applications. In: Center for Drug Evaluation and Research (CDER) and Center for Biologics Evaluation and Research (CBER), editor. 1998.
79. EMA. Guideline on the Environmental Risk Assessment of Medical Products for Human Use. London: European Medicines Agency, USE CFMPFH;2006. Report No.: EMEA/CHMP/SWP/4447/00 corr 1*.
80. DEFRA. Waste water treatment in the United Kingdom—2012. online. London: Department for Environment, Food and Rural Affairs, Department for Environment FaRA; 2012. Report No.: PB13811.
81. USEPA. Clean Watersheds Needs Survey 2008: Report to Congress. online. Washington: United States Environmental Protection Agency, Municipal Support Division SMB; 2008. Report No.: EPA-832-R-10-002.
82. US EPA. Report to Congress on the Impacts and Control of CSOs and SSOs. online. Washington D.C.: United States Environmental Protection Agency 2004. Report No.: EPA 833-R-04-001.
83. ASCE. 2013 Report Card for America's Infrastructure. online: American Society of Civil Engineers. 2013.
84. Kaegi R, Voegelin A, Ort C, Sinnet B, Thalmann B, Krismer J, et al. Fate and transformation of silver nanoparticles in urban wastewater systems. *Water Res.* 2013;47(12):3866–77. doi:10.1016/j.watres.2012.11.060.
85. Jarvie HP, Al-Obaidi H, King SM, Bowes MJ, Lawrence MJ, Drake AF, et al. Fate of silica nanoparticles in simulated primary wastewater treatment. *Environ Sci Technol.* 2009;43(22):8622–8. doi:10.1021/es901399q.
86. Johnson AC, Jürgens MD, Lawlor AJ, Cisowska I, Williams RJ. Particulate and colloidal silver in sewage effluent and sludge discharged from British wastewater treatment plants. *Chemosphere.* 2014;112:49–55. doi:10.1016/j.chemosphere.2014.03.039.
87. Eurostat. Guidance on classification of waste according to EWC-Stat categories: Supplement to the Manual for the Implementation of the Regulation (EC) No 2150/2002 on Waste Statistics. online: Commission of The European Communities: EUROSTAT. 2010.
88. USEPA. Municipal Solid Waste Generation, Recycling, and Disposal in the United States, Facts and Figures for 2011. online. Washington DC: United States Environmental Protection Agency 2013. Report No.: EPA530-F-13-001.
89. USEPA. United States Response UNEP Questionnaire for Paragraph 29 study Enclosure 4a April 2010. Revised May 2010. 2010. http://www.unep.org/chemicalsandwaste/Portals/9/Mercury/Documents/para29submissions/USA-Waste%20Incineration_revised%206-1-10.pdf. Accessed 19 Mar 2014.
90. DEFRA. Incineration of Municipal Solid waste. London: Department for Environment, Food and Rural Affairs. 2013. Report No.: PB13889.
91. Buffat P, Borel JP. Size effect on the melting temperature of gold particles. *Phys Rev A.* 1976;13(6):2287–98. doi:10.1103/PhysRevA.13.2287.
92. Lee J, Lee J, Tanaka T, Mori H. In situ atomic-scale observation of melting point suppression in nanometer-sized gold particles. *Nanotechnology.* 2009;20(47):475706. doi:10.1088/0957-4484/20/47/475706.
93. Dick K, Dhanasekaran T, Zhang Z, Meisel D. Size-dependent melting of silica-encapsulated gold nanoparticles. *J Am Chem Soc.* 2002;124(10):2312–7. doi:10.1021/ja017281a.
94. Nanda KK, Maisels A, Kruis FE, Rellinghaus B. Anomalous thermal behavior of gold nanostructures. *Europhys Lett (EPL).* 2007;80(5):56003. doi:10.1209/0295-5075/80/56003.
95. Luo W, Su K, Li K, Liao G, Hu N, Jia M. Substrate effect on the melting temperature of gold nanoparticles. *J Chem Phys.* 2012; doi:10.1063/1.4729910.
96. Kakumazaki J, Kato T, Sugawara K. Recovery of gold from incinerated sewage sludge ash by chlorination. *ACS Sustain Chem Eng.* 2014;2(10):2297–300. doi:10.1021/sc5002484.
97. Honig RE, Kramer DA. Vapor pressure data for the solid and liquid elements. RCA Laboratories, David Sarnoff Research Center; 1969.
98. Walser T, Limbach LK, Brogioli R, Erisman E, Flamigni L, Hattendorf B et al. Persistence of engineered nanoparticles in a municipal solid-waste incineration plant. *Nat Nano.* 2012;7(8):520–4. doi:<http://www.nature.com/nnano/journal/vaop/ncurrent/abs/nnano.2012.64.html#supplementary-information>.
99. RTI International. Memorandum: Inventory of Hospital/Medical/Infectious Waste Incinerators Potentially Covered by the Proposed Section 111(d)/129 Federal Plan 2012. Report No.: EPA Contract No. EP-D-07-019.
100. AmuthaRani D, Boccaccini AR, Deegan D, Cheeseman CR. Air pollution control residues from waste incineration: current UK situation and assessment of alternative technologies. *Waste Manag.* 2008;28(11):2279–92. doi:10.1016/j.wasman.2007.10.007.
101. Ørnebjerger H, Franck J, Lamers F, Angotti F, Morin R, Brunner M, et al. Management of bottom ash from WTE plants: an overview of management options and treatment methods. Copenhagen, Denmark: International Solid Waste Association; 2006.
102. Mari M, Domingo JL. Toxic emissions from crematories: a review. *Environ Int.* 2010;36(1):131–7. doi:10.1016/j.envint.2009.09.006.
103. Asharani PV, Iianwu Y, Gong Z, Valiyaveetil S. Comparison of the toxicity of silver, gold and platinum nanoparticles in developing zebrafish embryos. *Nanotoxicology.* 2011;5(1):43–54. doi:10.3109/17435390.2010.489207.
104. Bar-Ilan O, Albrecht RM, Fako VE, Furgeson DY. Toxicity Assessments of Multisized Gold and Silver Nanoparticles in Zebrafish Embryos. *Small.* 2009;5(16):1897–910. doi:10.1002/smll.200801716.
105. ECHA. Guidance on information requirements and chemical safety assessment: Chapter R.10: Characterisation of dose [concentration]-response for environment: European Chemicals Agency. 2008.

RESEARCH

Open Access



Effect of nanoparticles on red clover and its symbiotic microorganisms

Janine Moll^{1,2}, Alexander Gogos¹, Thomas D. Bucheli¹, Franco Widmer¹ and Marcel G. A. van der Heijden^{1,2,3*}

Abstract

Background: Nanoparticles are produced and used worldwide and are released to the environment, e.g., into soil systems. Titanium dioxide (TiO₂) nanoparticles (NPs), carbon nanotubes (CNTs) and cerium dioxide (CeO₂) NPs are among the ten most produced NPs and it is therefore important to test, whether these NPs affect plants and symbiotic microorganisms that help plants to acquire nutrients. In this part of a joint companion study, we spiked an agricultural soil with TiO₂ NPs, multi walled CNTs (MWCNTs), and CeO₂ NPs and we examined effects of these NP on red clover, biological nitrogen fixation by rhizobia and on root colonization of arbuscular mycorrhizal fungi (AMF). We also tested whether effects depended on the concentrations of the applied NPs.

Results: Plant biomass and AMF root colonization were not negatively affected by NP exposure. The number of flowers was statistically lower in pots treated with 3 mg kg⁻¹ MWCNT, and nitrogen fixation slightly increased at 3000 mg kg⁻¹ MWCNT.

Conclusions: This study revealed that red clover was more sensitive to MWCNTs than TiO₂ and CeO₂ NPs. Further studies are necessary for finding general patterns and investigating mechanisms behind the effects of NPs on plants and plant symbionts.

Keywords: Nanomaterials, Agriculture, Crop, Beneficial soil microbes, Ecosystem services

Background

Titanium dioxide (TiO₂) nanoparticles (NPs), carbon nanotubes (CNTs) and cerium dioxide (CeO₂) NPs are among the ten most produced NPs worldwide [1]. The production and use of these NPs leads to increasing concentrations in the soil system. Estimated material-flow in sludge treated soils for Europe are 2380 t y⁻¹ and 0.771 t y⁻¹ for TiO₂ and CNTs, respectively [2]. For CeO₂ 1400 t y⁻¹ are assumed to end up in sludge treated soils worldwide [1]. Thus, all of these three NP types are unintentionally released into the soil ecosystem. One NP type that needs special attention regarding risk assessment in soils is TiO₂ because these NPs are listed in patents and publications targeted as additives of plant protection products [3, 4]. Thus, if such products were released to the market and applied in the fields, higher concentrations of

TiO₂ NPs would be expected in soils. Due to the potential for increasing amounts of NPs that enter the soil system, it is important to test, whether these NPs affect plants and beneficial soil microorganisms that associate with plant roots and assist plants to acquire nutrients.

Several studies investigated effects of TiO₂ NPs, CNTs and CeO₂ NPs on either plants or microorganisms with variable results. For TiO₂ NPs, contrasting results were found and plant biomass was either decreased or not affected when grown in soil with enhanced TiO₂ NP concentrations [5–7]. Soil microbial community structures were shown to be altered when treated with TiO₂ NPs [7–9]. Also CNTs affected plants and soil microbial community structures: the number of flowers and fruits of tomatoes increased, and bacterial community structure changed [10]. In contrast, in another study with much higher CNT concentrations, soil microbial community structure was not affected [11]. Most often, ecotoxicological tests with NPs (TiO₂, CeO₂ and CNTs) in soil systems are either performed with plants, or with

*Correspondence: marcel.vanderheijden@agroscope.admin.ch

¹ Agroscope, Institute for Sustainability Sciences ISS, 8046 Zurich, Switzerland

Full list of author information is available at the end of the article

microorganisms, but the symbiosis of plants and soil microorganisms has rarely been investigated. Plant symbionts provide important ecosystem functions as e.g., nitrogen-fixation by rhizobia in legumes or phosphorus acquisition by arbuscular mycorrhizal fungi (AMF) [12]. One example is red clover which is used for animal feeding and as green manure. Red clover associates with nitrogen-fixing rhizobia bacteria (rhizobia) [13, 14]. Up to $373 \text{ kg N ha}^{-1} \text{ y}^{-1}$ can be fixed by these bacteria in root nodules of red clover plants [15]. Additionally, red clover performs a second symbiosis with AMF [12, 16–18]. These fungi provide plants with soil nutrients, especially immobile nutrients such as phosphorus. Up to 90 % of plant phosphorus is provided by AMF [18]. The two microbial symbionts, AMF and rhizobia, conduct important ecosystem functions [12], and thus it is important to assess whether nitrogen fixation and root colonization by AMF are affected by NPs.

Earlier studies showed that NPs had adverse effect on the legume-rhizobia symbiosis. For soybeans it has been reported that CeO_2 NPs diminished nitrogen fixation [19], and no effects of TiO_2 and Fe_3O_4 NPs on nodule colonization were found [20]. For barrel clover it has been reported that the number of nodules was decreased and gene expression altered when exposed to biosolids containing Ag, ZnO and TiO_2 NPs [21, 22]. Peas revealed a delayed nitrogen fixation when exposed to TiO_2 and ZnO in hydroponic systems [23, 24], and for faba beans, nodulation and nitrogenase activity were delayed by Ag NPs [25]. AMF root colonization has been reported to not being affected in soybeans exposed to TiO_2 and Fe_3O_4 NPs [20], while colonization of white clover roots was increased by Ag and FeO NPs [26]. Because of these effects on legume-rhizobia and AMF systems, it is important to assess whether root colonization by AMF and nitrogen fixation in soil-grown red clover are affected by NPs, e.g. TiO_2 , CeO_2 and CNTs, because these effects might be species and NP dependent. To our best knowledge, there are no studies available on the effects of CNTs on legume-rhizobia-AMF systems.

In the present study, we investigated the effects of three different NP types, i.e., TiO_2 NPs, multi-walled CNTs (MWCNTs) and CeO_2 NPs, on red clover growth, biological nitrogen fixation with rhizobia and on root colonization of AMF in a soil system. We investigated if these NPs affect (1) plant growth, (2) biological nitrogen fixation in plants, (3) AMF root colonization, and (4) phosphorus uptake by red clover. As positive control we chose $\text{ZnSO}_4 \cdot 7\text{H}_2\text{O}$ because Zn^{2+} was reported to decrease plant growth and affect nitrogen fixation of legumes [27]. Effective soil elemental titanium and MWCNT (black carbon) concentrations, their vertical translocation and plant uptake were investigated in detail in a companion paper [28].

Results

Red clover plants were exposed for 14 weeks to agricultural soil spiked with different concentrations of NPs, i.e., TiO_2 NPs (P25), a bigger non-nanomaterial [29] TiO_2 particle (NNM- TiO_2 , 20 % particles $<100 \text{ nm}$), MWCNTs, CeO_2 NPs and a ZnSO_4 treatment. The biomass of red clover plants did not differ between NP spiked substrate and controls without NP addition, both for root and shoot dry weight separately and for total plant dry weight (Fig. 1; Additional file 1: Table S1). Total plant dry weight and effective titanium content per pot were correlated explaining 20 % of variance (Pearson's correlation: $p = 0.041$, $r = 0.45$). The root-shoot ratio was 0.49 ± 0.04 on average, and was also not affected by the presence of NPs ($p > 0.05$). The number of flowers decreased in the 3 mg MWCNT kg^{-1} soil treatment by 34 % ($p = 0.049$, Fig. 1; Additional file 1: Table S1). The higher concentration of 3000 mg MWCNT kg^{-1} exhibited a similar decrease in mean number of flowers (33 %), but the variation was higher and therefore the number of flowers was not significantly different from the control plants ($p = 0.160$).

In addition to plant performance, the interaction of red clover with rhizobia was investigated. All harvested red clover plants contained root nodules and the root nodules had a reddish color which indicates that they fixed nitrogen [14]. In addition, the percentage of fixed nitrogen was assessed based on the ^{15}N concentrations of clover and a reference plant (rye grass; see formula 1 in the “Methods” section). The percentages of fixed nitrogen of control red clover plants and NP treated plants were compared, and confirmed that biological nitrogen fixation took place (Fig. 2). All of the treated red clover plants fixed nitrogen and NP application did not affect nitrogen fixation levels in most of the treatments. Only in the 3000 mg MWCNT kg^{-1} treatment, biological nitrogen fixation was increased by 8 % ($p = 0.016$). Pearson's correlation revealed a correlation of nitrogen fixation and total biomass of $r = 0.28$ ($p = 0.012$).

The second symbiotic partner of red clover, AMF, was assessed by determining root colonization by staining fungal tissue and counting fungal structures by microscopy [30, 31]. In addition the phosphorus content of red clover shoots was assessed, as AMF can contribute significantly to plant P nutrition. Total root colonization by AMF, i.e., % arbuscules, vesicles and hyphae per investigated root intersection, was similar in all treatments (on average $51 \pm 4 \%$; Additional file 1: Figure S1). Also the arbuscular and vesicular colonization revealed no differences between the control and NP treatments (average 23 ± 3 and $6 \pm 2 \%$, respectively;

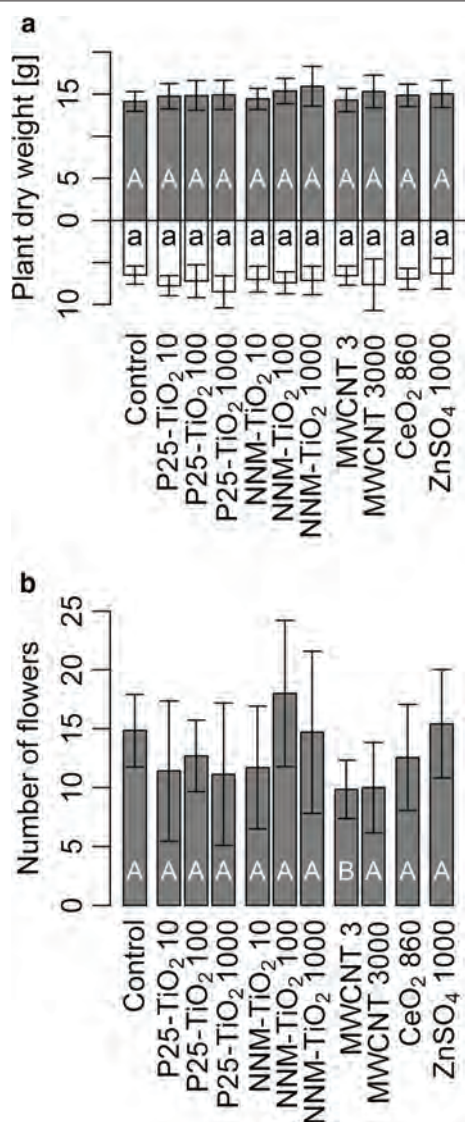


Fig. 1 Plant weight and flowers. **a** Red clover plant dry weight divided in shoot (grey) and root (white), and **b** number of flowers per pot at the end of the 3 month exposure for control, TiO₂ (P25, non-nanomaterial NNM), MWCNT, CeO₂ NPs, and ZnSO₄·7H₂O. The number behind the treatment name is the nominal concentration in mg kg⁻¹. Error bars show the standard deviations (n = 7). Capital letters show significant differences for shoot biomass and number of flowers, and small letters for root biomass compared to the control plants (p ≤ 0.05). The two blocks of starting time were included in the statistical model

Table 1). Phosphorus concentrations of the red clover shoots were not affected in any of the treatments (Additional file 1: Figure S1b, Table S1). Plant phosphorus content and total root colonization by AMF were not correlated (Pearson correlation coefficient: $p = 0.199$; $r = 0.15$).

Discussion

In the present study effects of different NPs, i.e., TiO₂ NPs, MWCNTs and CeO₂ NPs, on red clover and its symbiosis with rhizobia and AMF were assessed in a soil system. Both tested TiO₂ treatments (i.e. P25 and NNM-TiO₂) in all concentrations did not affect plant biomass in our experiment. The absence of effects of TiO₂ NPs on plant biomass are in agreement with other studies, using different plant species. For example plant growth was not affected when soybeans and corn were exposed to 200 mg TiO₂ NP kg⁻¹ [7] and when tomatoes were exposed to concentrations between 1000 and 5000 mg P25 TiO₂ NP kg⁻¹ [6]. However, in wheat 90 mg TiO₂ NPs kg⁻¹ was shown to decrease plant biomass by 13 % [5]. MWCNTs did not affect red clover biomass in our experiment. Contrary to our findings, MWCNTs have been reported to increase biomass of tomatoes exposed to 50 and 200 µg ml⁻¹ MWCNTs per plant [10]. In our experiment red clover biomass did not respond to the CeO₂ NP treatment, which is in agreement to a study using CeO₂ NPs at concentrations between 0.1 and 1 g kg⁻¹ in an experiment with soybeans [19]. Thus, effects on plant biomass might be influenced by plant species (as shown for the TiO₂ NPs and MWCNTs) as well as by NP type. All of the above cited studies used different soils. Depending on soil properties, NPs might be differently bound to soil particles [32] which could influence the exposure and the effects of NPs on plants.

The number of flower heads was not affected in both TiO₂ and CeO₂ NP treatments at all tested concentrations. However, MWCNTs decreased number of flowers by 34 % ($p = 0.049$) at the lower concentration (3 mg kg⁻¹). The higher MWCNT concentration showed a similar decrease of flower number (33 %), but the variance between the samples was higher and there was no statistically significant difference ($p = 0.16$). Our results indicate that the number of flowers is sensitive to MWCNTs. Khodakovskaya et al. showed that the number of flower increased significantly, when watered weekly with 50 ml of 50 and 200 µg ml⁻¹ MWCNTs per pot for 9 weeks [10]. The direction of the effect was in contrast to our observations. Nevertheless, the number of flowers was affected and further research is needed to determine the mechanism responsible for the effects of MWCNT on flowering.

To test effects of NPs on biological nitrogen fixation, the natural abundance of ¹⁵N was determined in the red clover shoots and in a reference plant (rye grass) and subsequently the fraction of biological fixed nitrogen in red clover was assessed (see “Methods” section). No nitrogen was added to the pots because increasing the availability of mineral nitrogen has been reported to decline nitrogen fixation rate progressively [33]. The percentage of fixed

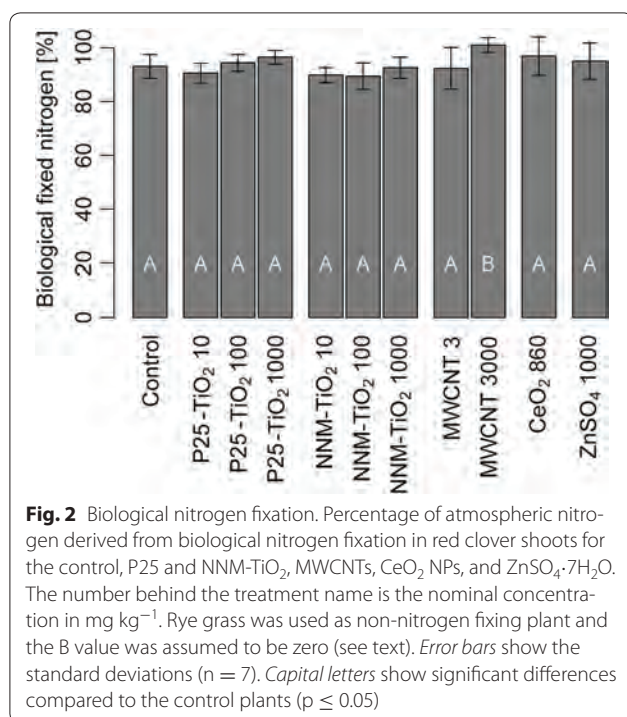


Table 1 Mean values and standard deviation of the arbuscular and vesicular root colonization

	Arbuscular coloni- zation (%)		Vesicular colo- nization (%)	
	Mean	SD	Mean	SD
Control	23	8	4	2
P25-TiO ₂ 10 mg kg ⁻¹	22	7	3	3
P25-TiO ₂ 100 mg kg ⁻¹	22	8	6	9
P25-TiO ₂ 1000 mg kg ⁻¹	21	10	8	7
NNM-TiO ₂ 10 mg kg ⁻¹	19	10	7	5
NNM-TiO ₂ 100 mg kg ⁻¹	24	11	6	3
NNM-TiO ₂ 1000 mg kg ⁻¹	25	11	7	8
CNT 3 mg kg ⁻¹	20	9	2	2
CNT 3000 mg kg ⁻¹	29	7	5	5
CeO ₂ 860 mg kg ⁻¹	24	9	8	5
ZnSO ₄ ·7H ₂ O 1000 mg kg ⁻¹	27	8	6	4

nitrogen was high and ranged between 89 and 100 % and was not affected by the TiO₂ NPs in our experiment. These results contrast those of another study performed in a hydroponic system using pea and rhizobia [23]. This study showed that nodulation was negatively affected and that the nitrogen fixation was delayed when TiO₂ NPs were present. However, it needs to be tested whether the results from hydroponic systems can be directly extrapolated to soil systems. In soils, TiO₂ NPs interact with

soil particles and are probably heteroaggregated with soil particles such as clay minerals [32]. Thus, the plant roots in soils might be less exposed to the NPs than in hydroponic systems and therefore roots and nodules might be less affected in soils, as indicated by the limited transport of TiO₂ NPs in soils in our experiment [28]. For the higher concentration of MWCNTs (3000 mg kg⁻¹), nitrogen fixation increased by 8 % (p = 0.01) compared to the control and 100 % of the nitrogen content in the shoots originated from nitrogen fixation. Even though the biomass and total nitrogen content of these MWCNT treated plants were not different from those in the control treatment, correlation between biologically fixed nitrogen and total biomass over all treatments was significant but only 8 % of the variation could be explained (R² = 0.08; p = 0.012). This indicates that enhanced nitrogen fixation had only a small beneficial effect on plant growth. In our experiment, nitrogen fixation was not affected by CeO₂ NPs. For soybeans however, the CeO₂ NPs have been reported to decrease nitrogen fixation potential up to 80 % [19]. This reference investigated a different plant species and effects of NPs might be plant and rhizobia species specific [19]. Also the use of different soils with different soil characteristics might influence the results. Further experiments are needed to consolidate our understanding of the mechanisms of how NPs affect nitrogen fixation.

Total arbuscular, as well as vesicular root colonization of red clover by AMF were not affected in any of the treatments. In support of this finding, but again with another plant species, Burke et al. [20] reported no effects of TiO₂ NPs on AMF root colonization in soybeans using a DNA based approach instead of counting the root colonization. AMF provide plants with nutrient, such as phosphorus [17, 34]. Therefore we assessed phosphorus content in red clover shoots at the harvest. Phosphorus content of red clover shoots was not affected in any of the treatments and there was no correlation between plant phosphorus content and total AMF root colonization (p = 0.2). Again, for TiO₂ NPs this is in agreement with Burke et al. who did not find differences in phosphorus content of soybean leaves [20]. Even though root colonization was not affected by the tested NPs in our experiments, community structure of AMFs in soils might change as shown in Burke et al. [7].

Contrary to our expectations, the ZnSO₄ control did not affect any of the measured endpoints. It is known that Zn²⁺ availability is limited at high soil pH conditions [35]. Soil pH was 7.7 [28] and the concentration added was probably not high enough to release enough free Zn²⁺ to cause harmful effects.

The amount of NPs applied to the soil was high and partly outside the exposure range expected in the field.

They were chosen to represent a potential agricultural application scenario, where fluxes between several micrograms to grams of NPs per kilogram of soil are estimated [3]. The highest concentration also simulates accidental spill during transport or pollution in industrial areas or in the field. In our experiment also lower concentrations, i.e. 10 and 100 mg kg⁻¹ soil, were tested. This approach ensures that potential negative effects can be detected before a NP is widely used and applied. This approach also facilitates the detection of potential harmful NPs in comparison to non-toxic or less harmful NP. Moreover, in order to be able to detect and measure concentrations of some NPs in the environment (e.g. titanium oxides for this study), high amounts have to be added because element like titanium occur naturally in the soil and the concentrations added need to be higher as natural background levels. For instance, for TiO₂ NPs the lowest concentration of 10 mg kg⁻¹ is realistic in comparison with estimations for soils treated with NP containing plant protection products, while the highest tested concentration (1000 mg kg⁻¹) rather represents a worst case scenario [3]. For MWCNTs, yearly increases of estimated environmental concentrations are estimated to range from 5 to 990 ng kg y⁻¹ [2]. Hence, both tested concentrations in our experiment are above natural values and represent an upper limit. The addition of these high concentrations was necessary to distinguish the added MWCNTs from the black carbon background of the soil [28, 36]. New methods are currently being developed to distinguish NPs from natural backgrounds as reviewed by others [37, 38]. Further research is needed to measure and characterize NPs in soils at predicted environmental concentrations, both for fate and behavior studies, and to accompany environmentally relevant ecotoxicological tests.

Conclusions

The investigated TiO₂ NPs and CeO₂ NPs did not affect red clover growth, biological nitrogen fixation and AMF root colonization. Opposite to other studies with TiO₂ and CeO₂ that observed effects on N fixing legumes, no effects were observed here with red clover. Further research is needed to search for general patterns and investigate the mechanisms behind such effects. MWCNTs increased nitrogen fixation and decreased the number of flowers compared to the control treatment, which might affect fitness of red clover. However, these effects occurred at concentrations much higher than expected in the environment.

Methods

NPs used for the experiment

P25 (Sigma Aldrich, USA, art. No. 718467) with a particle size of 29 ± 9 nm [28] was used as representative for TiO₂

NPs. In addition, NNM-TiO₂ (Sigma Aldrich, USA, Art. No. 232033) with an average particle size of 145 ± 46 nm [28] was used as non-nano-material, i.e. less than 50 % NPs [29]. MWCNTs were purchased from Cheap Tubes Inc. (USA). They had a length of 10–30 µm, outer diameter of 20–30 nm, a purity of >95 % and an elemental carbon content of >98 % (Additional file 1: Table S2) [28]. CeO₂ NPs (Sigma Aldrich, USA, art. No. 700290) had a diameter of less than 50 nm with cubic crystal structure according to the manufacturer's specifications.

Mixing NPs into the soil

For preparing the substrate, soil classified as brown earth with a sandy loamy to loamy fine fraction was collected from an agricultural field at Agroscope Institute for Sustainability Sciences in Zurich, Switzerland (coordinates N47° 25' 39.564" E8° 31' 20.04"). For this, the top 5 cm were removed and the underlying 15 cm soil were collected and sieved (<0.5 cm). The soil was mixed with quartz sand (50 % v/v) and then characterized as described by Gogos et al. (Additional file 1: Table S3) [28]. Nutrient contents in the mixture were 37.6 mg kg⁻¹ phosphorus and 85.3 mg kg⁻¹ potassium determined by ammonium acetate EDTA extraction [39]. Soil pH was 7.7. Each of the different NPs was premixed in 300 g substrate (soil and sand) on an overhead mixer (Turbula T2F, Switzerland) in 500 ml Schott bottles by adding 0.3, 3 and 30 g of P25 or NNM-TiO₂, 90 mg and 88 g MWCNTs, 25 g CeO₂ NPs and 30 g ZnSO₄·7H₂O (Sigma Aldrich, USA, art. No. Z0251), respectively. P25 (30 g) and MWCNTs (88 g) revealed a too large volume for the 500 ml Schott bottles, necessitating the division of the soil and additives into several bottles (300 g of substrate for each bottle). For P25 15 g were added to two Schott bottles, and for MWCNTs 22 g were added to four bottles. Each of these pre-mixtures was diluted with substrate to a total volume of 30 kg and mixed in a cement mixer for 6 h.

Experimental setup

Pots were prepared by gluing PVC-sewer pipes (15 cm diameter, 20 cm long) on a plastic board with a ball valve as draining device (Fig. 3). A plastic mesh (Propyltex 500 µm, Sefar, Switzerland) was placed on the top of the valve to prevent blockage of the valve by the substrate. Pots were filled with a 500 g quartz sand layer as drainage and 3.3 kg spiked substrate or control substrate. Seven replications per treatment were prepared, i.e., control, P25, NNM-TiO₂, MWCNT, CeO₂ NPs, and ZnSO₄·7H₂O. Total elemental titanium, black carbon (BC, for MWCNT treatments) and elemental cerium concentrations were determined in the substrate as described in the accompanying study [28]. Average total elemental titanium concentration of the

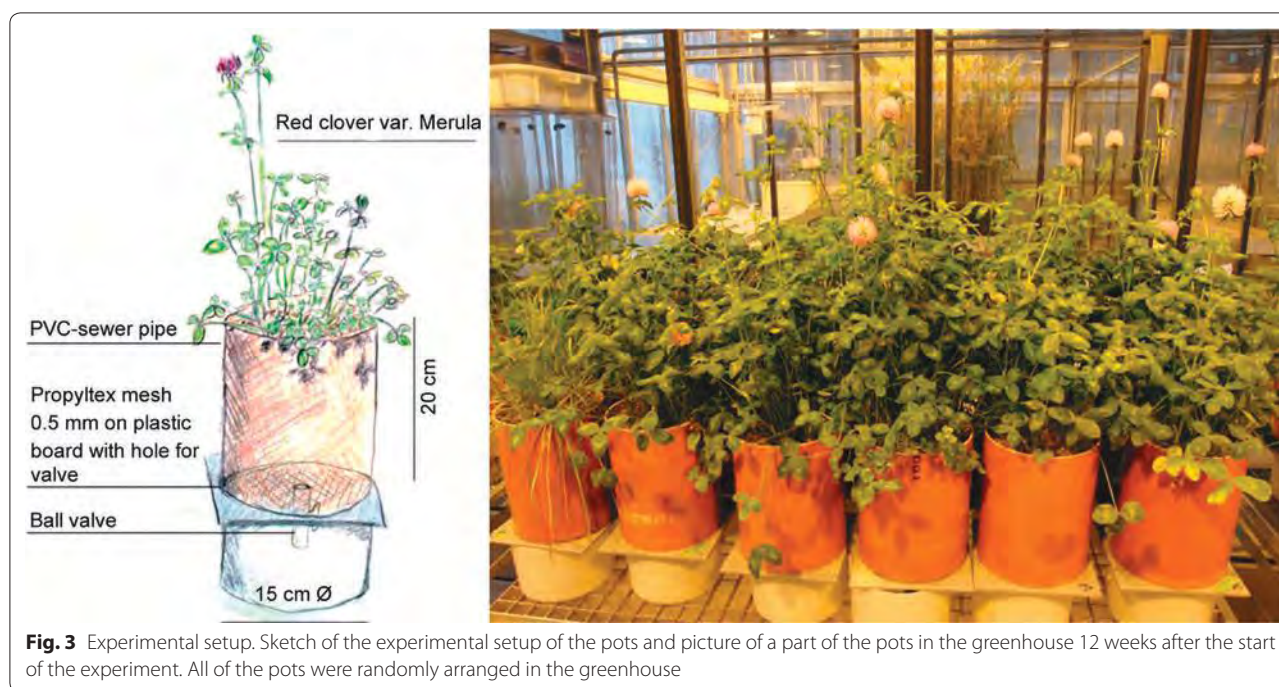


Fig. 3 Experimental setup. Sketch of the experimental setup of the pots and picture of a part of the pots in the greenhouse 12 weeks after the start of the experiment. All of the pots were randomly arranged in the greenhouse

highest tested concentrations was determined at the end of the experiment using X-ray fluorescence (XRF) and was 1332 ± 100 for the control treatment without titanium, 2059 ± 105 for 1000 mg kg^{-1} (nominal) P25 and $2007 \pm 79 \text{ mg kg}^{-1}$ for the NNM-TiO₂ treated soils, respectively [28]. For MWCNT the background of BC in control soils was on average $0.50 \pm 0.06 \text{ mg g}^{-1}$ and BC concentration in MWCNT 3000 mg kg^{-1} treated soil was $2400 \pm 100 \text{ mg kg}^{-1}$ as quantified by chemothermal oxidation [28]. Average elemental cerium concentration in the 830 mg kg^{-1} CeO₂ treatment was $416 \pm 19 \text{ mg kg}^{-1}$ determined with XRF at the end of the experiment.

Cultivation of red clover in NP spiked substrate

Red clover (*Trifolium pratense* var. Merula) was germinated on filter paper for 5 days. Thereafter, seven seedlings of equal size were transferred to the pots with substrate spiked with NPs or control soils in a greenhouse ($16 \text{ h } 25^\circ \text{C } 300 \text{ W m}^{-2}$, and $8 \text{ h } 16^\circ \text{C}$ in the dark). In addition seven pots with ryegrass (*Lolium perenne* var. Arolus) were prepared in the same way. These plants were grown because a non-nitrogen-fixing plant was needed to estimate biological fixed nitrogen in red clover (see below). The experiment was started in two blocks ($n = 4$ and 3 , respectively), time-shifted with 1 week difference. All pots were regularly watered to keep the water holding capacity between 60 and 70 % (controlled by weighing and adding every time the same amount of water to all of the pots). Clover was fertilized after 6 and 9 weeks with 10 ml of

KH₂PO₄ (5 mM), MgSO₄·7H₂O (1 mM), KCl (50 μM), H₃BO₃ (25 μM), MnSO₄·H₂O (1.3 μM), ZnSO₄·7H₂O (2 μM), CuSO₄·5H₂O (0.5 μM), (NH₄)₆Mo₇O₂₇·4H₂O (0.5 μM), and Fe(III) EDTA (20 μM). This is comparable to a phosphorus addition of 1.7 kg P ha^{-1} .

After 14 weeks NP exposure of red clover, the number of flowers (flower heads) was determined and the plant shoots were harvested. Soil cores were taken to assess NP concentration as described in Gogos et al. [28]. Roots were separated from the soil and washed. Then the roots were cut in 1 cm pieces, mixed in water and a randomized root subsample of approximately 2 g was taken for determining the AMF colonization. Roots were padded with a paper towel and weighed. The subsample was weighed separately and then stored at 4°C in 50 % ethanol in Falcon tubes until the colonization was determined. The remaining roots as well as the red clover and ryegrass shoots were dried at 70°C until they reached constant dry weight and dry weight of roots, shoots and total biomass (root + shoot weight) were determined. The dry weight of the AMF colonization root sample was calculated using the dry/wet weight ratio of the root sample. This AMF sample dry weight was added to the total root dry weight. Shoots of red clover and ryegrass were ground with a centrifugation mill (0.2 mm sieve, Retsch ZM200, Germany) and 2 mg samples were sent for ¹⁵N analysis by isotope ratio mass spectrometry at the stable isotope facility at Saskatchewan University (Canada). Root colonization of AMF was analyzed by microscopy

following the protocols of Vierheilig et al. [31] for staining the roots and McGonigle et al. [30] for counting the AMF structures. In short, roots were rinsed with deionized water, and transferred to 10 ml 10 % KOH for 20 min at 80 °C. Roots were rinsed again with water and stained in 5 % (v/v) ink (Parker Quink, black) in vinegar for 15 min at 80 °C. After rinsing the stained roots, they were transferred to 50 % glycerol for storage until root colonization was assessed. For microscopy, the root pieces were aligned in parallel onto a glass slide, covered with 50 % glycerol, and the roots were covered with a cover slip [30]. AMF structures in plant roots, i.e., hyphae, arbuscules, and vesicles, were counted for 100 intersections as described by McGonigle et al. [30]. Phosphorus content of shoots was assessed by ICP-OES using a hydrochloric acid digestion of the ashed residues [40].

Nitrogen fixation [%] was calculated using Eq. 1 where B is the value of $\delta^{15}\text{N}$ of shoots of plants, that are fully dependent upon nitrogen fixation [33]. For our experiment, a B value of 0 was assumed which reflects $\delta^{15}\text{N}$ of plants that are totally dependent on nitrogen fixation. The reference plant $\delta^{15}\text{N}$ was derived from the ryegrass shoots.

$$\% \text{ Nitrogen fixation} = \frac{\delta^{15}\text{N of reference plant} - \delta^{15}\text{N of N}_2 \text{ fixing plant}}{\delta^{15}\text{N of reference plant} - B} \times \frac{100}{1} \quad (1)$$

Statistics

All statistical analyses were performed with R [41]. A generalized linear model with Gaussian distribution was applied to determine differences of each treatment to the control. Thereby the two blocks of the different starting dates of the pot experiment were included as error term. The model was analyzed for homogeneity (Bartlett test) and normality (Shapiro test). Additionally a Dunnett test was performed (R library SimComp) using adjusted p-values for multiple testing [42] when normality and homogeneity were fulfilled. For non-normal residuals or inhomogeneous data, a Mann–Whitney test was used and p-values were adjusted for multiple testing according to Benjamini and Hochberg [43]. Pearson's correlations were calculated with the R command cor.test.

Additional file

Additional file 1. Supplementary information on arbuscular mycorrhizal fungal root colonization, multi walled carbon nanotubes (MWCNT) characterization, and soil properties.

Abbreviations

AMF: arbuscular mycorrhizal fungi; CeO_2 : cerium dioxide; CNT: carbon nanotubes; MWCNT: multiwalled carbon nanotubes; ^{15}N : nitrogen isotope; NNM- TiO_2 : non-nanomaterial titanium dioxide; NP: nanoparticle; TiO_2 : titanium dioxide.

Authors' contributions

JM carried out the study, analyzed data and wrote the manuscript. AG performed the physical–chemical NP analyses and revised the manuscript. MGAvdH, TDB, and FW participated in the design of the study and revised the manuscript. All authors read and approved the final manuscript.

Author details

¹ Agroscope, Institute for Sustainability Sciences ISS, 8046 Zurich, Switzerland. ² Plant-Microbe-Interactions, Department of Biology, Utrecht University, 3508 TB Utrecht, The Netherlands. ³ Institute of Evolutionary Biology and Environmental Studies, University of Zurich, Winterthurerstrasse 190, 8057 Zurich, Switzerland.

Acknowledgements

We thank Florian Klingenfuss for providing assistance for harvesting the experiment.

Competing interests

The authors declare that they have no competing interests.

Funding

This work is part of the project "Effects of NANOparticles on beneficial soil Microbes and CROPS (NANOMICROPS)", within the Swiss National Research Programme NRP 64 "Opportunities and Risks of Nanomaterials". We thank the Swiss National Science Foundation (SNF) for financial support.

Received: 21 January 2016 Accepted: 22 April 2016

Published online: 10 May 2016

References

- Keller A, McFerran S, Lazareva A, Suh S. Global life cycle releases of engineered nanomaterials. *J Nanopart Res*. 2013;15:1–17.
- Sun TY, Gottschalk F, Hungerbühler K, Nowack B. Comprehensive probabilistic modelling of environmental emissions of engineered nanomaterials. *Environ Pollut*. 2014;185:69–76.
- Gogos A, Knauer K, Bucheli TD. Nanomaterials in plant protection and fertilization: current state, foreseen applications, and research priorities. *J Agric Food Chem*. 2012;60:9781–92.
- Khot LR, Sankaran S, Maja JM, Ehsani R, Schuster EW. Applications of nanomaterials in agricultural production and crop protection: a review. *Crop Prot*. 2012;35:64–70.
- Du WC, Sun YY, Ji R, Zhu JG, Wu JC, Guo HY. TiO_2 and ZnO nanoparticles negatively affect wheat growth and soil enzyme activities in agricultural soil. *J Environ Monit*. 2011;13:822–8.
- Song U, Jun H, Waldman B, Roh J, Kim Y, Yi J, Lee EJ. Functional analyses of nanoparticle toxicity: a comparative study of the effects of TiO_2 and Ag on tomatoes (*Lycopersicon esculentum*). *Ecotoxicol Environ Saf*. 2013;93:60–7.
- Burke DJ, Zhu S, Pablico-Lansigan MP, Hewins CR, Samia ACS. Titanium oxide nanoparticle effects on composition of soil microbial communities and plant performance. *Biol Fertility Soils*. 2014;50:1169–73.
- Ge Y, Schimel JP, Holden PA. Identification of soil bacteria susceptible to TiO_2 and ZnO nanoparticles. *Appl Environ Microbiol*. 2012;78:6749–58.
- Ge YG, Schimel JP, Holden PA. Evidence for negative effects of TiO_2 and ZnO nanoparticles on soil bacterial communities. *Environ Sci Technol*. 2011;45:1659–64.
- Khodakovskaya MV, Kim B-S, Kim JN, Alimohammadi M, Dervishi E, Mustafa T, Cernigla CE. Carbon nanotubes as plant growth regulators: effects on tomato growth, reproductive system, and soil microbial community. *Small*. 2013;9:115–23.
- Shrestha B, Acosta-Martinez V, Cox SB, Green MJ, Li S, Cañas-Carrell JE. An evaluation of the impact of multiwalled carbon nanotubes on soil microbial community structure and functioning. *J Hazard Mater*. 2013;261:188–97.
- van der Heijden MGA, Bruin Sd, Luckerhoff L, van Logtestijn RSP, Schlaeppli K. A widespread plant-fungal-bacterial symbiosis promotes plant biodiversity, plant nutrition and seedling recruitment. *ISME J*. 2016;10(2):389–99.

13. Heidstra R, Bisseling T. Nod factor-induced host responses and mechanisms of Nod factor perception. *New Phytol.* 1996;133:25–43.
14. Somasegaran P, Hoben HJ. *Handbook for Rhizobia*. New York: Springer-Verlag; 1994.
15. Carlsson G, Huss-Danell K. Nitrogen fixation in perennial forage legumes in the field. *Plant Soil.* 2003;253:353–72.
16. Smith FA, Smith SE. What is the significance of the arbuscular mycorrhizal colonisation of many economically important crop plants? *Plant Soil.* 2011;348:63–79.
17. Smith SE, Read D. 5-Mineral nutrition, toxic element accumulation and water relations of arbuscular mycorrhizal plants. In: Read SES, editor. *Mycorrhizal symbiosis*. 3rd ed. London: Academic Press; 2008. p. 145–8.
18. van der Heijden MGA, Martin FM, Selosse M-A, Sanders IR. Mycorrhizal ecology and evolution: the past, the present, and the future. *New Phytol.* 2015;205:1406–23.
19. Priester JH, Ge Y, Mielke RE, Horst AM, Moritz SC, Espinosa K, Gelb J, Walker SL, Nisbet RM, An Y-J, et al. Soybean susceptibility to manufactured nanomaterials with evidence for food quality and soil fertility interruption. *Proc Natl Acad Sci USA.* 2012;109:E2451–6.
20. Burke DJ, Pietrasiak N, Situ SF, Abenojar EC, Porche M, Kraj P, Lakliang Y, Samia ACS. Iron oxide and titanium dioxide nanoparticle effects on plant performance and root associated microbes. *Int J Mol Sci.* 2015;16:23630–50.
21. Chen C, Unrine JM, Judy JD, Lewis RW, Guo J, McNear DH Jr, Tsyusko OV. Toxicogenomic responses of the model legume *Medicago truncatula* to aged biosolids containing a mixture of nanomaterials (TiO₂, Ag, and ZnO) from a pilot wastewater treatment plant. *Environ Sci Technol.* 2015;49:8759–68.
22. Judy JD, McNear DH, Chen C, Lewis RW, Tsyusko OV, Bertsch PM, Rao W, Stegemeier J, Lowry GV, McGrath SP, et al. Nanomaterials in biosolids inhibit nodulation, shift microbial community composition, and result in increased metal uptake relative to bulk/dissolved metals. *Environ Sci Technol.* 2015;49:8751–8.
23. Fan R, Huang YC, Grusak MA, Huang CP, Sherrier DJ. Effects of nano-TiO₂ on the agronomically-relevant *Rhizobium*-legume symbiosis. *Sci Total Environ.* 2014;466–467:50–512.
24. Huang YC, Fan R, Grusak MA, Sherrier JD, Huang C. Effects of nano-ZnO on the agronomically relevant *Rhizobium*-legume symbiosis. *Sci Total Environ.* 2014;497:78–90.
25. Abd-Alla MH, Nafady NA, Khalaf DM. Assessment of silver nanoparticles contamination on faba bean-*Rhizobium leguminosarum* bv. *viciae*-*Glomus aggregatum* symbiosis: implications for induction of autophagy process in root nodule. *Agric Ecosyst Environ.* 2016;218:163–77.
26. Feng Y, Cui X, He S, Dong G, Chen M, Wang J, Lin X. The role of metal nanoparticles in influencing arbuscular mycorrhizal fungi effects on plant growth. *Environ Sci Technol.* 2013;47(16):9496–504.
27. Vesper SJ, Weidensaul TC. Effects of cadmium, nickel, copper, and zinc on nitrogen fixation by soybeans. *Water Air Soil Poll.* 1978;9:413–22.
28. Gogos A, Moll J, Klingenfuss F, van der Heijden M, Irin F, Green M, Zenobi R, Bucheli T. Vertical transport and plant uptake of nanoparticles in a soil mesocosm experiment. *J Nanobiotechnol* (in press).
29. Commission recommendation on the definition of nanomaterial (<http://eur-lex.europa.eu/LexUriServ/LexUriServ.do?uri=OJ:L:2011:275:0038:0040:EN:PDF>).
30. McGonigle TP, Miller MH, Evans DG, Fairchild GL, Swan JA. A new method which gives an objective measure of colonization of roots by vesicular arbuscular mycorrhizal fungi. *New Phytol.* 1990;115:495–501.
31. Vierheilig H, Coughlan AP, Wyss U, Piche Y. Ink and vinegar, a simple staining technique for arbuscular-mycorrhizal fungi. *Appl Environ Microbiol.* 1998;64:5004–7.
32. Fang J, Shan X-q, Wen B, Lin J-m, Owens G. Stability of titania nanoparticles in soil suspensions and transport in saturated homogeneous soil columns. *Environ Pollut.* 2009;157:1101–9.
33. Unkovich M, Herridge D, Peoples M, Cadisch G, Boddey B, Giller K, Alves B, Chalk P. Measuring plant-associated nitrogen fixation in agricultural systems. Bruce: ACIAR; 2008.
34. Van Der Heijden MGA, Bardgett RD, Van Straalen NM. The unseen majority: soil microbes as drivers of plant diversity and productivity in terrestrial ecosystems. *Ecol Lett.* 2008;11:296–310.
35. Lindsay WL. Zinc in soils and plant nutrition. In: Brady NC, editor. *Advances in agronomy*, vol. 24. Cambridge: Academic Press; 1972. p. 147–86.
36. Sobek A, Bucheli TD. Testing the resistance of single- and multi-walled carbon nanotubes to chemothermal oxidation used to isolate soots from environmental samples. *Environ Pollut.* 2009;157:1065–71.
37. Farré M, Sanchis J, Barceló D. Analysis and assessment of the occurrence, the fate and the behavior of nanomaterials in the environment. *TrAC Trends Anal Chem.* 2011;30:517–27.
38. Von der Kammer F, Ferguson PL, Holden PA, Mason A, Rogers KR, Klaine SJ, Koelmans AA, Horne N, Unrine JM. Analysis of engineered nanomaterials in complex matrices (environment and biota): general considerations and conceptual case studies. *Environ Toxicol Chem.* 2012;31:32–49.
39. Stünzi H. The soil P extraction with ammonium acetate EDTA (AAE10). *Agrarforschung.* 2006;13:448–93.
40. Bassler R. Ausgewählte Elemente in pflanzlichem Material und Futtermitteln mit ICP-OES. In: VDLUFA-Methodenbuch—Band III—Die chemische Untersuchung von Futtermitteln. Vol 3; 1993.
41. R Core Team. R: a language and environment for statistical computing. Vienna: R Foundation for Statistical Computing; 2014.
42. Hasler M, Hothorn LA. A Dunnett-type procedure for multiple endpoints. *Int J Biostat.* 2011;7:1–15.
43. Benjamini Y, Hochberg Y. Controlling the false discovery rate: a practical and powerful approach to multiple testing. *J Roy Stat Soc Ser B (Stat Method).* 1995;57:289–300.

Submit your next manuscript to BioMed Central and we will help you at every step:

- We accept pre-submission inquiries
- Our selector tool helps you to find the most relevant journal
- We provide round the clock customer support
- Convenient online submission
- Thorough peer review
- Inclusion in PubMed and all major indexing services
- Maximum visibility for your research

Submit your manuscript at
www.biomedcentral.com/submit



RESEARCH

Open Access



Vertical transport and plant uptake of nanoparticles in a soil mesocosm experiment

Alexander Gogos^{1,2}, Janine Moll¹, Florian Klingenfuss¹, Marcel van der Heijden¹, Fahmida Irin³, Micah J. Green⁴, Renato Zenobi² and Thomas D. Bucheli^{1*}

Abstract

Background: Agricultural soils represent a potential sink for increasing amounts of different nanomaterials that nowadays inevitably enter the environment. Knowledge on the relation between their actual exposure concentrations and biological effects on crops and symbiotic organisms is therefore of high importance. In this part of a joint companion study, we describe the vertical translocation as well as plant uptake of three different titanium dioxide (nano-)particles (TiO₂ NPs) and multi-walled carbon nanotubes (MWCNTs) within a pot experiment with homogeneously spiked natural agricultural soil and two plant species (red clover and wheat).

Results: TiO₂ NPs exhibited limited mobility from soil to leachates and did not induce significant titanium uptake into both plant species, although average concentrations were doubled from 4 to 8 mg/kg Ti at the highest exposures. While the mobility of MWCNTs in soil was limited as well, microwave-induced heating suggested MWCNT-plant uptake independent of the exposure concentration.

Conclusions: Quantification of actual exposure concentrations with a series of analytical methods confirmed nominal ones in soil mesocosms with red clover and wheat and pointed to low mobility and limited plant uptake of titanium dioxide nanoparticles and carbon nanotubes.

Keywords: Nanomaterials, Black carbon, Soil leachate, Multi-angle light scattering, Microwave induced heating, Wheat, Red clover

Background

It is scientifically ascertained that, due to their increased production and use, nanomaterials (NMs) will inevitably enter the environment [1], including soils. The currently most produced NMs are titanium dioxide nanoparticles (TiO₂ NPs) [2]. They are used in diverse applications such as paints, UV-protection, photovoltaics and photocatalysis [3], but also as a food additive [4]. Carbon nanotubes (CNTs) are closing the gap in the last years, with 10-fold increased production volumes since 2006 [5]. Due to their extraordinary mechanical and electrical properties, CNTs are mostly used as building blocks in light-weight composite materials as well as electronics.

These particles can enter soils via different pathways [1, 6]. Application of biosolids to landfills and irrigation with surface waters is most likely for TiO₂ NPs, while CNTs may enter soils via landfills and atmospheric deposition [7]. These types of release are unintentional, however, also applications in plant protection and fertilization have been foreseen [8, 9], which may lead to severely increased fluxes of these NP into soils. Apart from the positive effects and functions that are envisioned for agricultural applications of TiO₂ NPs and CNTs [8, 9], such as protection of active ingredients and increased plant growth, respectively, also negative effects on microorganisms and plants have been reported [10–12].

The enduring uncertainty regarding the environmental safety of NMs highlights the need for a thorough risk assessment of these materials, which includes the study of their effects on organisms and the ecosystem as well as their fate. However, the analysis of NMs such as TiO₂ and

*Correspondence: thomas.bucheli@agroscope.admin.ch

¹ Agroscope, Institute for Sustainability Sciences ISS, 8046 Zurich, Switzerland

Full list of author information is available at the end of the article

CNTs in complex systems such as real soils is challenging in many ways. For both, elemental analysis alone is not sufficient to trace the particles due to high elemental background concentrations of Ti and carbon.

Therefore, most studies until now used simplified laboratory systems as well as specifically labeled particles for eased detection to investigate both NM transport through porous media as well as plant uptake, often without confirmation of actual exposure concentrations. For example, TiO₂ NP transport was investigated in sand columns under well controlled conditions [13, 14]. Fang et al. [15] studied TiO₂ NP transport through soil columns at very high concentrations (40 g/kg). However, vertical translocation of both TiO₂ NPs and CNTs has neither been investigated yet in large pot experiments or field studies, nor in the presence of plants. Plant uptake was shown for TiO₂ NP in hydroponic exposure systems at high concentrations [16, 17]. In contrast, in a more realistic exposure setting using natural soil amended with TiO₂ NPs, Du et al. [12] found no uptake of Ti into wheat. Also, CNTs were shown to be taken up into plants [18–20] from hydroponic systems. However, until now, no data is available for CNT uptake from natural soils, in which CNT transport and subsequent availability to plants could be different due to their high interactions with the soil matrix [21–23].

Here, we investigated the vertical distribution and leaching behavior of three different TiO₂ (nano-)particles [P25, E171 and a non-nanomaterial TiO₂ (NNM TiO₂)] and the vertical distribution of a multi-walled CNT (MWCNT) within two elaborate pot exposure studies with red clover (*Trifolium pratense*) [24] and spring wheat (*Triticum spp.*) [25] in natural soil, and quantified their fractions in aboveground parts of the plants. We used recently developed methods such as microwave induced heating (MIH) [26] and asymmetric flow field-flow fractionation coupled to multi-angle light scattering (aF4-MALS) [27] to detect and quantify unlabeled MWCNTs in plant and soil samples, respectively. We additionally imaged root cross sections of exposed plants using (scanning) transmission electron microscopy. All data from this study were gathered to accompany two corresponding effect studies with actual, rather than nominal exposure concentrations. These studies examined the functionality of an agricultural ecosystem in presence of the NMs with regard to nitrogen fixation by the red clover-rhizobium symbiosis, as well as root colonization by arbuscular mycorrhizal fungi of both red clover [24] and wheat [25].

Methods

Chemicals and nanoparticles

Food grade E171 TiO₂ particles were obtained from Sachtleben Chemie GmbH (Duisburg, Germany). All

other chemicals and TiO₂ nanoparticles were purchased from Sigma-Aldrich (Buchs, Switzerland). Uncoated titanium containing NPs were selected to represent different primary particle size ranges; average primary particle sizes were determined by TEM image analysis and were 29 ± 9 (P25, $n = 92$), 92 ± 31 (E171, $n = 52$) and 145 ± 46 nm (NNM TiO₂, $n = 49$), see also Additional file 1: Figure S1. Anatase was the dominating crystal structure in all of the used particles. However, P25 also contains 20 % rutile, according to the manufacturer.

Multi-walled carbon nanotubes were purchased from Cheap Tubes Inc. (Brattleboro, VT). They were declared to have a length of 10–30 μ m, and outer diameter of 20–30 nm, a purity of >95 % and an elemental carbon content of >98 %. The MWCNTs were used as received without further purification. Further characterization of the MWCNTs used was carried out and described in [27, 28]. All parameters were confirmed to be within the specified ranges with the exception of CNT length. The latter could only be determined in suspension, where it may have been altered due to sonication necessary for dispersing the particles.

Soil

A natural soil was collected from an agricultural field at the facility of Agroscope, Zurich (N47° 25' 39.564" E8° 31' 20.04"). The soil was classified as brown earth with a sandy loamy to loamy fine fraction. The top layer (5 cm) of the soil was removed and approximately 0.9 m³ of the underlying 15 cm topsoil were sampled. The soil was then sieved <5 mm, homogenized by shoveling it three times from one soil pile to another, and stored in a dry place until it was used in both red clover and wheat experiments.

Spiking of the soil with NPs

Particle concentrations were selected to represent potential agricultural exposure scenarios as well as analytically accessible and potentially toxicologically effective concentrations. In a potential agricultural exposure scenario, fluxes from pesticide or fertilizer formulations may range from several micrograms to grams of NMs per kilogram of soil, depending on the formulation [8]. Thus, low doses (1, 10 mg/kg) were included as well as high doses.

For the spiking process, the soil was firstly blended with quartz sand (50 % v/v) to facilitate the recovery of below-ground plant organs after harvest. The properties of the soil-sand mixture are listed in Table 1. First, 300 g of the sand-soil mixture were each mixed with (i) 0.03 g (wheat experiment only), 0.3 g (red clover experiment only), 3 and 30 g of TiO₂ NPs (both experiments), and (ii) 90 mg and 88 g MWCNT powder (clover experiment only), each in a 500 mL glass bottle which was rotated in

Table 1 Properties of the soil-quartz mixture (50:50 v/v) administered to the pots

	Value	StDev
Org. C %	0.55	0.03
CEC mmol+/kg	6	
CaCO ₃ %	2.6	
pH	7.7	
Max. WHC g H ₂ O/g dry soil	0.308	
Sand %	86.1	0
Silt %	6.3	0
Clay %	6.7	0.5

a powder mixer (Turbula® T 2 F, Willy A. Bachofen AG, Basel, Switzerland) for 30 min. For P25 and MWCNTs, the highest particle amounts resulted in a volume too big for the glass bottles. Therefore, these were split in two and four aliquots, respectively, and each aliquot mixed with 300 g sand-soil mixture.

Into a cement mixer, 30 kg (including the pre-mixture) of a fresh sand-soil mixture (50 % v/v) were added, to yield final nominal NP concentrations of 1, 10, 100 or 1000 mg/kg, respectively, for TiO₂ NPs, and 3 or 2933 mg/kg for MWCNTs. The mixing chamber was covered with a plastic sheet to avoid dust formation and run for 6 h. The soil was not dried before mixing to avoid changes to the microbial community structure, also investigated in Moll et al. [25]. Actual exposure concentrations were verified by X-ray fluorescence spectroscopy (XRF, for TiO₂) and chemo-thermal oxidation at 375 °C [28] [CTO-375, for MWCNTs/Black Carbon (BC)] analysis as described below.

General experimental design

A detailed description of the general setup, design and execution of the underlying exposure experiments is given in [24, 25]. In brief, for each plant type seven pot replicates were generated for each NP treatment, consisting of seven plants per pot for red clover and three for wheat. Non-plant controls were not performed because these two studies were primarily designed to observe possible biological effects of the NP treatments. Each pot was filled with a drainage layer of sand (0.5 L, 520 g) and 3.3 kg soil (corresponding to 2.9 L). Each pot was kept at 50–60 % (wheat) and 60–70 % (red clover) of the total water holding capacity (WHC, Table 1) during the entire experiment. Plants were grown over a period of 14 weeks (red clover) and 12 weeks (wheat) in a greenhouse with a 16 h light period (light intensity of 300 W m⁻²) and a 25/16 °C light/dark temperature regime. Wheat plants were fertilized weekly starting after week 3. Red clover plants were fertilized after 6 and 9 weeks, respectively. The composition of the nutrient solutions is given in the Additional file 1.

Sampling of soil cores

Soil cores were sampled at the day of harvest from each pot using a conventional soil driller with a 2 cm diameter. Two cores were taken per pot and each divided into three depths (0–5, 5–10 and 10–15 cm). For each depth, both subsamples were joined into one and stored in plastic bags at 4 °C until further processing.

Titanium analysis in soils with XRF

The soil samples from the cores were dried at 60 °C until a constant weight resulted, and ground to a fine powder using a Retsch ZM400 Ball Mill (Retsch GmbH, Haan, Germany) with a tungsten carbide bead at a frequency of 25/s for 5 min. Four grams of ground soil were homogenously mixed with 0.9 g of wax and pressed to a 32 mm tablet at 15 tons. Tablets were analyzed using an energy-dispersive XRF spectrometer (XEPOS, SPECTRO Analytical Instruments GmbH, Kleve, Germany). For correction of matrix effects, standard additions of the respective material to the soil were performed. For quality assurance we also analyzed a certified lake sediment reference sample (LKSD1, CANMET Mining and Mineral Sciences Laboratories, Ontario, Canada) with recoveries for Ti of >95 %.

Titanium analysis in leachates with ICP-OES

A week before harvest, each pot was watered with 520 mL tap water, leading to approx. 110 % WHC. Consequently, 45 mL of leachate were collected through a valve at the bottom of the pots. The leachate was analyzed on the same day without any further treatment using inductively-coupled plasma optical emission spectrometry (ICP-OES) (ARCOS, SPECTRO Analytical Instruments GmbH). For quality control, an external Ti containing standard solution (ICAL, Bernd Kraft GmbH, Duisburg, Germany) was analyzed. The instrumental limit of quantification for Ti was determined at 22 µg/L.

MWCNT analysis of soil with CTO-375

The CTO-375 procedure used in this study is described in detail in Sobek and Bucheli [28] as well as specifically for this work in the Additional file 1. This method quantifies total soil BC, which also encompasses MWCNT-carbon. We analyzed the soil samples taken from the cores, as well as the bulk spiked soil before the experiment. For the latter, six random grab samples of approx. 10 g were taken from the spiked pile.

MWCNT analysis of soil with aF4-MALS

The method for MWCNT detection using aF4-MALS is described in detail by Gogos et al. [27]. Briefly, 120 mg of dry and ground soil from the cores were extracted with 10 mL of a 2 % sodium deoxycholate/0.05 % sodium azide

solution, sonicated three times for 10 min using a high power sonication bath (720 W, Bandelin, Switzerland) and centrifuged at 17,500 g for 10 min. The supernatant was then used as a working suspension. This procedure was performed for each replicate of each soil depth. Afterwards, the replicates of each depth were joined to form a collective sample and analyzed using aF4-MALS, which generates a shape factor ρ from the radius of gyration and the hydrodynamic radius for each time point in the aF4 fractogram. The difference in ρ ($\Delta\rho$) compared to native soil is then used to detect the MWCNTs [27]. The method detection limit (MDL) of the present study is presented and further discussed in the “Results and discussion” section.

Titanium analysis of plants with ICP-OES

Due to their high importance for agricultural scenarios, from both plants, the parts used as food or feed were analyzed, i.e. the whole aboveground red clover, and the wheat grains. Dried plant samples were ground to a fine powder using a Retsch ZM200 centrifugal mill (Retsch GmbH). Subsamples (100 mg) were digested in a mixture of 0.2 mL hydrofluoric acid, 1.5 mL nitric acid and 0.2 mL hydrogen peroxide using a microwave (Ultraslave, MLS, Germany). The sample volume was subsequently adjusted to 50 mL. Digested samples were analyzed using ICP-OES (CIROS, SPECTRO Analytical Instruments GmbH). For quality assurance we also analyzed an industrial sludge reference sample (standard reference material SRM 2782, NIST, Gaithersburg, US) with recoveries for Ti of >85 %.

MWCNT analysis of plants with MIH

Dry plant material was ground to a fine powder as described before. The amount of MWCNT uptake was then quantified by MIH, which is described in detail by Irin et al. [26]. MWCNTs have a high microwave absorption capacity, which results in a rapid rise in temperature within a very short microwave exposure time. Original method development included the generation of a calibration curve using the thermal response as a function of known CNTs spiked into Alfalfa (*Medicago sativa*) root samples.

Utilizing the data from Irin et al. [26], a new calibration curve was generated, where the slope of the curve depends on the respective nanomaterial and the intercept on the sample type. To this end, first, the initial slope was corrected using a factor based on the ratio of the source nanomaterials (MWCNTs of this study) microwave sensitivity and the one of the Irin et al. study. The sensitivity was determined by exposing ~1 mg of MWCNT powder to 30 W microwave power (2.45 GHz frequency) and recording the final temperature rise immediately (within

1 s) with a temperature rise (ΔT) of 346 °C. Second, the intercept was corrected based on the control plant microwave response. Additional file 1: Figure S2 shows the renormalized calibration curve for MWCNTs at 50 W (6 s). The plant samples from the controls and the two MWCNT treatments were then tested at 50 W over 6 s and the quantity of MWCNT uptake were calculated using this new calibration curve. The limit of detection (LOD) as well as the limit of quantification (LOQ) were calculated based on the temperature rise from five measurements of control plant samples (blank signal) according to Keith et al. [29] (3 and 10 σ above the blank signal, respectively).

Transmission electron microscopy of root cross sections

Fresh root samples were washed with tap water and prefixed in 2.5 % glutaraldehyde in phosphate buffered saline directly on the day of harvest and stored at 4 °C until processing. Ultrathin cross Sects. (70 nm thickness) were obtained by cutting root samples embedded in epoxy-resin using an ultramicrotome (Ultracut E, Leica, Wetzlar, Germany). The detailed sample preparation steps are provided in the Additional file 1. Ultrathin sections were imaged using a TEM (Tecnai G2 Spirit, FEI, Hillsboro, USA), coupled to an energy-dispersive X-ray (EDX) spectroscope (X-Max, 80 mm², Oxford Instruments, Abingdon, UK) as well as a STEM (HD-2700-Cs, Hitachi, Japan) coupled to an EDX system as well (EDAX, NJ).

Statistics

In the case of normal distributed residuals and homogeneous data, an analysis of variance (ANOVA) was applied. If these model assumptions were not fulfilled, a Mann–Whitney test was conducted. All statistical analyses were done with the software R (version 3.01, the R Foundation for Statistical Computing) integrated in RStudio (version 0.97.551, RStudio, Boston, MA).

Results and discussion

Vertical soil distribution and leaching of Ti

Only the highest exposure concentration (1000 mg/kg) was analytically accessible using XRF, i.e., standard deviations among the replicates were in the order of the added Ti amount in samples spiked with <1000 mg/kg TiO₂. Actual dry weight exposure concentrations of Ti were almost always slightly higher at the time of harvest than the initial nominal ones predicted from native and added Ti amounts, probably due to the residual water content in soils at the time of spiking (Fig. 1b, c, e, f). However, the differences were minimal (2.5–7.6 %) and overall not statistically significant (except for Fig. 1c, P25 1000 mg/kg, 5–10 cm), indicating that the employed spiking procedure was rather reliable. The control soils in the wheat

experiment were systematically—though not significantly—lower in Ti content and showed higher standard deviations compared to the controls in the red clover experiment. This unexpected result may be explained by the fact that the two experiments were conducted independently using different subsets of the native soil and

also highlights the necessity to verify actual exposure concentrations.

No statistically significant difference could be found between the different soil layers in any of the treatments (Fig. 1). Still, some trends could be observed; the distribution profiles of Ti in the control and in the P25

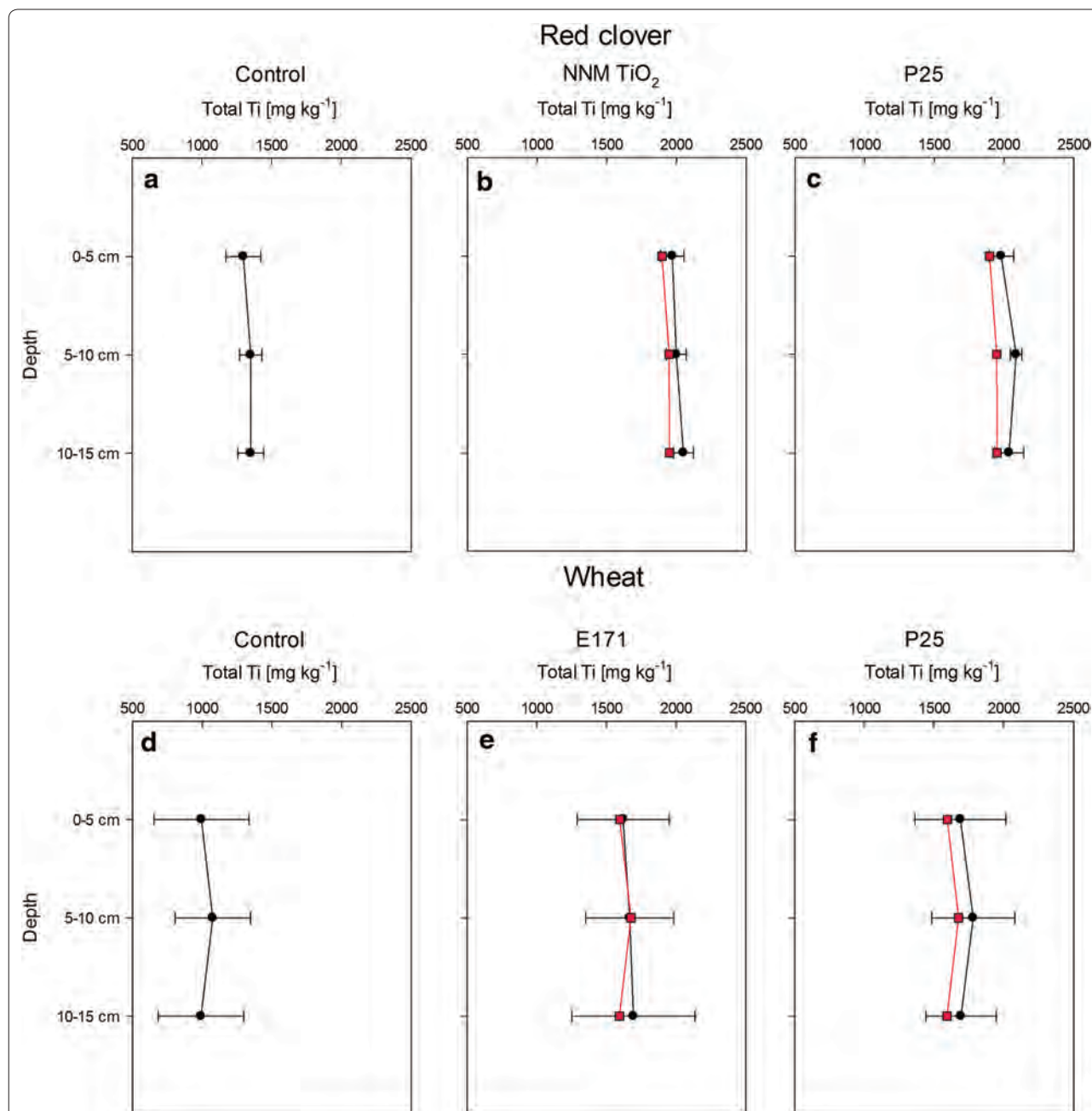


Fig. 1 Vertical distributions of elemental Ti as determined by XRF analysis for three depths and for two different exposure experiments: **a–c** Red clover controls and red clover exposed to 1000 mg/kg of NNM TiO_2 and P25 and **d–f** Wheat controls and wheat exposed to 1000 mg/kg of E171 and P25. Error bars show the standard deviation of seven replicates. Red squares show the predicted concentrations based on the control values and the nominal amount of Ti that was added as TiO_2 NPs

(80 % anatase, 20 % rutile) treatments were similar, with a tendency to slightly higher concentrations in the middle layer in both red clover and wheat pots. In contrast, the distribution profiles of the two pure anatase particles (NNM and E171) both tended towards elevated concentrations in the lowest part.

In addition, Ti concentrations in leachates of these two treatments were significantly elevated compared to the controls (Fig. 2, $p < 0.05$), thus it can be assumed that the elevated Ti originated from eluting TiO_2 NPs. However, the leached Ti amount—even in the treatments showing significantly higher concentrations—was very low and constituted not more than 10^{-4} % of the initial spiked Ti amount. In a dedicated transport study by Fang et al. [15], a soil with comparable properties (sandy loam, denoted as “JS soil”) showed a medium to high permeability for TiO_2 NPs, attributed to the soil’s high sand content. A breakthrough of Ti in this soil started to occur after 1 pore volume. In our case, 520 mL of water was added to the pots (equivalent to 30 mm of precipitation) to collect the leachate, which correspond to 0.4 pore volumes only (1.24 L pore volume at full WHC). Thus, the added water amount was too low to initiate quantitative elution and

would therefore explain the relatively low Ti concentration in the leachate after collection.

The observed difference in mobility (both in terms of Ti profiles and leachate content) may partly be explained by differences in the isoelectric point (IEP) of the TiO_2 particles: while the more mobile NNM TiO_2 and E171 exhibited a very low IEP of 2.2 (see Additional file 1: Figure S3), the one of P25 was 5.1, being much closer to the soil pH (7.7, see Table 1) and indicating a lesser colloidal stability [30]. TiO_2 NPs with low IEPs may thus have a higher tendency to reach the groundwater and should thus be avoided in applications where this might be of relevance, e.g., when used as a component of a plant protection product [8, 9].

Vertical soil distribution of BC/MWCNTs

Figure 3 shows the BC distribution as well as the shape factor difference ($\Delta\rho$) for the different soil depths of the 2933 mg/kg MWCNT amended red clover pots. As with Ti, only the highest MWCNT concentration was analytically accessible. The total background BC in the control soil was 0.50 ± 0.06 mg/g ($n = 4$). The specific recovery of the employed MWCNT in the soil over the

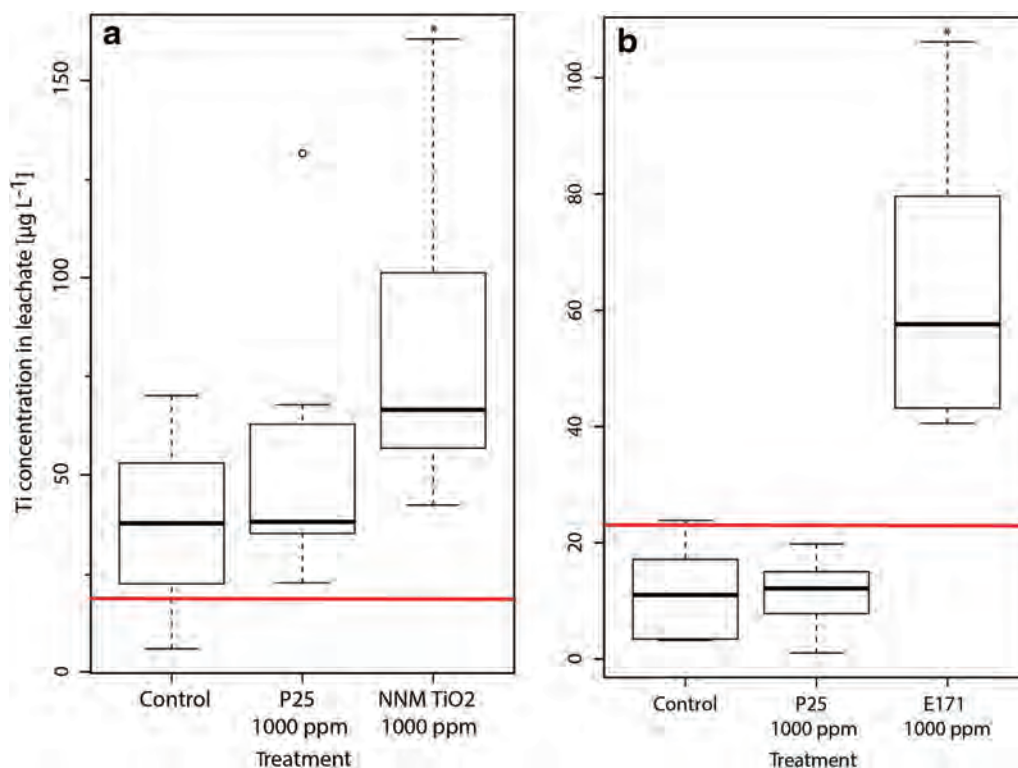
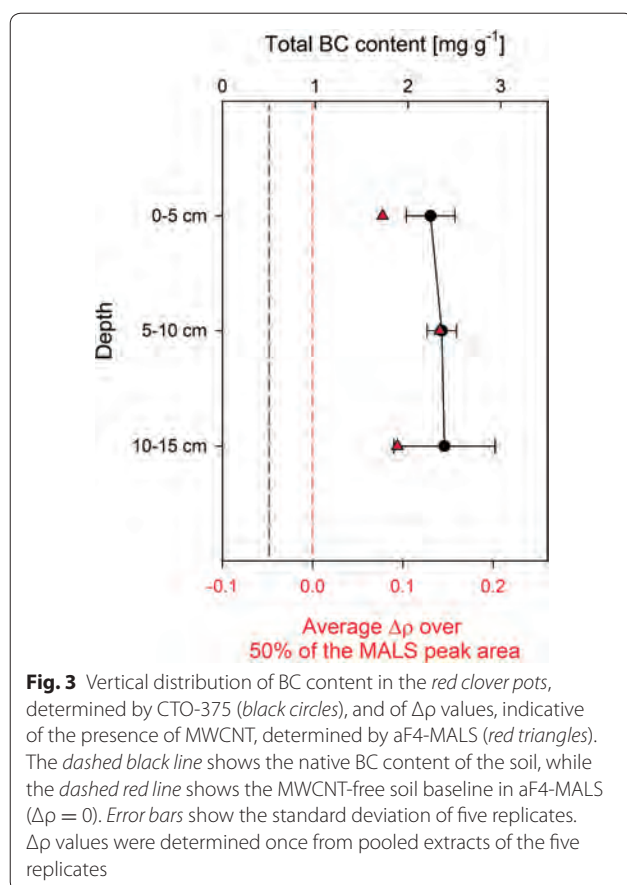


Fig. 2 Boxplots (solid line = median) showing the Ti content of the leachates in the clover (a, each treatment $n = 7$) and wheat (b, each treatment $n = 6$) experiment. The LOQ is indicated with a solid red line. Significant difference ($p < 0.05$) of a treatment compared to the respective controls is indicated with an asterisk. The lower and upper borders of the boxes represent the 25th and 75th percentile, respectively. Whiskers represent maximum and minimum values, circles indicate outliers



CTO-375 method was $85 \pm 13\%$ ($n = 18$, determined by standard addition). Therefore, the expected total BC concentration in the 2933 mg/kg MWCNT amended pots after CTO-375 can be calculated as follows: $(2933 \times 0.85) + 500 = 2993$ mg/kg. However, the average BC content in the spiked soil before filling into the pots was lower than expected, with 2400 ± 100 mg/kg ($n = 6$), corresponding to 80 % of the expected BC concentration. Eventually, losses during the large scale mixing procedure could have contributed to these lower values. The variability of 4 % however suggests that the employed spiking procedure still resulted in a rather homogenous MWCNT distribution before the experiment. After the experiment, the average BC content quantified over all soil depths was 2330 ± 280 mg/kg, corresponding to $78 \pm 12\%$ ($n = 15$) of the total expected BC concentration, with no significant difference between the layers. The average value was comparable to the BC content quantified before the experiment. However, precision, expressed by relative standard deviations, increased from 4 % (original spiked soil) to 12 % (aged soil). This increase in variability of the BC content may be associated with partial transport and/or aging (i.e. physiochemical

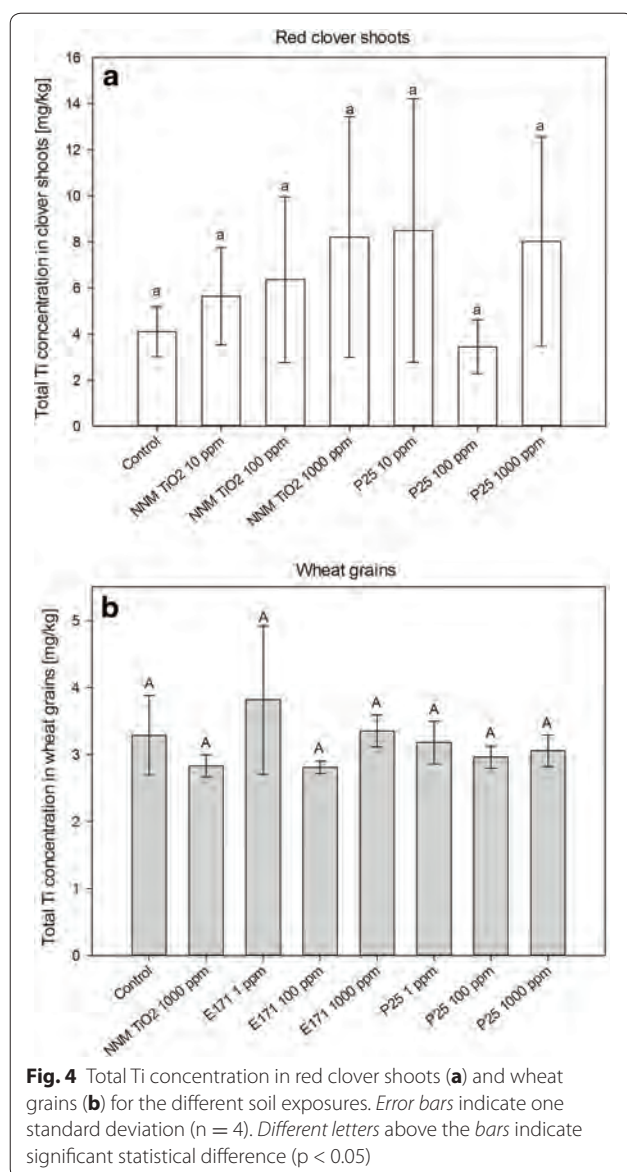
modification of the particles, influencing their survival in CTO-375) of MWCNTs during the experiment.

To orthogonally observe the MWCNT behavior between the different layers with a second method, we also measured the cores with aF4-MALS [27]. With the soil of the present study, the MDL was at a $\Delta\rho$ of 0.099, corresponding to a CTO-determined MWCNT content of approx. 2 mg/g (Fig. 3), which is slightly lower than with the soil used in Gogos et al. (4 mg/g) [27]. The soil layers showed $\Delta\rho$ values of 0.078, 0.141 and 0.094 in descending order (Fig. 3). Thus, only the value of the middle layer was above the MDL. In combination with the results from CTO-375 and the increase in variability compared to the initial spike, this suggests a limited transport of the MWCNTs in the experiment. Such a low mobility would be in accordance to a dedicated soil transport study by Kasel et al. [22]. Using 14-C labeled functionalized MWCNTs, they found no detectable breakthrough in a comparable soil (loamy sand, denoted as “KAL” soil) even at water contents close to saturation (96 %).

Plant uptake of Ti

With 4.1 mg/kg, the determined Ti concentration in the red clover control plant material (Fig. 4a) was in the range of literature values for a plant species of the same family (*M. sativa*, a legume which also forms a symbiosis with rhizobia) and total soil Ti [31]. After treatment with TiO_2 (nano-)particles, the average shoot Ti content of the red clover plants increased to 8 mg/kg at the highest exposure concentration of both NNM TiO_2 and P25 (Fig. 4a). For NNM TiO_2 , the average Ti content was rising with the exposure concentration, whereas for P25 no such trend could be observed. However, variability within the treatments was relatively high, and no statistical difference between the different treatments was observed. Therefore, the Ti-content in the red clover plants was not dependent on a NNM or NM exposure.

To elucidate whether the nevertheless elevated Ti contents within the red clover shoots was related to the uptake of actual TiO_2 (nano-)particles, we investigated cross sections of these roots with TEM and EDX elemental analysis. In red clover roots treated with NNM TiO_2 , Ti containing particles with a similar morphology to the employed particles (Additional file 1: Figure S1A) were observed at the root surface (Fig. 5a, A1) but never inside the root cells. Some of these particles also contained Si (Fig. 5 A1, Particle 2) pointing to a possible natural origin of the particles. However, the absence of NNM TiO_2 particles within the investigated thin sections does not necessarily disprove particle uptake, as it is not possible to representatively sample a whole plant root in this way.



In red clover roots treated with P25, only very few Ti containing nano-sized particles were found inside plant cells. The particle B1 in Fig. 5 shows a clear Ti EDX peak and is morphologically similar to the employed P25 particles (Additional file 1: elongated hexagon/Figure S1C). In addition, the oxygen peak in particle B1 is more distinct than in the other particles/objects, suggesting that the particle may consist of titanium-oxide/dioxide.

With an average of 3.3 mg/kg, the Ti content in the control wheat grains was slightly lower compared to red clover. In this case however, after treatment with TiO₂ NPs, the average Ti content in the grains remained approx. constant (Fig. 4b). Thus, both for red clover shoots and wheat grains, no significant difference in Ti

uptake between the different treatments and the controls could be found.

While no data is available for red clover plants, Larue et al. [32] and Servin et al. [16] demonstrated that nano-TiO₂ can be taken up into wheat and cucumber, respectively, under extreme conditions (direct hydroponic exposure, high concentrations). Larue et al. [32] reported contents of up to 109 mg/kg Ti inside wheat roots, whereas Ti content in wheat leaves was below their LOD. To date, quantitative uptake data for aboveground plant material grown in natural TiO₂ NP spiked soil however is available only from one study performed with wheat plants [12]. Therein, the Ti content of wheat grains was in the same range as in our study, with no significant uptake, confirming our observations. However, only one exposure concentration was employed (approx. 100 mg/kg TiO₂ NPs), so no comparison can be made with regard to concentration dependent trends.

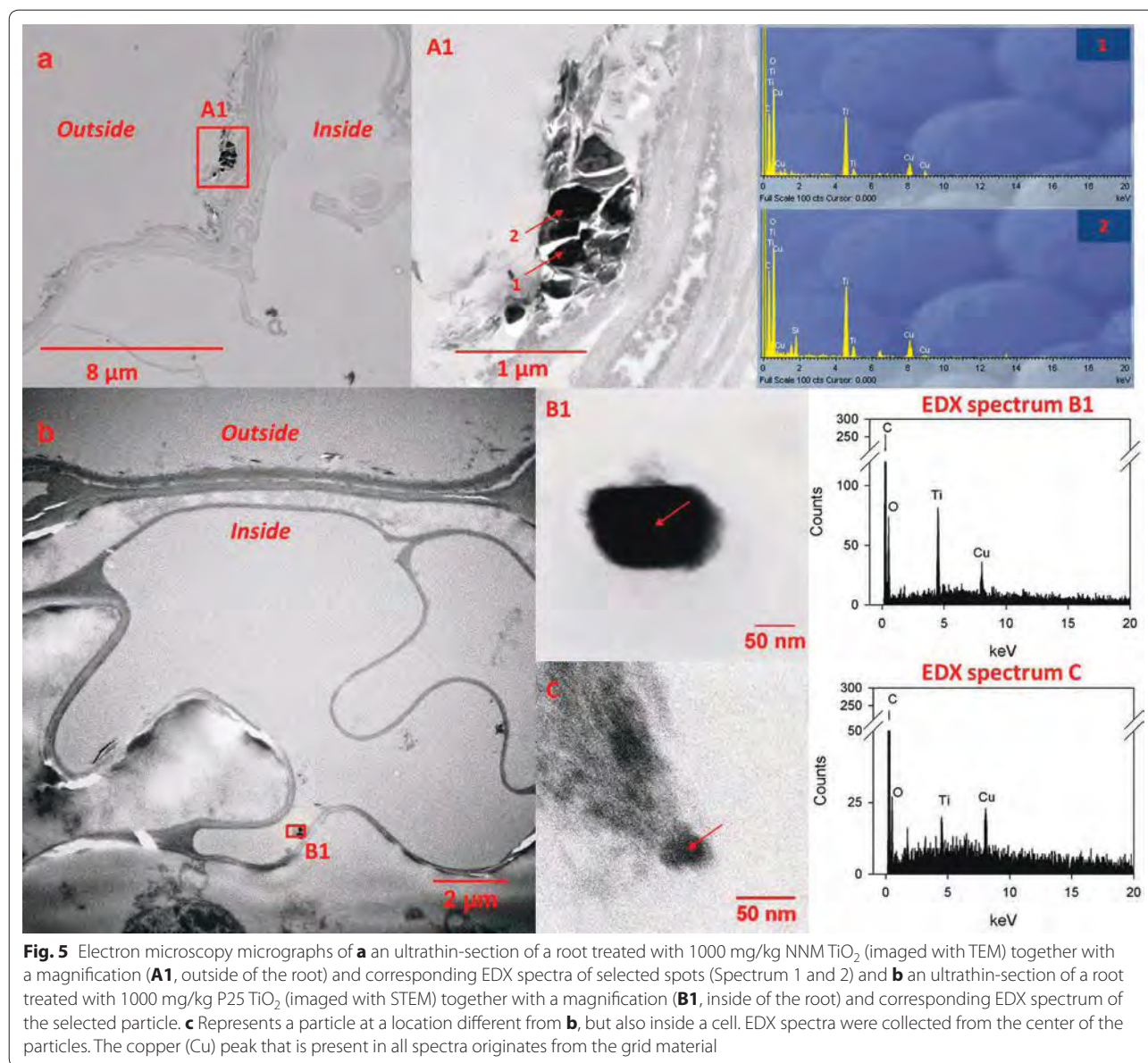
Altogether, our results suggest that Ti (-NP) uptake to red clover plants from real soils is insignificant. The biological data [24, 25] may represent another indirect piece of evidence, as for all endpoints (root and shoot biomass, number of flowers, nitrogen fixation and arbuscular mycorrhizal colonization), no significant effect of the treatments were observed for both plants.

Plant uptake of MWCNTs

Figure 6 shows the temperature rise (ΔT , °C) of dry red clover shoot material from the two MWCNT treatments. The LOD of the MIH method [26] was calculated to be at $\Delta T = 76$ °C (corresponding to a 16 $\mu\text{g/g}$ MWCNT content) and the LOQ at $\Delta T = 117$ °C (corresponding to a 55 $\mu\text{g/g}$ MWCNT content).

A large fraction of the values was located in the region between LOD and LOQ, and can thus be considered as MWCNT detections (60 % of the values in case of the 3 mg/kg treatment and 43 % in case of the 2933 mg/kg treatment). The values above the LOQ represent MWCNT contents of 68 (3 mg/kg treatment, n = 1) and 99 $\mu\text{g/g}$ (2933 mg/kg treatment, n = 1).

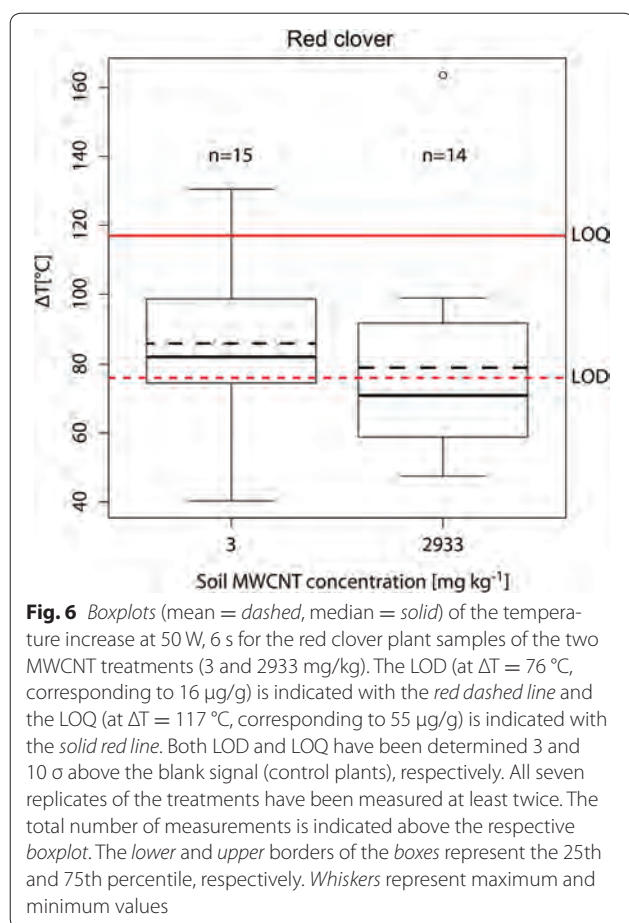
Taking into account the average dry weight of the red clover plants (14.3 g for the 3 mg/kg treatment and 15.3 g for the 2933 mg/kg treatment, see also Moll et al. [24]), the two cases with values above the LOD would correspond to a total amount of MWCNTs of 0.97 and 1.5 mg taken up into the plants per pot in the two treatments, respectively. This means that 9.8 % of the initial MWCNT amount in the soil would have been translocated to the shoots in the 3 mg/kg treatment. Conversely, in the 2933 mg/kg treatment, only 0.015 % of the initial amount would have been translocated. It is interesting to note that the MWCNT uptake was independent from the applied MWCNT concentration. In addition,



we observed that within the MWCNT treatments, a significant reduction of flowering occurred (see Moll et al. [24]), which was not concentration dependent as well.

Uptake of CNTs into a plant cell is likely to be limited to the fraction dispersed in water. MWCNTs however are highly hydrophobic and prone to homo- as well as hetero-agglomeration with soil constituents. This in turn may result in a very small fraction of MWCNTs that remains well dispersed in the soil pore water. In addition, the plant surface may act as a filter that becomes clogged over time. However, further experiments are needed to explain this intriguing result.

We tried to orthogonally confirm the observed MWCNT uptake by using TEM imaging on cross sections of the plant roots. Khodakovskaya et al. [18] and Tripathi et al. [19] provided such optical evidence for CNT uptake from hydroponic solutions. However, in our case, the sole use of TEM was not conclusive. Additional file 1: Figure S4A shows a MWCNT-like particle that was observed within a plant root cell of the MWCNT treatment. This particle showed structural and dimensional similarity to the native MWCNTs administered to the pots (Additional file 1: Figure S4B). Still, this observation remained the only one



within a number of cross sections that were manually inspected.

We then made additional attempts to screen the samples for the presence of MWCNTs with confocal Raman spectroscopy (Additional file 1: Figure S5). However, this approach requires that the sample is free (or almost free) of carbon allotropes (native carbon or contaminations), such as soot and amorphous carbon. In principle, Raman spectroscopy has enough sensitivity to detect single MWCNTs, but we observed that the spectra of MWCNTs and other carbon allotropes as well as cell wall material (i.e. lignin [33], which is present in clover roots [34]) had a large overlap which made the screening difficult.

While the exact amount of MWCNTs taken up could not be fully quantified and optical confirmation is still not entirely affirmed, based on the specificity of the MIH method, it is still suggested that MWCNTs were taken up and translocated to the aboveground part of the plant in some cases. Studies that reported plant uptake or cellular localization of CNTs until now were performed in hydroponic cultures, where the particles were freely available for interactions with the root [18, 19, 35, 36]. Uptake

from soil would thus constitute a novelty; however, due to the lack of an orthogonal confirmation of the observed uptake, this result should be interpreted with care.

Conclusions

In this part of a combined effect and exposure study we placed emphasis on a rigorous confirmation of actual NP exposure concentrations. To achieve this goal we applied an array of analytical techniques to the soil and plant samples, of which some are novel and used for the first time in this kind of effect studies. In particular, this includes the combination of CTO-375 and aF4-MALS that showed that MWCNTs exhibited a rather limited mobility in the soil, as well as MIH that showed a concentration independent uptake of MWCNTs into some plants. In addition, the battery of analytical techniques confirmed the relatively constant exposure situation in both TiO_2 NP and MWCNT treatments over several months, with only subtle changes in concentrations, which could however be explained qualitatively with underlying NP/soil properties, distribution processes and experimental conditions.

Additional file

Additional file 1. Figure S1. Bright field TEM micrographs and size information of TiO_2 particles. **Figure S2.** MIH calibration curve. **Figure S3.** Dependence of the ζ -potential [mV] of TiO_2 particles on pH. **Figure S4.** Transmission electron microscopy micrographs of a potential CNT structure. **Figure S5.** Raman spectra of the employed MWCNT powder and plant samples. **Text.** Composition of fertilizers, MWCNT analysis of soil with CTO-375. Detailed sample preparation steps of root cross sections for analysis using transmission electron microscopy.

Authors' contributions

AG carried out physical-chemical analyses (CTO-375, aF4-MALS, XRF, ICP-OES) as well as the transmission electron microscopy and wrote the manuscript. JM designed and conducted the red clover exposure experiment. FK performed the leachate measurements and conducted the wheat exposure experiment. MvdH participated in the design of the exposure study. FI conducted MIH measurements, and FI and MJG analyzed the data. MJG and RZ edited parts of the manuscript. TDB conceived of the study, and participated in its design and coordination and helped to write the manuscript. All authors read and approved the final manuscript.

Author details

¹ Agroscope, Institute for Sustainability Sciences ISS, 8046 Zurich, Switzerland. ² Department of Chemistry and Applied Biosciences, ETH Zurich, 8093 Zurich, Switzerland. ³ Department of Chemical Engineering, Texas Tech University, Lubbock, TX, USA. ⁴ Artie McFerrin Department of Chemical Engineering, Texas A&M University, College Station, TX, USA.

Acknowledgements

This work is part of the project "Effects of NANOparticles on beneficial soil Microbes and CROPS (NANOMICROPS)", within the Swiss National Research Programme NRP 64 "Opportunities and Risks of Nanomaterials". We thank the Swiss National Science Foundation (SNF) for financial support. Andres Kaech, Ursula Lüthi and the team at the center for microscopy and image analysis (ZMB), University of Zurich are gratefully acknowledged for TEM support. We also thank Jacek Szczerbiński for his support in the confocal Raman

microscopy, Franziska Blum for help with the BC analysis as well as Ralf Kaegi and Brian Sinnet for their help with the plant Ti determination and the possibility to carry out the XRF analyses in their lab.

Competing interests

The authors declare that they have no competing interests.

Received: 21 January 2016 Accepted: 6 May 2016

Published online: 08 June 2016

References

- Nowack B, Ranville JF, Diamond S, Gallego-Urrea JA, Metcalfe C, Rose J, et al. Potential scenarios for nanomaterial release and subsequent alteration in the environment. *Environ Toxicol Chem*. 2012;31(1):50–9.
- Piccinno F, Gottschalk F, Seeger S, Nowack B. Industrial production quantities and uses of ten engineered nanomaterials in Europe and the world. *J Nanopart Res*. 2012;14(9):1–11.
- Chen X, Mao SS. Titanium dioxide nanomaterials: synthesis, properties, modifications, and applications. *Chem Rev*. 2007;107(7):2891–959.
- Weir A, Westerhoff P, Fabricius L, Hristovski K, von Goetz N. Titanium dioxide nanoparticles in food and personal care products. *Environ Sci Technol*. 2012;46(4):2242–50.
- De Volder MFL, Tawfik SH, Baughman RH, Hart AJ. Carbon nanotubes: present and future commercial applications. *Science*. 2013;339(6119):535–9.
- Petersen EJ, Zhang L, Mattison NT, O'Carroll DM, Whelton AJ, Uddin N, et al. Potential release pathways, environmental fate, and ecological risks of carbon nanotubes. *Environ Sci Technol*. 2011;45(23):9837–56.
- Gottschalk F, Sonderer T, Scholz RW, Nowack B. Possibilities and limitations of modeling environmental exposure to engineered nanomaterials by probabilistic material flow analysis. *Environ Toxicol Chem*. 2010;29(5):1036–48.
- Gogos A, Knauer K, Bucheli TD. Nanomaterials in plant protection and fertilization: current state, foreseen applications, and research priorities. *J Agric Food Chem*. 2012;60(39):9781–92.
- Kah M, Beulke S, Tiede K, Hofmann T. Nanopesticides: state of knowledge, environmental fate, and exposure modeling. *Crit Rev Environ Sci Technol*. 2012;43(16):1823–67.
- Tong Z, Bischoff M, Nies LF, Myer P, Applegate B, Turco RF. Response of soil microorganisms to as-produced and functionalized single-wall carbon nanotubes (SWNTs). *Environ Sci Technol*. 2012;46(24):13471–9.
- Ge YG, Schimel JP, Holden PA. Evidence for negative effects of TiO₂ and ZnO nanoparticles on soil bacterial communities. *Environ Sci Technol*. 2011;45(4):1659–64.
- Du WC, Sun YY, Ji R, Zhu JG, Wu JC, Guo HY. TiO₂ and ZnO nanoparticles negatively affect wheat growth and soil enzyme activities in agricultural soil. *J Environ Monit*. 2011;13(4):822–8.
- Chen G, Liu X, Su C. Transport and retention of TiO₂ rutile nanoparticles in saturated porous media under low-ionic-strength conditions: measurements and mechanisms. *Langmuir*. 2011;27(9):5393–402.
- Solovitch N, Labille J, Rose J, Chaurand P, Borschneck D, Wiesner MR, et al. Concurrent aggregation and deposition of TiO₂ nanoparticles in a sandy porous media. *Environ Sci Technol*. 2010;44(13):4897–902.
- Fang J, Shan XQ, Wen B, Lin JM, Owens G. Stability of titania nanoparticles in soil suspensions and transport in saturated homogeneous soil columns. *Environ Pollut*. 2009;157(4):1101–9.
- Servin AD, Castillo-Michel H, Hernandez-Viezas JA, Diaz BC, Peralta-Videa JR, Gardea-Torresdey JL. Synchrotron micro-XRF and micro-XANES confirmation of the uptake and translocation of TiO₂ nanoparticles in cucumber (*Cucumis sativus*) plants. *Environ Sci Technol*. 2012;46(14):7637–43.
- Larue C, Veronesi G, Flank A-M, Surble S, Herlin-Boime N, Carriere M. Comparative uptake and impact of TiO₂ nanoparticles in wheat and rapeseed. *J Toxicol Environ Health Part A*. 2012;75(13–15):722–34.
- Khodakovskaya M, Dervishi E, Mahmood M, Xu Y, Li ZR, Watanabe F, et al. Carbon nanotubes are able to penetrate plant seed coat and dramatically affect seed germination and plant growth. *ACS Nano*. 2009;3(10):3221–7.
- Tripathi S, Sonkar SK, Sarkar S. Growth stimulation of gram (*Cicer arietinum*) plant by water soluble carbon nanotubes. *Nanoscale*. 2011;3(3):1176–81.
- Liu QL, Chen B, Wang QL, Shi XL, Xiao ZY, Lin JX, et al. Carbon nanotubes as molecular transporters for walled plant cells. *Nano Lett*. 2009;9(3):1007–10.
- Jaisi DP, Elimelech M. Single-walled carbon nanotubes exhibit limited transport in soil columns. *Environ Sci Technol*. 2009;43:9161–6.
- Kasel D, Bradford SA, Šimůnek J, Pütz T, Vereecken H, Klumpp E. Limited transport of functionalized multi-walled carbon nanotubes in two natural soils. *Environ Pollut*. 2013;180:152–8.
- Tian Y, Gao B, Wang Y, Morales VL, Carpena RM, Huang Q, et al. Deposition and transport of functionalized carbon nanotubes in water-saturated sand columns. *J Hazard Mater*. 2012;213–214:265–72.
- Moll J, Gogos A, Bucheli TD, Widmer F, van der Heijden MGA. Effect of nanoparticles on red clover and its symbiotic micro-organisms. *J Nanobiotechnol*. 2016;14:36.
- Moll J, Klingensuss F, Widmer F, Gogos A, Bucheli TD, et al. Assessing the effects of titanium dioxide nanoparticles on soil microbial communities and wheat growth. in preparation.
- Irin F, Shrestha B, Canas JE, Saed MA, Green MJ. Detection of carbon nanotubes in biological samples through microwave-induced heating. *Carbon*. 2012;50(12):4441–9.
- Gogos A, Kaegi R, Zenobi R, Bucheli TD. Capabilities of asymmetric flow field-flow fractionation coupled to multi-angle light scattering to detect carbon nanotubes in soot and soil. *Environ Sci Nano*. 2014;1(6):584–94.
- Sobek A, Bucheli TD. Testing the resistance of single- and multi-walled carbon nanotubes to chemothermal oxidation used to isolate soots from environmental samples. *Environ Pollut*. 2009;157(4):1065–71.
- Keith LH, Crummett W, Deegan J, Libby RA, Taylor JK, Wentler G. Principles of environmental analysis. *Anal Chem*. 1983;55(14):2210–8.
- Dunphy Guzman KA, Finnegan MP, Banfield JF. Influence of surface potential on aggregation and transport of titania nanoparticles. *Environ Sci Technol*. 2006;40(24):7688–93.
- Dumon JC, Ernst WHO. Titanium in Plants. *J Plant Physiol*. 1988;133(2):203–9.
- Larue C, Laurette J, Herlin-Boime N, Khodja H, Fayard B, Flank A-M, et al. Accumulation, translocation and impact of TiO₂ nanoparticles in wheat (*Triticum aestivum* spp.): influence of diameter and crystal phase. *Sci Total Environ*. 2012;431:197–208.
- Gierlinger N, Schwanninger M. The potential of Raman microscopy and Raman imaging in plant research. *Spectrosc-Int J*. 2007;21(2):69–89.
- de Neergaard A, Hauggaard-Nielsen H, Jensen LS, Magid J. Decomposition of white clover (*Trifolium repens*) and ryegrass (*Lolium perenne*) components: C and N dynamics simulated with the DAISY soil organic matter submodel. *Eur J Agron*. 2002;16(1):43–55.
- Lin SJ, Reppert J, Hu Q, Hudson JS, Reid ML, Ratnikova TA, et al. Uptake, translocation, and transmission of carbon nanomaterials in rice plants. *Small*. 2009;5(10):1128–32.
- Serag MF, Kaji N, Gaillard C, Okamoto Y, Terasaka K, Jabasini M, et al. Trafficking and subcellular localization of multiwalled carbon nanotubes in plant cells. *ACS Nano*. 2011;5(1):493–9.

Submit your next manuscript to BioMed Central and we will help you at every step:

- We accept pre-submission inquiries
- Our selector tool helps you to find the most relevant journal
- We provide round the clock customer support
- Convenient online submission
- Thorough peer review
- Inclusion in PubMed and all major indexing services
- Maximum visibility for your research

Submit your manuscript at
www.biomedcentral.com/submit



REVIEW

Open Access



Critical review of the safety assessment of nano-structured silica additives in food

Hans Christian Winkler¹, Mark Suter² and Hanspeter Naegeli^{1*}

Abstract

The development of nano-materials is viewed as one of the most important technological advances of the 21st century and new applications of nano-sized particles in the production, processing, packaging or storage of food are expected to emerge soon. This trend of growing commercialization of engineered nano-particles as part of modern diet will substantially increase oral exposure. Contrary to the proven benefits of nano-materials, however, possible adverse health effects have generally received less attention. This problem is very well illustrated by nano-structured synthetic amorphous silica (SAS), which is a common food additive since several decades although the relevant risk assessment has never been satisfactorily completed. A no observed adverse effect level of 2500 mg SAS particles/kg body weight per day was derived from the only available long-term administration study in rodents. However, extrapolation to a safe daily intake for humans is problematic due to limitations of this chronic animal study and knowledge gaps as to possible local intestinal effects of SAS particles, primarily on the gut-associated lymphoid system. This uncertainty is aggravated by digestion experiments indicating that dietary SAS particles preserve their nano-sized structure when reaching the intestinal lumen. An important aspect is whether food-borne particles like SAS alter the function of dendritic cells that, embedded in the intestinal mucosa, act as first-line sentinels of foreign materials. We conclude that nano-particles do not represent a completely new threat and that most potential risks can be assessed following procedures established for conventional chemical hazards. However, specific properties of food-borne nano-particles should be further examined and, for that purpose, in vitro tests with decision-making cells of the immune system are needed to complement existing in vivo studies.

Keywords: Aerosil, Corona, Dendritic cells, E 551, Food toxicology, Lymphoid tissue, Nanomaterial, SAS, Synthetic amorphous silica, Silicium dioxide

Background

The use of nanotechnology has many potentially beneficial applications in food production, processing and storage. The largest share of predicted markets involves nano-sized coatings of food-packaging materials that optimize mechanical properties or exert antimicrobial activity. In the future, nano-sized additives may be deliberately included to modify food properties such as taste, sensation, color, texture, consistency or shelf life, to fortify basic foods with nutrients and vitamins or to enhance bioavailability. An emerging application in the food industry includes, for example, the use of nano-Fe

particles for iron supplementation. Nano-sized materials might further be employed as indicators of food quality and freshness, or to ensure traceability [1–3]. In contrast to these novel developments, nano-structured silica has been on the market as a food additive since around 50 years. In the United States, the Food and Drug Administration allows up to 2 % by weight of such silica particles to be added to food [4]. Within the European Union (EU), Commission Regulation 1129/2011 sets a maximum level for silica of 1 % by weight in dried powdered foodstuffs [5]. Silica particles may thus be regarded as a paradigmatic case for the safety assessment of nano-material applications in the food industry.

A European Commission Recommendation defines nano-materials as having one dimension not exceeding 100 nm [6]. However, there is no solid scientific ground

*Correspondence: naegeli@vetpharm.uzh.ch

¹ Institute of Pharmacology and Toxicology, University of Zurich-Vetsuisse, Winterthurerstrasse 260, 8057 Zurich, Switzerland

Full list of author information is available at the end of the article

to propose a strict size boundary and the prefix “nano” does not make a substance automatically harmful. Nevertheless, the nano-size scale changes the material characteristics as compared to larger particles or the same substance in a dissolved state. Nano-sized materials display an increased surface-to-mass ratio that enhances their reactivity compared to larger structures [7, 8]. Also, nano-sized particles easily penetrate intact cell membranes thus conferring the potential for trafficking across biological barriers including the epithelium of the gastrointestinal tract [9–13]. Until now, the health effects of nano-particles have been studied mainly in relation to a respiratory uptake [14]. Considering their widespread food-related uses, however, there is an urgent need to review the suitability of oral toxicity and risk assessment studies addressing the long-term safety of nano-structured silica.

Synthetic amorphous silica

Silicon (Si) is a metalloid displaying an atomic weight of 28. The terms “silicium” and “silica” refer to naturally occurring or anthropogenic materials composed of silicon dioxide (SiO₂), which appears in two major forms, i.e., crystalline and amorphous. Synthetic amorphous silica (SAS) is widely applied to processed foods and registered by the EU as a food additive with the code E 551 [15]. The main purpose of SAS particles in the food industry is to prevent poor flow or “caking”, particularly in powdered products. SAS particles are additionally employed as a thickener in pastes or as a carrier of flavors, and also to clarify beverages and control foaming [16–18].

Silica particles exist in large amounts in nature and it is acknowledged that they have been dietary constituents throughout human evolution. However, the risk assessment of silica discussed in this review is limited to man-made materials introduced as food additives. In 1942, Harry Kloepfer (a chemist working at Degussa, now Evonik) invented the Aerosil procedure for the production of SAS particles intended for the food industry [19, 20]. Following a standard pyrogenic process, also known as flame hydrolysis, silicon tetrachloride is burned in a hydrogen flame at temperatures of 1000–2500 °C, generating silica nano-particles with a diameter of ~10 nm [21]. This material is denoted pyrogenic or fumed silica referring to the above production method. In an alternative wet route of synthesis, nanostructured SAS particles denoted as precipitated silica, silica gel or hydrous silica, are produced from alkali metal silicates dissolved in water and reacted with sulphuric acid. In the EU, only synthetic particles obtained by these pyrogenic or wet processes are allowed as food additive [15]. All SAS products aggregate into larger particles with sizes in the order

of 100 nm, which further agglomerate to form micron-sized structures [14, 22]. The term “aggregate” describes an assembly of particles held together by strong forces such as covalent or metallic bonds. “Agglomerates” of particles appear as a consequence of weak forces like van der Waals interactions, hydrogen bonding, electrostatic attractions or adhesion by surface tensions. SAS materials are hydrophilic but can be rendered hydrophobic, thus reducing their moisture uptake, by subsequent surface modifications.

Oral toxicity studies using SAS particles

A synopsis of animal studies addressing the oral safety of SAS particles was published by the European Centre for Ecotoxicology and Toxicology of Chemicals (ECETOC) [23] and, more recently, by the Organization for Economic Co-operation and Development (OECD) [24]. No mortality or adverse signs resulted from acute exposure by single oral administrations of hydrophilic SAS particles to rodents at doses of up to 5000 mg per kg body weight. A sub-acute (28-day) study was carried out by oral gavage administration of hydrophilic SAS particles to Wistar rats. The daily doses ranged between 100 and 1000 mg/kg body weight. None of the monitored endpoints (clinical signs, food consumption, body weight, behavioral tests, hematology, clinical chemistry parameters, organ weights, macroscopic pathology and histological examinations) revealed any substance-related abnormalities [25].

In a sub-chronic (90-day) toxicity study carried out in Charles River rats with daily doses of up to 3500 mg/kg body weight, hydrophilic SAS particles included in the feed did not elicit systemic toxicity and did not affect growth rate, food consumption or survival [26]. Also, no macroscopic or microscopic changes were observed in post-mortem analyses of the organs of exposed animals. A more detailed 90-day toxicity study was conducted in Wistar rats with in-diet administrations of hydrophilic SAS particles (up to 4000 mg/kg body weight daily). Endpoints included general condition and survival, behavior, water intake, food consumption, body weight, hematology, clinical chemistry, urinary analysis, organ weights, macroscopic pathology and histological examinations. As observed in the previous sub-chronic study, none of these parameters revealed any effects ascribed to SAS ingestion [27]. Sub-chronic dietary exposure studies were also carried out with hydrophobic SAS particles not permitted as food additive in the EU. In one case [28], no treatment-related abnormalities were reported except minimal changes in the thyroid gland morphology of male rats exposed to 2000 and 4000 mg/kg body weight daily. In another repeated dose toxicity study with hydrophobic SAS particles [29, 30], Wistar rats were exposed

via the diet for 5 weeks at 0 (control), 500 or 1000 mg/kg body weight per day, and for 8 weeks at progressively increasing SAS doses from 2000 to 16,000 mg/kg body weight per day. Animals in these high-dose group developed severe atrophy of the liver detected by microscopic examination, which was also observed to a milder degree in the 1000-mg/kg dose group.

Further effects on the liver were described in more recent reports, thus converging on a potential systemic hazard of SAS particles (Table 1). In one repeated oral toxicity study, BALB/c mice were exposed for 10 weeks to hydrophilic nano- or micron-sized silica particles prepared from rice husk (not permitted as food additive in the EU) [31]. The inclusion rate in feed was 1 % (wt/wt) translating to an expected oral uptake of 1500 mg/kg body weight per day. The animal group fed the nano-particles showed a significantly higher serum level of alanine aminotransferase (a biomarker of liver injury) compared to untreated controls or animals tested with micro-sized silica. In the histologic examination of tissues from mice exposed to nano-particles, but not in those exposed to micro-particles, there was an appearance of fatty liver characterized by abnormally frequent lipid droplets in hepatocytes. Further liver reactions were detected in a repeated dose toxicity study in Sprague–Dawley rats [32]. The animals were exposed via feed to hydrophilic SAS particles obtained from Evonik (denoted “Evonik-SAS”) or from the Joint Research Centre of the European Commission (denoted “JRC-SAS”). Both materials were produced by flame hydrolysis but differed in their surface area, i.e., 380 and 200 m²/g for “Evonik-SAS” and “JRC-SAS”, respectively. These particles were delivered with the feed at different daily doses (between 100 and 2500 mg/kg body weight) for 28 days, whereby the exposure was extended to 84 days for the highest dose groups. No treatment-related effects were observed after 28 days. However, following 84 days of exposure, the occurrence of periportal liver fibrosis was higher than in control animals (Table 1). This increase in the frequency of liver fibrosis was significant in the JRC-SAS-treated animals ($p = 0.02$) but slightly below statistical significance ($p = 0.07$) in the Evonik-SAS-treated group. The

histological effects were not accompanied by changes in clinical chemistry. Notably, this experiment also included some immunological parameters like IgG and IgM levels in blood, lymphocyte proliferation, as well as cytokine release from in vitro activated lymphocytes. None of the tested immunological endpoints were affected in any of the dose groups.

Long-term dietary studies in rats [33] were used for the risk assessment of human exposure. Groups of 40 Fischer rats were fed 0 (control), 1.25, 2.5 and 5 % (wt/wt) hydrophilic SAS particles for 103 consecutive weeks. The design of this chronic bioassay is outlined for the high-dose group in Table 2. The feed was not examined for possible nutritional imbalances [34]. There were no test substance-related effects on food consumption, overall survival, clinical laboratory or hematologic results and microscopic pathology findings. Liver weights were significantly reduced in the females fed 2.5 and 5 % SAS particles and this effect might be a consequence of the lower body weight attained in these two higher dose groups relative to controls and animals in the 1.25 % inclusion group. It is retrospectively not possible to distinguish whether the effect on liver weight represents an adverse reaction to SAS ingestion or whether it is an indirect consequence of a possible nutritional imbalance not directly related to SAS exposure. Notably, SAS-treated males displayed isolated cases of hyperplastic nodules in the liver and pheochromocytomas in the adrenal gland, but none of the control animals had such rare lesions. A long-term study in B6C3F1 mice involved groups of 40 animals fed 0 (control), 1.25, 2.5 and 5 % (wt/wt) SAS particles for 93 weeks [33]. Again, the feed was not examined for nutritional imbalances. The growth rate was significantly reduced in the mice of the high-dose group only at the end of the first 10 study weeks. Food consumption was significantly increased in the males fed 2.5 and 5 % SAS particles but no other substance-related differences came to light. The treatment had no effect on clinical chemistry, hematologic results and macroscopic as well as microscopic pathology findings. Recently, the European Commission Scientific Committee on Consumer Safety pointed out that these long-term studies

Table 1 Oral repeated dose toxicity studies with amorphous silica yielding liver effects

Species	Study length	Effect	LOAEL	NOAEL	Reference
Wistar rats	5–8 weeks	Liver atrophy	1000 mg/kg body weight per day	500 mg/kg body weight per day	[29, 30]
Balb/c mice	10 weeks	Fatty liver	1500 mg/kg body weight per day	NA	[31]
Sprague–Dawley rats	12 weeks	Periportal liver fibrosis	810 mg/kg body weight per day	NA	[32]
Fischer rats	103 weeks	Reduced liver weight	1000 mg/kg body weight per day	500 mg/kg body weight per day	[33]

Delivery of particles was by inclusion into the feed. This table proposes LOAEL (lowest observed adverse effect level) and NOAEL (no observed adverse effect level) values that differ from those purported in previous risk assessment reports. Other oral repeated dose studies [25–27] did not elicit adverse effects

Table 2 Outline of the chronic toxicity study with SAS particles carried out in rats

	Weeks of feeding						
	0	5	15	30	50	81	103
Body weight (g)	108 ± 6	174 ± 9	223 ± 11	253 ± 10	310 ± 18	364 ± 26	359 ± 56
Feed intake (g/day)		11.1 ± 0.4	10.4 ± 0.4	10.2 ± 0.5	11.9 ± 0.8	13.2 ± 0.8	12.7 ± 2.7
SAS intake (g/kg body weight per day)		3.2	2.3	2.0	1.9	1.8	1.8

Summarized data from the oral chronic toxicity study in Fischer rats [33]. This table illustrates the relationship between body weight, feed intake and daily doses in the females of the highest dose group, where the feed was supplemented with 5 % (wt/wt) SAS particles. When corrected for the actual feed intake, the daily dose of SAS particles was between 1.8 and 2.0 g/kg body weight during most of the study period

in rodents cannot be considered as adequate for risk assessment because it is not clear whether the research was conducted under generally accepted guidelines and because the test material was not properly described [35].

To summarize, a critical analysis of existing oral repeated dose studies in rodents reveals data gaps and uncertainties limiting their predictive value for the risk assessment of human dietary exposure. Some studies were based on poorly characterized particles in terms of composition, impurities or physico-chemical properties, and most reports lacked an assessment of particle size distribution.

Oral bioavailability and systemic distribution

Little is known on the intestinal absorption of nano-sized SAS particles and the potential to disseminate into tissues. A limited systemic uptake following oral ingestion cannot be ruled out although none of the tested SAS particles were shown to bio-accumulate [19]. This is illustrated by a repeated dose kinetic study, in which rats were administered SAS particles via gavage at a low dose of 20 mg/kg body weight during 5 consecutive days [36, 37]. On the sixth day of the study, measurements by quadrupole inductively coupled plasma mass spectrometry (ICP-MS) revealed only slightly elevated silicon levels in liver and spleen. The gastrointestinal absorption after administration of SAS particles, estimated from these silicon measurements in tissues and not considering a concurrent excretion, ranged between 0.03 and 0.06 % of the total oral dose [38]. In another repeated dose study already presented above, rats were administered SAS particles via feed for 28 days, with continued administration in the high-dose group for up to 84 days. Silicon contents were measured at days 29 and 84 by ICP-MS in liver, spleen, kidney, brain and testis. Conversion of the resulting silicon levels to assumed silica concentrations in tissues, again not considering concomitant excretion processes, indicated an overall oral bioavailability of 0.02 % or less [32]. The highest silica concentration (up to ~300 mg/kg tissue against a physiologic background below the limit of detection) was found in the spleen of SAS-exposed animals. So far, no SAS particles have been

detected in mesenteric lymph nodes or any other organ after oral uptake and, therefore, it is not clear whether the observed silicon residues exist in a particulate form or rather in a dissolved state, for example as orthosilicic acid.

Another key issue that has not yet been investigated with regard to bioavailability and systemic distribution is the effect of biomolecules bound to nano-particles changing their surface properties [38]. In particular, SAS nano-particles are known to be decorated by proteins, for example fibrinogen or apolipoprotein A1, as soon as they get in contact with biological fluids [39]. The term “protein corona” was introduced to describe the attachment of plasma proteins to the surface of nano-particles [40, 41]. One possible effect of this corona is that it mediates the uptake of nano-particles into cells and organs including the liver, thus influencing bioavailability and tissue distribution [42].

Human exposure

To obtain realistic dietary exposure values for a European population, Dekkers and colleagues [18] selected food products from a local supermarket (ready-to-eat meals, soups, sauces, coffee creamers, pancake mixes, seasonings and supplements) based on declarations for the presence of E 551. Next, the total silica concentration in these products was determined by inductively coupled plasma atomic emission spectrometry (ICP-AES). Then, dietary intake estimates of these products for the population were calculated using a Dutch food consumption survey [43]. Based on estimated consumption and silica levels, the resulting daily dietary intake was 9.4 mg SAS particles per kg body weight. This total daily quantity includes all SAS particles regardless of their degree of aggregation or agglomeration. Hydrodynamic chromatography with inductively coupled plasma mass spectrometry (HDC-ICPMS) showed that up to ~40 % of SAS particles detected in food products display an external diameter <200 nm [18].

The next question was whether the SAS particles in commercial food products would be destroyed in the digestive tract or rather withstand gastrointestinal

conditions. Using an in vitro system mimicking human gastric digestion, it could be demonstrated that nano-structured silica forms agglomerates under acidic conditions resembling the milieu of the stomach. By switching the conditions to those imitating the subsequent intestinal digestion stage, however, these large agglomerates disintegrate readily into nano-sized silica structures. In light of these in vitro findings, it was concluded that up to ~80 % of orally ingested SAS particles withstand gastric dissolution and display a nano-sized range once they reach the intestinal lumen [44].

Inadequacies of existing risk assessments

Nano-particles are neither inherently toxic nor inherently safe and possible adverse effects should be tested case-by-case. In principle, a standard assessment with $\text{risk} = \text{hazard} \times \text{exposure}$, which includes hazard identification, hazard characterization, exposure assessment and risk characterization, is applicable to nano-materials in food [21, 45, 46].

The United Kingdom Food Standards Agency Expert group on Vitamins and Minerals (EVM) performed an assessment of the oral safety of SAS particles, yielding a safe upper dietary level for daily consumption of 1500 mg SAS particles per day for adults [34]. This upper safety limit was calculated from the only available long-term toxicity study in rats [33], despite its limitations recently reiterated by the Scientific Committee on Consumer Safety [35]. The EVM experts noted that oral exposure to SAS particles for 103 consecutive weeks elicited effects on body weight and absolute liver weight (concerning the groups with a 2.5 and 5 % dietary inclusion rate). However, they attributed this outcome to possible nutritional imbalances, not adjusted in these two higher dose groups and considered unlikely to be relevant for humans. On this basis, the EVM group concluded that the no observed adverse effect level (NOAEL) is equivalent to the highest dose tested, i.e. 5 % SAS (wt/wt) in the diet. In the absence of further information or studies explaining the reduction in body and liver weight, we advocate a more cautious approach by deriving from the same study a lower NOAEL equivalent to the 1.25 % inclusion rate, also in view of the emergence of liver hyperplastic nodules and adrenal pheochromocytomas recorded in a few SAS-treated males but never in controls [33]. This more cautious interpretation is supported by a recent, above-described study [32] revealing periportal liver fibrosis in SAS-exposed rats.

As indicated, the EVM expert group opted for a NOAEL of 5 % dietary inclusion and further estimated that this translates by default to a daily dose of 2.5 g/kg body weight. After introducing an uncertainty factor of 100 (to adjust for inter-species as well as inter-individual

variations in sensitivity), the derived safe upper level for lifetime daily consumption of SAS particles was 25 mg/kg per day, equivalent to 1500 mg per day for a 60-kg adult. In terms of elemental silicon, the “safe” upper limit for daily consumption is 12 mg/kg body weight per day (equivalent to 700 mg for a 60-kg adult). In 2004, the Scientific Panel on Dietetic Products, Nutrition and Allergies (NDA Panel) at the European Food Safety Authority concluded for silicon that “there are no suitable data for dose—response for establishment of an upper level” [47]. In 2009, however, the Scientific Panel on Food Additives and Nutrient Sources added to Food (ANS Panel) took into consideration the risk assessment carried out by the EVM experts and adopted their proposed upper limit of 1500 mg per day when assessing silicon dioxide as food additive [46]. It remains to be mentioned that default intake calculations made by translating a 5 % inclusion in the feed of rats to an assumed ingestion of 2.5 g/kg per day seem incorrect as the actual daily dose of SAS particles, determined from feed consumption in the high-dose group, was around 1.9 g/kg body weight during most of the study period (Table 2). Similarly, the lower inclusion rates of 1.25 and 2.5 % correspond to daily oral doses of around 0.5 and 1 g/kg, respectively. To summarize, several gaps in both study design and interpretation of results diminish the predictability of the only available long-term bioassays in rodents addressing the oral safety of SAS particles.

Potential for local effects in the gastrointestinal tract

Depending on the nature of identified hazards that raise concerns, the canonical risk characterization may need to be complemented with endpoints that are not routinely assessed in the toxicological evaluation of chemicals. For example, a nano-Trojan horse hypothesis has previously been proposed in view of the observation that, in human lung epithelial cells exposed to Co_3O_4 or Mn_3O_4 nano-particles, the generation of reactive oxygen species (ROS) was higher than in controls exposed to an equivalent concentration of dissolved cobalt or manganese salts [10]. It is equally conceivable that the binding of luminal antigens to SAS particles could aid their delivery to reactive cells of the gastrointestinal tract. In this respect, we note in particular that none of the above-reviewed studies examined local effects on the lymphoid tissue of the gastrointestinal mucosa. Rather than causing ROS production, SAS particles have been implicated in the release of pro-inflammatory cytokines (see below).

Although the function of the immune system is to safeguard the host against invasive pathogens, the steady-state gastrointestinal tract is geared towards immune silencing or tolerance to avoid futile reactions

to innocuous food antigens and beneficial commensal microorganisms [48, 49]. Upon oral exposure, foreign particles encounter a single layer of mucous membrane lining the digestive tract. This large vulnerable surface is defended by the gut-associated lymphoid tissue, which consists of loosely organized clusters of lymphoid cells and more organized Peyer's patches. Nano-particles including those made of silica are known to penetrate this lymphoid tissue underlying the epithelial barrier [50–53], where they may disrupt the critical balance between tolerance to harmless food constituents and commensals on the one hand and inflammatory reactions towards pathogens on the other hand [54, 55]. Specific analyses of Peyer's patches are not mentioned in the available sub-chronic and chronic toxicity studies in rodents and, therefore, it is not possible to ascertain whether delayed local effects on the gut-associated lymphoid system were adequately excluded.

Previous studies highlighted the fact that there is one critical site in which food-borne nano-particles accumulate during lifelong exposure, i.e., in “pigment cells” of the gut-associated lymphoid tissue where the earliest signs of inflammatory bowel disease (IBD) are noted (reviewed in [56–58]). This is a wide group of chronic conditions ranging from Crohn's disease (affecting all segments of the digestive tract) to ulcerative colitis (restricted to the large bowel, [59]). The main gatekeepers of tolerance in the intestinal system, as well as major mediators of adverse reactions like IBD, are specialized antigen-presenting cells known as dendritic cells [60]. They act as scavengers of foreign materials by extending branched and rapidly changing projections across the epithelial barrier into the gut lumen and taking up particles by endocytosis [61]. Particles are also delivered directly to dendritic cells after their passage through microfold cells (M-cells) in the intestinal mucosa. In this way, dendritic cells filter out a volume of up to 1500 μm^3 , which equals their own cell volume, per hour [62]. Unlike other antigen-presenting cells, dendritic cells constitutively express class II major histocompatibility complexes and, in response to pathogen recognition, display co-stimulatory surface glycoproteins and produce inflammatory cytokines. For these reasons, dendritic cells constitute potent activators of the innate immune system and also polyvalent drivers of T lymphocytes [63, 64]. As nano-particles are in the same size range as many proteins or common viruses, it is not surprising to find that, by virtue of their function in probing the environment for intruding insults, dendritic cells capture nano-particles in an efficient manner [65–67].

It was shown that endotoxin-activated dendritic cells release the potent pro-inflammatory cytokine interleukin-1 β (IL-1 β) upon incubation with SAS nano-particles [68]. Mechanistically, this response has been

linked to activation of the inflammasome complex, which in turn cleaves the pro-IL-1 β precursor protein to release active IL-1 β . In view of this finding, it will be of pivotal importance to determine how steady-state dendritic cells like those residing in the normal non-inflammatory intestinal mucosa react to the presence of food-borne SAS particles. IBD has a multi-factorial origin with genetic susceptibility, gut microflora and a dysfunction of the mucosal immune system as main drivers [60]. Additionally, various dietary factors have been implicated in the increasing incidence of IBD and several authors raised the concern that food-borne nano-particles may contribute to initiating this chronic inflammatory disease [69–71]. Inadvertent stimulation of the immune system by nano-particles could trigger a reaction sequence that abrogates tolerance to food constituents and commensal bacteria and thereby favor immune-mediated conditions with the hallmarks of IBD (reviewed by [72]).

Conclusions

Previous and current controversies on hormone or antibiotic residues in food illustrate that nutrition is a highly emotional area in the public perception. The finding that SAS particles activate the inflammasome and, hence, are not biologically inert is intriguing because this type of nano-structured material has been employed since decades as food additive and is so far considered to be safe for consumers. Based on a critical review of existing oral toxicity studies, however, we consider that adverse effects from food-borne SAS particles cannot be excluded. Table 1 summarizes independent repeated dose studies that reached much the same conclusion with an oral NOAEL of 500 mg per kg body weight and a lowest observed adverse effect level (LOAEL) in the range of 810–1500 mg per kg body weight. Therefore, we advocate a prudent approach by taking the oral NOAEL of 500 mg/kg, based on body and liver weights in the 103-week feeding study in rats, as point of departure for the risk assessment of SAS particles. This NOAEL is lower than previously proposed [34] but, as summarized in Table 1, is consistent with the outcome (liver atrophy) of a 8-week feeding study and the liver effects (periportal fibrosis) in a 12-week feeding study, both in rats, at daily doses of 810–1000 mg/kg body weight. By applying a default uncertainty factor of 100 (to adjust for inter-species and inter-individual variations in sensitivity), this NOAEL would yield a safe upper level for the lifetime intake of SAS particles of 5 mg/kg body weight per day. The estimated consumption by a European population of 9.4 mg per kg body weight and day would, therefore, suggest that the dietary exposure to SAS particles should be reduced to remain, even with a worst case exposure scenario, below this newly proposed safety threshold of

5 mg/kg daily. Importantly, further studies are needed to investigate local effects of SAS particles in the gastrointestinal system, particularly on the gut-associated lymphoid tissue and embedded dendritic cells. In a broader perspective, mechanistic in vitro studies at different levels of biological complexity are necessary to understand in depth how food-borne nano-particles may influence the delicate balance between immune tolerance and inflammatory responses that depends on the proper function of dendritic cells in the intestinal mucosa. This research direction is crucial to eventually address the concern that the higher occurrence of IBD may be in part a consequence of the lifelong ingestion of nano-sized or nano-structured food additives increasingly used in the modern diet.

Abbreviations

ANS: Scientific Panel on Food Additives and Nutrient Sources added to Food; E 551: synthetic amorphous silica (food additive); ECETOC: European Centre for ecotoxicology and toxicology of chemicals; EU: European Union; EVM: Food Standards Agency Expert group on vitamins and minerals; HDC-ICPMS: hydrodynamic chromatography with inductively coupled plasma mass spectrometry; IBD: inflammatory bowel disease; ICP-AES: inductively coupled plasma atomic emission spectrometry; Ig: immunoglobulin; IL-1 β : interleukin-1 β ; JRC: Joint Research Centre of the European Commission; LOAEL: lowest observed adverse effect level; NDA: Scientific Panel on dietetic products, nutrition and allergies; NOAEL: no observed adverse effect level; OECD: Organization for Economic Co-operation and Development; ROS: reactive oxygen species; SAS: synthetic amorphous silica.

Authors' contributions

HCW, HN and MS wrote the manuscript. All authors read and approved the final manuscript.

Author details

¹ Institute of Pharmacology and Toxicology, University of Zurich-Vetsuisse, Winterthurerstrasse 260, 8057 Zurich, Switzerland. ² Immunology Division, Vetsuisse Faculty, University of Zurich, Winterthurerstrasse 260, 8057 Zurich, Switzerland.

Acknowledgements

Research in the author's laboratory was supported by the National Research Program "Opportunities and Risks of Nanomaterials" Grant 406440-141619 and by grant FK-15-053 from the "Forschungskredit" of the University of Zurich.

Competing interests

The authors declare that they have no competing interests.

Received: 1 December 2015 Accepted: 3 May 2016

Published online: 10 June 2016

References

- Chaudhry Q, Scotter M, Blackburn J, Ross B, Boxall A, Castle L, et al. Applications and implications of nanotechnologies for the food sector. *Food Addit Contam Part A*. 2008;25:241–58.
- Puddu M, Paunescu D, Stark WJ, Grass RN. Magnetically recoverable, thermostable, hydrophobic DNA/silica encapsulates and their application as invisible oil tags. *ACS Nano*. 2014;8:2677–85.
- Hilty FM, Arnold M, Hilbe M, Teleki A, Knijnenburg JTN, Ehrensperger F, et al. Iron from nanocompounds containing iron and zinc is highly bioavailable in rats without tissue accumulation. *Nat Nanotechnol*. 2010;5:374–80.
- US FDA 2015. United States Food and Drug Administration. Code of Federal Regulations Title 21, 21CFR172.480. 2015. <http://www.accessdata.fda.gov/scripts/cdrh/cfdocs/cfCFR/CFRSearch.cfm?fr=172.480>. Accessed 25 Apr 2016.
- Union European. Commission regulation (EU) No 1129/2011 of 11 November 2011 amending Annex II to Regulation (EC) No 1333/2008 of the European Parliament and of the Council by establishing a Union list of food additives. *Off J Eur Union*. 2011;295:1–177.
- Union European. Commission recommendation of 18 October 2011 on the definition of nanomaterial (2011/696/EU). *Off J Eur Union*. 2011;275:38–40.
- Oberdörster G. Toxicology of ultrafine particles: in vivo studies. *Philos Trans R Soc A Math Phys Eng Sci*. 2000;358:2719–40.
- Donaldson K, Stone V, Clouter A, Renwick L, MacNee W. Ultrafine particles. *Occup Environ Med*. 2001;58:211–6.
- Oberdörster G, Sharp Z, Atudorei V, Elder A, Gelein R, Kreyling W, et al. Translocation of inhaled ultrafine particles to the brain. *Inhal Toxicol*. 2004;16:437–45.
- Limbach LK, Li Y, Grass RN, Brunner TJ, Hintermann MA, Müller M, et al. Oxide nanoparticle uptake in human lung fibroblasts: effects of particle size, agglomeration, and diffusion at low concentrations. *Environ Sci Technol*. 2005;39:9370–6.
- Lankveld DPK, Van Loveren H, Baken KA, Vandebriel RJ. In vitro testing for direct immunotoxicity: state of the art. *Methods Mol Biol*. 2010;598:401–23.
- Landsiedel R, Fabian E, Ma-Hock L, van Ravenzwaay B, Wohlleben W, Wiench K, et al. Toxicology/biokinetics of nanomaterials. *Arch Toxicol*. 2012;86:1021–60.
- Mou Y, Chen B, Zhang Y, Hou Y, Xie H, Xia G, et al. Influence of synthetic superparamagnetic iron oxide on dendritic cells. *Int J Nanomedicine*. 2011;6:1779–86.
- Napierska D, Thomassen LC, Lison D, Martens JA, Hoet PH. The nanosilica hazard: another variable entity. *Part Fibre Toxicol*. 2010;7:39.
- European Union. Commission Regulation (EU) No 231/2012 of 9 March 2012 laying down specifications for food additives listed in Annexes II and III to Regulation (EC) No 1333/2008 of the European Parliament and of the Council. *Off J Eur Union*. 2012;2012(83):1–295.
- Marinova KG, Denkov ND, Branlard P, Giraud Y, Deruelle M. Optimal hydrophobicity of silica in mixed oil-silica antifoams. *Langmuir*. 2002;18:3399–403.
- Wang P, Zhu Y, Yang X, Chen A. Prolonged-release performance of perfume encapsulated by tailoring mesoporous silica spheres. *Flavour Fragr J*. 2008;23:29–34.
- Dekkers S, Krystek P, Peters RJB, Lankveld DPK, Bokkers BGH, van Hoeven-Arentzen PH, et al. Presence and risks of nanosilica in food products. *Nanotoxicology*. 2011;5:393–405.
- Fruijtier-Pöloth C. The toxicological mode of action and the safety of synthetic amorphous silica-a nanostructured material. *Toxicology*. 2012;294.
- Maynard AD. Old materials, new challenges? *Nat Nanotechnol*. 2014;9:658–9.
- SCENIHR 2007. Scientific Committee on Emerging and Newly-Identified Health Risks. The existing and proposed definitions relating to products of nanotechnologies, 29 November 2007. http://ec.europa.eu/health/archive/ph_risk/committees/04_scenihr/docs/scenihr_o_012.pdf. Accessed 25 Apr 2016.
- ELC 2009. Federation of European Food Additives; Food enzymes and food cultures industries. food additives and nanotechnologies. 2009. http://elc-eu.org/uploads/news_documents/2009-10_Food_additives_and_nanotechnologies_-_ELC_position.pdf. Accessed 25 Apr 2016.
- ECETOC 2006. European Centre for Ecotoxicology and Toxicology of Chemicals. Synthetic Amorphous Silica (CAS No. 7631-86-9), JACC REPORT No. 51. 2006. <http://members.ecetoc.org/Documents/Document/JACC051.pdf>. Accessed 25 Apr 2016.
- OECD 2015. Organization for economic co-operation and development. Dossier on silicon dioxide, Series on the safety of manufactured nanomaterials No. 51. 2015. <http://www.oecd.org/chemicalsafety/nanosafety/silicon-dioxide-manufactured-nanomaterial.htm>. Accessed 25 Apr 2016.
- Lewin G. 28-day oral toxicity study of synthetic amorphous silica in wistar (WU) rats. CEFIC, Brussels, Belgium. 2011. Unpublished report, described in OECD 2015. <http://www.oecd.org/chemicalsafety/nanosafety/silicon-dioxide-manufactured-nanomaterial.htm>. Accessed 25 Apr 2016.

26. Elsea JR. Cab-O-Sil (fluffy), ninety-day dietary feeding, supplement to progress reports dated January 8, and May 6, 1958, final report. Hazleton Laboratories, Falls Church, Virginia. Cabot, Tuscula, Illinois, USA. 1958. Unpublished report, described in SCCS 2015. http://ec.europa.eu/health/scientific_committees/consumer_safety/docs/sccs_o_175.pdf. Accessed 25 Apr 2016.
27. Til H, Hollanders M, Beems R. Subchronic (13 week) oral toxicity study in rats. Evonik Degussa, Germany. 1981. Unpublished report, described in OECD 2015. <http://www.oecd.org/chemicalsafety/nanosafety/silicon-dioxide-manufactured-nanomaterial.htm>. Accessed 25 Apr 2016.
28. Rutter HA, Shott LD. 13-week dietary administration - rats, silane-treated Cab-O-Sil, final report, project 178-114. Hazleton Laboratories, Falls Church, Virginia. Cabot, Billerica, MA, USA. 1970. Unpublished report, described in ECETOC 2006. <http://members.ecetoc.org/Documents/Document/JACC051.pdf>. Accessed 25 Apr 2016.
29. Leuschner F. Über die subakute Toxizität von R972. Degussa, Hanau, Germany. 1964. Unpublished report, described in ECETOC 2006. http://members.ecetoc.org/Documents/Document/JACC_051.pdf. Accessed 25 Apr 2016.
30. Pliess G. Histologische Befunde bei Versuchsratten, Medikament R972. Laboratorium für Pharmakologie und Toxikologie, Hamburg, Germany. Degussa, Frankfurt am Main, Germany. 1964. Unpublished report, described in ECETOC 2006. <http://members.ecetoc.org/Documents/Document/JACC051.pdf>. Accessed 25 Apr 2016.
31. So SJ, Jang IS, Han CS. Effect of micro/nano silica particle feeding for mice. *J Nanosci Nanotechnol*. 2008;8:5367–71.
32. van der Zande M, Vandebril RJ, Groot MJ, Kramer E, Herrera Rivera ZE, Rasmussen K, et al. Sub-chronic toxicity study in rats orally exposed to nanostructured silica. *Part Fibre Toxicol*. 2014;11:8.
33. Takizawa Y, Hirasawa F, Noritomi E, Aida M, Tsunoda H, Uesugi S. Oral ingestion of silyd to mice and rats and its chronic toxicity and carcinogenicity. *Acta Med Biol*. 1988;36:27–56.
34. UK Food Standards Agency 2003. Safe upper levels for vitamins and minerals: report of the expert group on vitamins and minerals. 2003. <http://cot.food.gov.uk/sites/default/files/vitamin2003.pdf>. Accessed 25 Apr 2016.
35. SCCS 2015. Scientific Committee on Consumer Safety. Opinion on silica, hydrated silica, and silica surface modified with alkyl silylates (nano form). 2015. http://ec.europa.eu/health/scientific_committees/consumer_safety/docs/sccs_o_175.pdf. Accessed 25 Apr 2016.
36. van Kesteren PCE, Cubadda F, Bouwmeester H, van Eijkeren JCH, Dekkers S, de Jong WH, et al. Novel insights into the risk assessment of the nano-material synthetic amorphous silica, additive E551, in food. *Nanotoxicology*. 2015;9:442–52.
37. NANOGENOTOX 2013. Facilitating the safety evaluation of manufactured nanomaterials by characterising their potential genotoxic hazard. 2013. http://www.nanogenotox.eu/index.php?option=com_content&view=article&id=136&Itemid=158. Accessed 25 Apr 2016.
38. Nel AE, Mädler L, Velegol D, Xia T, Hoek EMV, Somasundaran P, et al. Understanding biophysics/chemical interactions at the nano-bio interface. *Nat Mater*. 2009;8:543–57.
39. Ruh H, Kühl B, Brenner-Weiss G, Hopf C, Diabaté S, Weiss C. Identification of serum proteins bound to industrial nanomaterials. *Toxicol Lett*. 2012;208:41–50.
40. Cedervall T, Lynch I, Lindman S, Berggard T, Thulin E, Nilsson H, et al. Understanding the nanoparticle-protein corona using methods to quantify exchange rates and affinities of proteins for nanoparticles. *Proc Natl Acad Sci U S A*. 2007;104:2050–5.
41. Lundqvist M, Stigler J, Elia G, Lynch I, Cedervall T, Dawson KA. Nanoparticle size and surface properties determine the protein corona with possible implications for biological impacts. *Proc Natl Acad Sci U S A*. 2008;105:14265–70.
42. Nagayama S, Ogawara K, Kukuoka Y, Higaki K, Kimura T. Time-dependent changes in opsonin amount associated on nanoparticles alter their hepatic uptake characteristics. *Int J Pharm*. 2007;342:215–21.
43. Kistemaker C, Bouman M, Hulshof K. Consumption of separate products by Dutch population groups-Dutch National Food Consumption Survey 1997–1998. Zeist, TNO-Nutrition Food Res Institute, TNO-report. 1998;98:812.
44. Peters R, Kramer E, Oomen AG, Herrera Rivera ZE, Oegema G, Tromp PC, et al. Presence of nano-sized silica during in vitro digestion of foods containing silica as a food additive. *ACS Nano*. 2012;6:2441–51.
45. Warheit DB. How meaningful are the results of nanotoxicity studies in the absence of adequate material characterization? *Toxicol Sci*. 2008;101:183–5.
46. European Food Safety Authority. Scientific opinion of the panel on food additives and nutrient sources added to food on calcium silicate, silicon dioxide and silicic acid gel added for nutritional purposes to food supplements following a request from the European Commission. EFSA J. 2009;1132:1–24.
47. European Food Safety Authority. Opinion of the Scientific Panel on Dietetic Products, nutrition and allergies on a request from the commission related to the tolerable upper intake level of silicon (Request N° EFSA-Q-2003-018). EFSA J. 2004;60:1–11.
48. Ley RE, Hamady M, Lozupone C, Turnbaugh PJ, Ramey RR, Bircher JS, et al. Evolution of mammals and their gut microbes. *Science*. 2008;320:1647–51.
49. Bogunovic M, Ginhoux F, Helft J, Shang L, Hashimoto D, Greter M, et al. Origin of the lamina propria dendritic cell network. *Immunity*. 2009;31:513–25.
50. Sass W, Dreyer HP, Seifert J. Rapid insorption of small particles in the gut. *Am J Gastroenterol*. 1990;85:255–60.
51. des Rieux A, Fievez V, Garinot M, Schneider Y-J, Pr  at V. Nanoparticles as potential oral delivery systems of proteins and vaccines: a mechanistic approach. *J Control Release*. 2006;116:1–27.
52. Awaad A, Nakamura M, Ishimura K. Imaging of size-dependent uptake and identification of novel pathways in mouse Peyer's patches using fluorescent organosilica particles. *Nanomedicine*. 2012;8:627–36.
53. Powell JJ, Thomas-McKay E, Thoree V, Robertson J, Hewitt RE, Skepper JN, et al. An endogenous nanomineral chaperones luminal antigen and peptidoglycan to intestinal immune cells. *Nat Nanotechnol*. 2015;10:361–9.
54. Bekiaris V, Persson EK, Agace WW. Intestinal dendritic cells in the regulation of mucosal immunity. *Immunol Rev*. 2014;260:86–101.
55. Toda T, Yoshino S. Amorphous nanosilica particles block induction of oral tolerance in mice. *J Immunotoxicol*. 2016;18:1–6.
56. Evans SM, Ashwood P, Warley A, Berisha F, Thompson RPH, Powell JJ. The role of dietary microparticles and calcium in apoptosis and interleukin-1  release of intestinal macrophages. *Gastroenterology*. 2002;123:1543–53.
57. Lomer MCE, Thompson RPH, Powell JJ. Fine and ultrafine particles of the diet: influence on the mucosal immune response and association with Crohn's disease. *Proc Nutr Soc*. 2002;61:123–30.
58. Mazmanian SK, Round JL, Kasper DL. A microbial symbiosis factor prevents intestinal inflammatory disease. *Nature*. 2008;453:620–5.
59. Lucendo AJ, De Rezende LC. Importance of nutrition in inflammatory bowel disease. *World J Gastroenterol*. 2009;15:2081–8.
60. Bates J, Diehl L. Dendritic cells in IBD pathogenesis: an area of therapeutic opportunity? *J Pathol*. 2014;232:112–20.
61. Rescigno M. Before they were gut dendritic cells. *Immunity*. 2009;31:454–6.
62. Sallusto F, Cella M, Danieli C, Lanzavecchia A. Dendritic cells use macropinocytosis and the mannose receptor to concentrate macromolecules in the major histocompatibility complex class II compartment: downregulation by cytokines and bacterial products. *J Exp Med*. 1995;182:389–400.
63. Steinman RM, Lustig DS, Cohn ZA. Identification of a novel cell type in peripheral lymphoid organs of mice. 3. Functional properties in vivo. *J Exp Med*. 1974;139:1431–45.
64. Banchereau J, Steinman RM. Dendritic cells and the control of immunity. *Nature*. 1998;392:245–52.
65. Manolova V, Flace A, Bauer M, Schwarz K, Saudan P, Bachmann MF. Nanoparticles target distinct dendritic cell populations according to their size. *Eur J Immunol*. 2008;38:1404–13.
66. Li A, Qin L, Zhu D, Zhu R, Sun J, Wang S. Signalling pathways involved in the activation of dendritic cells by layered double hydroxide nanoparticles. *Biomaterials*. 2010;31:748–56.
67. M  ller L, Riediker M, Wick P, Mohr M, Gehr P, Rothen-Rutishauser B. Oxidative stress and inflammation response after nanoparticle exposure: differences between human lung cell monocultures and an advanced three-dimensional model of the human epithelial airways. *J R Soc Inter-face*. 2010;7(Suppl 1):S27–40.
68. Winter M, Beer H-D, Hornung V, Kr  mer U, Schins RPF, F  rster I. Activation of the inflammasome by amorphous silica and TiO2 nanoparticles in murine dendritic cells. *Nanotoxicology*. 2011;5:326–40.

69. Tetley TD. Health effects of nanomaterials. *Biochem Soc Trans*. 2007;35:527–31.
70. Powell JJ, Faria N, Thomas-McKay E, Pele LC. Origin and fate of dietary nanoparticles and microparticles in the gastrointestinal tract. *J Autoimmun*. 2010;34:J226–33.
71. Hummel TZ, Kindermann A, Stokkers PCF, Benninga MA, ten Kate FJW. Exogenous pigment in Peyer patches of children suspected of having IBD. *J Pediatr Gastroenterol Nutr*. 2014;58:477–80.
72. Zolnik BS, González-Fernández Á, Sadrieh N, Dobrovolskaia MA. Nanoparticles and the immune system. *Endocrinology*. 2010;151:458–65.

Submit your next manuscript to BioMed Central and we will help you at every step:

- We accept pre-submission inquiries
- Our selector tool helps you to find the most relevant journal
- We provide round the clock customer support
- Convenient online submission
- Thorough peer review
- Inclusion in PubMed and all major indexing services
- Maximum visibility for your research

Submit your manuscript at
www.biomedcentral.com/submit



RESEARCH

Open Access



Photoinduced effects of m-tetrahydroxyphenylchlorin loaded lipid nanoemulsions on multicellular tumor spheroids

Doris Hinger^{1*} , Fabrice Navarro^{2,3}, Andres Käch⁴, Jean-Sébastien Thomann^{2,3}, Frédérique Mittler^{2,3}, Anne-Claude Couffin^{2,3} and Caroline Maake¹

Abstract

Background: Photosensitizers are used in photodynamic therapy (PDT) to destruct tumor cells, however, their limited solubility and specificity hampers routine use, which may be overcome by encapsulation. Several promising novel nanoparticulate drug carriers including liposomes, polymeric nanoparticles, metallic nanoparticles and lipid nanocomposites have been developed. However, many of them contain components that would not meet safety standards of regulatory bodies and due to difficulties of the manufacturing processes, reproducibility and scale up procedures these drugs may eventually not reach the clinics. Recently, we have designed a novel lipid nanostructured carrier, namely Lipidots, consisting of nontoxic and FDA approved ingredients as promising vehicle for the approved photosensitizer m-tetrahydroxyphenylchlorin (mTHPC).

Results: In this study we tested Lipidots of two different sizes (50 and 120 nm) and assessed their photodynamic potential in 3-dimensional multicellular cancer spheroids. Microscopically, the intracellular accumulation kinetics of mTHPC were retarded after encapsulation. However, after activation mTHPC entrapped into 50 nm particles destroyed cancer spheroids as efficiently as the free drug. Cell death and gene expression studies provide evidence that encapsulation may lead to different cell killing modes in PDT.

Conclusions: Since ATP viability assays showed that the carriers were nontoxic and that encapsulation reduced dark toxicity of mTHPC we conclude that our 50 nm photosensitizer carriers may be beneficial for clinical PDT applications.

Keywords: Nanoemulsion, Biocompatibility, mTHPC, Photodynamic therapy, Spheroids, Lipid nanoparticles

Background

A wealth of publications report on the development of promising novel nanoparticulate drug carriers including liposomes [1], polymeric nanoparticles [2], metallic nanoparticles [3] and lipid nanocomposites [4]. However, many of them contain components that would not meet safety standards of regulatory bodies such as the European Medicines Agency (EMA) or the US food and drug administration (FDA) [5]. Furthermore, due to difficulties

of the manufacturing processes, reproducibility and scale up procedures these drugs may eventually not translate into the clinics.

Recently, we have designed a novel lipid nanostructured carrier, namely Lipidots, consisting of nontoxic and FDA approved ingredients: wax and soybean oil serve as core components and lecithin as membranous hull with a polyethylene glycol (PEG) coating [6]. Containing only natural compounds, they are likely to be broken down and removed or recycled by the body [7]. Lipidots may be utilized and adapted for many different applications such as fluorescent imaging probes, contrast agent carriers, or targeted drug delivery [8]. They offer the possibility

*Correspondence: doris.hinger@uzh.ch

¹ Institute of Anatomy, University of Zurich, Winterthurerstrasse 190, 8057 Zurich, Switzerland

Full list of author information is available at the end of the article

to tune the viscosity of their lipid core, thereby adapting the release of an encapsulated compound to the desired profile [9]. Moreover, Lipidots can be manufactured with high colloidal stability at laboratory and industrial scales using ultrasonics or high pressure homogenization [6].

An interesting future application of Lipidots may be in the context of photodynamic therapy (PDT), a modality which is currently receiving increasing clinical attention as a promising anti-cancer treatment [10]. PDT principles rely on the activation of a light-sensitive drug (the photosensitizer, PS), which, through oxidative reaction cascades of type I and type II leads to the generation of cytotoxic reactive oxygen species (ROS) and strictly localized cell death. Remarkably, PDT has the potential to overcome disadvantages of standard oncologic regimes such as surgery, chemo- or radiotherapy because it is minimal invasive, bears little risk for the development of resistance and lacks severe side effects [11]. However, the efficiency of PDT critically depends on a high local accumulation of the PS at the tumor site. But since many potent PSs are hydrophobic, they tend to aggregate in aqueous environments (e.g. after intravenous injection), with negative consequences for their biodistribution and photoactivity, which can eventually lead to unsatisfactory therapeutic effects [12]. With the aim to improve PDT applications, various PSs have been entrapped into nanocarriers, including e.g. Photophrin, hypocrellin A, chlorin e6, tetraarylporphyrin, the near infrared dye indocyanine green [13] or the powerful FDA approved second generation PS m-tetrahydroxyphenylchlorin (mTHPC) [14].

In a previous study we have reported on the successful and reproducible encapsulation of mTHPC (generic name: Temoporfin) into Lipidots and their extensive characterization [15]. While our physico-chemical and photophysical data indicate that these particles may be well suited for PDT applications, results about their biological activity are only very preliminary yet [15]. In the present study we have thus set out to investigate PDT effects of mTHPC-loaded Lipidots for the first time in an advanced in vitro 3-dimensional (3D) head and neck cancer cell model. To estimate their potential for clinical PDT use, we produced Lipidots with two sizes (50 and 120 nm) and, after mTHPC encapsulation, compared their in vitro effects to free mTHPC in terms of light-induced toxicity, penetration properties, dispersion behaviour, PDT effects, cell death mechanisms and gene expression patterns.

Methods

Chemicals

mTHPC was obtained from Biolitec, Jena, Germany as powder. A stock solution of 1.47 mM (1 mg/mL) in 100 % ethanol was prepared and stored at 4 °C in the dark. 1,1'-dioctadecyl-3,3,3',3'-tetramethylindodicarbocyanine

perchlorate (DiD) was purchased from Life Technologies (Carlsbad, USA). If not otherwise indicated, chemicals were purchased from Sigma-Aldrich, Buchs, Switzerland.

Nanoparticle preparation

Lipidots were prepared according to Delmas et al. [9] and Navarro et al. [15]. Briefly, the manufacturing process consists of mixing an aqueous phase and a lipid phase which are separately prepared, including on the one hand MyrjS40 surfactant dissolved into 1X phosphate buffered saline (PBS) (154 mM NaCl, 0.1 M Na₂HPO₄, pH 7.4) and on the other hand soybean oil and wax (Suppocire NB) under melted state. The ultrasonication step is performed using a VCX750 ultrasonic processor during 20 min (power input 190 W, 3-mm probe diameter, Sonics). MTHPC was incorporated into the lipid mixture as a concentrated solution in ethyl acetate and after vacuum elimination of organic solvent, the oily phase was added to the aqueous phase and emulsification was performed as previously described [15]. For 50 nm Lipidots, the dispersion is composed of 37.5 % (w/w) of lipid phase (with a lecithin/PEG surfactant weight ratio of 0.19 and a surfactant/core weight ratio of 1.20) whereas for 120 nm Lipidots, the dispersion is composed of 43.0 % (w/w) of lipid phase (with a lecithin/PEG surfactant weight ratio of 0.21 and a surfactant/core weight ratio of 3.0). The Lipidots were loaded with mTHPC (thereafter called M-Lipidots) at two different ratios of numbers of PS per nanoparticle for 50 and 120 nm-sized Lipidots, respectively (920 and 4600 molecules of mTHPC/particle, respectively). The mTHPC concentrations were determined by high-performance liquid chromatography (HPLC) analysis. HPLC of prepared samples was carried out on a Sunfire C18 column (250 mm × 4.6 mm, i.d. 5 µm) at 30 °C. The mTHPC compound was eluted at 2.10 min using a isocratic mobile phase of acetonitrile/H₂O trifluoroacetic acid, 0.1 %: 9/1 at 1 mL/min flow rate after injection of 30 µL. The UV detection is operated at 425 nm. The mTHPC concentrations were assessed using a calibration curve in the range of 1–12 µg/mL. For comparisons at constant PS content, all working solutions were diluted using PBS to obtain equivalent mTHPC amounts in solution to be added in cell culture media for PDT treatment (3.67, 7.34, 14.69 µM mTHPC content). For in vitro additional fluorescence imaging and flow cytometry purposes, dye-doped nanoparticles, thereafter called D-Lipidots, were prepared as previously described [16] by incorporating DiD lipophilic indocyanine into the oily core of 50 nm Lipidots.

Monolayer cell culture

CAL-33 tongue squamous cell carcinoma cells (DSMZ, Braunschweig, Germany), were grown in RPMI without

phenol red, 10 % FCS, 2 mM Glutamax (Life Technologies), and 1 % Penicillin/Streptomycin (Life Technologies). Cells were kept in 75 cm² cell culture flasks at 5 % CO₂ and 37 °C. Cell counting was performed with a Neubauer chamber (Laboroptik Ltd., Lancing, UK) on an aliquot of cells after staining with 0.1 % (w/v) nigrosin in PBS.

Spheroid cell culture

The bottoms of 96 well plates were coated with 65 µL 1.5 % (w/v) agarose (Life Technologies) in cell culture medium without supplements. 3D cell culture spheroids were prepared by putting 96 drops of 5000 CAL-33 cells in 10 µL complete cell culture medium on the inner side of the lid of a 96 well plate. Then the lids with the hanging drops were put back on the plates and incubated for 24 h. Thereafter, 190 µL of complete cell culture medium was added to the wells and the drops were spun down shortly in a centrifuge (Virion, Zürich, Switzerland) and incubated for another 72 h. By that time the spheroids had reached an average diameter of 200 µm and were immediately used for the experiments [17].

Light microscopy

Monolayer cells

CAL-33 cells were seeded on 12 mm glass cover slips (Karl Hecht, Sondheim, Germany) and incubated with 7.34 µM mTHPC or M-Lipidots or 1 µM D-Lipidots in cell culture medium for up to 28 h in the dark. The cover slips were washed twice with PBS and subsequently fixed for 20 min with 4 % (w/v) formaldehyde (FA)/PBS. After washing they were mounted on microscopic slides (Menzel, Braunschweig, Germany) with Glycergel (Dako, Glostrup, Denmark) and analyzed with a confocal laser scanning microscope (Leica SP5, Heerbrugg, Switzerland). MTHPC was excited at 488 nm and fluorescence was detected between 590–660 nm. Images were analyzed with the imaging software Imaris (Bitplane, Belfast, UK).

Spheroids

Spheroids were incubated with 7.34 µM of mTHPC or M-Lipidots in 100 µL cell culture medium for up to 28 h in 96 well plates in the dark. Spheroids were picked with a 1 mL pipette and transferred to microcentrifuge tubes. After washing twice with PBS spheroids were fixed in 4 % (w/v) FA/PBS for 1 h, washed in PBS and analyzed in 18-well µ-slides (IBIDI) by widefield fluorescence microscopy (Leica DMI 6000) or confocal laser scanning microscopy (Leica, SP5). Per time point, 3–5 images were acquired using differential interference contrast (DIC) and epifluorescence and mean fluorescence was calculated from regions of interest (ROIs) which were drawn

around the cell assemblies in the DIC channel with Leica AS lite software. Confocal laser scanning microscopy (Leica SP5) was performed on 3–5 fixed spheroids per condition with a 20× objective (HC Plan APO). After spheroid integrity was confirmed by DIC imaging, optical sectioning was performed with an argon laser at 488 nm for excitation of mTHPC. Pictures from the center of the spheroids were taken and processed with the imaging software Imaris (Bitplane, Belfast, UK).

Cytotoxicity assessment

Spheroids were incubated with 3.67, 7.34 and 14.69 µM of mTHPC or M-Lipidots for 24 h in 96 well plates in the dark. Substance-mediated damage (i.e. dark toxicity) was assessed by either measuring spheroid areas as ROIs with widefield microscopy and the Leica AS imaging software or by means of an ATP luciferase viability assay (Promega, Fitchburg, USA). For the ATP luciferase viability assay 100 µL of Cell Viability Assay solution was added to each well after drug incubation, the contents were mixed by pipetting and the plate was transferred for 20 min to a shaker. Subsequently bioluminescence was measured in a microplate reader (Biotek, Vermont, USA).

Phototoxicity assessment

Spheroids were incubated with 3.67, 7.34 and 14.69 µM of mTHPC or M-Lipidots for 24 h in 96 well plates in the dark. Subsequently the plates were subjected to PDT by illuminating with white light from 2.5 cm above (3440 lx; fluorescent tube SYLVA-NIA standard F15 W/154, daylight) for 20 min. To ensure an even illumination, the outer rim of the well plates was never used for experimentation and the sequence of samples within the plate was changed between repetitions. Spheroid areas were microscopically determined as described above and cell survival was determined by ATP luciferase viability assay 5 h after irradiation as described above.

Apoptosis assay

Spheroids were incubated with 7.34 µM mTHPC or M-Lipidots for 24 h. After illuminating for 1 min (conditions as described above) spheroids were incubated for another 1.5 h with 100 µL 15 µM Hoechst 33342 and 30× Flica reagent (FAM Flica Poly Caspase kit, ImmunoChemistry Technologies, Enzo Life Sciences, Lausen, Switzerland). The spheroids were subsequently harvested with a 1 mL pipette and transferred to microcentrifuge tubes. After washing twice with wash buffer (FAM Flica Poly Caspase Kit) they were fixed for 1 h in fixing solution (FAM Flica Poly Caspase Kit) and analyzed in 18 well µ-slides (IBIDI) with a confocal laser scanning microscope (Leica SP5, Heerbrugg, Switzerland) within 24 h.

Electron microscopy

Spheroids were incubated for 24 h with 3.67 μ M mTHPC or 50 nm M-Lipidots and irradiated for 1 min as described above. One hour after light treatment they were washed and fixed and sequentially treated with OsO_4 and uranylacetate. After dehydration they were embedded in Epon/Araldite and sections were contrasted with uranyl acetate and lead citrate. They were examined with a CM100 transmission electron microscope (FEI, Eindhoven, The Netherlands) or with an Auriga 40 scanning electron microscope (Zeiss, Oberkochen, Germany). For a more detailed description see Additional file 1.

Quantitative reverse transcription polymerase chain reaction (qRT-PCR)

A total of 120 spheroids were incubated with 3.67 μ M mTHPC or 50 nm M-Lipidots for 24 h. After illuminating for 1 min as described spheroids were incubated for another 2 h, subsequently harvested with a 1 mL pipette and transferred to microcentrifuge tubes. They were washed twice with PBS and resuspended in 600 μ L lysis buffer (Qiagen, Venlo, The Netherlands), vortexed vigorously and passed 30 times through a 1 mL syringe with a 20 gauge needle. Total RNA was extracted with the RNeasy Micro Kit (Qiagen) as described per manufacturer's instructions, processed with a cNDA synthesis kit (Qiagen) and the obtained cDNA used for a quantitative PCR array (Human Cancer Drug Targets RT² Profiler PCR Array, Qiagen). For further details please refer to the Additional file 1.

Flow cytometry

Flow cytometry analysis of the interaction of fluorescent D-Lipidots with cells was performed using a 9 colors FACS BD LSR2 equipped with lasers emitting at 488 and 633 nm (BD, Franklin Lakes, USA). CAL-33 cells were seeded at a density of 10^5 cells per well in 12 well plates and incubated for 24 h. D-Lipidots with a diameter of 50 nm were incubated at the corresponding concentration of 1 μ M DiD in presence of cell monolayers for 2, 3 or 6 h in complete cell culture medium. Thereafter, cells were rinsed with PBS ($\times 2$), harvested by the addition of trypsin followed by a centrifugation, and then fixed with 2 % FA before flow cytometry analysis. 10,000 to 20,000 events were recorded. The data from fluorescence measurements at an emission wavelength of 660 nm for DiD were analyzed using DIVA v8.1 software (BD) by using the overlay option.

Statistical evaluation and graphical modelling

Two-way ANOVA of cell toxicity and phototoxicity data was analyzed from at least two independent experiments and five replicates per condition. Means

are plotted \pm standard deviations. Statistics and graphical plots were established and analyzed with GraphPad Prism software (Graphpad Software, La Jolla, USA).

Results

Nanoparticle preparation

To investigate the effect of particle size and PS payload on transport and delivery, two series of nanoparticles were prepared with two different payloads. For the 50 nm nanoparticles, mTHPC was incorporated with a content of 920 molecules/particle whereas for 120 nm particles, the amount of mTHPC was estimated at 4600 molecules/particle. Therefore one 120 nm nanoparticle contains fivefold more molecules of mTHPC than one 50 nm nanoparticle. Expressed in equivalent mTHPC concentration (3.67, 7.34 and 14.69 μ M) the solution of 50 nm nanoparticles contains fivefold more particles than the solution of 120 nm particles. As observed in our preliminary study [15], mTHPC was efficiently encapsulated into lipid nanoparticles without affecting neither the colloidal properties of the carrier nor photophysical properties of the loaded PS. Indeed, an aggregation of mTHPC inside the lipid core of nanoparticles can be observed only for 50 nm particle at high payload (>4 %w/w total lipid, data not published). Estimated from the whole excipients initially incorporated in the Lipidot formulation, mTHPC was loaded in our study at 2.8 and 1.0 % w/w for 50 and 120 nm particles, respectively (Table 1).

Particle size and size distribution of lipid nanoparticles

Dynamic light scattering (DLS) technique was used to determine the particle hydrodynamic diameter (in nm), particle size distribution (expressed by polydispersity index PDI) using Zetasizer Nano ZS (Malvern Instruments, France). At least three different nanoparticle batches (lipid dispersed phase weight fraction: 10 %) are measured per condition. Data were expressed as mean \pm standard deviation of three independent measurements performed at 25 °C (Table 1).

Lipidot size drives uptake kinetics in CAL-33 cells

Using confocal laser scanning microscopy and CAL-33 monolayers and spheroids, uptake of 50 and 120 nm M-Lipidots was investigated over time and compared to free mTHPC (Fig. 1). In CAL-33 monolayer cultures, fluorescence of free mTHPC could be readily detected after 2 h of incubation as a diffuse signal throughout the cytoplasm, sparing the nucleus. In contrast, no fluorescence from our nanoparticle formulations was apparent at this time point. Only after 6 h both sizes of M-Lipidots were visible with the same distribution pattern as free mTHPC, however, the fluorescence was markedly weaker with 120 nm M-Lipidots compared

Table 1 Physicochemical characterization of Lipidots

	Lipid (mg/mL)	Number of particles/mL	MTHPC molecules/particle	mTHPC (µg/mL)	Drug loading ^a	Hydrodynamic diameter (nm)	Poly-dispersity index
50 nm M-Lipidot	50	7.27565×10^{14}	~920	722	2.8 %	47.7 ± 1.1	0.153 ± 0.01
120 nm M-Lipidot	50	5.26306×10^{13}	~4600	262	1.0 %	111.2 ± 2.2	0.103 ± 0.01
50 nm Lipidot ^b	50	7.27565×10^{14}	–	–	–	49.5 ± 1.5	0.170 ± 0.07
120 nm Lipidot ^b	50	5.26306×10^{13}	–	–	–	95.4 ± 3.4	0.120 ± 0.05

Data with standard deviation

^a Expressed w/w of total lipids (included in nanoparticle formulation)

^b Empty Lipidots

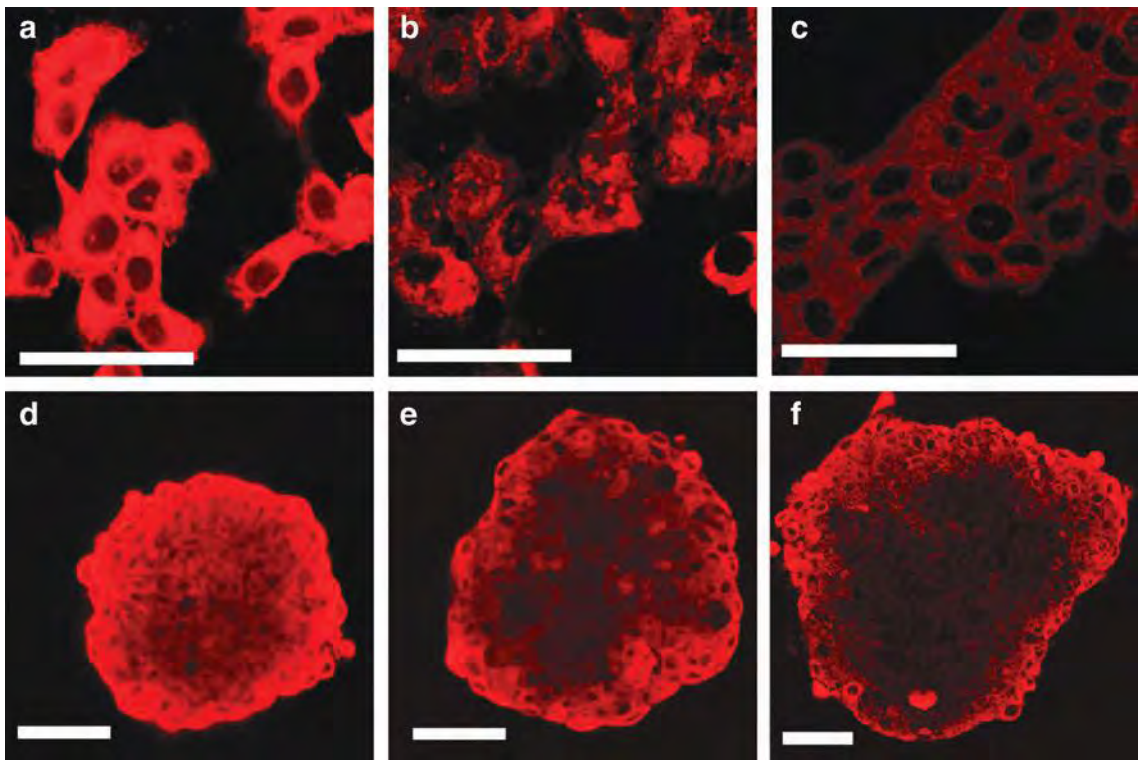
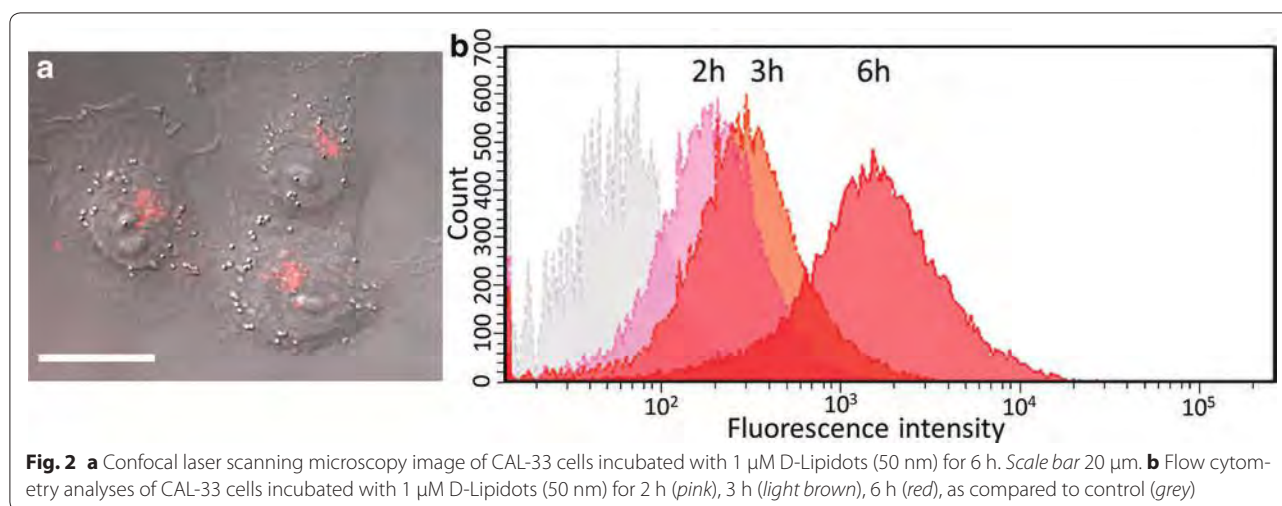


Fig. 1 Confocal laser scanning microscopy images of CAL-33 cells incubated for 28 h with free mTHPC (**a, d**), 50 nm M-Lipidots (**b, e**) and 120 nm M-Lipidots (**c, f**) in monolayers (**a–c**) and spheroids (**d–f**). Concentration for all treatments: 7.34 µM mTHPC. Scale bar 50 µm

to 50 nm M-Lipidots. The intracellular distribution pattern stayed similar until 28 h but fluorescence accumulated over time for all formulations (Fig. 1a–c). To obtain further information with regard to uptake kinetics, flow cytometry was used to measure in CAL-33 the fluorescence of 50 nm D-Lipidots over time (Fig. 2). These 50 nm D-Lipidots show the same accumulation behavior as 50 nm M-Lipidots (Fig. 2a), but are better suited for flow cytometry applications. Data confirmed microscopic observations in CAL-33 cells, showing an increase of fluorescence intensity after 6 h of incubation as compared to earlier time points (Fig. 2b).

To better predict the in vivo behavior, uptake was then investigated in CAL-33 spheroids (Fig. 1d–f). In this 3D model of an avascular mini tumor, free mTHPC accumulated in the outer cell layer at about the same time as in monolayer cells (2 h), however, it took up to 6 h until the PS was penetrating further into the spheroid. Eventually it reached the spheroid core at 24 h with a modest overall fluorescence increase until 28 h. At these late time points, fluorescence signals showed a homogeneous distribution within the spheroid. The weaker fluorescent signals of 50 nm M-Lipidots were apparent in the outer cell layers after 4 h, and continued to penetrate slowly deeper into



the spheroid center. At 28 h the core was fluorescent, but the signal displayed a more punctuate and less homogeneous pattern. Compared to 50 nm M-Lipidots, penetration of 120 nm M-Lipidots was retarded, most of which did not reach the center even at 28 h as evidenced by a less fluorescent spheroid core.

Semiquantitative analyses of microscopy data confirmed that time dependent uptake curves were different between free mTHPC and M-Lipidots in the spheroid model (Fig. 3). Free mTHPC was taken up in a nonlinear, asymptotical way with high initial uptake rates and quickly decreasing rates over time whereas 120 nm M-Lipidots were taken up by the spheroid in an almost linear fashion during the whole time of the experiment at a very low initial uptake rate. The uptake curve of the 50 nm M-Lipidots presents an uptake in a nonlinear way but at a lower initial uptake rate as free mTHPC. Based on uptake studies, further studies were therefore performed after a 24 h exposure to the compounds.

The nanoformulations are less cytotoxic than the free substance at high drug concentrations

To obtain information about a possible cytotoxicity of our nanocarriers, we first tested empty Lipidots by means of an ATP luciferase viability assay that measures cell viability in CAL-33 spheroids (Fig. 4a). A comparison revealed that both 50 and 120 nm Lipidots are well tolerated for concentrations of particles corresponding to the equivalent mTHPC concentration from 0 to 14.69 μM (± 69.3 –692.9 μg/mL lipid [50 nm]; 190.7 μg/mL–1.90 mg/mL lipid [120 nm]), with the smaller particles being slightly superior ($p < 0.01$). While the 50 nm particles did not exhibit any toxicity at the tested concentrations the 120 nm particles reduced viability by 10 %. As a next step, cytotoxic effects of PS-loaded M-Lipidots

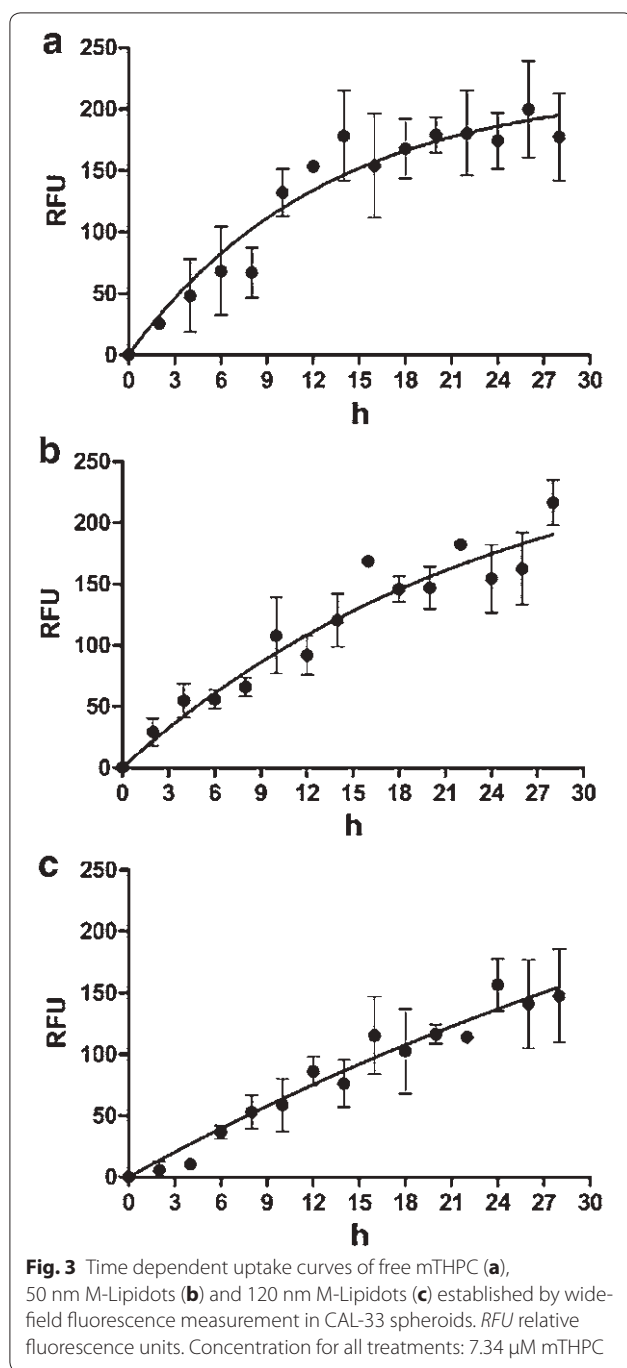
were compared to free mTHPC in CAL-33 spheroids (Fig. 4b). While free mTHPC showed a clear toxicity (68 % viability) in the dark at the highest concentration tested (14.69 μM), encapsulation of mTHPC into Lipidots resulted in a significantly reduced dark toxic effect (78 % viability with the 50 nm Lipidots; 86 % viability with the 120 nm Lipidots, $p < 0.001$).

The 50 nm M-Lipidots show high photodynamic potency similar to free mTHPC

The PDT effects mediated by M-Lipidots or free mTHPC were investigated in CAL-33 spheroids (Figs. 5, 6). Our microscopic analyses showed that PDT with both free mTHPC and 50 nm M-Lipidots induced a pronounced and comparable destruction of the spheroids (Fig. 5). Although the size reduction was difficult to microscopically measure under conditions of high destruction, the results correlated with the respective ATP luciferase viability assays (Fig. 6b). The 50 nm Lipidots as well as free mTHPC reduced spheroid sizes by 100 % at higher concentrations ($p < 0.001$). However, after PDT with 120 nm M-Lipidots, even at the highest concentration (14.69 μM), only mild phototoxic effects were visible with size reductions by only 34 % (Figs. 5, 6a, $p < 0.001$). These limited PDT effects of 120 nm M-Lipidots could also be confirmed by ATP luciferase viability assays (Fig. 6b). Viability after PDT with the highest concentration (14.69 μM) was 1.8 % with mTHPC, 6.6 % with the 50 nm particles and 66.2 % with the 120 nm particles ($p < 0.001$).

Free mTHPC causes apoptosis and necrosis while 50 nm M-Lipidots cause mostly apoptosis

By “FLICA” apoptosis assays high pan-caspase activity was detected in CAL-33 spheroids after PDT with 50 nm M-Lipidots (Fig. 7c) and, to a lesser extent, after



treatment with free mTHPC and irradiation (Fig. 7b). Very low caspase staining occurred after PDT with 120 nm M-Lipidots (Fig. 7d) which was barely more intense than staining of control spheroids (Fig. 7a).

An investigation of CAL-33 spheroids at the ultra-structural level with electron microscopy confirmed different modes of cell death as observed after PDT with mTHPC or 50 nm M-Lipidots (Fig. 8). Untreated

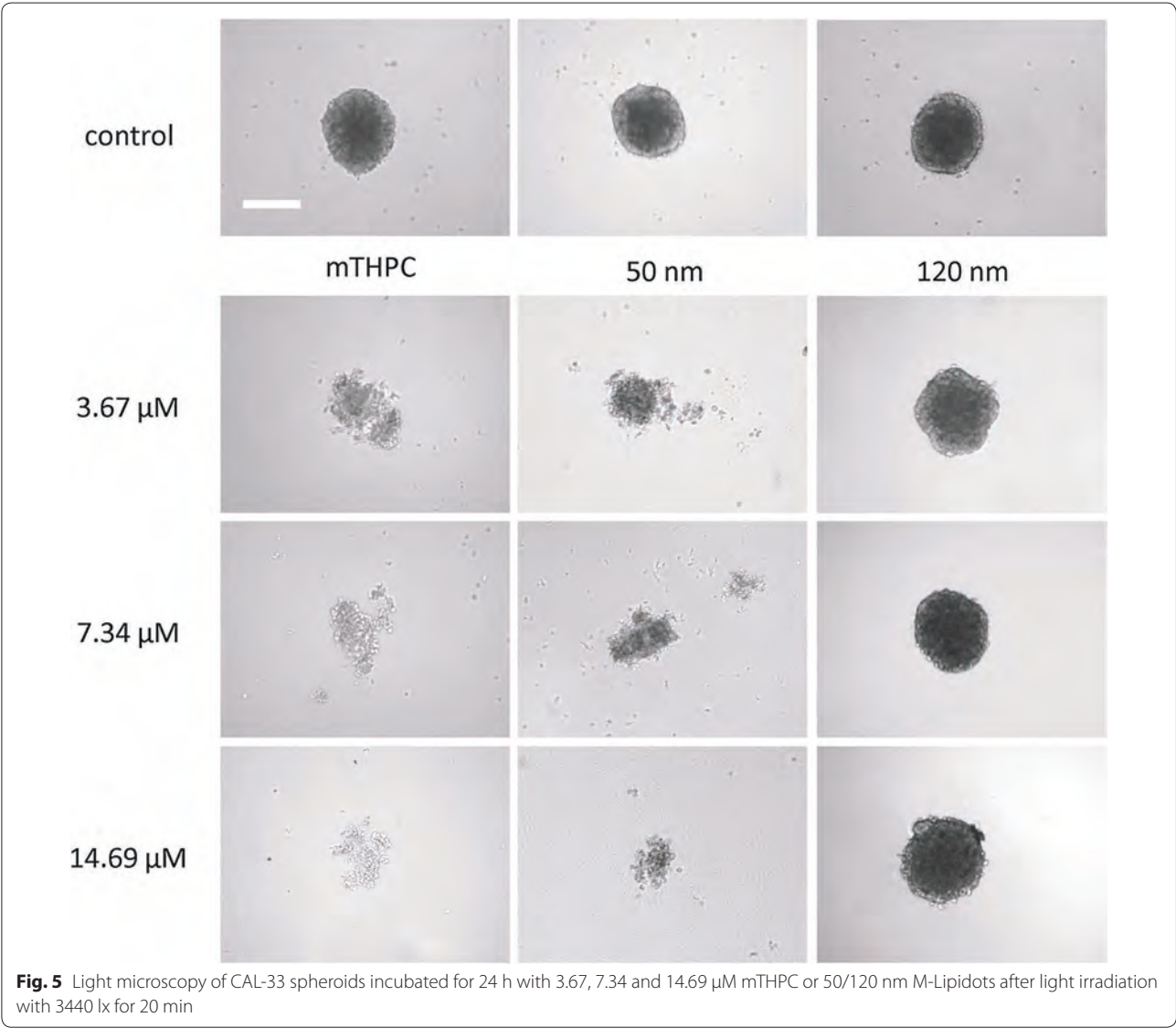
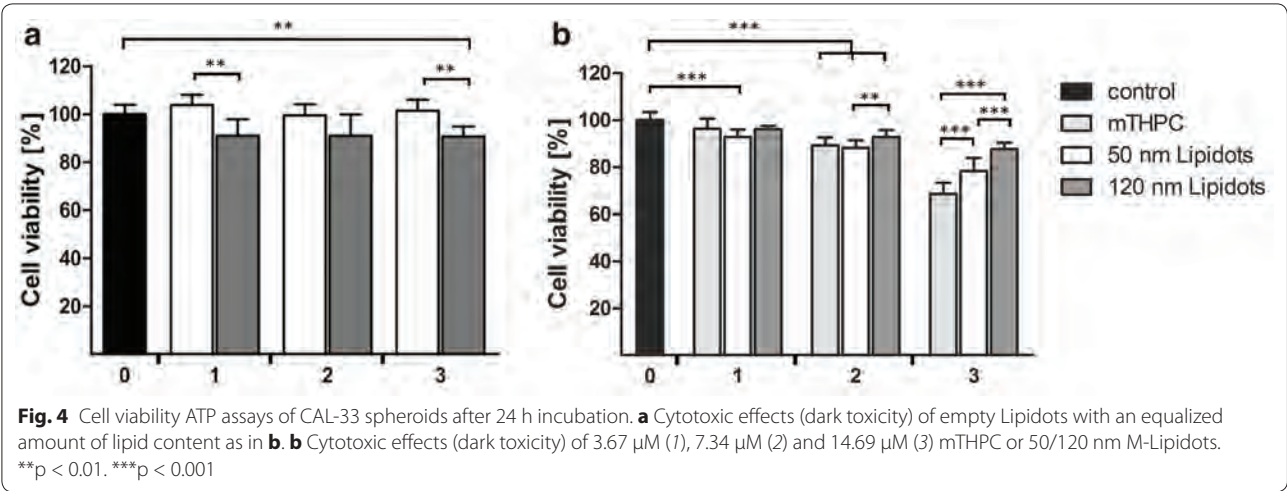
controls showed intact spheroid structures and most cells displayed well preserved cell organelles (Fig. 8a, d). MTHPC-induced PDT seemed to disrupt spheroid structure as a whole, causing cells to die either in an apoptotic or in a necrotic manner (Fig. 8b, e). Apoptosis was recognizable by the condensed chromatin structure and well preserved cell membranes of some dying cells. However, necrotic features like destroyed cell organelles and membranous cellular debris were present as well. Inside several cells inclusion bodies with grainy deposits were visible that may be aggregated and contrasted mTHPC (Fig. 8g). PDT with 50 nm M-Lipidots was primarily damaging the spheroid center leaving an outer rim of cells intact under these conditions (Fig. 8c). In the spheroid center cells were primarily showing features of apoptotic cell death, as described above (Fig. 8f). Additionally, in the outer cell layer, close to the cytoplasmic membrane, vesicles with enclosed sphere-like structures of about 50 nm were present that may represent M-Lipidots (Fig. 8h).

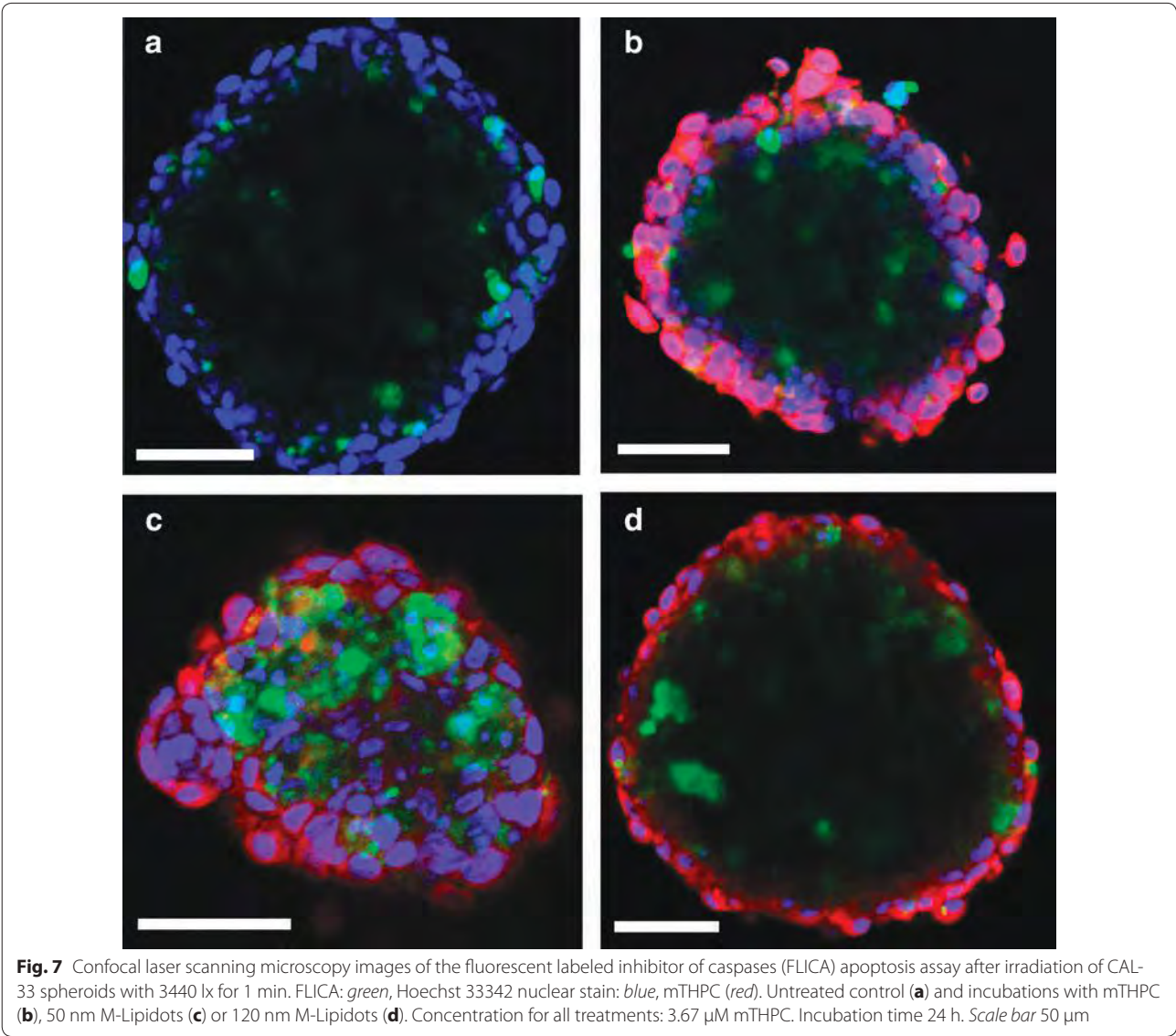
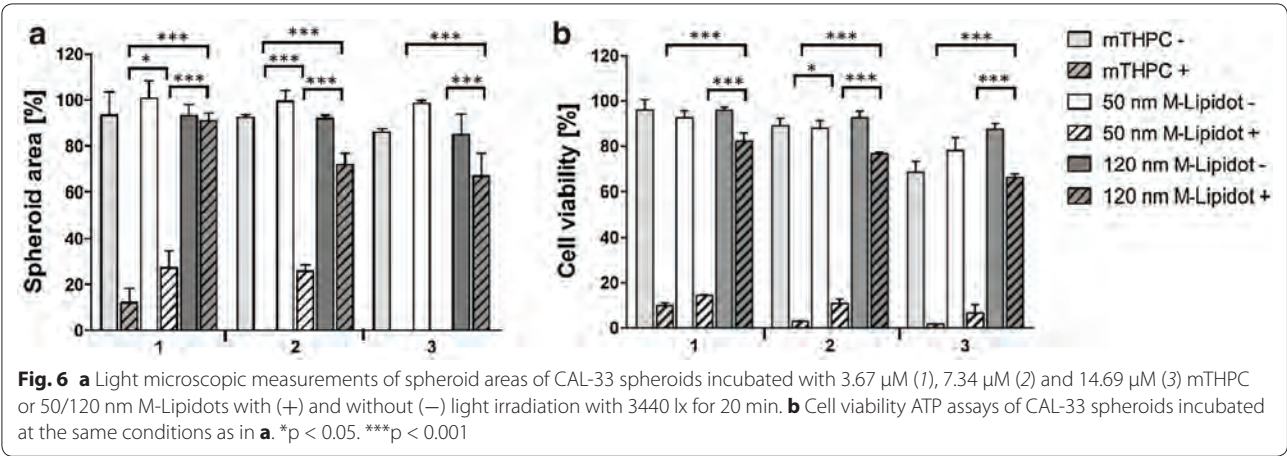
Lipidot-PDT affects similar pathways as mTHPC-PDT

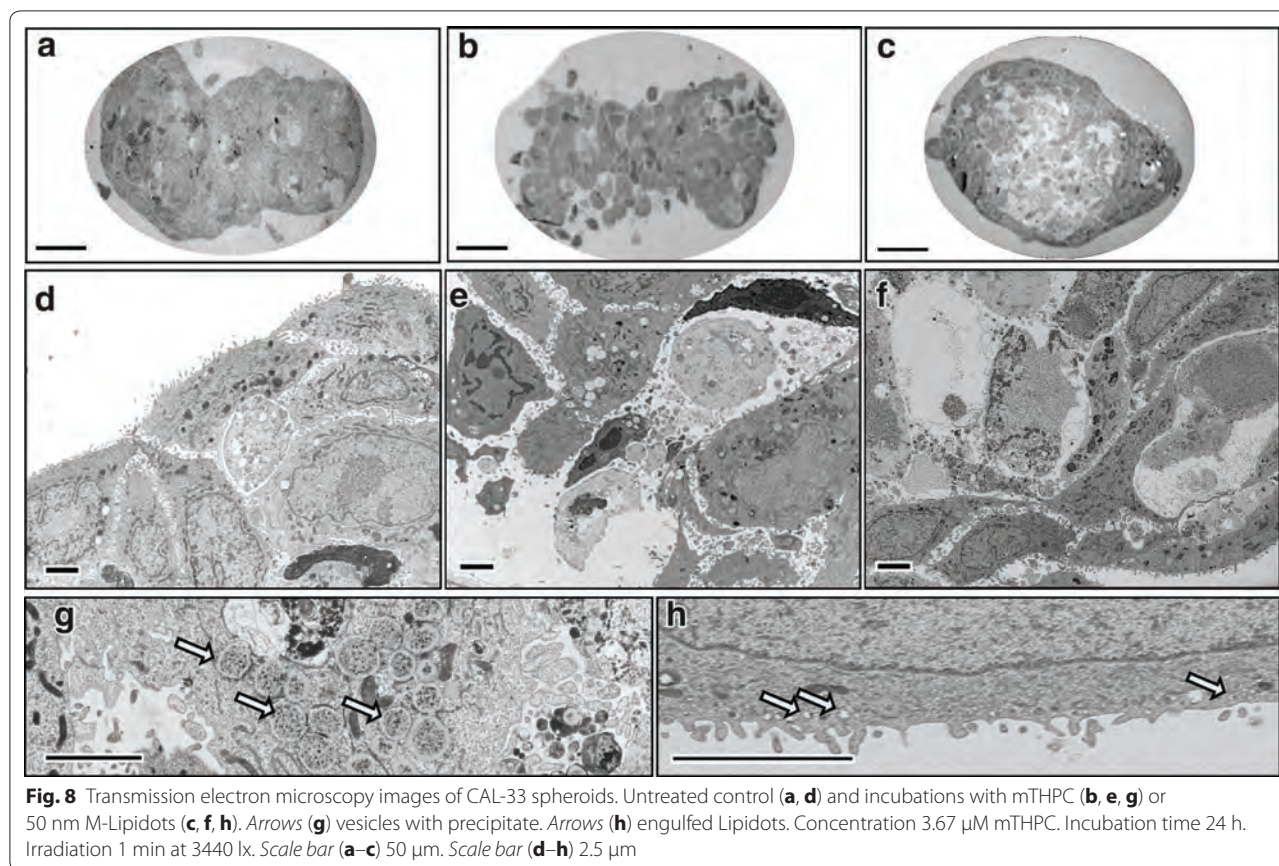
To further explore possible differences between mTHPC- and 50 nm M-Lipidot-mediated PDT, we analyzed the expression of 84 known cancer drug target genes by means of qRT-PCR (Fig. 9). Compared to the untreated control, no gross differences in overall expression patterns could be discovered after PDT, since the same 33 genes were upregulated after both regimes. However, the upregulation was generally stronger after mTHPC-PDT. This was e.g. obvious for the expression of PTGS2, TXNRD1, AKT1, NFKB1, EGFR, PIK3C3, NRAS, PLK2, PLK3, RHOB, and HSP90AA1, where a more than two-fold higher upregulation was found after mTHPC-PDT compared to M-Lipidot-PDT. However, it should be noted that the same pathways were affected in the same direction (only upregulation, no downregulation) after both PDT regimes. Among others, we detected signs for abnormal regulation of KRAS and NRAS and an increase of transcription factors ATF2, HIF1A, NFKB1, TP53 despite of the upregulation of histone deacetylases HDAC1, HDAC2 and HDAC4. Genes that were not expressed and/or unaltered after both PDT regimes are summarized in Additional file 1: Table S1.

Discussion

The powerful PS mTHPC is approved in several European countries for palliative PDT of patients with advanced head and neck cancer. However, mTHPC formulations that e.g. improve solubility of this highly hydrophobic drug, reduce its dark toxicity, enhance its intratumoral accumulation and/or increase PDT efficacy would be beneficial for systemic clinical applications [18].







Recently, we introduced solid lipid nanoparticles as stable, easy to produce and efficient carriers for mTHPC [15]. However, while physico-chemical and photophysical evaluations indicated their excellent suitability for PDT, only scarce information is available yet with regard to their behavior in biological systems. In the present study we have therefore chosen an advanced in vitro cancer spheroid model to investigate for the first time PDT effects of these particles (called M-Lipidots) at the cellular level and compare it to effects of free mTHPC. Cancer spheroids are multicellular 3D grown minitumors that display features which better mimic the biology of solid tumors than standard monolayer cultures, among others in terms of intercellular contacts, matrix deposition, physiological barriers, cellular inhomogeneity or proliferation properties [19]. Also with regard to ROS diffusion and PS penetration a 3D environment may be advantageous. Spheroids have thus been proposed not only as superior predictive platforms for testing of drugs but also of drug delivery systems [20].

Since diameters of Lipidots can be reliably adjusted between 30 and 120 nm by varying wax, oil and surfactant content [15], we have here included two exemplary sizes of mTHPC-Lipidots, namely 50 and 120 nm.

In both, monolayer cultures (that served as a reference) and spheroids, we found that free mTHPC was taken up in a shorter time frame compared to mTHPC encapsulated into Lipidots. The quicker and higher accumulation of free mTHPC may be explained by the fact that lipophilic PSs can bind to serum proteins and uptake can be mediated by low lipid density protein receptors, which is considered an efficient mechanism [18]. For in vivo applications this slower accumulation of M-Lipidots must of course be considered but may be outweighed by advantages of Lipidot's PEG chains that offer a stealth mechanism to avoid fast recognition by the immune system [21].

Our experiments further indicated favored uptake and superior spheroid penetration properties of the 50 nm M-Lipidots over the 120 nm M-Lipidots. These results are in accordance with most literature reports for other nanocomposites which suggest a size dependency of the uptake behavior and smaller diameters being more readily internalized by cells in monolayers [22]. There are fewer studies investigating size dependent penetration of nanoparticles into spheroids, however, in a work with gold nanocomposites the authors also reported a superior uptake of smaller 50 nm particles over larger 100 nm

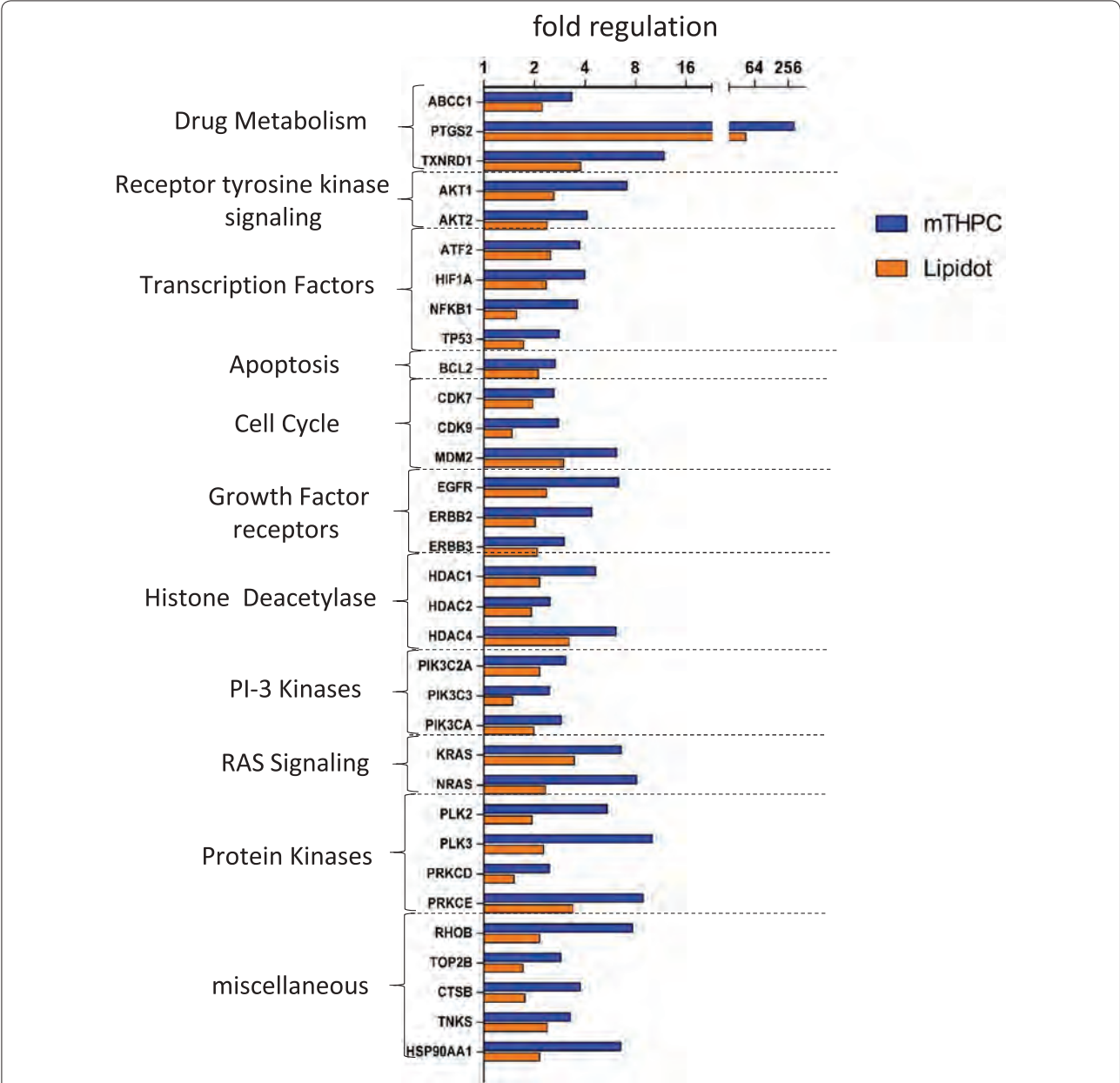


Fig. 9 Fold expression change in spheroids after 24 h incubation with 3.67 μ M mTHPC or 50 nm M-Lipidots and light illumination from 2.5 cm above with white light for 1 min at 3440 lx. Gene expression data was normalized against an untreated control and the RPLP0 house keeping gene. *CFTR/MRP* ATP-Binding Cassette, Sub-Family C, *ABCC1* Member 1, *PTGS2* Prostaglandin-Endoperoxide Synthase 2, *TXNRD1* Thioredoxin Reductase 1, *AKT1* V-Akt Murine Thymoma Viral Oncogene Homolog 1, *AKT2* V-Akt Murine Thymoma Viral Oncogene Homolog 2, *ATF2* Activating Transcription Factor 2, *HIF1A* Hypoxia Inducible Factor 1, Alpha Subunit, *NFKB1* Nuclear Factor Of Kappa Light Polypeptide Gene Enhancer In B-Cells 1, *TP53* Tumor Protein P53, *BCL2* B Cell CLL/Lymphoma 2, *CDK7* Cyclin-Dependent Kinase 7, *CDK9* Cyclin-Dependent Kinase 9, *MDM2* MDM2 Proto-Oncogene, E3, *EGFR* Epidermal Growth Factor Receptor, *ERBB2* Erb-B2 Receptor Tyrosine Kinase 2, *ERBB3* Erb-B2 Receptor Tyrosine Kinase 3, *HDAC1* Histone Deacetylase 1, *HDAC2* Histone Deacetylase 2, *HDAC4* Histone Deacetylase 4, *PIK3C2A* Phosphatidylinositol-4-Phosphate 3-Kinase, Catalytic Subunit Type 2 Alpha, *PIK3C3* Phosphatidylinositol 3-Kinase, Catalytic Subunit Type 3, *PIK3CA* Phosphatidylinositol-4,5-Bisphosphate 3-Kinase, Catalytic Subunit Alpha, *KRAS* Kirsten Rat Sarcoma Viral Oncogene Homolog, *V-Ras* Neuroblastoma RAS Viral, *NRAS* Oncogene Homolog, *PLK2* Polo-Like Kinase 2, *PLK3* Polo-Like Kinase 3, *PRKCD* Protein Kinase C, Delta, *PRKCE* Protein Kinase C, Epsilon, *RHOB* Ras Homolog Family Member B, *TOP2B* Topoisomerase (DNA) II Beta 180 kDa, *CTSB* Cathepsin B, *TNKS* Tankyrase, and Heat Shock Protein 90 kDa Alpha (Cytosolic), Class A Member 1 (HSP90AA1)

ones [23]. However, we cannot exclude that the stronger fluorescence signal observed after incubation with 50 nm M-Lipidots may also be due to the fact that five-fold more particles were present in the working solution of 50 nm M-Lipidots compared to 120 nm M-Lipidots. This is related to manufacturing processes and the aim to reach equivalent mTHPC concentrations with both M-Lipidot sizes. Furthermore, fluorescence with the nanoparticles was markedly weaker when compared to free mTHPC which is why we cannot exclude that quenching effects occur in the presence of cells.

For the following PDT experiments, we used a white light source rather than a laser to activate the PS. In a previous study we have shown that this is perfectly feasible and may be advantageous to detect (subtle) differences between effects of treatment regimes [24]. With the aim to preserve some morphology and avoid complete RNA degradation [25, 26] for our microscopic and RNA studies, we furthermore had to reduce the illumination time from 20 to 1 min. We observed a strong and comparable light-induced destruction of spheroids exposed to free mTHPC or 50 nm M-Lipidots. This similar PDT efficiency was despite our observation of a slightly different microscopic fluorescence distribution pattern within the spheroid of free mTHPC and M-Lipidots, respectively. The observed PDT effects complemented our previous study, where we have shown in a cell-free environment that 30, 50 and 100 nm mTHPC-Lipidots are capable of producing high quantum yields after illumination and that singlet oxygen may diffuse through the Lipidot shell to the surrounding [15]. As predicted because of their observed delayed and weaker cellular uptake, 120 nm M-Lipidots caused almost no PDT effects under the applied mild activation conditions. While effects may be improved with stronger illumination regimes, we have shown previously that ROS diffusion from larger Lipidots is anyway worse than from smaller ones [15].

From EM studies and the apoptosis assay, it was evident that spheroid centers were more damaged after PDT with the 50 nm Lipidots, although fluorescence accumulation was highest at the spheroid periphery. We propose that a decreasing nutrient gradient towards the spheroid center may render those cells more susceptible to PDT, and therefore also low PS doses will be sufficient to kill them.

Although PDT with both the free PS as well as the 50 nm M-Lipidots efficiently destroyed spheroids, underlying mechanisms turned out to feature differences under our experimental conditions, i.e. necrosis and apoptosis with mTHPC-PDT, and apoptosis with 50 nm M-Lipidot-PDT. The reasons for that are not clear yet. While it is well known that the subcellular localization of a PS governs PDT cell death pathways [27], we found similar

cytoplasmic fluorescence patterns of mTHPC with both formulations. However, necrotic mechanisms have been reported to occur with stronger cellular photodamage [27]. Since light doses were the same, it may therefore be speculated that under the same conditions treatment with M-Lipidots initiated slightly milder PDT effects than free mTHPC. Whether this is a consequence of quantitative PS uptake, exact intracellular distribution or the nanocarrier has to be investigated.

Stronger photodamage after PDT with free mTHPC may also be concluded from our RNA expression studies where we detected always a more pronounced gene regulation. For several genes a more than two-fold higher upregulation was found after mTHPC-PDT compared to M-Lipidot-PDT. As the same pathways were affected in the same direction (only upregulation, no downregulation) after both PDT regimes, it indicates common mechanisms of free and Lipidot-encapsulated mTHPC. The changed expression patterns reflect the cell's complex acute responses to (oxidative) stress due to our PDT regimes. Many of the upregulated genes may have dual roles for apoptosis or anti-apoptosis and it is not clear yet whether we observe the cell's efforts to initiate rescue mechanisms or the beginning of cell death. Apparently, many different pathways are dysregulated in parallel. Among others, we detected signs for abnormal regulation of the RAS signalling pathway, chromatin remodeling or an increase of transcription factor RNA despite of the upregulation of histone deacetylases.

In accordance with our previous studies with 30, 50 and 100 nm particles in MCF-7 monolayer cultures [14] the biocompatibility of empty 50 and 120 nm Lipidots could be here confirmed for CAL-33 spheroids. The observed slightly higher cytotoxicity of 120 nm Lipidots may be caused by their increased lipid concentration compared to 50 nm Lipidots, as observed before [14]. However, this difference may not be biologically relevant, leaving more than 90 % of cells vital.

Dark toxicity of PSs is an important issue for clinical PDT applications that may cause detrimental effects on healthy cells. This also applies to the strong PS mTHPC for which cytotoxic effects without light activation are well known. In our spheroid model we could demonstrate that the encapsulation of mTHPC into Lipidots significantly reduced unwanted dark toxicity of this PS at high concentrations. However, we cannot exclude that the lower toxicity is at least partially due to a lower uptake of mTHPC into the cells. Still, considering the outstanding biocompatibility of our carrier it may allow for systemic applications of higher doses of mTHPC for improved PDT without the risk for light-independent effects in patients.

Various different approaches have been proposed in the past, including the development of e.g. liposomal mTHPC formulations [28, 29] or the encapsulation of mTHPC into nanoparticles composed of poly(lactic-co-glycolic acid) [30], poly(lactic-co-glycolic acid)-b-poly(ethylene glycol) [31], poly(ethylene glycol) methacrylate-co-2-(diisopropylamino)ethyl methacrylate copolymers [32], human serum albumin [33], organic-modified silica [34] or calcium phosphate. [35] These studies describe promising carriers for mTHPC by improving solubility and reducing dark toxicity however it is not possible to directly compare them as very different model systems were used in each case. Furthermore, nanotoxicology will be very different depending on the materials used in the formulation and can differ greatly between in vitro and in vivo studies.

The 50 nm Lipidots display several favorable characteristics with regard to in vivo applications. Concerning size Tang et al. [36] e.g. could show in vivo that tumor permeation and retention of 50 nm silica particles (the EPR effect) was superior to smaller 20 nm ones and larger 200 nm ones. Furthermore, in two of our former in vivo studies with Lipidots as carrier for indocyanine green we could report on high chemical stability of the particles of over 6 months and a prolonged tumor labelling of over 1 day [7, 37]. Additionally, Lipidots displayed good long-term plasma stability and tolerability with low hemolytic activity [7, 37].

Conclusions

In conclusion, in an advanced 3D cell culture model, 50 nm Lipidots have presented themselves as nontoxic nanocarriers for hydrophobic photosensitizers such as mTHPC that preserve its functionality in PDT. Lipidots are not only fully biocompatible and easy to produce, but may solve two important problems of mTHPC that currently prevent a more widespread clinical use of this efficient PS by rendering it water soluble and reducing its dark toxicity. The slightly milder PDT effects with M-Lipidots may be beneficial in certain clinical settings, e.g. where an apoptotic cell death (without inflammation) is clinically preferred, such as for tumor ablation.

Additional file

Additional file 1. Additional material.

Abbreviations

PDT: photodynamic therapy; PS: photosensitizer; FDA: (US) food and drug administration; mTHPC: m-tetrahydroxyphenylchlorin; ATP: adenosine triphosphate; EMA: European Medicines Agency; PEG: polyethylene glycol; ROS: reactive oxygen species; DiD: 1,1'-dioctadecyl-3,3',3'-tetramethylindodicarbocyanine perchlorate; PBS: phosphate buffered saline; FA: formaldehyde; ROI: region of interest; CDNA: complementary DNA; FLICA:

fluorochrome-labeled inhibitor of caspases; M-Lipidots: mTHPC loaded Lipidots; D-Lipidots: dye loaded Lipidots; QRT-PCR: quantitative reverse transcription polymerase chain reaction.

Authors' contributions

DH carried out the culturing of cells, spheroid cell culture, cell toxicity studies, confocal microscopy, uptake studies, phototoxicity studies, apoptosis assay, PCR, preparation of samples for electron microscopy, all data analysis and preparation of the manuscript. FN cultured cells and did flow cytometry analysis, he also helped to improve the manuscript. JST and FM prepared the nanoparticles for the studies and did also the physicochemical characterization under supervision of ACC. ACC also helped to improve the manuscript. AK analyzed the samples for electron microscopy and took images, edited images and helped to improve the sections in the manuscript on microscopy. CM supervised DH and significantly contributed to the writing and adaptation of the manuscript. All authors read and approved the final manuscript.

Author details

¹ Institute of Anatomy, University of Zurich, Winterthurerstrasse 190, 8057 Zurich, Switzerland. ² Technologies for Biology and Healthcare Division, CEA, LETI, MINATEC Campus, Commissariat à l'Énergie Atomique et aux Énergies Alternatives (CEA), 38054 Grenoble, France. ³ Université Grenoble Alpes, 38000 Grenoble, France. ⁴ Center for Microscopy and Image Analysis, University of Zurich, Winterthurerstrasse 190, 8057 Zurich, Switzerland.

Acknowledgements

We are thankful to the Center for Microscopy and Image Analysis of the University of Zurich (especially to Gery Barmettler, Bruno Guhl and Ursula Lüthi) for their help with electron microscopy. We also want to thank Biolitec Research, Jena, Germany for kindly providing mTHPC for our study. The study was supported by the FP7 ERA-net EuroNanoMed project TARGET-PDT (31NM30-131004/1).

Competing interests

The authors declare that they have no competing interests. Patent: Goutayer M, Navarro F, Robert V, Texier I, Encapsulation of lipophilic or amphiphilic therapeutic agents into nano-emulsions, Granted on 14/08/2008, WO2010018222.

Received: 16 June 2016 Accepted: 29 August 2016

Published online: 07 September 2016

References

- Samad A, Sultana Y, Aqil M. Liposomal drug delivery systems: an update review. *Curr Drug Deliv*. 2007;4:297–305.
- Masood F. Polymeric nanoparticles for targeted drug delivery system for cancer therapy. *Mater Sci Eng C Mater Biol Appl*. 2016;60:569–78.
- Sharma H, Mishra PK, Talegaonkar S, Vaidya B. Metal nanoparticles: a theranostic nanotool against cancer. *Drug Discov Today*. 2015;20:1143–51.
- Naseri N, Valizadeh H, Zakeri-Milani P. Solid lipid nanoparticles and nanostructured lipid carriers: structure. Preparation and application. *Adv Pharm Bull*. 2015;5:305–13.
- Eifler AC, Thaxton CS. Nanoparticle therapeutics: FDA approval, clinical trials, regulatory pathways, and case study. *Methods Mol Biol*. 2011;726:325–38.
- Delmas T, Piraux H, Couffin AC, Texier I, Vinet F, Poulin P, et al. How to prepare and stabilize very small nanoemulsions. *Langmuir*. 2011;27:1683–92.
- Navarro FP, Mittler F, Berger M, Jossierand V, Gravier J, Vinet F, et al. Cell tolerability and biodistribution in mice of indocyanine green-loaded lipid nanoparticles. *J Biomed Nanotechnol*. 2012;8:594–604.
- Texier I, Goutayer M, Da Silva A, Guyon L, Djakeri N, Jossierand V, et al. Cyanine-loaded lipid nanoparticles for improved in vivo fluorescence imaging. *J Biomed Opt*. 2009;14:54005–11.
- Delmas T, Couffin AC, Bayle PA, De Crécy F, Neumann E, Vinet F, et al. Preparation and characterization of highly stable lipid nanoparticles with amorphous core of tuneable viscosity. *J Colloid Interface Sci*. 2011;360:471–81.
- Benov L. Photodynamic therapy: current status and future directions. *Med Princ Pract*. 2015;24(Suppl 1):14–28.

11. Triesscheijn M, Baas P, Schellens JHM, Stewart FA. Photodynamic therapy in oncology. *Oncologist*. 2006;11:1034–44.
12. Dolmans DEJGJ, Fukumura D, Jain RK. Photodynamic therapy for cancer. *Nat Rev Cancer*. 2003;3:375–80.
13. Bahmani B, Bacon D, Anvari B. Erythrocyte-derived photo-theranostic agents: hybrid nano-vesicles containing indocyanine green for near infrared imaging and therapeutic applications. *Sci Rep*. 2013;3:2180.
14. Debele TA, Peng S, Tsai H-C. Drug carrier for photodynamic cancer therapy. *Int J Mol Sci*. 2015;16:22094–136.
15. Navarro FP, Creusat G, Frochet C, Moussaron A, Verhille M, Vanderesse R, et al. Preparation and characterization of mTHPC-loaded solid lipid nanoparticles for photodynamic therapy. *J Photochem Photobiol B Biol*. 2014;130:161–9.
16. Gravier J, Navarro FP, Delmas T, Mittler F, Couffin A-C, Vinet F, et al. Lipidots: competitive organic alternative to quantum dots for in vivo fluorescence imaging. *J Biomed Opt*. 2011;16:096013.
17. Besic Gyenge E, Darphin X, Wirth A, Pieleus U, Walt H, Bredell M, et al. Uptake and fate of surface modified silica nanoparticles in head and neck squamous cell carcinoma. *J Nanobiotechnol*. 2011;9:32.
18. Senge MO, Brandt JC. Temoporfin (Foscan®; 5,10,15,20-Tetra(m-hydroxyphenyl)chlorin)—a second-generation photosensitizer. *Photochem Photobiol*. 2011;87:1240–96.
19. Leong DT, Ng KW. Probing the relevance of 3D cancer models in nanomedicine research. *Adv Drug Deliv Rev*. 2014;79–80:95–106.
20. Sambale F, Lavrentieva A, Stahl F, Blume C, Stiesch M, Kasper C, et al. Three dimensional spheroid cell culture for nanoparticle safety testing. *J Biotechnol*. 2015;205:120–9.
21. Gref R, Lück M, Quéllec P, Marchand M, Dellacherie E, Harnisch S, et al. 'Stealth' corona-core nanoparticles surface modified by polyethylene glycol (PEG): influences of the corona (PEG chain length and surface density) and of the core composition on phagocytic uptake and plasma protein adsorption. *Colloids Surf B Biointerfaces*. 2000;18:301–13.
22. Shang L, Nienhaus K, Nienhaus GU. Engineered nanoparticles interacting with cells: size matters. *J Nanobiotechnol*. 2014;12:5.
23. Huo S, Ma H, Huang K, Liu J, Wei T, Jin S, et al. Superior penetration and retention behavior of 50 nm gold nanoparticles in tumors. *Cancer Res*. 2013;73:319–30.
24. Gyenge EB, Luscher D, Forny P, Antoniol M, Geisberger G, Walt H, et al. Photodynamic mechanisms induced by a combination of hypericin and a chlorin based-photosensitizer in head and neck squamous cell carcinoma cells. *Photochem Photobiol*. 2013;89:150–62.
25. Buytaert E, Matroule JY, Durinck S, Close P, Kocanova S, Vandenheede JR, et al. Molecular effectors and modulators of hypericin-mediated cell death in bladder cancer cells. *Oncogene*. 2008;27:1916–29.
26. Song J, Wei Y, Chen Q, Xing D. Cyclooxygenase 2-mediated apoptotic and inflammatory responses in photodynamic therapy treated breast adenocarcinoma cells and xenografts. *J Photochem Photobiol B*. 2014;134:27–36.
27. Mroz P, Yaroslavsky A, Kharkwal GB, Hamblin MR. Cell death pathways in photodynamic therapy of cancer. *Cancers (Basel)*. 2011;3:2516–39.
28. Buchholz J, Kaser-Hotz B, Khan T, Bley CR, Melzer K, Schwendener R, et al. Optimizing photodynamic therapy: in vivo pharmacokinetics of liposomal meta-(tetrahydroxyphenyl) chlorin in feline squamous cell carcinoma. *Clin Cancer Res*. 2005;11:7538–44.
29. Molinari A, Colone M, Calcabrini A, Stringaro A, Toccaceli L, Arancia G, et al. Cationic liposomes, loaded with m-THPC, in photodynamic therapy for malignant glioma. *Toxicol In Vitro*. 2007;21:230–4.
30. Low K, Knobloch T, Wagner S, Wiehe A, Engel A, Langer K, et al. Comparison of intracellular accumulation and cytotoxicity of free mTHPC and mTHPC-loaded PLGA nanoparticles in human colon carcinoma cells. *Nanotechnology*. 2011;22:245102.
31. Villa Nova M, Janas C, Schmidt M, Ulshoefer T, Grafe S, Schiffmann S, et al. Nanocarriers for photodynamic therapy-rational formulation design and medium-scale manufacture. *Int J Pharm*. 2015;491:250–60.
32. Peng C-L, Yang L-Y, Luo T-Y, Lai P-S, Yang S-J, Lin W-J, et al. Development of pH sensitive 2-(diisopropylamino)ethyl methacrylate based nanoparticles for photodynamic therapy. *Nanotechnology*. 2010;21:155103.
33. Preuss A, Chen K, Hackbarth S, Wacker M, Langer K, Roder B. Photosensitizer loaded HSA nanoparticles II: in vitro investigations. *Int J Pharm*. 2011;404:308–16.
34. Compagnin C, Baù L, Mognato M, Celotti L, Miotto G, Arduini M, et al. The cellular uptake of meta-tetra(hydroxyphenyl)chlorin entrapped in organically modified silica nanoparticles is mediated by serum proteins. *Nanotechnology*. 2009;20:345101.
35. Haedicke K, Kozlova D, Grafe S, Teichgraber U, Eppel M, Hilger I. Multi-functional calcium phosphate nanoparticles for combining near-infrared fluorescence imaging and photodynamic therapy. *Acta Biomater*. 2015;14:197–207.
36. Tang L, Yang X, Yin Q, Cai K, Wang H, Chaudhury I, et al. Investigating the optimal size of anticancer nanomedicine. *Proc Natl Acad Sci USA*. 2014;111:15344–9.
37. Navarro FP, Berger M, Guillermet S, Josserand V, Guyon L, Neumann E, et al. Lipid nanoparticle vectorization of indocyanine green improves fluorescence imaging for tumor diagnosis and lymph node resection. *J Biomed Nanotechnol*. 2012;8:730–41.

Submit your next manuscript to BioMed Central and we will help you at every step:

- We accept pre-submission inquiries
- Our selector tool helps you to find the most relevant journal
- We provide round the clock customer support
- Convenient online submission
- Thorough peer review
- Inclusion in PubMed and all major indexing services
- Maximum visibility for your research

Submit your manuscript at
www.biomedcentral.com/submit




RESEARCH

Open Access



Lipid nanoemulsions and liposomes improve photodynamic treatment efficacy and tolerance in CAL-33 tumor bearing nude mice

Doris Hinger^{1*} , Susanna Gräfe², Fabrice Navarro^{3,4}, Bernhard Spingler⁵, Devaraj Pandiarajan⁵, Heinrich Walt⁶, Anne-Claude Couffin^{3,4} and Caroline Maake¹

Abstract

Background: Photodynamic therapy (PDT) as promising alternative to conventional cancer treatments works by irradiation of a photosensitizer (PS) with light, which creates reactive oxygen species and singlet oxygen ($^1\text{O}_2$), that damage the tumor. However, a routine use is hindered by the PS's poor water solubility and extended cutaneous photosensitivity of patients after treatment. In our study we sought to overcome these limitations by encapsulation of the PS m-tetrahydroxyphenylchlorin (mTHPC) into a biocompatible nanoemulsion (Lipidots).

Results: In CAL-33 tumor bearing nude mice we compared the Lipidots to the existing liposomal mTHPC nanoformulation Foslip and the approved mTHPC formulation Foscan. We established biodistribution profiles via fluorescence measurements in vivo and high performance liquid chromatography (HPLC) analysis. All formulations accumulated in the tumors and we could determine the optimum treatment time point for each substance (8 h for mTHPC, 24 h for Foslip and 72 h for the Lipidots). We used two different light doses (10 and 20 J/cm²) and evaluated immediate PDT effects 48 h after treatment and long term effects 14 days later. We also analyzed tumors by histological analysis and performing reverse transcription real-time PCR with RNA extracts. Concerning tumor destruction Foslip was superior to Lipidots and Foscan while with regard to tolerance and side effects Lipidots were giving the best results.

Conclusions: We could demonstrate in our study that nanoformulations are superior to the free PS mTHPC. The development of a potent nanoformulation is of major importance because the free PS is related to several issues such as poor bioavailability, solubility and increased photosensitivity of patients. We could show in this study that Foslip is very potent in destroying the tumors itself. However, because the Lipidots' biocompatibility is outstanding and superior to the liposomes we plan to carry out further investigations and protocol optimization. Both nanoformulations show great potential to revolutionize PDT in the future.

Keywords: Nanoemulsion, mTHPC, Head and neck cancer, PDT, Liposome

Background

Photodynamic therapy (PDT) has received more attention in recent years as attractive alternative to conventional cancer treatments such as chemotherapy, surgery

or radiotherapy [1, 2]. The principle of photodestruction on which it relies on works by exposure of a so called photosensitizer (PS) to light of an appropriate wavelength, which in turn depends on the kind of PS used. The PS reacts with oxygen upon irradiation and generates reactive oxygen species (ROS) and singlet oxygen ($^1\text{O}_2$) which damage surrounding tissue [3–5]. However, the short lifetime of singlet oxygen ($<0.04 \mu\text{s}$) and low diffusion potential with a small radius of action ($0.02 \mu\text{m}$)

*Correspondence: doris.hinger@uzh.ch

¹ Institute of Anatomy, University of Zurich, Winterthurerstrasse 190, Zurich 8057, Switzerland

Full list of author information is available at the end of the article

limits the damage to the irradiated spot [6]. In addition to this direct killing of malignant cells [7] tumor destruction can also be accomplished by targeting the tumor associated vessels [8]. However, a third possibility is to create longer lasting effects via stimulation of the immune system which subsequently may prevent tumor recurrence [9].

PDT is a strictly local modality that offers certain advantages over established anti-cancer regimes. It is e.g. minimally invasive, does not have a maximal lifetime dose and can therefore be repeated [1], gives an excellent cosmetic and functional outcome [10], does not produce drug resistance [11], and is not associated with severe systemic side effects [12]. PSs are preferentially taken up by malignant cells and therefore exhibit an inherent selectivity [13]. For this reason PSs can also be used as imaging probes in photodiagnosis (PDD) [14]. However, the selectivity leaves still room for improvement. The currently most widely used PSs are porphyrin derivatives. In an attempt to improve their optical properties modifications to the porphyrin structure have been made and led to the discovery of several second generation PSs like phthalocyanines [15] and chlorins [16]. The powerful chlorin PS *m*-tetrahydroxyphenylchlorin (mTHPC) is a well characterized substance and was highly successful in various *in vitro*, *in vivo* studies and clinical trials which has ultimately led to its approval for palliative treatment of head and neck cancer in Europe [17–20]. Although very promising its routine use in the clinic is hampered by poor water solubility which leads to aggregation, problematic systemic administration and suboptimal biodistribution. Moreover extended photosensitivity of patients after treatment impairs applicability [5, 21].

A possible solution to these drawbacks can be offered by encapsulation of PSs into nanocarriers. With this approach several problems could be tackled at once. First of all the solubility can be drastically improved, easing intravenous injections. Furthermore cancer selectivity could be increased by passive targeting, profiting from the enhanced permeability and retention effect (EPR) of nanoparticles in solid tumors [22]. Due to the high payload of nanoformulations, accumulation of greater pharmacological PS doses within the tumor may be facilitated, which could improve PDT effects by lowering the risk of an unwanted photosensitivity of healthy tissues, such as the skin.

We recently developed a biocompatible nanoemulsion (Lipidots) [23] as carrier for mTHPC with excellent optical properties which we subsequently tested in two *in vitro* studies [24, 25]. It could be demonstrated that Lipidots can significantly lower the dark toxicity of mTHPC while maintaining its photodynamic activity. In the course of our research we identified the most

promising Lipidot formulation which we decided to further test *in vivo*.

In the present study we compared this novel mTHPC nanoemulsion (Lipidots) with a liposomal mTHPC formulation (Foslip) [26], which has been shown to produce promising results with regard to tumor destruction in cats [27, 28], and the approved mTHPC formulation (Foscan), in CAL-33 tumor bearing nude mice.

Methods

Drug and nanoparticle preparation

MTHPC and the liposomal mTHPC formulation Foslip were obtained from Biolitec Research GmbH, Jena, Germany as powder. A stock solution of 1 mg/mL Foscan was prepared by dissolving the mTHPC powder in a 40/60 ethanol/propylene glycol mixture and filtered through a syringe filter (0.22 µm pore size; TPP, Trasadingen, Switzerland). Foslip (20 mg/mL DPPC/DPPG, 2.2 mM mTHPC, 50 mg/mL Glucose) was reconstituted with sterile water, giving a stock solution of 1.5 mg/mL (\approx 2.2 mM) mTHPC content, with an average particle size of 135 nm and a polydispersity index (PDI) of 0.089. A nanoemulsion containing mTHPC (Lipidots, 50 mg/mL lipid, 1.06 mM mTHPC) with an average particle diameter of 50 nm and a PDI of 0.17 was prepared according to Delmas et al. [23] and Navarro et al. [24].

Briefly, Lipidots were manufactured by selecting the suitable weight ratios of core/shell excipients to design 50 nm diameter nanoparticles. The dispersion is composed of 37.5 % (w/w) of lipid phase (with a lecithin/PEG surfactant weight ratio of 0.19 and a surfactant/core weight ratio of 1.20). The Lipidots were loaded with 920 molecules of mTHPC/particle. MTHPC was incorporated into the lipid mixture as a concentrated solution in ethyl acetate and after vacuum elimination of organic solvent, the oily phase was added to the aqueous phase and emulsification was performed as previously described [24]. The mTHPC concentrations were determined by high-performance liquid chromatography (HPLC) analysis. Separation was achieved on a Sunfire C18 column (250 mm \times 4.6 mm, i.d. 5 µm) at 30 °C. The mTHPC compound was eluted at 2.10 min using a isocratic mobile phase of acetonitrile/H₂O trifluoroacetic acid, 0.1 %: 9/1 at 1 mL/min flow rate after injection of 30 µL. The UV detection is operated at 425 nm. The mTHPC concentrations were assessed using a calibration curve in the range of 1–12 µg/mL. Physicochemical characterization data of Lipidots can be found in the supplements (Additional file 1: Table S1).

All solutions were stored at four degrees Celsius in the dark and further diluted with sterile phosphate buffered saline (PBS) for injection (0.15 mg/kg mTHPC).

If not otherwise indicated, all chemicals were purchased from Sigma-Aldrich, Buchs, Switzerland.

Cell culture

CAL-33, tongue squamous cell carcinoma cells (DSMZ, Braunschweig, Germany), were grown in RPMI-1640 medium without phenol red and with 10 % fetal calf serum (FCS), 2 mM Glutamax (Life Technologies, Carlsbad, USA), 1 % Penicillin/Streptomycin as supplements. Cells were kept in 75 cm² cell culture flasks at 5 % CO₂ and 37 °C. Cell counting was performed with a Neubauer chamber (Laboroptik Ltd., Lancing, UK) on an aliquot of cells after staining with 0.1 % (w/v) nigrosin in PBS.

Husbandry conditions of mice & tumor model

Female immune deficient CD1-*Foxn1*^{nu} nude mice (4–6 weeks old) were obtained from Charles River, Sulzfeld, Germany. The mice were kept as groups of 5 in individually ventilated cages (IVC) under specific pathogen free (SPF) conditions and provided with food and water ad libitum. To establish the tumor model 9 mice each were subcutaneously injected into the right flank with 1.0×10^6 , 1.5×10^6 or 2.0×10^6 CAL-33 cells in 0.1 mL ringer lactate (Kantonsapotheke, Zurich, Switzerland) using a 26 G needle and one mL syringe (B. Braun, Melsungen, Germany). The animals were examined at least every third day for up to 42 days. Upon examination the mice were weighed and scored for abnormalities in behavior and appearance. Tumor sizes were measured with a Vernier caliper.

All animal experiments were implemented with approval of the Swiss cantonal ethics committee for animal experiments (No. 156/2012).

Biodistribution studies

To determine pharmacokinetics Foscan, Foslip and Lipidots were injected intravenously into 10 mice each at a final concentration of 0.15 mg mTHPC/kg bodyweight (bw). Fluorescence measurements were carried out four, 8, 12, 24, 48 and 72 h after drug injection, by pressing the optic fiber of a spectrometer (PDT fluorometer; JETI Technische Instrumente GmbH, Jena, Germany) on three different spots on the tumor while holding the mice restrained. Three different spots on the skin were also analyzed as a reference. After the last measurement the mice were sacrificed and the tissues (tumor, skin, liver, spleen, kidney) were weighed, cut in small pieces and snap frozen in liquid nitrogen. For HPLC analysis the tissue was freeze dried (Christ Freeze drying system Alpha 1–4 LSC). The resulting powdered tissue was weighed and approximately 10–20 mg was transferred to a two milliliter reaction tube. Then 1.5 mL of methanol:DMSO (3:5, v:v) was added followed by immediate mixing for

three times five sec using a vortex mixer (Merck Eurolab, MELB 1719) operating at 2400 rpm and then incubated at 60 °C while continuously shaking for at least 12 h. All samples were then spun at 16,000g in a centrifuge (Microfuge, Heraeus, Germany) for 5 min. One milliliter of each supernatant was transferred to a HPLC vial and analysed by HPLC. The HPLC system consisted of the solvent module “System Gold 126” (Beckman Coulter, Brea, USA), autosampler “Triathlon” (Spark), fluorescence detector “RF-10A XL” (Shimadzu, Kyoto, Japan) with SS420x interface set for excitation wavelength at 410 nm and for emission wavelength at 654 nm, online degasser (ERC3415 alpha, ERC), column thermostat Jet-Stream Plus set at 30 °C (Thermotechnic Products), column LiChroCART250-4 with Purospher STAR RP-18 endcapped and guard column LiChroCART4-4 with Purospher STAR RP-18e endcapped (Merck). The mobile phase was composed of acetonitril: 0.1 % trifluoroacetic acid in water (57.5:42.5 v/v) and the flow rate set at 1 mL/min. The retention time for mTHPC was about 10 min and the injection volume was 50 µL. The measuring range was from 0.25 to 100 pg/µL ($r^2 = 0.9998$) and the detection limit 0.05 pg/µL. The software used was 32 Karat Software, Version 5.0, Build 1021 (Beckman Coulter). The tissue concentration of mTHPC was determined from a calibration curve constructed by plotting the peak height of mTHPC standard solutions versus their concentrations. The calibration was linear within this range.

In vivo PDT

Before treatment 90 tumor-bearing mice were injected subcutaneously with 1.5 mg/kg bw of the painkiller Metacam (Kantonsapotheke). Subsequently they were intravenously injected with one of the drug formulations (± 0.15 mg mTHPC/kg bw) and treated at the optimum time point according to the biodistribution study. For laser irradiation the mice were covered with a surgical drape, leaving only the tumor unprotected (\pm an irradiation area of 1.5 cm in diameter). Mice were held restrained tightly and irradiated with a Ceralas PDT laser 652 (Biolitec) for either 100 or 200 s (± 10 or 20 J/cm²; 100 mW/cm²). To monitor treatment effects tumor sizes were measured with a Vernier Caliper every 3 days and all mice were photographed with an 8 MP camera (Samsung, Seoul, South Korea) before treatment and up to 14 days later.

Histology and Immunohistochemistry

In order to screen for short term and long term PDT effects 48 h and 14 days after laser irradiation half of the mice ($n = 45$) were sacrificed in each group. Liver, kidney, spleen and tumor were taken and rinsed with PBS. The organs were subsequently fixed with four per cent

formaldehyde (FA)/PBS for 12 h and transferred to PBS or snap frozen in liquid nitrogen. FA fixed samples were dehydrated with an increasing alcohol series and embedded in paraffin. Five micrometer sections were cut and transferred to Superfrost glass slides (Thermo Fisher, Waltham, USA). The sections were deparaffinized and either stained with haematoxylin and eosin or processed for immunohistochemistry. For the latter the slides were washed repeatedly in Tris buffered saline (TBS) and blocked for 30 min in 1 % bovine serum albumin (BSA)/TBS. The slides were incubated with an anti-ki-67 antibody (Abcam, #ab15580, Cambridge, UK) over night at four degrees Celsius (1:100 in TBS). All following steps were performed at room temperature. After another washing step with TBS anti-rabbit-biotin antibody (BioScience Products AG, Emmenbrücke, Switzerland) was added (1:100 in BSA/TBS) for 30 min. After washing with TBS, the slides were incubated with Streptavidin Peroxidase (Biospa, Milano, Italy, 1:100 in TBS) for 30 min. Another washing step with TBS followed, then the endogenous peroxidase was blocked by placing the slides in 0.3 % H₂O₂/TBS for 20 min. After another washing step with TBS the slides were incubated with 0.7 mg/mL 3,3'-diaminobenzidine/H₂O for 3–20 min. The slides were washed with dH₂O and mounted with glycergel (Dako, Glostrup, Denmark).

Quantitative reverse transcriptase polymerase chain reaction (qRT-PCR)

Twenty mg frozen tumor tissue was transferred to MagNALyser Green Beads tubes (Roche, Basel, Switzerland) and 600 microliter lysis buffer (RNeasy Mini Kit, Qiagen, Venlo, The Netherlands) was added. Tissue homogenization was carried out according to manufacturer's instructions with a Precellys 24 Homogenizer (Bertin, Montigny le Bretonneux, France). The lysate was centrifuged for 1 min at 11.000g and transferred to RNeasy Mini Spin columns (Qiagen). RNA extraction was performed according to manufacturer's protocols. Five hundred

ng of purified RNA were subsequently used for cDNA synthesis with QuantiTect Reverse Transcription Kit (Qiagen), which was carried out according to the manufacturer's recommendations. QRT-PCR was performed with hydrolysis probes from a Universal Probe Library (Roche) on a LightCycler 480 (Roche). The PCR program consisted of an activation phase of 10 min at 95 °C followed by 45 cycles with 15 s at 95 °C and 1 min at 60 °C. Data was analyzed with the LightCycler480 software and REST software (<http://www.gene-quantification.de>). Primer sequences are listed in Table 1.

Data analysis and statistics

For the measurement of tumor volumes (V) the following formula was used: $V = \frac{\pi}{6} \times L \times W^2$; where L corresponds to the length of the tumor and W to width of the tumor.

All groups consisted of at least five individuals.

Measurement raw data was transformed by square root transformation and 1-way ANOVA was performed on data sets of day zero, five and 14 after treatment.

Results

The HNSCC model in nude mice worked best with a subcutaneously injected inoculation volume of 100 µL ringer lactate solution containing 1.5×10^6 CAL-33 cells. While for the concentrations 1×10^6 and 2×10^6 cells no exponential tumor growth phase was reached (Additional file 1: Fig. S1 A,C), after injection of 1.5×10^6 cells solid tumors with a calculated average volume of 150 mm³ developed within 24 days (Additional file 1: Fig. S1 B).

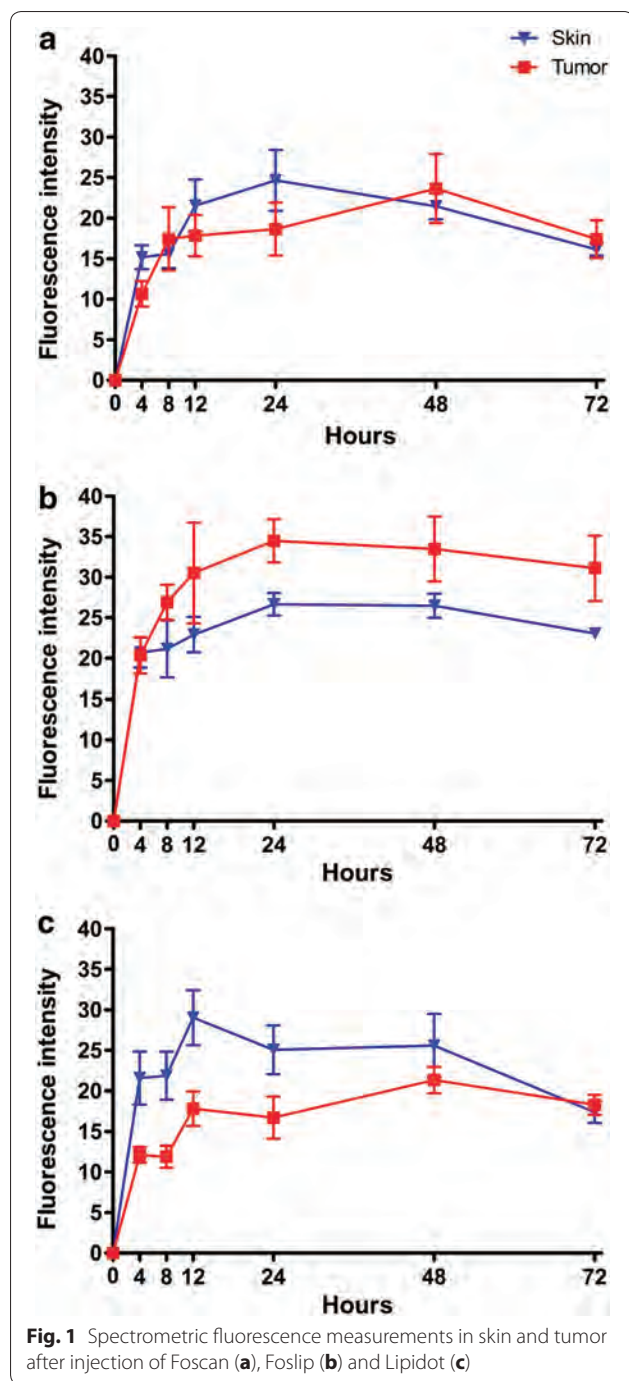
The biodistribution profile established by spectroscopic fluorescence measurements of mTHPC revealed that all formulations accumulated in the tumor but the distribution patterns were different for the three substances (Fig. 1). After Foscan injection the fluorescence in the tumor increased fast until 8 and then the curve reached a plateau. Tumor and skin accumulations were

Table 1 Sequences of primers

Gene	Primer forward 5'–3'	Primer reverse 5'–3'	Probe
Human GAPDH	CAGCAAGAGCACAAAGAGGAA	GTGGTGCGGGACTGAGTGT	#3
Human TACSTD	AGAGAGGGAGTGAGAGAAATTAAGG	GCGACTCCCTTTTCGTTCTT	#23
Human MMP7	GCTGACATCATGATTGGCTTT	TCTCCTCCGAGACCTGTCC	#72
Human ALDH1A3	TGGTGCTTTAAATGTCAGG	TATTCGGCCAAAGCGTATTC	#53
Human MKI67	CCAAAAGAAAGTCTCTGGTAATGC	CCTGATGGTTGAGGCTGTTC	#39
Human GLUT1	CTTTTCGTTAACCGCTTTGG	CGAGAAGCCCATGAGCAC	#62

Probe numbers relate to the Universal Probe Library (Roche)

GAPDH Glyceraldehyde 3-phosphate dehydrogenase; *TACSTD2* Tumor-Associated Calcium Signal Transducer 2; *MMP7* Matrix Metalloproteinase-7; *ALDH1A3* Aldehyde Dehydrogenase 1 Family, Member A3; *MKI67* Marker of Proliferation Ki-67; *GLUT1* Glucose Transporter 1

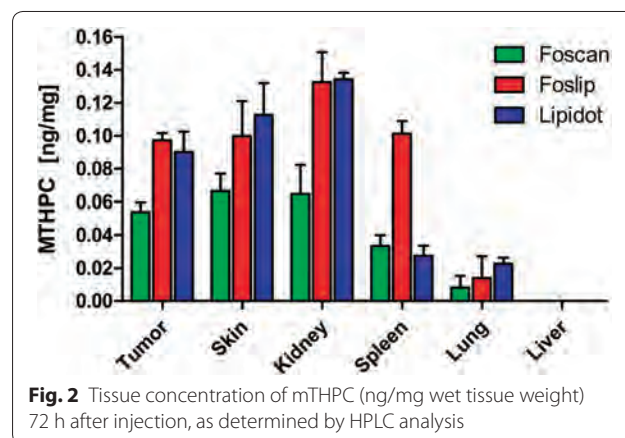


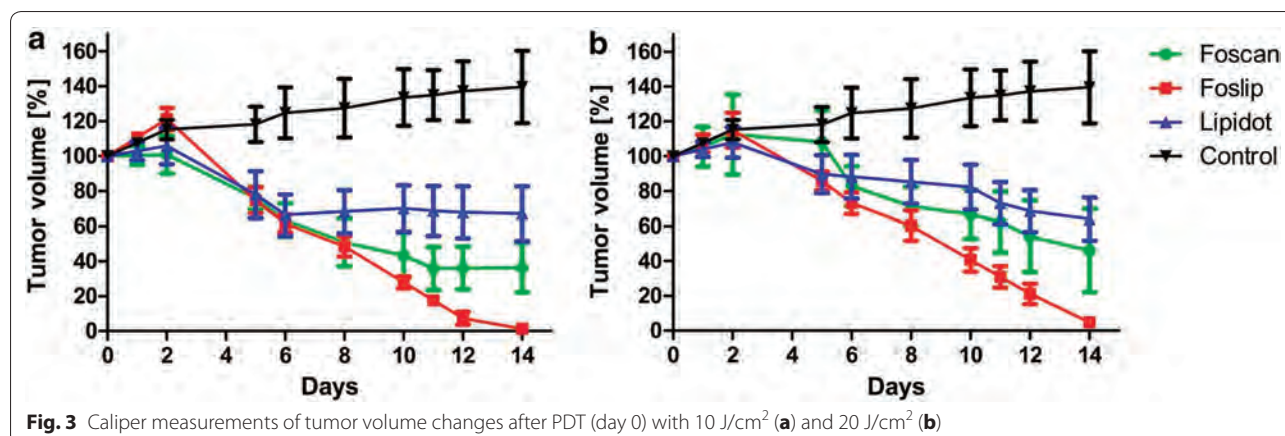
rather similar in trend but after 8 h, 48 h and 72 h slightly higher tumor fluorescence could be detected. Therefore 8 h was selected as the optimum drug–light interval for Foscan (Fig. 1a). Foslip accumulation in the tumor rose sharply until 12 h with the curve flattening afterwards. The detected fluorescence was higher in the tumor when compared to skin between 24 and 72 h. Accordingly 24 h was chosen as ideal treatment timepoint for Foslip

(Fig. 1b). Lipidots accumulated strongly in the skin, peaking at 12 h after injection. Fluorescence accumulation within the tumor was increasing over time but was delayed when compared to skin. Forty eight hours after injection Lipidots started to be cleared from the skin while accumulation within the tumor persisted. Although accumulation in the tumor was not higher 72 h was chosen as drug–light interval when less Lipidots were present in the skin (Fig. 1c). As a result of these fluorescence biodistribution profiles, the drug–light interval selected and applied for all further in vivo experiments are 8 h for Foscan, 24 h for Foslip and 72 h for Lipidot.

HPLC analysis confirmed mTHPC accumulation in the tumor 72 h after injection of all drug formulations (Fig. 2). Concentrations of Lipidots and Foslip were comparable, while the mTHPC concentration was lower with the Foscan formulation at this time point. Kidneys as well as skin showed high accumulation with Lipidots and Foslip and lower accumulation with Foscan. Foslip concentration was also high in the spleen whereas Lipidots and Foscan were present in this organ to a much lower extent. Very low concentrations were found in the lung with all three formulations and no drug could be detected in the liver with either formulation at 72 h.

Therapeutic effects after PDT treatment, analyzed by tumor size measurements indicated a treatment response to all three drug formulations (Fig. 3). The best results were accomplished by Foslip induced PDT which finally resulted in complete tumor remission with both light doses (10 and 20 J/cm²; 100 mW/cm²) (Fig. 3a, b). Foscan-PDT was also effective but tumors stopped to decrease further in size after 12 days with the lower light dose of 10 J/cm² (Fig. 3a). Tumor residues of around 40 % of the initial tumor volume (i.e. before treatment) were still present 14 days later with both light doses (Fig. 3a, b). Lipidots, although diminishing the tumor masses significantly failed to decrease the tumor size further after





6 days with the lower light dose (Fig. 3a). The higher light dose (20 J/cm²) resulted in continuous reduction of tumor masses down to around 60 % of the initial tumor volume (Fig. 3b). Fourteen days after treatment Foslip was significantly superior to both, Foscan and Lipidots at lower light doses ($p < 0.05$) and significantly superior to Lipidots at higher light doses ($p < 0.01$).

Forty eight hours after Foscan and Foslip mediated PDT skin burns were visible at the irradiated spot with both light doses but only slight burns occurred after Lipidot-PDT, even with the higher light dose (Figs. 4, 5). One week after PDT necrotic tissue and crusts were visible with all three drug formulations at both light doses. Fourteen days after Foslip-PDT visible tumor masses had disappeared completely and the skin had healed with minimal scarring. Tumors treated with Foscan-PDT had diminished significantly in size and the skin had started to heal but small crusts and residual tumor tissue remained. Lipidot-PDT treated tumors had also diminished in size after 14 days but with this formulation an outer rim of the tumor remained with a crust from destroyed tissue in the middle. Generally the destructive effects as well as the burning of the skin were more severe with the higher light dose in all cases which, however, did not seem to affect healing negatively.

A drop of body weight was observed in mice after Foscan and Foslip mediated PDT but more severe in case of Foscan (Fig. 6a). Also the higher light dose lead to a stronger body weight drop (Fig. 6b). Lipidots on the other hand did not result in any loss of body weight with neither light dose. If anything it delayed the body weight gain of the juvenile mice slightly (Fig. 6a, b).

A change in behavior of mice during and after administration of Foscan was apparent. The mice curled upon injection, which seemed to be painful to the rodents. Also during and after PDT the mice struggled and tried to avoid strongly to be touched, despite being treated

with analgesics. Foslip and Lipidot injections as well as PDT seemed to be well tolerated with mice not showing any unusual behavior.

Histological analysis was in accordance with caliper measurements revealing vascularized vital CAL-33 tumors in untreated mice (Fig. 7a). Forty eight hours after Foscan mediated PDT the tumors showed clear features of destruction with lamellar appearing tumor parts and flattened cells (Fig. 7a). Lipidot-PDT created the same lamellar features but a larger area in the outer part of the tumors appeared to be left intact (Fig. 7c). Foslip-PDT, however, led to lamellar parts and strongly flattened cells throughout the whole tumor mass (Fig. 7d).

To distinguish between vital, proliferating cancerous and damaged tumor tissue a proliferation marker (ki-67) was used (Fig. 8). Antibody staining supported the tumor size measurements confirming diminished proliferation corresponding to less ki-67 expressing cells 48 h after PDT with all formulations. Foscan-PDT treated tumors showed little ki-67 positive cells when compared to untreated tumors after 48 h (Fig. 8b). Tumors after Lipidot mediated PDT still exhibited several ki-67 positive cells but less than untreated controls (Fig. 8c) and tumors that had been subjected to Foslip-PDT exhibited no ki-67 stained cells at all (Fig. 8d).

Histological and immunohistochemical analyses of tumors 14 days after treatment supported caliper measurement data. Tumors which had been subjected to Foslip-PDT were completely eradicated just leaving fibrotic scar tissue behind. Tumors after Foscan-PDT were not fully destroyed leaving some tumor tissue intact while the tumors after Lipidot-PDT were only partly destroyed with some cells positive for ki-67, thus still proliferating (data not shown).

Possible side effects of the treatments were investigated by analyzing livers, kidneys and spleens 48 h and 14 days after PDT. Liver damage was recognizable by deformed



Fig. 4 Images of tumors after PDT with 10 J/cm². The irradiation area had a diameter of 1.5 cm (circle)



Fig. 5 Images of tumors after PDT with 20 J/cm². The irradiation area had a diameter of 1.5 cm (circle)

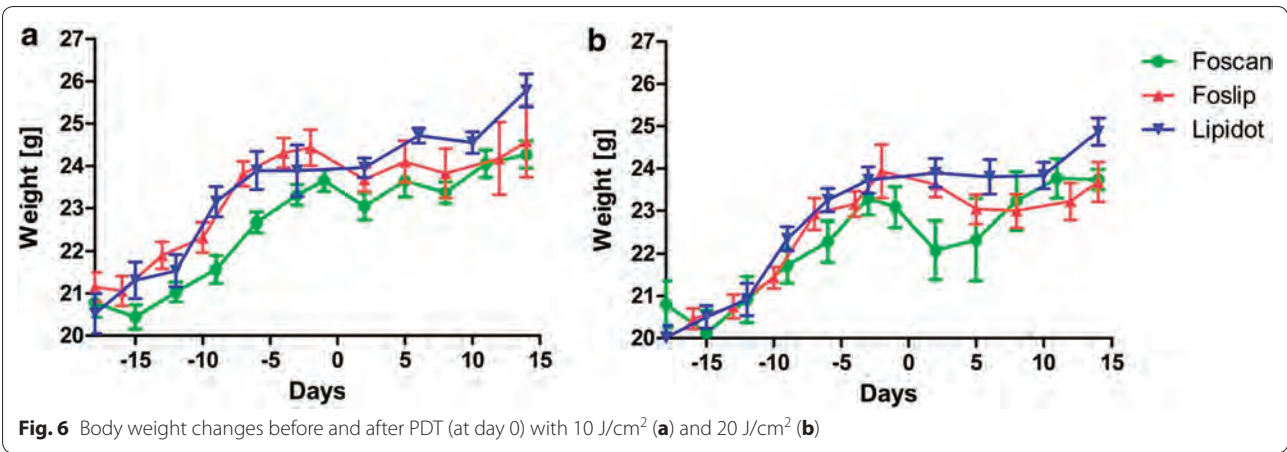


Fig. 6 Body weight changes before and after PDT (at day 0) with 10 J/cm² (a) and 20 J/cm² (b)

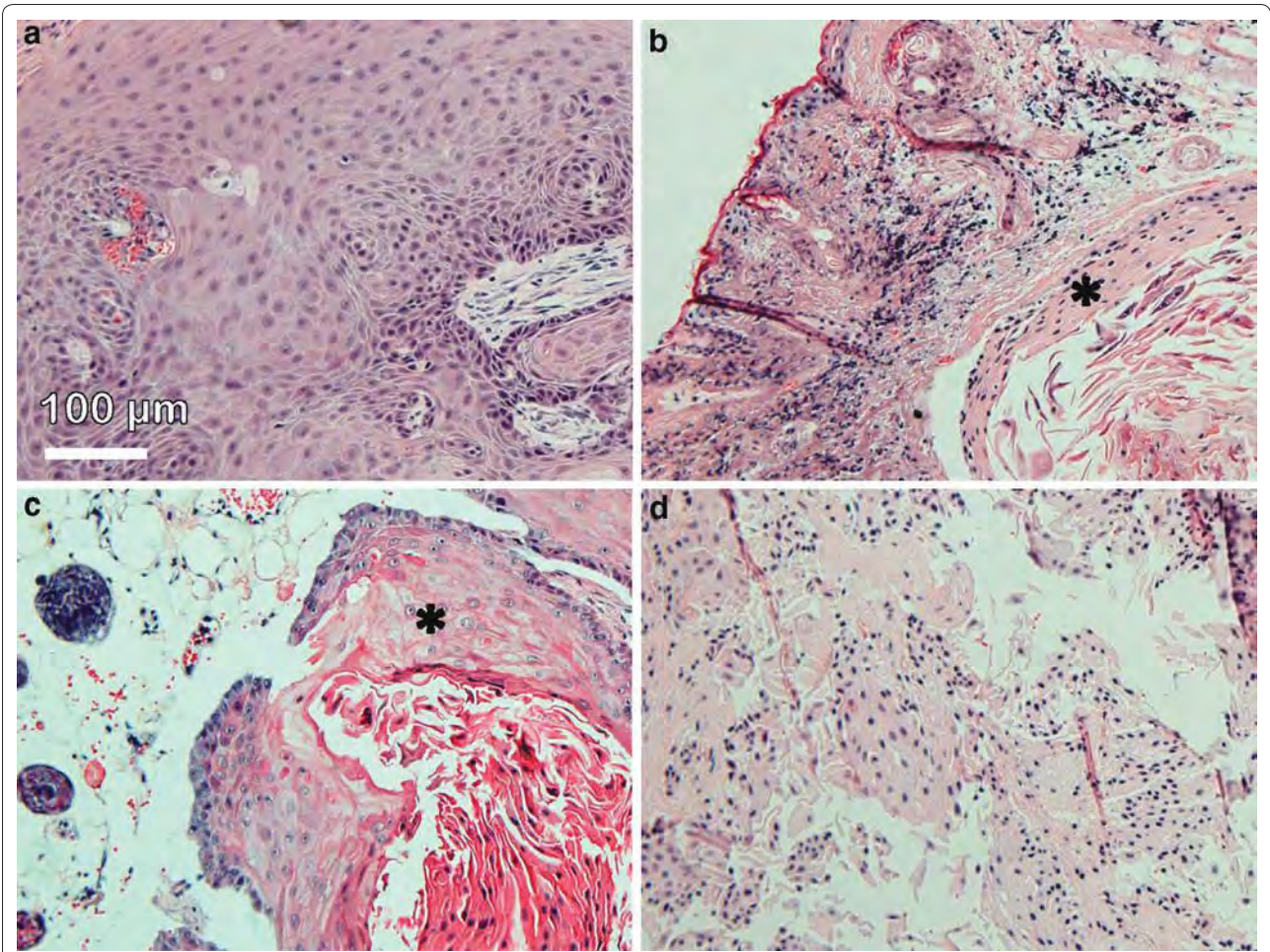


Fig. 7 H&E stain of CAL-33 tumors. **a** Untreated control tumor. Tumor 48 h after PDT with Foscan (**b**), Lipidot (**c**) and Foslip (**d**). Laser light irradiation 20 J/cm². Asterisk (**b**, **c**): tumor tissue. **a**, **d**: only tumor tissue

blood vessels and condensed nuclei of hepatocytes 48 h after Foscan and Foslip mediated PDT but not after Lipidot-PDT. However, the morphological changes were

reversible as 14 days later all livers displayed similar morphological appearance. No damage of other organs was detectable neither 48 h after nor 14 days after PDT.

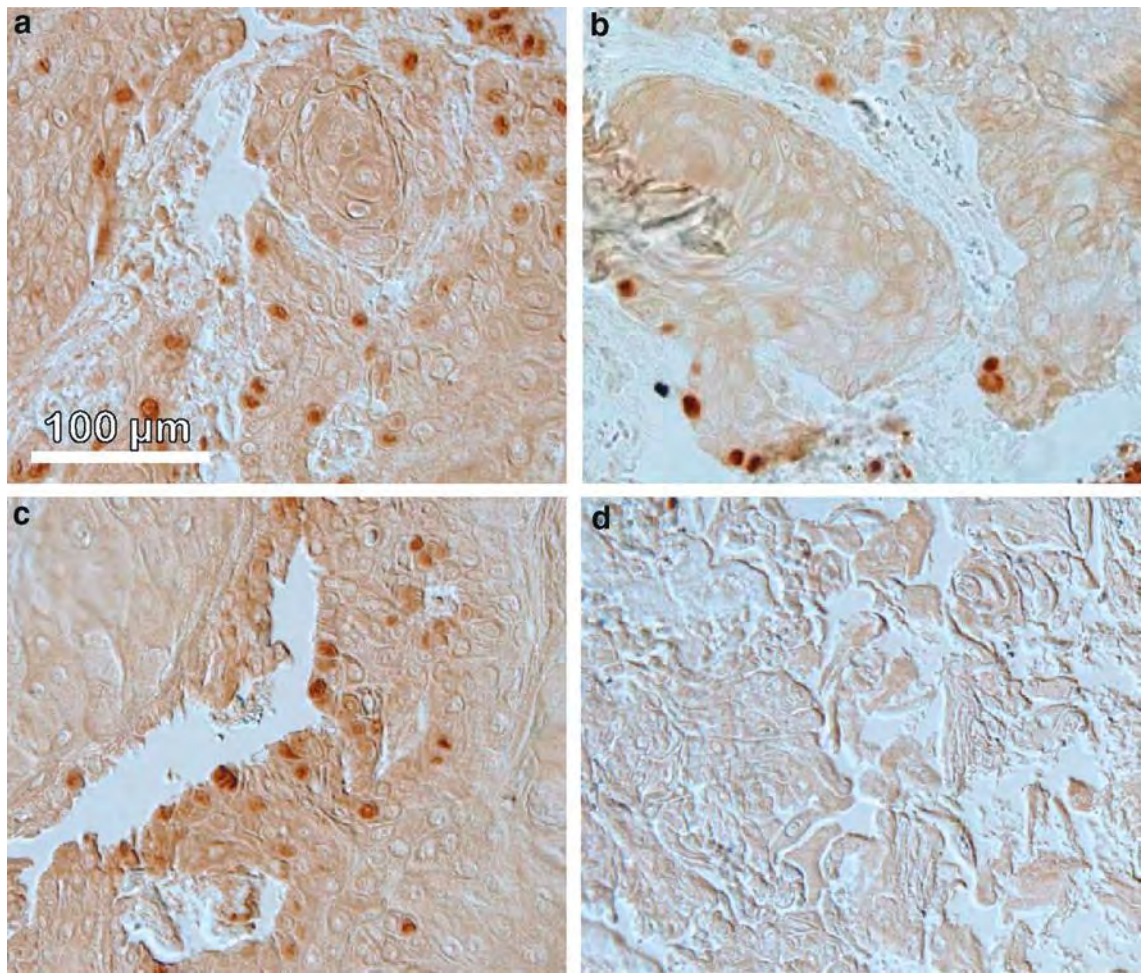


Fig. 8 Ki-67 immunohistochemistry for CAL-33 tumors. **a** Untreated control tumor. Tumor 48 h after PDT with Foscan (**b**), Lipidot (**c**) and Foslip (**d**). Laser light irradiation 20 J/cm²

We tested possible expression changes of five genes (TACSTD, MMP7, ALDH1A3, MKI67, GLUT1) in tumors 48 h and 14 days after mTHPC and Lipidot mediated PDT compared to untreated tumor controls (Fig. 9). Foslip-PDT destroyed the tumors completely and therefore no RT-PCR analysis was performed. MMP7 and ALDH1A3, that are stem cell markers for squamous cell carcinoma [29, 30], were not expressed in neither treated nor untreated tumors. TACSTD as marker for tumor aggressiveness [31] was not present in relevant abundance either. GLUT1, that may reflect the grade of malignancy [32], showed upregulation 48 h after mTHPC mediated PDT but not after Lipidot-PDT. However, these alterations were not present 14 days later. The proliferation marker gene MKI67 [33] did not reveal a significant

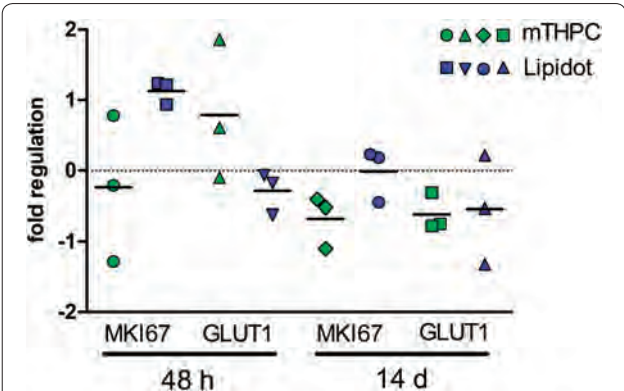


Fig. 9 QRT-PCR data from tumors 48 h and 14 days after mTHPC-PDT and Lipidot-PDT. Laser light irradiation 20 J/cm²

expression change although it was expressed to a slightly higher extent in tumors after Lipidot-PDT when compared to tumors that had been exposed to Foscan-PDT.

Discussion

Many preclinical studies provide evidence that PDT has great potential as anti-cancer modality. However, the hurdles of limited solubility of photosensitizers and photosensitivity of patients hamper routine use in the clinics and made encapsulation of PSs into nanocomposites an attractive option. Recently, the successful encapsulation of mTHPC in several nanocarriers had been described, such as polymeric nanoparticles [34, 35] and calcium phosphate nanoparticles [36]. In a similar approach in our former studies we presented the successful encapsulation of mTHPC into fully biocompatible and biodegradable lipid nanoemulsions and showed first data in monolayer cells [23, 24]. In our subsequent investigations in multicellular tumor spheroids we identified a formulation with a high mTHPC payload that featured the same excellent PDT effects as the free mTHPC but with a reduced dark toxicity (Lipidots) [25]. This nanoemulsion consists of a phospholipid (lecithin) monolayer, protected by a PEG-shell with a soybean/wax core, where mTHPC is incorporated. The average particle diameter of the most promising formulation was 50 nm with a PDI of 0.17 and a zeta potential close to -7 mV.

In the present study we now report for the first time on in vivo PDT with these novel PS-loaded Lipidots using a cancer xenograft nude mouse model. To better compare PDT effects of Lipidots, we included treatments with the conventional and approved mTHPC formulation Foscan [37–39] as well as the liposomal mTHPC formulation, Foslip, that already gave promising results in the treatment of cancer in cats [28, 40] and mice [40–42]. The liposomes in the Foslip solution had an average particle size of 135 nm and a PDI of 0.089 with a zeta potential of around -13 mV.

One of the prerequisites for successful PDT is a high accumulation of the PS within the tumor site. While it is known that PSs are preferentially taken up by cancer cells compared to normal cells [13], in vivo intratumoral doses of PSs may actually often be low due to solubility problems and/or interactions with plasma proteins [42]. Increasing the PS dose, however, bears the risk of high circulating PS amounts and photosensitivity of skin and eyes.

We here showed that after intravenous injection Foscan accumulates in cancer xenografts and that treatment with Foscan-PDT significantly reduced tumor volumes under the selected conditions. However, our histological analyses confirmed that Foscan-mediated PDT did leave tumor residues behind in most cases. These residues were

still present 14 days after treatment. Our HPLC data indicated a lower cancer accumulation of Foscan when compared to the other formulations 72 h after injection. The low accumulation, probably due to solubility problems, might be an explanation for the suboptimal PDT success. Also the other organs presented with less mTHPC content in the case of Foscan. Apart from solubility issues, an interaction with plasma proteins or, when taking into account the late time point of the HPLC measurement, faster systemic clearance could be at work.

Immunohistochemistry with ki-67 antibodies revealed that after Foscan-PDT, proliferating cells were still present in these samples but not more than in untreated cancers. Since elevated ki-67 is thought to be indicative for an unfavorable prognosis in head and neck cancers [43], incomplete PDT apparently did not select for this phenotype. To further characterize surviving tumor cells after PDT with Foscan, we performed qPCR studies for selected genes. Gene expression analyses revealed that cancer stem cell markers MMP7 and ALDH1A3 were neither transcribed before nor after PDT in CAL-33 cells. However, one genetic marker of tumor aggressiveness, GLUT1, was upregulated after Foscan-PDT. To the best of our knowledge, this is the first report on an increase of GLUT1 mRNA due to Foscan-PDT. The upregulation may have been the result of a PDT-related acute stress response as GLUT1 has previously been described as cell stress response gene [44]. However, 14 days after Foscan-PDT GLUT1 expression returned to control levels, suggesting that no permanent cell transformation into a GLUT1-related aggressive subtype had taken place. Although in our model remaining tumor cells did not start to proliferate in an aggressive manner we cannot exclude that they changed their phenotype. It is known that PDT can cause resistance in tumor cells under certain conditions and an acute stress response is one of them [11]. Thus, it would be interesting to investigate PDT resistance mechanisms in a follow up study by irradiating the tumors repeatedly.

Despite the different nature of the nanoformulations both, Lipidots and Foslip, accumulated in the xenografts and could reduce tumor volumes significantly after PDT. The observed slower cancer accumulation rate of Lipidots compared to Foscan is in line with our previous in vitro results from cancer spheroids [25] where penetration of Lipidots into the spheroid core was delayed. However, while tumor residues were still present after Lipidot-PDT, Foslip mediated PDT could eradicate the cancers completely. After Lipidot-PDT primarily the outer rim of the tumor seemed to be left intact, which was confirmed by histological analyses. Interestingly, we have observed a similar outcome already in our previous in vitro study with multicellular tumor spheroids

[25] where spheroids were dying in the center but outer cell layers were left intact. The reason for this phenomenon is not clear yet. We can only speculate that e.g. the cells in the center are more susceptible to PDT due to poor nutrient supply or that in the outer layers a kind of quenching effect might occur. Another possible explanation could be that the particles stay intact when entering the cell and are therefore less accessible for light activation. Ki-67 staining also revealed proliferating cells after Lipidot PDT as seen in the case of Foscan, while after Foslip PDT no such cells were present. QRT-PCR data showed no GLUT1 upregulation after PDT for neither of the particles, indicating that encapsulation changes certain cellular effects of the PS *in vivo*. This result is well in line with our previous *in vitro* results where we could show that encapsulation into Lipidots can dampen the expression response after mTHPC mediated PDT for a wide range of genes [25]. With regard to drug resistance encapsulation might thereby offer an advantage over the use of the free formulation.

Both particles, Lipidots and Foslip, contain the same drug and drug amounts were kept constant for all formulations. Furthermore, 72 h after injection quantitative HPLC analysis showed similar mTHPC amounts in the xenograft for both nanoformulations. According to these observations the difference in therapy outcome is most likely due to the nanoparticle itself.

While in the Foscan solution mTHPC is solubilized by use of a solvent consisting of propylene glycol/alcohol in the liposomes the PS, because of its amphiphilic nature, is entrapped in the phospholipid bilayer. In contrast in the nanoemulsion (Lipidots) with a phospholipid monolayer hull the PS is incorporated into the oil/wax core. Due to the different structure cells might interact with each nanoparticle in a different way and might cause or might not cause PS release by an uptake event. Furthermore, it is well known that the nature of the particle can have a major impact on its later subcellular localization, which is an import factor for the success of PDT [45]. Additionally both particles consist of different lipids and contain different lipid amounts in their formulation which is fivefold higher in the case of Lipidots.

From our biodistribution studies we have chosen drug–light intervals of 8 h and 24 h for Foscan and Foslip, respectively. To avoid high PS levels in the skin, for Lipidots, we extended the drug–light interval to 72 h. The idea behind this approach was to minimize the damage to healthy tissue by irradiation and to reduce the risk of subsequent scarring. However, with careful shielding as in our study, an earlier treatment time point might have been advantageous, since it has been shown that the drug–light interval determines in which compartment the PS accumulates preferentially. It has

been demonstrated e.g. by Lassalle et al. [46] that at early time points Foslip is circulating mostly within the blood stream, only after several hours it can reach the tumor site and at later time points it is mainly located within the cancers of mammary carcinoma bearing nude mice. It might have been the case that at the late treatment time point blood vessels were not affected by PDT, which would have been necessary to avoid subsequent tumor regrowth. In the present study, biodistribution was investigated by two complementary methods, i.e. spectrometric fluorescence *in vivo* measurements and HPLC endpoint analyses. Clearly, certain discrepancies between results of these methods arose that may have been caused by different optical measurement conditions after injection of the formulations that were most likely influenced by differences in subcellular distribution, aggregation behavior or localization of the PS within the tissue. It is well known that the nature of the nanocarrier may have a strong influence on these parameters, which can in turn lead to decreased detectability by methods that rely on fluorescence and might ultimately hamper a treatment response. Considering the different size and composition of the nanocarriers a distinctively different biodistribution profile was to be expected.

However, differences in the detectability made it very difficult to predict the optimal treatment time point. On the other hand, use of HPLC detection for all treatment time points would have called for a huge amount of rodents, which we deliberately refrained from. Nevertheless a better correlation between fluorescence measurements and HPLC should be established for future experiments.

Furthermore, it has to be stated that for successful PDT, dosimetry, that means the appropriate drug and light dose, as well as the optimal drug–light interval are of uttermost importance. In the case of Foscan and Foslip appropriate treatment schemes had already been established previously [28, 46], while for Lipidots no such protocol exists. We therefore cannot exclude that the drug–light interval used in our mouse model was not optimal for all substances, especially for the Lipidot formulation.

A factor which is often neglected in the therapy of cancer patients is their overall constitution. Because their body is already massively weakened by the disease it is of uttermost importance that the administered drugs do not unnecessarily deteriorate their health status by causing additional side effects. When it comes to treatment tolerance Lipidots were clearly performing best. Convenient, painless injection, no change in behavior of mice and no body weight loss indicate a highly biocompatible nanoformulation. In contrast Foscan was problematic in this regard, causing painful injections and severe weight loss.

Foslip was also superior to Foscan in this matter. Injections were unproblematic; however a slight weight loss was apparent. Furthermore our HPLC data showed high spleen accumulation only for Foslip, which leads to the conclusion that it is particularly susceptible to elimination from the blood stream via the reticuloendothelial system. Given the fact, that the particles are not protected by a PEG layer, it is not surprising that they are inferior to Lipidots in this regard.

As evidenced by histology, both Foslip and Foscan caused acute liver toxicity while the Lipidots seemingly had no such effect. However, 14 days after treatment all livers morphologically recovered. This is in line with our HPLC data which showed that already after 72 h no mTHPC was detectable in the livers, pointing towards a fast liver clearance as it had already been shown by Roviers et al. [47].

The high skin accumulation of Lipidots after systemic injection was a surprising finding as not much can be found in the literature concerning this phenomenon. Moreover no real explanations are given. However, many studies about topical nanoparticle administration and skin distribution exist. One explanation for prolonged skin accumulation in a study by Mittal et al. is e.g. a possible accumulation in hair follicles [48]. It would be very interesting to study the distribution of Lipidots in the mouse skin to investigate if this is the case and to determine their exact localization. These results might further clarify the interestingly different particle behaviour of both nanoformulations.

We also detected high mTHPC accumulation in the kidney with both nanoformulations. Bearing in mind that both intact particles are generally regarded as being too big for fast effective renal clearance [49] it is not surprising to still find mTHPC traces in this organ after 72 h, as clearance may be retarded through encapsulation. Therefore it can be assumed that free mTHPC will be cleared faster from the kidneys. Furthermore the overall biodistribution of mTHPC is expected to be worse due to solubility issues and unspecific aggregation.

Interestingly, despite the high mTHPC load, the kidney did not show signs of histological impairment, neither did other organs. Although we did not test for specific markers of organ function, we propose that none of the mTHPC formulations used cause severe side effects in kidney, spleen, lung and liver.

Conclusions

In conclusion we could confirm in our study the superiority of nanoformulations to the free PS mTHPC. Bearing in mind that the free substance is related to several issues such as poor bioavailability, solubility and increased photosensitivity of patients the development of

a potent nanoformulation is a necessity. We could show that Foslip on the one hand is very effective in destroying the tumors itself. However, because the Lipidots' biocompatibility is outstanding and superior to the liposomes we declare further investigations and protocol optimization a priority in the future.

Additional file

Additional file 1: Fig.S1. CAL-33 tumor model in CD1-Foxn1^{nu} nude mice. Tumor growth after injection with 1 x 10⁶ CAL-33 cells (A), 1.5 x 10⁶ CAL-33 cells (B) and 2 x 10⁶ CAL-33 cells. **Table S1.** Physicochemical characterization data of Lipidots.

Abbreviations

PDT: photodynamic therapy; PS: photosensitizer; ¹O₂: singlet oxygen; MTHPC: m-tetrahydroxyphenylchlorin; HPLC: high performance liquid chromatography; QRT-PCR: quantitative reverse transcriptase polymerase chain reaction; ROS: reactive oxygen species; PDD: photodynamic diagnosis; EPR: enhanced permeability and retention; DPPC: 1,2-Dipalmitoyl-sn-glycero-3-phosphocholine; DPPG: 1,2-Dipalmitoyl-sn-glycero-3-phosphorylglycerol sodium salt; PDI: polydispersity index; PEG: polyethylene glycol; PBS: phosphate buffered saline; IVC: individually ventilated cage; SPF: specific pathogen free; BW: body weight; FA: formaldehyde; TBS: tris buffered saline; BSA: bovine serum albumine; CDNA: complementary DNA; ANOVA: analysis of variance; HNSCC: head and neck squamous cell carcinoma; GAPDH: Glyceraldehyde 3-phosphate dehydrogenase; TACSTD2: Tumor-Associated Calcium Signal Transducer 2; MMP7: Matrix Metalloproteinase-7; ALDH1A3: Aldehyde Dehydrogenase 1 Family, Member A3; MKI67: Marker of Proliferation Ki-67; GLUT1: Glucose Transporter 1.

Authors' contributions

DH was culturing the cells, planning the experiments, taking care of the mice, carrying out biodistribution measurements, performing in vivo PDT, measuring tumor volumes, analyzing datasets, doing histology, dissecting mice, carrying out qRT-PCR and preparing the manuscript. SG was advising DH on animal experimentation, supervising mTHPC extraction and HPLC analysis from mouse organs and helping to improve the manuscript. ACC was preparing the Lipidots for the study, quality analysis was done by FN. Both helped with preparation of the manuscript. BS and DP were analyzing the Lipidot and Foslip shipments for mTHPC content by HPLC at the University of Zurich before we were using them for animal experiments. HW and CM were significantly contributing to the writing and adaption of the manuscript, furthermore CM was supervising DH. All authors read and approved the final manuscript.

Author details

¹ Institute of Anatomy, University of Zurich, Winterthurerstrasse 190, Zurich 8057, Switzerland. ² Biolitec Research GmbH, Otto-Schott-Str. 15, 07745 Jena, Germany. ³ CEA, LETI, MINATEC Campus, Commissariat à l'Énergie Atomique et aux Énergies Alternatives (CEA), Technologies for Biology and Healthcare Division, 38054 Grenoble, France. ⁴ Université Grenoble Alpes, Grenoble 38000, France. ⁵ Department of Inorganic Chemistry, University of Zurich, Winterthurerstrasse 190, Zurich 8057, Switzerland. ⁶ Department of Cranio-Maxillofacial Surgery, University Hospital Zurich, Frauenklinikstrasse 24, Zurich 8091, Switzerland.

Acknowledgements

We are thankful to Dr. Pilar Ruiz Sanchez for helping with the mouse experiments. Furthermore, we want to thank Dr. med. vet. Carla Rohrer-Bley and Dr. med. vet. Monika Bochmann from the Tierspital, Zurich for providing the laser for our study.

Competing interests

The authors declare that they have no competing interests.

Availability of data and material

Additional material is available at <https://figshare.com/s/3b6fc2f1edfbf1030422>.

Ethical approval

All animal experiments were implemented with approval of the Swiss cantonal ethics committee for animal experiments (No. 156/2012).

Funding

The study was supported by the FP7 ERA-net EuroNanoMed project TARGET-PDT (31NM30-131004/1). We also thank the Swiss government for giving an ESKAS fellowship to Dr. D. Pandiarajan.

Received: 16 June 2016 Accepted: 27 September 2016

Published online: 03 October 2016

References

- Nyst HJ, Tan IB, Stewart FA, Balm AJM. Is photodynamic therapy a good alternative to surgery and radiotherapy in the treatment of head and neck cancer? *Photodiagnosis Photodyn Ther*. 2009;6:3–11.
- Jones HJ, Vernon DI, Brown SB. Photodynamic therapy effect of m-THPC (Foscan) in vivo: correlation with pharmacokinetics. *Br J Cancer*. 2003;89:398–404.
- Dolmans DEJGJ, Fukumura D, Jain RK. Photodynamic therapy for cancer. *Nat Rev Cancer*. 2003;3:375–80.
- Wilson BC. Photodynamic therapy for cancer: principles. *Can J Gastroenterol*. 2002;16:393–6.
- Vrouenraets MB, Visser GWM, Snow GB, van Dongen GAMS. Basic principles, applications in oncology and improved selectivity of photodynamic therapy. *Anticancer Res*. 2003;23:505–22.
- Moan J, Berg K. The photodegradation of porphyrins in cells can be used to estimate the lifetime of singlet oxygen. *Photochem Photobiol*. 1991;53:549–53.
- Henderson BW, et al. Tumor Destruction and Kinetics of Tumor Cell Death in Two Experimental Mouse Tumors following Photodynamic Therapy. *Cancer Res*. 1985;45:572–6.
- Fingar VH, et al. Analysis of acute vascular damage after photodynamic therapy using benzoporphyrin derivative (BPD). *Br J Cancer*. 1999;79:1702–8.
- Korbelik M, Dougherty GJ. Photodynamic therapy-mediated immune response against subcutaneous mouse tumors. *Cancer Res*. 1999;59:1941–6.
- Biel M. Advances in photodynamic therapy for the treatment of head and neck cancers. *Lasers Surg Med*. 2006;38:349–55.
- Casas A, DiVenosa G, Hasan T, AlBatlle. Mechanisms of resistance to photodynamic therapy. *Curr Med Chem*. 2011;18:2486–515.
- Kelly JF, Snell ME, Berenbaum MC. Photodynamic destruction of human bladder carcinoma. *Br J Cancer*. 1975;31:237–44.
- Dougherty TJ, et al. Photodynamic therapy. *J Natl Cancer Inst*. 1998;90:889–905.
- Stummer W, Reulen HJ, Novotny A, Stepp H, Tonn JC. Fluorescence-guided resections of malignant gliomas—an overview. *Acta Neurochir Suppl*. 2003;88:9–12.
- Ben-Hur E, Rosenthal I. The phthalocyanines: a new class of mammalian cells photosensitizers with a potential for cancer phototherapy. *Int J Radiat Biol Relat Stud Phys Chem Med*. 1985;47:145–7.
- Gomer CJ. Preclinical examination of first and second generation photosensitizers used in photodynamic therapy. *Photochem Photobiol*. 1991;54:1093–107.
- Bonnett R, White RD, Winfield UJ, Berenbaum MC. Hydroporphyrins of the meso-tetra(hydroxyphenyl)porphyrin series as tumour photosensitizers. *Biochem J*. 1989;261:277–80.
- EMA-European Medicines Agency—European Public Assessment Report for Foscan. <http://www.ema.europa.eu>. Accessed 28 Mar 2016.
- Leung WN, Sun X, Mak NK, Yow CM. Photodynamic effects of mTHPC on human colon adenocarcinoma cells: photocytotoxicity, subcellular localization and apoptosis. *Photochem Photobiol*. 2002;75:406–11.
- Peng Q, Moan J, Ma L, Nesland JM. Uptake, localization, and photodynamic effect of meso-tetra (hydroxyphenyl) porphine and its corresponding chlorin in normal and tumor tissues of mice bearing mammary carcinoma. *Cancer Res*. 1995;55:2620–6.
- Jori G. Tumour photosensitizers: approaches to enhance the selectivity and efficiency of photodynamic therapy. *J Photochem Photobiol B Biol*. 1996;36:87–93.
- Kobayashi H, Watanabe R, Choyce PL. Improving conventional enhanced permeability and retention (EPR) effects; what is the appropriate target? *Theranostics*. 2014;4:81–9.
- Delmas T, et al. Preparation and characterization of highly stable lipid nanoparticles with amorphous core of tuneable viscosity. *J Colloid Interface Sci*. 2011;360:471–81.
- Navarro FP, et al. Preparation and characterization of mTHPC-loaded solid lipid nanoparticles for photodynamic therapy. *J Photochem Photobiol B Biol*. 2014;130:161–9.
- Hinger D, et al. Photoinduced effects of M-tetrahydroxyphenylchlorin loaded lipid nanoemulsions on multicellular tumor spheroids. *J Nanobiotechnol*. 2016;14:68.
- Kuntsche J, Freisleben I, Steiniger F, Fahr A. Temoporfin-loaded liposomes: physicochemical characterization. *Eur J Pharm Sci*. 2010;40:305–15.
- Buchholz J, et al. Photodynamic therapy of feline cutaneous squamous cell carcinoma using a newly developed liposomal photosensitizer: preliminary results concerning drug safety and efficacy. *J Vet Intern Med*. 2007;21:770–5.
- Buchholz J, et al. Optimizing photodynamic therapy: in vivo pharmacokinetics of liposomal meta-(tetrahydroxyphenyl) chlorin in feline squamous cell carcinoma. *Clin Cancer Res*. 2005;11:7538–44.
- Liu D, et al. Association between polymorphisms in the promoter regions of matrix metalloproteinases (MMPs) and risk of cancer metastasis: a meta-analysis. *PLoS One*. 2012;7:e31251.
- Masood R, et al. A novel orthotopic mouse model of head and neck cancer and lymph node metastasis. *Oncogenesis*. 2013;2:e68.
- Shvartsur A, Bonavida B. Trop2 and its overexpression in cancers: regulation and clinical/therapeutic implications. *Genes Cancer*. 2015;6:84–105.
- Ayala FRR, et al. GLUT1 and GLUT3 as potential prognostic markers for oral squamous cell carcinoma. *Molecules*. 2010;15:2374–87.
- Birajdar SS, et al. Expression of Ki-67 in normal oral epithelium, leukoplakic oral epithelium and oral squamous cell carcinoma. *J Oral Maxillofac Pathol*. 2014;18:169–76.
- Rojnik M, et al. In vitro and in vivo characterization of temoporfin-loaded PEGylated PLGA nanoparticles for use in photodynamic therapy. *Nanomedicine (Lond)*. 2012;7:663–77.
- Villa Nova M, et al. Nanocarriers for photodynamic therapy-rational formulation design and medium-scale manufacture. *Int J Pharm*. 2015;491:250–260.
- Haedicke K, et al. Multifunctional calcium phosphate nanoparticles for combining near-infrared fluorescence imaging and photodynamic therapy. *Acta Biomater*. 2015;14:197–207.
- Friedberg JS, et al. A phase I study of Foscan-mediated photodynamic therapy and surgery in patients with mesothelioma. *Ann Thorac Surg*. 2003;75:952–9.
- Kniebuhler G, et al. Photodynamic therapy for cholangiocarcinoma using low dose mTHPC (Foscan((R))). *Photodiagnosis Photodyn Ther*. 2013;10:220–8.
- Stoker SD, et al. Photodynamic therapy as salvage therapy for patients with nasopharyngeal carcinoma experiencing local failures following definitive radiotherapy. *Photodiagnosis Photodyn Ther*. 2015. doi:10.1016/j.pdpdt.2015.04.005.
- Buchholz J, et al. Photodynamic therapy of feline cutaneous squamous cell carcinoma using a newly developed liposomal photosensitizer: preliminary results concerning drug safety and efficacy. *J Vet Intern Med*. 2007;21:770–5.
- Svensson J, et al. Tumor selectivity at short times following systemic administration of a liposomal temoporfin formulation in a murine tumor model. *Photochem Photobiol*. 2007;83:1211–9.
- Allison BA, Pritchard PH, Richter AM, Levy JG. The plasma distribution of benzoporphyrin derivative and the effects of plasma lipoproteins on its biodistribution. *Photochem Photobiol*. 1990;52:501–7.

43. Szentkuti G, et al. Correlations between prognosis and regional biomarker profiles in head and neck squamous cell carcinomas. *Pathol Oncol Res*. 2015;21:643–50.
44. Wertheimer E, Sasson S, Cerasi E, Ben-Neriah Y. The ubiquitous glucose transporter GLUT-1 belongs to the glucose-regulated protein family of stress-inducible proteins. *Proc Natl Acad Sci USA*. 1991;88:2525–9.
45. Hsieh Y-J, Wu C-C, Chang C-J, Yu J-S. Subcellular localization of Photofrin determines the death phenotype of human epidermoid carcinoma A431 cells triggered by photodynamic therapy: when plasma membranes are the main targets. *J Cell Physiol*. 2003;194:363–75.
46. Lassalle HP, et al. Correlation between in vivo pharmacokinetics, intratumoral distribution and photodynamic efficiency of liposomal mTHPC. *J Control Release*. 2009;134:118–24.
47. Rovers JP, et al. Effective treatment of liver metastases with photodynamic therapy, using the second-generation photosensitizer meta-tetra(hydroxyphenyl)chlorin (mTHPC), in a rat model. *Br J Cancer*. 1999;81:600–8.
48. Mittal A, et al. Non-invasive delivery of nanoparticles to hair follicles: a perspective for transcutaneous immunization. *Vaccine*. 2013;31:3442–51.
49. Choi HS, et al. Renal clearance of nanoparticles. *Nat Biotechnol*. 2007;25:1165–70.

Submit your next manuscript to BioMed Central and we will help you at every step:

- We accept pre-submission inquiries
- Our selector tool helps you to find the most relevant journal
- We provide round the clock customer support
- Convenient online submission
- Thorough peer review
- Inclusion in PubMed and all major indexing services
- Maximum visibility for your research

Submit your manuscript at
www.biomedcentral.com/submit



RESEARCH

Open Access



Release of copper-amended particles from micronized copper-pressure-treated wood during mechanical abrasion

Chiara Civardi^{1,2*}, Lukas Schlagenhauf^{3,4,5†}, Jean-Pierre Kaiser⁶, Cordula Hirsch⁶, Claudio Mucchino⁷, Adrian Wichser^{4,6}, Peter Wick⁶ and Francis W. M. R. Schwarze^{1*}

Abstract

Background: We investigated the particles released due to abrasion of wood surfaces pressure-treated with micronized copper azole (MCA) wood preservative and we gathered preliminary data on its in vitro cytotoxicity for lung cells. The data were compared with particles released after abrasion of untreated, water (0% MCA)-pressure-treated, chromated copper (CC)-pressure-treated wood, and varnished wood. Size, morphology, and composition of the released particles were analyzed.

Results: Our results indicate that the abrasion of MCA-pressure-treated wood does not cause an additional release of nanoparticles from the unreacted copper (Cu) carbonate nanoparticles from of the MCA formulation. However, a small amount of released Cu was detected in the nanosized fraction of wood dust, which could penetrate the deep lungs. The acute cytotoxicity studies were performed on a human lung epithelial cell line and human macrophages derived from a monocytic cell line. These cell types are likely to encounter the released wood particles after inhalation.

Conclusions: Our findings indicate that under the experimental conditions chosen, MCA does not pose a specific additional nano-risk, i.e. there is no additional release of nanoparticles and no specific nano-toxicity for lung epithelial cells and macrophages.

Keywords: Cytotoxicity, Copper particles, Debris, Exposure, Inhalation, Wood dust

Background

Thousands of tons of wood chips and sawdust are being generated each day by industry, domestic environment, or improper disposal of debris. Further, the presence of wood preservatives may pose an environmental and human health risk due to release of toxic metals like arsenic and copper (Cu). Such an exposure pathway has already been recognized for various preservatives, in particular for chromated Cu arsenate (CCA) [1, 2]. We are currently experiencing an increased use of particulate Cu

wood preservatives in order to effectively protect wood from decay and lengthen its service life. More specifically, basic Cu carbonate particulate systems with a size range between 1 nm and 25 µm were introduced for wood protection in the US market in 2006 [3]. This has resulted in more than 11,800,000 m³ of wood treated with micronized Cu (MC) formulations [4], which corresponds to over 75% of residential lumbers produced in the US [4].

Micronized Cu wood preservatives include a nanosized fraction of basic Cu carbonate, which may be of high concern: there is a strong indication that different Cu-based nanoparticles (NPs) have a high toxicity for aquatic organisms [5–10], terrestrial plants [11], mammals [12–17], and humans [18–23].

To date, the environmental fate of Cu carbonate particles from MC-pressure-treated wood has mostly assessed their leachability [24–28]. However particles generated

*Correspondence: civardic@student.ethz.ch; francis.schwarze@empa.ch

†Chiara Civardi and Lukas Schlagenhauf contributed equally to this work

¹ Laboratory for Applied Wood Materials, Empa, Lerchenfeldstrasse 5, 9014 St. Gallen, Switzerland

² Institute for Building Materials, ETH, Stefano-Franscini-Platz 3, 8093 Zurich, Switzerland

Full list of author information is available at the end of the article

by abrasion of MC-treated wood may be more hazardous than wood dust untreated or treated with conventional wood preservatives, due to the presence of Cu-based NPs. Platten et al. [29] and Santiago-Rodríguez et al. [30] recently assessed how exposure to Cu from wood dust originated from MC-pressure-treated wood can occur via dermal transfer or oral ingestion. Therefore, it is extremely important to determine the dust composition that can be inhaled after exposure—occupational or not—to abraded particles from MC-pressure-treated wood and its hazard to human lungs.

The current study characterizes the particles released from MC azole (MCA)-pressure-treated wood and compares them with particles generated from wood untreated, pressure-treated with the conventional wood preservative chromated Cu (CC), and with varnished untreated and MCA-pressure-treated wood. Subsequently, it assesses acute cytotoxic reactions of MCA, its components tebuconazole and Cu^{2+} , as well as particles abraded from MCA-, CC-pressure treated wood and untreated wood to lung epithelial cells and macrophages.

Methods

MC characterization

We used a commercially available MC azole (MCA) formulation. This is the same as the formulation with high amount of tebuconazole MCA_HTBA we used in a previous investigation [31]. A full characterization of the Cu particles in the MCA formulation is available from the latter study. To summarize briefly, the measured particle size distribution of MCA was 104 ± 1.7 nm with an average zeta potential of -21 ± 0.4 mV.

Wood sample preparation

Octagonal specimens of Scots pine (*Pinus sylvestris* L.) sapwood (90 mm diameter \times 20 mm height) were used for the abrasion study. The specimens were prepared and pressure-treated with 2% aqueous suspensions of MCA or CC reference preservative, prepared according to the European standard ENV 807 [32]. After an 8-week drying procedure, some of the MCA-pressure-treated samples were coated three times with intervals of 24 h with a primer, i.e. solution of deck lacquer (90%) and white spirit (10%). The control materials were composed of: untreated wood samples and samples pressure-treated with a 0% MCA solution in distilled water, varnished untreated wood samples.

Abrasion setup

The experimental setup has been described by Schlagenhaut et al. [33]. To simulate the abrasive process, a Taber Abraser (Model 5135, Taber, North Tonawanda, NY) was used. While the wood sample rotates, the Taber Abraser

uses one abrasive wheel that abrades the sample continuously at the point of contact. The sample rotates 60 times/min and the weight applied on the wheel is 0.75 kg. The samples were abraded with S-42 sandpaper strips (Taber) mounted on a CS-0 (Taber) rubber wheel. A conductive silicone tube (TSI) with a rectangular inlet at the tube entrance with a 4.8 mm^2 suction area was placed directly behind the abrasion area to collect the particles. The air flow was driven by a pump (N816.1.2KN.18, KNF, Germany). Devices for aerosol characterization and particle collection were included in the tubing system.

Wood dust characterization

The generated particles were characterized in triplicates both in the aerosol form by particle size distribution measurements with an aerodynamic particle sizer (APS, Model 3321, TSI, Shoreview, MN) and a scanning mobility particle sizer (SMPS) consisting of a differential mobility analyzer (DMA) equipped with a long DMA column (Model 3080, TSI) and a condensation particle counter (CPC) (Model 3775, TSI). During each measurement, three particle size distributions were recorded. The recording time for each distribution was 195 s. The background distribution (without abrasive processes) of each experiment was measured three times. The experimental setup was verified by means of an atomizer aerosol generator (Model 3079, TSI). The particle size distributions obtained were processed as described by Schlagenhaut et al. [33]. In addition, the particles were collected on stubs and analyzed by means of scanning electron microscopy (SEM, Hitachi S-4800; Hitachi High-Technologies US and Canada, Illinois, USA). The stubs were plasma gold-sputtered (Polaron Equipment, SEM coating Unit E5100, Kontron AG, Switzerland; 5 mA, 1 mbar) prior to image acquisition.

The presence of Cu in the generated particles was assessed in the collected particles through ICP-MS (PerkinElmer Elan 6100, detection limit: $0.004 \mu\text{g/L}$) and two distinct ICP-OES (Perkin-Elmer OPTIMA 3000, Jobin-Yvon HORIBA Ultima 2, detection limit for both instruments: 0.005 mg/L) instruments. In this way, we could benefit from the two different detection limits, as well as identify any effect of the instrumentation and—especially—of sample preparation on the detected amount of Cu. Analyses were carried out on the whole size range of abraded particles and on particles $<1 \mu\text{m}$ collected on Nucleopore track-etch membrane filter (111106, pore size $0.2 \mu\text{m}$, Whatman, UK). For ICP-MS and Perkin-Elmer OPTIMA 3000 ICP-OES Cu content analysis, the collected particles were dissolved nitric acid (HNO_3 , 65%, Supra Pure) and hydrogen peroxide (H_2O_2 , 30%, Supra Pure) and subsequently underwent microwave digestion (MLS 1200 MEGA, Milestone, Leutkirch,

Germany). Cu plasma standard solutions (1 g/L) were used for calibration. For Jobin–Yvon HORIBA Ultima 2 ICP-OES analysis a similar procedure was used, but without the addition of hydrogen peroxide. The detector voltage was set using a 100 mg/L standard solution, while a 7 levels calibration curve was employed for quantification.

Cell culture

The human alveolar epithelial cell line A549 (ATCC: CCL-185) was grown in Roswell Park Memorial Institute (RPMI-1640) medium (Sigma-Aldrich) supplemented with 10% fetal calf serum (FCS) (Lonza), 2 mM L-glutamine (Gibco), 50 µg/mL penicillin (Gibco), 50 µg/mL streptomycin (Gibco), and 100 µg/mL neomycin (Gibco) at 37 °C in a humidified atmosphere containing 5% carbon dioxide (CO₂, hereafter referred to as complete cell culture medium and standard growth conditions, respectively). Cells were subcultured at approximately 80–90% confluency once a week using 0.5% Trypsin–EDTA (Sigma-Aldrich).

Formation of reactive oxygen species (ROS)

The formation of ROS in A549 cells was determined using the 2',7'-dichlorodihydrofluorescein-diacetate assay (H₂DCF-DA), as described by Roesslein et al. [34]. For experimental details see Additional file 1.

Cell viability

To assess mitochondrial activity as a measure of cell viability/cell death in A549 cells Cell Titer96[®] Aqueous One Solution (Promega) containing 3-(4,5-dimethylthiazol-2-yl)-5-(3-carboxymethoxy phenyl)-2-(4-sulphophenyl)-2H (MTS) as a water-soluble tetrazolium compound was used according to the manufacturer's protocol. In brief, 1.5×10^4 A549 cells were seeded in 200 µL complete cell culture medium in a 96-well plate and grown over night under standard growth conditions. Thereafter medium was removed and cells were incubated for 3 or 24 h in 200 µL complete cell culture medium containing the respective stimuli (abraded particles from MCA-, CC-pressure-treated wood or untreated wood, or eluates derived thereof as described below). Cadmium sulfate (CdSO₄) in different concentrations served as positive control, untreated cells as negative control. After appropriate incubation times (3, 24 h) medium was replaced by 120 µL of MTS working solution (composed of 20 µL MTS plus 100 µL of phenol-red-free RPMI-1640 w/o supplements) per well and cells were incubated for 60 min at standard growth conditions. Absorption was detected at 490 nm using an ELx800 microplate reader (BioTEK Instruments).

Data processing

Blank samples treated exactly the same way but containing no cells were run with every cell-based assay. Values given in the graphs are blank-corrected and subsequently normalized to the untreated sample. The mean of at least three independent experiments (each run with technical triplicates) and the corresponding standard deviations are shown.

Sample preparation for cytotoxicity analysis

Cytotoxicity was assessed in two different scenarios: (i) Abraded particles released from MCA-, CC-pressure-treated as well as untreated wood were diluted in appropriate media and directly applied to cultured cells. (ii) Eluates from the same abraded particles were used to assess the cytotoxicity of active soluble components contained in and released from the wood. Therefore, 4 mg of abraded wood particles per mL elution medium were incubated for 24 h at 37 °C on a rotating platform. Supernatant was collected after centrifugation at 500g for 5 min. Elution medium for ROS detection was Hank's Balanced Salt Solution (HBSS; for experimental details see Additional file 1). For cell viability assessment and cytokine detection (see Additional file 1) eluates were produced in phenol-red free RPMI (without supplements) which was supplemented after centrifugation with 10% FCS, 2 mM L-glutamine, 50 µg/mL penicillin, 50 µg/mL streptomycin, and 100 µg/mL neomycin. The HBSS supernatant as well as the supplemented RPMI supernatant contain the highest possible amount of released components and were labeled "100% eluate". Serial 1:2 dilutions were performed in the respective media and concordantly termed "50, 25%, etc. eluates".

Determination of Cu content in eluates

The Cu content in eluates of the abraded particles from untreated, CC- and MCA-pressure-treated wood was determined by ICP-MS (Sector Field SF-ICP-MS Element 2 from Thermo Finnigan, detection limit: 0.004 µg/L). Prior to analysis, the specimens were acidified with nitric acid (HNO₃, 65%, Supra Pure) and hydrogen peroxide (H₂O₂, 30%, Supra Pure) and subsequently underwent microwave digestion (MLS 1200 MEGA, Milestone, Leutkirch, Germany). Cu plasma standard solutions (1 g/L) were used for calibration.

Production of cytokines. The release of the pro-inflammatory cytokine TNF-α was assessed in macrophages derived from the monocytic cell line THP-1 (ATCC: TIB-202) using the Ready-SET-Go![®] Elisa kit (eBioscience) according to the manufacturer's protocol. For cell culture conditions and experimental details see Additional file 1.

Results and discussion

Wood dust particle size

The particle size distributions for the different wood samples (untreated, 2% MCA-pressure-treated, 2% CC-pressure-treated, 0% MCA-pressure-treated, varnished, 2% MCA-pressure-treated and varnished) are shown in Fig. 1(a, b). More specific, Fig. 1a represents the particle size distributions measured by SMPS below 1 μm , while Fig. 1b presents the distributions measured by APS above 1 μm . All the samples show a similar pattern below 1 μm , with peaks at about 400 nm; while two different outlines are visible above 1 μm : one for the abraded particles from varnished samples, and another for the abraded particles of unvarnished samples. In the first case the peak is between 700 nm and 1.3 μm , while in the second one it is around 2.3 μm . Therefore, the set up maximizes the release of coarse (PM10), fine (PM2.5) and ultrafine particles (generally defined as smaller than 100 nm). These three particle size fractions are commonly associated with adverse health effects in humans, as demonstrated by Schwartz et al. [35], Raaschou-Nielsen et al. [36], and Oberdörster et al. [37]. In addition, the setting fitted the purpose of detecting any variation in the generated wood dust at the nanoscale, which may have occurred due to the presence of Cu carbonate NPs. In any case, no additional release of a nanosized fraction was observed for the 2% MCA-treated wood.

We could observe how the application of varnishes influences the particle size released increasing the average dimensions, reducing the exposure to ultrafine particles.

The APS results on the aerodynamic particle diameter are in good agreement with the study from Thorpe and Brown [38], in which the wood dust size distribution after different sanding processes was assessed. The mean particle diameter was comprised between 1.52 and 2.65 μm . However, further different abrasive processes, e.g. cutting, grinding, welding, may cause the release of wood dust with different particle size distributions. Despite that, as our abrasive set up maximizes the release of coarse, fine and ultrafine particles, we can suppose that different abrasive processes would not release more nanoparticles than our system.

Our tests focused on Scots pine only, however different wood species may release particles that differ in the size distribution, due to the wood properties, as demonstrated by Lehmann and Fröhlich [39] and Ratnasingam et al. [40]. In the case of MCA-treated wood, the wood species features may also influence the amount of Cu carbonate particles present in the wood after impregnation.

In terms of human exposure, our results indicate that a fraction of the abraded particles produced by the different wood samples could penetrate the lower airways

(tracheo-bronchiolar regions or even the alveolar sacs), due to their small size. The application of varnishes alter the size distribution of the abraded particles and by that would shift the particle deposition to the nasopharyngeal and tracheo-bronchiolar regions [41]. However, the broad size range of the particles does not allow a precise quantification of particle deposition in the respiratory tract.

Wood dust particle morphology

The generated particles from untreated, CC-, and MCA-pressure-treated wood were morphologically assessed by SEM (Fig. 1c–e). Visual inspection of all the SEM images collected confirmed the presence of particles below 10 μm , as well as the presence of bigger particles (10² μm), beyond the APS and SMPS detection limits adopted. In addition, no difference between the different wood samples (Fig. 1d, e) was encountered, indicating no mechanical alteration due to the wood treatments, in accordance with the APS and SMPS results. In all cases, the generated particles appeared mostly fibrous, although irregular and heterogeneous in shape and size. The surfaces were not always flat.

Various studies reported similar features from SEM investigations on wood dust from various wood species [42, 43]. In particular, Mazzoli and Favoni [44] reported no difference in wood dust particle size and morphology from different wood species, suggesting no dissimilarity for in vitro cytotoxicity. However, wood species that are documented to be carcinogenic, e.g. beech [45], were not assessed. In that case, different structures responsible for the increased adverse effects may be observed. In addition, the abrasive process may also generate wood dust particles that differ in size and morphology.

Cu content in wood dust

By means of ICP-OES and ICP-MS analyses we could assess the different concentrations of Cu in wood dust from untreated and MCA-pressure-treated wood samples, as shown in Table 1. Combining the ICP-OES and ICP-MS results, which are concordant, we determined a baseline amount of Cu in untreated wood at 0.01 ± 0.02 mg/g. Similarly, when the wood was varnished the baseline amount was found at 0.02 ± 0.01 mg/g. When MCA-pressure-treated wood was abraded, the amount of Cu released was 2.02 ± 0.09 mg/g, corresponding to 0.20% w/w of the total amount of treated wood, and it drastically reduced when varnish was applied (0.23 ± 0.01 mg/g). This difference may be due to the higher release of varnish instead of wood, therefore implying that varnishes may prevent release of Cu during mechanical abrasion of treated wood. The amount of Cu release was almost double in CC-pressure-treated

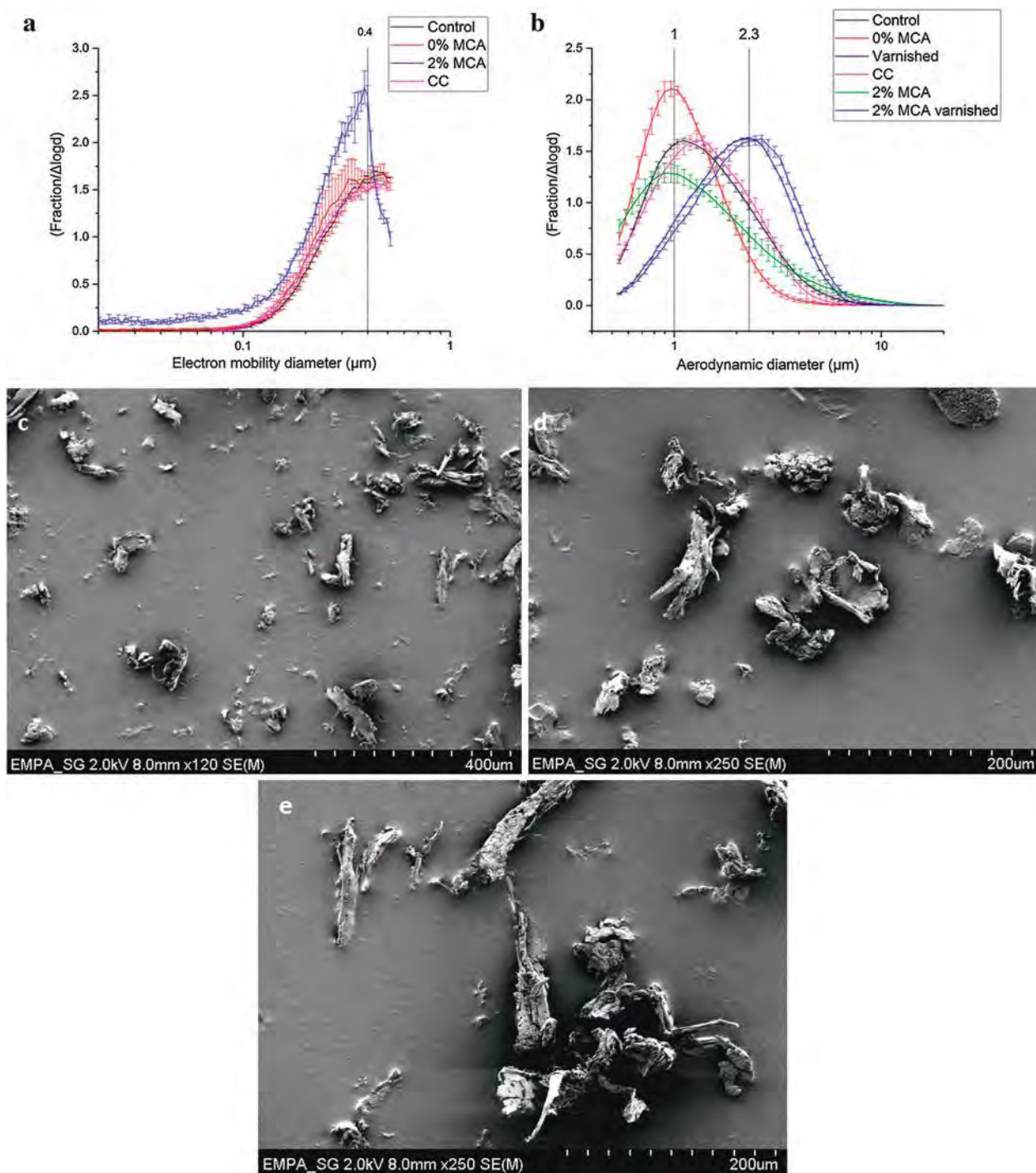


Fig. 1 Characterization of the abraded particles. **a** Particle size distributions of untreated wood (control), water-treated wood (0% MCA), MCA-treated wood (2% MCA), and CC-treated wood (CC) measured by SMPS. Most of the abraded particles had a diameter of 400 nm. Data represented as mean of three repetitions. **b** Particle size distributions of untreated wood (control), water-treated wood (0% MCA), varnished wood (varnished), CC-treated wood (CC), MCA-treated wood (2% MCA), and varnished MCA-treated wood (2% MCA varnished) measured by APS. Most of the abraded particles had a diameter of about 1 μm . When varnish is applied, the average diameter shifts towards 2.3 μm . Data represented as mean of three repetitions. **c, d** SEM images of wood dust generated by the abrasion process on 2% MCA-treated wood. **e** SEM image of wood dust generated by the abrasion process on untreated wood (control)

Table 1 Cu content in sawdust particles and eluates thereof

Wood treatment	$\mu\text{g Cu/mg}$ abraded particles	$\mu\text{g Cu/mL}$ medium (eluates ^a) [release in %]
Untreated	0.01 ± 0.02	0.01 ± 0.01
MCA-pressure treated	2.02 ± 0.09	0.36 ± 0.01 [4.4%]
CC-pressure treated	4.26 ± 0.01	0.75 ± 0.01 [4.4%]
RPMI medium (w/o wood)	na	0.00 ± 0.01

^a 4 mg abraded particles were incubated in 1 mL phenolred free RPMI for 24 h at 37 °C on a rotating platform; after centrifugation at 500 g for 5 min supernatants were further processed for ICP-MS measurements

wood (4.26 ± 0.01 mg/g). This is due to differences in the formulations: in fact, the amount of Cu in the initial CC formulation doubles the amount in MCA. Since 2% is an economically feasible concentration, generally used in the timber industry, the result indicate that at similar dilutions (2%) MCA-pressure-treated wood would release less Cu due to mechanical abrasion. The percentage of Cu released from MCA-pressure-treated wood is in good agreement with studies on indoor sawing of CCA-treated wood: Decker et al. [46] reported 0.3% Cu in wood dust, while Nygren et al. [47] 0.1%. In addition, a comparison can be made between our results and the ones from the less invasive wiping experiment reported in the EPA report [24]. In fact, in the latter, the amount of Cu released from MCA-pressure-treated wood was lower and comprised between 0.0135 and 0.072 mg.

The amount of Cu detected in the wood dust nanosized fraction was below the Cu concentration in the whole wood dust, both from untreated and MCA-pressure-treated wood. In particular the concentration of Cu in the nanosized dust generated by MCA-pressure-treated wood was 1.50 ± 0.30 mg/g (0.15% w/w). Therefore, combining these data with the SMPS results we can conclude that most of the Cu released was bound to the larger wood particles, however a small amount of Cu bound to the nanosized fraction would deposit in the deep lungs, if inhaled. Therefore, toxicological studies are required to fully assess the hazard on human health.

Cytotoxicity assessment

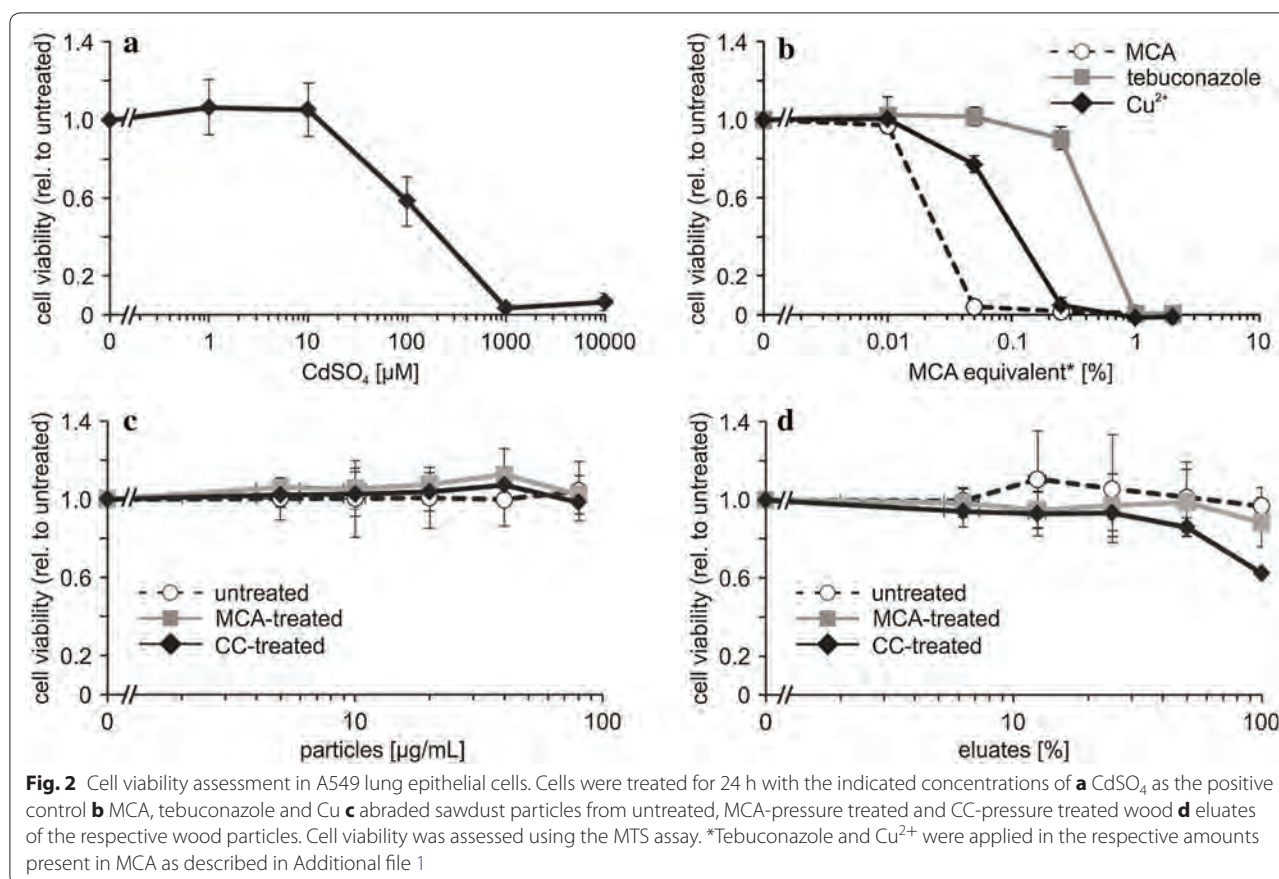
The most critical exposure route for sawdust particles is the lung. Therefore, we focused our *in vitro* study on the lung epithelial cell line A549 and macrophages differentiated from the monocytic cell line THP-1. Both cell types are likely to be among the first cell types getting in touch with inhaled particles. We investigated potential adverse effects of sawdust particles abraded from untreated wood, MCA-pressure treated wood and CC-pressure treated wood. Furthermore, to assess the effects caused by soluble compounds, rather than by wood dust per se, eluates from these three types of wood particles were included in the cytotoxicity evaluation. These results were compared to the toxicity induced by direct

treatment of lung epithelial cells with MCA and its active components tebuconazole and Cu^{2+} ions from copper sulfate pentahydrate ($\text{CuSO}_4 \cdot 5\text{H}_2\text{O}$).

According to the ROS paradigm [34] the interaction of (nano) particles with cells is likely to induce elevated cellular levels of ROS. Subsequent oxidative stress reactions can then cause severe damage to biomolecules (proteins, lipids and nucleic acids), induce inflammatory reactions and finally lead to cell death. Therefore we initially assessed the overproduction of ROS using the DCF assay. As shown in Additional file 1: Figure S1, only the positive controls Sin-1 and MWCNT led to a considerable increase of ROS levels in A549 cells. All eluates and abrasion particles tested did not elevate ROS formation. However, cell death can also be triggered by ROS independent pathways. We therefore investigated cell viability of A549 lung epithelial cells using the MTS assay. The assay internal positive control CdSO_4 induces cell death in a dose-dependent manner (Fig. 2a) thus indicating that toxicity can be reliably detected under the experimental conditions.

The cytotoxicity of MCA itself was determined up to a concentration of 2% (v/v) in cell culture medium. In parallel, its active compounds tebuconazole and Cu^{2+} were analyzed in equivalent amounts (Fig. 2b; Additional file 1). Our results reveal a toxicity ranking of tebuconazole < Cu^{2+} < MCA, which indicates an additive effect of tebuconazole and Cu^{2+} . Further, our results suggest that the cytotoxicity of MCA is likely to be caused by Cu^{2+} ions than nanoparticles.

The highest, technically feasible, concentration of abraded particles that could be applied to A549 cells was $80 \mu\text{g/mL}$ equaling to a growth area of $47 \mu\text{g/cm}^2$. For all three types of sawdust particles no cytotoxicity could be detected up to this concentration and over an incubation period of 24 h (Fig. 2c). According to Table 1 the highest amount of $80 \mu\text{g}$ particles from MCA- or CC-pressure-treated wood contain 0.16 or $0.34 \mu\text{g Cu}^{2+}$, respectively. Measurements of eluates of the respective abraded particles revealed that only a fraction of 4.4% of Cu^{2+} is released into the medium over a period of 24 h (Table 1). Therefore we do not expect concentrations above $0.007 \mu\text{g/mL}$ or $0.015 \mu\text{g/mL Cu}^{2+}$ for the two samples,



respectively. In relation to Fig. 2b, where Cu^{2+} ion cytotoxicity starts above 5 $\mu\text{g}/\text{mL}$ ($=0.01\%$), these values appear very low. However, the following considerations will relate the chosen in vitro doses to an inhalation scenario for wood workers. If we consider an inhalation volume of 1.9 L per breath and roughly 26 breathes per min during heavy exercise [48] we can assume a total volume of 24 m^3 air to be inhaled during an 8 h working day. According to Decker et al. [46], wood dust concentrations in air may range from 0.6 mg/m^3 (sampled at outdoor working sites over a period of 229 min) to a maximum of 49 mg/m^3 (sampled during indoor sanding operations over a period of 127 min). With these data a total amount of 3.8–555 mg inhaled particles per working day can be estimated. Considering 102 m^2 of total lung surface area [49] and assuming all the wood dust particles to be deposited in the lung we can estimate a total deposited amount of wood dust particles of 0.004–0.545 $\mu\text{g}/\text{cm}^2$. In this scenario the 47 $\mu\text{g}/\text{cm}^2$ in vitro dose is a rather high concentration mimicking a repeated exposure over at least 17 weeks (indoor) to a whole lifetime (49 working years; outdoor). Nevertheless, spatially restricted effects due to particle deposition, cellular uptake of particles and potential intracellular Cu^{2+} release cannot be addressed,

neither by in vitro toxicity tests nor by the above demonstrated exposure calculations. In summary the doses chosen in the present study adequately reflect a worst case exposure scenario for wood workers.

Furthermore, we analyzed eluates produced from the three types of abraded wood particles and assessed the cytotoxicity of soluble factors released from the sawdust on A549 cells. As shown in Fig. 2d no cytotoxicity could be detected after 24 h of incubation with eluates from untreated as well as MCA-pressure-treated wood. Eluates from CC-pressure-treated wood particles reduced cell viability at the highest concentration tested to 63% viable cells compared to untreated control cultures. This highest eluate concentration (Table 1) contained only 0.8 $\mu\text{g}/\text{mL}$ Cu^{2+} . As Cu^{2+} ion cytotoxicity started at concentrations beyond 5 $\mu\text{g}/\text{mL}$ ($=0.01\%$) (Fig. 2b) Cu^{2+} is most likely not the main reason for the observed effect, but rather chromium. Further investigations are necessary to prove a real human hazard from CC-pressure-treated wood, which was not the scope of the present study. Besides that, our results clearly indicate that there is no additional nano-specific effect, as abraded particles from MCA-pressure-treated wood as well as eluates thereof did not induce any cytotoxicity under the experimental

conditions tested. This provides further evidence to the hypothesis that Cu^{2+} ions rather than nanoparticles are responsible for any adverse effects.

Besides cell viability, inflammatory reactions at sublethal concentrations can be an indication for non-acute but nevertheless relevant adverse effects. Therefore we assessed the release of the pro-inflammatory cytokine $\text{TNF-}\alpha$ from immune responsive cells in vitro using the enzyme-linked immunosorbent assay (ELISA) technique. We used macrophages differentiated from THP-1 monocytes as the model cell line. Initially, cell viability was investigated to assure sublethal concentrations were applied for subsequent cytokine release experiments. THP-1 macrophages were exposed to the respective stimuli for 8 h and cell viability was assessed using the MTS assay. For technical details see Additional file 1. CdSO_4 served again as the assay internal positive control and induced cytotoxicity in a dose-dependent manner (Additional file 1: Figure S2a). Following the same experimental design as described for A549 cells MCA and its active components tebuconazole and Cu^{2+} were applied in equivalent amounts (Additional file 1: Figure S2b). In this case, the effects of Cu^{2+} and MCA were comparable, therefore even in this case the effects from MCA appear to be caused by Cu^{2+} ions rather than nanoparticles. Cell viability was affected at concentrations above 0.05% MCA in a dose-dependent manner. All three abraded wood particle types (up to 80 $\mu\text{g/mL}$) as well as eluates thereof did not induce an adverse response (Additional file 1: Figure S2c, d) in THP-1 macrophages. Accordingly, for cytokine release measurements MCA, tebuconazole and Cu^{2+} were used at concentrations below 0.05% MCA-equivalents and abraded wood particles were used up to 80 $\mu\text{g/mL}$. Lower eluate concentrations (6.25 to 25.00%) showed an increase in cell viability rather than a decrease. Therefore we used concentrations below 25.00% for ELISA experiments. Treatment with the positive control lipopolysaccharides (LPS) led to a 16- and 25-fold increase in $\text{TNF-}\alpha$ release at 10 and 100 ng/mL LPS, respectively (Additional file 1: Figure S3). However, no significant release of $\text{TNF-}\alpha$ could be observed after treatment with MCA, its active components, abraded wood particles or eluates thereof at any of the concentrations tested (Additional file 1: Figure S3). Thus, even in this case no specific nano effect was observed.

In summary our findings on the cytotoxicity reveal (1) a toxicity ranking of tebuconazole < Cu^{2+} < MCA (2) no induction of cytotoxicity for abraded particles up to 80 $\mu\text{g/mL}$ (3) only a minor toxicity was found for the highest concentration of eluates resulting from CC-pressure-treated wood, which was only observed for A549 lung epithelial cells, and it is likely due to the presence of chromium in the formulation; most importantly

(4) no additional nano hazard (caused by the presence of Cu-based NPs per se) was identified. Furthermore, our cytotoxicity study indicates low adverse effects for low-frequency consumer exposure. However, woodworkers can be continuously exposed to wood dust, in particular since dust-exposed woodworkers do not always wear appropriate respirators approved for wood dust [50]. The wood being processed may have been pressure-treated with Cu-based formulations, and the particles released can increase the adverse effects due to the presence of Cu. However, MCA is likely to be the safest alternative: no nano hazard was evidenced, and the amount of Cu, especially easily bioavailable Cu, in CC was double the amount in MCA. Furthermore, both types of human cells tested showed lower adverse effects (higher cell viability) when compared to cells exposed to CC. In conclusion, the abrasion of MCA-pressure-treated wood does not constitute a nano-specific risk. Nonetheless, further more advanced toxicity studies on tissues and in vivo are required.

Additional file

Additional file 1: Figures S1, S2, S3. Concentration considerations of MCA components; Formation of reactive oxygen species (ROS); Culture conditions and cell viability assessment of THP-1 cells; Production of cytokines.

Authors' contributions

The manuscript was written through contributions of all authors. All authors read and approved the final manuscript.

Author details

¹ Laboratory for Applied Wood Materials, Empa, Lerchenfeldstrasse 5, 9014 St. Gallen, Switzerland. ² Institute for Building Materials, ETH, Stefano-Franscini-Platz 3, 8093 Zurich, Switzerland. ³ Empa, Functional Polymers, Dübendorf, Switzerland. ⁴ Empa, Analytical Chemistry, Dübendorf, Switzerland. ⁵ Institute for Environmental Engineering, ETH, Zurich, Switzerland. ⁶ Particles-Biology Interactions, Empa, St. Gallen, Switzerland. ⁷ Dipartimento di Chimica, Università degli Studi di Parma, Parma, Italy.

Acknowledgements

The work was financially supported by the Swiss National Research Foundation (Grant No. 406440_141618). We are indebted to Alexandra Rippl for the cytokine analysis and the maintenance of the cell cultures, to Daniel Heer for the technical support, to He Xu for the zeta potential measurements, and to David Kistler for the ICP-MS analysis.

Competing interests

The authors declare that they have no competing interests.

Data availability

All the data are available within the manuscript and the additional files.

Funding sources

The study was financially supported by the Swiss National Research Foundation (NRP 64, Grant No. 406440_141618). The funders had no role in study design, data collection and analysis, decision to publish, or preparation of the manuscript.

Received: 31 August 2016 Accepted: 22 November 2016

Published online: 28 November 2016

References

- Jambeck JR, Townsend TG, Solo-Gabriele HM. Landfill disposal of CCA-treated wood with construction and demolition (C&D) debris: arsenic, chromium, and copper concentrations in leachate. *Environ Sci Technol*. 2008;42(15):5740–5.
- Townsend T, Solo-Gabriele H, Tolaymat T, Stook K, Hosein N. Chromium, copper, and arsenic concentrations in soil underneath CCA-treated wood structures. *Soil Sediment Contam*. 2003;12(6):779–98.
- Osmose. Consumer safety and product performance of micronized copper technology confirmed. Osmose press release. 2009. <http://www.prnewswire.com/news-releases/consumer-safety-and-product-performance-of-micronized-copper-technology-confirmed-65722682.html>.
- Freeman BMH, McIntyre CR. A Comprehensive review of copper-based wood preservatives with a focus on new micronized or dispersed copper systems. *For Prod J*. 2008;58(11):6–27.
- Blinova I, Ivask A, Heinlaan M, Mortimer M, Kahru A. Ecotoxicity of nanoparticles of CuO and ZnO in natural water. *Environ Pollut*. 2010;158(1):41–7.
- Griffitt RJ, Weil R, Hyndman K, Denslow N, Powers K, Taylor D, Barber DS. Exposure to copper nanoparticles causes gill injury and acute lethality in zebrafish (*Danio rerio*). *Environ Sci Technol*. 2007;41:8178–86.
- Heinlaan M, Kahru A, Kasemets K, Arbeille B, Prensier G, Dubourguier H-C. Changes in the *Daphnia magna* midgut upon ingestion of copper oxide nanoparticles: a transmission electron microscopy study. *Water Res*. 2011;45(1):179–90.
- Heinlaan M, Ivask A, Blinova I, Dubourguier H-C, Kahru A. Toxicity of nanosized and bulk ZnO, CuO and TiO₂ to bacteria *Vibrio fischeri* and crustaceans *Daphnia magna* and *Thamnocephalus platyurus*. *Chemosphere*. 2008;71(7):1308–16.
- Shaw BJ, Al-Bairuty G, Handy RD. Effects of waterborne copper nanoparticles and copper sulphate on rainbow trout (*Oncorhynchus mykiss*): physiology and accumulation. *Aquat Toxicol*. 2012;116–117:90–101.
- Shi J, Abid AD, Kennedy IM, Hristovaa KR, Silk WK. To duckweeds (*Landoltia punctata*), nanoparticulate copper oxide is more inhibitory than the soluble copper in the bulk solution. *Environ Pollut*. 2011;159(5):1277–82.
- Atha DH, Wang H, Petersen EJ, Cleveland D, Holbrook RD, Jaruga P, Dizdaroğlu M, Xing B, Nelson BC. Copper oxide nanoparticle mediated DNA damage in terrestrial plant models. *Environ Sci Technol*. 2012;46(3):1819–27.
- Bondarenko O, Juganson K, Ivask A, Kasemets K, Mortimer M, Kahru A. Toxicity of Ag, CuO and ZnO nanoparticles to selected environmentally relevant test organisms and mammalian cells in vitro: a critical review. *Arch Toxicol*. 2013;87:1181–200.
- Chen Z, Meng H, Xing G, Chen C, Zhao Y, Jia G, Wang T, Yuan H, Ye C, Zhao F, et al. Acute toxicological effects of copper nanoparticles in vivo. *Toxicol Lett*. 2006;163(2):109–20.
- Lei R, Wu C, Yang B, Ma H, Shi C, Wang Q, Wang Q, Yuan Y, Liao M. Integrated metabolomic analysis of the nano-sized copper particle-induced hepatotoxicity and nephrotoxicity in rats: a rapid in vivo screening method for nanotoxicity. *Toxicol Appl Pharmacol*. 2008;232(2):292–301.
- Manna P, Ghosh M, Ghosh J, Das J, Sil PC. Liver dysfunction and cellular damage: role of IκBα/NF-κB, MAPKs and mitochondrial signal. *Nanotoxicology*. 2012;6(1):1–21.
- Sarkar A, Das J, Manna P, Sil PC. Nano-copper induces oxidative stress and apoptosis in kidney via both extrinsic and intrinsic pathways. *Toxicology*. 2011;290(2–3):209–18.
- Meng H, Chen Z, Xing G, Yuan H, Chen C, Zhao F, Zhang C, Zhao Y. Ultrahigh reactivity provokes nanotoxicity: explanation of oral toxicity of nano-copper particles. *Toxicol Lett*. 2007;175(1–3):102–10.
- Huang Y-W, Wu C, Aronstam RS. Toxicity of transition metal oxide nanoparticles: recent insights from in vitro studies. *Materials*. 2010;3(10):4842–59.
- Karlsson HL, Cronholm P, Gustafsson J, Möller L. Copper oxide nanoparticles are highly toxic: a comparison between metal oxide nanoparticles and carbon nanotubes. *Chem Res Toxicol*. 2008;21:1726–32.
- Karlsson HL, Holgersson A, Möller L. Mechanisms related to the genotoxicity of particles in the subway and from other sources. *Chem Res Toxicol*. 2008;21(3):726–31.
- Karlsson HL, Gustafsson J, Cronholm P, Möller L. Size-dependent toxicity of metal oxide particles—a comparison between nano- and micrometer size. *Toxicol Lett*. 2009;188(2):112–8.
- Lanone S, Rogerieux F, Geys J, Dupont A, Maillot-Marechal E, Boczkowski J, Lacroix G, Hoet P. Comparative toxicity of 24 manufactured nanoparticles in human alveolar epithelial and macrophage cell lines. Part I. *Fibre Toxicol*. 2009;6:14.
- Midander K, Cronholm P, Karlsson HL, Elihn K, Möller L, Leygraf C, Wallinder IO. Surface characteristics, copper release, and toxicity of nano- and micrometer-sized copper and copper(II) oxide particles: a cross-disciplinary study. *Small*. 2009;5(3):389–99.
- US Environmental Protection Agency. Release of micronized copper particles from pressure-treated wood. 600/R-14/365. 2014. <http://www.epa.gov/ord>.
- Stirling R, Ruddick JNR, Morris PI. Characterization of copper in leachates from ACQ- and MCQ-treated wood and its effect on basidiospore germination. *Wood Fiber Sci*. 2015;47(3):1–8.
- Stirling R, Morris PI. Mobility of copper from MCQ in shell-treated wood exposed above ground. IRG/WP 10-30534. Stockholm: International Research Group on Wood Protection; 2010.
- Kartal SN, Green F, Clausen CA. Do the unique properties of nanometals affect leachability or efficacy against fungi and termites? *Int Biodeterior Biodegrad*. 2009;63(4):490–5.
- Wang L, Kamdem P. Copper leached from micronized copper quaternary (MCQ) treated wood: influence of the amount of copper in the formulations. In: proceedings of the 55th international convention of society of wood science and technology, 27–31 Aug 2012, Beijing; 2012. Paper PS-66. <http://www.swst.org/meetings/AM12/pdfs/papers/PS-66.pdf>. Accessed Aug 2016.
- Platten WE, Sylvest N, Warren C, Arambewela M, Harmon S, Bradham K, Rogers K, Thomas T, Luxton TP. Estimating dermal transfer of copper particles from the surfaces of pressure-treated lumber and implications for exposure. *Sci Total Environ*. 2016;548–549:441–9.
- Santiago-Rodríguez L, Griggs JL, Bradham KD, Nelson C, Luxton T, Platten WE, Rogers KR. Assessment of the bioaccessibility of micronized copper wood in synthetic stomach fluid. *Environ Nanotechnol Monit Manag*. 2015;4:85–92.
- Civardi C, Schubert M, Fey A, Wick P, Schwarze FW. Micronized copper wood preservatives: efficacy of ion, nano, and bulk copper against the brown rot fungus *Rhodonia placenta*. *PLoS ONE*. 2015;10(11):e0142578.
- European Committee for Standardization. ENV 807. Wood preservatives-determination of the effectiveness against soft rotting micro-fungi and other soil inhabiting micro-organisms. Brussels:BSI; 2001.
- Schlagenhauf L, Chu BTT, Buha J, Nüesch F, Wang J. Release of carbon nanotubes from an epoxy-based nanocomposite during an abrasion process. *Environ Sci Technol*. 2012;46(13):7366–72.
- Roesslein M, Hirsch C, Kaiser JP, Krug HF, Wick P. Comparability of in vitro tests for bioactive nanoparticles: a common assay to detect reactive oxygen species as an example. *Int J Mol Sci*. 2013;14(12):24320–37.
- Schwartz J, Dockery DW, Neas LM. Is daily mortality associated specifically with fine particles? *J Air Waste Manag Assoc*. 1996;46(10):927–39.
- Raaschou-Nielsen O, Andersen ZJ, Beelen R, Samoli E, Stafoggia M, Weinmayr G, Hoffmann B, Fischer P, Nieuwenhuijsen MJ, Brunekreef B, et al. Air pollution and lung cancer incidence in 17 European cohorts: prospective analyses from the European study of cohorts for air pollution effects (ESCAPE). *Lancet Oncol*. 2013;14(9):813–22.
- Oberdörster G, Celein RM, Ferin J, Weiss B. Association of particulate air pollution and acute mortality: involvement of ultrafine particles? *Inhal Toxicol*. 1995;7(1):111–24.
- Thorpe A, Brown RC. Measurements of the effectiveness of dust extraction systems of hand sanders used on wood. *Ann Occup Hyg*. 1994;38(3):279–302.
- Lehmann E, Fröhlich N. Particle size distribution of wood dust at the workplace. *J Aerosol Sci*. 1988;19(7):1433–6.
- Ratnasingam J, Scholz F, Natthondan V, Graham M. Dust-generation characteristics of hardwoods during sanding processes. *Eur J Wood Wood Prod*. 2011;69(1):127–31.
- Oberdörster G, Oberdörster E, Oberdörster J. Nanotoxicology: an emerging discipline evolving from studies of ultrafine particles. *Environ Health Perspect*. 2005;113(7):823–39.
- Atuanya CU, Ibhade AO. AOA. Characterization of Okhuen (*Brachystegia nigerica*) wood as a potential reinforcement for polymer composites. *Int J Eng Technol*. 2011;11(4):52–9.

43. Gómez Yepes ME, Cremades LV. Characterization of wood dust from furniture by scanning electron microscopy and energy-dispersive X-ray analysis. *Ind Health*. 2011;49(4):492–500.
44. Mazzoli A, Favoni O. Particle size, size distribution and morphological evaluation of airborne dust particles of diverse woods by scanning electron microscopy and image processing program. *Powder Technol*. 2012;225:65–71.
45. Klein RG, Schmezer P, Amelung F, Schroeder HG, Woeste W, Wolf J. Carcinogenicity assays of wood dust and wood additives in rats exposed by long-term inhalation. *Int Arch Occup Environ Health*. 2001;74(2):109–18.
46. Decker P, Cohen B, Butala JH, Gordon T. Exposure to wood dust and heavy metals in worker using CCA pressure-treated wood. *AIHA J*. 2002;63(2):166–71.
47. Nygren O, Nilsson CA, Lindahl R. Occupational exposure to chromium, copper and arsenic during work with impregnated wood in joinery shops. *Ann Occup Hyg*. 1992;36(5):509–17.
48. Gangwa S, Brown JS, Wang A, Houck KA, Dix DJ, Kavlock RJ, Cohen Hubal EA. Informing selection of nanomaterial concentrations for ToxCast in vitro testing based on occupational exposure potential. *Environ Health Perspect*. 2011;119(11):1539–46.
49. Sargent LM, Porter DW, Staska LM, Hubbs AF, Lowry DT, Battelli L, Siegrist KJ, Kashon ML, Mercer RR, Bauer AK, et al. Promotion of lung adenocarcinoma following inhalation exposure to multi-walled carbon nanotubes. *Part Fibre Toxicol*. 2014;11:3.
50. Alwis U, Mandryk J, Hocking AD, Lee J, Mayhew T, Baker W. Dust exposures in the wood processing industry. *Am Ind Hyg Assoc J*. 1999;60(5):641–6.

Submit your next manuscript to BioMed Central and we will help you at every step:

- We accept pre-submission inquiries
- Our selector tool helps you to find the most relevant journal
- We provide round the clock customer support
- Convenient online submission
- Thorough peer review
- Inclusion in PubMed and all major indexing services
- Maximum visibility for your research

Submit your manuscript at
www.biomedcentral.com/submit



REVIEW

Open Access



A critical review of the current knowledge regarding the biological impact of nanocellulose

C. Endes^{1,2†}, S. Camarero-Espinosa^{1,2†}, S. Mueller¹, E. J. Foster^{1,3}, A. Petri-Fink¹, B. Rothen-Rutishauser¹, C. Weder¹ and M. J. D. Clift^{1,4*}

Abstract

Several forms of nanocellulose, notably cellulose nanocrystals and nanofibrillated cellulose, exhibit attractive property matrices and are potentially useful for a large number of industrial applications. These include the paper and cardboard industry, use as reinforcing filler in polymer composites, basis for low-density foams, additive in adhesives and paints, as well as a wide variety of food, hygiene, cosmetic, and medical products. Although the commercial exploitation of nanocellulose has already commenced, little is known as to the potential biological impact of nanocellulose, particularly in its raw form. This review provides a comprehensive and critical review of the current state of knowledge of nanocellulose in this format. Overall, the data seems to suggest that when investigated under realistic doses and exposure scenarios, nanocellulose has a limited associated toxic potential, albeit certain forms of nanocellulose can be associated with more hazardous biological behavior due to their specific physical characteristics.

Keywords: Nanocellulose, Cellulose nanocrystals, Human health, Risk, Exposure, Hazard, Nanofibers, Nano-object-cell interactions, Nanotoxicology

Background

Since the emergence of nanotechnology as a field in its own right, a continuously increasing number of new nanomaterials have been developed, which are potentially useful for applications that range from healthcare products to high-performance engineering materials [1–3]. Several forms of nanocellulose, in their raw format, have been demonstrated to exhibit attractive property matrices and are potentially useful for the paper industry, as a reinforcing filler in polymer composites, basis for low-density foams, in packaging materials, additive in colloidal systems such as adhesives and paints, zero-calorie filler/thickener/stabilizer in a wide variety of food products, and in hygiene, cosmetic, and medical products [4, 5]. Although (microcrystalline) cellulose has long

been used in healthcare products such as wound healing tissue and dialysis membranes, as well as a food additive, little is known as to the potential adverse biological impact of its nanoscale variants, whose commercial exploitation only begun in the last few years [6, 7].

Cellulose, the most abundant polymer in the world, is found in plant cell-walls, certain sea creatures, e.g. tunicates, and algae, e.g. *Valonia*. It is also produced by several bacteria such as *Acetobacter xylinum* [8–11]. Cellulose is a carbohydrate, whose repeat unit is constituted by two anhydroglucose units that are linked by a β -1,4 glycosidic bond. Cellulose chains assemble via complex inter- and intramolecular H-bonding into crystalline structures [12, 13]. Crystalline sheets pack in a parallel fashion, building up filiform structures that can be isolated from the native material as cellulose nanocrystals (CNCs), which are also referred to as nanocrystalline cellulose (NCC) or cellulose nanowhiskers (CNWs). These rod-shaped, high-aspect-ratio nanoparticles (HARN; aspect ratio = length/diameter ≥ 3 [14]) exhibit a diameter of 5–40 nm and a length that can vary from

*Correspondence: m.j.d.clift@swansea.ac.uk

[†]C. Endes, S. Camarero-Espinosa contributed equally as first author

⁴ In Vitro Toxicology Group, Swansea University Medical School, Singleton Park Campus, Swansea SA2 8PP, Wales, UK

Full list of author information is available at the end of the article

100–500 nm, when derived from plant sources, or from 1–3 μm when extracted from tunicates or algae (Fig. 1) [15–19]. In plant-derived cellulose, CNCs are further integrated into longer fibers that are composed of amorphous and crystalline domains and are commonly referred to as cellulose nanofibrils (CNF), nanofibrillated cellulose (NFC) or microfibrillated cellulose (MFC) [15, 20]. Thus, deconstruction of the hierarchical structure of plant cellulose by mechanical treatment and/or enzymatic [21] or chemical [22] treatments permits the isolation of CNFs [23]. The degradation of cellulose pulp into CNCs is generally achieved by hydrolysis of the non-crystalline domains with mineral acids such as hydrochloric [18], sulfuric [9, 24] or phosphoric acid [25]. In the case of the latter two acids, a frequently observed side-reaction is the formation of sulfate or phosphate ester groups with the surface hydroxyl groups of nanocellulose. The degree of functionalization and the nature of the functional groups determine the charge density and thereby the dispersibility of nanocellulose in liquid solvents or polymer matrices. The presence of surface ester groups also negatively affects the thermal stability of the nanocellulose and may affect their toxicological behavior [26, 27]. Bacterial cellulose (BC) is produced by bacteria in the form of continuous fibers with a diameter of 3–8 nm, which assemble into macroscopic meshes of high purity and crystallinity [11, 28, 29].

The high degree of crystallinity and the uniaxial orientation of the polymer chains bestow CNCs with an extraordinarily high stiffness (120–168 GPa) and strength [30, 31]. Other attractive features include a low density, low cost, the renewable nature of the source, and biodegradability. The high density of surface hydroxyl groups allow CNCs to interact with another and also polymeric matrix materials via H-bonding, which promotes very efficient stress transfer and makes CNCs ideal candidates as reinforcing fillers for polymers [9, 32]. It was shown that the H-bonding interactions can be switched “off” on demand, i.e. by exposure to a competing hydrogen-bond forming agent, and this has enabled the fabrication of stimuli responsive materials whose stiffness can be changed over several orders of magnitude [9, 33, 34]. CNCs can further form lyotropic phases, display a high surface area, and the abundance of surface hydroxyl groups makes the chemical modification of the surface readily possible. All these features make CNCs and other nanocellulose types interesting for a broad range of new applications including, use as a reinforcing filler in polymer nanocomposites [35, 36], the basis for stimuli responsive materials [9, 37, 38], as a nucleating agent [39, 40], a carrier for the controlled delivery of molecules [41], biosensors [42], and a component of tissue engineering scaffolds [43, 44]. In addition, the substitution of microcrystalline cellulose, which has long been used

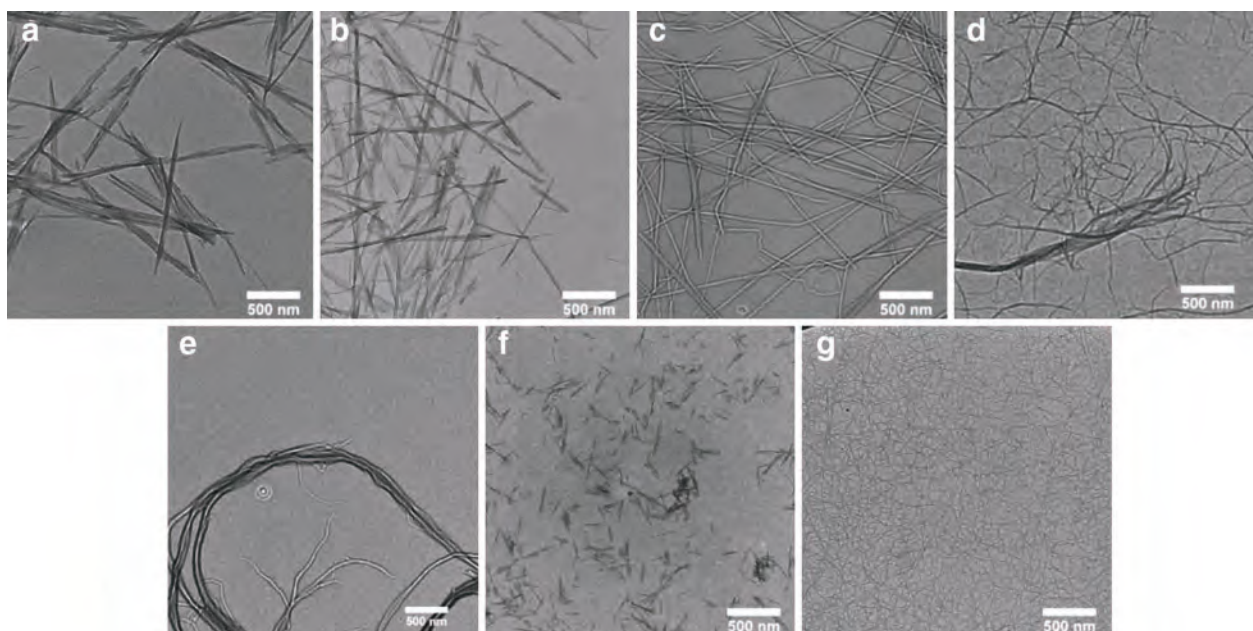


Fig. 1 Transmission electron microscopy images of selected nanocellulose types. CNCs isolated by HCl (a) and H_2SO_4 hydrolysis (b) from bacterial cellulose, H_2SO_4 hydrolysis from tunicate mantles (c) or wood pulp (f) and nanofibrillated cellulose obtained by enzymatic (d), mechanical (e), or 2,2,6,6-tetramethylpiperidiny-1-oxyl (TEMPO) mediated oxidative (g) degradation of wood pulp. The figure is reprinted with permission from Sacui et al. [96] © (2014) American Chemical Society

as rheology modifier in food products and cosmetic formulations, and as an excipient in tablets, with nanocellulose types can be envisioned to bring significant benefits beyond those described above.

The commercial production of CNCs and NFC has recently been launched and a gross world product of \$600 billion is expected by 2020 [45]. For example, based on the technology developed by FPIInovations and under the supervision of Domtar (Domtar Corporation, Montreal, Canada), CelluForce® built a semi-commercial facility in 2010 with a capacity to produce 1000 kg CNCs per day [46, 47], whilst Innventia® reported a production of 100 kg CNFs per day in 2011 [48]. Several other entities have in the meantime installed production facilities for CNFs and CNCs that expand these initial capacities. The manufacturing of final products such as coatings, packaging materials, composite materials, aerogels for insulation or water filtration containing different types of nanocellulose has already commenced [49, 50]. Given these developments, the potential human health risks associated with exposure to these nanomaterials, especially in the form of respirable nanofibers as either a final product (e.g. in food and health care products), after extraction from a more complex material (e.g. after aging and degradation of a polymer nanocomposite or mechanical treatment of the latter), or at production or processing facilities (e.g. occupational exposure) must be understood [51, 52]. This is considered for all main portals of entry to the human body, including the skin, gastrointestinal tract, systemic circulation, and arguably, the most important, the lung [53]. The latter is considered the primary route of exposure to humans for any nanoparticle released into the environment (including, and especially, an occupational scenario) [54].

Since the first findings regarding the adverse biological impact of HARN, and their potential association with lung diseases were identified [55], special attention is being paid to the toxicology of engineered nanofibers [56]. The most prominently known fact surrounding fibers, is that exposure to asbestos fibers was associated with the development of epidemic lung disease states such as fibrosis, asbestosis, lung cancer, mesothelioma and pleural plaques [57]. Further studies on the toxicology of synthetic vitreous fibers (SVF), which are a group of inorganic materials containing aluminum or calcium silicates, led to the development of the fiber pathogenicity paradigm [58–60]. The *fiber paradigm* states that the length of a fiber is a key parameter that impacts the ability of a macrophage to phagocytize it; this results in frustrated phagocytosis [58], subsequent stimulation of inflammatory factors leading towards potential fibrosis or carcinogenic effects if the fiber is too long. However, the length is not the unique parameter involved in the

toxicology of fibers; indeed the biopersistence of a fiber has been specifically identified as the key factor governing the biological response following (chronic) exposure [58, 61].

The fiber paradigm therefore highlights the importance of the form, shape and biological interaction of a substance when brought into contact with mammalian cells/tissue(s). Based on this understanding, and with the development of a disease commonly referred to as 'brown lung', observed in workers of the cotton industry exposed to cotton dust [62–64], several studies investigated the possible health risks associated with cellulosic materials. Tatrai et al. [65] administered a single dose intratracheally (15 mg) of either cellulose powder, pine wood dust or a fiber-free extract from the same wood dust and observed after one month following exposure, granulomatous inflammation, fibrosis and alveolitis in vivo. The authors also observed in microscopic studies the presence of birefringent fibrous structures in the cytoplasm of formed multinucleated giant cells. However, these effects were not observed in fiber-free samples. In addition, other parameters such as the biopersistence of cellulose have been evaluated in several studies in vivo [66, 67] and in vitro [68]. Davis [67] reported in a 28-day inhalation study with rats the formation of alveolitis and granulomata. By contrast, a further in vivo study conducted by Warheit et al. [66], that involved a 2-week inhalation period, no significant pulmonary effects were detected 3 months post exposure following exposure to microcellulose. Nevertheless, the authors reported the extremely limited rate of clearance of the fibers from the lungs of the animals which, as mentioned before, is an important parameter in fiber toxicology. Muhle et al. [69] also conducted an in vivo study and reported, after one year of exposure, a higher durability of cellulose fibers in the lung of rats (2 mg dose intratracheally) than chrysotile, a common form of asbestos. The biopersistence of cellulose nanofibers was also assessed in vitro using artificial lung airway lining fluid and macrophage phagolysosomal fluid, further supporting the durability of cellulosic fibers in a biological environment [68]. In light of these findings, and in further consideration of the differences between bulk and nanoscale materials, there is an imperative need to understand the potential hazard posed by nanocellulose, due to its nanoscale (1–100 nm) dimensions [53]. As a result, a number of studies have recently been conducted to shed light on this aspect. The objective of the present review is to summarize and critically discuss this recent work, and elucidate which key indicators can be utilized in the future in order to safely apply nanocellulose in different industries. It is important to note, that the discussion centered around this review is based upon the raw form of nanocellulose, and not that

already applied in e.g. a polymer matrix. For a comprehensive review on applied forms of nanocellulose, please refer to [5].

Life-cycle of nanocellulose

In order to evaluate the potential risk of any form of nanocellulose towards human health and the environment, its life-cycle must be studied in order to identify and analyze possible high- and low-risk scenarios. During the life-cycle of any manufactured nanomaterial, and product containing nanomaterials, several stages can be identified (Fig. 2): production of raw materials (Stage 1), manufacture (Stage 2), transportation (Stage 3), consumer use (Stage 4) and disposal (Stage 5). In a new life-cycle risk assessment framework (NANO LCRA) proposed by Shatkin and Kim [70], the different exposure scenarios during the life-cycle of nanocellulose in food packaging were evaluated and ranked as a function of the potential, magnitude, likelihood and frequency of the hazard. The authors identified the top four exposure scenarios to be (1) inhalation of dry, raw material by a facility employee during production, (2) application of dry, raw nanocellulose to create a film and inhalation during manufacturing, (3) inhalation of dry, raw nanocellulose powder during mixing with other materials to manufacture a product, and (4) inhalation by incidental contact with the raw form of nanocellulose. It has to be noted that transportation was not considered during evaluation of the life-cycle and that the risk assessment was performed for a specific application of nanocellulose, e.g. construction materials. However, analysis of the data suggests that the main exposure route would be the inhalation of (raw) nanocellulose, in whatever form, within an occupational setting. It is also important to note that the first

exposure scenario at a consumer level appeared in tenth position, notably as the inhalation of sprayed wet nanoparticles [70]. It must be emphasized, however, that for other applications, such as the production of reinforced materials or the use as a food additive for example, other factors would have to be taken into consideration. In the case of polymer nanocomposites, for example, the release and inhalation of cellulose/polymer particles during processing steps such as drilling, cutting, and sanding, might be a concern [71]. Moreover, for many applications such as uses in healthcare products, cellulose might be surface functionalized, imparting new properties to the material and possibly triggering the need of an independent case study [72, 73].

Although first studies suggest that the inhalation of raw CNCs or CNFs would be the main exposure route for humans, little is known about the exposure concentrations or doses [74]. These parameters will strongly depend on each scenario, i.e., exposure concentrations in occupational activities are likely to be higher than those in consumer applications. Vartiainen et al. [75] measured the occupational exposure during grinding and spray-drying activities in a CNF production pilot plant. Under normal working conditions, e.g., with the grinding device placed inside a fume hood, the measured particle concentration in the air was as low as <4.000 particles/cm³ with some peaks reaching >8.000 particles/cm³. When the measurement was carried out inside the fume hood, the measured particle concentration reached 41.000 particles/cm³ with 75% of particles ranging between 10 and 30 nm in diameter. Similarly, during spray-drying the average particle concentration near the instrument was <10.000 particles/cm³ with a particle diameter between 20 and 60 nm. These findings suggest

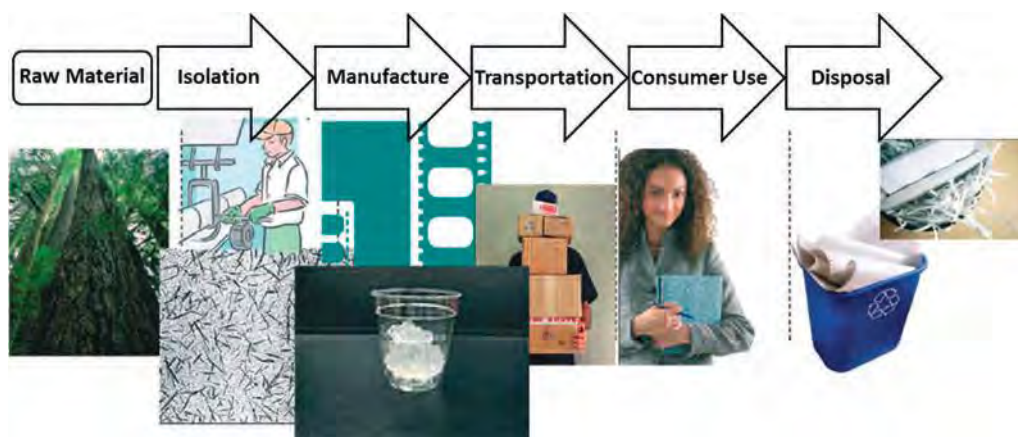


Fig. 2 Life cycle of nanocellulose based composite materials where 5 different stages can be identified: production of raw materials or isolation (Stage 1), manufacture (Stage 2), transportation (Stage 3), consumer use (Stage 4) and disposal (Stage 5). Adapted from Shatkin et al. [70], with permission of The Royal Society of Chemistry

that humans can be readily exposed to nanocellulose in a variety of occupational settings at heightened concentrations. Nonetheless, understanding of the impact of chronic, repeated exposure to these airborne concentrations to human health however, remains, at best, limited.

Biological impact of nanocellulose

Since human exposure, and to a lesser extent based on the current understanding, environmental exposure, to nanocellulose has been shown to be of a significant increase to normal airborne particle concentrations [75], and further to the concerns surrounding the potential hazard associated with HARN and nanomaterials in general [58], understanding of the structure–activity relationship of nanocellulose is vital. The purpose of the remainder of this review therefore, is to provide a critical overview of research directed towards exploring the biological impact and potential hazard of nanocellulose. An overview of key studies is provided in Table 1. In Table 1, together with the physical characteristics of the nanocellulose investigated, a description of the test system utilized, as well as the results of tests designed to assess cytotoxicity, (pro-)inflammatory response following nanocellulose exposure, the oxidative stress status of the biological system studied, as well as the potential for nanocellulose to elicit genotoxicity. Throughout the particle and fiber toxicology field, these endpoints are recognized as the most important drivers of nanomaterial toxicity [54]. For convenience, Table 1 provides a brief summary of the overall conclusions from each of these studies, although it is acknowledged that in some cases the entries may be overly simplified. It is important to further highlight that the biological systems highlighted through the main text and in Table 1 cover both in vitro, in vivo and ecosystem orientated models. This is a considered approach to convey the current understanding of the biological impact of raw nanocellulose, and its varying forms (which also change study-by-study) in terms of the biological response measured.

Cytotoxicity

One of the first important studies regarding the ecotoxicological impact of cellulose nanocrystals derived from ‘kraft pulp’ (CNC dimensions: $200 \times 10 \times 5$ nm) was published by Kovacs et al. in 2010 [76]. The authors presented results from a realistic exposure scenario, i.e., suspension experiments with relevant dose ranges (0.03–10 g/L), that were based on the potential effluent in the vicinity of a CNC production site. The study included aquatic organisms from all trophic levels from bacteria, algae, crustacean, cnidarian to fish and investigated acute lethality (LC_{50} = the lethal concentration that reduces the biological system population to 50% viability),

reproduction, growth, morphology, embryo development and cytotoxicity. Taking all results into consideration, the authors summarized the outcome as “non-concerning”.

Further to this, several studies on cellulose-human interactions confirmed the limited toxic potential of nanocellulose in terms of cytotoxicity in various experimental systems [77, 78]. A sophisticated triple-cell co-culture model of the human epithelial tissue barrier (formulated of a layer of epithelial cells, complemented by human blood monocyte derived macrophages and dendritic cells on the apical and basolateral sides respectively) was used in a study that showed no significant cytotoxicity of two different CNC types isolated from cotton ($170 \pm 72 \times 19 \pm 7$ nm) and tunicates ($2.3 \pm 1.4 \mu\text{m} \times 31 \pm 7$ nm) that were deposited onto the cells in realistic doses (0.14 ± 0.04 , 0.81 ± 0.03 and $1.57 \pm 0.03 \mu\text{g}/\text{cm}^2$) from aerosolized water-based suspensions [79, 80]. However, clearance, albeit based upon a dose, time and CNC-dependent manner, of deposited CNCs by macrophages was observed when cells were exposed to both of these types CNCs, with a lower efficiency associated with the tunicate CNCs (Fig. 3) [79]. Jeong and co-workers used bacterial cellulose (BC; no dimensions given [81]) in in vitro experiments with human umbilical vein endothelial cells (HUVECs) [81]. Neither of their experiments measuring cytotoxicity via the MTT assay, observing the morphology with light microscopy or assessing apoptosis/necrosis (Annexin V/Propidium Iodide staining) and cell-cycle via flow cytometry, showed significant altered outcomes after 24 or 48 h towards the exposure to high BC concentrations (0.1–1 mg/mL) compared to the negative control. Furthermore, in vivo exposure of 0.5–5 mg/mL BC administered via intraperitoneal injection to C57/Bl6 male mice showed no adverse effects after 7 days in comparison to sham exposures. Similar results with BC ($50\text{--}1500 \times 3\text{--}5$ nm) were obtained by Moreira et al. [82] who could not detect significant changes in morphology or proliferation rates of mouse fibroblasts (3T3) and Chinese hamster ovary cells (CHO) in exposures ranging from 0.1–1 mg/mL.

However, there are also studies that have shown cytotoxic effects upon exposure to nanocellulose. Mahmoud and co-workers investigated uptake and membrane integrity in human embryonic kidney cells (HEK 293) and Sf9 insect cells and found that exposure to 0.1 mg/mL of negatively charged CNCs (ζ -potential -46.4 mV), which had been isolated from enzyme treated flax fibers ($130\text{--}200 \times 10\text{--}20$ nm) and labeled with FITC (fluorescein isothiocyanate), led to membrane rupture under physiological pH in contrast to exposure to positively charged, RBITC-labeled (rhodamine B isothiocyanate) CNCs (ζ -potential 8.7 mV) [83]. Similar cytotoxic

Table 1 Succinct overview of the key findings regarding the biological impact of nanocellulose samples studied within the literature

First author	Year	Ref	Nano-cellulose type	Dimensions	Test system	Cytotoxicity	Inflammatory response	Oxidative stress	Genotoxicity	Main conclusions from study
Moreira	2009	[82]	BC	50–1500 × 3–5 nm	3T3 fibroblasts, Chinese Hamster ovary cells	–	n/a	n/a	–	Benign material, beware of material modifications
Kovacs	2010	[76]	NCC	200 × 10 × 5 nm	Rainbow trout, <i>Daphnia magna</i> , <i>Ceriodaphnia dubia</i> , Fathead minnow, <i>Vibrio fischeri</i> , <i>Pseudokirchneriella subcapitata</i> , <i>Hydra attenuate</i> , <i>Danio rerio</i> , Rainbow trout hepatocyte cells	–	n/a	n/a	–	Low toxicity potential and low environmental risk
Jeong	2010	[81]	BC	n/a	Human umbilical vein epithelial cells; C57/BL6 mouse model	–	n/a	n/a	n/a	Suitability for tissue engineering
Mahmoud	2010	[83]	CNC	130–200 × 10–20 nm	Human embryonic kidney cells (HEK 293) and <i>Spodoptera frugiperda</i> Ovary cells (Sf9)	+	n/a	n/a	n/a	Surface charge influences toxicity and uptake
Clift	2011	[91]	CNC	220 ± 6.7 × 15 ± 5 nm	3D Co-culture (A549 epithelial cells, combined with human blood monocyte derived macrophages (MDM) and dendritic cells (MDDC))	–	+	n/a	n/a	Length, stiffness and possibly origin affect CNC-cell interactions
Male	2012	[77]	NCC	120–140 × 3–6 nm	Chinese Hamster lung cells (V79) and <i>Spodoptera frugiperda</i> ovary cells (Sf9)	–	n/a	n/a	n/a	Origin/extraction, treatment and carboxylic acid content influence toxicity
Dong	2012	[78]	CNC	181 ± 9 × 5.0 ± 0.2 nm	Human brain microvascular endothelial cells (HBMEC), mouse endothelial brain cells (bEnd.3), RAW 264.7 macrophages, human breast epithelial cells (MCF-10A, MDA-MB-231 and MDA-MB-468), human hepatocyte cells (KB), prostate cancer cells (PC-3), Rat brain fibroblasts (C6)	–	n/a	n/a	n/a	Low unspecific uptake, no cytotoxicity appropriate for biomedical applications
de Lima	2012	[87]	CNF	White: 135 ± 50 × 14 ± 4 nm, Brown: 140 ± 45 × 11 ± 3 nm, Green: 180 ± 45 × 13 ± 2 nm, Ruby: 130 ± 25 × 10 ± 4 nm, Curaua: 80–170 × 6–10 nm	<i>Allium cepa</i> , 3T3 fibroblasts, and lymphocytes	+	n/a	n/a	+	Genotoxicity depends on cell type and color used
Hannukainen	2012	[93]	NFC	n/a	BEAS 2B epithelial cells	–	n/a	–	+	Elucidation of limited genotoxicity
Pereira	2013	[88]	CNF	85–225 µm × 6–18 nm	Bovine fibroblasts	+	n/a	+	n/a	High dose of CNF exposure leads to negative cell effects
Pereira	2014	[84]	CNF	85–225 µm × 6–18 nm	<i>Chlorella vulgaris</i>	+	n/a	+	n/a	CNF exposure can affect algal viability and growth

Table 1 continued

First author	Year	Ref	Nano-cellulose type	Dimensions	Test system	Cytotoxicity	Inflammatory response	Oxidative stress	Genotoxicity	Main conclusions from study
Endes	2014	[80]	CNC	Cotton: $170 \pm 72 \times 19 \pm 7$ nm Tunicate: $2.3 \pm 1.4 \mu\text{m} \times 31 \pm 7$ nm	3D Co-culture [A549 epithelial cells, monocyte derived macrophages (MDM) and dendritic cells (MDDC)]	–	–	–	n/a	Benign nature of CNCs, independent of their dimensions
Hanif	2014	[86]	CNC	256 ± 64.8 nm 140.5 ± 37.5 nm 108.4 ± 94.8 nm 1174 ± 338.7 nm	3T3 fibroblasts and human colon epithelial cells (HCT116)	+	n/a	n/a	n/a	Cytotoxicity observed for concentrations below $250 \mu\text{g/mL}$, dimensions irrelevant
Catalan	2014	[85]	CNC	$135 \pm 5 \times 7.3 \pm 0.2$ nm	BEAS 2B epithelial cells and human blood monocyte derived macrophages	+	–	n/a	–	55% cytotoxicity mainly $\geq 100 \mu\text{g/mL}$
Yanamala	2014	[90]	CNC	90.19 ± 3.03 nm 207.9 ± 49 nm n/a	C57BL/6 mouse model	+	+	+	n/a	Nanocellulose dimensions rather than the source exert a strong influence on the biological response
Stefaniak	2014	[68]	CNC, CNF	$\sim 105 \times 10$ nm, $\sim 165 \times 11$ nm	RAW 264.7 macrophages	n/a	n/a	Cell free + in vitro	n/a	High biodegradability
Endes	2015	[79]	CNC	Cotton: $237 \pm 118 \times 29 \pm 13$ nm Tunicate: $2244 \pm 1687 \times 30 \pm 8$ nm	3D Co-culture [A549 epithelial cells, monocyte derived macrophages (MDM) and dendritic cells (MDDC)] @ Air-Liquid Interface	–	n/a	n/a	n/a	Length and concentration have a significant effect on CNC-cell interactions
Colic	2015	[89]	CNF	$33 \pm 2.5 \mu\text{m} \times 10\text{--}70$ nm	Mouse fibroblasts (L929), thymocytes, and peripheral blood mononuclear cells (PBMCs)	+	+	–	n/a	High concentration leads to observed effects
Shvedova	2016	[94]	CNC	158 ± 97 nm $\times 54 \pm 17$ nm	C57BL/6 mouse model	+	+	+	+	Male mice exhibit significantly higher adverse pulmonary effects compared to female mice (gender differences)
Farcas	2016	[95]	CNC	158 ± 97 nm $\times 54 \pm 17$ nm	<i>Cauda epididymal</i> sperm samples	+	+	+	+	Pulmonary exposure of CNC affects male mice reproduction system

These are structured, as referred to in the main text, as to the main biochemical endpoints studied within the field, including, *Cytotoxicity*, *Inflammatory Response*, *Oxidative Stress* and *Genotoxicity*. For each endpoint, + response was observed and – no response observed; n/a not investigated). The final column highlights a brief, considered statement of the outcome of the referenced study. Studies are presented in the chronological order that they were published into the public domain

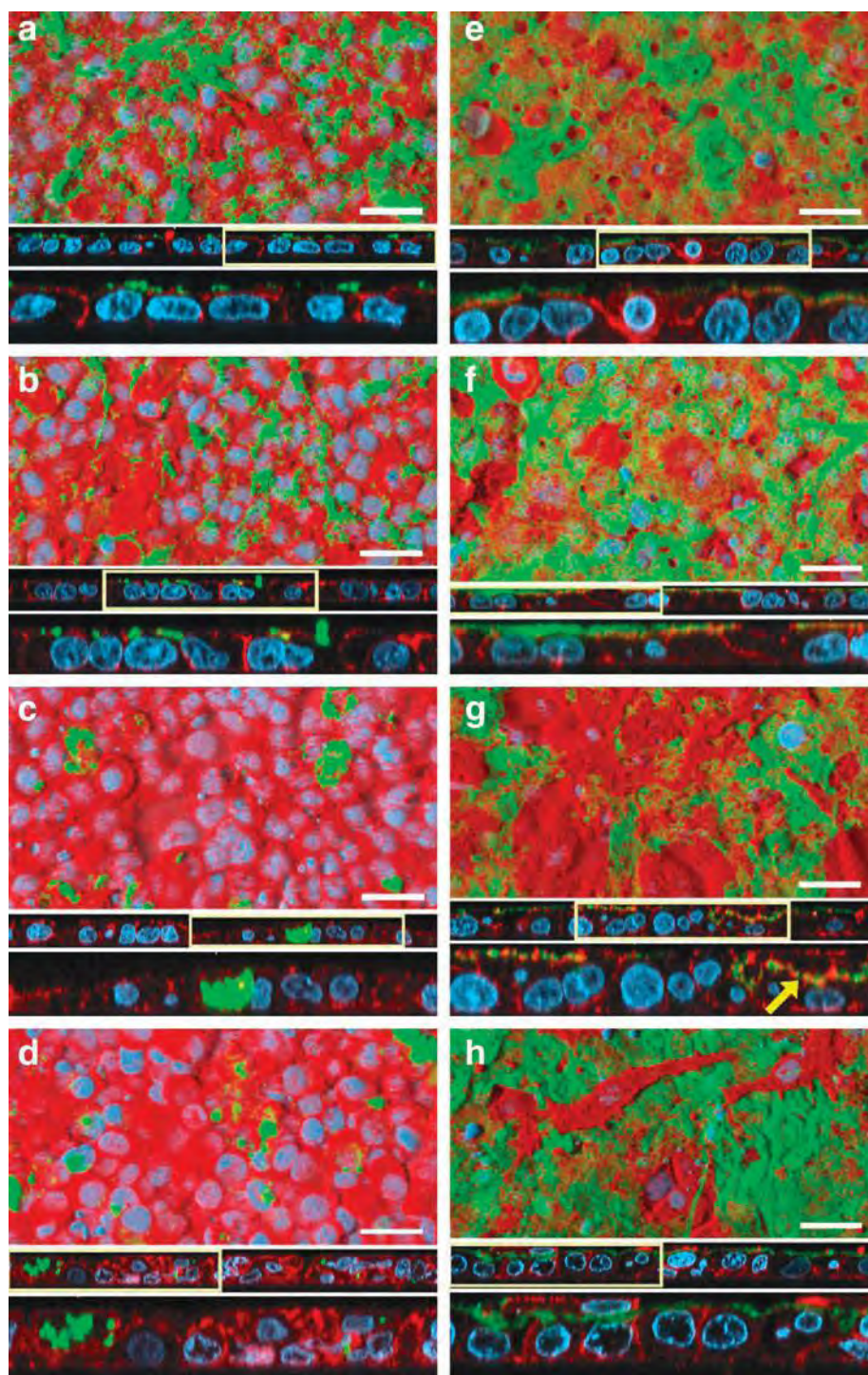


Fig. 3 Length dependent clearance of CNCs by macrophages. Confocal laser scanning microscopy images of the triple-cell co-culture model exposed to $0.56 \pm 0.25 \mu\text{g}/\text{cm}^2$ rhodamine-labeled CNCs isolated from cotton (green **a–d**) or $0.67 \pm 0.09 \mu\text{g}/\text{cm}^2$ CNCs isolated from tunicates (**e–h**) via the ALICE system. Co-cultures were either immediately fixed (**a, e**), or after 1 (**b, f**), 24 (**c, g**), or 48 h (**d, h**) post exposure and stained for cytoskeleton (red) and nuclei (cyan). Images are presented as surface rendering (top), xz-projection of the z-stacks (middle), or twofold optical zoom (bottom). Boxes indicate digitally enlarged ($\times 2$) areas. Arrow shows fiber-F-actin interactions. Scale bars 30 μm . Reprinted with permission from Endes et al. [79] © 2015 American Chemical Society

reactions were also reported using typical CNCs in exposures to algae [84] or bronchial cells (BEAS 2B) [85]. However, in both studies extremely high nanocellulose concentrations in respect to mammalian cell culture (0.25–5 mg/mL) were used [86–88]. Of note in this regard is the study by Colic and co-authors [89], who showed that only the exposure to extremely high concentrations of long, entangled cellulose nanofibrils ($33 \pm 2.5 \mu\text{m} \times 10\text{--}10 \text{ nm}$; $0.25\text{--}1 \text{ mg/mL}$), the highest one covering the L929 monolayers almost completely, lead to impaired metabolic activity and reduced cell proliferation [89]. Furthermore in vivo, Yanamala measured elevated cytotoxicity (as determined by an increase in the activity of the enzyme lactate dehydrogenase) after the aspiration of wood pulp derived CNCs in mice (50, 100 and 200 $\mu\text{g}/\text{mouse}$), detecting similar strong reactions in the context of cytotoxicity compared to asbestos aspiration (50 $\mu\text{g}/\text{mouse}$) [90].

Overall, the incidence of benign results in terms of cytotoxicity, viability and impact upon mammalian cell morphology seems to be prevalent in the current literature upon the risk of nanocellulose. Despite this, the existence of adverse effects observed following nanocellulose exposure has to be taken into consideration when evaluating the total hazard posed by this material. Summarizing, single, low doses administration of nanocelluloses hint at the non-hazardous nature of nanocellulose, yet lack a degree of realism when considering human exposure. The importance of relevant exposure systems (cell type), dose, nanocellulose type/treatment/origin together with a clear material characterization is especially highlighted by the seemingly directly opposing results obtained by Mahmoud and co-authors (0.1 mg/mL FITC-labeled CNCs elicit cytotoxicity in human embryonic kidney cells (HEK 293) ovary cells (Sf9)) [83] vs. Dong et al. (0.01–0.05 mg/mL FITC-labeled CNCs induce no measurable cytotoxicity in a wide range of barrier and immune cell types in vitro) [78].

Inflammation

One of the key aspects of the nanoparticle-cell interaction is the potential for nanoparticles to elucidate a (pro-)inflammatory response from the cellular system being studied. In a realistic in vitro model of the human epithelial tissue barrier, it has been demonstrated that the exposure to CNCs does not induce a significant amount of (pro-)inflammatory mediators tumor necrosis factor- α (TNF- α) and interleukin-8 (IL-8), in contrast to asbestos fibers [91, 80]. The latter study [80] involved CNCs isolated from cotton ($170 \pm 72 \times 19 \pm 7 \text{ nm}$) and tunicates ($2.3 \pm 1.4 \mu\text{m} \times 31 \pm 7 \text{ nm}$) that were applied via nebulizing aqueous suspensions at a concentration

range from 0.14 ± 0.04 to $1.57 \pm 0.03 \mu\text{g}/\text{cm}^2$ by an air-liquid exposure approach. These results are underpinned by a study of Catalan et al., who exposed monocyte derived macrophage monocultures to 30–300 $\mu\text{g}/\text{mL}$ cotton CNCs ($135 \pm 5 \times 7.3 \pm 0.2 \text{ nm}$) with no detection of TNF- α and IL-1 β in comparison to microcrystalline cellulose (CNC aggregates that were micron-sized) [92]. Interestingly, Colic and co-workers showed an anti-inflammatory influence of cellulose nanofibril exposures on PBMCs (peripheral blood mononuclear cells) in vitro, as measured by downregulation of IL-2, IFN- γ (interferon- γ) and IL-17, of which was only observed at considered high doses (0.25–1 mg/mL) [89]. However, Clift et al. ($220 \pm 6.7 \times 15 \pm 5 \text{ nm}$) [91], who used the same 3D triple-cell co-culture model of the human epithelial tissue barrier highlighted above and applied CNCs via aqueous suspensions, showed an increase in IL-8 response when exposed to 30 $\mu\text{g}/\text{mL}$ cotton CNCs. An extensive screening study by Yanamala and colleagues that explored the administration of CNCs after different processing steps (wood pulp CNCs applied as isolated in suspension and kept in suspension vs. isolated and freeze dried to powder before re-suspension) found that both preparations of CNCs have the potential to induce inflammatory effects following pharyngeal aspiration in mice [90]. The authors detected significantly elevated pulmonary influxes of total cells, especially PBMCs compared to negative controls and mice exposed to asbestos. Increased expression of cytokines (IL-1 α , IL-1 β , IL-5, IL-6, IL-12 p40, G-CSF, GM-CSF, KC, MCP-1, MIP-1 α , MIP-1 β , and TNF- α) involved in acute inflammatory reactions compared to the control could be detected. Interestingly, depending on the pre-treatment from which the CNCs were applied, either a T-helper cell subtype 1 (Th1) mediated immune response (freeze dried before resuspension) or the induction of a Th2 associated response (only suspension) could be observed.

Despite the data discussed the above paragraph (Table 1), there remains a prominent lack of coherent data to substantially, and specifically evaluate the potential of nanocellulose to pose a relevant hazard towards human health via an inflammatory immune response. Nevertheless, the existing studies point out that the physico-chemical characteristics, especially the aggregation status, of CNCs can have a (direct) detrimental impact towards elucidating a (pro-)inflammatory response [90]. Moreover, overload exposures often mask the underlying specific mechanisms of toxicity and can only point at a general direction of potential hazard. In terms of inflammation, especially the chronic or repeated low dose exposure as the most realistic scenario for human exposure must be focused upon in future research.

Oxidative stress

Little is known about the radical forming potential of nanocellulose in cell-free and cellular environments, with studies mainly reporting insignificant impact on the oxidative stress status of the cells unless extremely high concentrations are applied (cotton CNFs, 85–225 $\mu\text{m} \times 6\text{--}18\text{ nm}$; 2–5 mg/mL, bovine fibroblasts), similar to the endpoints of cytotoxicity and inflammation [88]. Only a few studies include the measurement of radical oxygen species formation [68, 89], the activity of antioxidant enzymes such as superoxide dismutase (SOD) or peroxiredoxin [88], and the depletion of antioxidant peptides such as glutathione [80, 89]. Interestingly, Stefaniak et al. observed significantly increased radical formation ($\cdot\text{OH}$) by CNCs ($\sim 105 \times 10\text{ nm}$) and CNFs ($\sim 165 \times 11\text{ nm}$) in a cell free experiment in contrast to benchmark MCC ($<10\text{ }\mu\text{m} \times <2\text{ }\mu\text{m}$) with absent, consecutive cellular reactions in macrophages [68]. These results are especially alarming as the study also revealed a high durability in artificial lung fluid. In summary, it has been commonly reported that no significant oxidative stress is evident in vitro following nanocellulose exposure, i.e. using cotton ($170 \pm 72 \times 19 \pm 7\text{ nm}$) or tunicate ($2.3 \pm 1.4\text{ }\mu\text{m} \times 31 \pm 7\text{ nm}$) CNCs ($0.14 \pm 0.04\text{--}1.57 \pm 0.03\text{ }\mu\text{g}/\text{cm}^2$) in the human epithelial tissue barrier model previously described [80], nanofibrillated celluloses ($9.5\text{--}950\text{ }\mu\text{g}/\text{cm}^2$) on bronchial cells (BEAS 2B) [93], CNFs in high dose experiments with bovine fibroblasts ($85\text{--}225\text{ }\mu\text{m} \times 6\text{--}18\text{ nm}$; 2–5 mg/mL) [88] and CNFs in lower doses to human fibroblasts (L929; $>10\text{ }\mu\text{m} \times 10\text{--}35\text{ nm}$; $31.5\text{ }\mu\text{g}/\text{mL}$ – $1\text{ mg}/\text{mL}$) [89]. However, measurable biological effects were shown by Pereira et al. as a slight increase in SOD activity in the algae *Chlorella vulgaris* after exposure to 1, 50 and $100\text{ }\mu\text{g}/\text{mL}$ cotton CNFs ($85\text{--}225\text{ }\mu\text{m} \times 6\text{--}18\text{ nm}$) [88].

The oxidative stress status of a cell has a relevant influence most importantly in chronic exposures where it, together with its intrinsic biopersistence, can lead to severe damage and resulting disease as seen with other HARN materials [56]. The findings in cell-free experiments Stefaniak and colleagues [68] should point out the importance to substantiate the research in this direction regarding the potential adverse biological impact of nanocellulose.

Genotoxicity

In recent years the investigation of damage to or changes in the genetic information within a cell induced by nanoparticle exposure came into focus; including the measurement of DNA strand breaks, formation of micronuclei and the potential for mutagenicity. Only a few studies have so far investigated the genotoxic influence of nanocellulose. Although the typical dimensions of

nanocellulose result in an unlikeliness of nuclear translocation however is not to be excluded without further evidence. Nevertheless, the hindrance of cell-division, viability or indirect genotoxicity has to be especially highlighted when surface functionalizations are used to alter the bare and so far benign surface of nanocellulose.

Of the studies pertinent to this biological endpoint regarding nanocellulose, no effects in terms of micronuclei formation could be observed with BEAS 2B cells at low concentrations of cotton CNCs ($2.5\text{--}100\text{ }\mu\text{g}/\text{mL}$; $135 \pm 5 \times 7.3 \pm 0.2\text{ nm}$) over 48 h [92]. Kovacs et al. reported no changes in DNA quality after exposures to up to 2 mg/mL kraft pulp CNCs ($200 \times 10 \times 5\text{ nm}$) in primary rainbow trout hepatocytes [76]. Similar results were obtained when CNCs isolated from BC ($50\text{--}1500 \times 3\text{--}5\text{ nm}$) were used in a comet assay and the AMES test in a concentration of 0.1–1 mg/mL after 48 h [82]. However, 0.01–1% white, colored cotton and curaua nanofibers (white $135 \pm 50 \times 14 \pm 4\text{ nm}$, brown $140 \pm 45 \times 11 \pm 3\text{ nm}$, green $180 \pm 45 \times 13 \pm 2\text{ nm}$, ruby $130 \pm 25 \times 10 \pm 4\text{ nm}$ and curaua: $80\text{--}170 \times 6\text{--}10\text{ nm}$) showed the ability to induce negative changes in the relative mitotic index and chromosomal aberration of *Allium cepa* cells as well as DNA strand breaks in concentrations of 0.1% of brown cotton and curaua fibers in animal cells (human lymphocytes, 3T3 mouse fibroblasts) [87]. Furthermore, Hannukainen et al. reported a potential genotoxic effect by the exposure of BEAS 2B epithelial cells to NFC ($950\text{ }\mu\text{g}/\text{cm}^2$; 24 h) measured by the comet assay [93].

Finally, important recent research has shown that some CNCs are able to induce all four biological endpoints, highlighting that through complex cellular cascades, that all four biochemical processes can induce deleterious effects, albeit only in males in vivo. In recent studies by Shvedova et al., and Farcas et al., it has been shown that following pulmonary exposure of CNCs to C57BL/6 mice, that, after analysis over a chronic period, male mice were more susceptible to exhibit increased cytotoxicity, which was further associated with a heightened inflammatory and oxidative stress response compared to female mice. Further evidence was shown that these biochemical effects led to significant genotoxicity [94]. In a further study, a similar author team elucidated further that the genotoxic effects were highly detrimental to the male reproductive system [95].

Summary

It is apparent from the research conducted regarding the potential hazard posed by various forms of nanocellulose, especially towards human and environmental health, that the current understanding of its structure–activity relationship is equivocal and incoherent. Whilst a multitude

of studies show the overall benign nature of nanocellulose, others stress the potential for adverse effects (overview Table 1).

It appears that many of the observed differences can be attributed to the variation in cell systems, material origin, treatment and characterization, cell exposure doses reaching non-realistic concentrations of nanocellulose, exposure scenarios or the lack of thorough characterization of the administered CNCs and/or the biological systems used. Some studies focus on the inhalation route as one of the main entry portals for particulates in occupational settings [79, 80, 91, 92, 96]. Others focus on the reaction of immune cells as important drivers of toxicity [90]. Some of the observed cellular responses are the result of heavily overloaded systems and the outcomes, therefore, are deemed to be an effect of the dose and not the nanomaterials themselves [88]. So far, the approach of most of the experiments is a general hazard assessment with little regard to realistic exposure doses, particle characteristics during exposure, time frames or exposure scenarios. Additionally, due to the nature of nanocellulose it is challenging to track it during uptake and fate due to a lack of analytical methods feasible to measure nanocellulose in biological systems. Therefore, the morphological impact or organ distribution after exposure is limited. Nevertheless, the overall results could be interpreted that most of the studies hint at a limited hazard potential of nanocellulose. From the data highlighting a potential hazard associated with nanocellulose however, such possibilities can be circumvented or diminished by avoiding those nanocellulose types with extreme length ($>5\ \mu\text{m}$), overload doses or in a physical format that induces biological adverse effects such as freeze-dried and re-suspended powder. It seems that the limiting factor in guiding the scientific output regarding nanocellulose toxicity is the lacking knowledge of incidence and in situ exposure doses as well as the specific types of nanocellulose mostly used, i.e. commercial products should be tested instead of in house products. Clear understanding of the specific physical and chemical properties of currently produced and used nanocellulose and realistic exposure doses is of the utmost importance and inevitable.

Finally, data in acute exposure scenarios reported upon the structure–activity relationship of nanocelluloses indicate that they do not pose as greater risk to human (and environment) health as other HARN currently being produced and potentially used in similar applications (e.g. CNTs). Until further results elucidate the potential of adverse health/environmental effects posed by nanocellulose, avoiding exposure with specialized personal protection gear and release is the best way for protection. Clarity must be obtained as to the health implications of low dose, chronic and repeated exposure to nanocellulose

in its many different forms, as this holds the key to their potential advantageous use across a multitude of disciplines and applications.

Abbreviations

ALI: air–liquid interface; BC: bacterial cellulose; CHO: Chinese Hamster Ovary cells; CNC: cellulose nanocrystal; CNF: cellulose nanofibril/fiber; CNT: carbon nanotube; CNW: cellulose nanowhisker; CSF: colony stimulating factor; FITC: fluorescein isothiocyanate; G-CSF: granulocyte-CSF; HARN: high aspect-ratio nanoparticles; HEK 293: human embryonic kidney cells; IL: interleukin; INF: interferon; KC: keratinocyte chemoattractant; LC₅₀: lethal concentration (indicating 50% loss in viability); LDH: lactate dehydrogenase; MCP: monocyte chemoattractant protein; MFC: microfibrillated cellulose; MIP: macrophage inflammatory protein; MTT: 3-(4,5-dimethylthiazol-2-yl)-2,5-diphenyltetrazolium bromide; NCC: nanocrystalline cellulose; NFC: nanofibrillated cellulose; PBMC: peripheral blood mononuclear cell; RBITC: rhodamine-B-isothiocyanate; Sf9: *Spodoptera frugiperda* ovary cells; SOD: superoxide dismutase; SVF: synthetic vitreous fibers; TNF: tumor necrosis factor.

Authors' contributions

CE and SCE reviewed the literature, drafted and wrote significant portions of the manuscript. CW and MJDC created the reviews' concept and edited the manuscript. All authors critically reviewed the manuscript. All authors read and approved the final manuscript.

Author details

¹ Adolphe Merkle Institute, University of Fribourg, Chemin des Verdiers 4, 1700 Fribourg, Switzerland. ² Australian Institute for Bioengineering and Nanotechnology (AIBN), Cnr College Rd & Cooper Rd, Building 75, Brisbane, QLD 4072, Australia. ³ Department of Materials Science and Engineering, Macromolecules Innovation Institute (MII), Virginia Polytechnic Institute and State University (Virginia Tech), 213 Holden Hall, 445 Old Turner Street, Blacksburg, VA, 24061, USA. ⁴ In Vitro Toxicology Group, Swansea University Medical School, Singleton Park Campus, Swansea SA2 8PP, Wales, UK.

Acknowledgements

The authors wish to thank the Swiss National Science Foundation, particularly the National Research Programme 64 (Project #406440_131264/1) and the Adolphe Merkle Foundation for financial support.

Competing interests

The authors declare no competing interests. The authors are entirely responsible for the content of the review of the opinions contained within it.

Received: 2 September 2016 Accepted: 18 November 2016

Published online: 01 December 2016

References

- Duncan TV. Applications of nanotechnology in food packaging and food safety: barrier materials, antimicrobials and sensors. *J Colloid Interface Sci.* 2011;363(1):1–24. doi:10.1016/j.jcis.2011.07.017.
- Hanus MJ, Harris AT. Nanotechnology innovations for the construction industry. *Prog Mater Sci.* 2013;58(7):1056–102. doi:10.1016/j.pmatsci.2013.04.001.
- Rao CNR, Cheetham AK. Science and technology of nanomaterials: current status and future prospects. *J Mater Chem.* 2001;11(12):2887–94. doi:10.1039/B105058N.
- Klemm D, Kramer F, Moritz S, Lindström T, Ankerfors M, Gray D, et al. Nanocelluloses: a new family of nature-based materials. *Angew Chem Int Ed.* 2011;50(24):5438–66. doi:10.1002/anie.201001273.
- Eichhorn SJ, Dufresne A, Aranguren M, Marcovich NE, Capadona JR, Rowan SJ, et al. Review: current international research into cellulose nanofibres and nanocomposites. *J Mater Sci.* 2010;45(1):1–33. doi:10.1007/s10853-009-3874-0.
- Jorfi M, Foster EJ. Recent advances in nanocellulose for biomedical applications. *J Appl Polymer Sci.* 2015;132(14):41719. doi:10.1002/app.41719.

7. Lin N, Dufresne A. Nanocellulose in biomedicine: current status and future prospect. *Eur Polymer J*. 2014;59:302–25. doi:10.1016/j.eurpolymj.2014.07.025.
8. Ranby BG. Aqueous colloidal solutions of cellulose micelles. *Acta Chem Scand*. 1949;3(5):649–50. doi:10.3891/acta.chem.scand.03-0649.
9. Capadona JR, Shanmuganathan K, Tyler DJ, Rowan SJ, Weder C. Stimuli-responsive polymer nanocomposites inspired by the sea cucumber dermis. *Science*. 2008;319(5868):1370–4. doi:10.1126/science.1153307.
10. Mueller S, Weder C, Foster EJ. Isolation of cellulose nanocrystals from pseudostems of banana plants. *RSC Advances*. 2014;4(2):907–15. doi:10.1039/c3ra46390g.
11. Petersen N, Gatenholm P. Bacterial cellulose-based materials and medical devices: current state and perspectives. *Appl Microbiol Biotechnol*. 2011;91(5):1277–86. doi:10.1007/s00253-011-3432-y.
12. Šturcová A, His I, Apperley DC, Sugiyama J, Jarvis MC. Structural details of crystalline cellulose from higher plants. *Biomacromolecules*. 2004;5(4):1333–9. doi:10.1021/bm034517p.
13. VanderHart DL, Atalla RH. Studies of microstructure in native celluloses using solid-state carbon-13 NMR. *Macromolecules*. 1984;17(8):1465–72. doi:10.1021/ma00138a009.
14. Poland CA, Duffin R, Kinloch I, Maynard A, Wallace WAH, Seaton A, et al. Carbon nanotubes introduced into the abdominal cavity of mice show asbestos-like pathogenicity in a pilot study. *Nat Nanotechnol*. 2008;3(7):423–8. doi:10.1038/nnano.2008.111.
15. Moon RJ, Martini A, Nairn J, Simonsen J, Youngblood J. Cellulose nanomaterials review: structure, properties and nanocomposites. *Chem Soc Rev*. 2011;40(7):3941–94. doi:10.1039/c0cs00108b.
16. Šturcová A, Davies GR, Eichhorn SJ. Elastic modulus and stress-transfer properties of tunicate cellulose whiskers. *Biomacromolecules*. 2005;6(2):1055–61. doi:10.1021/bm049291k.
17. De Souza Lima MM, Wong JT, Paillet M, Borsali R, Pecora R. Translational and rotational dynamics of rodlike cellulose whiskers. *Langmuir*. 2002;19(1):24–9. doi:10.1021/la020475z.
18. Araki J, Wada M, Kuga S, Okano T. Flow properties of microcrystalline cellulose suspension prepared by acid treatment of native cellulose. *Colloids Surf A Physicochem Eng Asp*. 1998;142(1):75–82. doi:10.1016/s0927-7757(98)00404-x.
19. Hua K, Carlsson DO, Alander E, Lindstrom T, Stromme M, Mhryanyan A, et al. Translational study between structure and biological response of nanocellulose from wood and green algae. *RSC Adv*. 2014;4(6):2892–903. doi:10.1039/c3ra45553j.
20. Habibi Y, Lucia LA, Rojas OJ. Cellulose Nanocrystals: chemistry, Self-Assembly, and Applications. *Chem Rev*. 2010;110(6):3479–500. doi:10.1021/cr900339v.
21. Henriksson M, Henriksson G, Berglund LA, Lindstrom T. An environmentally friendly method for enzyme-assisted preparation of microfibrillated cellulose (MFC) nanofibers. *Eur Polymer J*. 2007;43(8):3434–41. doi:10.1016/j.eurpolymj.2007.05.038.
22. Saito T, Kimura S, Nishiyama Y, Isogai A. Cellulose nanofibers prepared by TEMPO-mediated oxidation of native cellulose. *Biomacromolecules*. 2007;8(8):2485–91. doi:10.1021/bm0703970.
23. Isogai A, Saito T, Fukuzumi H. TEMPO-oxidized cellulose nanofibers. *Nanoscale*. 2011;3(1):71–85. doi:10.1039/C0NR00583E.
24. Dong XM, Revol JF, Gray DG. Effect of microcrystallite preparation conditions on the formation of colloid crystals of cellulose. *Cellulose*. 1998;5(1):19–32.
25. Camarero Espinosa S, Kuhnt T, Foster EJ, Weder C. Isolation of thermally stable cellulose nanocrystals by phosphoric acid hydrolysis. *Biomacromolecules*. 2013;14(4):1223–30. doi:10.1021/bm400219u.
26. Wang N, Ding E, Cheng R. Thermal degradation behaviors of spherical cellulose nanocrystals with sulfate groups. *Polymer*. 2007;48(12):3486–93. doi:10.1016/j.polymer.2007.03.062.
27. Roman M, Winter WT. Effect of sulfate groups from sulfuric acid hydrolysis on the thermal degradation behavior of bacterial cellulose. *Biomacromolecules*. 2004;5(5):1671–7. doi:10.1021/bm034519+.
28. Rambo CR, Recouvreur DOS, Carminatti CA, Pitlovancic AK, Antônio RV, Porto LM. Template assisted synthesis of porous nanofibrous cellulose membranes for tissue engineering. *Mater Sci Eng C*. 2008;28(4):549–54. doi:10.1016/j.msec.2007.11.011.
29. Klemm D, Schumann D, Uhardt U, Marsch S. Bacterial synthesized cellulose—artificial blood vessels for microsurgery. *Prog Polym Sci*. 2001;26(9):1561–603. doi:10.1016/s0079-6700(01)00021-1.
30. Tashiro K, Kobayashi M. Theoretical evaluation of 3-dimensional elastic-constants of native and regenerated celluloses—role of hydrogen-bonds. *Polymer*. 1991;32(8):1516–30. doi:10.1016/0032-3861(91)90435-l.
31. Meyer KH, Lotmar W. Sur l'élasticité de la cellulose. (Sur la constitution de la partie cristallisée de la cellulose IV). *Helv Chim Acta*. 1936;19(1):68–86. doi:10.1002/hlca.19360190110.
32. Favier V, Canova GR, Shrivastava SC, Cavaille JY. Mechanical percolation in cellulose whisker nanocomposites. *Polym Eng Sci*. 1997;37(10):1732–9. doi:10.1002/pen.11821.
33. Capadona JR, Van Den Berg O, Capadona LA, Schroeter M, Rowan SJ, Tyler DJ, et al. A versatile approach for the processing of polymer nanocomposites with self-assembled nanofibre templates. *Nat Nanotechnol*. 2007;2(12):765–9. doi:10.1038/nnano.2007.379.
34. Shanmuganathan K, Capadona JR, Rowan SJ, Weder C. Bio-inspired mechanically-adaptive nanocomposites derived from cotton cellulose whiskers. *J Mater Chem*. 2010;20(1):180–6. doi:10.1039/b916130a.
35. Sapkota J, Jorfi M, Weder C, Foster EJ. Reinforcing poly(ethylene) with cellulose nanocrystals. *Macromol Rapid Commun*. 2014;35(20):1747–53. doi:10.1002/marc.201400382.
36. Mueller S, Sapkota J, Nicharat A, Zimmermann T, Tingaut P, Weder C, et al. Influence of the nanofiber dimensions on the properties of nanocellulose/poly(vinyl alcohol) aerogels. *J Appl Polymer Sci*. 2015. doi:10.1002/app.41740.
37. Biyani MV, Foster EJ, Weder C. Light-healable supramolecular nanocomposites based on modified cellulose nanocrystals. *ACS Macro Lett*. 2013;2(3):236–40. doi:10.1021/mz400059w.
38. Annamalai PK, Dagnon KL, Monemian S, Foster EJ, Rowan SJ, Weder C. Water-responsive mechanically adaptive nanocomposites based on styrene-butadiene rubber and cellulose nanocrystals-processing matters. *ACS Appl Mater Interfaces*. 2014;6(2):967–76. doi:10.1021/am404382x.
39. Camarero-Espinosa S, Boday DJ, Weder C, Foster EJ. Cellulose nanocrystal driven crystallization of poly(D, L-lactide) and improvement of the thermomechanical properties. *J Appl Polym Sci*. 2015;132(10):41607. doi:10.1002/app.41607.
40. Pei A, Zhou Q, Berglund LA. Functionalized cellulose nanocrystals as biobased nucleation agents in poly(L-lactide) (PLLA)—crystallization and mechanical property effects. *Compos Sci Technol*. 2010;70(5):815–21. doi:10.1016/j.compscitech.2010.01.018.
41. Kuhnt T, Herrmann A, Benczedi D, Foster EJ, Weder C. Functionalized cellulose nanocrystals as nanocarriers for sustained fragrance release. *Polymer Chem*. 2015;6(36):6553–62. doi:10.1039/C5PY00944H.
42. Schyrr B, Pasche S, Voirin G, Weder C, Simon YC, Foster EJ. Biosensors based on porous cellulose nanocrystal-poly(vinyl alcohol) scaffolds. *ACS Appl Mater Interfaces*. 2014;6(15):12674–83. doi:10.1021/am502670u.
43. Muller FA, Muller L, Hofmann I, Greil P, Wenzel MM, Staudenmaier R. Cellulose-based scaffold materials for cartilage tissue engineering. *Biomaterials*. 2006;27(21):3955–63. doi:10.1016/j.biomaterials.2006.02.031.
44. Camarero-Espinosa S, Rothen-Rutishauser B, Foster EJ, Weder C. Articular cartilage: from formation to tissue engineering. *Biomater Sci*. 2016;4(5):734–67. doi:10.1039/C6BM00068A.
45. TAPPI. International nanocellulose standards-The need and purpose of standards for nanocellulosic materials. TAPPI: Norcross, 2011. <http://www.tappinano.org>. Accessed 29 Aug 2016.
46. http://cellulforce.com/en/product_plant.php. Accessed 29 Aug 2016.
47. ASPI. Domtar expands into nanotechnology. ASPI News. 2012;9(2):4–5.
48. Inventia. <http://www.tappi.org/Downloads/Conference-Papers/2011/2011-TAPPI-International-Conference-on-Nanotechnology-for-Renewable-Materials/11NANO44.aspx>.
49. Cowie J, Bilek EM, Wegner TH, Shatkin JA. Market projections of cellulose nanomaterial-enabled products—part 2: volume estimates. *TAPPI J*. 2014;13(6):57–69.
50. Shatkin JA, Wegner TH, Bilek EM, Cowie J. Market projections of cellulose nanomaterial-enabled products—part 1: applications. *TAPPI J*. 2014;13(5):9–16.
51. Roman M. Toxicity of cellulose nanocrystals: a review. *Ind Biotechnol*. 2015;11(1):25–33. doi:10.1089/ind.2014.0024.

52. Warheit DB, Reed KL, Webb TR. Man-made respirable-sized organic fibers: what do we know about their toxicological profiles? *Ind Health*. 2001;39(2):119–25. doi:10.2486/indhealth.39.119.
53. Camarero-Espinosa S, Endes C, Mueller S, Petri-Fink A, Rothen-Rutishauser B, Weder C, et al. Elucidating the potential biological impact of cellulose nanocrystals. *Fibers*. 2016;4(3):21.
54. Stone V, Miller MR, Clift MJD, Elder A, Mills NL, Moller P, et al. Nanomaterials vs ambient ultrafine particles: an opportunity to exchange toxicology knowledge. *Environ Health Perspect*. 2016. doi:10.1289/EHP424.
55. Poland CA, Duffin R, Kinloch I, Maynard A, Wallace WAH, Seaton A, et al. Carbon nanotubes introduced into the abdominal cavity of mice show asbestos-like pathogenicity in a pilot study. *Nat Nano*. 2008;3(7):423–8.
56. Donaldson K, Murphy FA, Duffin R, Poland CA. Asbestos, carbon nanotubes and the pleural mesothelium: a review of the hypothesis regarding the role of long fibre retention in the parietal pleura, inflammation and mesothelioma. *Particle Fibre Toxicol*. 2010;7:5.
57. Becklake MR. Asbestos-related diseases of lung and other organs—their epidemiology and implications for clinical practice. *Am Rev Respir Dis*. 1976;114(1):187–227.
58. Donaldson K, Tran CL. An introduction to the short-term toxicology of respirable industrial fibres. *Mutation Res Fundam Mol Mech Mutagen*. 2004;553(1–2):5–9. doi:10.1016/j.mrfmmm.2004.06.011.
59. Bernstein DM. Synthetic vitreous fibers: a review toxicology, epidemiology and regulations. *Crit Rev Toxicol*. 2007;37(10):839–86. doi:10.1080/10408440701524592.
60. Wick P, Clift MJD, Rösslein M, Rothen-Rutishauser B. A brief summary of carbon nanotubes science and technology: a health and safety perspective. *ChemSusChem*. 2011;4(7):905–11. doi:10.1002/cssc.201100161.
61. Donaldson K, Brown RC, Brown GM. New perspectives on basic mechanisms in lung disease. 5. Respirable industrial fibres: mechanisms of pathogenicity. *Thorax*. 1993;48(4):390–5. doi:10.1136/thx.48.4.390.
62. Furness G, Maitland HB. Studies on cotton dust in relation to byssinosis. 1. Bacteria and fungi in cotton dust. *Br J Ind Med*. 1952;9(2):138–45.
63. Niven RM, Pickering CAC. Byssinosis: a review. *Thorax*. 1996;51(6):632–7.
64. Pickering CAC, Niven R. Byssinosis and other cotton-related diseases. Hunter's diseases of occupations, 10th Edn. CRC Press, Taylor and Francis Group, Boca Raton. 2010.
65. Tatrai E, Adamis Z, Bohm U, Meretey K, Ungvary G. Role of cellulose in wood dust-induced fibrosing alveo-bronchiolitis in rat. *J Appl Toxicol*. 1995;15(1):45–8.
66. Warheit DB, Snajdr SI, Harstsky MA, Frame SR. Advances in the prevention of occupational respiratory diseases. International Congress Series, Amsterdam: Elsevier Science; 1998. p. 579–89.
67. Davis JMG. The need for standardized testing procedures for all products capable of liberating respirable fibers—the example of materials based on cellulose. *Br J Ind Med*. 1993;50(2):187–90.
68. Stefaniak AB, Seehra MS, Fix NR, Leonard SS. Lung biodegradability and free radical production of cellulose nanomaterials. *Inhal Toxicol*. 2014;26(12):733–49. doi:10.3109/08958378.2014.948650.
69. Muhle H, Ernst H, Bellmann B. Investigation of the durability of cellulose fibres in rat lungs. *Ann Occup Hyg*. 1997;41(Supplement 1):184–8.
70. Shatkin JA, Kim B. Cellulose nanomaterials: life cycle risk assessment, and environmental health and safety roadmap. *Environ Sci Nano*. 2015;5(2):477–99.
71. Köhler AR, Som C, Helland A, Gottschalk F. Studying the potential release of carbon nanotubes throughout the application life cycle. *J Clean Prod*. 2008;16(8–9):927–37. doi:10.1016/j.jclepro.2007.04.007.
72. Albanese A, Tang PS, Chan WCW. The Effect of nanoparticle size, shape, and surface chemistry on biological systems. In: Yarmush ML, editor. Annual review of biomedical engineering, vol 14. Annual Review of Biomedical Engineering; 2012. p. 1–16.
73. Clift MJD, Rothen-Rutishauser B, Brown DM, Duffin R, Donaldson K, Proudfoot L, et al. The impact of different nanoparticle surface chemistry and size on uptake and toxicity in a murine macrophage cell line. *Toxicol Appl Pharmacol*. 2008;232(3):418–27. doi:10.1016/j.taap.2008.06.009.
74. Donaldson K, Schinwald A, Murphy F, Cho W-S, Duffin R, Lang T, et al. The biologically effective dose in inhalation nanotoxicology. *Acc Chem Res*. 2013;46(3):723–32. doi:10.1021/ar300092y.
75. Vartiainen J, Pohler T, Sirola K, Pylkkanen L, Alenius H, Hokkinen J, et al. Health and environmental safety aspects of friction grinding and spray drying of microfibrillated cellulose. *Cellulose*. 2011;18(3):775–86. doi:10.1007/s10570-011-9501-7.
76. Kovacs T, Naish V, O'Connor B, Blaise C, Gagne F, Hall L, et al. An ecotoxicological characterization of nanocrystalline cellulose (NCC). *Nanotoxicology*. 2010;4(3):255–70. doi:10.3109/17435391003628713.
77. Male KB, Leung ACW, Montes J, Kamen A, Luong JHT. Probing inhibitory effects of nanocrystalline cellulose: inhibition versus surface charge. *Nanoscale*. 2012;4(4):1373–9. doi:10.1039/c2nr11886f.
78. Dong S, Hirani AA, Colacino KR, Lee YW, Roman M. Cytotoxicity and cellular uptake of cellulose nanocrystals. *Nano LIFE*. 2012;02(03):1241006. doi:10.1142/S1793984412410061.
79. Endes C, Mueller S, Kinnear C, Vanhecke D, Foster EJ, Petri-Fink A, et al. Fate of cellulose nanocrystal aerosols deposited on the lung cell surface in vitro. *Biomacromolecules*. 2015;16(4):1267–75. doi:10.1021/acs.biomac.5b00055.
80. Endes C, Schmid O, Kinnear C, Mueller S, Camarero-Espinosa S, Vanhecke D, et al. An in vitro testing strategy towards mimicking the inhalation of high aspect ratio nanoparticles. *Particle Fibre Toxicol*. 2014;11(1):40.
81. Jeong SI, Lee SE, Yang H, Jin YH, Park CS, Park YS. Toxicologic evaluation of bacterial synthesized cellulose in endothelial cells and animals. *Mol Cell Toxicol*. 2010;6(4):373–80. doi:10.1007/s13273-010-0049-7.
82. Moreira S, Silva NB, Almeida-Lima J, Oliveira Rocha HA, Batistuzzo Medeiros SR, Alves C Jr, et al. BC nanofibres: in vitro study of genotoxicity and cell proliferation. *Toxicol Lett*. 2009;189(3):235–41. doi:10.1016/j.toxlet.2009.06.849.
83. Mahmoud KA, Mena JA, Male KB, Hrapovic S, Kamen A, Luong JHT. Effect of surface charge on the cellular uptake and cytotoxicity of fluorescent labeled cellulose nanocrystals. *ACS Appl Mater Interfaces*. 2010;2(10):2924–32. doi:10.1021/am100622z.
84. Pereira M, Mouton L, Yepremian C, Couto A, Lo J, Marconcini J, et al. Ecotoxicological effects of carbon nanotubes and cellulose nanofibers in *Chlorella vulgaris*. *J Nanobiotechnol*. 2014;12(1):15.
85. Catalan J, Ilves M, Jarventaus H, Hannukainen KS, Kontturi E, Vanhala E, et al. Genotoxic and immunotoxic effects of cellulose nanocrystals in vitro. *Environ Mol Mutagen*. 2014;56(2):171–82.
86. Hanif Z, Ahmed FR, Shin SW, Kim Y-K, Um SH. Size- and dose-dependent toxicity of cellulose nanocrystals (CNC) on human fibroblasts and colon adenocarcinoma. *Colloids Surf B Biointerfaces*. 2014;119:162–5. doi:10.1016/j.colsurfb.2014.04.018.
87. de Lima R, Feitosa LO, Maruyama CR, Barga MA, Yamawaki PC, Vieira LJ, et al. Evaluation of the genotoxicity of cellulose nanofibers. *Int J Nanomed*. 2012;7:3555–65. doi:10.2147/ijn.s30596.
88. Pereira MM, Raposo NRB, Brayner R, Teixeira EM, Oliveira V, Quintao CCR, et al. Cytotoxicity and expression of genes involved in the cellular stress response and apoptosis in mammalian fibroblast exposed to cotton cellulose nanofibers. *Nanotechnology*. 2013;24(7):075103.
89. Colic M, Mihajlovic D, Mathew A, Naseri N, Kokol V. Cytocompatibility and immunomodulatory properties of wood based nanofibrillated cellulose. *Cellulose*. 2015;22(1):763–78. doi:10.1007/s10570-014-0524-8.
90. Yanamala N, Farcas MT, Hatfield MK, Kisin ER, Kagan VE, Geraci CL, et al. In vivo evaluation of the pulmonary toxicity of cellulose nanocrystals: a renewable and sustainable nanomaterial of the future. *ACS Sustain Chem Eng*. 2014;2(7):1691–8. doi:10.1021/sc500153k.
91. Clift MJD, Foster EJ, Vanhecke D, Studer D, Wick P, Gehr P, et al. Investigating the interaction of cellulose nanofibers derived from cotton with a sophisticated 3D human lung cell coculture. *Biomacromolecules*. 2011;12(10):3666–73. doi:10.1021/bm200865j.
92. Catalan J, Ilves M, Jarventaus H, Hannukainen K-S, Kontturi E, Vanhala E, et al. Genotoxic and immunotoxic effects of cellulose nanocrystals in vitro. *Environ Mol Mutagen*. 2015;56(2):171–82. doi:10.1002/em.21913.
93. Hannukainen KS, Suhonen S, Savolainen K, Norppa H. Genotoxicity of nanofibrillated cellulose in vitro as measured by enzyme comet assay. *Toxicol Lett*. 2012;211:571. doi:10.1016/j.toxlet.2012.03.276.

- 94 Shvedova AA, Kisin ER, Yanamala N, Farcas MT, Menas AL, Williams A, Fournier PM, Reynolds JS, Gutkin DW, Star A, Reiner RS, Halappanavar S, Kagan VE. Gender differences in murine pulmonary responses elicited by cellulose nanocrystals. *Part Fibre Toxicol*. 2016;13(1):28. doi:[10.1186/s12989-016-0140-x](https://doi.org/10.1186/s12989-016-0140-x).
- 95 Farcas MT, Kisin ER, Menas AL, Gutkin DW, Star A, Reiner RS, Yanamala N, Savolainen K, Shvedova AA. Pulmonary exposure to cellulose nanocrystals caused deleterious effects to reproductive system in male mice. *J Toxicol Environ Health A*. 2016;24:1–14.
- 96 Sacui IA, Nieuwendaal RC, Burnett DJ, Stranick SJ, Jorfi M, Weder C, et al. Comparison of the properties of cellulose nanocrystals and cellulose nanofibrils isolated from bacteria, tunicate, and wood processed using acid, enzymatic, mechanical, and oxidative methods. *ACS Appl Mater Interfaces*. 2014;6(9):6127–38. doi:[10.1021/am500359f](https://doi.org/10.1021/am500359f).

Submit your next manuscript to BioMed Central
and we will help you at every step:

- We accept pre-submission inquiries
- Our selector tool helps you to find the most relevant journal
- We provide round the clock customer support
- Convenient online submission
- Thorough peer review
- Inclusion in PubMed and all major indexing services
- Maximum visibility for your research

Submit your manuscript at
www.biomedcentral.com/submit



REVIEW

Open Access



Interaction of biomedical nanoparticles with the pulmonary immune system

Fabian Blank^{1*}, Kleanthis Fytianos², Emilie Seydoux¹, Laura Rodriguez-Lorenzo², Alke Petri-Fink^{2,3}, Christophe von Garnier¹ and Barbara Rothen-Rutishauser²

Abstract

Engineered nanoparticles (NPs) offer site-specific delivery, deposition and cellular uptake due to their unique physicochemical properties and were shown to modulate immune responses. The respiratory tract with its vast surface area is an attractive target organ for innovative immunomodulatory therapeutic applications by pulmonary administration of such NPs, enabling interactions with resident antigen-presenting cells (APCs), such as dendritic cells and macrophages. Depending on the respiratory tract compartment, e.g. conducting airways, lung parenchyma, or lung draining lymph nodes, APCs extensively vary in their number, morphology, phenotype, and function. Unique characteristics and plasticity render APC populations ideal targets for inhaled specific immunomodulators. Modulation of immune responses may operate in different steps of the immune cell-antigen interaction, i.e. antigen uptake, trafficking, processing, and presentation to T cells. Meticulous analysis of the immunomodulatory potential, as well as pharmacologic and biocompatibility testing of inhalable NPs is required to develop novel strategies for the treatment of respiratory disorders such as allergic asthma. The safe-by-design and characterization of such NPs requires well coordinated interdisciplinary research uniting engineers, chemists biologists and respiratory physicians. In this review we will focus on in vivo data available to facilitate the design of nanocarrier-based strategies using NPs to modulate pulmonary immune responses.

Keywords: Biomedical nanoparticles, Immune-modulation, Specific targeting, Pulmonary antigen presenting cells, In vivo models

Background

The human respiratory tract provides a vast epithelial surface area for air conduction and gas-exchange with a combined surface area that is about 150 m². In particular, the gas exchange region provides the major part of surface, where the structural barrier between air and blood is reduced to a mean arithmetic thickness of 2.2 µm or thinner tissue layers in the alveoli [1]. The vast surface and direct contact with environment makes lung the most important portal of entry for inhaled xenobiotics such as particulate matter (reviewed in [2]). This has raised concerns that particles may cause respiratory disease or trigger adverse effects as seen with ambient

combustion-derived particles recognized as an important cause of cardiovascular morbidity and mortality in areas with air pollution [3–5]. On the other hand, the unique lung characteristics render this organ ideal for novel biomedical applications by inhalation of specifically designed nanomaterials [6]. Nano-sized carriers [e.g. mainly nanoparticles (NPs) with all three dimensions below 100 nm (ISO/TS, 2008)] have been proposed as promising novel diagnostic, therapeutic, and vaccination approaches for a variety of human diseases [7–9].

Drug delivery through the pulmonary route offers several advantages over oral or parenteral delivery. This is primarily due to the presence of a dense vasculature, the circumvention of the first pass effect, and a lower concentration of drug-metabolizing enzymes in the lung combined with the highly dispersed nature of an aerosol [10, 11]. Furthermore, size-dependent deposition and size-dependent uptake by specific immune cell subsets (as

*Correspondence: fabian.blank@dkf.unibe.ch

¹ Respiratory Medicine, Bern University Hospital, University of Bern, Murtenstrasse 50, 3008 Bern, Switzerland

Full list of author information is available at the end of the article

discussed later) in the pulmonary compartment may lead to modulation specific downstream immune responses with reduced side-effects due to targeted delivery by NPs. Novel NPs may be employed to deliver drugs or may act as immunomodulators, either on the entire lung surface or by targeting a particular cell population localized in a specific compartment of the respiratory tract. Knowledge about the anatomical compartments in the respiratory tract and resident cells is a prerequisite to understand the interplay between APCs and inhalable NPs. In addition, each NP type requires thorough characterization and testing *in vitro*, before being considered for animal experimentation and clinical applications. Characterization begins during and immediately after synthesis of NPs to monitor physicochemical properties, size, shape and stability. In a subsequent step, cell-free assays can be employed to investigate how particles interact with constituents of biological solutions, such as free proteins and enzymes [12, 13]. Mechanisms of particle-cell interaction and cytotoxicity are investigated by *in vitro* experiments using either cell mono-cultures or more advanced and complex 3D co-culture systems that simulate specific human organs or organ compartments [13]. To study effects of NPs on the entire organism, *in vivo* animal models are necessary in species that represent appropriate models for the human anatomy, physiology, and immunology as closely as possible. Extensive short, intermediate and longterm *in vivo* characterization of both unwanted biological effects and efficacy of particle are a prerequisite before clinical testing can be performed. Such a cascade of characterization of biocompatibility and immunogenicity on multiple levels of increasing complexity will allow the development of NPs of acceptable safety and accurately defined effects regarding targeting, interplay with target cells/tissues and persistence. In particular safety regarding toxicological and immunomodulatory effects of newly developed biomedical NPs should be of major concern.

In this review we will summarize the anatomy of the respiratory tract regarding the different immune cell subsets which are populating its diverse compartments. Furthermore, we will focus on recently emerged *in vivo* models to monitor the immunomodulatory potential of biomedical NPs while discussing characteristics of potential biomedical NPs, which are important in order to modulate immune responses in the lung.

General anatomy of the respiratory tract

As previously outlined, the lung provides an attractive portal of entry in the human body for non-invasive applications using biomedical NPs. Detailed knowledge on the macroscopic structure of the lung anatomy, i.e. different compartments; and in particular the distribution and

function of immune cells within different compartments of the respiratory tract is crucial to develop and engineer specific inhalable NPs. The human respiratory tract is structurally designed for gas exchange in the human body through a huge internal surface area of about 150 m² (i.e. alveoli and airways) closely enmeshed with a dense capillary network [1]. The respiratory tract is anatomically subdivided into four regions: (1) the extra thoracic region comprising the anterior nose and the posterior nasal passages, larynx, pharynx and mouth; (2) the bronchial region consisting of the trachea and bronchi; (3) the bronchiolar region consisting of bronchioles and terminal bronchioles; and finally (4) the alveolar-interstitial region consisting of respiratory bronchioles (bronchioles with some alveoli apposed), the alveolar ducts and sacs with their alveoli and the interstitial connective tissue, inside the interalveolar septa.

The epithelial tissue changes its architectural and cellular characteristics from the upper airway to the periphery. Beginning at the trachea/bronchi, the airway epithelium is pseudostratified with ciliated epithelial cells, i.e. mucociliary escalator, and at the level of smaller bronchioles it is of cuboidal appearance. Toward the lung periphery, the alveoli are lined by squamous cells, the alveolar type I epithelial cells which cover about 95% of the surface and share a basement membrane with the endothelial cells covering the pulmonary capillaries, and also contain alveolar type II epithelial cells, which secrete lung surfactant (surface active agent) to prevent alveolar collapse [14, 15]. The structural barrier between air and blood is reduced to a mean arithmetic thickness of 2.2 µm or thinner tissue layers in the alveoli [1]. More than 40 different cell types, amongst others different types of epithelial cells, endothelial cells, fibroblasts, nerve cells, lymphoid cells, gland cells, dendritic cells and macrophages, add to the complexity of the epithelium in the lung. All four regions in the respiratory tract contain lymphatic tissue or specific components of it [14].

There are approximately 400 million alveoli in the lungs [16], with a combined surface area that is about 140 m² and with an alveolar epithelium which can be as thin as 0.1 µm [1, 15]. The interstitium of the alveolar septum is for most parts extremely thin and endothelial cells, which cover the inner surface of the capillaries, fuse with basement membranes of epithelial cells to minimize the air-blood barrier. At the thicker parts, where the basement membranes of endothelial and epithelial cells are separated, elastic fibers, collagen fibrils bundles as well as fibroblasts are present in the extracellular matrix. This large surface area, combined with an extremely thin barrier between the pulmonary lumen and the capillaries, creates conditions that are well suited for efficient gas transfer [14].

Lung barriers and particle clearance

A series of structural and functional barriers protect the respiratory system against both harmful and innocuous xenobiotics [17]. The airway mucosa, with its respiratory epithelium sealed by apically localized tight junction complexes, provides a mechanical barrier that protects against effects of inhaled and on the lung cell surface deposited xenobiotics. Furthermore, ciliated epithelial cells and mucus producing goblet cells, together with locally produced secreted immunoglobulins (mainly IgA), provide effective mechanisms for mucociliary clearance of inhaled particulate antigens [18]. In addition, airway epithelial cells have key roles in the regulation of lung homeostasis by secretion of a range of regulatory and effector molecules (e.g. mucins, surfactant proteins, complement and complement cleavage products, antimicrobial peptides) that are involved in front-line defence against pathogens [19].

The clearance kinetics in the lung periphery is much slower due to the absence of mucociliary action, and particles are eliminated by (1) phagocytosis with subsequent transport by macrophages, (2) dendritic cells with trafficking to draining lymph nodes, as well as (3) direct translocation via the air-blood tissue barrier into the circulation. All these mechanisms by which the particles are eliminated from the inner surface of the respiratory tract have to be taken into account for the design of new NPs [20].

The immune system in the respiratory tract

APCs such as alveolar and interstitial macrophages, as well as dendritic cells (DCs) (Fig. 1), play an important role in the regulation of the immune response.

Respiratory tract macrophages play an important role in the maintenance of immunological homeostasis and host defense. In the lungs the key population is composed of alveolar macrophages. Under steady state conditions, the most important function of alveolar macrophages is phagocytosis and sequestration of antigen from the immune system to shield local tissues from the development of specific immune responses [21]. Alveolar macrophages have been shown to take up most of the particulate material that is delivered intranasally [22]. Since alveolar macrophages do not migrate to the lung draining lymph nodes [23], their antigen presentation capabilities are limited to interact with local effector T cells only, in contrast to pulmonary dendritic cells which, as professional antigen presenting cells, migrate to the lymph nodes in order to activate naive T cells and to direct their differentiation into effector T cells, as described later. Besides clearance of inhaled particulates, macrophages are involved in diverse functions that are achieved by the plasticity of these cells that, depending on signals

present in their microenvironment, can polarize into a plethora of different phenotypes [24, 25]. Cytokines, such as interferon (IFN)- γ and tumor necrosis factor (TNF)- α , or bacterial products, such as lipopolysaccharide (LPS), induce polarization of macrophages into a proinflammatory phenotype through the transcription factor IFN regulatory factor 5 (IRF5). Such macrophages were conventionally named M1-dominant macrophages and release proinflammatory cytokines interleukin (IL)-12, IL-1 β , and TNF- α . They are thus important in host defense against intracellular pathogens [24, 26]. Furthermore, macrophages induced by the proallergic asthma cytokines IL-4 and IL-13, in the past conventionally also known as M2 macrophages that are important in wound healing and host defense against helminth infections. This macrophage subset is characterized by upregulation of the mannose receptor (CD206) and, in mice, production of the chitinase-like protein YM1. However, recent literature has challenged the existence of an M1 and M2 paradigm of macrophage activation and proposed a more complex system of macrophage polarization [27]. Another macrophage phenotype consists of anti-inflammatory macrophages that are induced by compounds and mediators such as corticosteroids, IL-10, or prostaglandin E₂ PGE₂. Such anti-inflammatory macrophages are also characterized by upregulation of CD206, but produce the anti-inflammatory cytokine IL-10 [28].

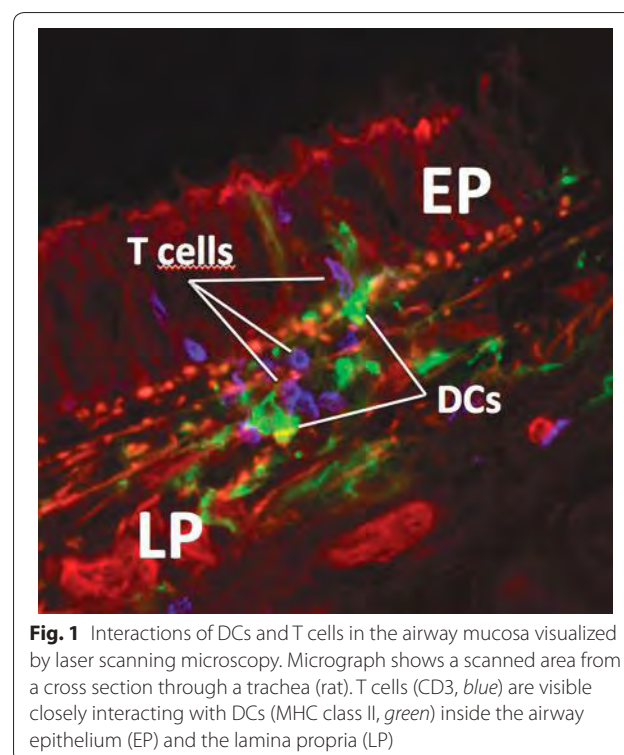


Fig. 1 Interactions of DCs and T cells in the airway mucosa visualized by laser scanning microscopy. Micrograph shows a scanned area from a cross section through a trachea (rat). T cells (CD3, blue) are visible closely interacting with DCs (MHC class II, green) inside the airway epithelium (EP) and the lamina propria (LP)

The mucosa of the airways and the lung parenchyma also contains dense networks of DCs that develop early in life [29]. DCs are professional APCs that link innate and adaptive immunity, and therefore occupy a key role in regulating the body's immune responses [30]. They are strategically positioned for antigen uptake both within and directly below the surface epithelium and extend protrusions into the airway lumen [31], or the alveolar space [32] similar to what has been demonstrated for DCs in intestinal tissue where DCs have been shown to form tight junction complexes with epithelial cells [33]. This characteristic suggests that DCs can sample directly, both from the airway lumen and the alveolar space [32] through the intact epithelium [31] by the expression of adherens and tight junction proteins which might help to preserve the epithelial integrity in a trans-epithelial network [34]. Morphologically characterized by dendrite-like projections DCs are the most potent APC population able to provide T cell activation (Fig. 1) [35].

Potential pathogens are 'sensed' through pattern recognition receptors (PRRs) that interact with pathogen associated molecular patterns (PAMPs), triggering innate and adaptive immunity [36]. In DCs, activation through the PRRs leads to upregulation of the chemokine receptor CCR7 (CD197; the ligand is CCL19/ECL) that is essential for DC migration from the site of pathogen encounter to lymph nodes, where activation of naive T cells occurs. In this process of trafficking to the lymph nodes DCs differentiate from a so-called 'immature' state (high capacity for antigen uptake, low capacity for T cell activation) to a 'mature' state (low capacity for antigen uptake, high capacity for T-cell activation) [37]. Following migration to lymph nodes, DCs face their most important task: that is to instruct T cells to respond to presented antigen in the most appropriate way. The type and activation state of the DC, the dose of antigen, as well as the nature of concomitant micro-environmental factors present at the time of antigen encounter determine the nature of the resulting T cell response [37]. Conventionally, three different outcomes for effector T cells have been distinguished: T helper 1 (Th1), T helper 2 (Th2) and regulatory T cells (Treg). A Th1 response is characterized by the production of IFN- γ and TNF by T cells. It is the normal outcome after an exposure of DCs to viruses or bacteria. It is also the basis of the delayed type hypersensitivity reaction. Th2 differentiation usually occurs following contact with extracellular parasites and involves the production of cytokines IL-4, IL-5, IL-9, and IL-13 resulting in IgE production and accumulation of eosinophils and mast cells. Furthermore, in allergic asthma, as nonpathogenic environmental antigens are able to induce an inappropriate Th2 response and become allergens, such as the house dust mite allergen Der p1. The third outcome is the

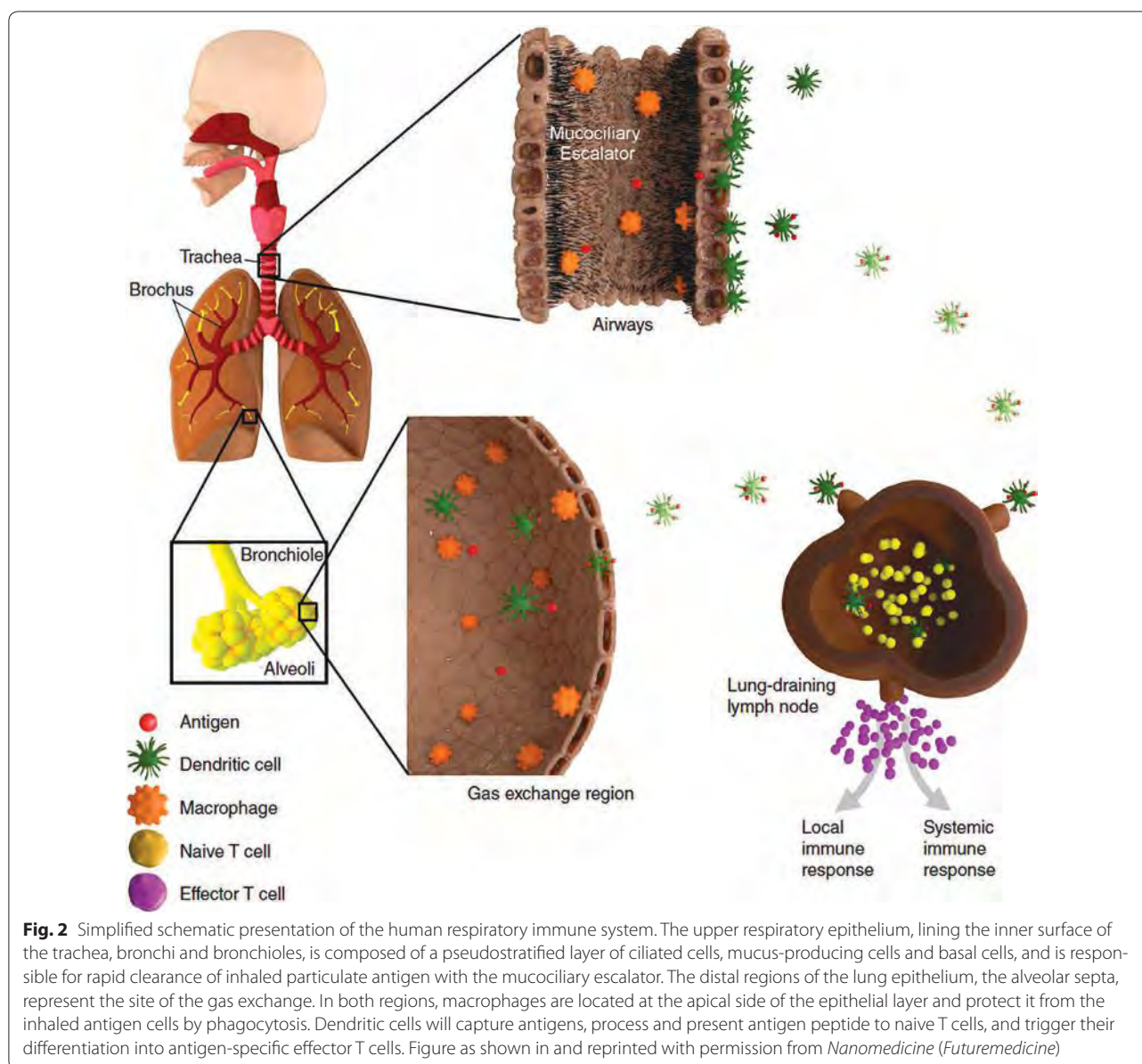
induction of regulatory T cells that produce immunosuppressive cytokines such as IL-10 or TGF- β . This describes probably the most prevalent response in steady-state conditions, as it forms a constant safeguard against the induction of inappropriate inflammatory reactions to harmless antigen [37]. It has become increasingly evident that T cell functions are considerably more complex and heterogeneous than originally assumed. In particular, the potential key role of Th17 cells in disease pathogenesis has been described. As an example, some asthma patients have been described to develop a more type 17 associated disease with dominance of neutrophils rather than eosinophils [38]. An additional conceptual development has emerged with the role of airway epithelial cells in driving the selection of disease-related T cell phenotypes through the expression of potent T cell modulatory molecules (discussed in [19]).

T cells are also found in varying numbers in the airways and the lung parenchyma. In the airways they are found intraepithelially and within the underlying lamina propria. As in the gut, most intraepithelial T cells express CD8, whereas CD4⁺ T cells are more frequently localized the lamina propria. Both subsets mainly have an effector- and/or memory-cell phenotype [19]. Both in vitro and in vivo studies have shown that T cell proliferation upon NP treatment can be affected [8, 22, 39–41]. T cells are thus promising targets for future therapies using biomedical NPs.

The lamina propria of the airways also contains mast cells and plasma cells (mainly producing polymeric IgA) and some loosely distributed B cells. Aside from their central role in antibody production, it is possible that B cells also contribute to local antigen presentation, given the recent demonstration of such a function for B cells in the lymph nodes that drain the lungs [42]. Figure 2 shows a simplified illustration of the innate and adaptive immune response in the respiratory tract.

Particle deposition in different lung compartments

According to the particle size, it can be predicted in which compartment particles will be predominantly deposit in the lung [10, 43]. Larger particles (1–10 μm) preferentially deposit in trachea and bronchi, whereas smaller particles (i.e. NPs) tend to deposit in the deeper regions of the lung (i.e. small airways and alveoli). Inhaled particles may be deposited in the lung by impaction, sedimentation and diffusion as described in detail in [44]. While impaction is generally observed with particles greater than 5 μm , sedimentation is seen with particles with sufficient mass and a size of 1–5 μm in diameter. Finally diffusion is observed mainly with the smallest particles (Table 1). Therefore, solely depending on the size of particles or aerosol droplets, different compartments of the respiratory tract and specific



subpopulations of immune cells may be targeted. In addition a recent study has shown that depending on size and charge particles deposited on the respiratory mucus are either locally trapped or can diffuse freely [45].

A large number of different studies in the recent years has also demonstrated that characteristics of NPs like size, shape, surface charge, and surface modification all play an important role in affecting the fate of the particles in the respiratory tract with particle size, surface charge and surface modification being among the most important. Deposition in the respiratory tract depends, however, mainly on particle size due to the fact that different mechanisms of particle deposition are defined based on this characteristic.

Based on size-dependent pulmonary deposition NPs can be used to primarily target distal lung compartments for prolonged persistence, since in these anatomical areas there is only slow removal by alveolar macrophages compared to the proximal lung compartments like the conducting airways. Prolonged persistence allows NPs to interact with cells of interest for a longer time in order to become effective locally by remaining in the lung compartment or systemically by crossing the air-blood barrier. In particular the interaction of NPs with pulmonary immune cells is of great interest, since NPs can be easily applied in the lungs and immediately get in contact with different cells of the immune system after deposition. A number of recent studies has characterized how inhaled

Table 1 Correlation between compartments of lung deposition, the mechanism of deposition and particle size

Location	Size (μm)	Mechanism
Primary bronchi	5–10	Impaction
Secondary bronchi	1–5	Sedimentation
Bronchioles	1–3	Sedimentation
Alveoli	0.5–1	Brownian motion

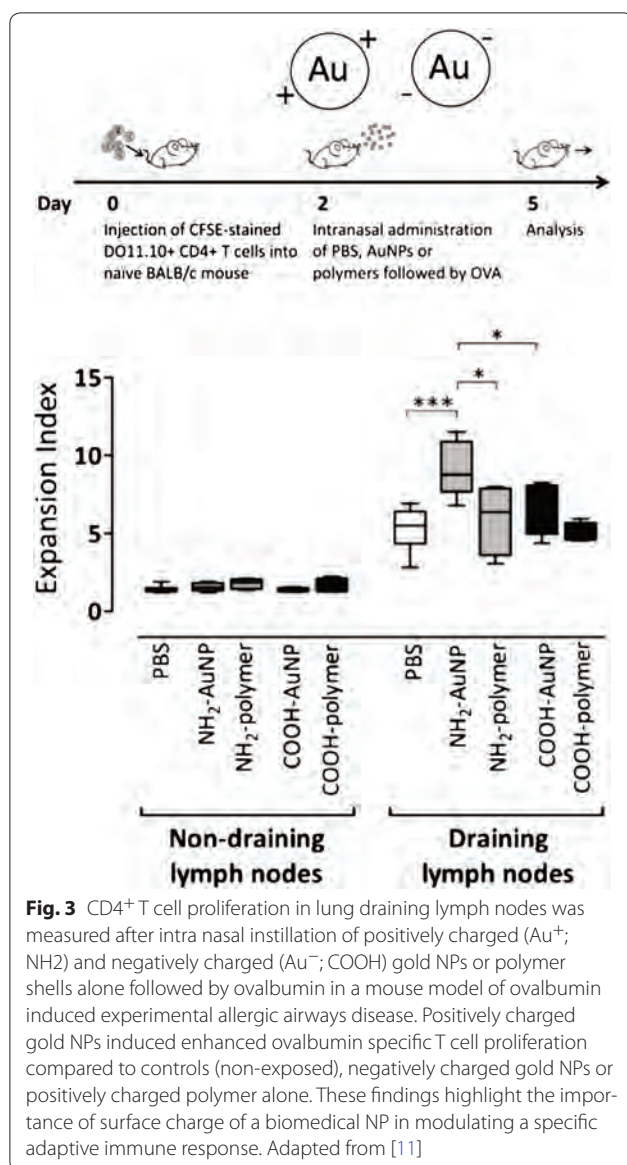
NPs affect immune cells in the lung and provide valuable information for the development of novel biomedical tools for pulmonary delivery.

Immunomodulatory potential of NPs in in vivo models

The highly complex organization of the pulmonary immune system characterised by a multitude of cell–cell interactions across different respiratory tract compartments, highlights the essential requirement to investigate the fate and effects of inhalable biomedical NPs. Hence in vivo models are a crucial step in the optimization of potential biomedical NPs following initial development through in vitro investigations [13] before clinical studies can be considered. In the following paragraph promising nanocarriers and treatment strategies, which have been tested in in vivo models, i.e. mainly rodents, are discussed and compared.

Screening for NP characteristics relevant for translocation in the respiratory tract, Choi et al. utilized different NPs by varying material, size, shape, as well as surface charge, and correlated these properties with translocation in the body and adverse health effects, after lung instillation in rat models [46]. Briefly, administration of non-cationic NPs with a size of approximately 30 nm or smaller resulted in a maximal translocation to mediastinal lymph nodes and the bloodstream due to insufficient clearance. The authors suggested to employ chemical modifications to adapt size and the charge of NPs, so the adverse health effects may be minimized. Focusing on particle size, we employed in a recently reported in vivo study polystyrene (PS) NPs intra-nasally in mice, and demonstrated size-dependent uptake, trafficking, and modulation of downstream immune responses [22]. Compared to larger NPs, those with a diameter of 20–50 nm were preferentially captured and trafficked by pulmonary DCs to lung draining lymph nodes, while very low or no lymphatic drainage was observed with any other particle size. In particular, 20 nm PS NPs co-administered together with the model antigen ovalbumin (OVA) induced significantly enhanced activation of antigen-specific T cells, compared to results obtained with larger 1000 nm particles [22]. In contrast, a similar study done by Hardy and co-workers showed

a prophylactic inhibitory effect of 50 nm neutral amino acid glycine (PS50G) NPs: Intratracheally instilled PS50G NPs did not exacerbate but instead inhibited key features of allergic airway inflammation including lung airway and parenchymal inflammation, airway epithelial mucus production, and serum allergen-specific IgE and allergen-specific Th2 cytokines in the lung-draining lymph node after allergen challenge 1 month later. Furthermore, PS50G NPs themselves did not induce any inflammatory response or oxidative stress in the lungs. Finally, PS50G NPs suppressed the ability of CD11b^{hi} DCs in the draining lymph nodes of allergen-challenged mice to induce proliferation of OVA-specific CD4⁺ T cells [41]. A follow-up study of the same group using the same PS50G (50 nm) and larger PS500G (500 nm) nanoparticles, investigated the uptake by antigen presenting cell populations in the lung parenchyma and the lung draining lymph nodes following intra-tracheal instillation in naive mice. It was found that PS50G were preferentially taken up by alveolar and non-alveolar macrophages, B cells, and CD11b⁺ and CD103⁺ DC in the lung. However, in the lung draining lymph nodes, only DCs were found to contain particles, demonstrating transport of NPs to the lymph nodes exclusively by DCs. Consistent with our findings, this study excluded particle translocation via lymphatic drainage. However, both particle sizes decreased frequencies of stimulatory allergen-laden DC in the lung draining lymph nodes, with the smaller particles having the more pronounced effect. The authors from these studies concluded that in allergic airway inflammation PS50G but not PS500G significantly inhibited adaptive allergen-specific immunity [47]. Another study with results similar to our findings investigated the trafficking of intranasal instilled 500 nm PS beads from the respiratory tract to the mediastinal lymph nodes, in which the majority of particles was captured by alveolar macrophages, but particles were also detected in a small number of DCs that had migrated to the T cell-rich areas of the mediastinal lymph nodes [23]. Additional studies have shown that polylactid-co-Glycolid (PLGA) NPs (approximately 200 nm) and dendrimers (<10 nm) may be functionalized with siRNA or drugs while surface charge can be controlled during synthesis of NPs [48–50]. Focusing on pulmonary deposition following inhalation, Taratula et al. [51] successfully delivered a high concentration of inhalable lipid-NP-based drug to the respiratory tract of mice. In this study, pulmonary deposition was more efficient compared to intravenous injection of the same drug, in terms of organ distribution, lung tumor targeting, and anti-cancer activity. These studies demonstrate a significant effect of particle size in the modulation of innate and adaptive immune responses in the respiratory tract. Particle size has therefore to be



taken in consideration for the development of biomedical carriers for the use in pulmonary applications.

As already discussed above, not only particle size but also surface charge of an engineered NP may affect pulmonary immune cells and modulate downstream immune responses. In order to address how surface charge of a pulmonary administered NP may affect its fate and modulate a specific immune response, we employed modified gold NPs (AuNPs) (Fig. 3). The AuNPs were coated with polyvinyl alcohol (PVA) containing either positively (NH₂) or negatively (COOH) charged functional groups [52]. Following intra-nasal instillation in a mouse model, all pulmonary APC subsets preferentially took up positively charged AuNPs, compared to negatively charged AuNPs. Also, positively

charged AuNPs generated an enhanced ovalbumin-specific CD4⁺ T cell stimulation in lung draining lymph nodes compared to negatively charged AuNPs. An additional salient finding in this study was that intact positively charged AuNPs were necessary, as immune responses were not affected when the positively charged polymer was utilized alone. Another recent study also demonstrated improved therapeutic effects of a particulate biomedical carrier compared to its soluble counterpart: In this study solid lipid nanoparticles (SLNs) of Yuxingcao essential oil (YEO) with different particle size (200, 400 and 800 nm) were prepared using Compritol 888 ATO as lipid and polyvinyl alcohol as an emulsifier. Following intra-tracheal administration in rats, YEO loaded SLNs not only prolonged pulmonary retention up to 24 h, but also increased area under the curve values (15.4, 18.2 and 26.3 µg/g h for SLN-200, SLN-400 and SLN-800, respectively) by 4.5–7.7 folds compared to the intra-tracheal dosed YEO solution and by 257–438 folds to the intravenously dosed YEO solution, respectively. These results demonstrated a promising inhalable particulate carrier with improved local bioavailability [53]. Furthermore, a similar study showing effects of surface charge following administration to the lung was conducted to understand the biological impact of superparamagnetic iron oxide NPs (SPIONs) and their surface-modification with polyethylene glycol having either negative (i.e. carboxyl) or positive (i.e. amine) functional groups in a 1-month longitudinal study using a mouse model. Genetic assessment revealed enhanced expression of chemokine ligand 17 (CCL-17) and IL-10 biomarkers following SPIONs administration compared to surface-modified NPs. However, SPIONs with carboxyl terminal showed a slightly prominent effect compared to amine modification [54]. A further study used cationic carbon dots for pulmonary delivery of DNA. Administration of particle-DNA complexes to mouse lungs demonstrated that these new carriers achieved similar efficiency but lower toxicity compared to GL67A, a golden standard lipid based transfection reagent for gene delivery to the lungs. The authors suggested that post-functionalization of these nanoparticles with polyethylene glycol (PEG) or targeting moieties should even improve their efficiency and in vivo biocompatibility [55]. Another recent in vivo study performed with hydrogel rod-shaped NPs of different surface charge also confirmed enhanced uptake of positively charged NPs by alveolar macrophages and different subsets of pulmonary DC, with enhanced trafficking to lung draining lymph nodes, as compared to negatively charged NPs. The authors concluded that cationic NPs are endowed with an enhanced immunomodulatory potential in the respiratory tract [56]. All these in vivo findings underline

that size, surface charge and intact conformation of engineered NPs play an important role in modulating downstream immune responses in the respiratory tract [11]. The studies discussed above highlight that different attributes of NPs such as size and surface charge may become important triggers to re-program adaptive immune responses in the respiratory tract. Inhalable NPs may therefore be designed to specifically modulate pulmonary immune responses, either towards an immune-therapy to reprogram allergic responses, or vaccination to generate protective immunity against a respiratory pathogen. To prevent triggering of excessive inflammatory responses that may jeopardise gaseous exchange, meticulous development of inhalable NPs through in depth characterisation of in vivo effects is the final, but most crucial step in pre-clinical development.

Conclusions

The lung with its extensive internal surface harboring different immune cell populations, provides a non-invasive and promising target organ for novel therapies with inhalable nanoparticles. NP engineering approaches is a promising technique for non-invasive and cost-effective pulmonary drug delivery to treat respiratory tract disorder. Specific NP properties such as material, size and surface modification that can be used to stimulate or to inhibit a specific immune reaction may be specifically designed for the treatment of immune disease, such as allergic asthma. In order to achieve this, close collaboration and interdisciplinary research between physicians, biologists, chemists and material scientists is essential. Furthermore, careful design, thorough characterization and process control in the entire NP synthesis procedure is required in order to assure high-quality NP batches with repeatedly reproducible and accurate results. Sophisticated approaches using relevant animal models can play a major role in this development since they can provide straight-forward and reliable data which can be the baseline of such developments.

Authors' contributions

FB, KF, ES, LR, AF, CvG and BR participated in the planning, design and coordination of the manuscript. FB, BR, and CvG drafted the manuscript. All authors read and approved the final manuscript.

Author details

¹ Respiratory Medicine, Bern University Hospital, University of Bern, Murtenstrasse 50, 3008 Bern, Switzerland. ² Adolphe Merkle Institute, University of Fribourg, Fribourg, Switzerland. ³ Chemistry Department, University of Fribourg, Fribourg, Switzerland.

Competing interests

The authors declare that they have no competing interests.

Availability of data and supporting materials

Data sharing not applicable to this article as no datasets were generated or analysed during the current study.

Ethical approval and consent to participate

Ethical approval and consent to participate is not applicable to this article as no data were generated or analysed during the current study.

Funding

This study was supported by the Swiss National Science Foundation National Research Program NRP-64 on Opportunities and Risks of Nanomaterials (Grant Number: 406440-131266/1), the R'Equip grant from the Swiss National Science Foundation Nr. 316030_145003 and the Adolphe Merkle Foundation.

Received: 2 September 2016 Accepted: 26 December 2016

Published online: 09 January 2017

References

- Gehr P, Bachofen M, Weibel E. The normal human lung: ultrastructure and morphometric estimation of diffusion capacity. *Respir Physiol*. 1978;32:121–40.
- Gehr P, Mühlfeld C, Rothen-Rutishauser B, Blank F. Particle-lung interactions. Informa healthcare USA, Inc.; 2010.
- Mills NL, et al. Adverse cardiovascular effects of air pollution. *Nat Clin Pract Cardiovasc Med*. 2009;6:36–44.
- Wichmann HE, et al. Daily mortality and fine and ultrafine particles in Erfurt, Germany part I: role of particle number and particle mass. *Res Rep*. 2000;98:5–94.
- Oberdörster G. Pulmonary effects of inhaled ultrafine particles. *Int Arch Occup Env Heal*. 2001;74:1–8.
- Müller L, Lehmann AD, Johnston BD, Blank F, Wick P, Fink A. Handbook of nanotoxicology, nanomedicine and stem cell use in toxicology. In: Sahu SC, Da C, editors. Hoboken: Wiley; 2014.
- Foged C, Brodin B, Frokjaer S, Sundblad A. Particle size and surface charge affect particle uptake by human dendritic cells in an in vitro model. *Int J Pharm*. 2005;298:315–22.
- Nembrini C, et al. Nanoparticle conjugation of antigen enhances cytotoxic T-cell responses in pulmonary vaccination. *PNAS*. 2011;108:E989–97.
- Zrazhevskiy P, Sena M, Gao X. Designing multifunctional quantum dots for bioimaging, detection, and drug delivery. *Chem Soc Rev*. 2010;39:4326–54.
- Patton JS, Byron PR. Inhaling medicines: delivering drugs to the body through the lungs. *Nat Rev*. 2007;6:67–74.
- Seydoux E, et al. Pulmonary delivery of cationic gold nanoparticles boost antigen-specific CD4+ T cell proliferation. *Nanomedicine*. 2016. doi:10.1016/j.nano.2016.02.020.
- Moore TL, et al. Nanoparticle colloidal stability in cell culture media and impact on cellular interactions. *Chem Soc Rev*. 2015;44:6287–305.
- Fytianos K, et al. Current in vitro approaches to assess nanoparticle interactions with lung cells. *Nanomedicine (Lond)*. 2016;11:2457–69.
- Ochs M, Weibel ER. McGray-HillMedia; 2008.
- Weibel ER. Principles and methods for the morphometric study of the lung and other organs. *Lab Invest*. 1963;12:131–55.
- Ochs M, et al. The number of alveoli in the human lung. *Am J Respir Crit Care Med*. 2004;169:120–4.
- Nicod LP. Lung defences: an overview. *Eur Respir Rev*. 2005;14:45–50.
- Kilburn KH. A hypothesis for pulmonary clearance and its implications. *Am Rev Respir Dis*. 1968;98:449–63.
- Holt PG, Strickland DH, Wikström ME, Jahnsen FL. Regulation of immunological homeostasis in the respiratory tract. *Nat Rev Immunol*. 2008;8:142–52.
- Moller WK, Schmid WG, Semmler-Behnke O, Schulz M. Particle-lung interactions. In: Barbara BF, editors; 2010.
- MacLean JA, et al. Sequestration of inhaled particulate antigens by lung phagocytes A mechanism for the effective inhibition of pulmonary cell-mediated immunity. *Am J Pathol*. 1996;148:657–66.
- Blank F, et al. Size-dependent uptake of particles by pulmonary antigen-presenting cell populations and trafficking to regional lymph nodes. *Am J Respir Cell Mol Biol*. 2013;49:67–77.
- Jakubzick C, Tacke F, Llodra J, van Rooijen N, Randolph GJ. Modulation of dendritic cell trafficking to and from the airways. *J Immunol*. 2006;176:3578–84.

24. Mosser DM, Edwards JP. Exploring the full spectrum of macrophage activation. *Nat Rev Immunol*. 2008;8:958–69.
25. Xue J, et al. Transcriptome-based network analysis reveals a spectrum model of human macrophage activation. *Immunity*. 2014;40:274–88.
26. Krausgruber T, et al. IRF5 promotes inflammatory macrophage polarization and TH1–TH17 responses. *Nat Immunol*. 2011;12:231–8.
27. Martinez FO, Gordon S. The M1 and M2 paradigm of macrophage activation time for reassessment. *F1000Prime Rep*. 2014;6:13.
28. Biswas SK, Mantovani A. Macrophage plasticity and interaction with lymphocyte subsets: cancer as a paradigm. *Nat Immunol*. 2010;11:889–96.
29. Nelson DJ, McMenamin C, McWilliam AS, Brennan M, Holt PG. Development of the airway intraepithelial dendritic cell network in the rat from class II major histocompatibility (Ia)-negative precursors: differential regulation of Ia expression at different levels of the respiratory tract. *J Exp Med*. 1994;179:203–12.
30. Banchereau J, Steinman RM. Dendritic cells and the control of immunity. *Nature*. 1998;392:245–52.
31. Jahnsen FL, et al. Accelerated antigen sampling and transport by airway mucosal dendritic cells following inhalation of a bacterial stimulus. *J Immunol*. 2006;177:5861–7.
32. Thornton EE, et al. Spatiotemporally separated antigen uptake by alveolar dendritic cells and airway presentation to T cells in the lung. *J Exp Med*. 2012;209:1183–99.
33. Rescigno M, et al. Dendritic cells express tight junction proteins and penetrate gut epithelial monolayers to sample bacteria. *Nat Immunol*. 2001;2:361–7.
34. Blank F, et al. Macrophages and dendritic cells express tight junction proteins and exchange particles in an in vitro model of the human airway wall. *Immunobiology*. 2011;216:86–95.
35. Demedts I, Bracke K, Maes T, Joos G, Brusselle G. Different roles for human lung dendritic cell subsets in pulmonary immune defense mechanisms. *Am J Respir Cell Mol Biol*. 2006;35:387–93.
36. Iwasaki A. Role of autophagy in innate viral recognition. *Autophagy*. 2007;3:354–6.
37. Vermaelen K, Pauwels R. Pulmonary dendritic cells. *Am J Respir Crit Care Med*. 2005;172:530–51.
38. Manni ML, et al. The complex relationship between inflammation and lung function in severe asthma. *Mucosal Immunol*. 2014;7:1186–98.
39. Frick SU, et al. Functionalized polystyrene nanoparticles trigger human dendritic cell maturation resulting in enhanced CD4+ T cell activation. *Macromol Biosci*. 2012;12:1637–47.
40. Blank F, et al. Biomedical nanoparticles modulate specific CD4+ T cell stimulation by inhibition of antigen processing in dendritic cells. *Nanotoxicology*. 2011;5:606–21.
41. Hardy CL, et al. Inert 50-nm polystyrene nanoparticles that modify pulmonary dendritic cell function and inhibit allergic airway inflammation. *J Immunol*. 2012;188:1431–41.
42. Lund FE, et al. B cells are required for generation of protective effector and memory CD4 cells in response to *Pneumocystis* lung infection. *J Immunol*. 2006;176:6147–54.
43. Heyder J, Gebhart J, Rudolf G, Schiller CF, Stahlhofen W. Deposition of particles in the human respiratory tract in the size range 0.005–15 μm . *J Aerosol Sci*. 1986;17:811–25.
44. Tena AF, Clará PC. Deposition of inhaled particles in lungs. *Arch Broncho-neumol*. 2012;48:240–6.
45. Murgia X, et al. Size-limited penetration of nanoparticles into porcine respiratory mucus after aerosol deposition. *Biomacromolecules*. 2016;17:1536–42.
46. Choi HS, et al. Rapid translocation of nanoparticles from the lung air-spaces to the body. *Nat Biotechnol*. 2010;28:1300–3.
47. Hardy CL, et al. Differential uptake of nanoparticles and microparticles by pulmonary APC subsets induces discrete immunological imprints. *J Immunol*. 2013;191:5278–90.
48. Muttill P, et al. Pulmonary immunization of guinea pigs with diphtheria CRM-197 antigen as nanoparticle aggregate dry powders enhance local and systemic immune responses. *AAPS J*. 2010;12:699–707.
49. Ryan G, et al. Pulmonary administration of PEGylated polylysine dendrimers: absorption from the lung versus retention within the lung is highly size-dependent. *Mol Pharm*. 2013;10:2986–95.
50. Thomas C, Rawat A, Hope-Weeks L, Ahsan F. Aerosolized PLA and PLGA nanoparticles enhance humoral, mucosal and cytokine responses to hepatitis B vaccine. *Mol Pharm*. 2011;8:405–15.
51. Taratula O, Kuzmov A, Shah M, Garbuzenko O, Minko T. Nanostructured lipid carriers as multifunctional nanomedicine platform for pulmonary co-delivery of anticancer drugs and siRNA. *J Control Release*. 2013;171:349–57.
52. Rodriguez-Lorenzo L, et al. Fluorescence-encoded gold nanoparticles: library design and modulation of cellular uptake into dendritic cells. *Small*. 2014;10:1341–50.
53. Zhao Y, et al. Solid lipid nanoparticles for sustained pulmonary delivery of Yuxingcao essential oil: preparation, characterization and in vivo evaluation. *Int J Pharm*. 2016;516:364–71.
54. Al Faraj A, Shaik AP, Shaik AS. Effect of surface coating on the biocompatibility and in vivo MRI detection of iron oxide nanoparticles after intrapulmonary administration. *Nanotoxicology*. 2015;9:825–34.
55. Pierrat P, et al. Efficient in vitro and in vivo pulmonary delivery of nucleic acid by carbon dot-based nanocarriers. *Biomaterials*. 2015;51:290–302.
56. Fromen CA, et al. Nanoparticle surface charge impacts distribution, uptake and lymph node trafficking by pulmonary antigen-presenting cells. *Nanomed Nanotechnol Biol Med*. 2016;12:677–87.

Submit your next manuscript to BioMed Central and we will help you at every step:

- We accept pre-submission inquiries
- Our selector tool helps you to find the most relevant journal
- We provide round the clock customer support
- Convenient online submission
- Thorough peer review
- Inclusion in PubMed and all major indexing services
- Maximum visibility for your research

Submit your manuscript at
www.biomedcentral.com/submit



REVIEW

Open Access



Transformation of the released asbestos, carbon fibers and carbon nanotubes from composite materials and the changes of their potential health impacts

Jing Wang^{1,2*} , Lukas Schlagenhauf^{1,2} and Ari Setyan^{1,2}

Abstract

Composite materials with fibrous reinforcement often provide superior mechanical, thermal, electrical and optical properties than the matrix. Asbestos, carbon fibers and carbon nanotubes (CNTs) have been widely used in composites with profound impacts not only on technology and economy but also on human health and environment. A large number of studies have been dedicated to the release of fibrous particles from composites. Here we focus on the transformation of the fibrous fillers after their release, especially the change of the properties essential for the health impacts. Asbestos fibers exist in a large number of products and the end-of-the-life treatment of asbestos-containing materials poses potential risks. Thermal treatment can transform asbestos to non-hazardous phase which provides opportunities of safe disposal of asbestos-containing materials by incineration, but challenges still exist. Carbon fibers with diameters in the range of 5–10 μm are not considered to be respirable, however, during the release process from composites, the carbon fibers may be split along the fiber axis, generating smaller and respirable fibers. CNTs may be exposed on the surface of the composites or released as free standing fibers, which have lengths shorter than the original ones. CNTs have high thermal stability and may be exposed after thermal treatment of the composites and still keep their structural integrity. Due to the transformation of the fibrous fillers during the release process, their toxicity may be significantly different from the virgin fibers, which should be taken into account in the risk assessment of fiber-containing composites.

Background

A composite material can be defined as a combination of two or more materials that results in better properties than those of the individual components used alone [1]. The composite materials may be preferred because they are stronger, lighter, or less expensive when compared to traditional materials [2]. The components forming the composites can be divided into two main categories: matrix and reinforcement. The continuous phase is the matrix, which can be a polymer, metal, or ceramic [1]. The reinforcement usually adds the strength and stiffness.

In most cases, the reinforcement is harder, stronger, and stiffer than the matrix [1]. Fibers with high length-to-diameter ratios are common reinforcement materials. Asbestos fibers were widely used as reinforcement in cement to improve the tensile strength and heat resistance. The most common asbestos-containing industrial material produced worldwide has been cement-asbestos [3]. Carbon fibers with diameters 5–10 μm are used in polymer matrices. With the development of material technology, fibers with smaller diameters are getting popular. Carbon nanotubes (CNTs) with diameters below 100 nm exhibit properties including high strength and tensile stiffness, chirality-dependent electrical conductivity, increased thermal conductivity and one of the highest Young's modulus [4], therefore they have been considered as a nanofiller for composites.

*Correspondence: jing.wang@ifu.baug.ethz.ch

¹ Institute of Environmental Engineering, ETH Zurich, 8093 Zurich, Switzerland

Full list of author information is available at the end of the article

With the wide applications of fiber-reinforced composites, there come the possibilities of release of the fibers and exposure to workers and consumers. Due to their dimensions, as well as chemical and elemental composition, concerns as to the human health risk associated with exposure to respirable fibers have been vehemently raised [5–7]. The toxicity of fibers is generally determined by the three “D’s”: dose, dimension, and durability [8]. The small aerodynamic diameters of thin fibers enable deposition beyond the ciliated airways. Donaldson et al. [9] provided a schematic with direct comparison between the CNTs and asbestos, showing that the long asbestos and long and stiff CNTs deposit in the parietal pleura and the macrophage cells cannot completely engulf such fibers, resulting in incomplete or frustrated phagocytosis, which leads to oxidative stress and inflammation. In contrast, the short asbestos and compact, entangled CNTs could be cleared by the macrophage cells. The frustrated phagocytosis effect is not limited to CNTs or asbestos, but applicable for high aspect ratio particles [9]. The correlation between biopersistence and adverse pulmonary effects has been demonstrated [10], while the fiber material is of minor importance [11]. Fibers with good biopersistence produce chronic pulmonary inflammation and interstitial fibrosis; if very biopersistent, fibrosis is followed by lung cancer and/or pleural mesothelioma [8]. Defined by the World Health Organization (WHO), respirable fibers have a length above 5 μm , a diameter below 3 μm , and an aspect ratio (length/diameter) above or equal to 3 [12]. The recommended permissible exposure limit (PEL) by the Occupational Safety and Health Administration (OSHA) is 1 respirable fiber/ cm^3 for an 8 h time weighed average [8]. There remains an impending need to undertake research initiatives that focus specifically upon determining the real advantages posed by nanofibers, as well as underpinning their conceivable risk to human health. Both are inextricably linked, and therefore by devising a thorough understanding of the synthesis and production of nanofibers to their potential application and disposal is essential in gaining an insight as to the risk they may pose to human health [6].

The fibers in composite materials can be released to the environment in different phases of the life time of the products, including production and processing, service life, and disposal [13]. Wear and tear, cutting, drilling, sanding, machining, exposure to UV light and heat, chemical erosion, and combustion can all possibly lead to release of fibrous fillers after production. The released fibers may be free standing or partially embedded in the matrix material. Harper et al. [14] suggested that CNT-containing fragments may be turned into household dust. The physical and chemical properties of the fibers can be altered by the mechanical, chemical or thermal energy

input during the release process. Therefore, the dimension and biopersistence of the released fibers may be different from the original materials, e.g. asbestos could be entirely transformed to a mixture of non hazardous silicate phases by thermal treatment; large carbon fibers can be turned into respirable fibers; nanotubes may be oxidized or shortened. It follows that the risk assessment of the composites cannot be solely based on the properties of the fibers put into the composites, but on the properties of the fibers released from the composites, with the understanding that the properties before and after release are closely linked. This review is not intended to be an exhaustive review of the release studies. Instead, it focuses on the transformation of the fibrous fillers after their release from composites, especially the change of the properties essential for the health impacts.

Transformation of the asbestos from construction materials

Background

Asbestos is a family of six natural silicate minerals, containing long chains of silicon and oxygen that give rise to the fibrous nature of the mineral [15]. Asbestos is recognized as a carcinogen and it has been more than 30 years since the first national ban on asbestos in 1983 by Iceland [16]. To date, all the EU member states have banned usage of all forms of asbestos [17]. However, asbestos fibers still exist in a large number of products and the end-of-the-life treatment of asbestos-containing materials poses potential risks. An estimated 20% of buildings in the US still contain products such as shingles, cement pipes and insulation made from chrysotile asbestos [15]. Yet well-maintained asbestos in buildings will not spontaneously shed fibers into the air. Instead decay, renovation or demolition of the structures can lead to the release of fibers [15].

The most common methodology of asbestos waste management is the disposal in special landfills for toxic and hazardous wastes [18]. However, identifying an appropriate location for the installation of these landfills is difficult, due to the specific requirements of these sites according to current legislation and due to common operational difficulties [18].

Waste incineration is becoming a popular method to significantly reduce the volume of the deposited waste and to avoid soil contamination. For example, the current Swiss Technical Ordinance on Waste demands that all combustible waste has to be burned before deposition. Therefore landfilling of wastes containing asbestos and high fraction of organic contents are forbidden. Incineration of such wastes in municipal solid waste incineration (MSWI) plants and deposition of the slags and filter ashes afterward seem to be a solution, because it is known that

thermal treatment could destroy the fibrous structure of the asbestos, transforming the asbestos to non-hazardous materials [19, 20].

Standard detection methods for asbestos fibers are usually based on filter collection and microscopic inspection. The National Institute for Occupational Safety and Health (NIOSH) has four standard methods for the analysis of asbestos fibers [21–24]. Two of them are for the analysis of filter samples by microscopy (phase contrast microscopy for method 7400, and transmission electron microscopy TEM for method 7402). The two other methods are for the analysis of powder samples, either by X-ray diffraction (method 9000) or by polarized light microscopy (method 9002). The EPA has also a standard method for the analysis of asbestos. Their procedure involves two mandatory steps of analysis by microscopy (a stereomicroscopic examination, followed by polarized light microscopy) for the qualitative classification of the fibers. The amount of asbestos in a residue can then be quantified by gravimetry, X-ray diffraction (XRD), polarized light microscopy, or analytical electron microscopy. There are also several other standard methods available e.g. [25, 26]. Many previous studies used electron

microscopy and XRD to investigate the modification of the asbestos after thermal treatment.

Transformation of asbestos by thermal treatment

Gualtieri and Tartaglia [20] reported that asbestos could be entirely transformed to a mixture of non-hazardous silicate phases throughout a thermal treatment at 1000–1250 °C and to a silicate glass at $T > 1250$ °C. They investigated four samples, including a pure serpentine asbestos, a pure amphibole asbestos, a commercial asbestos containing material utilized in the past for asbestos–cement pipes, and a commercial asbestos–cement for external roof pipes. Initially the pure asbestos samples had lengths over 10 μm and diameters less than 1 μm (Fig. 1a). After the thermal treatment, the asbestos samples lost the fibrous morphology and were transformed to non-hazardous silicate phases (Fig. 1b). The construction material samples had asbestos fibers dispersed in the heterogeneous matrix (Fig. 1c). The thermal treatment resulted in crystals of the silicate phases in place of the fibers (Fig. 1d). The authors also described the recycle of the thermally treated asbestos containing samples as a raw material for glass ceramics and traditional ceramics.

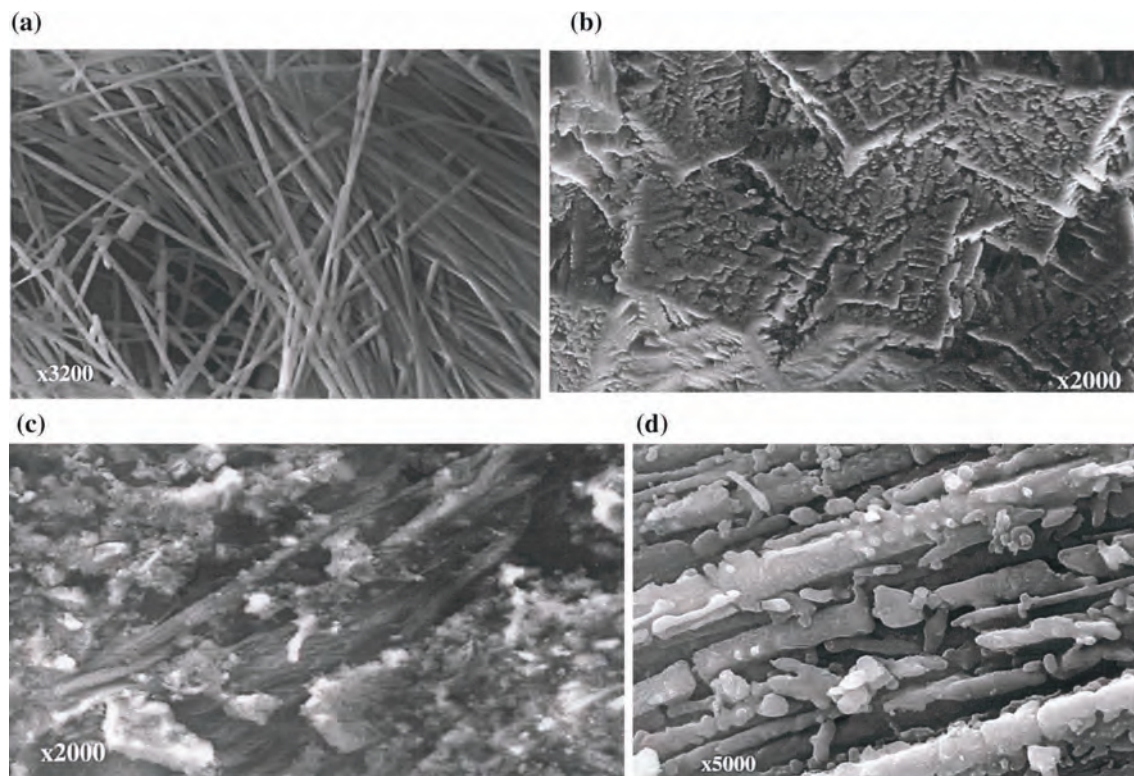


Fig. 1 SEM images of **a** the initial sample of a pure amphibole asbestos; **b** the pure amphibole asbestos sample after thermal treatment; **c** the initial sample of a commercial asbestos–cement for external roofs pipes; **d** the asbestos–cement sample after thermal treatment. (Adapted from [20], with the permission of Elsevier)

Gualtieri et al. [27] used time-resolved synchrotron powder diffraction to follow the thermal transformation of a cement-asbestos sample. The instrumentation allowed for the observation of metastable phases during the transformation of asbestos fibers into non-fibrous crystalline phases. The changing gas atmosphere in the closed system was shown to affect the final composition of the recrystallized product.

Gualtieri et al. [3] used environmental scanning electron microscopy to follow in situ the thermal transformation of chrysotile fibers present in cement-asbestos. It was found that the reaction kinetics of thermal transformation of chrysotile was highly slowed down in the presence of water vapor in the experimental chamber with respect to He. This was explained by chemisorbed water on the surface of the fibers which affected the dehydroxylation reaction and consequently the recrystallization into Mg-silicates.

Zaremba et al. [28] reported the possibility of detoxification of chrysotile asbestos through a low temperature heating and grinding treatment. They found that an isothermal treatment at 650 °C for at least 3 h caused the complete dehydroxylation of chrysotile $\text{Mg}_3\text{Si}_2\text{O}_5(\text{OH})_4$. Transformation of the dehydroxylated phase to forsterite Mg_2SiO_4 was obtained by heat treatment in the range 650–725 °C. In addition, it was easily milled to pulverulent-shape material by mechanical milling.

Kusiorowski et al. [29] investigated thermal decomposition of 10 different samples of raw natural asbestos. They found that different temperatures were required (about 700–800 °C for chrysotile and more than 900 °C for amphibole asbestos). As a result of this process, the mineral structure was changed through dehydroxylation which led to the formation of X-ray amorphous and anhydrous phase. Kusiorowski et al. [30] extended their study to three asbestos–cement samples from different factories. Calcination of asbestos–cement wastes at ~1000 °C was sufficient to totally destroy the dangerous structure of asbestos. No significant differences in thermal decomposition among the types of asbestos–cement samples used were observed.

Yamamoto et al. [31] investigated simulated slag samples produced by high-temperature melting of asbestos-containing wastes. Fiber concentrations were below the quantification limit of their TEM-based method in all samples.

Transformation of the asbestos by the thermal treatment can be identified not only by microscopy, but also by other analytical techniques. Gualtieri et al. [27] used the synchrotron powder diffraction to observe the phase change of asbestos fibers. The Fourier transform infrared spectroscopy (FT-IR) spectra of asbestos normally show a characteristic double peak at 3640–3680/cm

corresponding to the OH-stretching vibration. Upon thermal decomposition, the double peak disappeared [30]. Heating the samples causes appreciable other changes in their FT-IR spectra, which provides important information about the structural transformations. For instance, Kusiorowski et al. [29] showed that a characteristic triplet in the region 935–1080/cm, which is typical of the Si–O–Si stretches in the silica network, was clearly shifted toward lower frequencies.

Discussion

The cited studies show that thermal treatment can be an effective solution to transform both raw asbestos samples and asbestos-containing construction materials into non-hazardous phase. Effective treatment of asbestos-containing cement wastes needs about 1000 °C. During the incineration process, asbestos may stay embedded or be liberated from the matrix and carried away by the air flow and thermal plume. Therefore, the asbestos may remain in the slag or become free standing. According to the directives of the European Union on the incineration of wastes, the gas resulting from the process must reach at least 850 °C. Moreover, if hazardous wastes contain more than 1% of halogenated organic substances, the temperature has to be raised to 1100 °C for at least 2 s during incineration [32]. Therefore, the temperature in the incineration processes may or may not be high enough for effective treatment of asbestos-containing wastes.

Currently there is no uniform practice in Switzerland regarding the incineration of wastes that contain asbestos in MSWIs and some MSWIs do accept small volumes [33]. In addition, the temperature is heterogeneous in an incinerator therefore asbestos fibers may have different degrees of thermal decomposition. The liberated asbestos may have long enough residence time in the incinerator to be thermally transformed; they may settle down as part of the slag or be carried by the flue gas and captured as part of the filter ashes. The distribution fractions are not known. Further studies are needed to investigate the fate and stability of asbestos fibers in MSWIs and to assess the risks for the operators and environment.

Transformation of the released carbon fibers from composites

Background

Carbon fibers are fibrous structures composed mostly of carbon atoms, which can be derived from organic fibers by subjecting them to high temperatures that drive off the non-carbon components [8]. Carbon fibers have been used in high performance applications from airplanes to automobiles and from satellites to sporting goods [34]. Carbonized fibers include carbon (amorphous) and graphite (crystalline; made by further heating amorphous

carbon fibers) [8]. All commercial carbon fibers produced today are based on rayon (a cellulose-based polymer), PAN (polyacrylonitrile fiber) or pitch (a tar-like mixture of hundreds of branched organic compounds) [34]. PAN-based fibers have superior tensile strength; pitch-based fibers are unique in their ability to achieve ultrahigh Young's modulus and thermal conductivity [34].

Carbon fiber reinforced polymer (CFRP) composites have gained great attention due to their interesting combination of strength, durability, high strength-to-weight ratios and corrosion resistance [35]. They are finding increasing applications in architecture, aerospace, automotive, and sporting goods industry [35, 36]. Release of carbon fibers from CFRPs has been observed during machining [37–40] and during tensile strength tests [41]. The fiber content of CFRPs is often above 50 vol% which means that the produced dust during machining or tensile tests consists mainly of materials from the fibers. Besides fibers with the same diameter as the embedded fibers in the composite, respirable fibers with smaller diameters were also generated, indicating transformation of the embedded fibers during the process.

Previous studies showed that the toxicity of carbon fibers depended on their sizes. Holt and Horne [39] exposed guinea pigs to dust obtained by feeding PAN-based carbon fibers into a hammer mill. The nonfibrous particles in the dust were phagocytosed. The few carbon fibers found in the lung that were longer than 5 μm were still extracellular after 27 weeks and they were uncoated. No pathological effects were observed. Warheit et al. [42] exposed rats to PAN-based carbon fibers which were 9 μm in diameter and considered to be non-respirable. They had no effect on any of the parameters tested. In the same study, the pitch-based carbon fibers with <2 μm aerodynamic diameter produced a dose-dependent transient inflammatory response in the lungs of exposed rats. Martin et al. [43] investigated the cytotoxicity of particles generated during machining of CFRP composites (characterized by [38]). For two samples they saw a slight toxicity, but as the particles consisted of fibers and matrix materials, it was not clear what caused the effect.

Carbon fiber release from composites and transformation

Holt and Horne [39] fed PAN-based carbon fibers into a hammer mill and examined the dust taken from the air in the dusting chamber. They observed fibers about 10 μm in diameter and >100 μm long, which might have the same diameter as the original ones. Only low concentrations of dust of respirable size were produced and less than 1% of the respirable carbon particles were fibrous. The respirable black fibers had diameters about 1–2.5 μm and lengths up to 15 μm . They were possibly fragmented

fibers from the original ones, though the authors did not explain where these smaller fibers were from. It appeared that the authors used an optical microscope therefore the size resolution was limited. The authors used the generated dust for toxicity tests in guinea pigs and found no adverse effects.

Henry et al. [44] analyzed airborne dust during preparation and machining of carbon fiber composites at a PAN-based production facility and reported 0.01–0.0002 f/ml (mean diameters >6 μm and mean lengths >30 μm). Gieske et al. [45] reported concentrations of 0.001–0.05 f/ml (mean diameters >5.5 μm and mean lengths >900 μm) during various phases of carbon fiber production. Based on the data they reviewed, Warheit et al. [8] suggested that released carbon fibers tended to be non-respirable—diameters were 3.9–7.8 μm and lengths were 32.8–2342 μm .

Mazumder et al. [40] investigated aerodynamic and morphological properties of the fibers and fiber fragments released from commercial laminates containing carbon and graphite fibers during cutting, grinding and by thermal degradation. The virgin fiber diameters were 5.8–8.0 μm and fiber volume content was about 60%. The authors found that mechanical chopping of virgin carbon fibers produced sharp-edged fiber like particles in the respirable size range. When the composites were subjected to grinding, fibers were often exposed from their polymer matrix, and the released particles contained small fibers and fragments with irregular shapes, and a significant number of fibers having smaller diameters than the original ones and sharp edges because of fibrillation. The authors showed electron micrographs demonstrating how the fiber could split, generating particles with irregular shapes and often with sharp edges. It was estimated that about 90% did not have such sharp edges. They concluded that fiber fragments in the sub-micrometer range could be generated during the machining process.

Mazumder et al. [40] exposed virgin carbon fibers to a temperature of 850 $^{\circ}\text{C}$ for 4.5 h. They observed that the fibers underwent significant fragmentation during oxidation, and apparently lost their crystalline property. Debris in this process from carbon fibers primarily consisted of amorphous carbon particles rather than fiber like particles. When the particles released from grinding of the composites were heated, the epoxy resin evaporated quickly at temperatures above 400 $^{\circ}\text{C}$, then the vapor condensed to form respirable particles.

Boatman et al. [38] performed machining operations on six carbon fiber/epoxy composites and analyzed the released dust. By microscopy, bulk particles ranged from 7 to 11 μm in diameter, with mean aspect ratios from 4

to 8:1. The relative fractions of respirable to total mass of bulk samples were <3%. The authors concluded that under their machining protocols, dusts at the tool face contained few particles of respirable size with no evidence of splitting of fibers longitudinally.

Bello et al. [37] investigated release of airborne particles during dry and wet cutting of composites containing CNTs and carbon fibers. The carbon fibers had nominal diameter of 6–7 μm and broken fibers of about the same diameter were observed in the dust. Fibers which might have originated from fracturing of the carbon fibers along their axis were identified, which were typically thinner, longer, and had higher aspect ratios than those associated with the broken carbon fibers. Bello et al. [46] performed drilling on the same composites and again found both carbon fibers fractured perpendicular to the fiber axis and split fragments along the axis.

Schlagenhauf et al. [41] investigated the fiber release and possible risk for the operating staff in two CFRP cable tensile tests. The carbon fibers had a filament diameter of 5 μm and were pre-impregnated by an epoxy polymer resin matrix. The fiber volume fraction was 60% in the cables. The tensile tests involved first loading the cables with very high elastic energy, then releasing the energy abruptly in the failure event, which caused the cable to rupture and induced a vast amount of dust. Measurements with aerosol devices and examination of the filter samples showed that the cable failure caused release of particles and free-standing fibers whereof a fraction had diameters below 3 μm and thus were respirable according to WHO [12]. The measured peak fiber concentration of 0.76 fibers/ cm^3 and calculated concentration of 0.07 fibers/ cm^3 for an 8 h time weighed average were below the PEL of 1 respirable fiber/ cm^3 given by OSHA. The peak fiber concentration was close to the PEL indicating needs for protective measures for the workers during and immediately after the tensile tests.

Example SEM and TEM images from the study of Schlagenhauf et al. [41] are shown in Fig. 2. Some collected fibers had the original diameter of 5 μm and relatively smooth surface decorated by residual particles. These fibers were not considered to be respirable according to the WHO criteria. There were also more fibers which appeared to be split during the cable failure and could be respirable due to the diameters below 3 μm . Further, fragmented particles from the composite matrix and fibers, whereof most had diameters below 10 μm , were also collected. The TEM images show a few fibers with a diameter below 1 μm . The morphologies of the released fibers suggested that the embedded fibers were not only severed perpendicular to the fiber axis, but also along the fiber axis in many instances, causing respirable fibers with smaller diameters.

Discussion

The studies reviewed here demonstrate that the carbon fibers with diameters 5–10 μm embedded in composites can be released by mechanical operations. The released fibers may be broken perpendicular to the fiber axis, thus with the same diameters as the original ones; they may also be fractured or split along the fiber axis, leading to respirable fibers with smaller diameters. This splitting can be explained by the micro structure of the fibers. Diefendorf and Tokarsky [47] described carbon fibers as composed of a ladder structure of graphite layers that are aligned parallel to the fiber axis. Endo and Dresselhaus [48] described several different carbon fiber structures. The PAN-based fibers consist of small carbon structural units preferentially aligned with the carbon hexagonal segments parallel to the fiber axis, and the intertwined morphology is responsible for the high mechanical strength of the PAN-based fibers. The mesophase pitch-based fibers consist of well aligned graphitic layers nearly parallel to the fiber axis, and this high degree of crystallinity is responsible for their high modulus or stiffness. The vapor grown fibers consist of coaxial cylindrical graphene sheets and are closely related to multiwall carbon nanotubes. The graphite whiskers [49] were reported to have the scroll structure of rolled up graphite sheets. The bonds between the graphitic layers or sheets or small carbon structural units are relatively weak and susceptible to fragmentation. The fibers used by Schlagenhauf et al. [41] were PAN-based (Tenax[®] IMS 60, Teijin, Tokyo, Japan) and the split fiber in the first panel of Fig. 2 showing that a small carbon structural unit broke off from the large fiber. Mazumder et al. [40] described some of their observed fragmented fibers with shattered outer graphite structure, exposing the inner core of the fiber. These fibers seemed to have the scroll structure of rolled up graphite sheets.

Thermal treatment can cause both asbestos and carbon fibers to lose their fibrous structures. However, the mechanisms are different. The asbestos is subjected to the dehydroxylation reaction and consequently the recrystallization into the silicate phase. The carbon fibers may undergo fragmentation during oxidation, lose their crystalline property and turn into amorphous carbon particles.

Transformation of the released carbon nanotubes

Background

CNTs represent a type of fascinating nanomaterial which gained numerous applications due to their special mechanical, electrical, thermal and optical properties [4, 50, 51]. As filler in composites, CNTs can lead to superior or additional properties compared to their neat matrix materials including tensile strength and Young's modulus

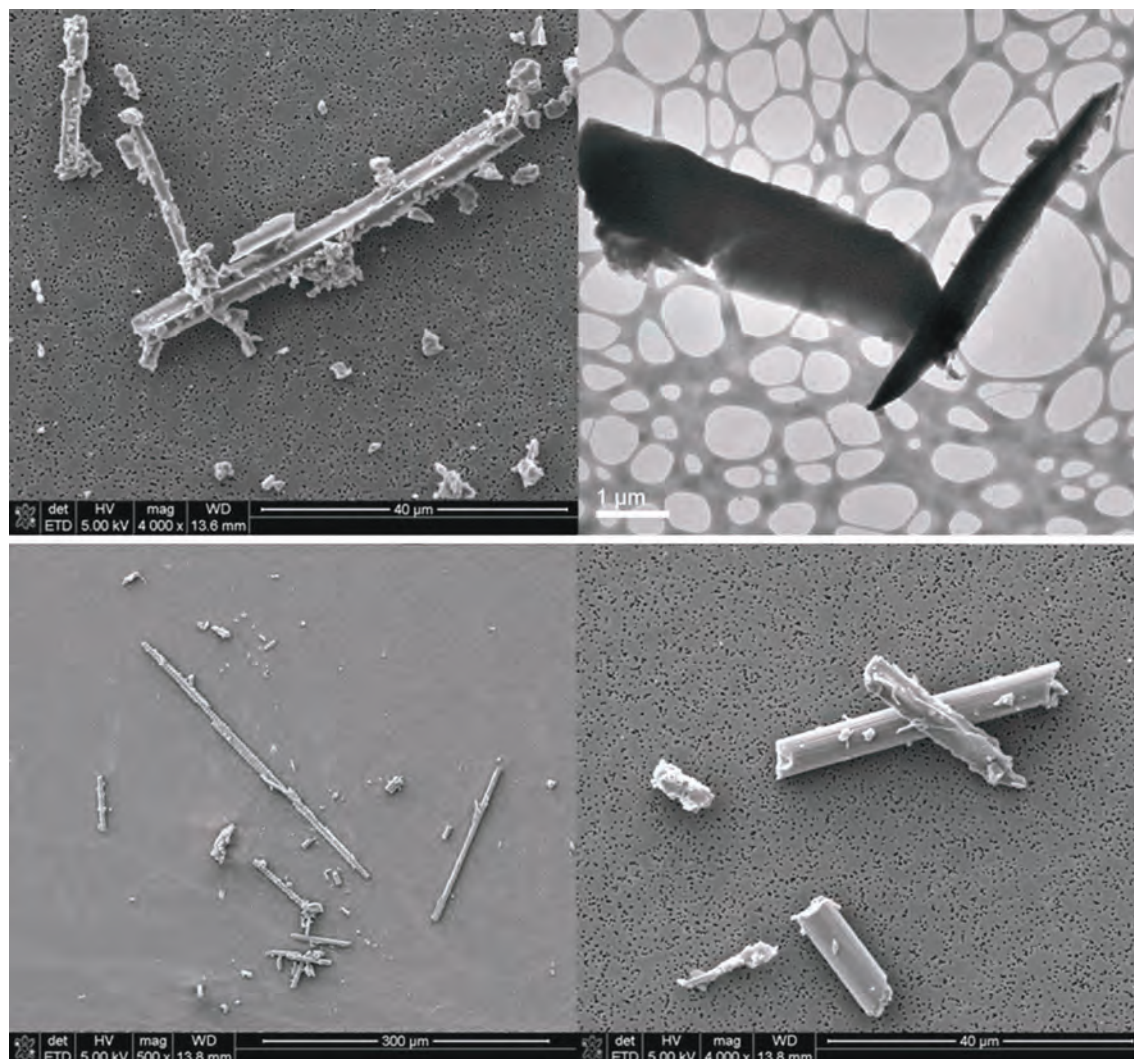


Fig. 2 Example SEM and TEM images of the released particles following the rupture of CFRP cables in the tensile strength test. (Partially adapted from [41])

[52], energy absorption [53], improved scratch and wear resistance [54], electrical and thermal conductivity [55, 56], fire resistance [57], and optical properties [58].

CNTs are also one of the most heavily studied nanomaterials for their potential impacts on human and environment [59–67] among the others). Therefore, voluminous studies have been dedicated to the release of CNTs from composites [13, 14, 37, 46, 68–88]. The release of CNTs by mechanical stresses and weathering or a combination of them has been widely investigated.

Another possible release route is by thermal treatment which decomposes the polymer matrix and exposes the CNTs. CNTs possess high thermal stability. Pang et al. [89] studied the oxidation of CNTs by thermogravimetric analysis (TGA) in air. The maximum rate of weight loss took place at 695 °C at a heating rate of 1 °C/min. The

oxidative stability of CNTs is dependent on the defects and tube diameter [90]. The defects are present at the ends, bends, Y-junctions, and kinks in nanotubes and they contribute to a decrease in the oxidative stability. A smaller diameter results in a higher degree of curvature and subsequently a higher reactivity toward oxygen. Bom et al. [90] showed that thermal annealing could remove the defects and improve the thermal stability of the multiple wall carbon nanotubes (MWCNTs). By annealing at 2800 °C, Bom et al. showed the oxidative stability enhancements of MWCNTs was 155 °C, and complete decomposition of the annealed MWCNTs needed temperatures around 800 °C. CNTs are considered to be a promising flame retardant to replace the conventional halogenated ones [57]. The CNT nanocomposites may be exposed to high temperatures in a fire accident, in

incineration plants, or in a thermal treatment intended to recover the CNTs for reuse. The scenarios will be discussed.

Transformation of the released CNTs from composites

In the study of Bello et al. [37] composites containing CNTs and carbon fibers were subjected to dry and wet cutting. Although release of chopped and split carbon fibers was reported, no released CNTs were detected. In a subsequent study, Bello et al. [46] performed drilling on the composites and observed release of clusters of CNT aggregates. In both of the above studies, the authors observed submicron fibers with at least one nanoscale dimension without discussing their origins. The CNTs in the carbon-fiber based composites were reported to be 8 nm in average diameter and 100–150 μm long [37]. The released CNT aggregates had complex morphology and the diameter and length of the involved CNTs were not reported.

Cena and Peters [69] reported that weighing bulk CNTs and sanding epoxy containing CNTs generated few airborne nano-sized particles. Sanding epoxy containing CNTs might generate micrometer-sized particles with CNTs protruding from the main particle core. The protruding CNTs had diameters (~ 25 nm) in the range of the original CNTs (10–50 nm). No free standing CNTs were found. Huang et al. [74] reported more results for sanding epoxy sticks with CNTs. Similar results were obtained in that protruding CNTs with diameters around 25 nm were observed. The authors did not detect rod shaped particles from micrographs, except for the tests conducted with 4% CNT epoxy, in which particles with features consistent with free CNTs were observed.

Schlagenhauf et al. [80] used the Taber Abraser to perform abrasion on a CNT/epoxy composite, for which the properties were reported in Hollertz et al. [55]. MWCNTs (Baytubes, C150p) with 1–10 μm lengths and 13–16 nm outer mean diameters were used to produce the composites. The MWCNT mass content was 0.1 or 1% and they were dispersed in the epoxy resin by three-roll milling at a gap pressure of 1 MPa. The composite preparation process evidently reduced the CNT lengths to about 0.7 ± 0.2 μm [55]. After abrasion, protruding CNTs from the released epoxy particles were visible (Fig. 3a, b), and a non-negligible amount of free-standing CNTs (Fig. 3c–e) and agglomerates of CNTs were also found (Fig. 3f). The released CNTs had about the same diameters as the original ones. However, the average length of 19 imaged

free-standing CNTs was 304 ± 251 nm. Therefore the released CNTs were shortened during the abrasion process compared to the embedded ones. Schlagenhauf et al. [81] developed an ion labeling method to quantify the exposed CNTs in the respirable fraction of the abraded particles, and found approximately 4000 ppm of the MWCNTs were released as protruding or free-standing MWCNTs (which could contact lung cells upon inhalation) and approximately 40 ppm as free-standing MWCNTs in the worst-case scenario.

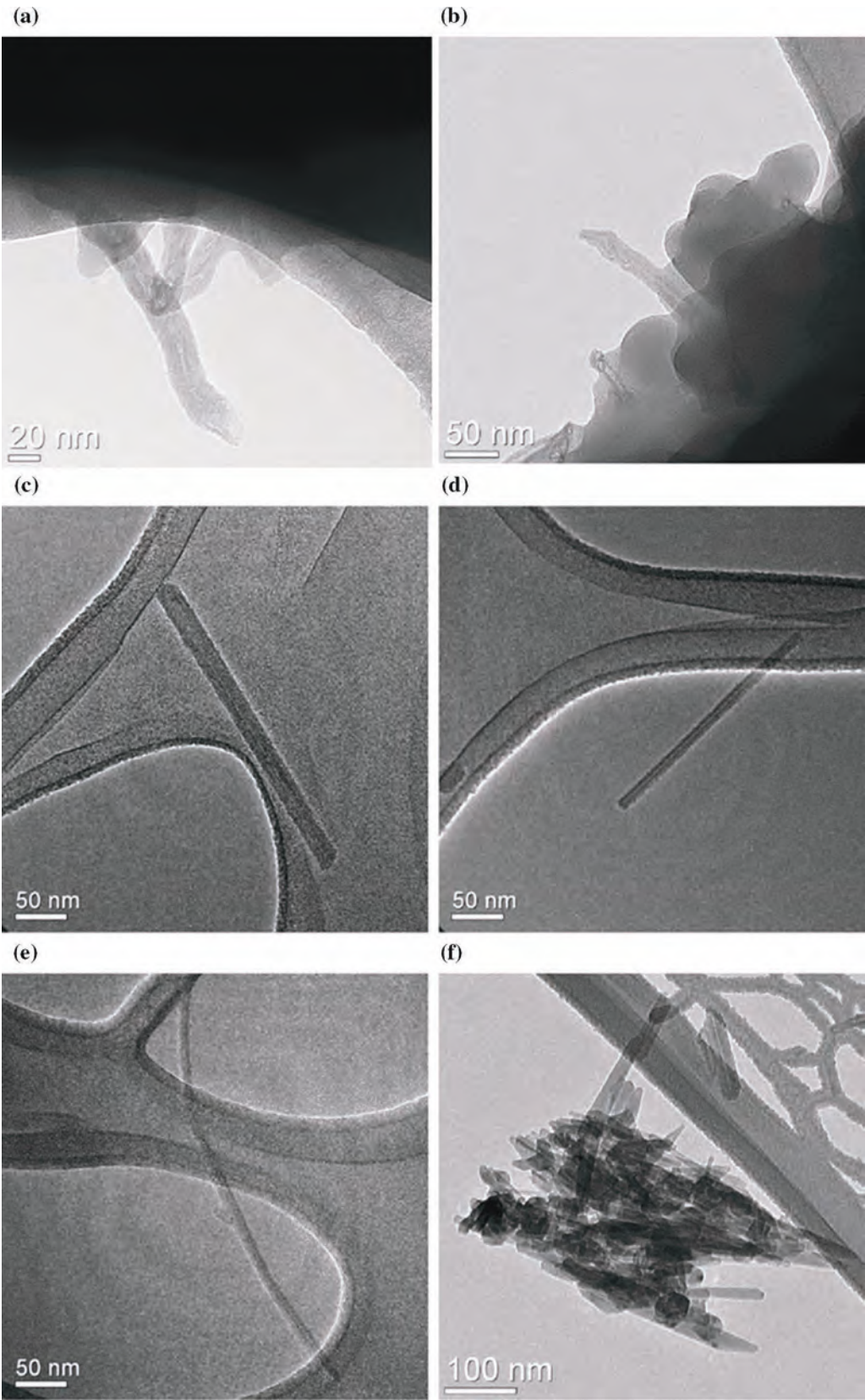
Golanski et al. [71] performed abrasion on polycarbonate, epoxy and PA (polyamide) polymer composites containing CNTs up to 4 wt%. They developed practical tools inducing non-standardized high stresses such as mechanical shocks and hard scratches simulated by a metallic brush. No release of CNTs was measured for the samples with well dispersed CNTs, however for the samples with poorly distributed CNTs, individual free standing CNTs were observed on TEM grids. The CNTs used in the study had an external diameter of 12 nm. The authors did not give size information for the released free standing CNTs.

Ogura et al. [91] investigated the particle release caused by the grinding of polystyrene-based composites containing 5 wt% single-wall carbon nanotubes (SWCNTs). Free-standing CNTs were not observed, whereas micron-sized particles with protruding fibers speculated to be CNTs were observed. The CNTs had a tube diameter of approximately 3 nm and it is difficult to confirm the fibers were CNTs from the SEM images of the released particles.

Nguyen et al. [77] and Petersen et al. [78] investigated the degradation of a CNT/epoxy nanocomposite under intensive UV-light. UV-light can cause oxidation of the polymer and chain scission therefore damage of the sample surface. The studies showed that the epoxy-rich surface layer of the nanocomposite was removed relatively rapidly, leaving a surface covered almost completely with a network of MWCNTs. The MWCNT network on the weathered epoxy surface was more mechanically resistant to scratching than the neat epoxy. The authors' analysis of released particles did not show free standing CNTs. The strong mechanical properties of the CNT network and the lack of broken CNTs implied that the UV exposure did not damage the integrity of the CNTs. Ging et al. [92] evaluated the degradation of a CNT/epoxy nanocomposite with neat and amino functionalized CNTs exposed to the combination of UV, moisture, mechanical

(see figure on next page.)

Fig. 3 TEM images of abraded particles from a CNT/Epoxy composite by the Taber Abraser. **a, b** Protruding CNTs from abraded particles of the 1 wt% CNT composite; **c–e** free-standing individual CNTs; **f** an agglomerate of CNTs with a couple of individual CNTs scattered nearby. (Partially adapted from [80])



stress and other factors. Several possible forms of CNTs were found on the composite surface by UV irradiation: completely unprotected and agglomerated CNTs; partially exposed CNTs fractured due to the crack formation originating from exposure; CNTs still encapsulated in the matrix; and fragments of the matrix.

Wohlleben et al. [87, 88] analyzed degradation scenarios for different nanocomposite materials. They found after long term weathering the polymer matrix (polyoxymethylene POM and thermoplastic polyurethane TPU) with embedded CNTs degraded and exposed the nanofiller as an entangled CNT network. Immersion in water did not lead to release of CNTs from the network. Hirth et al. [73] investigated sanding and weathering of CNT/epoxy nanocomposites and observed embedded or protruding CNTs in the released particles. The authors identified the protrusions from mechanically released fragments unambiguously as naked CNTs by chemically resolved microscopy. The protruding CNTs matched the morphology and diameter of original CNTs and formed a surface layer with length around 0.3 μm . The original CNTs had 10–50 nm outer diameter and 1–20 μm length. In the weathering experiments, protruding networks of CNTs remained after photochemical degradation of the matrix, and it took the worst case combinations of weathering plus high-shear wear to release free CNTs in the order of $\text{mg}/\text{m}^2/\text{year}$.

Schlagenhauf et al. [82] performed weathering studies on a CNT/epoxy nanocomposite by both UV exposure and immersion in water. In the UV exposure experiments, the authors did not observe the accumulated CNT layer on the degraded surface as in Nguyen et al. [77], Petersen et al. [78] and Wohlleben et al. [87, 88]. Instead, the results indicated that delamination occurred between the exposure times of 1000–1500 h and the top layer of the surface fell off the composite. The remaining surface was relatively smooth with low degrees of chemical degradation. The difference with other weathering studies might be due to the much larger thickness of the samples and lower relative humidity in Schlagenhauf et al. [82].

Kashiwagi et al. [57, 93, 94] performed a series of experiments to investigate the thermal degradation and flammability properties of CNT composites. Kashiwagi et al. [57] showed that MWCNTs enhanced the thermal stability of polypropylene (PP). They concluded that the flame retardant performance was achieved through the formation of a relatively uniform network-structured floccule layer covering the entire sample surface. This layer re-emitted much of the incident radiation back into the gas phase from its hot surface and thus reduced the transmitted flux to the receding PP layers below it, slowing the PP pyrolysis rate. This network-structured layer

was formed during cone calorimeter experiments below around 600 °C. Kashiwagi et al. [57] described the network-structured layer as partially oxidized CNTs embedded in an agglomerate composed of iron oxide primary particles. The iron was the catalyst for the used CNTs. Kashiwagi et al. [94] stated that the tubes in the network were more 'intertwined' and larger than those in the original sample. The tubes were also partially oxidized. The mass of the network layer was very close to the initial mass of carbon nanotubes in the original nanocomposite. Kashiwagi et al. [93] extended their studies to poly(methylmethacrylate) (PMMA), SWCNTs and carbon nanofibers and obtained similar results.

The formation of CNT network in the combustion residuals was confirmed in a number of studies of fire behaviors and flame retardants [95–99]. These studies covered different types of composite matrices such as polyamide 6 (PA6), silicone foams, polyethylene naphthalate (PEN), PP/wood flour and nanofillers including pristine CNTs, hydroxylated CNTs, carbon black, graphite and graphene.

In the recent years, several studies focusing on CNT release during thermal treatment of nanocomposites have been published. Bouillard et al. [68] used an acrylonitrile butadiene styrene (ABS) composite with 3 wt% of CNTs, combusted the sample in a furnace and collected released particles on TEM grids. The MWCNTs used for composite production had the mean outer diameter of 10–15 nm and length of 0.1–15 μm . They found that MWCNTs of about 12-nm diameter and 600-nm length were released to the air during combustion; these dimensions were very similar to those of the original MWCNTs. The released numbers were quite significant posing a possible sanitary risk in the case of accidental scenarios. The authors observed several isolated (not in bundle) CNT fibers, as well as CNT fibers in bundles. These CNTs had the catalysts remaining attached to their ends and had shapes and chemical speciation similar to those of the original MWCNTs.

Schlagenhauf et al. [83] thermally decomposed MWCNT/epoxy composites in a tube furnace under air or nitrogen atmosphere. The temperature was gradually increased and a large number of airborne particles were released at temperatures below 300 °C when air was used. The usage of a thermal denuder showed that only 0.01 wt% of the released mass consisted of non-volatile particles. A release of free-standing MWCNTs was not observed.

Sotiriou et al. [85, 86] setup a system to decompose composites in tube furnaces and characterize the released aerosols. In the experiments of a polyurethane (PU)/MWCNT composite at 500 and 800 °C, they found no CNTs in the released aerosols. Residual ash existed only

at 500 °C and numerous CNT protrusions were observed from the surface of the ash. The authors inferred that the CNTs were intact because 500 °C was below the expected oxidization temperature for MWCNTs. Singh et al. [84] extended the experiments to CNT composites with polypropylene and polycarbonate matrices and found no CNTs in the released aerosols as in previous studies.

Vilar et al. [100] investigated calcination as a method to recover nanomaterials from nanocomposites. They used PA6 composites containing pristine MWCNTs or MWCNTs modified to be more compatible with PA6. The calcination conditions were 410 °C during 3 h 30 min. The temperature was set with the consideration that the polymer was burned and CNTs did not suffer any change. Calcinated nanomaterials were characterized by FT-IR and TGA and neither of the two analyses showed any difference between the nanomaterials before and after calcinations. However, electron microscopy showed that the MWCNTs recovered from composites were with a small amount of attached polymer.

Discussion

The studies on release of CNTs from nanocomposites mostly focused on whether the CNTs were released; information on the transformation of the physical and chemical properties of the released CNTs is sparse. From the analytical point of view, it is difficult to obtain accurate measurement of the properties of released CNTs when they are scattered or embedded in fragments of the matrix, therefore to prove the change of properties. The number of studies showing release of free standing CNTs without any matrix material is very limited, and amount of the free CNTs usually did not allow sophisticated analysis.

The toxicity of the released CNTs together with the fragmented matrix particles can be different from the pristine CNTs, therefore, toxicity tests are important to understand the health impact of the particles released from composites, especially in the cases where CNT release is detected. These tests are different from the mechanistic toxicity study of the pristine material, as they are designed to answer practical questions related to real world applications. The toxicity of the released particles by mechanical abrasion from CNT-nanocomposites has been investigated by several in vitro and in vivo studies. Wohlleben et al. [87, 88], Ging et al. [92] and Saber et al. [101] did not detect release of the CNTs and found no additional toxic effect caused by the added nanofillers in comparison with the neat matrix materials. Schlagenhauf et al. [81, 82] observed protruding CNTs from matrix particles and some free standing CNTs, however, the toxicity tests revealed that the abraded particles did not induce any acute cytotoxic effects. Ging et al. [92] and

Schlagenhauf et al. [81, 82] all observed toxic effects of the virgin CNTs, but their no-effect observation from the released particles demonstrated that the health impact assessment needs to take the transformation during the release into account.

CNTs play distinct roles in the different scenarios where they are exposed to high temperatures. In the applications using CNTs as flame retardants, the CNTs are expected to form a protective network and impede the fire. In incineration plants, the ideal outcome is to decompose CNTs [14, 102] and to avoid exposure of CNTs to human. In recovery operations, the temperature needs to be high enough to burn off the polymer matrix but below the point where the CNTs are oxidized. The temperature dependence of the CNT's oxidative stability is obviously critical. The temperature in an accidental fire is not controllable. Using the more thermally stable CNTs in the retardant applications befits the "safe by design" concept. The temperatures in incineration and recovery operations should be set according to the goals. Different types of CNTs have different diameters and defects, thus variable thermal properties. The fact that the CNTs are embedded in the polymer matrix and interaction of CNTs with the molten matrix further complicate the situation. In case the CNTs and their agglomerates are liberated from the matrix, their mobility and transportation may be complex in the flue gas and thermal plume [103]. More studies for the thermal behavior of different types of CNT composites are needed to address the topic. Harper et al. [14] considered the release of CNTs from waste incineration to be low given CNTs can be combusted; even if the CNTs survive the incineration, they may end up in bottom ash or fly ash captured by the filters, and eventually in the landfill.

Summary

We reviewed studies on release of fibrous fillers in composites and identified a number of scenarios where the physical and chemical properties of the released fibers may be altered. A summary of the possible transformation of the released fibrous fillers is shown in Table 1.

The most important release scenario for asbestos now is the end-of-the-life treatment of asbestos-containing materials. A number of studies showed that thermal treatment transforms both raw asbestos samples and asbestos-containing construction materials into non-hazardous phase when the temperature was above about 1000 °C. The stability and fate of asbestos in real incineration operations with heterogeneous temperature and airflow still need further investigation.

Carbon fibers usually possess diameters in the range of 5–10 µm and are not considered respirable. However, mechanical operations on their composites can

Table 1 Summary of the possible transformation of the released fibrous fillers from composites

Fibrous filler	Composite matrix	Release process	Transformation of released fibers	References
Asbestos	Cement; other construction materials	Thermal treatment of about 1000 °C and above	Asbestos were transformed to non-hazardous silicate phase	Gualtieri and Tartaglia [20], Gualtieri et al. [3, 27], Kusiorowski et al. [30], Yamamoto et al. [31]
Different carbon fibers	Epoxy	Hammer mill, dry and wet cutting, grinding, drilling	Fibers split along the axis from the original fibers were released. They had smaller diameters and might be respirable	Holt and Horne [39], Mazumder et al. [40], Bello et al. [37, 46]
Different carbon fibers	Epoxy	Heating to 400 and 850 °C	At 850 °C, fibers underwent fragmentation during oxidation, and lost crystalline property	Mazumder et al. [40]
PAN-based carbon fibers	Polymer cable	Tensile stress test to cable failure	Respirable fibers split along the fiber axis from the original fibers were released	Schlagenhauf et al. [41]
CNTs	Epoxy	Sanding	CNTs protruding from fragments of matrix material had similar diameters as the original ones.	Cena and Peters [69], Huang et al. [56]
CNTs	Epoxy	Abrasion	Free standing single and agglomerated CNTs were released and had average length (304 nm) shorter than the CNTs in the matrix (0.7 µm)	Schlagenhauf et al. [80]
CNTs	Epoxy; POM; TPU	UV exposure	Surface of the sample was covered by a network of CNTs and their integrity was not damaged	Nguyen et al. [77], Petersen et al. [78], Wohleben et al. [87, 88]
CNTs	Epoxy	Combination of sanding and weathering	Protruding CNTs had the same diameter as the original ones and formed a surface layer with length around 0.3 µm, shorter than the original length of 1–20 µm	Hirth et al. [73]
CNTs; carbon nanofibers	PP; PMMA	Fire test	A protective CNT network was formed in the combustion residuals. The tubes in the network were more 'intertwined' and larger than the original ones. The tubes were partially oxidized. Iron catalysts were also oxidized	Kashiwagi et al. [57, 93, 94]
CNTs	ABS	Combustion	Free isolated and bundled CNTs were released to the air with dimensions similar to the original MWCNTs	Bouillard et al. [68]
CNTs	PU	Thermal decomposition	CNT protrusions were observed from the surface of the ash and CNTs were assumed to be intact	Sotiriou et al. [85, 86]
Pristine and compatibilized CNTs	PA6	Calcination	Recovered CNTs showed no difference from the original ones by FT-IR or TGA analysis but showed a small amount of attached polymer in TEM	Vilar et al. [100]

ABS acrylonitrile butadiene styrene, FT-IR Fourier transform infrared spectroscopy, PA6 polyamide 6, PMMA poly(methylmethacrylate), POM polyoxymethylene, PP polypropylene, PU polyurethane, TGA thermal gravimetric analysis, TPU thermoplastic polyurethane

cause release of not only fibers with the same diameter as the embedded fibers, but also smaller respirable fibers caused by splitting of fibers along the axis. For nanomaterials, the weight percentage in composites lies in the low single digit range causing no or only a low number of released fibers when machined. However, carbon fibers can make up more than 50% of the volume of composites, therefore the released amount of fibrous particles can be substantial. The health impact could be concerning if the split carbon fibers with respirable sizes are present.

For CNT composites exposed to mechanical forces, Schlagenhauf et al. [13] concluded that the expected release scenarios include free standing CNTs, agglomerated CNTs, and particles with- and without protruding CNTs. Due to the nature of the release caused by mechanical forces, the released CNTs are possibly on average shorter than the CNTs in the composite. In all the reviewed studies, the diameters of the released CNTs were in the same range as the original CNTs used in the composites. Normally during the release processes, the CNT concentration in air is too low for them to agglomerate. This means that the finding of released CNT agglomerates can indicate a poor distribution of the CNTs in the investigated nanocomposite. The possible shorter length of the released CNTs indicates less toxicity to pulmonary cells and generally less persistent in the lung [8, 63]. The release process probably does not increase the agglomeration degree of the CNTs, therefore possibly not causing increased toxicity associated with agglomerates [104, 105]. The toxicity studies so far found no additional toxic effect caused by the added CNTs in comparison with the neat matrix materials; the observation may be mainly due to the low amount of released CNTs.

UV exposure can degrade the matrix and expose a layer of CNTs on the sample surface. Fire or thermal treatment can decompose the matrix and leave a network of CNTs in the residuals. Previous studies indicated that these CNT network structures had good mechanical strength and the CNT integrity was generally not damaged. CNTs were not easily liberated from these intertwined network structures. However, combined stresses such as weathering followed by additional shaking, abrasion, runoff water, etc., may cause CNTs release [14]. CNTs released by thermal treatment may be partially oxidized. Some studies showed that the CNTs oxidized by strong acid were more toxic than pristine CNTs [106, 107]. More studies on the thermally oxidized CNTs are needed.

The transformation scenarios of the released fibers from composites lead to different changes of the potential health impacts of the fibers. Thermal treatment can destroy the fibrous structure of asbestos and transform asbestos into non-hazardous phase. Mechanical operations and heating at certain temperatures may cause

release of carbon fibers split along the fiber axis. The smaller diameters increase the deposition probability of the split carbon fibers in the gas exchange regions of the lung. The dose of such fibers may be high in occupational settings given the high volume fraction of carbon fibers in composites. Therefore the health impact of the embedded carbon fibers is probably increased following the transformation in the release process. A number of studies on the CNT release by mechanical operations, weathering and thermal treatment demonstrated that the released CNTs had similar diameters as the original ones, and the fiber integrity was largely undamaged. On the other hand, the released CNTs were on average shorter than the CNTs in the composite, therefore they would be easier to be cleared by the macrophage cells and less biopersistent. In summary, the released CNTs are possibly less harmful than the virgin CNTs.

Authors' contributions

JW developed the framework of the review and wrote the article; LS contributed to the reviews on carbon fibers and carbon nanotubes; AS contributed to the reviews on asbestos. All authors read and approved the final manuscript.

Author details

¹ Institute of Environmental Engineering, ETH Zurich, 8093 Zurich, Switzerland. ² Advanced Analytical Technologies, Empa, Ueberlandstrasse 129, 8600 Dübendorf, Switzerland.

Acknowledgements

The financial support of the Swiss National Science Foundation is acknowledged.

Competing interests

The authors declare that they have no competing interests.

Ethics approval and consent to participate

Results from several previous in vitro and in vivo studies are reviewed in this work but no new data are collected from biological tests in this work. Therefore, ethics approval and consent to participate are not needed.

Funding

This study was financed by the Swiss National Science Foundation (NFP 64), "Evaluation platform for safety and environment risks of carbon nanotube reinforced nanocomposites", 406440_131286.

Received: 15 November 2016 Accepted: 10 February 2017

Published online: 20 February 2017

References

1. Campbell FC. Structural composite materials. Almere: ASM International; 2010. p. 2010.
2. Gilmore C. Materials science and engineering properties. Scarborough: Nelson Education; 2014.
3. Gualtieri AF, Gualtieri ML, Meneghini C. In situ high-temperature synchrotron powder diffraction study of the thermal decomposition of cement-asbestos. *Powder Diffr.* 2008;23(4):323–8.
4. Robertson J. Realistic applications of CNTs. *Mater Today.* 2004;7:46–52.
5. Donaldson K, Aitken R, Tran L, Stone V, Duffin R, Forrest G, Alexander A. Carbon nanotubes: a review of their properties in relation to pulmonary toxicology and workplace safety. *Toxicol Sci.* 2006;92:5–22.
6. Petri-Fink A, Rothen-Rutishauser B, Clift MJ. Nanofibers: friend or foe? *Fibers.* 2016;4(3):25. doi:10.3390/fib4030025.

7. Wick P, Clift MJD, Rosslein M, Rothen-Rutishauser B. A brief summary of carbon nanotubes science and technology: a health and safety perspective. *ChemSusChem*. 2011;4:905–11.
8. Warheit DB, Hart GA, Hesterberg TW, et al. Potential pulmonary effects of man-made organic fiber (MMOF) dusts. *Crit Rev Toxicol*. 2001;31(6):697–736.
9. Donaldson K, Murphy FA, Duffin R, Poland CA. Asbestos, carbon nanotubes and the pleural mesothelium: a review of the hypothesis regarding the role of long fibre retention in the parietal pleura, inflammation and mesothelioma. *Part Fibre Toxicol*. 2010;7(1):5.
10. Hesterberg TW, Hart GA. Synthetic vitreous fibers: a review of toxicology research and its impact on hazard classification. *CRC Crit Rev Toxicol*. 2001;31(1):1–53.
11. Stanton MF, Wrench C. Mechanisms of mesothelioma induction with asbestos and fibrous glass. *J Natl Cancer Inst*. 1972;48(3):797–821.
12. WHO. Reference methods for measuring man-made mineral fibres (MMMF). Prepared by WHO/EURO Technical Committee for Evaluating MMMF. Copenhagen: World Health Organization; 1985.
13. Schlagenhauf L, Nüesch F, Wang J. Release of carbon nanotubes from polymer nanocomposites. *Fibers*. 2014;2(2):108–27.
14. Harper S, Wohlleben W, Doa M, Nowack B, Clancy S, Canady R, Maynard A. Measuring nanomaterial release from carbon nanotube composites: review of the state of the science. *Journal of Physics: Conference Series* (Vol. 617, No. 1, p. 012026). IOP Publishing; 2015.
15. Alleman JE, Mossman BT. Asbestos revisited. *Sci Am*. 1997;277:54–7.
16. Nishikawa K, Takahashi K, Karjalainen A, Wen CP, Furuya S, Hoshuyama T, Todoroki M, Kiyomoto Y, Wilson D, Higashi T, Ohtaki M, Pan GW, Wagner G. Recent mortality from pleural mesothelioma, historical patterns of asbestos use, and adoption of bans: a global assessment. *Environ Health Persp*. 2008;116(12):1675–80.
17. WHO. Elimination of asbestos-related diseases. Geneva: World Health Organization; 2006.
18. Gidarakos E, Anastasiadou K, Koumantakis E, Nikolaos S. Investigative studies for the use of an inactive asbestos mine as a disposal site for asbestos wastes. *J Hazard Mater*. 2008;153(3):955–65.
19. Boccaccini DN, Leonelli C, Rivasi MR, Romagnoli M, Veronesi P, Pellacani GC, Boccaccini AR. Recycling of microwave inertised asbestos containing waste in refractory materials. *J Eur Ceram Soc*. 2007;27:1855–8.
20. Gualtieri AF, Tartaglia A. Thermal decomposition of asbestos and recycling in traditional ceramics. *J Eur Ceram Soc*. 2000;20:1409–18.
21. NIOSH Method 7400 for the determination of asbestos and other fibers by phase contrast microscopy (PCM); 1994.
22. NIOSH Method 7402 for the determination of asbestos by transmission electron microscopy (TEM); 1994.
23. NIOSH Method 9000 for the determination of asbestos and chrysotile by X-ray diffraction (XRD); 1994.
24. NIOSH Method 9002 for the Determination of asbestos (bulk) by polarized light microscopy (PLM); 1994.
25. CARB Method 435 for the determination of asbestos content of serpentine aggregate; 1991.
26. ISO 10312, Ambient air—determination of asbestos fibres—direct-transfer transmission electron microscopy method; 1995.
27. Gualtieri AF, Gualtieri ML, Tonelli M. In situ ESEM study of the thermal decomposition of chrysotile asbestos in view of safe recycling of the transformation product. *J Hazard Mater*. 2008;156:260–6.
28. Zaremba T, Krzakala A, Piotrowski J, Garczorz D. Study on the thermal decomposition of chrysotile asbestos. *J Therm Anal Calorim*. 2010;101:479–85.
29. Kusiorowski R, Zaremba T, Piotrowski J, Adamek J. Thermal decomposition of different types of asbestos. *J Therm Anal Calorim*. 2012;109(2):693–704.
30. Kusiorowski R, Zaremba T, Piotrowski J, Gerle A. Thermal decomposition of asbestos-containing materials. *J Therm Anal Calorim*. 2013;113(1):179–88.
31. Yamamoto T, Kida A, Noma Y, Terazono A, Sakai S-I. Development of a testing method for asbestos fibers in treated materials of asbestos containing wastes by transmission electron microscopy. *Waste Manag*. 2014;34:536–41.
32. European Union Directive 2000/76/EC of the European Parliament and of the Council on the incineration of waste. 4 December 2000.
33. BAFU. Fate and stability of asbestos fibres in municipal solid waste incineration plants (MSWI)—incineration experiment, personal communication from the Swiss Federal Office for the Environment (BAFU); 2014.
34. ACS. American Chemical Society National Historic Chemical Landmarks. High performance carbon fibers. 2003. <http://www.acs.org/content/acs/en/education/whatischemistry/landmarks/carbonfibers.html>. Accessed 1 Nov 2016.
35. Piñero-Hernandez R, Dodds C, Hyde J, García-Serna J, Poliakov M, Lester E, Cocero MJ, Kingman S, Pickering S, Wong KH. Chemical recycling of carbon fibre reinforced composites in nearcritical and supercritical water. *Compos A Appl Sci Manuf*. 2008;39(3):454–61.
36. Sun H, Guo G, Memon SA, Xu W, Zhang Q, Zhu JH, Xing F. Recycling of carbon fibers from carbon fiber reinforced polymer using electrochemical method. *Compos A Appl Sci Manuf*. 2015;78:10–7.
37. Bello D, Wardle BL, Yamamoto N, et al. Exposure to nanoscale particles and fibers during machining of hybrid advanced composites containing carbon nanotubes. *J Nanopart Res*. 2009;11(1):231–49.
38. Boatman ES, Covert D, Kalman D, Luchtel D, Omenn GS. Physical, morphological, and chemical studies of dusts derived from the machining of composite-epoxy materials. *Environ Res*. 1988;45(2):242–55.
39. Holt PF, Horne M. Dust from carbon fibre. *Environ Res*. 1978;17:276–83.
40. Mazumder MK, Chang RJ, Bond RL. Aerodynamic and morphological properties of carbon-fiber aerosols. *Aerosol Sci Technol*. 1982;1(4):427–40.
41. Schlagenhauf L, Kuo YY, Michel S, Terrasi G, Wang J. Exposure assessment of a high-energy tensile test with large carbon fiber reinforced polymer cables. *J Occup Environ Hyg*. 2015;12(8):D178–83.
42. Warheit DB, Hansen JF, Carakostas MC, Hartsky MA. Acute inhalation toxicity studies in rats with a respirable-sized experimental carbon fiber: pulmonary biochemical and cellular effects. *Ann Occup Hyg*. 1995;18(1):769–76.
43. Martin TR, Meyer SW, Luchtel DR. An evaluation of the toxicity of carbon fiber composites for lung cells in vitro and in vivo. *Environ Res*. 1989;49:246–61.
44. Henry W, Melton C, Schmidt E. Method for measuring carbon fiber emissions from stationary sources. Washington, D.C.: US Environmental Protection Agency; 1982.
45. Gieseke J, Reif R, Schmidt E. Characterization of carbon fiber emissions from current and projected activities for the manufacture and disposal of carbon fiber products. US Environmental Protection Agency (EPA), EPA-600/3-84-021; 1984.
46. Bello D, Wardle BL, Zhang J, Yamamoto N, Santeufemio C, Hallock M, Virji MA. Characterization of exposures to nanoscale particles and fibers during solid core drilling of hybrid carbon nanotube advanced composites. *Int J Occup Environ Health*. 2010;16:434–50.
47. Diefendorf RJ, Tokarsky E. High-performance carbon fibers. *Polym Eng Sci*. 1975;15(3):150–9.
48. Endo M, Dresselhaus MS. Carbon fibers and carbon nanotubes. 2003. <http://web.mit.edu/tinytech/Nanostructures/Spring2003/MDresselhaus/i789.pdf>. Accessed 4 Nov 2016.
49. Bacon R. Filamentary Graphite and method for producing the same, US Patent # 2 957 756; 1960.
50. Ajayan PM, Zhou OZ. Applications of carbon nanotubes. In *Carbon nanotubes*. Berlin: Springer; 2001. p. 391–425.
51. De Volder MF, Tawfik SH, Baughman RH, Hart AJ. Carbon nanotubes: present and future commercial applications. *Science*. 2013;339:535–9.
52. Coleman JN, Khan U, Gun'ko YK. Mechanical reinforcement of polymers using carbon nanotubes. *Adv Mater*. 2006;18:689–706.
53. Sun LY, Gibson RF, Gordaninejad F, Suhr J. Energy absorption capability of nanocomposites: a review. *Compos Sci Technol*. 2009;69:2392–409.
54. Giraldo LF, Brostow W, Devaux E, Lopez BL, Perez LD. Scratch and wear resistance of polyamide 6 reinforced with multiwall carbon nanotubes. *J Nanosci Nanotechnol*. 2008;8:1–8.
55. Hollertz R, Chatterjee S, Gutmann H, Geiger T, Nueesch FA, Chu BTT. Improvement of toughness and electrical properties of epoxy composites with carbon nanotubes prepared by industrially relevant processes. *Nanotechnology*. 2011;22:12570.
56. Huang H, Liu CTH, Wu Y, Fan S. Aligned carbon nanotube composite films for thermal management. *Adv Mater*. 2005;17:1652–6.

57. Kashiwagi T, Grulke E, Hilding J, Harris R, Awad W, Douglas J. Thermal degradation and flammability properties of poly(propylene)/carbon nanotube composites. *Macromol Rapid Commun*. 2002;23:761–5.
58. Breuer O, Sundararaj U. Big returns from small fibers: a review of polymer/carbon nanotube composites. *Polym Compos*. 2004;25:630–45.
59. Du J, Wang S, You H, Zhao X. Understanding the toxicity of carbon nanotubes in the environment is crucial to the control of nanomaterials in producing and processing and the assessment of health risk for human: a review. *Environ Toxicol Pharmacol*. 2013;36:451–62.
60. Helland A, Wick P, Koehler A, Schmid K, Som C. Reviewing the environmental and human health knowledge base of carbon nanotubes. *Environ Health Perspect*. 2007;115:1125–31.
61. Ma-Hock L, Treumann S, Strauss V, Brill S, Luizi F, Mertler M, Wiench K, Gamer AO, van Ravenzwaay B, Landsiedel R. Inhalation Toxicity of multiwall carbon nanotubes in rats exposed for 3 months. *Toxicol Sci*. 2009;112:468–81.
62. Muller L, Riediker M, Wick P, Mohr M, Gehr P, Rothen-Rutishauser B. Oxidative stress and inflammation response after nanoparticle exposure: differences between human lung cell monocultures and an advanced three-dimensional model of the human epithelial airways. *J R Soc Interface*. 2010;7:S27–40.
63. Murphy FA, Poland CA, Duffin R, Donaldson K. Length dependent pleural inflammation and parietal pleural responses after deposition of carbon nanotubes in the pulmonary airspaces of mice. *Nanotoxicology*. 2013;7:1157–67.
64. Palomaki J, Valimaki E, Sund J, Vippola M, Clausen PA, Jensen KA, Savolainen K, Matikainen S, Alenius H. Long, Needle-like carbon nanotubes and asbestos activate the NLRP3 inflammasome through a similar mechanism. *ACS Nano*. 2011;5:6861–70.
65. Thurnherr T, Brandenberger C, Fischer K, Diener L, Manser P, Maeder-Althaus X, Kaiser JP, Krug HF, Rothen-Rutishauser B, Wick P. A comparison of acute and long-term effects of industrial multiwalled carbon nanotubes on human lung and immune cells in vitro. *Toxicol Lett*. 2011;200:176–86.
66. Porter DW, Hubbs AF, Chen BT, et al. Acute pulmonary dose-responses to inhaled multi-walled carbon nanotubes. *Nanotoxicology*. 2013;7:1179–94.
67. Pulskamp K, Diabate S, Krug HF. Carbon nanotubes show no sign of acute toxicity but induce intracellular reactive oxygen species in dependence on contaminants. *Toxicol Lett*. 2007;168:58–74.
68. Bouillard JX, R'Mili B, Moranviller D, Vignes A, Le Bihan O, Ustache A, Bomfim JA, Frejafon E. Nanosafety by design: risks from nanocomposite/nanowaste combustion. *J Nanopart Res*. 2013;15(4):1–11.
69. Cena LG, Peters TM. Characterization and control of airborne particles emitted during production of epoxy/carbon nanotube nanocomposites. *J Occup Environ Hyg*. 2011;8:86–92.
70. Duncan TV. Release of engineered nanomaterials from polymer nanocomposites: the effect of matrix degradation. *ACS Appl Mater Interfaces*. 2014;7(1):20–39.
71. Golanski L, Guiot A, Pras M, Malarde M, Tardif F. Release-ability of nano fillers from different nanomaterials (toward the acceptability of nanoproduct). *J Nanopart Res*. 2012;14:962. doi:10.1007/s11051-012-0962-x.
72. Hellmann A, Schmidt K, Ripperger S, Berges M. Release of ultrafine dusts during the machining of nanocomposites. *Gefahrst Reinhalt Luft*. 2012;72:473–6.
73. Hirth S, Cena L, Cox G, Tomović Ž, Peters T, Wohlleben W. Scenarios and methods that induce protruding or released CNTs after degradation of nanocomposite materials. *J Nanopart Res*. 2013;15(4):1–15.
74. Huang G, Park J, Cena L, Shelton B, Peters T. Evaluation of airborne particle emissions from commercial products containing carbon nanotubes. *J Nanopart Res*. 2012;14:1231.
75. Kingston C, Zepp R, Andraday A, Boverhof D, Fehir R, Hawkins D, Roberts J, Sayre P, Shelton B, Sultan Y, Vejins V, Wohlleben W. Release characteristics of selected carbon nanotube polymer composites. *Carbon*. 2014;68:33–57.
76. Methner M, Crawford C, Geraci C. Evaluation of the potential airborne release of carbon nanofibers during the preparation, grinding, and cutting of epoxy-based nanocomposite material. *J Occup Environ Hyg*. 2012;9:308–18.
77. Nguyen T, Pellegrin B, Bernard C, Gu X, Gorham JM, Stutzman P, Stanley D, Shapiro A, Byrd E, Hettenhouser R, Chin J. Fate of nanoparticles during life cycle of polymer nanocomposites. *J Phys Conf Series*. 2011;304:012060.
78. Petersen EJ, Lam T, Gorham JM, Scott KC, Long CJ, Stanley D, Sharma R, Alexander Liddle J, Pellegrin B, Nguyen T. Methods to assess the impact of UV irradiation on the surface chemistry and structure of multiwall carbon nanotube epoxy nanocomposites. *Carbon*. 2014;69:194–205.
79. Rhiem S, Barthel AK, Meyer-Plath A, Hennig MP, Wachtendorf V, Sturm H, Schäffer A, Maes HM. Release of 14 C-labelled carbon nanotubes from polycarbonate composites. *Environ Pollut*. 2016;215:356–65.
80. Schlagenhauf L, Chu BTT, Buha J, Nüesch F, Wang J. Release of carbon nanotubes from an epoxy-based nanocomposite during an abrasion process. *Environ Sci Technol*. 2012;46:7366–72.
81. Schlagenhauf L, Buerki-Thurnherr T, Kuo Y-Y, Wichser A, Nüesch F, Wick P, Wang J. Carbon nanotubes released from an epoxy-based nanocomposite: quantification and particle toxicity. *Environ Sci Technol*. 2015;49(17):10616–23.
82. Schlagenhauf L, Kianfar B, Buerki-Thurnherr T, Kuo Y-Y, Wichser A, Nüesch F, Wick P, Wang J. Weathering of a carbon nanotube/epoxy nanocomposite under UV light and in water bath: impact on abraded particles. *Nanoscale*. 2015;7:18524–36.
83. Schlagenhauf L, Kuo Y-Y, Bahk YK, Nüesch F, Wang J. Decomposition and particle release of a carbon nanotube/epoxy nanocomposite at elevated temperatures. *J Nanopart Res*. 2015;17:440.
84. Singh D, Sotiriou GA, Zhang F, Mead J, Bello D, Wohlleben W, Demokritou P. End-of-life thermal decomposition of nano-enabled polymers: effect of nanofiller loading and polymer matrix on by-products. *Environ Sci: Nano*. 2016;3:1293–305.
85. Sotiriou GA, Singh D, Zhang F, Chalbot MCG, Spielman-Sun E, Hoering L, Kavours IG, Lowry GV, Wohlleben W, Demokritou P. Thermal decomposition of nano-enabled thermoplastics: possible environmental health and safety implications. *J Hazard Mater*. 2016;305:87–95.
86. Sotiriou GA, Singh D, Zhang F, Wohlleben W, Chalbot MCG, Kavours IG, Demokritou P. An integrated methodology for the assessment of environmental health implications during thermal decomposition of nano-enabled products. *Environ Sci: Nano*. 2015;2(3):262–72.
87. Wohlleben W, Brill S, Meier MW, Mertler M, Cox G, Hirth S, von Vacano B, Kavours IG, Treumann S, Wiench K, et al. On the Lifecycle of Nanocomposites: comparing released fragments and their in-vivo hazards from three release mechanisms and four nanocomposites. *Small*. 2011;7:2384–95.
88. Wohlleben W, Meier MW, Vogel S, Landsiedel R, Cox G, Hirth S, Tomovic Z. Elastic CNT-polyurethane nanocomposites: synthesis, performance and assessment of fragments released during use. *Nanoscale*. 2013;5:369–80.
89. Pang LS, Saxby JD, Chatfield SP. Thermogravimetric analysis of carbon nanotubes and nanoparticles. *J Phys Chem*. 1993;97(27):6941–2.
90. Bom D, Andrews R, Jacques D, Anthony J, Chen B, Meier MS, Selegue JP. Thermogravimetric analysis of the oxidation of multiwalled carbon nanotubes: evidence for the role of defect sites in carbon nanotube chemistry. *Nano Lett*. 2002;2(6):615–9.
91. Ogura I, Kotake M, Shigeta M, Uejima M, Saito K, Hashimoto N, Kishimoto A. Potential release of carbon nanotubes from their composites during grinding. *NanoSafe 2012: International conferences on safe production and use of nanomaterials*. Vol 429, No 012049. 2013.
92. Ging J, Tejerina-Anton R, Ramakrishnan G, Nielsen M, Murphy K, Gorham JM, Nguyen T, Orlov A. Development of a conceptual framework for evaluation of nanomaterials release from nanocomposites: environmental and toxicological implications. *Sci Total Environ*. 2014;473:9–19.
93. Kashiwagi T, Du F, Douglas JF, Winey KI, Harris RH, Shields JR. Nanoparticle networks reduce the flammability of polymer nanocomposites. *Nat Mater*. 2005;4(12):928–33.
94. Kashiwagi T, Grulke E, Hilding J, Groth K, Harris R, Butler K, Shields J, Douglas J. Thermal and flammability properties of polypropylene/carbon nanotube nanocomposites. *Polymer*. 2004;45(12):4227–39.
95. Ditttrich B, Wartig KA, Hofmann D, Mülhaupt R, Scharfel B. Carbon black, multiwall carbon nanotubes, expanded graphite and functionalized graphene flame retarded polypropylene nanocomposites. *Polym Adv Technol*. 2013;24(10):916–26.
96. Fu S, Song P, Yang H, Jin Y, Lu F, Ye J, Wu Q. Effects of carbon nanotubes and its functionalization on the thermal and flammability properties of polypropylene/wood flour composites. *J Mater Sci*. 2010;45(13):3520–8.

97. Kim JY, Park HS, Kim SH. Thermal decomposition behavior of carbon-nanotube-reinforced poly (ethylene 2, 6-naphthalate) nanocomposites. *J Appl Polym Sci*. 2009;113(3):2008–17.
98. Schartel B, Pötschke P, Knoll U, Abdel-Goad M. Fire behaviour of polyamide 6/multiwall carbon nanotube nanocomposites. *Eur Polymer J*. 2005;41(5):1061–70.
99. Verdejo R, Barroso-Bujans F, Rodríguez-Pérez MA, de Saja JA, Arroyo M, López-Manchado MA. Carbon nanotubes provide self-extinguishing grade to silicone-based foams. *J Mater Chem*. 2008;18(33):3933–9.
100. Vilar G, Fernández-Rosas E, Puentes V, Jamier V, Aubouy L, Vázquez-Campos S. Monitoring migration and transformation of nanomaterials in polymeric composites during accelerated aging. *Journal of Physics: Conference Series* (Vol. 429, No. 1, p. 012044). IOP Publishing; 2013.
101. Saber AT, Mortensen A, Szarek J, Koponen IK, Levin M, Jacobsen NR, Pozzebon ME, Mucelli SP, Rickerby DG, Kling K, Atluri R. Epoxy composite dusts with and without carbon nanotubes cause similar pulmonary responses, but differences in liver histology in mice following pulmonary deposition. *Part Fibre Toxicol*. 2016;13(1):37.
102. Mueller NC, Buha J, Wang J, Ulrich A, Nowack B. Modeling the flows of engineered nanomaterials during waste handling. *Environ Sci: Process Impacts*. 2013;15(1):251–9.
103. Wang J, Bahk YK, Chen S-C, Pui DYH. Characteristics of airborne fractal-like agglomerates of carbon nanotubes. *Carbon*. 2015;93:441–50.
104. Bruinink A, Wang J, Wick P. Effect of particle agglomeration in nanotoxicology. *Arch Toxicol*. 2015;89(5):659–75.
105. Wick P, Manser P, Limbach LK, et al. The degree and kind of agglomeration affect carbon nanotube cytotoxicity. *Toxicol Lett*. 2007;168:121–31.
106. Bottini M, Bruckner S, Nika K, Bottini N, Bellucci S, Magrini A, Bergamaschi A, Mustelin T. Multi-walled carbon nanotubes induce T lymphocyte apoptosis. *Toxicol Lett*. 2006;160(2):121–6.
107. Pietroiusti A, Massimiani M, Fenoglio I, Colonna M, Valentini F, Palleschi G, Camaioni A, Magrini A, Siracusa G, Bergamaschi A, Sgambato A. Low doses of pristine and oxidized single-wall carbon nanotubes affect mammalian embryonic development. *ACS Nano*. 2011;5(6):4624–33.

Submit your next manuscript to BioMed Central and we will help you at every step:

- We accept pre-submission inquiries
- Our selector tool helps you to find the most relevant journal
- We provide round the clock customer support
- Convenient online submission
- Thorough peer review
- Inclusion in PubMed and all major indexing services
- Maximum visibility for your research

Submit your manuscript at
www.biomedcentral.com/submit



RESEARCH

Open Access



Interaction of silver nanoparticles with algae and fish cells: a side by side comparison

Yang Yue^{1,2,4}, Xiaomei Li^{1,2}, Laura Sigg^{1,3,5}, Marc J-F Suter^{1,3}, Smitha Pillai^{1,3}, Renata Behra^{1,3*} and Kristin Schirmer^{1,2,3*}

Abstract

Background: Silver nanoparticles (AgNP) are widely applied and can, upon use, be released into the aquatic environment. This raises concerns about potential impacts of AgNP on aquatic organisms. We here present a side by side comparison of the interaction of AgNP with two contrasting cell types: algal cells, using the algae *Euglena gracilis* as model, and fish cells, a cell line originating from rainbow trout (*Oncorhynchus mykiss*) gill (RTgill-W1). The comparison is based on the AgNP behavior in exposure media, toxicity, uptake and interaction with proteins.

Results: (1) The composition of exposure media affected AgNP behavior and toxicity to algae and fish cells. (2) The toxicity of AgNP to algae was mediated by dissolved silver while nanoparticle specific effects in addition to dissolved silver contributed to the toxicity of AgNP to fish cells. (3) AgNP did not enter into algal cells; they only adsorbed onto the cell surface. In contrast, AgNP were taken up by fish cells via endocytic pathways. (4) AgNP can bind to both extra-cellular and intracellular proteins and inhibit enzyme activity.

Conclusion: Our results showed that fish cells take up AgNP in contrast to algal cells, where AgNP sorbed onto the cell surface, which indicates that the cell wall of algae is a barrier to particle uptake. This particle behaviour results in different responses to AgNP exposure in algae and fish cells. Yet, proteins from both cell types can be affected by AgNP exposure: for algae, extracellular proteins secreted from cells for, e.g., nutrient acquisition. For fish cells, intracellular and/or membrane-bound proteins, such as the Na⁺/K⁺-ATPase, are susceptible to AgNP binding and functional impairment.

Keywords: AgNP, *Euglena gracilis*, RTgill-W1 cell line, Nanoparticle uptake, Nanoparticle toxicity, Nanoparticle-protein interactions

Background

Owing to their unique antimicrobial properties, silver nanoparticles (AgNP) are among the most widely used engineered nanoparticles in a variety of consumer products and medical applications, such as textiles and paints. With washing, rain and through other routes, these nanoparticles can be released into the environment, especially into the aquatic environment [1]. This raises concern about potential adverse effects in aquatic

organisms. On this background, the toxicity of AgNP to aquatic organisms has been tested on a variety of organisms, ranging from bacteria, to plants, fungi, algae, invertebrates and fish [2–4]. However, with few exceptions [5, 6], most studies did not clearly attribute toxicity to either direct effects of AgNP or to indirect effects of dissolved silver, which includes all the silver species in oxidized state Ag(I) in aqueous solution, such as Ag⁺, AgCl_n (aq) and AgOH (aq), stemming from AgNP.

Among aquatic organisms, algae and fish are two important models. As autotrophic organisms, algae are primary producers, i.e. they fix CO₂ to produce oxygen in the presence of light. They are at the base of the food

*Correspondence: renata.behra@eawag.ch; kristin.schirmer@eawag.ch

¹ Department of Environmental Toxicology, Eawag, Swiss Federal Institute of Aquatic Science and Technology, 8600 Dübendorf, Switzerland
Full list of author information is available at the end of the article

chain, serving as food to, e.g. water flea but also fish. Microalgae are single cell organisms surrounded by an inner plasma membrane and an outer semi-permeable cell wall of various compositions. The pores in such cell walls have a size estimated to be 5–20 nm. It helps the algae to maintain integrity and constitutes a primary site for interaction with the surrounding environment [7]. Algae connect with their environment by releasing, e.g. digestive enzymes, for nutrient acquisition. Whether algae have sophisticated mechanisms of particle uptake, such as via endocytosis (see below), is still a matter of debate. Accordingly, internalization of nanoparticles in algae was suggested in only a few studies [8, 9]. There was no evidence of nanoparticle uptake into algae in many other studies using electron microscope imaging and/or analysis of internalized metal in cells [10–14]. These findings emphasize the role of the algal surface as a potential barrier against nanoparticle entry into the cells, with the limitation likely being the pore size in the cell wall.

In contrast to microalgae, fish are heterotrophic, multiple organ- and tissue-based organisms. Fish are at a higher trophic level than algae but depend on the oxygen that algae and other autotrophic organisms produce. Depending on the species, fish can be consumers of algae or of other heterotrophs. With respect to environmental exposure to chemicals or nanoparticles, the fish gill is an important interface due to its large surface. The gill affords gas exchange between the external water environment and internal environment of the organism. In this exchange process, other substances, like metal nanoparticles and organic compounds, can interact with fish gill cells and eventually pass into the blood stream. Therefore, the fish gill can be considered a target of fish-nanoparticle interactions. Accordingly, AgNP were found to be most highly concentrated within gill and liver tissue of rainbow trout (*Oncorhynchus mykiss*) after a 10-day exposure [15]. In contrast to algae cells, fish gill cells, like all animal cells, are cell wall-free. Several kinds of endocytic pathways were proposed for nanoparticle incorporation into animal cells: clathrin-mediated endocytosis, caveolae-mediated endocytosis, macropinocytosis and phagocytosis [14, 16]. Once the vesicles carrying nanoparticles are internalized and detach from the plasma membrane, the vesicles are sorted and transported to different endocytic compartments. By these processes, nanoparticles are delivered to other subcellular compartments in endocytic pathways, from early endosome and multi-vesicular bodies to late endosomes and lysosomes [17].

Independent of the mechanism of particle uptake, nanoparticles tend to bind molecules from the surrounding environment owing to their big surface-to-mass ratio. During nanoparticle interaction with cells, proteins are

an important class of biomolecules that are prone to binding to nanoparticles, leading to a protein corona [18, 19]. With regard to extracellular proteins, such as the digestive proteins excreted by algae and bacteria, a so-called “eco-corona” can form [20, 21]. Intracellular proteins, on the other hand, can bind to particles upon uptake into cells. With the binding to nanoparticles, the properties and functions of proteins can change compared to unbound proteins. Thus, it is also important to understand to what extent nanoparticle-protein complexes impact on the properties of the proteins. Studies on the nanoparticle-protein interactions initially focused on single proteins. For example, Wigginton [22] found that AgNP inhibited tryptophanase (TNase) activity in the interaction with *E. coli* proteins and a dose-dependent inhibition of enzyme activity was observed for the incubation of citrate-coated AgNP with firefly luciferase [23]. In contrast to single protein-nanoparticle interactions, only few studies have thus far focused on identifying proteins that bind out of a complex mixture, especially in an intact intracellular environment [24, 25]. Such studies not only help identify the proteins most susceptible to particle binding but can also guide future research on single protein-particle interactions.

In order to shed light on the detailed mechanisms of interaction between AgNP and cells of algae and fish, we explored different aspects of AgNP-cell interactions, spanning AgNP behavior in exposure media, toxicity to cells, uptake and interaction with proteins. We aimed to critically compare the interaction of AgNP with contrasting cell types belonging to autotrophic vs. heterotrophic organisms in order to support a rational assessment of risks based on our previous studies [26–29]. A species of algae, *Euglena gracilis*, and a fish gill cell line, RTgill-W1 [30], originating from rainbow trout (*Oncorhynchus mykiss*), were selected to represent an autotrophic and a heterotrophic aquatic cellular system. The *Euglena gracilis* has no rigid cell wall but a flexible glycoprotein-containing pellicle, which aligns on the surface in longitudinal articulated stripes [31]. It was selected on purpose because nanoparticle uptake was thought to more likely occur in such an algae compared to one with a rigid cell wall. The RTgill-W1 cell line can survive in a simplified exposure medium, which provides the possibility to expose cells in medium that more closely mimics the aqueous environment a fish gill would face [32, 33]. Both algae and fish gill cell exposures were performed in minimal media supporting cell survival but not proliferation, in order to provide better controllable exposure and effect assessment for mechanistic studies. Here we focus on the comparative aspects of the outcome of our research. Unless noted otherwise, we will refer to *E.*

gracilis as “algal cells” and to the RTgill-W1 fish gill cell line as “fish cells”.

Results and discussion

The composition of exposure media significantly influences AgNP behavior

The size, zeta potential and dissolution of AgNP were tested over time in exposure media for algae and fish cells (Table 1). To avoid silver complexation, only 10 mM 3-morpholinopropanesulfonic acid (MOPS, pH 7.5) was used as exposure medium in algae experiments [26]. In the stock solution, the initial Z-average size and zeta potential of AgNP were 19.4 nm and −30 mV, respectively. AgNP were stable in this medium with an average size of 38–73 nm and a zeta potential of −23 to −28 mV up to 4 h of incubation [26]. For the fish cells, three kinds of exposure media were selected: L-15/ex, a regular, high ionic strength and high chloride cell culture medium based on Leibovitz’ 15 (L-15) [32, 34]; L-15/ex w/o Cl, a medium without chloride to avoid the formation of AgCl and study the role of chloride in silver ion and AgNP toxicity; and d-L-15/ex, a low ionic strength medium that more closely mimics fresh-water [27]. The AgNP moderately agglomerated (average size: 200–500 nm; Zeta potential: −15 mV) in L-15/ex medium. In L-15/ex w/o Cl medium, AgNP strongly agglomerated with an average size of 1000–1750 nm and a zeta potential of −10 mV. In d-L-15/ex medium, AgNP dispersed very well (average size: 40–100 nm; Zeta potential: −20 mV). Even though the size of AgNP increased up to 1750 nm, we found that large size AgNP were due to agglomeration [27], which is a reversible process and AgNP can easily be dispersed again [35]. The UV–Vis absorbance of AgNP in exposure media confirmed the different behavior of AgNP in the different media [26, 27]. Transmission electron microscopy (TEM) images of fish cells showed that single or slightly agglomerated AgNP were located in endosomes and lysosomes in fish cells, which indicates that fish cells took up AgNP in nanoscale [28].

The dissolution of AgNP, expressed as percentage of free to total silver, was comparable in MOPS and L-15/ex (~1.8%); dissolution was somewhat lower in L-15/ex w/o Cl and d-L-15/ex medium (~0.5%). Depending on the applied concentrations, this amounts to dissolved silver in the range of 1 nM to 2 μM (assuming 1–2% dissolution in 0.1–100 μM AgNP suspension). Upon contact with algae or fish cells, the uptake of dissolved silver shifts the AgNP/silver ion equilibrium and more silver ions are released. Furthermore, previous work reported that AgNP accumulated in mammalian cell endosomes and lysosomes displayed higher dissolution in these acidic environments than in a neutral environment [17, 36]. Therefore, we expect significant dissolution of AgNP in this process and used AgNO₃ as a dissolved silver control throughout.

The diverse behavior of AgNP in the different exposure media demonstrates the importance of accounting for nanoparticle characteristics in the respective exposure environments. The composition of the exposure media showed a strong influence, especially in terms of particle agglomeration but also in terms of dissolution. In high ionic strength medium, high concentrations of ions can break the electrical double layers surrounding the AgNP and thereby decrease the surface charge, which leads to AgNP agglomeration. In the presence of chloride, AgNP were more stable (compare L-15/ex medium to L-15/ex w/o Cl), which means chloride ions can stabilize AgNP, likely by binding to AgNP surfaces and contributing to a negative surface charge. In terms of AgNP dissolution, a higher percentage was found in L-15/ex with high chloride: chloride shifts the equilibrium of AgNP dissolution by complexing the dissolved silver.

AgNP adsorb to the algal cell surface but can be taken up by fish cells

To quantitatively relate AgNP/AgNO₃ exposure to the toxicity seen in algal and fish cells, cell-associated silver was quantified by inductively coupled plasma mass spectrometry (ICP-MS). Upon exposure to

Table 1 AgNP behavior in exposure media for algae and fish cells

	Algae exposure medium [26]	Fish cell exposure media [27]		
		L-15/ex	L-15/ex w/o Cl	d-L-15/ex
Medium ionic strength (mM)	3.44	173.0	177.1	72.0
Size of AgNP (nm)	38–73	200–500	1000–1750	40–100
Zeta potential of AgNP (mV)	−23 to −28	−15	−10	−20
Dissolution of AgNP (% of total Ag) ^a	1.7%	1.89%	0.67%	0.40%

^a The level of dissolution of AgNP represents the mean of dissolution data obtained using two different methods to separate dissolved silver from particles: ultrafiltration and ultracentrifugation. Values given are the mean of the average data obtained for each method, carried out three independent times

similar concentrations of AgNP or AgNO₃, the cell-associated silver in algae cells was comparable with the cell-associated silver which was reported for the alga *Chlamydomonas reinhardtii* [11]. Similarly, the cell-associated silver in RTgill-W1 cells was also comparable with the silver content in other vertebrate cell types, such as mouse erythroleukemia cells [37] and HepG2 cells [38].

At comparable external AgNO₃ exposure concentrations (0.1–0.5 μM), the silver content associated with algal cells was 2.4–4.2 times higher than in the fish cells (Fig. 1). This was probably due to the different compositions of the exposure media and the resulting different dissolved silver species. In the algal exposure medium, MOPS, almost all dissolved silver was present as free silver ions (Ag⁺) as predicted by Visual MINTEQ (V3.1, KTH, Sweden). Free silver ions are taken up via copper transporters in algae, as suggested in *C. reinhardtii*, *Pseudokirchneriella subcapitata* and *Chlorella pyrenoidosa* [39–41]. On the contrary, in fish cell exposure medium, only around 60% of dissolved silver was in the form of Ag⁺. The other 40% reacted with chloride and formed neutral or negatively charged complexes (AgCl_n⁽ⁿ⁻¹⁾⁻) [27]. Earlier research showed that Ag⁺ has a higher bioavailability than AgCl_n⁽ⁿ⁻¹⁾⁻ complexes in rainbow trout and Atlantic salmon [42], since Ag⁺ enters into gill cells via copper transporters and sodium channels, while AgCl₀(aq) may be taken up by simple diffusion [43].

In the case of AgNP exposure, the algal cells again had 2.5–4 times more cell-associated silver than the fish cells at 2.5–5 μM of external AgNP concentration (Fig. 1).

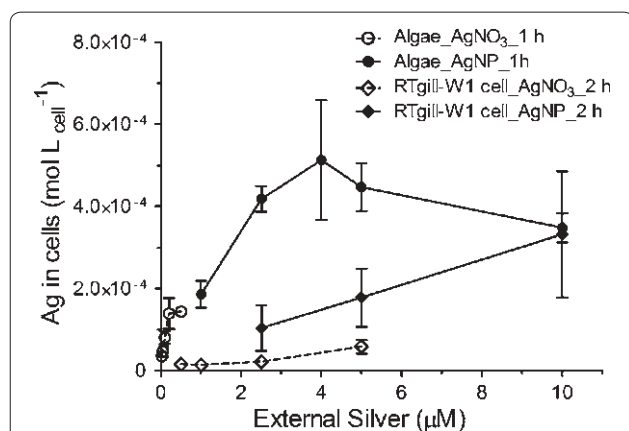


Fig. 1 Cell-associated silver in algae and fish cells. Cell-associated silver levels (mol/L_{cell}) were quantified by ICP-MS after exposure to AgNP and AgNO₃ for 1 h (algae) and 2 h (fish cells). The exposure of the algal cells was in MOPS; that of the fish cells in d-L-15/ex medium. The concentrations of silver (AgNP, AgNO₃) were selected based on the concentration response curves obtained for algae [26] and fish cells [28]. Cells were washed with cysteine solution to remove any loosely bound silver prior to extraction and analysis. Data presented as mean ± SD; n = 3

We attribute this difference to a higher overall exposure of the algal cells. There might be various factors influencing the level of cell-associated silver, e.g. kinetics of internalization into fish cells, sorption differences, ongoing dissolution at the interface between AgNP and cell surface, and abundance of metal transporters. Indeed, algae cells were exposed in suspension, allowing AgNP and AgNO₃ to interact from all sides with the cell surface (643 μm²/cell). In contrast, the fish cells were exposed as a cell monolayer sitting on a cell culture surface, which means only one side of the fish cells (half of the cell surface: 286 μm²/cell) was in immediate contact with AgNP or AgNO₃.

AgNP and silver ions elicit toxicity to algae and fish cells

The photosynthetic yield was assessed to study the time-dependent toxicity of AgNP and AgNO₃ in algae. The photosynthetic yield is an important parameter for evaluating the viability of algal cells as autotrophic organisms. In the fish cells, the overall metabolic activity was used as an endpoint upon AgNP and AgNO₃ exposure. Effective concentrations causing a 50% decline (EC50s) in photosynthetic yield and metabolic activity were calculated from dose–response curves derived with algal and fish cells. The EC50s ranged from 1.5 to 1.9 μM (0.16–0.21 mg/L) AgNP in algal cells and from 12.7 to 70.3 μM (1.37–7.59 mg/L) AgNP in fish cells (Fig. 2). In AgNO₃ exposures, EC50s were 0.09 μM (0.01 mg/L) in algae and 0.8–9.7 μM (0.09–1.05 mg/L) in the fish cells

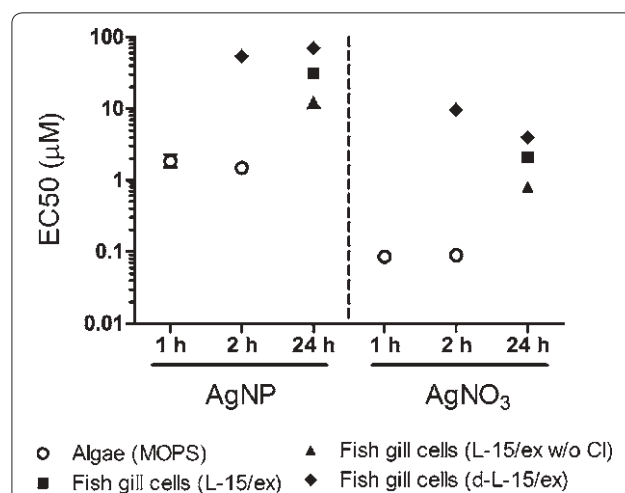


Fig. 2 EC50 values of AgNP and AgNO₃ in algae and fish cell exposures as a function of total silver. Times of exposure were selected based on the response of the respective cell type, with algal cells responding quickly with no further change in EC50 after 1 h whereas EC50 further decreased for fish cells over a 24 h period. Data presented as mean ± SD; n = 3. The error bars are smaller than the symbols due to the exponential scale in Y-axis

(Fig. 2). In the algae cell model, the EC50 values of AgNP determined in our study were comparable with EC50 values reported for other algal species [3, 44]. In the fish cell model, the EC50 values were similar to the EC50 values measured in other fish cell types [45, 46]. According to the categorization of toxic or non-toxic concentrations to aquatic organisms (<0.1 mg/L = extremely toxic; 0.1–1 mg/L = very toxic; 1–10 mg/L = toxic; 10–100 mg/L = harmful; >100 mg/L = non-toxic [47, 48]), we conclude that AgNP and AgNO₃ are toxic to both algae and fish cells.

When comparing these EC50s, both similarities and differences were found for algal and fish cells. In terms of similarities, AgNP induced significantly lower toxicity than AgNO₃ in both cell types if EC50s are expressed as a function of total silver present (Fig. 2). In terms of differences, algae were 10 to 100 times more sensitive than fish cells to both AgNP and AgNO₃ exposure. On the other hand, if EC50s are expressed as a function of dissolved silver in the respective exposure media, it was found that the toxicity of AgNP to algae is mediated solely by dissolved silver [26] while in fish cells, AgNP were found to induce toxicity by a nanoparticle specific effect as well as dissolved silver [27].

The media composition also had a strong effect on the toxicity of AgNP to fish cells (Fig. 2) [27]. Among the three fish cell exposure media, AgNP yielded highest toxicity in L-15/ex w/o Cl and lowest toxicity in d-L-15/ex. This difference correlates with the degree of AgNP agglomeration in the media: the strongly agglomerated AgNP (size: 1000–1750 nm) in L-15/ex w/o Cl induced a 2-times higher toxicity than moderately agglomerated

AgNP (size: 200–500 nm) in L-15/ex and 5-times higher toxicity than weakly agglomerated AgNP (size: 40–100 nm) in d-L-15/ex medium. Likely, the different degrees of agglomeration resulted in differing degrees of deposition of AgNP onto the fish cells, with the strongest agglomeration leading to highest cell exposure. This trend indicated that agglomeration and deposition could increase the interaction of AgNP with RTgill-W1 cell and induce higher toxicity. In the present exposure model, fish cells formed a cell layer on the bottom of the wells and AgNP suspensions were added on top. Previous modeling work showed that large size nanoparticles are transported faster than small nanoparticles due to deposition [49, 50]. Because of particle deposition on the cell monolayer, AgNP agglomeration may increase the interaction of AgNP with cells and thereby AgNP toxicity. Among the fish cell exposure media, d-L-15/ex medium maintains AgNP stability and better reflects the freshwater environment to which gill cells of freshwater fish would be exposed. Therefore, d-L-15/ex was selected to study the interaction of AgNP with fish cells in more detail.

The effects of AgNP and AgNO₃ to algae and fish cells were recalculated as a function of cell-associated silver (Fig. 3; Additional file 1: Table S1). The EC10s (concentrations leading to 10% effect compared to unexposed control) were used for comparison because effects were quantifiable based on experimental data under all conditions for this level of effect (see horizontal dashed line in Fig. 3). The EC10 of AgNP and AgNO₃ in algae are 1.40×10^{-4} and 3.55×10^{-4} mol/L_{cell}, respectively. The EC10 of AgNP and AgNO₃ in fish cells are 1.80×10^{-5}

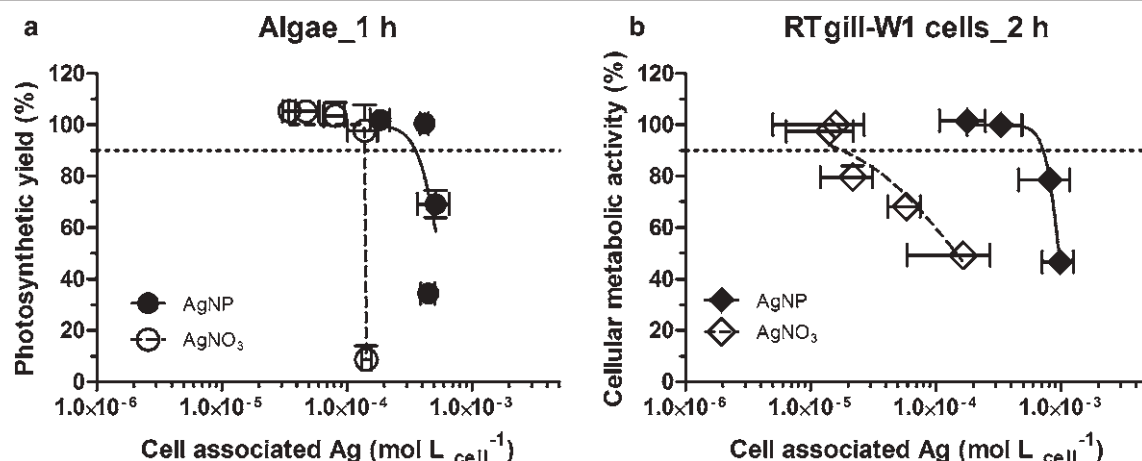


Fig. 3 Recalculation of the toxicity of AgNP and AgNO₃ to algae in MOPS **a** and fish cells in d-L15/ex medium **b** as a function of cell-associated silver. The dashed horizontal lines show the EC10 level. Each data point presents the mean of three independent experiments with the horizontal lines indicating the variation in cell-associated silver and the vertical lines the variation in effect (mean \pm SD, $n = 3$). All data are expressed as % of the respective unexposed control. Data presented as mean \pm SD; $n = 3$

and 7.22×10^{-4} mol/L_{cell}, respectively. In both cell models, the AgNO₃ concentration response curve is left of the AgNP concentration response curve, indicating stronger effects of AgNO₃. This can be interpreted as AgNP inducing toxicity via different mechanisms compared to AgNO₃. However, this difference between AgNO₃ and AgNP concentration response curves is much greater in the fish cells, demonstrating that fish cells respond strongly to a particle-specific impact, whereas in algae, dissolved silver is the dominant cause of toxicity.

The fact that no particle-specific effect was seen in algae suggested that AgNP were not incorporated into algae but that they may adhere to the algal surface from which Ag⁺ may dissolve and as such be taken up in the cells. To follow up on this hypothesis, the localization of cell-associated silver in algae was investigated by time-of-flight secondary ion mass spectrometry (TOF-SIMS), a qualitative and quantitative surface analysis. Indeed, the silver intensity from algae exposed to AgNP and AgNO₃ indicated a strong sorption of AgNP onto the algal surface [26]. In contrast, fish gill cells take up AgNP in an energy-dependent process: as demonstrated by TEM coupled with energy-dispersive X-ray analysis that localized the NPs in the endocytic compartments of the cells [28]. This latter finding corresponds to the work of others who confirmed metal nanoparticles uptake by vertebrate cells via endocytic pathways [51–53].

AgNP can bind cellular proteins and inhibit enzyme activity

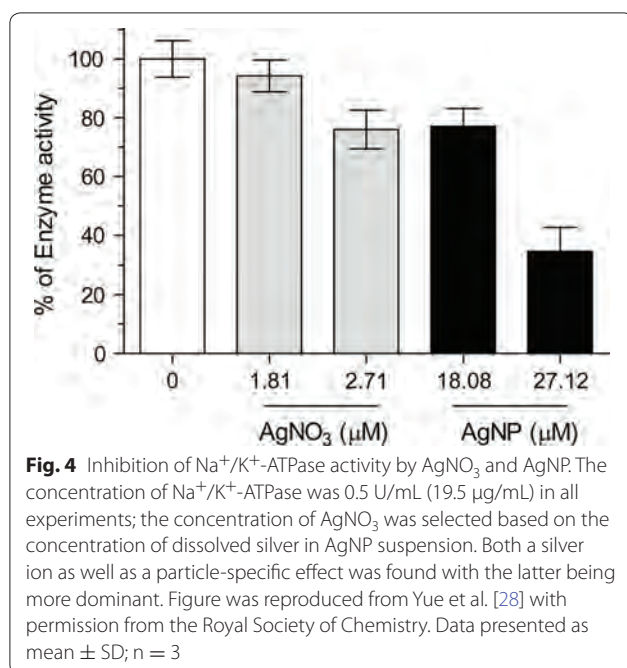
Considering the contrasting finding that algal cells do not take up AgNP while fish cells do, and the importance of the AgNP-protein binding in nano-bio interaction, we postulate that extracellular proteins are more important in terms of AgNP exposure for algae while intracellular proteins should be considered for fish cells. One important extracellular protein is alkaline phosphatase, an enzyme responsible for phosphorus acquisition. This enzyme is highly abundant in aquatic environments, and is produced by a wide range of organisms including bacteria, fungi, zooplankton and algae [54–56]. Previously, alkaline phosphatase activity in periphyton was shown to be unaffected [57] or stimulated [58] by AgNP. However, considering that algae within periphyton are embedded in a matrix of biomolecules forming a biofilm [59], other factors might influence direct interaction of AgNP with the enzyme, e.g. periphyton community continuously synthesizes and secretes enzymes, it could not be determined whether the absence of inhibitory effects was due to a lack of interaction with AgNP or whether any impact was masked by de-novo synthesis of the enzyme.

Indeed, studying the interaction of AgNP or AgNO₃ with isolated alkaline phosphatase showed that AgNP

have a particle-specific, inhibitory effect on alkaline phosphatase activity and that this inhibition depends on the sequences of addition of enzyme substrate or AgNP [29]. Other studies have reported on an inhibitory effect on extracellular enzymes by nanoparticles. For example, in the same study on periphyton cited above [57], inhibition of β -glucosidase and L-leucine aminopeptidase was attributed to dissolved silver and particle specific effects. Inhibitory effects of the same proteins were also seen in heterotrophic biofilm exposed to titanium dioxide nanoparticles [60]. Thus, understanding the mechanisms of interaction of extracellular proteins and nanoparticles in general is an important future direction.

In order to study the interaction of AgNP with intracellular proteins in fish cells, the AgNP-protein corona was recovered from intact endocytic compartments by a newly established method with subcellular fractionation. Proteins acquired from the AgNP-protein corona were identified by mass spectrometry and analyzed with Gene Ontology. A total of 383 proteins were identified in this way and broadly classified as belonging to cell membrane functions, uptake and vesicle-mediated transport and stress-response pathways [28]. These proteins regulate substance transport across the plasma membrane or play key roles in cell metabolic processes, such as Na⁺/K⁺-ATPase, Ca²⁺-ATPase, adaptor-related protein complex 1 (AP-1B1), caveolin 1, flotillin 1/2, EH-domain containing protein 1/2/4 and Rab Family Small GTPases (RAB5A, RAB7A, RAB18) [28]. Based on the identified proteins, the processing of AgNP in fish cells was reconstructed: AgNP were taken up by fish cells via endocytic processes and stored in endosomal/lysosomal compartments [28]. Binding to AgNP could impair the function of these proteins and subsequently disrupt the normal cell activity, which would relate to the decline of cell viability in RTgill-W1 cells exposed to AgNP. Some of these proteins were also identified in the corona of magnetic nanoparticles exposed to human lung epithelial cells (A549) and HeLa cells [24, 25]. This indicated that vertebrate cells take up metal nanoparticles via common pathways regardless of elemental composition or coating of particles, exposure conditions and cell types.

Among the proteins identified from fish cells, Na⁺/K⁺-ATPase was selected to study the effect of AgNP on corona proteins. Experiments on the isolated, single protein showed that the inhibition of enzyme activity is attributable primarily to a particle-specific rather than a dissolved silver ion effect (Fig. 4). Schultz reported that citrate coated AgNP, i.e. the same type of particle used in this work, led to a particle-specific inhibition of Na⁺/K⁺ ATPase activity in juvenile rainbow trout gill in vivo [61]. Thus, our in vitro study was confirmative of the findings



Conclusion

The results of the side by side comparison of AgNP-cell interactions for algal and fish cells are summarized in Table 2. The composition of exposure media influenced AgNP behavior and toxicity, highlighting once more the importance of characterizing nanoparticle speciation in the risk assessment of nanomaterials. Because of the barrier surrounding the cell membrane, AgNP cannot be taken up by algal cells but adsorb onto the cell surface instead, and toxicity is thus induced by dissolved silver. On the other hand, in fish cells, AgNP are taken up via endocytic pathways, causing toxicity by both dissolved silver and a nanoparticle specific effect. Thus, the cell type and structure are important features to be considered in nanotoxicity research. AgNP can bind extracellular proteins and inhibit enzyme activities via nanoparticle specific effects. Current work provides a first concrete attempt to study the interaction of AgNP with extracellular and intracellular proteins from aquatic organisms. For future assessment, this kind of knowledge not only aids in mechanism-based aquatic risk assessment but also helps designing safer nanoparticles.

in vivo and signifies a strategy to further investigate AgNP and other nanoparticles for their interaction with corona proteins, based on the protein list established as described above.

Methods

AgNP preparation and characterization

The citrate coated AgNP were purchased from NanoSys GmbH (Wolfhalden, Switzerland) as aqueous suspension

Table 2 Summary of the interaction of AgNP with algae and fish cells

	Algae	Fish cell
NP behavior	Slight agglomeration in MOPS medium	Slight agglomeration in d-L-15/ex medium and strong agglomeration in L-15/ex and L-15/ex w/o Cl media
Toxicity	Dissolved silver ^a	Dissolved silver ^a , nanoparticle-specific effect
Cellular uptake	No, adsorbed on algal surface	Yes, uptake via endocytic pathways
AgNP-protein interaction	Adsorption of extracellular enzyme on AgNP, inhibition of enzymatic activity	Cell membrane proteins and endocytic proteins binding to NP, inhibition of enzymatic activity
Cell structure and AgNP association		

^a Dissolved silver indicates all the silver species in oxidized state Ag(I) in aqueous solution, such as Ag⁺, AgCl_n (aq) and AgOH (aq), stemming from AgNP

with a concentration of 1 g/L (9.27 mM referring to the total silver, pH 6.46). The Z-average size and Zeta potential of AgNP in the stock solution were 19.4 nm and -30 mV, respectively. The stock AgNP solution was kept in the dark. A stock solution (10 mM) of AgNO_3 (Sigma-Aldrich, Switzerland) was prepared by dissolving AgNO_3 in nanopure water (16–18 M Ω /cm; Barnstead Nanopure Skan AG, Switzerland). The experimental solutions of AgNP and AgNO_3 were freshly prepared by adding AgNP and AgNO_3 stock solution into the respective exposure media and vortexing for 10 s. Unless specifically indicated, all chemicals were purchased from Sigma-Aldrich. As the work focused on the impacts of AgNP on algae and fish cells, we chose the respective AgNP and AgNO_3 concentrations to observe significant effects in the toxicity experiments. In the uptake experiments, the exposure concentrations were selected to meet the ICP-MS detection limit.

The AgNP were characterized in nanopure water and under experimental conditions in each exposure media. The Z-average size and zeta potential of the AgNP were measured by dynamic light scattering (DLS) and electrophoretic mobility using a Zetasizer (Nano ZS, Malvern Instruments, UK) [26, 27]. To measure the dissolution of AgNP in exposure medium, dissolved silver was separated by two methods: centrifugal ultrafiltration with a nominal molecular weight cut-off of 3 kDa (Amicon ultra-4 centrifugal filter units, Millipore, Germany) centrifuged at $3000\times g$ for 0.5 h (Megafuge 1.0R, Heraeus Instruments, Germany) and by ultra-centrifugation (CENTRIKON T-2000, KONTRON Instruments, Switzerland) at $145,000\times g$ for 3 h. The silver concentration was measured by Inductively Coupled Plasma Mass Spectrometry (ICP-MS, Element 2, Thermo Finnigan, Germany). The dissolution of AgNP was calculated by dividing the measured dissolved silver concentration to the related nominal total silver concentration. The average of the AgNP dissolution (Table 1) obtained by ultra-filtration and ultra-centrifugation was used for recalculation of the concentration–response curves as a function of dissolved silver (Fig. 3).

Algal culture and exposure of cells

The alga *E. gracilis* strain Z (Culture Collection of Algae, Göttingen, Germany) was cultured in the Talaquil medium (pH 7.5) supplemented with vitamins B1 and B12 [62] at 20°C under light–dark cycles of 12 h each on a shaker (Infors, Switzerland) with 90 rpm. The cell number and volume were measured by a particle counter (Beckman Coulter Z2, USA).

Before exposure to AgNO_3 and AgNP, exponentially grown algae were centrifuged at $2000\times g$ for 10 min and then re-suspended in MOPS. The final cell density for

toxicity assessment was 1.5×10^4 cell/mL. After exposure to AgNO_3 (0–400 nM) and AgNP (0–40 μM) for 1 and 2 h, to study toxic effects, the photosynthetic yield was measured by fluorometry using a PHYTO-PAM (Heinz Walz GmbH, Germany) [26]. The values were presented as percentage of controls, and were plotted as a function of measured total silver and cell-associated silver [26].

RTgill-W1 cell culture and exposure of cells

RTgill-W1 cells were routinely cultivated in L-15 medium (Invitrogen, Switzerland), supplemented with 5% fetal bovine serum (FBS, Gold, PAA Laboratories GmbH, Austria) and 1% penicillin/streptomycin (Sigma-Aldrich, Switzerland) in 75 cm² flasks. The L-15 medium containing these supplements is termed “complete L-15”. Cells are routinely cultured in the dark in normal atmosphere at 19°C .

For exposure to AgNO_3 (0–5 μM) and AgNP (0–100 μM), cells were seeded in 24-well microtiter plates or 25 cm² flasks, and cultured in complete L-15 medium. After being fully confluent, cell monolayers were washed with either L-15/ex, L-15/ex w/o Cl or d-L-15/ex. Then, 1 mL/well of AgNP or AgNO_3 suspension in the respective media was added to culture wells. Exposure proceeded for 2–24 h at 19°C . AlamarBlue (AB, Invitrogen, Switzerland) was used to measure the cellular metabolic activity to assess the toxicity of AgNP to fish gill cells [27, 32]. Before incubation with AlamarBlue, the AgNP suspension was removed and exposed cells were carefully washed with PBS to removed loosely adsorbed AgNP. Control experiments showed no interference of the silver with the AlamarBlue assay.

Uptake of AgNP by algae and fish cells

The algae were exposed to AgNP (0–10 μM) and AgNO_3 (0–500 nM) at a cell density of 1×10^5 cell/mL in order to meet the detection limit of the ICP-MS. After 1 h of exposure, the algae were washed to remove loosely bound AgNP with fresh medium or adsorbed silver ions by cysteine using the following protocol: algae exposed to AgNP or AgNO_3 were first centrifuged ($2000\times g$, 10 min) and resuspended in MOPS. After 2 wash cycles, the algae were re-suspended in cysteine–MOPS and gently stirred for 5 min. After washing, the algae were filtered (SM 16510, Sartorius) and digested for metal analysis [26].

To quantify the fish cell-associated silver, RTgill-W1 cells were cultured in 25 cm² flasks until confluency and then exposed to AgNP (2.5–10 μM) or AgNO_3 (0.5–5 μM) in d-L-15/ex medium. After exposure, the medium with AgNP or AgNO_3 was removed and cells were washed twice with cysteine for 5 min. Cells were then trypsinized. Detached cells were re-suspended in complete L-15 medium. Cell suspensions were

centrifuged at $1000\times g$ for 3 min to pellet the cells. Cell pellets were re-suspended in 550 μL PBS and the cell density determined by an electronic cell counter (CASY1 TCC, Schärfe System, Germany). A volume of 500 μL cell supernatant was digested for metal analysis [28].

Samples from algae and fish cell exposures were digested with 4.5 mL of 65% HNO_3 in a high-performance microwave digestion unit (MLS-1200 MEGA, Switzerland) at a maximum temperature of 195 $^{\circ}\text{C}$ for 20 min. The digests were diluted 50-times and measured by ICP-MS. The detection limit for ICP-MS quantitation of silver was 10 ng/L (1.0×10^{-5} mol/L_{cell} in the current work). The reliability of the measurements was determined using specific water references (M105A, IFA-Tull, Austria). As the volume of algal cells is larger than that of the fish cells, the measured cell associated silver was related to cell volume and expressed as mol/L_{cell} in order to be able to directly compare the cell-associated silver in algae and fish cells. The associated silver was also related to the cell number and expressed as mol per cell to be able to compare with other reports.

The localization of cell-associated silver in algae was checked by time-of-flight secondary ion mass spectrometry analysis (TOF-SIMS, ToF.SIMS 5 instrument, ION-TOF GmbH). The primary ion was 25 keV Bi^+ to ensure high sensitivity to silver and the sputtering time was 5.2 s leading to ablation of a few nanometers of the surface layer of the cell [26]. The AgNP uptake in fish cells was investigated by transmission electron microscopy (TEM, FEI Morgagni 268, 100 kV) and energy dispersive X-ray (EDX) spectroscopy analyses in a scanning transmission electron microscope (STEM, Hitachi HD-2700) [28].

Interaction of AgNP with proteins

Alkaline phosphatase (Sigma-Aldrich) was selected as a representative extracellular algal enzyme to study the interaction with AgNP. The effect of AgNP to alkaline phosphatase was assayed in MOPS by determining enzyme activity, using fluorescently linked 4-methylumbelliferyl phosphate disodium salt as substrate [29].

In fish cell exposures, to identify the proteins binding to AgNP in cells, AgNP-protein corona complexes were recovered from intact subcellular compartments isolated by subcellular fractionation and proteins lysed from the AgNP to be detected by mass spectrometry. The identified proteins were analyzed by DAVID (<http://david.abcc.ncifcrf.gov/>), a protein ontology analysis tool. Among the identified proteins, Na^+/K^+ -ATPase (Sigma-Aldrich, No. A7510) was selected to study the interaction of AgNP with intracellular proteins. The effect of AgNP on Na^+/K^+ -ATPase activity was measured in a buffer containing 20 mM Tris-HCl, 0.60 mM EDTA, 5 mM MgCl_2 , 3 mM

KCl and 133 mM NaCl (pH 7.8) and substrate, ATP (Sigma-Aldrich, No. A9062) [28].

Data analysis

All data were analyzed by GraphPad Prism (version 5.02 for Windows, USA). Fluorescent units obtained in the cell assays were converted to percent viability of control cells. Concentrations leading to 10% and 50% effect (EC_{10}s , EC_{50}s) were determined by nonlinear regression sigmoidal dose-response curve fitting using the Hill slope equation, and were presented as the mean of three independent experiments, with a 95% confidence interval. Data presented as mean \pm standard deviation, $n = 3$.

Additional file

Additional file 1: Table S1. EC_{10} and EC_{50} values, corresponding 95% Confidence Intervals, Hill slope and R^2 of AgNP and AgNO_3 concentration-response curves.

Authors' contributions

YY and XL carried out the study and analyzed data. YY and KS wrote the manuscript. LS, MJFS, SP, RB, and KS participated in the design of the study and revised the manuscript. All authors read and approved the final manuscript.

Author details

¹ Department of Environmental Toxicology, Eawag, Swiss Federal Institute of Aquatic Science and Technology, 8600 Dübendorf, Switzerland. ² School of Architecture, Civil and Environmental Engineering, École Polytechnique Fédérale de Lausanne, 1015 Lausanne, Switzerland. ³ Department of Environmental Systems Science (D-USYS), ETH-Zürich, 8092 Zürich, Switzerland. ⁴ Present Address: Department of Basic Sciences and Aquatic Medicine, Norwegian University of Life Sciences (NMBU), Oslo 0454, Norway. ⁵ Present Address: Wattstrasse 13a, 8307 Effretikon, Switzerland.

Acknowledgements

We thank D. Kistler (Eawag, Swiss Federal Institute of Aquatic Science and Technology, Dübendorf, Switzerland) for ICP-MS measurements.

Competing interests

The authors declare that they have no competing interests.

Funding

This research was part of "Interaction of metal nanoparticles with aquatic organisms (MeNanoqa)" project (Project Number: 406440-131240), which was supported by the Swiss National Science Foundation in the framework of the Swiss National Research Program 64 (NRP 64) "Opportunities and Risks of Nanomaterials".

Received: 2 September 2016 Accepted: 22 February 2017

Published online: 28 February 2017

References

1. Kaegi R, Sinnet B, Zuleeg S, Hagendorfer H, Mueller E, Vonbank R, Boller M, Burkhardt M. Release of silver nanoparticles from outdoor facades. *Environ Pollut*. 2010;158:2900–5.
2. Collin B, Auffan M, Johnson AC, Kaur I, Keller AA, Lazareva A, Lead JR, Ma X, Merrifield RC, Svendsen C, et al. Environmental release, fate and ecotoxicological effects of manufactured ceria nanomaterials. *Environ Sci Nano*. 2014;1:533–48.

3. Fabrega J, Luoma SN, Tyler CR, Galloway TS, Lead JR. Silver nanoparticles behaviour and effects in the aquatic environment. *Environ Int*. 2011;37:517–31.
4. Schultz AG, Boyle D, Chamot D, Ong KJ, Wilkinson KJ, McGeer JC, Sunahara G, Goss GG. Aquatic toxicity of manufactured nanomaterials: challenges and recommendations for future toxicity testing. *Environ Chem*. 2014;11:207–26.
5. Yang X, Gondikas AP, Marinakos SM, Auffan M, Liu J, Hsu-Kim H, Meyer JN. Mechanism of silver nanoparticle toxicity is dependent on dissolved silver and surface coating in *Caenorhabditis elegans*. *Environ Sci Technol*. 2011;46:1119–27.
6. Park E-J, Yi J, Kim Y, Choi K, Park K. Silver nanoparticles induce cytotoxicity by a Trojan-horse type mechanism. *Toxicol In Vitro*. 2010;24:872–8.
7. Fleischer A, O'Neill MA, Ehwald R. The pore size of non-graminaceous plant cell walls is rapidly decreased by borate ester cross-linking of the pectic polysaccharide rhamnogalacturonan II. *Plant Physiol*. 1999;121:829–38.
8. Taylor NS, Merrifield R, Williams TD, Chipman JK, Lead JR, Viant MR. Molecular toxicity of cerium oxide nanoparticles to the freshwater alga *Chlamydomonas reinhardtii* is associated with supra-environmental exposure concentrations. *Nanotoxicology*. 2016;10:32–41.
9. Wang Y, Miao AJ, Luo J, Wei ZB, Zhu JJ, Yang LY. Bioaccumulation of CdTe quantum dots in a freshwater alga *Ochromonas danica*: a kinetics study. *Environ Sci Technol*. 2013;47:10601–10.
10. Leclerc S, Wilkinson KJ. Bioaccumulation of nanosilver by *Chlamydomonas reinhardtii*—nanoparticle or the free ion? *Environ Sci Technol*. 2014;48:358–64.
11. Piccapietra F, Allué CG, Sigg L, Behra R. Intracellular silver accumulation in *Chlamydomonas reinhardtii* upon exposure to carbonate coated silver nanoparticles and silver nitrate. *Environ Sci Technol*. 2012;46:7390–7.
12. Röhder LA, Brandt T, Sigg L, Behra R. Influence of agglomeration of cerium oxide nanoparticles and speciation of cerium(III) on short term effects to the green algae *Chlamydomonas reinhardtii*. *Aquat Toxicol*. 2014;152:121–30.
13. Hoecke KV, Quik JTK, Mankiewicz-Boczek J, Schamphelaere KACD, Elsaesser A, Meeren Pvd, Barnes C, McKerr G, Howard CV, Meent DVD, et al. Fate and effects of CeO₂ nanoparticles in aquatic ecotoxicity tests. *Environ Sci Technol*. 2009;43:4537–46.
14. Behra R, Sigg L, Clift MJD, Herzog F, Minghetti M, Johnston B, Petri-Fink A, Rothen-Rutishauser B. Bioavailability of silver nanoparticles and ions: from a chemical and biochemical perspective. *J R Soc Interface*. 2013;10:20130396.
15. Scown TM, Goodhead RM, Johnston BD, Moger J, Baalousha M, Lead JR, van Aerle R, Iguchi T, Tyler CR. Assessment of cultured fish hepatocytes for studying cellular uptake and (eco)toxicity of nanoparticles. *Environ Chem*. 2010;7:36–49.
16. Stern S, Adisheshaiah P, Crist R. Autophagy and lysosomal dysfunction as emerging mechanisms of nanomaterial toxicity. *Part Fibre Toxicol*. 2012;9:20.
17. Canton I, Battaglia G. Endocytosis at the nanoscale. *Chem Soc Rev*. 2012;41:2718–39.
18. Nel AE, Madler L, Velegol D, Xia T, Hoek EMV, Somasundaran P, Klaessig F, Castranova V, Thompson M. Understanding biophysicochemical interactions at the nano-bio interface. *Nat Mater*. 2009;8:543–57.
19. Monopoli MP, Walczyk D, Campbell A, Elia G, Lynch I, Baldelli Bombelli F, Dawson KA. Physical–chemical aspects of protein corona: relevance to in vitro and in vivo biological impacts of nanoparticles. *J Am Chem Soc*. 2011;133:2525–34.
20. Lynch I, Dawson KA, Lead JR, Valsami-Jones E. Chapter 4-macromolecular coronas and their importance in nanotoxicology and nanoecotoxicology. *Front Nanosci*. 2014;7:127–56.
21. Schirmer K. Chapter 6-mechanisms of nanotoxicity. *Front Nanosci*. 2014;7:195–221.
22. Wigginton NS, Wigginton NS. Binding of silver nanoparticles to bacterial proteins depends on surface modifications and inhibits enzymatic activity. *Environ Sci Technol*. 2010;44:2163–8.
23. Aleksandr K, Feng D, Pengyu C, Monika M, Anne K, Pu Chun K. Interaction of firefly luciferase and silver nanoparticles and its impact on enzyme activity. *Nanotechnology*. 2013;24:345101.
24. Bertoli F, Davies G-L, Monopoli MP, Moloney M, Gun'ko YK, Salvati A, Dawson KA. Magnetic nanoparticles to recover cellular organelles and study the time resolved nanoparticle-cell interactome throughout uptake. *Small*. 2014;10:3307–15.
25. Hofmann D, Tenzer S, Bannwarth MB, Messerschmidt C, Glaser S-F, Schild H, Landfester K, Mäiländer V. Mass spectrometry and imaging analysis of nanoparticle-containing vesicles provide a mechanistic insight into cellular trafficking. *ACS Nano*. 2014;8:10077–88.
26. Li X, Schirmer K, Bernard L, Sigg L, Pillai S, Behra R. Silver nanoparticle toxicity and association with the alga *Euglena gracilis*. *Environ Sci Nano*. 2015;2:594–602.
27. Yue Y, Behra R, Sigg L, Fernández Freire P, Pillai S, Schirmer K. Toxicity of silver nanoparticles to a fish gill cell line: role of medium composition. *Nanotoxicology*. 2015;9:54–63.
28. Yue Y, Behra R, Sigg L, Suter MJF, Pillai S, Schirmer K. Silver nanoparticle-protein interactions in intact rainbow trout gill cells. *Environ Sci Nano*. 2016;3:1174–85.
29. Li X. Interactions of silver and polystyrene nanoparticles with algae. EPFL Ph.D. Thesis. 2015.
30. Bols NC, Barlian A, Chirinotrojo M, Caldwell SJ, Goegan P, Lee LEJ. Development of a cell-line from primary cultures of rainbow-trout, *Oncorhynchus mykiss* (Walbaum), gills. *J Fish Dis*. 1994;17:601–11.
31. Nakano Y, Urade Y, Urade R, Kitaoka S. Isolation, purification, and characterization of the pellicle of *Euglena gracilis*. *J Biochem*. 1987;102:1053–63.
32. Schirmer K, Chan AGJ, Greenberg BM, Dixon DG, Bols NC. Methodology for demonstrating and measuring the photocytotoxicity of fluoranthene to fish cells in culture. *Toxicol In Vitro*. 1997;11:107–19.
33. Dayeh VR, Schirmer K, Bols NC. Applying whole-water samples directly to fish cell cultures in order to evaluate the toxicity of industrial effluent. *Water Res*. 2002;36:3727–38.
34. Leibovitz A. The growth and maintenance of tissue–cell cultures in free gas exchange with the atmosphere. *Am J Epidemiol*. 1963;78:173–80.
35. Sigg L, Behra R, Groh K, Isaacson C, Odzak N, Piccapietra F, Röhder L, Schug H, Yue Y, Schirmer K. Chemical aspects of nanoparticle ecotoxicology. *Chimia*. 2014;68:806–11.
36. Setyawati MI, Yuan X, Xie J, Leong DT. The influence of lysosomal stability of silver nanomaterials on their toxicity to human cells. *Biomaterials*. 2014;35:6707–15.
37. Wang Z, Liu S, Ma J, Qu G, Wang X, Yu S, He J, Liu J, Xia T, Jiang G-B. Silver nanoparticles induced RNA polymerase-silver binding and RNA transcription inhibition in erythroid progenitor cells. *ACS Nano*. 2013;7:4171–86.
38. Liu W, Wu Y, Wang C, Li HC, Wang T, Liao CY, Cui L, Zhou QF, Yan B, Jiang GB. Impact of silver nanoparticles on human cells: effect of particle size. *Nanotoxicology*. 2010;4:319–30.
39. Fortin C, Campbell PGC. Silver uptake by the green alga *Chlamydomonas reinhardtii* in relation to chemical speciation: influence of chloride. *Environ Toxicol Chem*. 2000;19:2769–78.
40. Lee D-Y, Fortin C, Campbell PGC. Influence of chloride on silver uptake by two green algae, *Pseudokirchneriella subcapitata* and *Chlorella pyrenoidosa*. *Environ Toxicol Chem*. 2004;23:1012–8.
41. Pillai S, Behra R, Nestler H, Suter MJF, Sigg L, Schirmer K. Linking toxicity and adaptive responses across the transcriptome, proteome, and phenotype of *Chlamydomonas reinhardtii* exposed to silver. *Proc Natl Acad Sci USA*. 2014;111:3490–5.
42. Bury NR, Hogstrand C. Influence of Chloride and Metals on Silver Bioavailability to Atlantic Salmon (*Salmo salar*) and Rainbow Trout (*Oncorhynchus mykiss*) Yolk-Sac Fry. *Environ Sci Technol*. 2002;36:2884–8.
43. Wood CM. 1-Silver. In: Chris M, Wood APF, Brauner CJ, editors. Homeostasis and toxicology of non-essential metals. Cambridge: Academic Press; 2011. p. 1–65.
44. Bondarenko O, Juganson K, Ivask A, Kasemets K, Mortimer M, Kahru A. Toxicity of Ag, CuO and ZnO nanoparticles to selected environmentally relevant test organisms and mammalian cells in vitro: a critical review. *Arch Toxicol*. 2013;87:1181–200.
45. Connolly M, Fernandez-Cruz ML, Quesada-Garcia A, Alte L, Segner H, Navas MJ. Comparative cytotoxicity study of silver nanoparticles (AgNPs) in a Variety of rainbow trout cell lines (RTL-W1, RTH-149, RTG-2) and primary hepatocytes. *Int J Environ Res Public Health*. 2015;12:5386–405.
46. Minghetti M, Schirmer K. Effect of media composition on bioavailability and toxicity of silver and silver nanoparticles in fish intestinal cells (RTgutGC). *Nanotoxicology*. 2016;10:1526–34.
47. Sanderson H, Johnson DJ, Wilson CJ, Brain RA, Solomon KR. Probabilistic hazard assessment of environmentally occurring pharmaceuticals

- toxicity to fish, daphnids and algae by ECOSAR screening. *Toxicol Lett.* 2003;144:383–95.
48. Jemec A, Kahru A, Potthoff A, Drobne D, Heinlaan M, Böhme S, Geppert M, Novak S, Schirmer K, Rekulapally R, et al. An interlaboratory comparison of nanosilver characterisation and hazard identification: harmonising techniques for high quality data. *Environ Int.* 2016;87:20–32.
 49. Hinderliter P, Minard K, Orr G, Chrisler W, Thrall B, Pounds J, Teeguarden J. ISDD: a computational model of particle sedimentation, diffusion and target cell dosimetry for in vitro toxicity studies. *Part Fibre Toxicol.* 2010;7:36.
 50. Teeguarden JG, Hinderliter PM, Orr G, Thrall BD, Pounds JG. Particokinetics in vitro: dosimetry considerations for in vitro nanoparticle toxicity assessments. *Toxicol Sci.* 2007;95:300–12.
 51. Busch W, Bastian S, Trahorsch U, Iwe M, Kühnel D, Meißner T, Springer A, Gelinsky M, Richter V, Ikonomidou C, et al. Internalisation of engineered nanoparticles into mammalian cells in vitro: influence of cell type and particle properties. *J Nanopart Res.* 2011;13:293–310.
 52. García-Alonso J, Khan FR, Misra SK, Turmaine M, Smith BD, Rainbow PS, Luoma SN, Valsami-Jones E. Cellular internalization of silver nanoparticles in gut epithelia of the estuarine polychaete *Nereis diversicolor*. *Environ Sci Technol.* 2011;45:4630–6.
 53. Greulich C, Diendorf J, Simon T, Eggeler G, Eppler M, Köller M. Uptake and intracellular distribution of silver nanoparticles in human mesenchymal stem cells. *Acta Biomater.* 2011;7:347–54.
 54. Jansson M, Olsson H, Pettersson K. Phosphatases; origin, characteristics and function in lakes. In *Phosphorus in freshwater ecosystems*. Berlin: Springer; 1988. p. 157–75.
 55. Rier ST, Kuehn KA, Francoeur SN. Algal regulation of extracellular enzyme activity in stream microbial communities associated with inert substrata and detritus. *J North Am Benthol Soc.* 2007;26:439–49.
 56. Rose C, Axler RP. Uses of alkaline phosphatase activity in evaluating phytoplankton community phosphorus deficiency. *Hydrobiologia.* 1997;361:145–56.
 57. Gil-Allué C, Schirmer K, Tlili A, Gessner MO, Behra R. Silver nanoparticle effects on stream periphyton during short-term exposures. *Environ Sci Technol.* 2015;49:1165–72.
 58. Tlili A, Cornut J, Behra R, Gil-Allué C, Gessner MO. Harmful effects of silver nanoparticles on a complex detrital model system. *Nanotoxicology.* 2016;10:728–35.
 59. Stewart TJ, Traber J, Kroll A, Behra R, Sigg L. Characterization of extracellular polymeric substances (EPS) from periphyton using liquid chromatography-organic carbon detection—organic nitrogen detection (LC-OCD-OND). *Environ Sci Pollut Res.* 2013;20:3214–23.
 60. Schug H, Isaacson CW, Sigg L, Ammann AA, Schirmer K. Effect of TiO₂ nanoparticles and uv radiation on extracellular enzyme activity of intact heterotrophic biofilms. *Environ Sci Technol.* 2014;48:11620–8.
 61. Schultz AG, Ong KJ, MacCormack T, Ma G, Veinot JGC, Goss GG. Silver nanoparticles inhibit sodium uptake in juvenile rainbow trout (*Oncorhynchus mykiss*). *Environ Sci Technol.* 2012;46:10295–301.
 62. Le Faucheur S, Behra R, Sigg L. Phytochelatin induction, cadmium accumulation, and algal sensitivity to free cadmium ion in *Scenedesmus vacuolatus*. *Environ Toxicol Chem.* 2005;24:1731–7.

Submit your next manuscript to BioMed Central and we will help you at every step:

- We accept pre-submission inquiries
- Our selector tool helps you to find the most relevant journal
- We provide round the clock customer support
- Convenient online submission
- Thorough peer review
- Inclusion in PubMed and all major indexing services
- Maximum visibility for your research

Submit your manuscript at
www.biomedcentral.com/submit



REVIEW

Open Access



Non-invasive continuous monitoring of pro-oxidant effects of engineered nanoparticles on aquatic microorganisms

Christian Santschi^{1*}, Nadia Von Moos², Volodymyr B. Koman¹, Vera I. Slaveykova², Paul Bowen³ and Olivier J. F. Martin¹

Abstract

Engineered nanomaterials (ENMs) are key drivers for the development of highly sophisticated new technologies. As all new attainments, the rapidly increasing used of ENMs raise concerns about their safety for the environment and humans. There is growing evidence showing that if engineered nanomaterials are released into the environment, there is a possibility that they could cause harm to aquatic microorganisms. Among the divers effects triggering their toxicity the ability of ENMs to generate reactive oxygen species (ROS) capable of oxidizing biomolecules is currently considered a central mechanism of toxicity. Therefore, development of sensitive tools for quantification of the ROS generation and oxidative stress are highly sought. After briefly introducing ENMs-induced ROS generation and oxidative stress in the aquatic microorganisms (AMOs), this overview paper focuses on a new optical biosensor allowing sensitive and dynamic measurements of H_2O_2 in real-time using multiscattering enhanced absorption spectroscopy. Its principle is based on sensitive absorption measurements of the heme protein cytochrome *c* whose absorption spectrum alters with the oxidation state of constituent ferrous Fe^{II} and ferric Fe^{III} . For biological applications cytochrome *c* was embedded in porous random media resulting in an extended optical path length through multiple scattering of light, which lowers the limit of detection to a few nM of H_2O_2 . The sensor was also integrated in a microfluidic system containing micro-valves and sieves enabling more complex experimental conditions. To demonstrate its performance, abiotic absorption measurements of low concentrations of dye molecules and 10 nm gold particles were carried out achieving limits of detection in the low nM range. Other biologically relevant reactive oxygen species can be measured at sub- μM concentrations, which was shown for glucose and lactate through enzymatic reactions producing H_2O_2 . In ecotoxicological investigations H_2O_2 excreted by aquatic microorganisms exposed to various stressors were measured. Pro-oxidant effects of nano- TiO_2 and nano- CuO towards green alga *Chlamydomonas reinhardtii* were explored in various exposure media and under different light illuminations. Dynamics of Cd^{2+} induced effects on photosynthetic activity, sensitisation and recovery of cells of *C. reinhardtii* was also studied.

Keywords: Ecotoxicity, Nanomaterials, Reactive oxygen species, Oxidative stress, Hydrogen peroxide, Optical biosensor, Multiscattering, Absorption spectroscopy

Background

The material revolution engendered by nanotechnological advances in the last decades has not only enabled the

development of highly sophisticated fine-tuned materials for new applications but also confronted established risk assessment and regulatory affairs with new challenges: the possible (eco-)toxicological implications of the expected increment of engineered nanomaterials (ENMs) discharged into environmental compartments [1].

Natural water bodies, one environmental sink of discharged ENMs, are estimated to receive 0.4–7% of the total global mass flow of ENMs [2]. Once in the aquatic

*Correspondence: christian.santschi@epfl.ch

¹ Nanophotonics and Metrology Laboratory (NAM), École Polytechnique Fédérale de Lausanne, EPFL/IST/IMT/NAM, Station 11, 1015 Lausanne, Switzerland

Full list of author information is available at the end of the article



systems ENMs interact with different biotic and abiotic components and potentially harm different organisms [3]. There is currently an agreement [4] that three major phenomena drive the detrimental effects of the ENMs to aquatic organisms: (i) their dissolution, (ii) their organism-dependent cellular uptake and (iii) the induction of oxidative stress and consequent cellular damages. The ability of ENMs to generate reactive oxygen species (ROS) capable of oxidizing biomolecules is currently considered a central (but by no means sole) mechanism of toxicity, potentially leading to oxidative stress and damage (Fig. 1) [5–12].

It is postulated that increased levels of ROS and oxidative damage will occur in exposed organisms (despite the presence of basal or enhanced antioxidant defence systems of repair and replacement), which may be linked to some aspect of impaired biological functions at cellular or higher levels of organization [13]. Thus, from the nanoecotoxicological perspective seeking the elucidation of environmental hazards of ENMs, it follows that an in-depth understanding of their toxic mode of action, that is, of normal and ENM-stimulated ROS production as well as antioxidant levels in aquatic organisms is required. This will allow to quantitatively link the

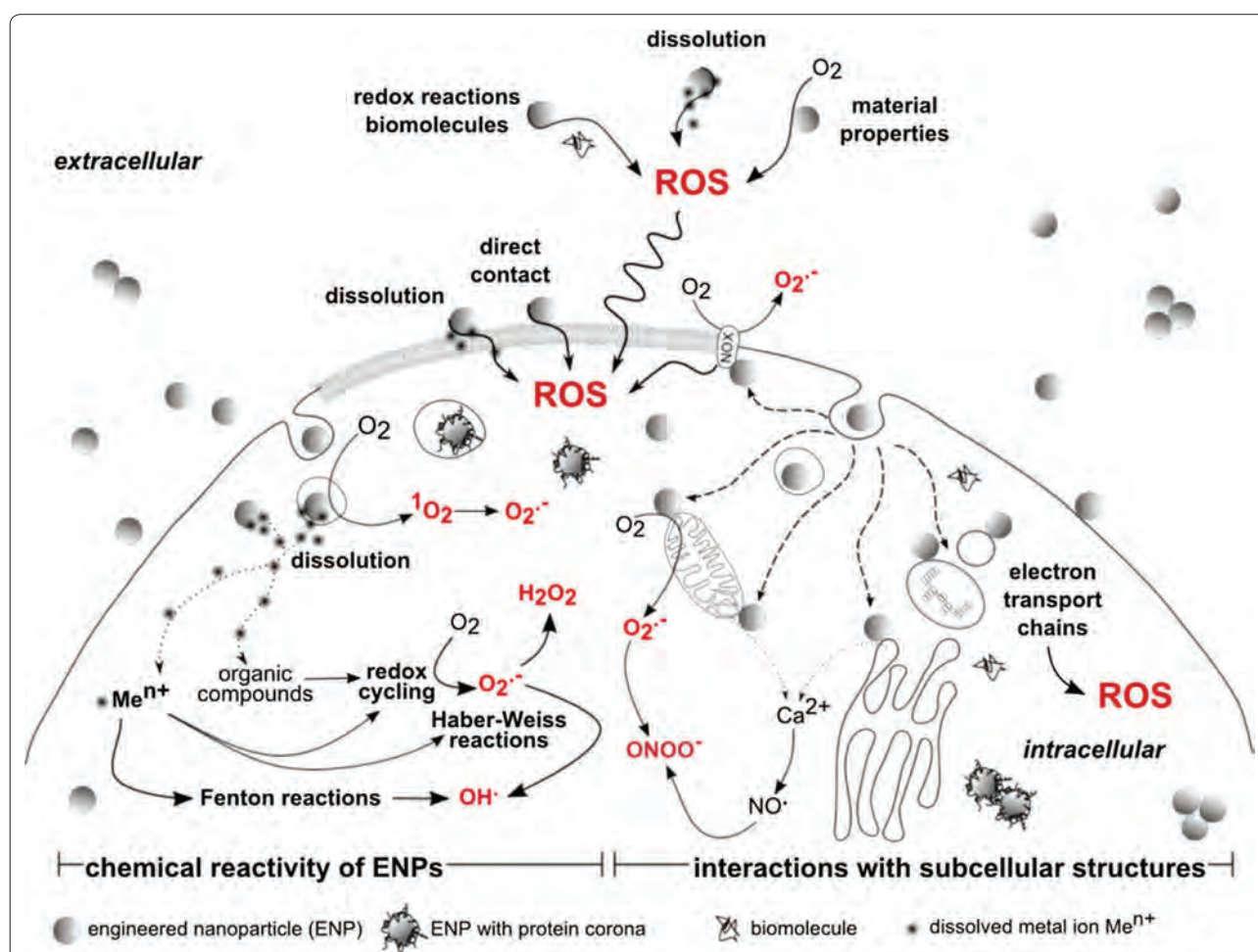


Fig. 1 Mechanisms of ROS generation by engineered nanomaterials via intracellular chemical reactivity (left hand side) or via physical interactions with subcellular compartments (right hand side). ENPs generate ROS by direct and indirect chemical reactions. Direct reactions involve the photoexcitation of O_2 , which yields singlet oxygen (1O_2) and superoxide ($O_2^{\cdot-}$). Indirect chemical reactions involve reactions between ENP constituents (e.g. metal ions, organic compounds) that engage in redox cycling that yields superoxide ($O_2^{\cdot-}$) and hydrogen peroxide (H_2O_2) or in hydroxyl radical (OH^{\cdot}) producing Fenton and Haber–Weiss reactions. ROS yielding interactions encompass the interference with electron transfer chains in chloroplasts, peroxisomes, mitochondria and the endoplasmic reticulum. Furthermore, interactions of ENPs and mitochondria or the endoplasmic reticulum can also cause a loss of organelle membrane integrity that triggers the release of Ca^{2+} ions from interior stores, which may activate ROS generating Ca^{2+} /calmodulin-dependent enzymes, i.e. certain nitrogen monoxide synthase isoforms that produce NO^{\cdot} . Interactions with NADPH oxidase (NOX) complexes in the cell membrane yield $O_2^{\cdot-}$ [29]. Illustration adapted from Unfried, Albrecht [29], not to proportion. Reprinted with permission from (*Nanotoxicology* 2014; 8: 605–630). Copyright (2014)

presence of ENMs with pro-oxidant processes and to estimate the expected degree by which ENM-stimulated oxidative damage may potentially affect overall health of organism.

Hence, there has been a keen interest in the detection and quantification of ROS in aqueous and biological systems, which is a technically tricky task due to their very low concentration in the pico- to micromolar range and their extremely short-lived nature with half times ranging from nanoseconds to hours [14]. Most conventional ROS sensing methods rely on exogenous probes or resulting endogenous reaction products and molecular biomarkers reflecting oxidative damage and antioxidant status [13, 15–17]; they suffer one major technical drawback—the invasive nature of the detection method itself [18].

The present article provides an overview of the main findings of the project “Non-invasive continuous monitoring of the interaction between nanoparticles and aquatic microorganisms” within in the framework of the Swiss National Research Program 64 on the Opportunities and Risk of Nanomaterials. The review begins with a brief introduction in the ENMs-induced ROS generation and oxidative stress in the aquatic microorganisms (AMOs) as well as short presentation of the existing detection techniques. The newly developed method for non-invasive quantification of extracellular H_2O_2 in real-time and monitoring with an unprecedented limit of detection is described, while its capabilities are illustrated by exploring the pro-oxidants effects of the ENMs to AMOs [18].

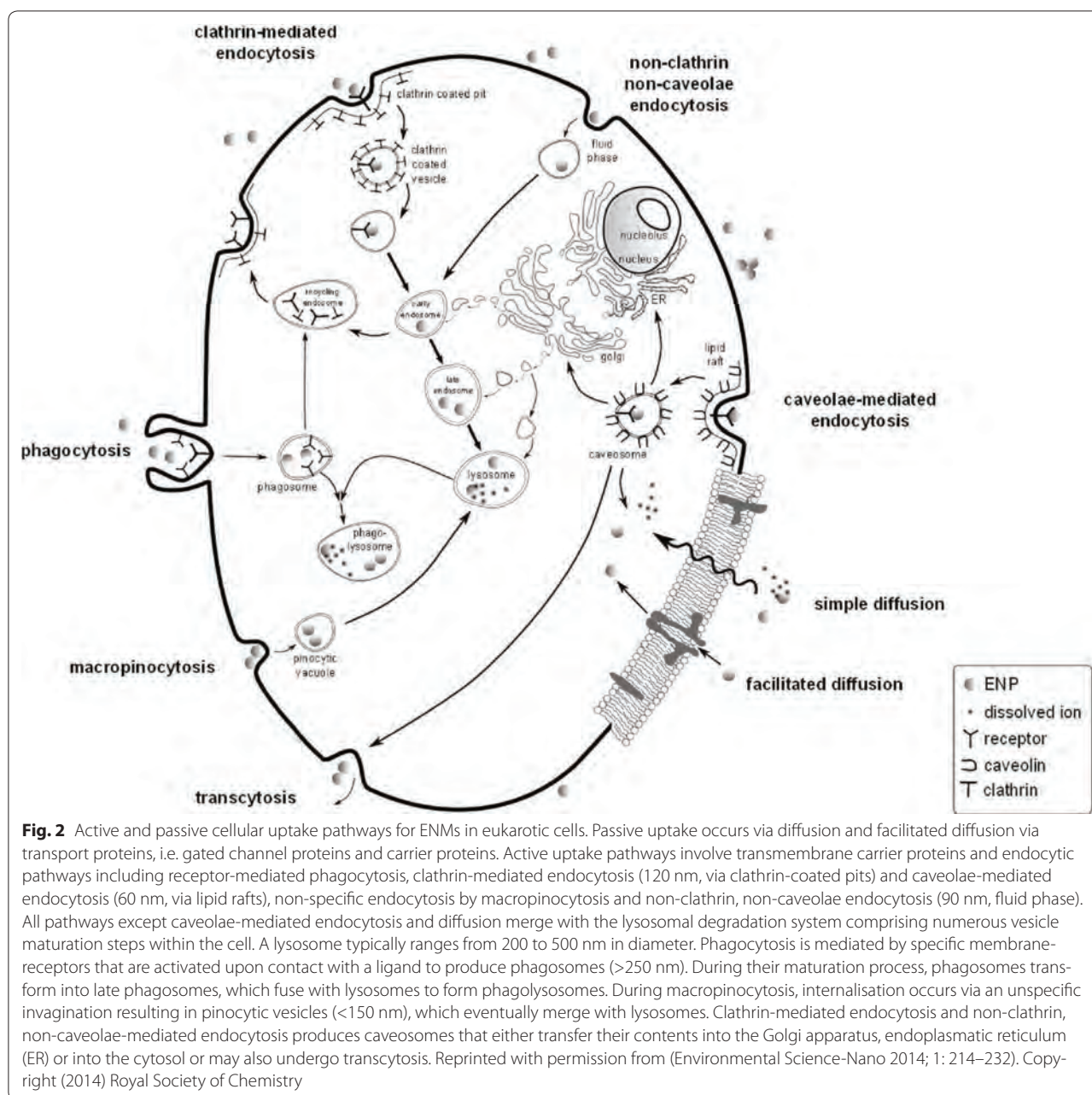
ENMs and oxidative stress in aquatic microorganisms

Investigations performed in the mid-90's led to the conclusion that nanoparticles have the ability to stimulate the generation of reactive oxygen (ROS) and nitrogen species (RNS) at or near the cell surface and to induce oxidative stress [10, 12, 19]. The oxidative stress hypothesis was successfully expanded into nanotoxicology and recognised as a major mechanism for nanoparticle induced effects [23]. Therefore, the impacts of ENMs on the pro-oxidant/antioxidant equilibrium can provide relevant information on their ecotoxicological importance [5].

The toxicity of metal and metal oxide ENMs to organisms can be classified in direct and indirect effects [20, 21]. Direct toxic effects are principally controlled by their chemical composition and surface reactivity. Indirect effects are mainly governed by physical restraints, the release of toxic ions or the production of ROS. The latter is thought to result in elevated cellular response classified as defence, pro-inflammatory effects and cytotoxicity [22]. Toxicological effects of ENMs may include (i) inflammation related to generation of ROS

and oxidative stress, depletion of glutathione and accumulation of oxidised glutathione in response to ROS generation, (ii) DNA and membrane damage, protein denaturation and immune reactivity, (iii) reduction or loss in photosynthetic activity in algae and plants. Direct toxic effects require, as a prerequisite, contact and adsorption of the ENMs with the AMOs [3, 23]. Once the ENMs are adsorbed, they may penetrate through the biological membrane and, therefore, be internalised (Fig. 2). Uptake mechanisms and different pathways leading to internalisation are discussed elsewhere [3, 4, 24]. It is important to note that ENMs can be internalised without necessarily inducing cytotoxicity, meaning that ENMs are not toxic per se [25]. However, ENMs are prone to adsorption of ambient pollutants, which can be transferred into the cells by ENMs acting as carriers (Trojan Horse effect). ENMs can trigger ROS formation extra- and intracellularly by direct and indirect chemical reactions [12] (Fig. 1). The mechanisms underlying the generation of the ROS in AMOs could involve (i) the release of metal ions from ENMs, (ii) the catalytic activity of ENMs and (iii) the redox properties at the particle surface. The pro-oxidant potential of ENMs strongly dependent of their chemical and physical properties, notably chemical composition and purity, particle size, shape and the resulting relative large reactive surface area and surface chemistry [7, 14]. For metal-containing ENMs, dissolution processes leading to ion release play a major role in terms of ecotoxicity. Many transition metal ions, such as Fe^{3+} , Cu^{2+} , Cr^{3+} are redox active and some of them, e.g. Fe and Cu can catalyse Fenton reactions yielding biologically highly reactive hydroxyl radicals OH^\bullet . The Haber–Weiss reactions in the presence of super oxide ions O_2^- can also reduce redox-active metal ions which further couple to the Fenton reactions. Hence, valence state and bioavailability of redox-active ions are strongly related to the generation of ROS. Numerous inorganic ENMs, such as Ag, Pt, TiO_2 , CeO_2 , ZnO, CuO, SiO_2 and different quantum dots were shown to generate ROS and induce oxidative stress in different organisms [5, 10, 12, 26–30]. Selected examples concerning ENM-induced oxidative stress or damage in microalgae, representative for aquatic phytoplankton are given in Table 1.

Photoactive ENMs including fullerenes and semiconducting metal oxides, such as TiO_2 , CuO, CeO_2 , ZnO and Al_2O_3 , can generate ROS when illuminated [43, 44]. It has been demonstrated that these ENMs, the most prominent being TiO_2 , can activate molecular oxygen radicals, 1O_2 and O_2^- , which belong, together with OH^\bullet , to the biologically most potent ROS. It is well known that those photoactive particles are primarily active at wavelength in the UV regime (<390 nm) but it has also been



demonstrated in several studies that TiO_2 is capable to induce oxidative stress in the absence of light.

Overall, environmental contaminants, including ENMs, have the capability to induce generation of ROS in AMOs and, consequently, to alter the cellular redox homeostasis leading to oxidative stress. Oxidative stress occurs as a result of (i) increase in oxidant generation, (ii) reduction of antioxidant protection and (iii) failure to repair oxidative damage [45].

Towards development of the novel tool for non-invasive monitoring of the pro-oxidant effects of engineered nanomaterials

Various approaches are available to determine oxidative stress [46]: (i) Quantification of radicals, including O_2^- , OH^\cdot and H_2O_2 , (ii) quantification of oxidative damage markers and (iii) quantification of antioxidants. A schematic illustration of the main approaches is displayed in Fig. 3. Superoxide O_2^- , represents one of the aboriginal

Table 1 Selected examples of ENM-induced oxidative stress or damage in microalgae

ENM	Algae	Media	Mechanism	Reference
TiO ₂	<i>C. reinhardtii</i>	SE	Generation of ROS by photocatalysis	[31]
TiO ₂ and UV light	<i>C. reinhardtii</i>	Lake water and MOPS buffer		[32]
TiO ₂	<i>Chlorella</i> sp.	OECD	Generation of intracellular ROS by HA	[33]
CdTe/CdS	<i>C. reinhardtii</i>	MES, MOPS, HEPES	Oxidative stress	[34]
Al ₂ O ₃ , SiO ₂ , ZnO and TiO ₂	<i>Chlorella</i> sp.	SE	ROS may not be the dominant mechanism for algal growth inhibition	[35]
Ag	<i>C. vulgaris</i> , <i>Dunaliella tertiolecta</i>	Growth medium BG-11	ROS induced lipid peroxidation and a decrease of cell viability	[36]
Pt	<i>C. reinhardtii</i> <i>P. subcapitata</i>	ISO 8692 medium and 4-fold diluted tris-acetate-phosphate medium	Substantial oxidative stress and negligible membrane damage; significant growth inhibition	[30]
Coated and uncoated CuO	<i>C. reinhardtii</i>	High salt medium	ROS formation may be the primary toxicity mechanism	[37]
CeO ₂	<i>P. subcapitata</i>	Standard US EPA	The oxidative activity is mediated by OH and initiation of lipid peroxidation	[38]
Core-shell CuO	<i>C. reinhardtii</i>	High salt growth medium	ROS are responsible for chlorophyll deterioration, significant decrease of PSII primary photochemistry	[39]
CuO	<i>C. reinhardtii</i>	Various media, lake water	Oxidative stress and damage of membrane integrity	[40]
CuO and light	<i>C. reinhardtii</i>	Synthetic fresh water	Chlorophyll bleaching, oxidative stress and membrane damage; CuO and UV-light has synergistic effect	[41]
TiO ₂ , CdTe and QDs	<i>C. reinhardtii</i>	CM growth medium	Lipid peroxidation induced by oxidative stress, QDs and TiO ₂ exhibit different mechanisms	[42]

forms of aerobic ROS. It is very reactive and short-living and can be converted to H₂O₂ through the reaction with SOD. H₂O₂ is one of the major and most stable ROS produced intracellularly by physiological and pathological processes and can cause oxidative damage. Its stability allows it to diffuse through the cell wall and can therefore be extracellularly detected [47]. Oxidative damage markers such as lipids, DNAs and proteins can be examined for alterations to quantify the extent of oxidative damage due to oxidative stress. Furthermore, several enzymes, such as SOD, CAT and GR, belonging to the antioxidative defence system, can be measured in order to quantify oxidative stress. Recent progress in fluorescent, luminescent and colorimetric ROS and RNS probes was comprehensively reviewed [48].

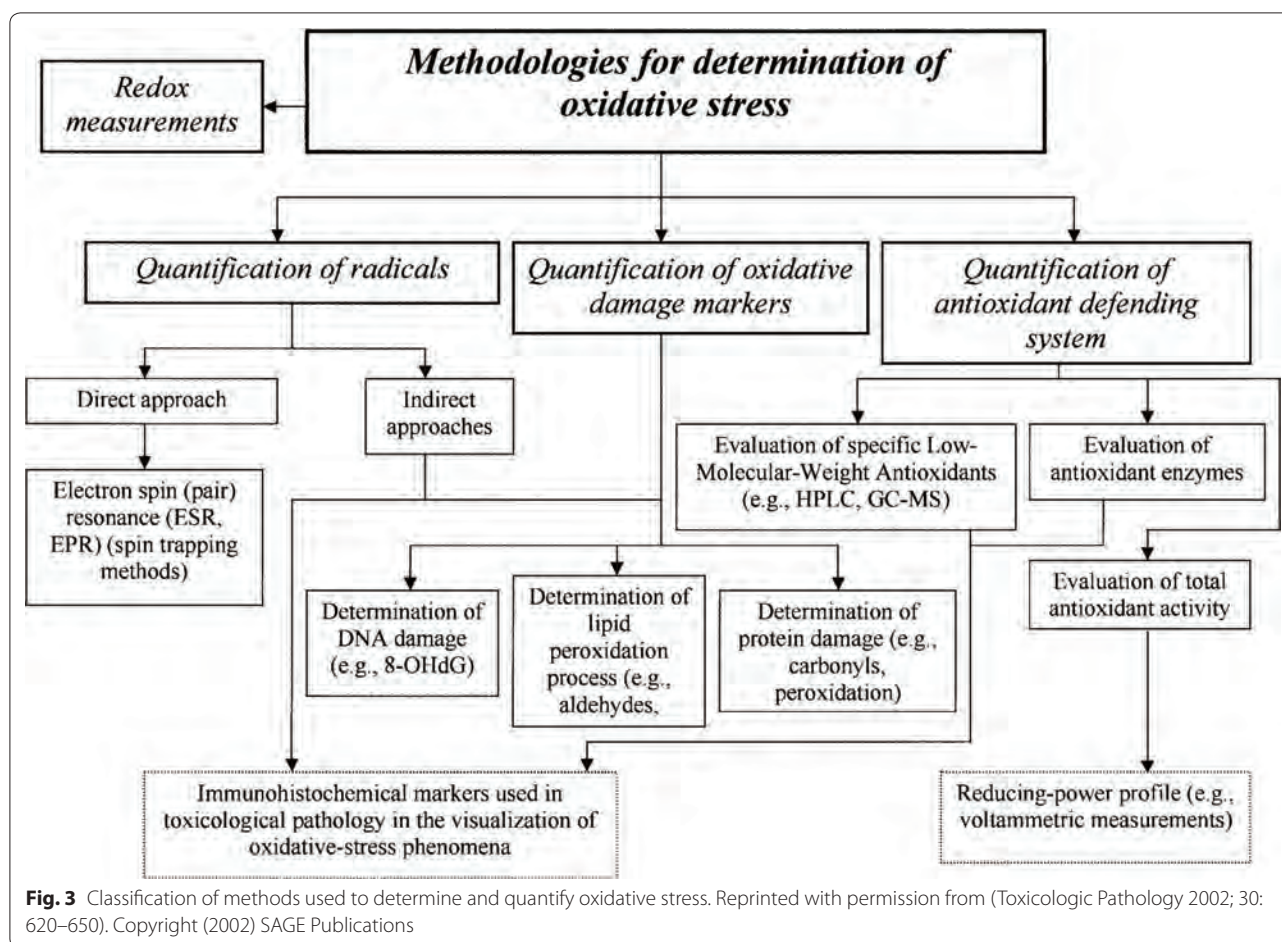
The above-mentioned oxidative stress “indicators” can provide a useful picture on the cell-ENM interactions. However, they are endpoint-based and qualitative, thus unable to provide quantitative information about the rate and amount of generated ROS. In addition they are often very laborious and fail to provide dynamic and continuous information on specific physiological phenomena happening at the exposed living cells.

Hereinafter a new, very sensitive detection scheme for continuous measurement of extracellular H₂O₂ based on multiscattering enhanced absorption spectroscopy is present. Its high sensitivity allows non-invasive and real time measurements of H₂O₂ related to aerobic cell activity, including oxidative stress. Stress-induced H₂O₂ can rapidly diffuse across plasma membranes [49, 50], is relatively long-lived (half-life 4–20 h, <1 s in living tissues) and, therefore, extracellular H₂O₂ could serve as an indicator of pro-oxidant processes [51–54]. A non-exhaustive list of H₂O₂ detection methods can be found in Table 2.

Fluorescent and chemi-luminescent methods exhibit low LODs in the nM range. However, a major drawback of those methods is their incompatibility with bioorganisms and they are therefore endpoint detection schemes.

Multiscattering enhanced absorption spectroscopy (MEAS)

Thanks to its versatility, absorption spectroscopy has become a popular method with a broad range of applications. Adsorption spectroscopy provides a fast, simple and inexpensive method for the detection of a wide

**Table 2** Selection of H₂O₂ detection methods [14]

Technique/probe	Observable	LOD	Application notes	Reference
Direct detection	Absorbance of H ₂ O ₂	mM		[55, 56]
Cyt c	Absorbance	nM	Optimal reaction in low ionic strength solutions	[57, 58]
Xylenolorange + Fe ³⁺	Absorbance of complex	μM	Carried out in acidic acids	[59]
Xylenolorange + Ti ⁴⁺	Absorbance of complex	μM	Carried out in acidic acids	[59]
Luminol	Chemi-luminescence	nM	Interference with Mn ²⁺ and Fe ³⁺	[60–62]
2,7-Dichlorodihydrofluorescein (DCFH)	Fluorescence of product	pM–nM	Can be oxidised by other ROS	[16, 63]
p-Hydroxyphenylacetic acid	Fluorescence of product	nM	Optimal reaction at pH > 8.5	[64, 65]

variety of targets [66]. Absorption spectroscopy can be applied in wide spectral span ranging from X-ray [67] to infrared light [68] and provides a beneficial tool for investigating biomolecules [69, 70]. In conventional absorption spectroscopy configurations the spectral light intensity, passed through the sample under test, is measured and normalised with respect to the intensity of the incident light. Knowing the optical path length (OPL) l through the sample and the absorption coefficient α of

the analyte of interest, its concentration can be determined using Beer-Lambert's law (1) [71].

$$\frac{I}{I_0} = e^{-\alpha Cl} \quad (1)$$

I_0 and I represent the light intensity before and after travelling through the sample, respectively. Long OPLs requires large amounts of analytes which are often costly, especially for biosamples.

Significant efforts have been put in the development of various techniques aiming to improve the sensitivity of absorption spectroscopy [72–74]. A simple and versatile technique, was presented by Koman et al. [75]. In order to extend the OPL and, thus, the sensitivity, advantages were taken from disordered media where the OPL is increased via multiple scattering since spatial variations of the refractive index prevent the light to follow the shortest trajectory. In a configuration containing suspended polystyrene (PS) beads, as schematically shown in Fig. 4, the limit of detection (LOD) was improved substantially [75].

In order to demonstrate its performance MEAS was carried out on low concentrations of phenol red, envy green and 10 nm gold nanoparticles (AuNP). The absorbance A of standard and multiscattering experiments are displayed in Fig. 5 [75]. Using this approach, sensitivity and LOD of commercially available bioassays can be improved. This has been shown for OxiSelect, an assay for H_2O_2 detection [75].

$$A = -\log\left(\frac{I}{I_0}\right) = Cl \quad (2)$$

According to Eq. (3) the sensitivity S for a certain analyte concentration becomes maximal. Hence, the OPL can be adjusted by selecting an adequate scatterer concentration and thereby optimised with respect to a specific application.

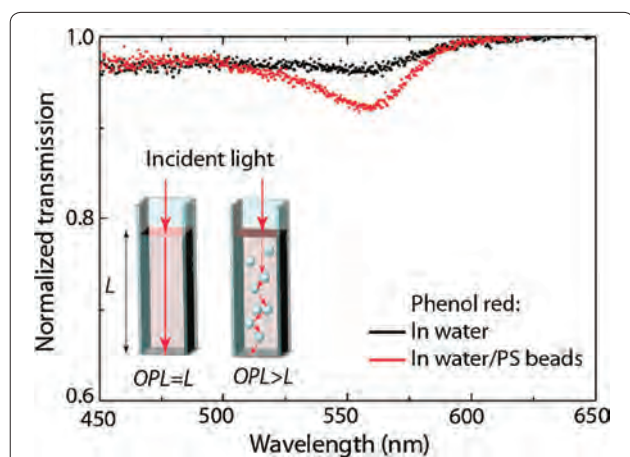


Fig. 4 The presence of scatterers (500 nm polystyrene beads) in the MEAS configuration enhances the OPL and, consequently, lowers the LOD. Principle and transmission measurements of the absorption of phenol red in conventional and MEAS configurations. Reprinted with permission from (*Analytical Chemistry* 2015; 87: 1536–1543). Copyright (2015) American Chemical Society

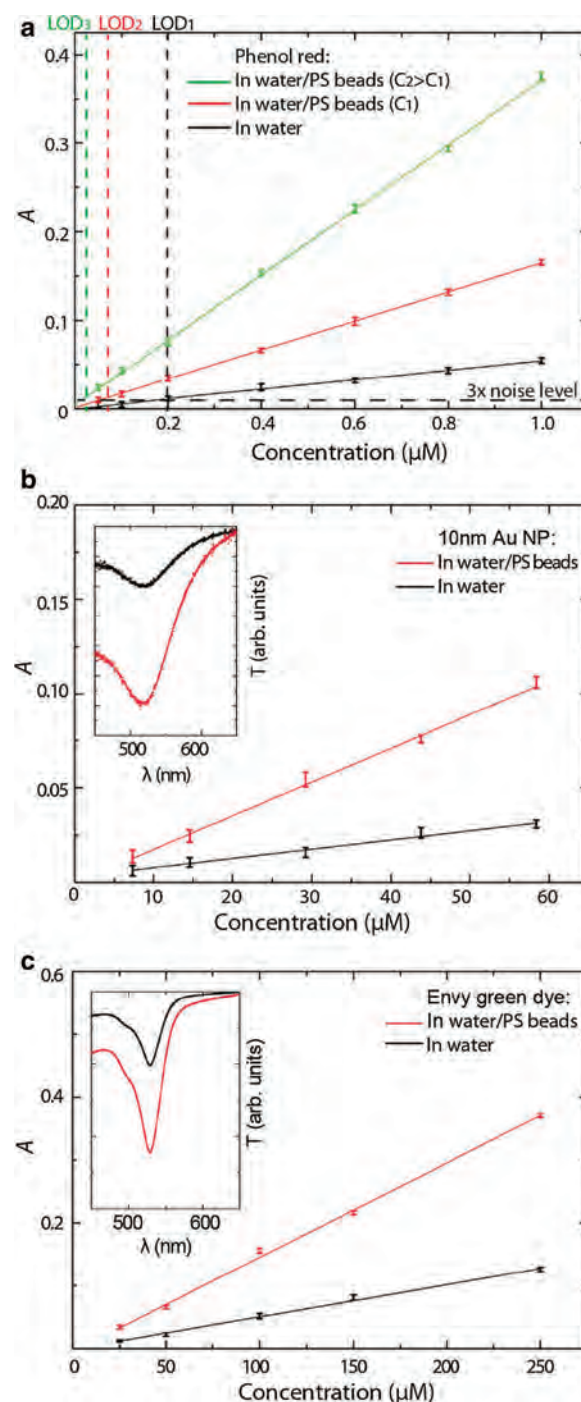
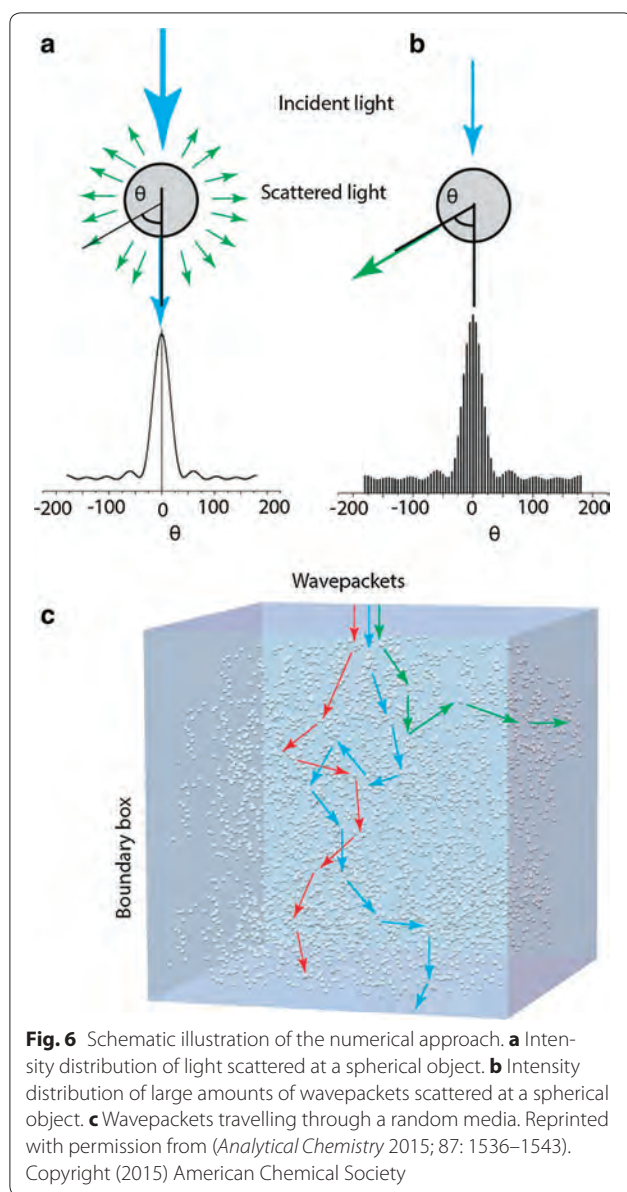


Fig. 5 Absorption enhancement for **a** phenol red, **b** 10 nm Au NPs and **c** envy green for different concentrations C of 500 nm PS scatterers: $C_1 = 0.6$ nM and $C_2 = 3$ nM. The insets in **b** and **c** show the normalised transmission spectrum T and the LOD is defined as 3 times the noise level. The error bars correspond to the standard deviation over five independent measurements. Reprinted with permission from (*Analytical Chemistry* 2015; 87: 1536–1543). Copyright (2015) American Chemical Society



$$S = \left| \frac{\partial}{\partial C} \frac{\Delta I}{I_0} \right| = \alpha l e^{-\alpha C l} \quad (3)$$

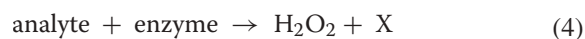
For a better understanding of the multiscattering phenomenon a probabilistic Monte Carlo approach was implemented (Fig. 6). Wavepackets are launched into the system containing randomly distributed PS beads. The random scattering angles were determined using Henyey-Greensteins approximation [76] which describes the scattering cross-section σ for an individual scatterer using Mie theory [77, 78]. The attenuation of each wavepacket was computed following Beer-Lambert's law (1) and, finally, the residues of the individual wavepackets leaving the system were summed together. In order

to achieve an appropriate accuracy the random trajectories of 10^8 wavepackets were calculated. The simulations showed excellent agreement with experimental results and allow prediction of OPLs for different concentrations, refractive indexes and sizes of the scatterers. Due to bead-bead interactions the proposed numerical approach is not accurate for high filling factors F [79] nevertheless, for $F < 10\%$ good numerical/experimental agreements were found [75].

Sensitive real-time detection of H_2O_2

MEAS was employed to improve the sensitivity for the detection of H_2O_2 in aqueous solutions. The detection principle is based on sensitive adsorption measurements of the heme protein cytochrome *c* (cyt *c*) [18], since the absorption spectrum of cyt *c* depends on the oxidation state of its heme group [80]. The catalytic redox behaviour of cyt *c* reduces H_2O_2 into water whereas the ferrous Fe^{II} heme group is oxidised into the ferric Fe^{III} heme group providing information on the H_2O_2 concentration in its environment. Cyt *c* exhibits three oxidation state-dependent absorption peaks in the visible range, namely, at $\lambda = 530$ nm in the oxidised and $\lambda = 520$ and $\lambda = 550$ nm in the reduced state. The absorption at $\lambda = 542$ nm and $\lambda = 556$ nm provide adequate reference signals since at those wavelengths the absorption is independent of the oxidation state (Fig. 7). The sensing molecules, cyt *c*, were embedded in a porous matrix consisting of either aggregated PS beads or a filter membrane. The aggregates were prepared as follows: PS beads were suspended in an aqueous solution of cyt *c* prior to addition of glutaraldehyde to crosslink cyt *c* resulting in cyt *c*/PS beads aggregates [18]. Transmission measurements were performed using an inverted microscope and the temporal evolution of a normalised average oxidation state coefficient ϕ ranging from 0 to 1 for completely oxidised and reduced cyt *c*, respectively, was determined. Calibration experiments carried out for this configuration with known concentrations of H_2O_2 revealed a LOD below 100 pM which enables continuous measurements of the dynamics of ROS produced by bioorganisms when undergoing stress situations [18].

Since H_2O_2 is the reaction product of many enzymatic reactions [Eq. (4)] [81], its real-time detection combined with those reactions enables the detection of further metabolites such as glucose and lactate.



Koman et al. presented a detection scheme for sensitive and real-time detection of those metabolites [40]. Taking advantage of the above presented multiscattering approach they were detected with sub-micromolar LODs. Moreover, this enzymatic approach allows real-time measurements of multiple analytes in parallel which

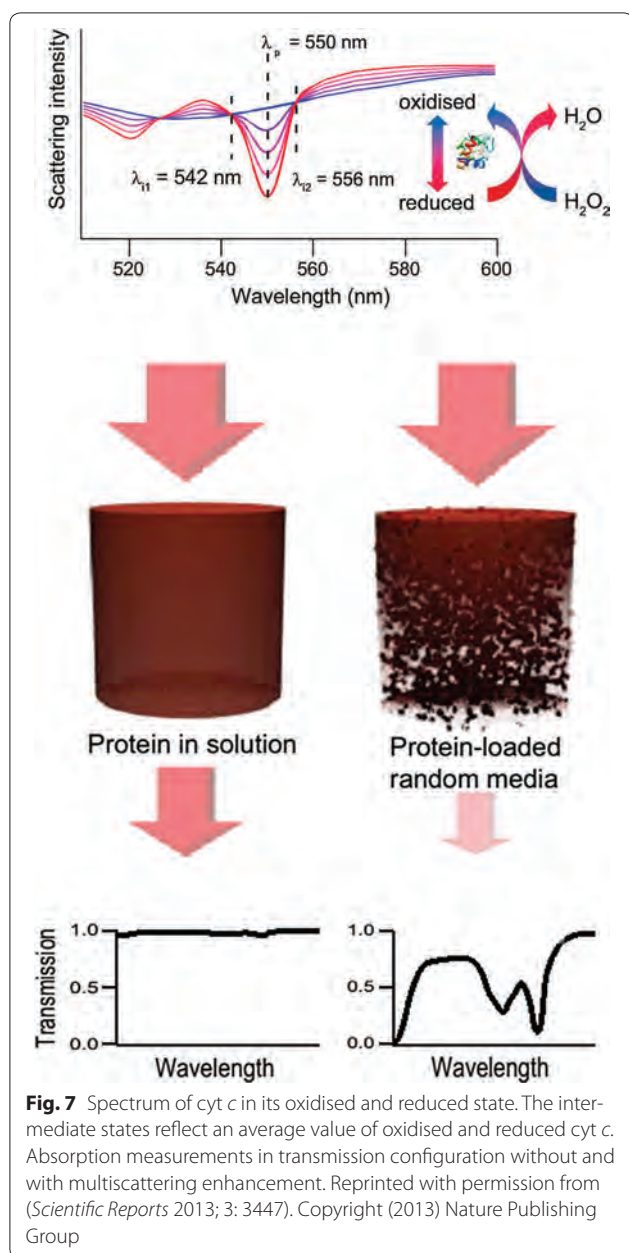


Fig. 7 Spectrum of cyt *c* in its oxidised and reduced state. The intermediate states reflect an average value of oxidised and reduced cyt *c*. Absorption measurements in transmission configuration without and with multiscattering enhancement. Reprinted with permission from (*Scientific Reports* 2013; 3: 3447). Copyright (2013) Nature Publishing Group

offers the possibility to follow the evolution of several metabolites. This feasibility has been demonstrated using the example of parallel detection of glucose and H_2O_2 .

Portable setup and microfluidic chip

To step towards reliable and sensitive routine H_2O_2 measurements, a portable setup containing a multiscattering sensing element was built (Fig. 8) [82]. An aqueous solution of cyt *c* was spotted onto a porous filter membrane using a microarray robot with a delivery volume of 5 nl of 4 mM cyt *c* solution. Subsequently,

the cyt *c* was crosslinked with vaporous glutaraldehyde in order to retain the cyt *c* in the membrane. Using the membrane approach the reproducibility of the amplification was remarkably improved compared to the aggregates described in the previous section. A closed chamber delimited by an o-ring and two glass cover slips was employed to carry out static experiments (Fig. 8a). The sensing element was placed at the bottom of the chamber prior to the measurements. Figure 9a shows the time evolution of ϕ in the static regime for different H_2O_2 concentrations in PBS buffer solution [82]. Measurements performed in this configuration exhibit a signal enhancement due to multiscattering, on the order of 5. In a further step the configuration was extended with a multi-layered microfluidic arrangement containing micro-valves and sieves [83], enabling more complex experimental sequences; for instance exposure/rinsing steps to study recovery or sensitisation of bioorganisms. Schematic overview and photographs of the principle of the portable oxidative stress sensor (POSS) are displayed in Fig. 10. The implementation of microsieves offers the possibility to perform experiments with non-adhering bioorganisms such as algae, which are retained in the reaction chamber as illustrated in Fig. 10h, i. The sensing element is placed in the microfluidic channel in order to minimise possible interferences between organisms and analytes. Figure 9b shows the differential oxidation state coefficient $\Delta\phi$ vs. H_2O_2 concentration for the static and microfluidic regime. $\Delta\phi$ defined as the difference between the initial value of $\phi_{t=0}$ and the value at time t : $\Delta\phi = \phi_{t=0} - \phi_t$. The calibration curve resembles a sigmoidal shape when increasing H_2O_2 concentration, which is typical for ligand binding assays and can be fitted using a 4-parameter logistic model [84]. For the given configuration with a porous membrane a LOD of 40 nM of H_2O_2 was achieved [82]. Exposing the sensing element to reducing agents the cyt *c* alters from its ferric Fe^{III} state to its ferrous Fe^{II} state. Hence, after reducing an oxidised sensing element can be reused. This has been shown by exposing the sensing spot to AA. Four consecutive oxidation/reduction cycles were carried out without lowering the performance of the sensor [82]. Furthermore, glucose and H_2O_2 and lactate and H_2O_2 were simultaneously measured adding glucose (GOx) and lactate oxidase (LOx), respectively, for the enzymatic conversion into H_2O_2 [Eq. (4)] [40]. Thus, to avoid that the fast conversion already takes place in the solution the oxidase was incorporated inside the sensing element. In practise, a mixture of oxidase and cyt *c* was deposited onto the filter membrane prior to crosslinking with glutaraldehyde, as described above for cyt *c*. An unambiguous measurement of glucose and lactate concentrations requires simultaneous measurements of the substrate (glucose and lactate

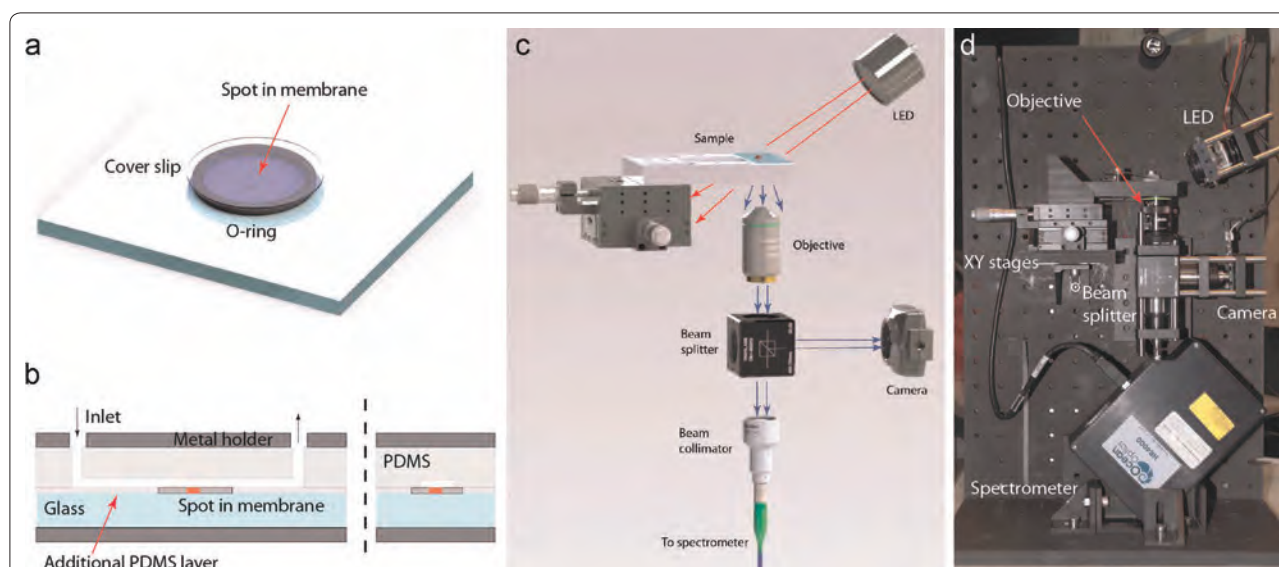


Fig. 8 Portable setup **(a)** closed chamber for static measurements, **(b)** microfluidic channel for flow experiments, **(c)** schematic drawing of the portable setup and **(d)** front view photograph. Reprinted with permission from (Biosensing and Bioelectronics 2015; 68: 245–252). Copyright (2015) Elsevier

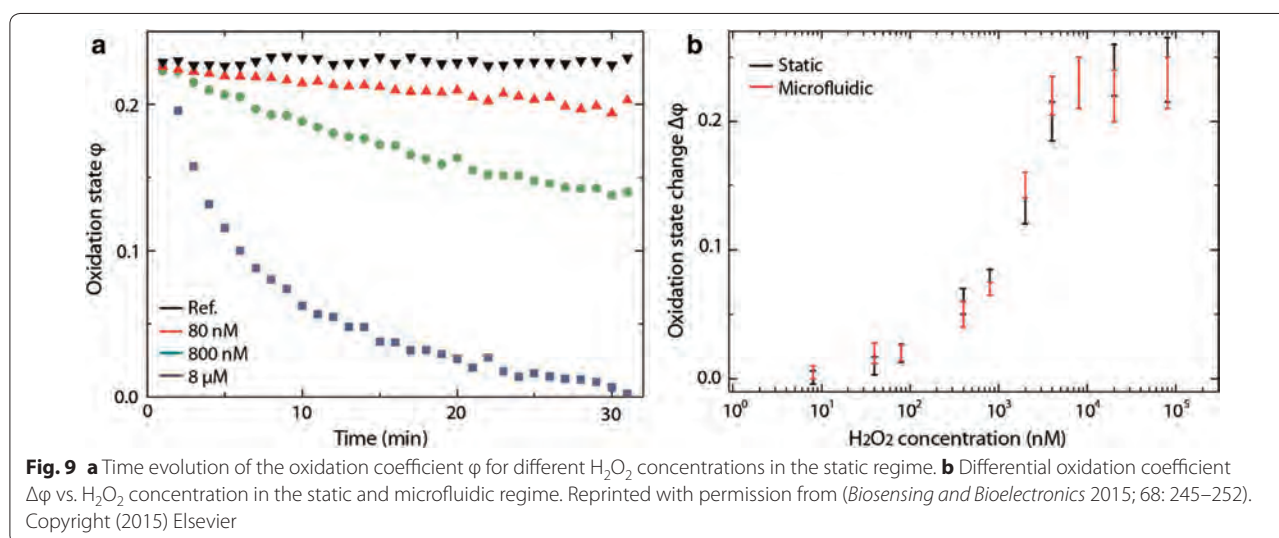


Fig. 9 **a** Time evolution of the oxidation coefficient ϕ for different H_2O_2 concentrations in the static regime. **b** Differential oxidation coefficient $\Delta\phi$ vs. H_2O_2 concentration in the static and microfluidic regime. Reprinted with permission from (Biosensing and Bioelectronics 2015; 68: 245–252). Copyright (2015) Elsevier

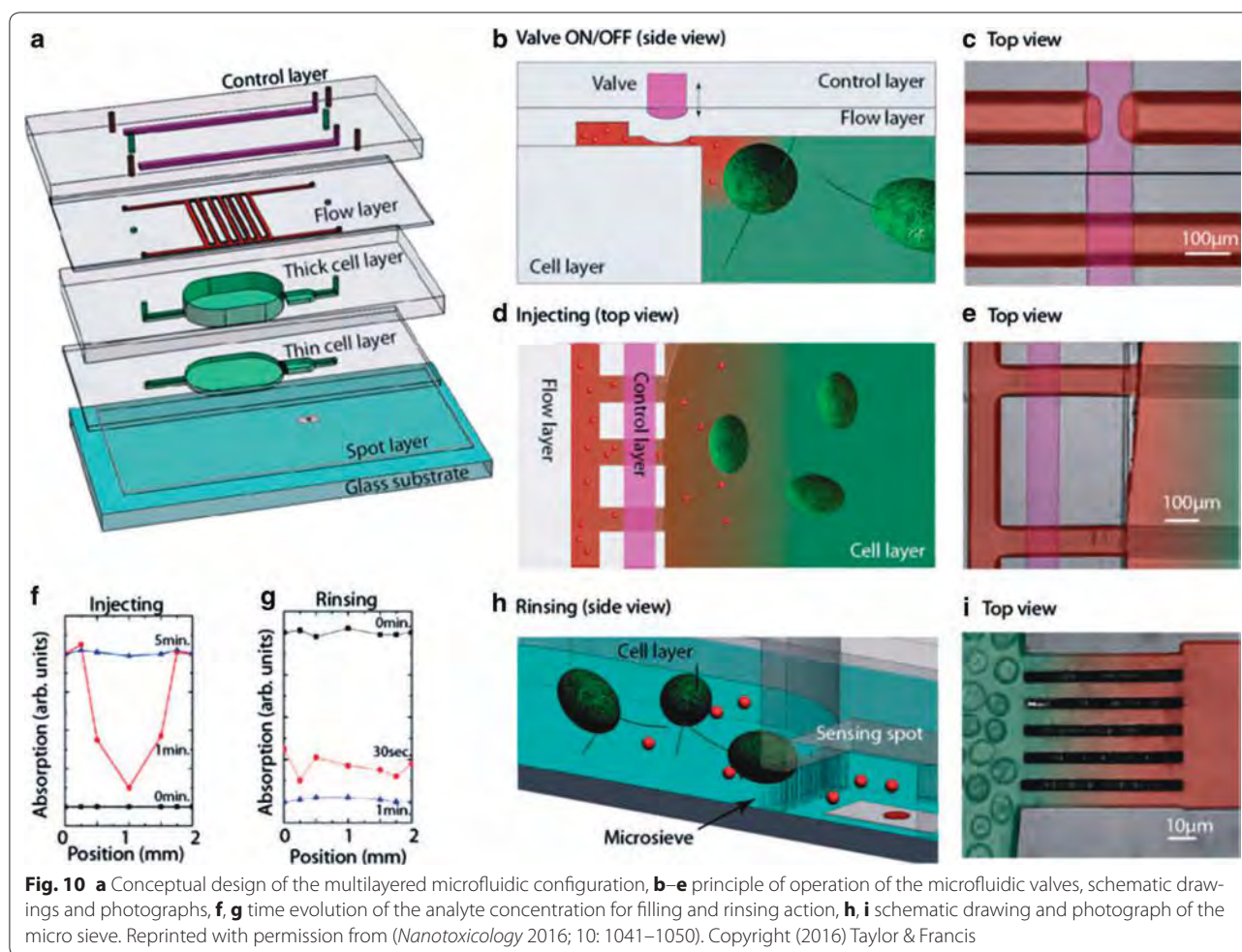
in the present cases) and H_2O_2 with subsequent subtraction of the background H_2O_2 contribution. For the sake of completeness, it should be mentioned that, due to diffusion issues, interferences were observed when placing the sensing elements for the substrate and H_2O_2 in the same chamber. This problem was solved by adapting the microfluidic configuration to separate the sensing elements [40]. Finally, LODs as low as 240 and 110 nM for lactate and glucose, respectively, were achieved for the configuration at hand.

Here ENM-induced H_2O_2 excretion by cells exposed to ENMs was monitored with a recently developed optical

biosensor in a portable setup (POSS; portable oxidative stress sensor) specifically designed for field experimentation [82]. In this way, POSS may contribute to the elucidation of ENM-specific pro-oxidant interactions with cells and thus help to narrow the gap between material innovation and sound risk assessment.

Selected applications to probe the pro-oxidant effect of nanoparticles to microalga *C. reinhardtii*

To demonstrate the performances of the developed sensing tool, the pro-oxidant effects of CuO and TiO₂ nanoparticles to green alga *C. reinhardtii*, a representative



model AMO are presented [32, 85] together with measurements of the potential to generate abiotic ROS as well as oxidative stress and membrane damage. These two ENMs were chosen since they have different properties—CuO nanoparticles have a tendency to dissolve, while nano-TiO₂ is rather inert; (ii) both have photocatalytic properties; (iii) nano-CuO is with relatively high toxic potential [86], while nano-TiO₂ is moderately toxic; (iv) they are of high environmental relevance given their increasing use in different products.

The nanoparticle-induced cellular pro-oxidant process in *C. reinhardtii* were studied using the newly developed cytochrome *c* biosensor for the continuous quantification of extracellular H₂O₂ and fluorescent probes (Cell-RoxGreen for oxidative stress and propidium iodide for membrane integrity [32, 41, 87]) in combination with flow cytometry. Both the dynamics of abiotic (ENM only) and biotic (ENM + cells) pro-oxidant processes related to the exposure of *C. reinhardtii* to nano-CuO and nano-TiO₂ are present below.

Nano-CuO

Chlamydomonas reinhardtii were exposed to CuO nanoparticles in five different media, namely TAP, MOPS, OECD, MES and Geneva lake water [85] and the biological responses including growth, size increase, chlorophyll autofluorescence, intracellular ROS and membrane damage were quantified.

The concentration of Cu ions dissolved from the nano-CuO in the different media increased in the order: MOPS < MES < Geneva lake water < OECD < TAP. Nano-CuO exposure induced oxidative stress and membrane damage, but the intensity of the effects was susceptible to medium and exposure duration [40]. Comparison of the exposure of *C. reinhardtii* to nano-CuO and released Cu²⁺ revealed that in all but one of the five different exposure media free ionic copper was likely the main toxicity-mediating factor. However, a threshold concentration of Cu²⁺ must be reached for biological effects to occur. However, a nano-CuO particle effect was observed in cells exposed in the Good's

buffer MOPS, in which nano-CuO dissolution was very low. These findings highlight how the dominant toxicity mediating factors change with exposure medium, time and the biological endpoint considered and thus demonstrate that nanotoxicity is a highly dynamic process. Furthermore, the observed ROS generation and oxidative stress observed in *C. reinhardtii* exposed to nano-CuO in lake water, were in line with the increasing extracellular H_2O_2 determined using the POSS (Fig. 11). Abiotic H_2O_2 formation by nano-CuO was also observed, but the values were much lower than those found in the presence of algae. Simultaneous exposure of *C. reinhardtii* to nano-CuO and simulated solar light induced synergistic effect in ROS generation, whereas exposure to ionic copper and the same solar simulated light conditions resulted in antagonistic effects [41, 87]. No measurable alterations in nano-CuO aggregation, copper dissolution or abiotic ROS production were found under the tested light irradiations suggesting that the synergistic effects are not associated with light-induced changes in nano-CuO properties in the exposure medium [40, 41]. Nano-CuO toxicity to microalgae is generally recognized to be associated with the amount of copper released by the nanoparticles [41]. However, the combined effects observed for light irradiation and CuO-NPs could not be explained with the measured copper dissolution suggesting that under stressful light conditions other mechanisms of actions might be involved.

Nano-TiO₂

The nano-TiO₂ exposure experiments were performed in MOPS and water sampled from lake of Geneva [32]. The observed pro-oxidant effects were strongly dependent on the exposure concentration and medium. In lake water exposures the proportion of cells affected by oxidative stress increased with the concentration of nano-TiO₂, with highest responses obtained for algae exposed to 100 and 200 mg L⁻¹ nano-TiO₂. Similarly, membrane damage predominantly occurred in lake water rather than in MOPS. UV light pre-treatment of TiO₂ enhanced median intracellular ROS levels in lake water exposure while no significant effect was found in MOPS.

In MOPS H_2O_2 concentrations ($c_{H_2O_2}$) determined using POSS were highest at the start and decayed to values close to the LOD after 60 min exposure (Fig. 12) in all treatments. $c_{H_2O_2}$ values were higher in UV pre-treated samples at nearly all concentrations (except 10 mg L⁻¹ nano-TiO₂). The initial $c_{H_2O_2}$ peaks are possibly due to the formation of hole/electron pairs and their subsequent photocatalytic reaction with H_2O and O_2 at the surface of the nano-TiO₂ particles [88]. Results suggest that nano-TiO₂ behaves as both peroxide source and sink through photocatalytic reactions at the surface of the nanoparticles. Experiments carried out with lake water did not exhibit initial peroxide peak concentrations after sonication. This may be explained by ROS quenching species in the form of dissolved organic

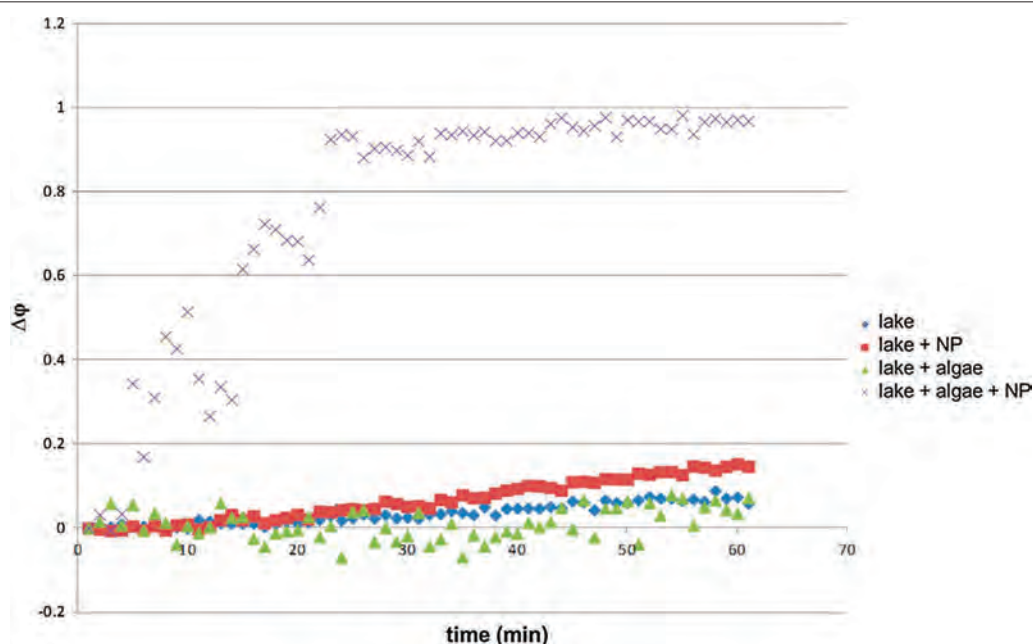


Fig. 11 Time evolution of the differential oxidation coefficient $\Delta\phi$ during an exposure for 60 min to nano-CuO, *C. reinhardtii* and nano-CuO and *C. reinhardtii* in lake water. A control experiment was carried out in lake water

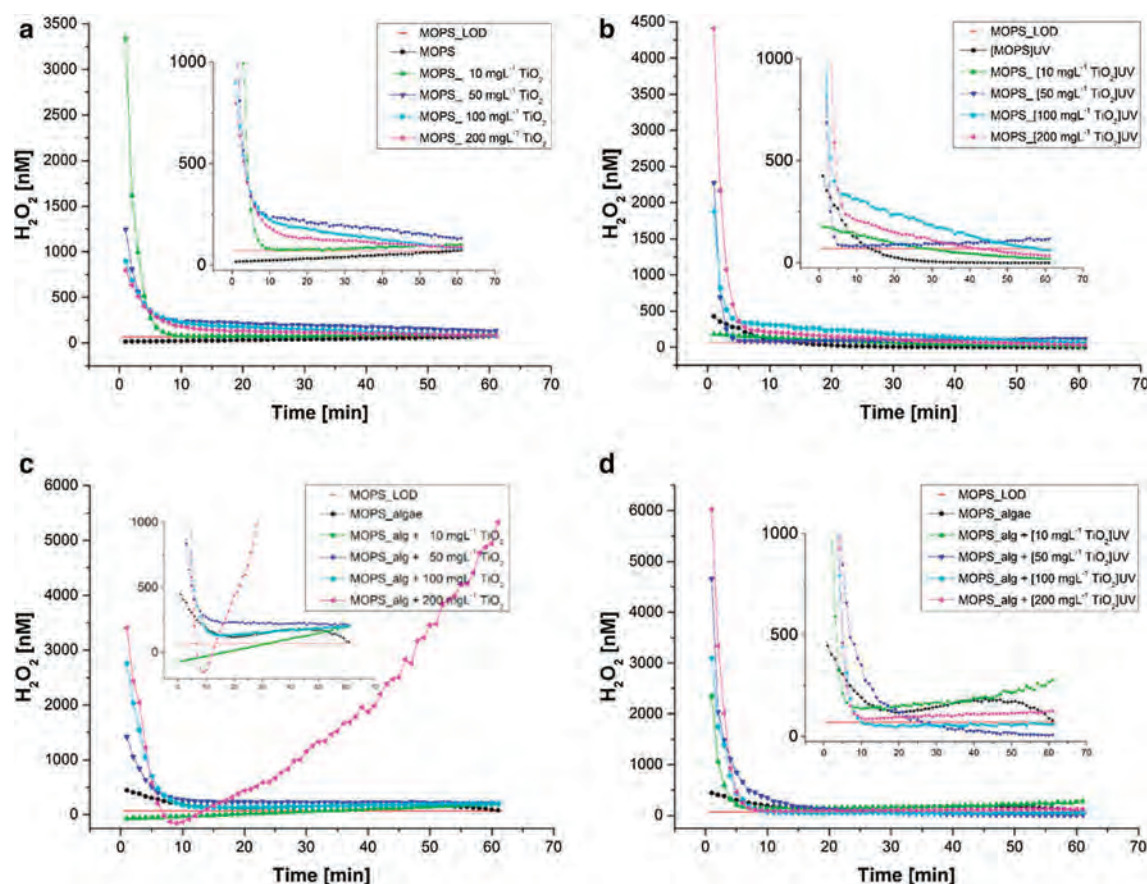


Fig. 12 Extracellular H_2O_2 [nM] ($c_{H_2O_2}$) produced during 60 min by four nano-TiO₂ concentrations with (b, d) and without UV pre-treatment (a, c) in abiotic (a, b) and biotic (c, d) conditions in the MOPS buffer: nano-TiO₂ only (a), nano-TiO₂ after 20 min UV pre-treatment (b), algae exposed to nano-TiO₂ (c) and algae exposed to UV pre-treated nano-TiO₂ (d). The horizontal red line represents the LOD and insets depict enlargements of the respective 0–1000 nM concentration range Reprinted with permission from (RSC Advances 2016; 6: 115271–115283). Copyright (2016) Royal Society of Chemistry

matter (DOM), which, in contrast to MOPS, are present in lake water.

The biotic exposure experiments revealed higher decay rates of the initial peaks at the beginning of the experiments, suggesting a peroxide annihilation by algae.

Overall, our findings showed that (i) irrespective of the medium, agglomerated nano-TiO₂ in the micrometer size range produced measurable abiotic H_2O_2 concentrations in biologically relevant media, which is enhanced by UV irradiation, (ii) $c_{H_2O_2}$ undergo decay and are highest in the first 10–20 min of exposure and (iii) the generation of H_2O_2 and/or the measured H_2O_2 concentration is a dynamic process modified by the ambient medium as well as nano-TiO₂ concentrations and the presence of cells.

Comparison of the extracellular H_2O_2 measurements and intracellular oxidative stress [32, 82] further showed significant differences between extracellular and intracellular pro-oxidant processes. Indeed, an increase of the intracellular oxidative stress was found under the

conditions where no significant increase in extracellular biotic H_2O_2 was measured. The above observation indicates that extracellular H_2O_2 measurements cannot directly serve as a predictor of cellular pro-oxidant processes or oxidative stress in *C. reinhardtii*, however, they provide valuable information about the extracellular dynamics of the most stable ROS in the extracellular medium.

Extracellular H_2O_2 measurements during altering illumination regimes

It is well known that light conditions influence the metabolic activity of algae and therefore cellular ROS generation [89, 90]. ROS released by photosynthetic organisms generally originate from the photosystems II and I [89, 90] (PSII and PSI) located in the thylakoid membrane of the chloroplast. Disturbances of the electron transport chain from PSII to PSI favour reduction of molecular oxygen O_2 to O_2^- which triggers a reaction cascade leading to the formation

of OH and H₂O₂ [91]. According to previous studies, chloroplast derived H₂O₂ is able to diffuse out of the chloroplast [92] and through the cell walls and is, therefore, present in the extracellular media. Here, we examined the dynamics of extracellular H₂O₂ during altering illumination regimes.

C. reinhardtii in model medium were exposed to 100 nM of Cd²⁺ in different light conditions [18].

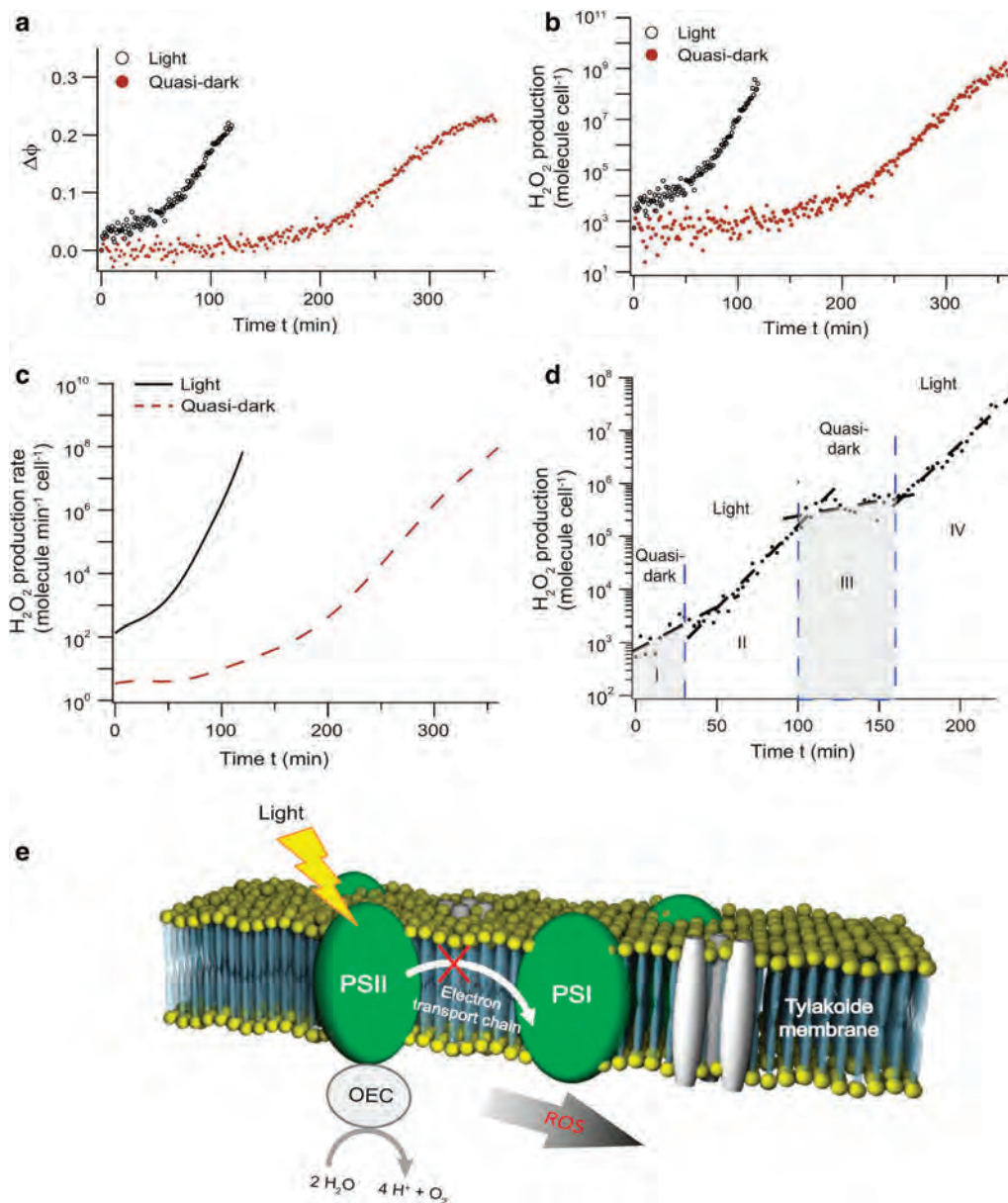


Fig. 13 Dark- and light-adapted *C. reinhardtii* are exposed to 100 nM of Cd(II). Time evolution of **(a)** the differential oxidation state coefficient $\Delta\phi$, **(b)** the H₂O₂ production and **(c)** the H₂O₂ production rate. After injection of Cd(II) the light-adapted algae under illumination start excreting H₂O₂ without delay, whereas there is a production delay under dark conditions. **(d)** ROS production for dark-adapted algae exposed to 100 nM of Cd(II) when the illumination is successively turned on and off during the measurement. **(e)** These data support the following action mechanism of Cd(II) on the photosynthetic apparatus of *C. reinhardtii*: Cd(II) binding to the plastoquinone pool disturbs the electron transport chain between PSII and PSI. Upstream, the light driven electron extraction from oxygen evolving complex (OEC) remains functional and generates light-dependant ROS at the PSII acceptor side. Reprinted with permission from (Scientific Reports 2013; 3: 3447). Copyright (2013) Nature Publishing Group

Figure 13 indicates an enhanced H_2O_2 production rate and no production delay under light conditions suggesting a correlation between ROS regulation and the activity of the photosystems.

Recovery and sensitisation

In contrast to end-point measurements, sensitive and non-invasive continuous H_2O_2 measurements enable the investigation of recovery and sensitisation. To demonstrate the practicability of such experiments the *C. reinhardtii* were repeatedly exposed to Cd^{2+} , using a microfluidic configuration as described above [83]. Cd^{2+} concentrations are typically <10 nM in fresh water. However, higher concentrations of Cd^{2+} were found in the exposure media containing CdSe quantum dots [5] or CdTe/CdS [34].

Extracellular H_2O_2 concentrations were measured while *C. reinhardtii* were exposed to 100 and 500 nM of Cd^{2+} [step (1)]. A subsequent rinsing [step (2)] and

further exposure to Cd^{2+} [step (3)], even at 100 nM, exhibits an increased H_2O_2 production rate compared to the previous exposure (Fig. 14).

1. 1st exposure of *C. reinhardtii* to $\text{Cd}^{2+} \rightarrow \text{H}_2\text{O}_2$ production
2. Rinsing
3. 2nd exposure of *C. reinhardtii* to $\text{Cd}^{2+} \rightarrow$ increased production rate of H_2O_2

This shows that exposure to even low concentration of Cd^{2+} leads to a sensitisation of exposed cells, thus suggesting an adverse impact on the health of microorganisms. In parallel, intracellular ROS was assessed based on the fluorescence intensity of de-esterified $\text{H}_2\text{DFC-DA}$ [93]. At high Cd^{2+} concentrations (500 nM) intra- and extracellular measurements correlated very well, confirming the suitability of extracellular H_2O_2 measurements as indicator of cellular stress. However, unlike extracellular H_2O_2

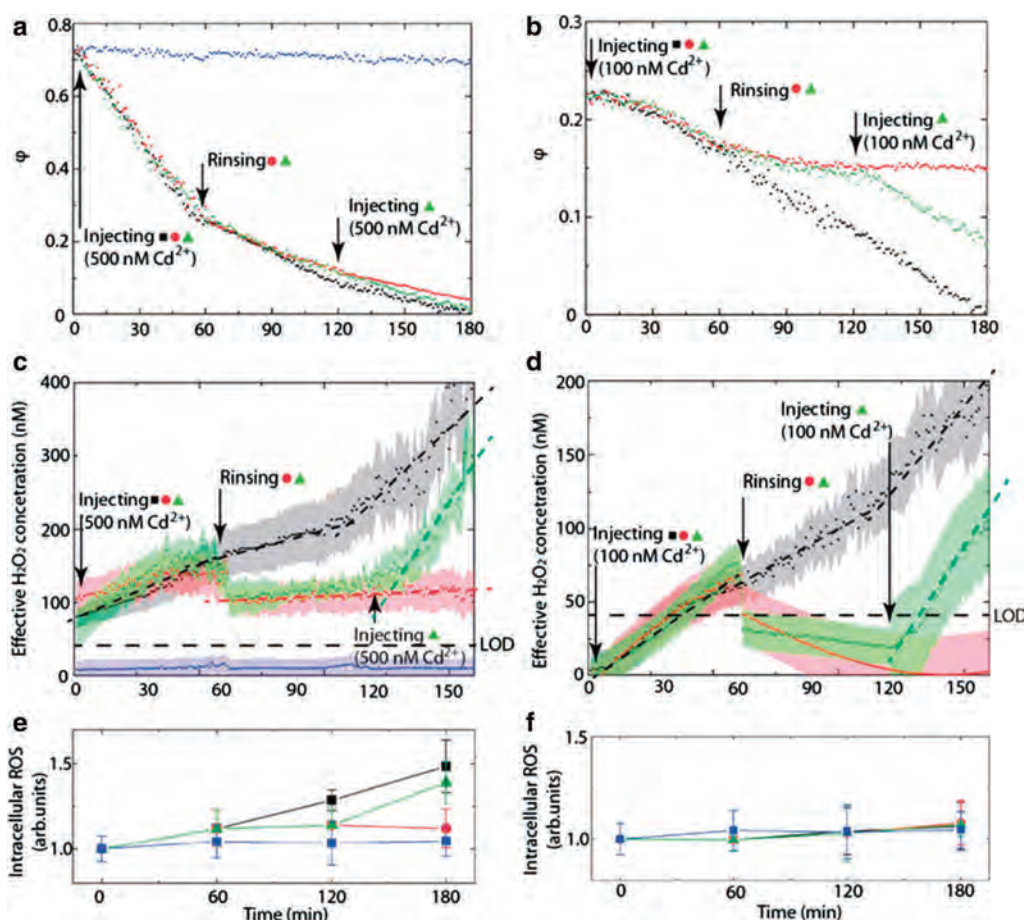


Fig. 14 Algae exposure to Cd^{2+} . Oxidative state coefficient ϕ versus time for: **a** 500 nM and **b** 100 nM exposure cycles. **c, d** Extracellular H_2O_2 concentration $C_{\text{H}_2\text{O}_2}$. Intracellular ROS measured a fluorescence method for **e** 500 and **f** 100 nM Cd^{2+} exposures for identical cycles as in **a** and **b**. Reprinted with permission from (Nanotoxicology 2016; 10: 1041–1050). Copyright (2016) Taylor & Francis

concentrations, intracellular levels remain stable in the 100 nM exposure, suggesting an efficient ROS/AOX regulation through the cell walls.

Conclusions and outlook

This review paper provides a short overview on nanoparticle toxicity for aquatic microorganisms based on the paradigm of oxidative stress and highlights the recent developments of an optical biosensor based on absorption measurements of cyt *c* for the sensitive, non-invasive and continuous measurement of H₂O₂. The use of this new tool for studying the pro-oxidant effects of ENMs to aquatic microorganisms was demonstrated by exposing the representative aquatic microorganism *C. reinhardtii* to nano-CuO and nano-TiO₂ in various exposure media and under different light treatments. Sensitive continuous measurements of extracellular H₂O₂ provided valuable information on both the potency of the studied nano-CuO and nano-TiO₂ to generate ROS as well as on the mechanisms of toxicity. The results were in good agreement with the oxidative stress and membrane damage results obtained under the same conditions using a combination of fluorescent staining with flow cytometry. The developed biosensor allows rapid measurement of the rate and amount of H₂O₂ measured in the extracellular medium in response to cell exposure to ENMs. Hence, detailed knowledge of the dynamics of H₂O₂ excretion can provide valuable insights into complex biological responses. The development of the portable setup and the multi-layered microfluidic chip with an integrated optical sensor for the continuous sensitive detection of extracellular H₂O₂ opens novel avenues for new types of exposure experiments, leading to a better understanding of ROS biology as well as to numerous opportunities for nanoecotoxicological studies. Developing and employing new sensing tools and methods enables conducting experiments under more realistic conditions such as environmental relevant concentrations, aged nanomaterials and simultaneous exposure to various stressors. Furthermore, studying the dynamics of cellular metabolites leads to new insights in the extremely complex adverse outcome pathways.

Abbreviations

ENMs: engineered nanomaterials; ROS: reactive oxygen species; AOX: antioxidant; AMO: aquatic microorganism; MEAS: multiscattering enhanced absorption spectroscopy; OPL: optical path length; LOD: limit of detection; POSS: portable oxidative stress sensor; AuNp: gold nanoparticle; cyt *c*: cytochrome *c*; PSI: photosystem I; PSII: photosystem II; MES: 2-(*N*-morpholino)ethanesulfonic acid; MOPS: 3-(*N*-morpholino)propanesulfonic acid; TAP: N-Tris[hydroxymethyl]methyl-3-aminopropanesulfonic acid; OECD: OECD standard media; DOM: dissolved organic matter; SOD: superoxide dismutase; CAT: catalase; GR: glutathione reductase; AA: ascorbic acid; HA: humic acid; SRFA: Suwannee River fulvic acid; EDTA: ethylenediaminetetraacetic acid.

Authors' contributions

CHS contributed to the development of the sensor and to the coordination of the experiments, NVM carried out the experiments on AMOs, VK contributed to the development of the sensor and the AMO experiments, VS coordinated the AMO experiments, PB coordinated the characterisation of the nano-particles, OJFM participated in the coordination of the study and manuscript writing, CHS, NVM and VS wrote the manuscript, all authors edited and approved the manuscript. All authors read and approved the final manuscript.

Author details

¹ Nanophotonics and Metrology Laboratory (NAM), École Polytechnique Fédérale de Lausanne, EPFL/IST/IMT/NAM, Station 11, 1015 Lausanne, Switzerland.

² Environmental Biogeochemistry and Ecotoxicology, Department F.-A. Forel for Environmental and Aquatic Sciences, Earth and Environmental Sciences, Faculty of Sciences, University of Geneva, 66, Bvd Carl-Vogt, 1211 Geneva, Switzerland. ³ Powder Technology Laboratory (LTP), École Polytechnique Fédérale de Lausanne, 1015 Lausanne, Switzerland.

Acknowledgements

This work was supported by the Swiss National Research Program NRP 64 Project No. 406440-131280/1 of the Swiss National Science Foundation.

Competing interests

The authors declare that they have no competing interests.

Availability of data and materials

Not applicable since it is a review article. Data are available from the original publications.

Consent for publication

We accept the submission conditions.

Funding

Swiss National Research Program NRP 64 Project No. 406440-131280/1 of the Swiss National Science Foundation.

Received: 20 December 2016 Accepted: 22 February 2017

Published online: 07 March 2017

References

1. Miller G, Wickson F. Risk analysis of nanomaterials: exposing nanotechnology's naked emperor. *Rev Policy Res*. 2015;32(4):485–512.
2. Keller AA, et al. Global life cycle releases of engineered nanomaterials. *J Nanopart Res*. 2013;15(6):1–17.
3. von Moos N, Bowen P, Slaveykova VI. Bioavailability of inorganic nanoparticles to planktonic bacteria and aquatic microalgae in freshwater. *Environ Sci Nano*. 2014;1(3):214–32.
4. Ivask A, et al. Mechanisms of toxic action of Ag, ZnO and CuO nanoparticles to selected ecotoxicological test organisms and mammalian cells in vitro: a comparative review. *Nanotoxicology*. 2014;8:57–71.
5. Burello E, Worth AP. A theoretical framework for predicting the oxidative stress potential of oxide nanoparticles. *Nanotoxicology*. 2011;5(2):228–35.
6. Zhang H, et al. Use of metal oxide nanoparticle band gap to develop a predictive paradigm for oxidative stress and acute pulmonary inflammation. *ACS Nano*. 2012;6(5):4349–68.
7. Nel A, et al. Toxic potential of materials at the nanolevel. *Science*. 2006;311(5761):622–7.
8. Djuricic AB, et al. Toxicity of metal oxide nanoparticles: mechanisms, characterization, and avoiding experimental artefacts. *Small*. 2015;11(1):26–44.
9. Xia T, et al. Comparison of the abilities of ambient and manufactured nanoparticles to induce cellular toxicity according to an oxidative stress paradigm. *Nano Lett*. 2006;6(8):1794–807.
10. Donaldson K, Beswick PH, Gilmour PS. Free radical activity associated with the surface of particles: a unifying factor in determining biological activity? *Toxicol Lett*. 1996;88(1–3):293–8.
11. Manke A, Wang L, Rojanasakul Y. Mechanisms of nanoparticle-induced oxidative stress and toxicity. *BioMed Res Int*. 2013;2013:118.

12. von Moos N, Slaveykova V. Oxidative stress induced by inorganic nanoparticles in bacteria and aquatic microalgae—state of the art and knowledge gaps. *Nanotoxicology*. 2014;8(6):605–30.
13. Livingstone DR. Contaminant-stimulated reactive oxygen species production and oxidative damage in aquatic organisms. *Mar Pollut Bull*. 2001;42(8):656–66.
14. Burns JM, et al. Methods for reactive oxygen species (ROS) detection in aqueous environments. *Aquat Sci*. 2012;74(4):683–734.
15. Bartosz G. Oxidative stress in plants. *Acta Physiol Plant*. 1997;19(1):47–64.
16. Gomes A, Fernandes E, Lima J. Fluorescence probes used for detection of reactive oxygen species. *J Biochem Biophys Methods*. 2005;65(2–3):45–80.
17. Valavanidis A, et al. Molecular biomarkers of oxidative stress in aquatic organisms in relation to toxic environmental pollutants. *Ecotoxicol Environ Saf*. 2006;64(2):178–89.
18. Suarez G, et al. Sensing the dynamics of oxidative stress using enhanced absorption in protein-loaded random media. *Sci Rep*. 2013;3:3447.
19. Lushchak VI. Environmentally induced oxidative stress in aquatic animals. *Aquat Toxicol*. 2011;101(1):13–30.
20. Quigg A, et al. Direct and indirect toxic effects of engineered nanoparticles on algae: role of natural organic matter. *Acs Sustain Chem Eng*. 2013;1(7):686–702.
21. Miao AJ, et al. The algal toxicity of silver engineered nanoparticles and detoxification by exopolymeric substances. *Environ Pollut*. 2009;157(11):3034–41.
22. Nel AE, et al. Understanding biophysicochemical interactions at the nano-bio interface. *Nat Mater*. 2009;8(7):543–57.
23. Neal AL. What can be inferred from bacterium-nanoparticle interactions about the potential consequences of environmental exposure to nanoparticles? *Ecotoxicology*. 2008;17(5):362–71.
24. Zhao F, et al. Cellular uptake, intracellular trafficking, and cytotoxicity of nanomaterials. *Small*. 2011;7(10):1322–37.
25. Auffan M, et al. Relation between the redox state of iron-based nanoparticles and their cytotoxicity toward *Escherichia coli*. *Environ Sci Technol*. 2008;42(17):6730–5.
26. Li KG, et al. Surface interactions affect the toxicity of engineered metal oxide nanoparticles toward *Paramecium*. *Chem Res Toxicol*. 2012;25(8):1675–81.
27. Brown DM, et al. Size-dependent proinflammatory effects of ultrafine polystyrene particles: a role for surface area and oxidative stress in the enhanced activity of ultrafines. *Toxicol Appl Pharmacol*. 2001;175(3):191–9.
28. Wilson MR, et al. Interactions between ultrafine particles and transition metals in vivo and in vitro. *Toxicol Appl Pharmacol*. 2002;184(3):172–9.
29. Unfried K, et al. Cellular responses to nanoparticles: target structures and mechanisms. *Nanotoxicology*. 2007;1(1):52–71.
30. Sorensen SN, et al. A multimethod approach for investigating algal toxicity of platinum nanoparticles. *Environ Sci Technol*. 2016;50(19):10635–43.
31. Chen LZ, et al. Toxicological effects of nanometer titanium dioxide (nano-TiO₂) on *Chlamydomonas reinhardtii*. *Ecotoxicol Environ Saf*. 2012;84:155–62.
32. von Moos N, et al. Pro-oxidant effects of nano-TiO₂ on *Chlamydomonas reinhardtii* during short-term exposure. *RSC Adv*. 2016;6(116):115271–83.
33. Lin DH, et al. The influence of dissolved and surface-bound humic acid on the toxicity of TiO₂ nanoparticles to *Chlorella* sp. *Water Res*. 2012;46(14):4477–87.
34. Domingos RF, et al. Bioaccumulation and effects of CdTe/CdS quantum dots on *Chlamydomonas reinhardtii*—nanoparticles or the free ions? *Environ Sci Technol*. 2011;45(18):7664–9.
35. Ji J, Long ZF, Lin DH. Toxicity of oxide nanoparticles to the green algae *Chlorella* sp. *Chem Eng J*. 2011;170(2–3):525–30.
36. Ouakroum A, et al. Inhibitory effects of silver nanoparticles in two green algae, *Chlorella vulgaris* and *Dunaliella tertiolecta*. *Ecotoxicol Environ Saf*. 2012;78:80–5.
37. Perreault F, et al. Polymer coating of copper oxide nanoparticles increases nanoparticles uptake and toxicity in the green alga *Chlamydomonas reinhardtii*. *Chemosphere*. 2012;87(11):1388–94.
38. Rogers NJ, et al. Physico-chemical behaviour and algal toxicity of nanoparticulate CeO₂ in freshwater. *Environ Chem*. 2010;7(1):50–60.
39. Saison C, et al. Effect of core-shell copper oxide nanoparticles on cell culture morphology and photosynthesis (photosystem II energy distribution) in the green alga, *Chlamydomonas reinhardtii*. *Aquat Toxicol*. 2010;96(2):109–14.
40. Koman VB, Santschi C, Martin OJF. Multiscattering-enhanced optical biosensor: multiplexed, non-invasive and continuous measurements of cellular processes. *Biomed Opt Express*. 2015;6(7):2353–65.
41. Cheloni G, Marti E, Slaveykova VI. Interactive effects of copper oxide nanoparticles and light to green alga *Chlamydomonas reinhardtii*. *Aquat Toxicol*. 2016;170:120–8.
42. Wang JX, et al. Toxicity assessment of manufactured nanomaterials using the unicellular green alga *Chlamydomonas reinhardtii*. *Chemosphere*. 2008;73(7):1121–8.
43. Adams LK, Lyon DY, Alvarez PJJ. Comparative eco-toxicity of nanoscale TiO₂, SiO₂, and ZnO water suspensions. *Water Res*. 2006;40(19):3527–32.
44. Brunet L, et al. Comparative photoactivity and antibacterial properties of C-60 fullerenes and TiO₂ nanoparticles. *Environ Sci Technol*. 2009;43(12):4355–60.
45. Kumari K, Khare A, Dange S. The applicability of oxidative stress biomarkers in assessing chromium induced toxicity in the fish *Labeo rohita*. *Biomed Res Int*. 2014;2014:1.
46. Nyska A, Kohen R. Oxidation of biological systems: oxidative stress phenomena, antioxidants, redox reactions, and methods for their quantification. *Toxicol Pathol*. 2002;30(6):620–50.
47. Armoza-Zvuloni R, Shaked Y. Release of hydrogen peroxide and antioxidants by the coral *Stylophora pistillata* to its external milieu. *Biogeosciences*. 2014;11(17):4587–98.
48. Chen X, et al. Recent progress in the development of fluorescent, luminescent and colorimetric probes for detection of reactive oxygen and nitrogen species. *Chem Soc Rev*. 2016;45(10):2976–3016.
49. Dynowski M, et al. Plant plasma membrane water channels conduct the signalling molecule H₂O₂. *Biochem J*. 2008;414:53–61.
50. Bienert GP, et al. Specific aquaporins facilitate the diffusion of H₂O₂ across membranes. *J Biol Chem*. 2007;282(2):1183–92.
51. Li C, et al. Electrochemical detection of extracellular hydrogen peroxide released from RAW 264.7 murine macrophage cells based on horseradish peroxidase-hydroxyapatite nanohybrids. *Analyst*. 2011;136(6):1116–23.
52. Gonzalez-Sanchez MI, et al. Electrochemical detection of extracellular hydrogen peroxide in *Arabidopsis thaliana*: a real-time marker of oxidative stress. *Plant Cell Environ*. 2013;36(4):869–78.
53. Demidchik V. Mechanisms of oxidative stress in plants: from classical chemistry to cell biology. *Environ Exp Bot*. 2015;109:212–28.
54. Halliwell B, Gutteridge JM. Free radicals in biology and medicine. 4th ed. Oxford: Oxford University Press Inc.; 2007.
55. Morgan MS, et al. Ultraviolet molar absorptivities of aqueous hydrogen peroxide and hydroperoxyl ion. *Anal Chim Acta*. 1988;215(1–2):325–9.
56. Lin CL, Rohatgi NK, Demore WB. Ultraviolet-absorption cross-section of hydrogen-peroxide. *Geophys Res Lett*. 1978;5(2):113–5.
57. Abrams R, Altschul AM, Hogness TR. Cytochrome c peroxidase II. The peroxidase-hydrogen peroxide complex. *J Biol Chem*. 1942;142(1):303–16.
58. Altschul AM, Abrams R, Hogness TR. Cytochrome c peroxidase. *J Biol Chem*. 1940;136(3):777–94.
59. Gupta BL. Microdetermination techniques for H₂O₂ in irradiated solutions. *Microchem J*. 1973;18(4):363–74.
60. Armstrong WA, Humphreys WG. A let independent dosimeter based on chemiluminescent determination of H₂O₂. *Can J Chem Back Year*. 1965;43(9):2576.
61. Malavolti NL, Pilosof D, Nieman TA. Optimization of experimental variables for the chemi-luminescent determination of glucose in microporous membrane flow cells. *Anal Chem*. 1984;56(12):2191–5.
62. Kok GL. Measurements of H₂O₂ in rainwater. *Atmos Environ*. 1980;14(6):653–6.
63. Keston AS, Brandt R. Fluorometric analysis of ultramicro quantities of H₂O₂. *Anal Biochem*. 1965;11(1):1.
64. Hwang H, Dasgupta PK. Fluorometric flow-injection determination of aqueous peroxides at nanomolar level using membrane reactors. *Anal Chem*. 1986;58(7):1521–4.
65. Lazrus AL, et al. Automated fluorometric method for hydrogen-peroxide in air. *Anal Chem*. 1986;58(3):594–7.
66. Barth A. Infrared spectroscopy of proteins. *Biochimica Et Biophysica Acta Bioenerg*. 2007;1767(9):1073–101.
67. Zubavichus Y, et al. X-ray absorption spectroscopy of the nucleotide bases at the carbon, nitrogen, and oxygen K-edges. *J Phys Chem B*. 2008;112(44):13711–6.

68. Zaera F. New advances in the use of infrared absorption spectroscopy for the characterization of heterogeneous catalytic reactions. *Chem Soc Rev*. 2014;43(22):7624–63.
69. Pradier C-M, et al. Specific binding of avidin to biotin immobilised on modified gold surfaces: fourier transform infrared reflection absorption spectroscopy analysis. *Surf Sci*. 2002;502–503:193–202.
70. Namjou K, et al. Determination of exhaled nitric oxide distributions in a diverse sample population using tunable diode laser absorption spectroscopy. *Appl Phys B Lasers Opt*. 2006;85(2–3):427–35.
71. Bohren CF, Huffman DR. Absorption and scattering of light by small particles. New York: Wiley; 1983.
72. Wong YH, Thomas RL, Hawkins GF. Surface and subsurface structure of solids by laser photoacoustic spectroscopy. *Appl Phys Lett*. 1978;32(9):538–9.
73. Greener J, Abbasi B, Kumacheva E. Attenuated total reflection Fourier transform infrared spectroscopy for on-chip monitoring of solute concentrations. *Lab Chip*. 2010;10(12):1561–6.
74. Okeefe A, Deacon DAG. Cavity ring-down optical spectrometer for absorption-measurements using pulsed laser sources. *Rev Sci Instrum*. 1988;59(12):2544–51.
75. Koman VB, Santschi C, Martin OJF. Multiscattering-enhanced absorption spectroscopy. *Anal Chem*. 2015;87(3):1536–43.
76. Henyey LG, Greenstein JL. Diffuse radiation in the galaxy. *Astrophys J*. 1941;93(1):70–83.
77. Uppu R, Tiwari AK, Mujumdar S. Coherent random lasing in diffusive resonant media. In: Chigrin DN, editor. Fourth international workshop on theoretical and computational nanophotonics. Amer Inst Physics: Melville; 2011.
78. Mujumdar S, et al. Monte Carlo calculations of spectral features in random lasing. *J Nanophoton*. 2010;4:39.
79. Liew SF, et al. Short-range order and near-field effects on optical scattering and structural coloration. *Opt Express*. 2011;19(9):8208–17.
80. Butt WD, Keilin D. Absorption Spectra and some other properties of cytochrome c and of its compounds with ligands. *Proc R Soc Ser B Biol Sci*. 1962;156(965):429.
81. Wilson R, Turner APF. Glucose oxidase: an ideal enzyme. *Biosens Bioelectron*. 1992;7(3):165–85.
82. Koman VB, et al. Portable oxidative stress sensor: dynamic and non-invasive measurements of extracellular H₂O₂ released by algae. *Biosens Bioelectron*. 2015;68:245–52.
83. Koman VB, et al. New insights into ROS dynamics: a multi-layered microfluidic chip for ecotoxicological studies on aquatic microorganisms. *Nanotoxicology*. 2016;10:1–10.
84. Findlay JWA, Dillard RF. Appropriate calibration curve fitting in ligand binding assays. *Aaps J*. 2007;9(2):E260–7.
85. von Moos N, Maillard L, Slaveykova VI. Dynamics of sub-lethal effects of nano-CuO on the microalga *Chlamydomonas reinhardtii* during short-term exposure. *Aquat Toxicol*. 2015;161:267–75.
86. Auffan M, et al. Chemical stability of metallic nanoparticles: a parameter controlling their potential cellular toxicity in vitro. *Environ Pollut*. 2009;157(4):1127–33.
87. Cheloni G, Cosio C, Slaveykova VI. Antagonistic and synergistic effects of light irradiation on the effects of copper on *Chlamydomonas reinhardtii*. *Aquat Toxicol*. 2014;155:275–82.
88. Cho M, et al. Linear correlation between inactivation of *E. coli* and OH radical concentration in TiO₂ photocatalytic disinfection. *Water Res*. 2004;38(4):1069–77.
89. Asada K. Production and scavenging of reactive oxygen species in chloroplasts and their functions. *Plant Physiol*. 2006;141(2):391–6.
90. Pospisil P. Production of reactive oxygen species by photosystem II. *Biochimica Et Biophysica Acta Bioenerg*. 2009;1787(10):1151–60.
91. Barber J. Photosynthetic energy conversion: natural and artificial. *Chem Soc Rev*. 2009;38(1):185–96.
92. Mubarakshina MM, Ivanov BN. The production and scavenging of reactive oxygen species in the plastoquinone pool of chloroplast thylakoid membranes. *Physiol Plant*. 2010;140(2):103–10.
93. Kim G, Lee YE, Kopelman R. Hydrogen peroxide (H₂O₂) detection with nanopores for biological applications: a mini-review. *Methods Mol Biol*. 2013;1028:101–14.

Submit your next manuscript to BioMed Central and we will help you at every step:

- We accept pre-submission inquiries
- Our selector tool helps you to find the most relevant journal
- We provide round the clock customer support
- Convenient online submission
- Thorough peer review
- Inclusion in PubMed and all major indexing services
- Maximum visibility for your research

Submit your manuscript at
www.biomedcentral.com/submit



RESEARCH

Open Access



Effects of silica nanoparticle exposure on mitochondrial function during neuronal differentiation

Angélique D. Ducray¹, Andrea Felser², Jana Zielinski¹, Aniela Bittner¹, Julia V. Bürgi¹, Jean-Marc Nuoffer², Martin Frenz³ and Meike Mevissen^{1*}

Abstract

Background: Nanomedicine offers a promising tool for therapies of brain diseases, but potential effects on neuronal health and neuronal differentiation need to be investigated to assess potential risks. The aim of this study was to investigate effects of silica-indocyanine green/poly (ϵ -caprolactone) nanoparticles (PCL-NPs) engineered for laser tissue soldering in the brain before and during differentiation of SH-SY5Y cells. Considering adaptations in mitochondrial homeostasis during neuronal differentiation, metabolic effects of PCL-NP exposure before and during neuronal differentiation were studied. In addition, kinases of the PI3 kinase (PI3-K/Akt) and the MAP kinase (MAP-K/ERK) pathways related to neuronal differentiation and mitochondrial function were investigated.

Results: Differentiation resulted in a decrease in the cellular respiration rate and the extracellular acidification rate (ECAR). PCL-NP exposure impaired mitochondrial function depending on the time of exposure. The cellular respiration rate was significantly reduced compared to differentiated controls when PCL-NPs were given before differentiation. The shift in ECAR was less pronounced in PCL-NP exposure during differentiation. Differentiation and PCL-NP exposure had no effect on expression levels and the enzymatic activity of respiratory chain complexes. The activity of the glycolytic enzyme phosphofructokinase was significantly reduced after differentiation with the effect being more pronounced after PCL-NP exposure before differentiation. The increase in mitochondrial membrane potential observed after differentiation was not found in SH-SY5Y cells exposed to PCL-NPs before differentiation. The cellular adenosine triphosphate (ATP) production significantly dropped during differentiation, and this effect was independent of the PCL-NP exposure. Differentiation and nanoparticle exposure had no effect on superoxide levels at the endpoint of the experiments. A slight decrease in the expression of the neuronal differentiation markers was found after PCL-NP exposure, but no morphological variation was observed.

Conclusions: PCL-NP exposure affects mitochondrial function depending on the time of exposure before and during neuronal differentiation. PCL-NP exposure during differentiation was associated with impaired mitochondrial function, which may affect differentiation. Considering the importance of adaptations in cellular respiration for neuronal differentiation and function, further studies are needed to unravel the underlying mechanisms and consequences to assess the possible risks including neurodegeneration.

Keywords: Nanomedicine, Silica-nanoparticle, Neuronal differentiation, Mitochondrial respiration

*Correspondence: meike.mevissen@vetsuisse.unibe.ch

¹ Division of Pharmacology and Toxicology, Vetsuisse Faculty, University of Bern, Laenggassstrasse 124, 3012 Bern, Switzerland
Full list of author information is available at the end of the article

Background

Nanomedicine offers promising possibilities for therapy of brain diseases as drug carriers, in tumor destruction and laser tissue soldering. In the latter application, silica nanoparticles embedded with bovine serum albumin in a biodegradable implant can be used for treatment of aneurysms in the brain [1, 2]. Despite several advantages compared to the conventional technique of suturing including speed, immediate water tightness, reduced tissue trauma, and faster wound healing, the nanoparticles may cause potential adverse effects once released from the biodegradable scaffold.

In previous studies, nanoparticle uptake and the underlying mechanisms and effects of these silica nanoparticles were studied in microglial cells, primary hippocampal cultures, neuron-like cells (SH-SY5Y) and organotypic brain slices [3–5]. Nanoparticle exposure did not result in increased cytotoxicity and apoptosis in microglial and neuron-like cell lines even though a transient depletion of glutathione was found indicating reactive oxygen species (ROS) formation [3]. Moreover, nanoparticles were demonstrated to be taken up by microglial cells in a time- and particle-dependent manner [4]; the uptake in primary hippocampal cultures was time- and concentration-dependent [5]. For all brain cells analyzed, no modulation of inflammatory cytokine secretion and autophagy was observed [4, 5], but neuronal differentiation markers including mitogen-activated protein kinase/extracellular signal-related kinase (MAP-K/ERK) 1/2 and phosphatidylinositol 3-kinase/serine/threonine specific protein kinase (PI3-K/Akt) kinases were shown to be downregulated after nanoparticle exposure [5].

Mitochondrial dynamics, trafficking, turnover, and biogenesis play key roles in regulating the functional health of neurons. Mitochondria do not only support the energy demands of neuronal electrophysiology, but also mediate calcium homeostasis, integration of cell death/survival signals, and fatty acid metabolism [6]. The limited glycolytic potential and uncontrolled mitophagy were demonstrated to be linked to neurodegeneration with the protein kinases ERK1/2 and PTEN-induced kinase 1 (PINK1) being involved [6]. Not surprisingly, perturbations in mitochondrial function have long been centrally implicated in the pathogenesis of Parkinson's disease [7, 8].

Mitochondria play an important role in cell metabolism during neuronal differentiation because this process requires metabolic adaptations [9], and the PI3-K/AKT and ERK pathways were reported to be required for the differentiation of retinoic acid (RA)—induced neuroblastoma cell differentiation [10]. MAP-K/ERK 1/2 was reported to be important for regulating mitochondrial function [11–13] as well as PI3-K/Akt/mechanistic

target of rapamycin (mTOR) being a regulator in glucose metabolism during neuronal differentiation [14]. Phosphorylation of c-Jun N-terminal kinase (JNK), ERK and p38 mitogen-activated kinase (p38) were found in primary astrocytes after exposure to zinc oxide (ZnO) nanoparticles [15]. Silver nanoparticles have demonstrated to induce impairment of mitochondrial oxidative phosphorylation [16] and exposure to titanium dioxide (TiO₂) nanoparticles significantly impaired mitochondrial function in a concentration- and time-dependent manner in astrocytes [17]. Silica nanoparticles effectively inhibited vascular endothelial growth factor (VEGF)—induced angiogenesis in vitro and ERK 1/2 activation [18].

Unlike other cells, neurons show limited glycolytic potential, and both insufficient and excessive mitophagy have been linked to neurodegeneration. Mitochondrial dynamics is important for neurogenesis and neuronal differentiation [9, 19].

An increase in glucose metabolism was demonstrated during neuronal differentiation with PI3K/Akt/mTOR signaling being a critical regulator in neuronal energy metabolism [14]. Activated MAP-Ks were shown to phosphorylate various transcription factors resulting in regulation of cell proliferation, differentiation, inflammatory responses, oxidative stress caused by ROS and apoptosis [20]. Kinases have been demonstrated to be involved in neurite elongation (PI3-K/Akt), neuronal survival and in synaptic plasticity (MAP-K/ERK) of neurons [21, 22]. Activation of kinases such as Akt and ERK and an increase in neuronal differentiation was shown after exposure of SH-SY5Y cells to silver nanoparticles [23].

Given the importance of mitochondrial function in neuronal health, an interaction with nanoparticles may have detrimental consequences. Our aims were to investigate the effects of poly-(ε-caprolactone) (PCL) silica nanoparticles on the respiratory capacity of differentiating SH-SY5Y cells and to analyze the effect of nanoparticle exposure on the expression and the activation of the protein kinases Akt and MAP-K before and during neuronal differentiation.

Methods

Cell culture

SH-SY5Y cells were obtained from ATCC (Manassas, VA, USA), and culturing as well as differentiation was done with some adaptations as previously described [5]. Briefly, at day in vitro (DIV) 0, SH-SY5Y cells were seeded at a density of 1×10^7 cells per T75 for Western samples, 8×10^4 cells per well in 24-well plates (Techno Plastic Products AG (TPP) Trasadingen, Switzerland) and maintained at non-differentiated state for 24 h in Dulbecco's Modified Eagle Medium (DMEM) GlutaMAXTM medium (Life Technologies, UK) sodium pyruvate [1 mM], L-glutamine

[2 mM], penicillin/streptomycin ([1 unit/ml], Life Technologies, UK) at 37 °C in an atmosphere of 5% CO₂.

For the first 3 days of differentiation, cells were exposed to the same medium with a reduced FBS concentration (5%) and supplemented with retinoic acid [10 µM] (RA, Sigma, St Louis, USA). For the last 3 days, SH-SY5Y cells were grown in DMEM with only 1% FBS with RA [10 µM]. PCL-NP exposure was performed before differentiation (NP DIFF) or during differentiation (DIFF NP DIFF) on DIV1 or DIV4, respectively. The cells were exposed to PCL-NPs in the same medium supplemented with 1% FBS for 24 h.

Nanoparticle exposure

Nanoparticle synthesis and characterization as well as the chemical and physical properties of the PCL-NPs have been described previously [3, 4, 24]. Briefly, a core shell nanoparticle system was developed consisting of a defined silica-core of 80 nm with a hydrophobic PCL coating acting as carrier system for ICG. The ICG dye was used as an absorbing dye for the laser-soldering procedure. These nanoparticles incorporating rhodamine dye in the silica-core (silica-RITC)-PCL were used to study their uptake into cells. The designed nanoparticles were characterized by scanning electron microscopy, infrared spectroscopy, dynamic light scattering, thermogravimetric analysis, fluorescence measurements, and two-photon microscopy. Size, shape, ICG concentrations, zeta potential (−25.4 mV), surface charge, surface chemistry and photo stability were evaluated and published previously [24]. A stock solution of [2.6×10^{11} PCL-NPs/ml] was prepared using 0.0025% DMSO (Sigma, USA) in Dulbecco's phosphate buffered saline (DPBS, Gibco, Life Technologies, UK). The stock solution was sonicated three times for 5 min with cooling steps in between to enable homogeneous nanoparticle suspension just before treatment of the cells. The final concentration of PCL-NPs [2.6×10^{10} PCL-NPs/ml] used for all experiments was obtained by dilution of the stock with culture medium containing 1% FBS as previously reported [4, 5].

Microplate-based respirometry

The mitochondrial oxygen consumption rate (OCR), which is a key metric of aerobic mitochondrial function, and the extracellular acidification rate (ECAR), which approximates glycolytic activity, were analyzed simultaneously using a standard mitochondrial stress test paradigm on the Seahorse Bioscience XF-24 analyzer (Agilent Technologies, CA, USA). Cells were assayed at DIV8 for OCR and ECAR measurements following the manufacturer's instructions (Agilent Technologies, CA, USA). For each group, five independent experiments were performed with five samples per experiment.

Before analysis, cells were washed three times with unbuffered assay media [DMEM (Sigma, Switzerland) diluted in water without phenol red supplemented with Glutamax (1X), sodium pyruvate [1 mM] and glutamine [2 mM], penicillin-streptomycin cocktail (1X) (Life Technologies, UK)] and incubated 1 h in a CO₂-free incubator at 37 °C. After the initial measurement of basal OCR and ECAR, sequential exposures to modulators of mitochondrial activity were injected in the microtiter plate. First, the inhibitor of ATP synthase oligomycin [1 µM] was added to determine leak respiration induced through passive proton leakage across the mitochondrial inner membrane. Next, the uncoupler of mitochondrial oxidative phosphorylation carbonyl cyanide-4-(trifluoromethoxy) phenylhydrazone (FCCP, [0.125 µM]) was added to assess maximally stimulated uncoupled respiration. Finally, the complex (C)III inhibitor, antimycin A [1 µM] together with CI inhibitor rotenone [1 µM], an inhibitor of mitochondrial NADH dehydrogenase, were added to determine extramitochondrial respiration. Optimal concentrations of oligomycin, FCCP, antimycin A and rotenone were determined before. Basal respiration or acidification was calculated using the mean of the four OCR or ECAR measurements before the first injection. Leak respiration and maximal respiration were calculated as the mean of three OCR measurement cycles after oligomycin or FCCP injection, respectively. Maximal acidification was calculated as the mean of three ECAR measurement cycles after oligomycin injection. OCR data were corrected for non-mitochondrial oxygen consumption under rotenone and antimycin A. After each experiment, cell numbers in each well were measured using the CyQUANT kit (Molecular Probes, OR, USA). OCR (pmol/min) and ECAR (mpH/min) values were normalized to corresponding cell numbers.

Enzymatic activities of respiratory chain complexes

SH-SY5Y cells were cultured as described above and harvested on DIV8. Briefly, cells were washed twice in cold HBSS, scraped and centrifuged at 4 °C at 2000 rpm for 5 min. Dried cell pellets were then frozen at −80 °C until used. For respiratory chain enzyme activity measurements, cells were mechanically homogenized and sonicated in buffer containing [25 mM] potassium phosphate (pH 7.2), [5 mM] MgCl₂, and [2.5 mg/ml] BSA. Activity measurements of reduced nicotinamide adenine dinucleotide (NADH) coenzyme Q reductase complex (C) I, succinate dehydrogenase (CII), ubiquinol-cytochrome c reductase (CIII), cytochrome c oxidase (CIV), Mg-ATPase (CV), and citrate synthase were determined separately by spectrophotometry as previously described [25].

Phosphofructokinase activity (PFK)

Phosphofructokinase measurements were done according to the manufacturer's datasheet (Phosphofructokinase Activity Colorimetric Assay Kit, Sigma, Switzerland). SH-SY5Y cells were seeded in T25 flasks (Techno Plastic Products AG (TPP), Trasadingen, Switzerland) at a density of 3×10^6 cells per flask and treated as previously described above. Briefly, the protein was extracted by scraping off cells in 1 mL HBSS and centrifuged at $13.200 \times g$ for 10 min. The buffer was removed and the pellet was dissolved in 200 μ L cold PFK assay buffer and centrifuged at $13.200 \times g$ for 10 min. The pellet was solubilized in 60 μ L cold PFK buffer and 50 μ L were transferred to a 96-well plate and a master mix consisting of PFK Assay Buffer, PFK Enzyme Mix, PFK Developer, ATP and PFK substrate was added. The absorbance (450 nm) was measured using a Synergy H1 multi-mode reader. The data were compared with the NADH standard curve ranging from [2 to 10 nmol]/well and values were normalized to 1 mg protein. The protein amount of each sample was determined with PierceTM 660 nm Protein Assay Reagent (Thermo Fisher Scientific, Switzerland).

Mitochondrial membrane potential

The mitochondrial membrane potential ($\Delta\Psi_m$) was determined using tetramethylrhodamine methyl ester (TMRM, Invitrogen, Thermo Fisher Scientific, Switzerland), a lipophilic cationic fluorescent probe which accumulates within mitochondria depending on their $\Delta\Psi_m$. The measurements were performed according to the supplier's instructions. SH-SY5Y cells were cultured as described above. Briefly, the provided Image-iT TMRM Reagent and TMRM were diluted to [100 nM] in 1% FBS/DMEM medium. At DIV8, the medium was replaced with the staining solution for 30 min at 37 °C. Successively, the cells were washed twice with HBSS and the signal was measured at an emission of 488 nm and an extinction of 570 nm with a Synergy H1 multi-mode reader. Consequently, the protein amount of each sample was determined with OPA as described. The values were normalized to 1 mg protein.

Cellular ATP levels

The amount of intracellular ATP was determined with the CellTiter-Glo[®] Luminescent Cell Viability Assay (Promega AG, Switzerland). SH-SY5Y cells were seeded in a 96-well plate at a density of 3.5×10^4 cells and cultured as described above. The measurements were performed according to the supplier's datasheet. Shortly, the CellTiter-Glo substrate was reconstituted in the CellTiter-Glo buffer and equilibrated to room temperature. Prior to the measurement (30 min) the plate was equilibrated

to room temperature. The staining solution was added, mixed with an orbital shaker for 2 min and incubated in the dark for 10 min to stabilize the signal. Following, the luminescence was measured with a Synergy H1 multi-mode reader with an integration time of 1 s. Finally, the protein amount of each sample was determined with OPA as described before. The values were normalized to 1 mg protein.

Superoxide measurements

Mitochondrial superoxide was measured with the MitoSOXTM Red mitochondrial superoxide indicator for live cell imaging (Molecular Probes, Thermo Fisher Scientific, Switzerland). SH-SY5Y cells were seeded in a 96-well plate (Huberlab, Switzerland) at a density of 3.5×10^4 cells and cultured as described above. The measurements were done according to the supplier's datasheet. Briefly, a [5 mM] stock solution of the provided MitoSOX reagent was prepared in DMSO and the stock solution was further diluted to a [5 μ M] working solution in Hank's balanced salt solution with calcium and magnesium (HBSS, Sigma, Switzerland). At DIV8, non-differentiated, differentiated as well as nanoparticle-treated SH-SY5Y cells were incubated with [5 μ M] MitoSOX working solution at 37 °C for 50 min after the cells were washed with HBSS. Fluorescence measurements were performed immediately at an emission of 510 nm and excitation of 580 nm with a Synergy H1 multi-mode reader (BioTek, Switzerland). Subsequently, the protein amount of each sample was determined using FluoraldehydeTM o-phthaldialdehyde reagent solution (OPA, Thermo Fisher Scientific, Switzerland) at an emission of 360 nm and an excitation of 460 nm. The results of the MitoSOX Assay were normalized to 1 mg protein.

Protein expression of differentiation markers and OXPHOS enzymes

SH-SY5Y cells were cultured as described above. On DIV7, protein extraction was performed and the samples were analyzed by Western Blot as described previously [5]. Briefly, SH-SY5Y cells were lysed in protein lysis buffer containing phosphatase (Sigma, Switzerland) and protease (Thermo ScientificTM, IL, Switzerland) cocktail inhibitors. The lysed cell suspension was incubated on ice for 15 min, sonicated for 10 s and finally centrifuged at high speed for 10 min at 4 °C. The protein content of the supernatant was quantified using the Pierce protein assay reagent (Bio-Rad Laboratories, CA, USA); 10 μ g of protein from each test sample were loaded and subsequently separated on 12% SDS-PAGE before the protein was transferred onto PVDF membrane (Sigma, USA) at 0.25 A for 1.5 h (PI3- and ERK-kinases, OXPHOS) or nitrocellulose membrane (Bio-Rad, Switzerland) at

0.35 A for 2 h (MAP-2) membranes. Blocking for 2 h in PBS 0.2% Tween, 5% milk was performed at room temperature. Subsequently, the primary antibodies, rabbit anti-phospho-Akt (1:1000), rabbit anti-Akt (1:1000), mouse anti-phospho-pMAP-K (ERK1/2) (1:2000), mouse anti-pMAP-K (ERK1/2) (1:2000) all from Cell Signaling Technology (MA, USA); mouse anti-MAP-2 (1:500) and the monoclonal mouse antibody anti- β -actin (1:10,000) both from Sigma (MO, USA); mouse anti-OXPHOS cocktail (1:1000) from Abcam (UK) were added for overnight incubation at 4 °C. The secondary antibodies, donkey-anti-rabbit and donkey-anti-mouse horseradish peroxidase (Thermo Scientific™, IL, USA) were applied accordingly at 1:10,000–1:20,000 for 2 h at room temperature. Chemiluminescent substrate (Advansta Western Bright Sirius Chemiluminescent, Witec, Switzerland) was used and chemiluminescence was detected using a luminescent image analyzer (LAS-3000 Imaging System from Fuji, Japan). Blot quantification was performed using ImageJ analysis (NIH, Bethesda, USA) measuring the ratio between the intensity of the obtained band of a specific marker versus the corresponding band of actin using arbitrary units.

Neuronal differentiation

Immunofluorescence staining was performed at the end of the culture period as previously described [5]. Briefly, cultures were fixed with 4% paraformaldehyde, blocking was performed with 10% normal horse serum in 0.4% Triton-X PBS before the primary antibody mouse anti- β -3-tubulin (1:500) (Sigma, Switzerland) was applied overnight at 4 °C in 0.4% Triton-X PBS. Finally, the secondary antibody [Alexa Fluor donkey anti-mouse 488 nm, Alexa Fluor anti-goat 488 nm (1:250) (Molecular Probes, Thermo Fisher Scientific, Switzerland)] was applied. Cell nuclei were counterstained using Hoechst 333,342 (1:10,000) (Molecular Probes, Thermo Fisher Scientific, Switzerland). Images were performed using a Zeiss Axio Imager Z1 coupled with an Apotome 1 (Carl Zeiss Vision Swiss AG, Feldbach, Switzerland).

Statistical analysis

Three to five independent experiments were performed for all parameters measured. Data at each stage were analyzed using a one-way ANOVA followed by Tukey's multiple comparison to compare the means of all treatments with the respective controls (GraphPad Software Inc., La Jolla, USA). For the protein quantification, three to four independent experiments were performed in duplicates for all analyses. A one-way ANOVA followed by the Dunnett's test was used for group comparisons. Data are presented as mean \pm standard error of the mean (SEM). p values ≤ 0.05 were considered significant.

Results

Oxygen consumption rate and extracellular acidification rate

To evaluate whether PCL-NP exposure before and during differentiation affected mitochondrial function, the oxygen consumption rate (OCR) and the extracellular acidification rate (ECAR) were analyzed in differentiated and undifferentiated SH-SY5Y cells. As shown in Fig. 1, the differentiation process led to a significant reduction (26.2%, $p \leq 0.05$) of basal OCR and a significant reduction (36.8%, $p \leq 0.0001$) of maximal respiration in SH-SY5Y cells when compared to undifferentiated control. PCL-NP exposure starting before differentiation was associated with a significantly decreased basal OCR compared to undifferentiated controls as well as differentiated controls (50.9 and 24.7%, respectively) as shown in Fig. 1b. Leak respiration was decreased compared to undifferentiated controls and differentiated controls, whereas maximal respiration was approximately the

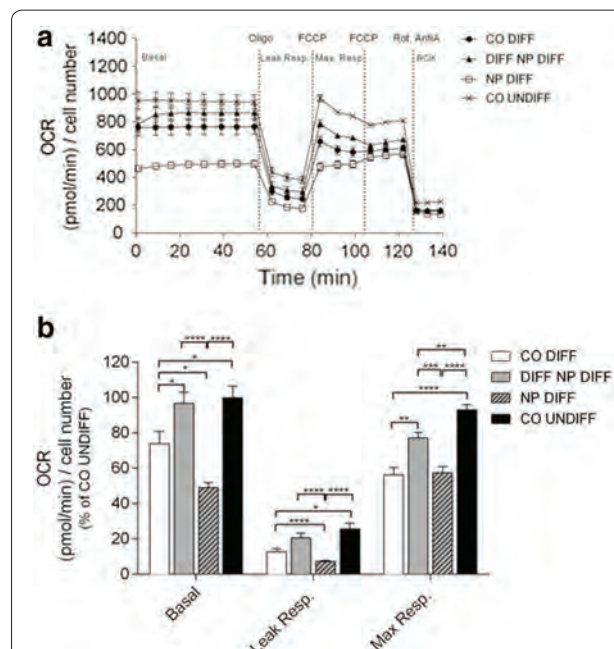


Fig. 1 The oxygen consumption rate (OCR) was measured using a Seahorse Biosciences XF24 Analyser in SH-SY5Y neuroblastoma cells exposed to PCL-NPs for 24 h before differentiation (NP DIFF) or during differentiation (DIFF NP DIFF) on day in vitro (DIV) 1 and DIV4, respectively. Untreated SH-SY5Y cells, either non-differentiated (CO UNDIFF) or differentiated for 6 days (CO DIFF), were analyzed in parallel (**a, b**). SH-SY5Y cells were exposed sequentially to each mitochondrial modulator of mitochondrial activity (oligomycin = Oligo, FCCP and rotenone/antimycin A = Rot, AntiA). The mean \pm SEM of the mitochondrial stress test on OCR are depicted over time (**a**). A quantitative analysis of the data is depicted in (**b**). Values represent the mean \pm SEM; $n = 5$ replicates of five independent experiments. * $p \leq 0.05$; ** $p \leq 0.01$; *** $p \leq 0.001$; **** $p \leq 0.0001$

same as in differentiated control cells, but lower compared to undifferentiated control cells.

The PCL-NP exposure initiated on the third day of differentiation resulted in a non-significant decrease (3.25%) in OCR as compared to undifferentiated controls, but a significant increase of 22.9% when compared to differentiated controls ($p \leq 0.05$) (Fig. 1b). Leak respiration and maximal respiratory capacity were significantly lower compared to undifferentiated controls, but significantly higher compared to differentiated control cells (Fig. 1b).

The maximal respiratory capacity for SH-SY5Y cells exposed to PCL-NPs started during differentiation was significantly lower compared to undifferentiated controls ($p \leq 0.01$), but significantly higher compared to differentiated control cells ($p \leq 0.01$) (Fig. 1b).

Under basal conditions, the ECAR was significantly decreased (41.4%) in differentiated cells compared to undifferentiated cells ($p \leq 0.001$) as illustrated in Fig. 2a, b. The ECAR in cells exposed to PCL-NPs before and

during differentiation was significantly lower compared to undifferentiated SH-SY5Y control cells with $p \leq 0.01$ and $p \leq 0.05$, respectively (Fig. 2b). No difference was found between differentiated SH-SY5Y cells devoid of nanoparticles and PCL-NP exposed cells.

The inhibition of ATP synthesis initiated by oligomycin resulted in an increase in ECAR in all four groups due to the inhibition of mitochondrial ATPase with a similar pattern for maximal acidification. The increase was 1.8-fold in undifferentiated cells and twofold in differentiated cells ($p \leq 0.01$) as shown in Fig. 2.

The cellular metabolic phenotypes are summarized in Fig. 2c. Whereas undifferentiated SH-SY5Y cells are characterized by a high cellular OCR and ECAR, differentiation process leads to a shift to lower OCR and ECAR levels. Exposures to nanoparticles before and during neuronal differentiation induce significant changes in the described shift in energy metabolism (OCR and ECAR).

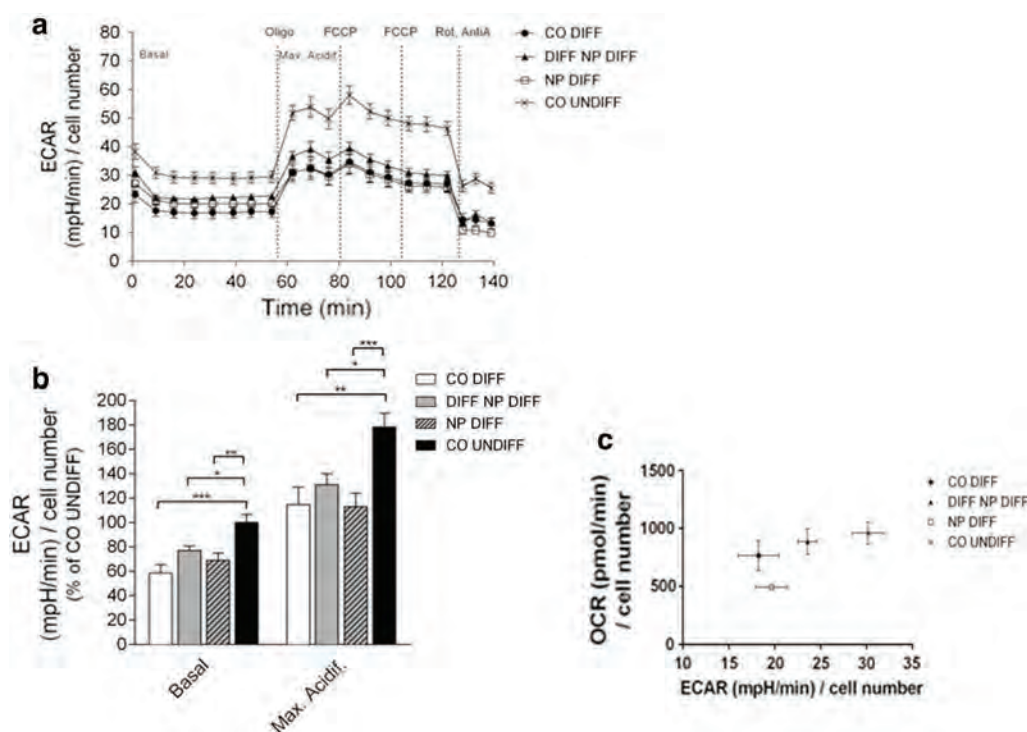


Fig. 2 The extracellular acidification rate (ECAR) was measured using a Seahorse Biosciences XF24 Analyser. The bioenergetic activity was analyzed in SH-SY5Y neuroblastoma cells exposed to PCL-NPs for 24 h before differentiation (NP DIFF) or during differentiation (DIFF NP DIFF) on day in vitro (DIV) 1 and DIV4, respectively. Untreated SH-SY5Y cells, either non-differentiated (CO UNDIFF) or differentiated for 6 days (CO DIFF), were analyzed in parallel (**a**, **b**). SH-SY5Y cells were exposed sequentially to each mitochondrial modulator of mitochondrial activity (oligomycin, FCCP and rotenone/actinomycin A). The mean \pm SEM of the mitochondrial stress test on ECAR are depicted over time (**a**). A quantitative analysis of the data is depicted in (**b**). Values represent the mean \pm SEM; $n = 5$ replicates of five independent experiments. * $p \leq 0.05$; ** $p \leq 0.01$; *** $p \leq 0.001$; **** $p \leq 0.0001$. The energy phenotype is depicted by ECAR on the x axis and the mitochondrial respiration is represented by the oxygen consumption rate (OCR) on the y axis. Bioenergetic profiling of SH-SY5Y cells (OCR versus ECAR) revealed decreased metabolic activity after exposure to PCL-NPs. Values represent the raw mean \pm SEM of each group (mean of the ECAR in abscissa/mean of the OCR in ordinate) (**c**)

Expression and activity of mitochondrial respiratory chain enzymes

In order to gain more information about the mechanism of the observed decrease in OCR measurements, Western blot analyses of subunits of each enzyme complex were

performed and enzymatic activities of all five respiratory chain complexes were quantified. As shown in Fig. 3, the protein content of selected subunits of enzyme complexes I to V of the respiratory chain revealed no significant change after PCL-NP exposure when compared to

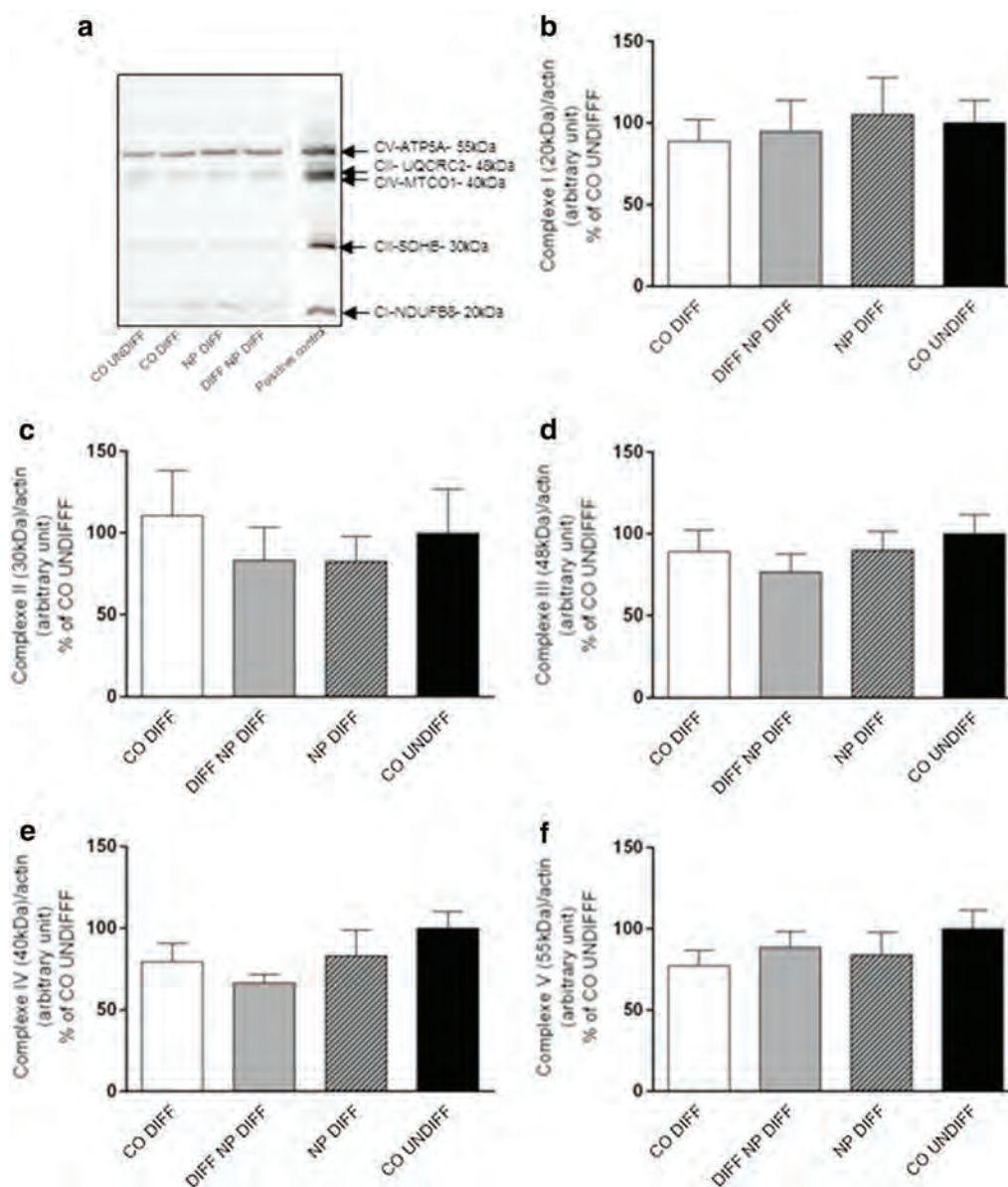


Fig. 3 Oxidative phosphorylation enzymes (OXPHOS) were analyzed to evaluate expression of mitochondrial chain complexes I to V in SH-SY5Y cells exposed to PCL-NPs (2.6×10^{10} PCL-NPs/ml) for 24 h before (DIV1, NP DIFF) or after (DIV4, DIFF NP DIFF) differentiation with retinoic acid. Untreated controls, undifferentiated SH-SY5Y cells (CO UNDIFF) and differentiated SH-SY5Y cells (CO DIFF) were performed in parallel. The following complexes or subunits of the complexes were analyzed: Accessory subunit of the mitochondrial membrane respiratory chain NADH dehydrogenase complex (CI) (CI-NDUFB8); iron-sulfur protein (IP) subunit of succinate dehydrogenase involved in CII (CII-SDHB); component of the ubiquinol-cytochrome c reductase of CIII (CIII-UQCRC2); catalytic subunit of cytochrome c oxidase of CIV (CIV-MTCO1), and mitochondrial membrane ATP synthase (F₁F₀ ATP synthase) or CV (CV-ATP5A). Representative Western blots are shown in (a). The histograms represent the ratio of each complex normalized to the corresponding actin (loading control) band CI (b), CII (c), CIII (d), CIV (e) and CV (f). Respective protein levels were assessed using digital quantification of immunoblots, and they are presented as relative intensity compared to total protein. The analysis was done using ImageJ. Values are expressed with arbitrary units. Error bars represent the mean + SEM

undifferentiated or differentiated control cells. In accordance, activity measurements of complexes I–V showed no significant variation (Table 1) independent of the cell differentiation and the nanoparticle exposure time.

Phosphofructokinase activity

Phosphofructokinase (PFK) activity in SH-SY5Y cells was found significantly decreased in differentiated controls in comparison to undifferentiated controls ($p \leq 0.05$) (Fig. 4a). In contrast to nanoparticle exposure during differentiation, nanoparticle exposure before differentiation, led to a significant decrease in PFK activity when compared to differentiated controls ($p \leq 0.0001$). PFK activity was also found to be significantly reduced in nanoparticle treated cells compared to undifferentiated control cells with the effect being more pronounced for nanoparticles applied before differentiation (Fig. 4a).

Mitochondrial membrane potential ($\Delta\Psi_m$), intracellular ATP and superoxide production

Mitochondrial membrane potential is a key indicator of the integrity of the membrane. As shown in Fig. 4b, differentiation of SH-SY5Y cells led to a significant increase in $\Delta\Psi_m$ compared to undifferentiated control cells ($p \leq 0.05$) as well as nanoparticle exposure during differentiation. In contrast, exposure to PCL-NPs before differentiation resulted in a significant reduction in $\Delta\Psi_m$ when compared to differentiated controls ($p \leq 0.0001$) and to undifferentiated controls ($p \leq 0.01$) (Fig. 4b).

As illustrated in Fig. 4c, significant differences in ATP production on DIV8 were observed between undifferentiated controls and differentiated controls ($p \leq 0.001$) and cells exposed to nanoparticles before differentiation ($p \leq 0.01$) and during differentiation ($p \leq 0.001$).

No significant variation in superoxide production was found when PCL-NP exposed groups and controls were compared (Fig. 5).

Effect of NP exposure on neuronal differentiation markers

Kinases have been demonstrated to be involved in neurite elongation (PI3-K/Akt) and in synaptic plasticity

(MAP-K/ERK) of neurons. Therefore, we investigated the effect of PCL-NP exposure on the expression of these kinases. A significant upregulation of the phosphorylated kinases Akt (P-Akt) ($p \leq 0.001$) and MAP-K (P-p42/44-MAP-K) ($p \leq 0.05$) was found in differentiated cells compared to undifferentiated SH-SY5Y cells as shown in Fig. 6a–e. PCL-NP exposure for 24 h before differentiation and during differentiation resulted in a significant upregulation of phosphorylated-Akt (P-Akt) ($p \leq 0.01$) of the same magnitude when compared to undifferentiated control SH-SY5Y cells on DIV6 (Fig. 6b). No difference between PCL-NP treated cells and differentiated control cells was found. Likewise, a decrease in both, P-p42-MAP-K and P-p44-MAP-K was seen in both PCL-NP exposed conditions in SH-SY5Y cells when compared to differentiated control cells. However, this effect was not statistically significant (Fig. 6d, e).

Differentiated SH-SY5Y cells showed a significant increase in the differentiation marker MAP-2 ($p \leq 0.05$) (Fig. 6f, g). Exposure to PCL-NPs before and during the differentiation resulted in a significant upregulation of this marker when compared to undifferentiated control cells ($p \leq 0.001$ and $p \leq 0.01$, respectively) as illustrated in Fig. 6g. The upregulation of MAP-2 after PCL-NP exposure was higher compared to differentiated controls, but the effect was not statistically significant.

Neuronal differentiation was analyzed using β -3-tubulin-staining and differentiated cells displayed typical neuronal morphology (Fig. 7). Neurite outgrowth was observed when undifferentiated control cells (Fig. 7a) and differentiated controls (Fig. 7b) were compared. Nanoparticle exposure (Fig. 7c, d) did not result in obvious cellular morphological differences when compared to differentiated control cells.

Discussion

A limited glycolytic potential has been linked to neurodegeneration and mitochondrial dynamics are important for neurodegeneration [9]. In contrast to astrocytes, neurons were reported to exhibit lower levels of glycolysis [26].

Table 1 Enzymatic activities of respiratory chain complexes

Experimental group	Citrate synthase activity (mU/mg protein)	Enzymatic complex activities (mU/mU citrate synthase)				
		CI	CII	CIII	CIV	CV
CO DIFF	111 \pm 7	0.1 \pm 0.01	0.15 \pm 0.01	0.13 \pm 0.01	0.18 \pm 0.01	0.39 \pm 0.03
DIFF NP DIFF	131 \pm 8	0.07 \pm 0.01	0.14 \pm 0.01	0.14 \pm 0.01	0.13 \pm 0.01	0.35 \pm 0.03
NP DIFF	127 \pm 9	0.08 \pm 0.01	0.16 \pm 0.02	0.14 \pm 0.01	0.15 \pm 0.01	0.37 \pm 0.05
CO UNDIFF	118 \pm 12	0.08 \pm 0.01	0.14 \pm 0.01	0.18 \pm 0.02	0.13 \pm 0.03	0.40 \pm 0.04

Enzymatic activities of respiratory chain complexes were measured on day in vitro 8 (DIV8) in undifferentiated control cells (CO UNDIFF), differentiated control cells (CO DIFF) and PCL-NPs exposed cells before (NP DIFF) or during (DIFF NP DIFF) differentiation. Values were estimated by the difference in activity levels measured in presence and absence of specific inhibitors; values are expressed as ratios to the mitochondrial marker enzyme citrate synthase (mU/mU citrate synthase) \pm S.E.M

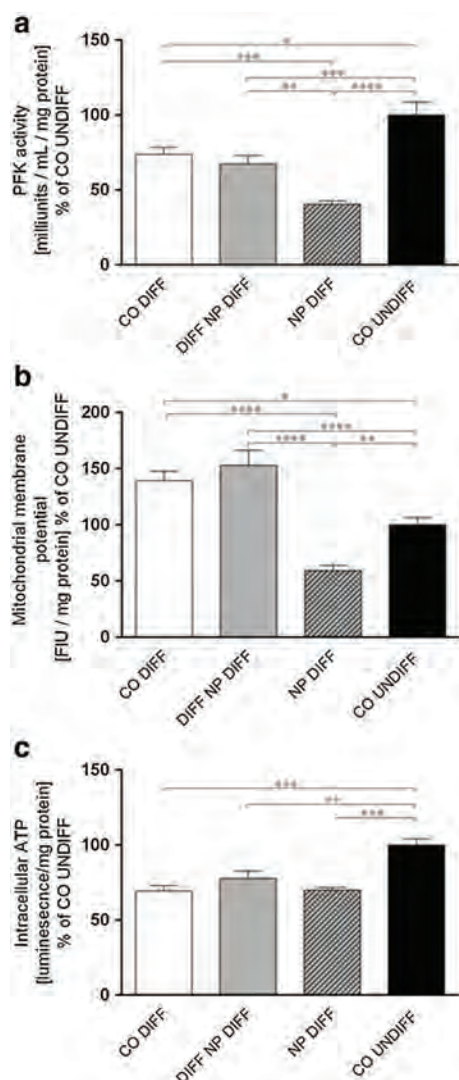


Fig. 4 Phosphofructokinase (PFK) activity (a), mitochondrial membrane potential ($\Delta\Psi_m$) (b) and ATP production (c) were assessed in SH-SY5Y cells undifferentiated controls (CO UNDIFF), differentiated controls (CO DIFF) and exposed to PCL-NPs before (NP DIFF) or during (DIFF NP DIFF) differentiation. The histograms represent values calculated as percent of undifferentiated controls. Values are expressed as milliunits/ml/mg protein for PKF activity (a), fluorescence intensity unit (FIU)/mg protein for $\Delta\Psi_m$ (b), as luminescence/mg protein for ATP production (c). Error bars represent the mean + SEM. Significant differences to undifferentiated and differentiated controls are labeled with asterisks (* $p \leq 0.05$; ** $p \leq 0.01$; *** $p \leq 0.001$; **** $p \leq 0.0001$)

Differentiation of SH-SY5Y cells resulted in changes in the cellular metabolism. As expected, the OCR and the intracellular ATP levels were decreased in differentiated SH-SY5Y cells compared to undifferentiated cells corroborating previous findings [27, 28]. Differentiated SH-SY5Y cells were reported to exhibit an elevated stimulation of mitochondrial respiration indicating an

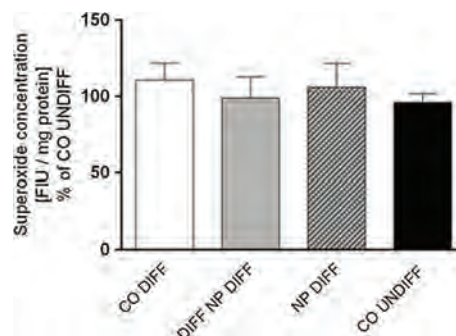
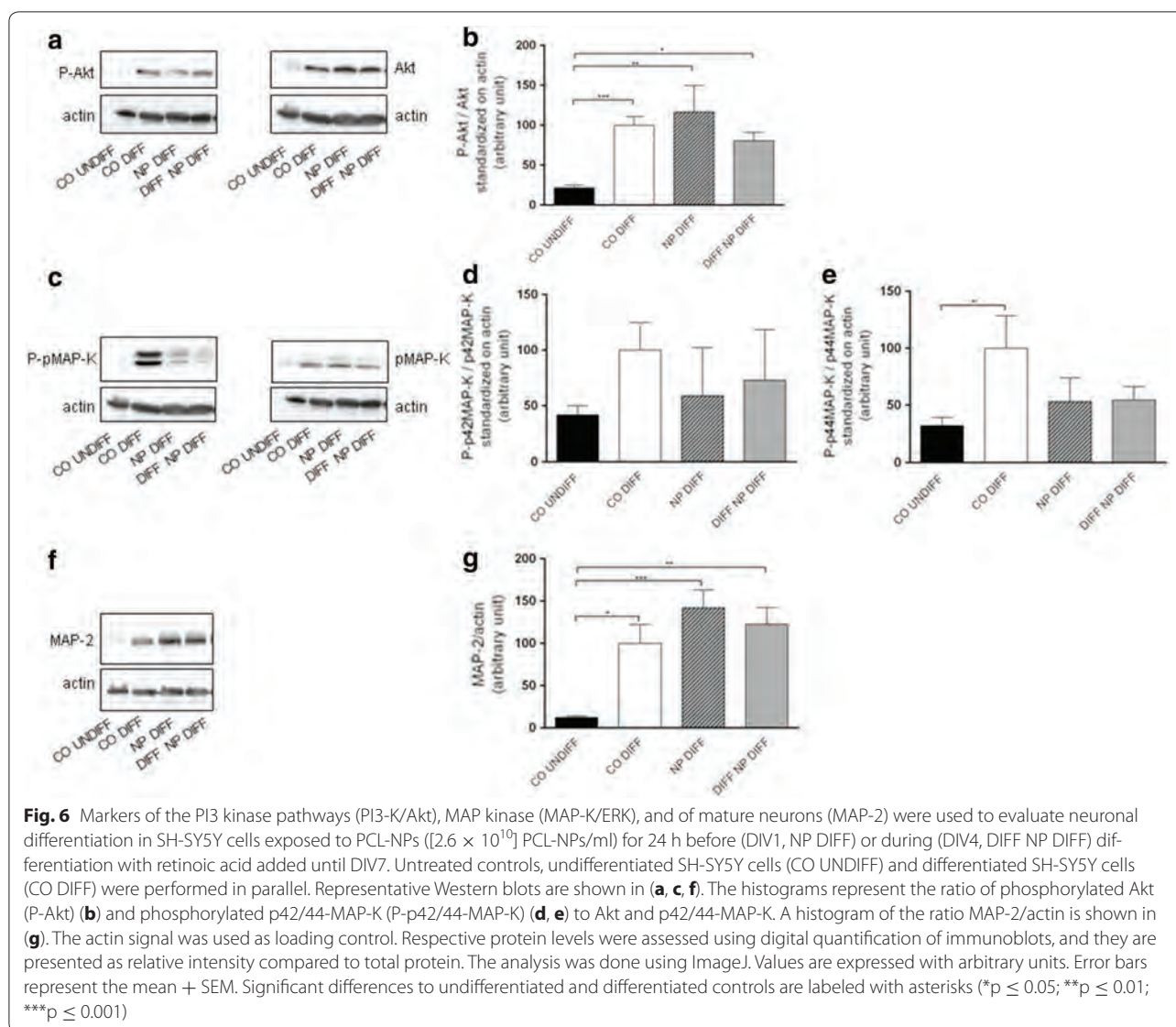


Fig. 5 Superoxide production was measured at DIV8 in SH-SY5Y cells exposed to PCL-NPs before (DIV1, NP DIFF) or during (DIV4, DIFF NP DIFF) differentiation with RA. Untreated controls, undifferentiated cells (CO UNDIFF) and differentiated cells (CO DIFF) were performed in parallel. Values are expressed as fluorescent intensity units (FIU)/mg protein; they are represented as percentage of undifferentiated control. Error bars represent the mean + SEM

increased mitochondrial reserve capacity compared to undifferentiated SH-SY5Y cells due to changes in mitochondrial metabolism [29, 30].

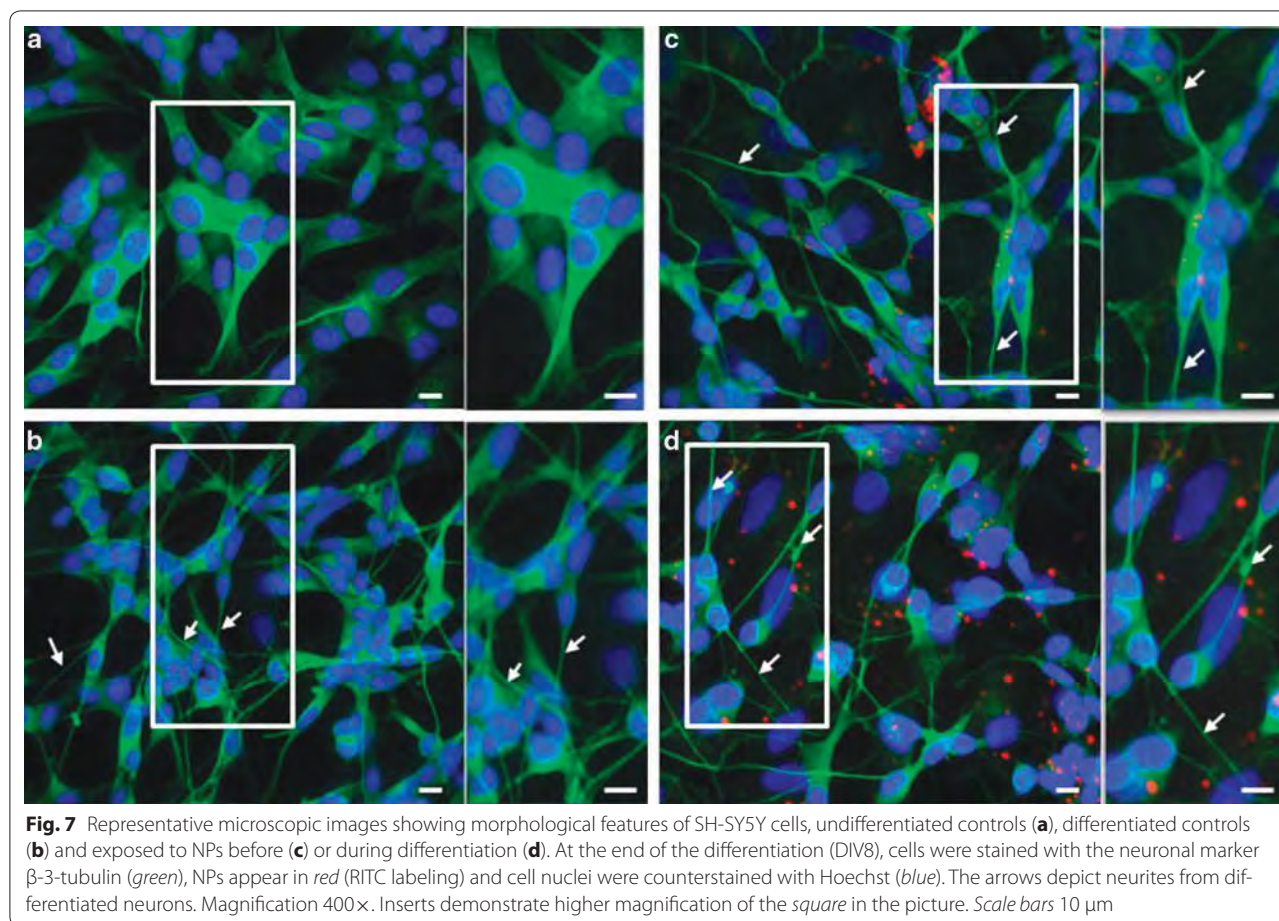
The basal OCR was significantly reduced after PCL-NP exposure before differentiation compared to differentiated cells, whereas an increase in OCR was measured when PCL-NPs were added to the cells during differentiation. Blockage or serious inhibition of the mitochondrial chain is detrimental for neuronal differentiation [31, 32]. ZnO nanoparticles were reported to induce apoptosis and decrease the mitochondrial membrane potential in primary astrocytes indicating that mitochondria are involved in ZnO nanoparticle-induced apoptosis. The nanoparticle exposure resulted in phosphorylation of c-Jun N-terminal kinase (JNK), ERK, and p38 mitogen activated protein kinase (p38 MAP-K) [14]. Silver nanoparticles showed a decoupling effect on mitochondria resulting in an impairment of mitochondrial oxidative phosphorylation [16]. In agreement with the observed increase in basal cellular respiration in PCL-NPs exposure during differentiation, TiO₂ nanoparticles increased the basal cellular respiration in human keratinocytes in a concentration-dependent manner [33].

In undifferentiated and differentiated SH-SY5Y control cells, a decrease in OCR occurred after the addition of the inhibitor of ATP synthase, oligomycin, with the drop being more pronounced in differentiated controls indicating that the mitochondrial oxygen consumption used for ATP synthesis increases during cellular differentiation. The observed increase in mitochondrial membrane potential in differentiated SH-SY5Y cells compared to undifferentiated cells has been described before [29]. The increase in membrane potential was also found after nanoparticle exposure during differentiation, whereas



nanoparticle exposure before differentiation resulted in a significant reduction of mitochondrial membrane potential indicating an impairment of mitochondrial metabolism. As the elevation in membrane potential has been demonstrated to be accompanied with differentiation [29], the nanoparticle exposure might impair differentiation. Silica-oxide nanoparticles were reported to reduce the membrane potential in hepatocytes [34], and a decrease in membrane potential was also demonstrated in human umbilical endothelial cells after exposure to 60 nm silica nanoparticles [35] corroborating our findings. Production of ATP by oxidative phosphorylation and especially dysfunction of this system has been related to the generation of superoxide, and its scavenging is accomplished by radical scavengers such as superoxide

dismutase [6]. PCL-NPs exposure before differentiation decreased basal OCR significantly more compared to differentiated control cells. In contrast, PCL-NP exposure during differentiation did not significantly change ATP production compared to differentiated control cells. Additional measurements showed that differentiation induced a significant decrease in ATP levels, but nanoparticle exposure had no effect on this parameter. In addition, the expression and the activity of the mitochondrial chain complexes I to V was not affected by nanoparticle exposure. In contrast, silica oxide nanoparticles were demonstrated to reduce the mitochondrial chain complexes I, III and IV in rat hepatocytes [34]. The smaller size of these nanoparticles as well as the different cell type may explain the different findings.



Acute nanoparticle exposure might increase leak respiration if given to undifferentiated cells causing acute stress. Hence, they are more vulnerable to mitochondrial uncoupling. In agreement with this hypothesis, transient ROS production was found in undifferentiated SH-SY5Y cells [3]. Superoxide production did not vary between all groups in this study. Previously, an increase in ROS production was found in undifferentiated cells [3]. Silica nanoparticles were also reported to increase superoxide levels in the corpus striatum of rats [36] and inhibited superoxide dismutase in human endothelial cells [35]. However, the physicochemical differences and/or the different species or cell type may explain the variable findings. It needs to be noted that distinct energy metabolism profiles were found in pluripotent stem cells, differentiated cells and cancer cells [37]. Recently, it was demonstrated that changes in mitochondrial function after Fe_3O_4 nanoparticle exposure were less pronounced in neuronal cells compared to astrocytes [38]. In the present study, cells were differentiated and the superoxide was measured after the differentiation period. Hence, the discrepancy may be due to the differentiation of the

cells and the time of the measurements. The production of oxygen radicals by HeLa cells and human hepatocytes after silica-quantum dots exposure was reported to reach a plateau already 40 min after exposure [39]. An increase in superoxide cannot be excluded in our study as it might have occurred right after the nanoparticle exposure or before the end of the differentiation period.

The uncoupled maximal respiration (OCR under FCCP) was significantly higher in undifferentiated cells compared to differentiated cells. PCL-NP exposure before differentiation did not change maximal respiration, whereas PCL-NP exposure during differentiation significantly increased maximal respiration compared to differentiated control cells. TiO_2 nanoparticle exposure was demonstrated to change mitochondrial membrane potential in rat primary hippocampal neurons [40], induce neuronal dysfunction in primary astrocytes [41], and decrease the activity of all mitochondrial respiratory chain complexes in brain tissue [42]. These findings corroborate our data despite the different composition of nanoparticles. In contrast, TiO_2 nanoparticles were reported to increase the OCR after rotenone

in keratinocytes [33]. Different material, size and charge of the nanoparticles and the difference in cell origin may account for this difference.

Mitochondria play an important role in cell metabolism during neuronal differentiation because neuronal cell differentiation requires metabolic adaptations [9]. A lower glycolytic activity was found in differentiated cells compared to undifferentiated cells, and PCL-NP exposure, independent of the time of exposure, was not significantly different from differentiated cells but significantly reduced compared to undifferentiated controls. Carbon monoxide supplementation was demonstrated to promote metabolic changes occurring during neuronal differentiation, namely, from glycolytic to oxidative metabolism [9]. Measurements of the activity of the key enzyme in glycolysis, PFK, showed a significant reduction between differentiated control cells and undifferentiated cells. PFK levels of cells exposed to PCL-NPs during differentiation did not vary compared to differentiated controls, but PFK levels were significantly reduced in cells where nanoparticles were given before differentiation. Cell differentiation was reported to be associated with metabolic changes and a metabolic shift from glycolysis to oxidative phosphorylation during neuronal differentiation has been demonstrated [19]. Moreover, artificial constitutive expression of hexokinase and lactate dehydrogenase was shown to result in cell death indicating that a decrease in glycolysis is essential for neuronal differentiation [43]. Thus the observed reduction of PFK activity in cells exposed to PCL-NPs before differentiation may affect differentiation. In contrary, an increase in glucose metabolism was found during neuronal differentiation with PI3-K/Akt/mTOR signaling being a critical regulator [14].

Neuronal differentiation

Kinases such as PI3-K/Akt and MAP-K/ERK are involved in neurite elongation, neuronal survival and synaptic plasticity of neurons [10, 21–23], and MAP-K/ERK was demonstrated to play a key role in mitochondrial function [44]. Recent data demonstrate that proliferative neuronal stem cells have high ROS levels, which is required for self-renewal and neurogenesis with underlying PI3-K/Akt signaling [45]. A significant increase in the differentiation markers (PI3-K/Akt and MAP-K/ERK) was found in differentiated SH-SY5Y compared to undifferentiated cells indicating that these kinases are involved in neuronal differentiation [46]. This finding is corroborating previously published data [5] and other studies also demonstrated that the PI3-K/Akt improved neurite elongation in primary hippocampal and cortical neurons [21, 22, 47]. However, PCL-NP exposure before and during differentiation did not significantly change

the expression of both kinases. In contrast, recently published results demonstrated a significant reduction of the differentiation markers used in this study, but neurite outgrowth was not significantly altered by exposure to PCL-NPs for 24 h before differentiation in SH-SY5Y cells [5]. The disparate findings may be explained by the differentiation protocol used in the current study as compared to the previous work; namely, a moderate FBS starvation during RA treatment. Starvation was only initiated after DIV3 (1% FBS) and the cells were incubated with 5% FBS for the first 3 days of differentiation. The expression of the neuronal marker MAP-2 was significantly increased in differentiated control cells and in cells exposed to PCL-NPs either before or during differentiation. Previously published data demonstrated a significantly reduced expression of MAP-2 in SH-SY5Y cells exposed to PCL-NP for 24 h before differentiation supporting this hypothesis. However, the trend towards a reduced expression of PI3-K/Akt and MAP-K/ERK was also found in the present study. In contrast to these findings, an activation of the kinases Akt and ERK after exposure to silver nanoparticles, enhanced neurite outgrowth, an increase in MAP-2 and an increased ROS production was reported [23]. ERK induction was found to be involved in mitochondrial degradation in SH-SY5Y cells used in an in vitro model for Parkinson disease with its activity being important for microphagy [48, 49].

The size (30 vs. 80 nm) and the different material may explain the disparate findings. Silica nanoparticles were shown to cause oxidative stress in endothelial cells via activation of the MAP-K/Nrf2 pathway and nuclear factor-kappaB signaling [50]. The same authors reported that amorphous silica nanoparticles induced ROS production mediated by MAP-K/Bcl-2 and PI3-K/Akt/mTOR signaling in endothelial cells. In that study, phosphorylated ERK, PI3-K/Akt, and mTOR were significantly decreased, whereas phosphorylated JNK and p38 MAP-K were increased after exposure to silica nanoparticles [51]. Despite the different cell origin, in our study, a decreased PI3-K/Akt and phosphorylated p42/44-MAP-K was found after PCL-NP exposure before and during differentiation in SH-SY5Y cells even though the effect was not statistically significant. As reported previously, PCL-NP exposure increased ROS production only transiently in SH-SY5Y cells [3]. Oxidative stress was demonstrated to activate MAP-K pathways [20]. Silver nanoparticles were shown to result in an increase in ROS and an activation of ERK and Akt supporting neuronal differentiation in SH-SY5Y cells. This was also demonstrated by an increased expression of the neuronal differentiation marker MAP-2 [23]. This finding is in agreement with our data, where PCL-NP exposure led to slightly increased levels of MAP-2.

Conclusions

PCL-NP exposure of SH-SY5Y cells affected mitochondrial function and the expression of differentiation markers in a time-dependent manner during differentiation. Considering the importance of adaptations in cellular respiration for neuronal differentiation and function, further studies addressing the regulation and the functional impact of PCL-NP exposure are needed to unravel the underlying mechanisms and consequences to assess the possible risks for using them in biomedical applications as impaired mitochondrial function may lead to neurodegeneration.

Abbreviations

ATP: adenosine triphosphate; C I-V: complexes I to V; DIV: day in vitro; DMEM: Dulbecco's Modified Eagle Medium; FBS: fetal bovine serum; ECAR: extracellular acidification rate; HBSS: Hank's balanced salt solution with calcium and magnesium; ICG: indocyanine green; MAP-2: microtubule associated protein-2; MAP-K/ERK: mitogen activated protein kinase/extracellular signal-related kinases; $\Delta\psi_m$: mitochondrial membrane potential; O_2 : oxygen; OCR: oxygen consumption rate; OPA: Fluoraldehyde™ o-phthalaldehyde reagent solution; PCL-NPs: silica-indocyanine green/poly-(ε-caprolactone) nanoparticles; PFK: phosphofructokinase; PI3-K/Akt/mTOR: phosphatidylinositol 3-kinase/serine/threonine specific protein kinase/mechanistic target of rapamycin; RA: retinoic acid; ROS: reactive oxygen species; SEM: standard error of the mean.

Authors' contributions

ADD performed all the experiments, analyzed the data and was a major contributor in writing the manuscript. AF contributed to acquisition of Seahorse data and OXPHOS activity, data analysis and interpretations. JZ contributed to acquisition of the ATP, superoxide, mitochondrial membrane potential and PFK measurements, data analysis; she wrote parts of the manuscript. AB contributed to the experimental work for cell culture and western blot. JB contributed to parts of the experimental work. J-MN was involved in editing the manuscript critically for important intellectual content. MF and MM were involved in writing and editing the manuscript and revising it critically for important intellectual content. All authors read and approved the final manuscript.

Author details

¹ Division of Pharmacology and Toxicology, Vetsuisse Faculty, University of Bern, Laenggassstrasse 124, 3012 Bern, Switzerland. ² Institute of Clinical Chemistry, University Hospital Bern, 3010 Bern, Switzerland. ³ Institute of Applied Physics, University of Bern, Sidlerstrasse 5, 3012 Bern, Switzerland.

Acknowledgements

The authors thank Nadja Peduto for helping with the cell culture work. Microscopy analysis was performed on equipment supported by the Microscopy Imaging Center, University of Bern, Switzerland.

Competing interests

The authors declare that they have no competing interests.

Availability of data and materials

The datasets generated and analyzed during the current study are available from the corresponding author on reasonable request.

Funding

This work was funded by the Swiss National Science Foundation (NRP64, Project #131297).

Publisher's Note

Springer Nature remains neutral with regard to jurisdictional claims in published maps and institutional affiliations.

Received: 13 January 2017 Accepted: 17 June 2017

Published online: 04 July 2017

References

- Bogni S, Schoni D, Constantinescu M, Wirth A, Vajtai I, Bregy A, Raabe A, Piele U, Frenz M, Reinert M. Tissue fusion, a new opportunity for sutureless bypass surgery. *Acta Neurochir Suppl*. 2011;112:45–53.
- Schoni DS, Bogni S, Bregy A, Wirth A, Raabe A, Vajtai I, Piele U, Reinert M, Frenz M. Nanoshell assisted laser soldering of vascular tissue. *Lasers Surg Med*. 2011;43:975–83.
- Koch F, Moller AM, Frenz M, Piele U, Kuehni-Boghenbor K, Mevissen M. An in vitro toxicity evaluation of gold-, PLLA- and PCL-coated silica nanoparticles in neuronal cells for nanoparticle-assisted laser-tissue soldering. *Toxicol In Vitro*. 2014;28:990–8.
- Zielinski J, Moller AM, Frenz M, Mevissen M. Evaluation of endocytosis of silica particles used in biodegradable implants in the brain. *Nanomedicine*. 2016;12:1603–13.
- Ducray AD, Stojilkovic A, Moller A, Stoffel MH, Widmer HR, Frenz M, Mevissen M. Uptake of silica nanoparticles in the brain and effects on neuronal differentiation using different in vitro models. *Nanomedicine*. 2016;13:1195–204.
- Gusdon AM, Chu CT. To eat or not to eat: neuronal metabolism, mitophagy, and parkinson's disease. *Antioxid Redox Signal*. 2011;14:1979–87.
- Mizuno Y, Ikebe S, Hattori N, Nakagawahattori Y, Mochizuki H, Tanaka M, Ozawa T. Role of mitochondria in the etiology and pathogenesis of parkinson's disease. *Biochim Biophys Acta-Mol Basis Dis*. 1995;1271:265–74.
- Zhu JH, Chu CT. Mitochondrial dysfunction in Parkinson's disease. *J Alzheimers Dis*. 2010;20:S325–34.
- Almeida AS, Vieira HL. Role of cell metabolism and mitochondrial function during adult neurogenesis. *Neurochem Res* 2017;42(6):1787–1794. doi:10.1007/s11064-016-2150-3.
- Qiao J, Paul P, Lee S, Qiao L, Josifi E, Tiao JR, Chung DH. PI3K/AKT and ERK regulate retinoic acid-induced neuroblastoma cellular differentiation. *Biochem Biophys Res Commun*. 2012;424:421–6.
- Nowak G, Clifton GL, Godwin ML, Bakajsova D. Activation of ERK1/2 pathway mediates oxidant-induced decreases in mitochondrial function in renal cells. *Am J Physiol Renal Physiol*. 2006;291:F840–55.
- Monick MM, Powers LS, Barrett CW, Hinde S, Ashare A, Groskreutz DJ, Nyunoya T, Coleman M, Spitz DR, Hunninghake GW. Constitutive ERK MAPK activity regulates macrophage ATP production and mitochondrial integrity. *J Immunol*. 2008;180:7485–96.
- Zhu JH, Horbinski C, Guo F, Watkins S, Uchiyama Y, Chu CT. Regulation of autophagy by extracellular signal-regulated protein kinases during 1-methyl-4-phenylpyridinium-induced cell death. *Am J Pathol*. 2007;170:75–86.
- Agostini M, Romeo F, Inoue S, Niklison-Chirou MV, Elia AJ, Dinsdale D, Morone N, Knight RA, Mak TW, Melino G. Metabolic reprogramming during neuronal differentiation. *Cell Death Differ*. 2016;23:1502–14.
- Wang J, Deng X, Zhang F, Chen D, Ding W. ZnO nanoparticle-induced oxidative stress triggers apoptosis by activating JNK signaling pathway in cultured primary astrocytes. *Nanoscale Res Lett*. 2014;9:117.
- Chichova M, Shkodrova M, Vasileva P, Kirilova K, Doncheva-Stoimenova D. Influence of silver nanoparticles on the activity of rat liver mitochondrial ATPase. *J Nanoparticle Res*. 2014;16:2243.
- Coccini T, Grandi S, Lonati D, Locatelli C, De Simone U. Comparative cellular toxicity of titanium dioxide nanoparticles on human astrocyte and neuronal cells after acute and prolonged exposure. *Neurotoxicology*. 2015;48:77–89.
- Jo DH, Kim JH, Yu YS, Lee TG, Kim JH. Antiangiogenic effect of silicate nanoparticle on retinal neovascularization induced by vascular endothelial growth factor. *Nanomedicine Nanotechnol Biol Med*. 2012;8:784–91.
- Almeida AS, Sonnewald U, Alves PM, Vieira HL. Carbon monoxide improves neuronal differentiation and yield by increasing the functioning and number of mitochondria. *J Neurochem*. 2016;138:423–35.
- Son Y, Cheong YK, Kim NH, Chung HT, Kang DG, Pae HO. Mitogen-activated protein kinases and reactive oxygen species: how can ROS activate MAPK pathways? *J Signal Transduct*. 2011;2011:792639.

21. Dijkhuizen PA, Ghosh A. BDNF regulates primary dendrite formation in cortical neurons via the PI3-kinase and MAP kinase signaling pathways. *J Neurobiol*. 2005;62:278–88.
22. Zheng J, Shen WH, Lu TJ, Zhou Y, Chen Q, Wang Z, Xiang T, Zhu YC, Zhang C, Duan S, Xiong ZQ. Clathrin-dependent endocytosis is required for TrkB-dependent Akt-mediated neuronal protection and dendritic growth. *J Biol Chem*. 2008;283:13280–8.
23. Dayem AA, Kim B, Gurunathan S, Choi HY, Yang G, Saha SK, Han D, Han J, Kim K, Kim JH, Cho SG. Biologically synthesized silver nanoparticles induce neuronal differentiation of SH-SY5Y cells via modulation of reactive oxygen species, phosphatases, and kinase signaling pathways. *Biotechnol J*. 2014;9:934–43.
24. Schonbachler A, Glaied O, Huwlyer J, Frenz M, Piesles U. Indocyanine green loaded biocompatible nanoparticles: stabilization of indocyanine green (ICG) using biocompatible silica-poly (epsilon-caprolactone) grafted nanocomposites. *J Photochem Photobiol A Chem*. 2013;261:12–9.
25. Schaller A, Hahn D, Jackson CB, Kern I, Chardot C, Belli DC, Gallati S, Nuoffer JM. Molecular and biochemical characterisation of a novel mutation in POLG associated with Alpers syndrome. *BMC Neurol*. 2011;11:4.
26. Almeida A, Almeida J, Bolanos JP, Moncada S. Different responses of astrocytes and neurons to nitric oxide: the role of glycolytically generated ATP in astrocyte protection. *Proc Natl Acad Sci USA*. 2001;98:15294–9.
27. Marosi K, Kim SW, Moehl K, Scheibye-Knudsen M, Cheng A, Cutler R, Camandola S, Mattson MP. 3-Hydroxybutyrate regulates energy metabolism and induces BDNF expression in cerebral cortical neurons. *J Neurochem*. 2016;139:769–81.
28. Jady AG, Nagy AM, Kohidi T, Ferenczi S, Tretter L, Madarasz E. Differentiation-dependent energy production and metabolite utilization: a comparative study on neural stem cells, neurons, and astrocytes. *Stem Cells Dev*. 2016;25:995–1005.
29. Schneider L, Giordano S, Zelickson BR, Johnson MS, Benavides GA, Ouyang X, Fineberg N, Darley-Usmar VM, Zhang J. Differentiation of SH-SY5Y cells to a neuronal phenotype changes cellular bioenergetics and the response to oxidative stress. *Free Radic Biol Med*. 2011;51:2007–17.
30. Kasahara A, Scorrano L. Mitochondria: from cell death executioners to regulators of cell differentiation. *Trends Cell Biol*. 2014;24:761–70.
31. Varum S, Rodrigues AS, Moura MB, Momcilovic O, Easley IV CA, Ramalho-Santos J, Van Houten B, Schatten G. Energy metabolism in human pluripotent stem cells and their differentiated counterparts. *PLoS ONE*. 2011;6:e20914.
32. Pereira SL, Graos M, Rodrigues AS, Anjo SI, Carvalho RA, Oliveira PJ, Arenas E, Ramalho-Santos J. Inhibition of mitochondrial complex III blocks neuronal differentiation and maintains embryonic stem cell pluripotency. *PLoS ONE*. 2013;8:e82095.
33. Tucci P, Porta G, Agostini M, Dinsdale D, Iavicoli I, Cain K, Finazzi-Agro A, Melino G, Willis A. Metabolic effects of TiO₂ nanoparticles, a common component of sunscreens and cosmetics, on human keratinocytes. *Cell Death Dis*. 2013;4:e549.
34. Xue Y, Chen Q, Ding T, Sun J. SiO₂ nanoparticle-induced impairment of mitochondrial energy metabolism in hepatocytes directly and through a Kupffer cell-mediated pathway in vitro. *Int J Nanomedicine*. 2014;9:2891–903.
35. Duan J, Yu Y, Li Y, Yu Y, Li Y, Zhou X, Huang P, Sun Z. Toxic effect of silica nanoparticles on endothelial cells through DNA damage response via Chk1-dependent G2/M checkpoint. *PLoS ONE*. 2013;8:e62087.
36. Parveen A, Rizvi SHM, Mahdi F, Tripathi S, Ahmad I, Shukla RK, Khanna VK, Singh R, Patel DK, Mahdi AA. Silica nanoparticles mediated neuronal cell death in corpus striatum of rat brain: implication of mitochondrial, endoplasmic reticulum and oxidative stress. *J Nanoparticle Res*. 2014;16:2664.
37. Zhang J, Nuebel E, Wisidagama DR, Setoguchi K, Hong JS, Van Horn CM, Imam SS, Vergnes L, Malone CS, Koehler CM, Teitell MA. Measuring energy metabolism in cultured cells, including human pluripotent stem cells and differentiated cells. *Nat Protoc*. 2012;7:1068–85.
38. Coccini T, Caloni F, Ramirez Cando LJ, De Simone U. Cytotoxicity and proliferative capacity impairment induced on human brain cell cultures after short- and long-term exposure to magnetite nanoparticles. *J Appl Toxicol*. 2017;37(3):361–373. doi:10.1002/jat.3367.
39. Fujioka K, Hiruoka M, Sato K, Manabe N, Miyasaka R, Hanada S, Hoshino A, Tilley RD, Manome Y, Hirakuri K, Yamamoto K. Luminescent passive-oxidized silicon quantum dots as biological staining labels and their cytotoxicity effects at high concentration. *Nanotechnology*. 2008;19:415102.
40. Sheng L, Ze Y, Wang L, Yu X, Hong J, Zhao X, Ze X, Liu D, Xu B, Zhu Y, et al. Mechanisms of TiO₂ nanoparticle-induced neuronal apoptosis in rat primary cultured hippocampal neurons. *J Biomed Mater Res A*. 2015;103:1141–9.
41. Wilson CL, Natarajan V, Hayward SL, Khalimonchuk O, Kidambi S. Mitochondrial dysfunction and loss of glutamate uptake in primary astrocytes exposed to titanium dioxide nanoparticles. *Nanoscale*. 2015;7:18477–88.
42. Costa CS, Ronconi JV, Daufenbach JF, Goncalves CL, Rezin GT, Streck EL, Paula MM. In vitro effects of silver nanoparticles on the mitochondrial respiratory chain. *Mol Cell Biochem*. 2010;342:51–6.
43. Zheng X, Boyer L, Jin M, Mertens J, Kim Y, Ma L, Ma L, Hamm M, Gage FH, Hunter T. Metabolic reprogramming during neuronal differentiation from aerobic glycolysis to neuronal oxidative phosphorylation. *Elife*. 2016;5:e13374.
44. Abrahamsen B, Zhao J, Asante CO, Cendan CM, Marsh S, Martinez-Barbera JP, Nassar MA, Dickenson AH, Wood JN. The cell and molecular basis of mechanical, cold, and inflammatory pain. *Science*. 2008;321:702–5.
45. Le Belle JE, Orozco NM, Paucar AA, Saxe JP, Mottahadeh J, Pyle AD, Wu H, Kornblum HI. Proliferative neural stem cells have high endogenous ROS levels that regulate self-renewal and neurogenesis in a PI3K/Akt-dependent manner. *Cell Stem Cell*. 2011;8:59–71.
46. Kunzler A, Zeidan-Chulia F, Gasparotto J, Girardi CS, Klafke K, Petiz LL, Bortolin RC, Rostirolla DC, Zanotto-Filho A, de Bittencourt Pasquali MA, et al. Changes in cell cycle and up-regulation of neuronal markers during SH-SY5Y neurodifferentiation by retinoic acid are mediated by reactive species production and oxidative stress. *Mol Neurobiol*. 2016. doi:10.1007/s12035-016-0189-4.
47. Lim CS, Walikonis RS. Hepatocyte growth factor and c-Met promote dendritic maturation during hippocampal neuron differentiation via the Akt pathway. *Cell Signal*. 2008;20:825–35.
48. Dagda RK, Zhu J, Kulich SM, Chu CT. Mitochondrially localized ERK2 regulates mitophagy and autophagic cell stress: implications for Parkinson's disease. *Autophagy*. 2008;4:770–82.
49. Zhu JH, Gusdon AM, Cimen H, Van Houten B, Koc E, Chu CT. Impaired mitochondrial biogenesis contributes to depletion of functional mitochondria in chronic MPP+ toxicity: dual roles for ERK1/2. *Cell Death Dis*. 2012;3:e312.
50. Guo C, Xia Y, Niu P, Jiang L, Duan J, Yu Y, Zhou X, Li Y, Sun Z. Silica nanoparticles induce oxidative stress, inflammation, and endothelial dysfunction in vitro via activation of the MAPK/Nrf2 pathway and nuclear factor-kappaB signaling. *Int J Nanomedicine*. 2015;10:1463–77.
51. Guo CX, Yang M, Jing L, Wang J, Yu Y, Li Y, Duan JC, Zhou XQ, Li YB, Sun ZW. Amorphous silica nanoparticles trigger vascular endothelial cell injury through apoptosis and autophagy via reactive oxygen species-mediated MAPK/Bcl-2 and PI3K/Akt/mTOR signaling. *Int J Nanomedicine*. 2016;11:5257–76.

RESEARCH

Open Access



Characteristics and properties of nano-LiCoO₂ synthesized by pre-organized single source precursors: Li-ion diffusivity, electrochemistry and biological assessment

Jean-Pierre Brog¹, Aurélien Crochet², Joël Seydoux¹, Martin J. D. Clift³ , Benoît Baichette¹, Sivarajakumar Maharajan¹, Hana Barosova³, Pierre Brodard⁴, Mariana Spodaryk⁵ , Andreas Züttel⁵ , Barbara Rothen-Rutishauser³ , Nam Hee Kwon^{1*} and Katharina M. Fromm^{1*}

Abstract

Background: LiCoO₂ is one of the most used cathode materials in Li-ion batteries. Its conventional synthesis requires high temperature (>800 °C) and long heating time (>24 h) to obtain the micronscale rhombohedral layered high-temperature phase of LiCoO₂ (HT-LCO). Nanoscale HT-LCO is of interest to improve the battery performance as the lithium (Li⁺) ion pathway is expected to be shorter in nanoparticles as compared to micron sized ones. Since batteries typically get recycled, the exposure to nanoparticles during this process needs to be evaluated.

Results: Several new single source precursors containing lithium (Li⁺) and cobalt (Co²⁺) ions, based on alkoxides and aryloxides have been structurally characterized and were thermally transformed into nanoscale HT-LCO at 450 °C within few hours. The size of the nanoparticles depends on the precursor, determining the electrochemical performance. The Li-ion diffusion coefficients of our LiCoO₂ nanoparticles improved at least by a factor of 10 compared to commercial one, while showing good reversibility upon charging and discharging. The hazard of occupational exposure to nanoparticles during battery recycling was investigated with an in vitro multicellular lung model.

Conclusions: Our heterobimetallic single source precursors allow to dramatically reduce the production temperature and time for HT-LCO. The obtained nanoparticles of LiCoO₂ have faster kinetics for Li⁺ insertion/extraction compared to microparticles. Overall, nano-sized LiCoO₂ particles indicate a lower cytotoxic and (*pro*-)inflammogenic potential in vitro compared to their micron-sized counterparts. However, nanoparticles aggregate in air and behave partially like microparticles.

Keywords: Single source precursors, Nano-LiCoO₂, Li⁺ Diffusion coefficient, Li-ion batteries, Nanoparticle hazard

Background

Lithium cobalt oxide LiCoO₂ has been the most commonly used cathode material in rechargeable Li-ion batteries since Goodenough first introduced the reversible reaction of Li-ions in the structure [1]. The structures of Li_{1-x}CoO₂ have been extensively studied as a function of

lithium de-intercalation, leading to several phase transformations from rhombohedral with 0.06 < x < 0.25 [2–5], via monoclinic with x = 0.5 [2, 3], to hexagonal for 0.66 < x < 0.83 [6, 7], and a second hexagonal phase, O1, for 0.88 < x < 1 [6–8].

The layered structure of lithiated LiCoO₂ exhibits two crystal structures depending on the temperature during synthesis and the preparation method. LiCoO₂ produced at low temperature (~400 °C) (LT-LCO) has a cubic spinel structure with the space group Fd3 m [9, 10] while the phase synthesized at high temperature (>850 °C,

*Correspondence: namhee.kwon@unifr.ch; katharina.fromm@unifr.ch

¹ Department of Chemistry, University of Fribourg, Chemin du Musée 9, 1700 Fribourg, Switzerland

Full list of author information is available at the end of the article

HT-LCO) has a rhombohedral layered structure [11]. LT-LCO shows a large hysteresis between the intercalation and de-intercalation of lithium ions [12–14], which is due to the mixing of Co^{3+} and Li^+ in the structure, preventing the formation of layered pathways for Li-ion diffusion. The material is therefore calcined at higher temperature to yield HT-LCO, which possesses alternating planes of Co^{3+} and Li^+ cations in the hexagonal ABCABC oxygen packing [15], providing superior electrochemical properties in Li-ion batteries [16].

Industrially, two starting materials, typically Li_2CO_3 and Co_3O_4 , are heated in a two-step process to yield first at a temperature of $<600^\circ\text{C}$ for 24 h under O_2 the LT-LCO. A second calcination step at 900°C for >12 h under O_2 [17] yields the HT-LCO [18–20]. Such a prolonged calcination process at high temperature causes however coarsening of the particles and evaporation of lithium [21]. Various synthetic methods have thus been investigated to avoid the high temperature process, with the aim to obtain the rhombohedral layered structure of HT-LCO, e.g. sol–gel [22–25], hydrothermal [26], or precipitation [16]. However, low temperature syntheses formed mostly the cubic spinel LT-LiCoO_2 , which is not favorable for Li^+ insertion/extraction. Thus, calcination at high temperature $>800^\circ\text{C}$ was always required in a second step to use the so-produced material in Li-ion battery cathodes [16].

Another access to the layered structure of HT-LCO uses metal–organic single source precursors based on alkoxides or aryloxides, in which the metal ions are already preorganized. Indeed, the synthesis of heterobimetallic alkoxides and/or aryloxides can provide a facile route for obtaining soluble, volatile, and generally monomeric species, that can thus serve as valuable precursors for making metal oxides under rather mild conditions [27–36]. For example, Buzzeo published homoleptic cobalt phenolate compounds of the type $\text{K}_2[\text{Co}(\text{OAr})_4]$ ($\text{OAr} = \text{OC}_6\text{F}_5^-$ or $3,5\text{-OC}_6\text{H}_3(\text{CF}_3)_2^-$), in which the effect of fluorination of phenoxide on $(\text{K18C6})_2[\text{Co}(\text{OAr})_4]$ is highlighted [37]. Boyle et al. published lithium cobalt double aryloxide compounds obtained from $\text{LiN}(\text{SiMe}_3)_2$, $\text{CoN}(\text{SiMe}_3)_2$ in THF and subsequent addition of an aryl alcohol. They obtained nanoparticles of LiCoO_2 by thin film formation [38], but did not characterize them electrochemically. Nanoparticles of HT-LCO have the advantage to offer shorter diffusion lengths for the Li-ions as compared to the commercial, micron-sized particles from which only $\sim 50\%$ of Li-ions can be used [26, 35]. On the other hand, since batteries are typically also shredded upon recycling, the use of nanomaterials in batteries might present a certain danger, which requires a risk management for new materials.

In this context, we present here new molecular precursors using simple ligands such as phenoxide and alkoxides with a low amount of carbon atoms that can produce nano-HT-LCO at quite low temperature. We have tested the new materials for their electrochemical properties in cathodes and their Li-ion diffusion coefficients were determined. In order to evaluate possible material hazards, the nanoparticles of HT-LCO were exposed directly at the air–liquid interface (ALI) using a well-established *in vitro* multicellular lung model [39]. The lung was chosen as an experimental tissue, since it can be considered by far the most important portal of entry for aerosolized nanoparticles into the human body [40–46]. Although various aspects of nanoparticles toxicity have already been described and studied in the recent literature, almost no studies were carried out in the domain of battery cathode nanoparticles.

Methods

Materials and reagents

Cobalt chloride (CoCl_2) (dry or hydrated with two H_2O), lithium phenoxide (LiOPh) in tetrahydrofuran (THF), lithium *iso*-propoxide (LiO^iPr) in THF, ethanol (technical grade and analytical grade), tetramethylethylenediamine (TMEDA), dioxane, dimethoxyethane (DME), pyridine (Py), heptane and micron-sized HT- LiCoO_2 were purchased from Sigma-Aldrich (Switzerland). Lithium *tert*-butoxide (LiO^tBu) in THF, lithium methoxide (LiOMe) in methanol, lithium ethoxide (LiOEt) in THF and THF (dry and over molecular sieves) were purchased from Acros Organics (Belgium). Deionized water was produced in house by double distillation.

Synthesis of bimetallic complexes [47]

All experiments were carried out under an inert argon atmosphere, using Schlenk techniques [48]. All solvents were bought dried and were stored over molecular sieve. The elemental analysis of the compounds turned out to be difficult to obtain due to the instability of most compounds in air, based on the loss of (coordinated) solvent.

The compounds $[\text{Co}(\text{OPh})_4\text{Li}_2(\text{THF})_4]$ (1), $[\text{Co}(\text{OPh})_4\text{Li}_2(\text{THF})_4]\cdot\text{THF}$ (2), $[\text{Co}(\text{OPh})_4\text{Li}_2(\text{THF})_2(\text{H}_2\text{O})(\text{THF})_2]$ (3), $[\text{Co}(\text{OPh})_4\text{Li}_2(\text{TMEDA})_2]$ (4), $[\text{Co}(\text{OPh})_4\text{Li}_2(\text{dioxane})_2]_n$ (5), $[\text{Co}(\text{OPh})_4\text{Li}_2(\text{DME})_2]$ (6), $[\text{Co}(\text{OPh})_4\text{Li}_2(\text{Py})_4]$ (7), $[\text{Co}_2(\text{O}^t\text{Bu})_6\text{Li}_4(\text{THF})_2]$ (8), $[\text{Co}_2(\text{O}^t\text{Bu})_2(\text{OPh})_4\text{Li}_2(\text{THF})_4]$ (9), $[\text{Co}_2(\text{O}^i\text{Pr})_6\text{Li}_2(\text{THF})_2]$ (10), $[\text{Co}_2(\text{OEt})_{12}\text{Li}_8(\text{THF})_{8-10}]$ (11), and $[\text{Co}_2(\text{OMe})_6\text{Li}_2(\text{THF})_2(\text{MeOH})_2]$ (12) were synthesized using CoCl_2 as starting material and reacting it with the corresponding lithium aryloxide or alkoxide. In a typical reaction procedure, dried CoCl_2 is dissolved in dry THF under heating to reflux. After stirring for 30 min, aliquots of LiOR ($\text{R} = \text{Ph}, ^t\text{Bu}, ^i\text{Pr}, \text{Et}, \text{Me}$)

are added. The mixture is heated to reflux, stirred during 30 min and then concentrated. Layering the concentrated solution with a non-solvent, respectively solvent exchange lead to single crystalline material for compounds **1–5** and **9**, while powders were obtained for **6–8** and **10–12**. Table 1 resumes the reaction conditions for all compounds, with detailed synthesis protocols and IR-analyses given in the Additional file 1: Text 1.

Calcination to LiCoO₂

Among the so obtained precursors, compounds **1**, **8–12** were heated up to 450 °C for 1 h and 500 °C for 2 h at an average rate of 18 °C/min under an air flow of 8 l/min in a muffle furnace equipped with an evacuation smoke-stack for combustion gases. The black powder obtained was then cooled to room temperature within 5 min in air. The black/grey powder was next washed by centrifugation three times with water and two times with ethanol in order to remove LiCl. The clean and dry oxide nanopowder was finally annealed using an average ramp of 17 °C/min up to 600 °C for 80 min to remove low temperature oxide phase impurities. These materials were used for the biohazard tests. LiCoO₂ prepared with LiOMe and LiO^tBu was calcined further until 700 °C for 30 min to measure charge/discharge capacities at different current densities.

Characterization

Single crystal X-ray structures

Single crystals of compounds **1–5** and **9** were mounted on a loop and all geometric and intensity data were taken from these crystals. Data collection using Mo-K_{α1} radiation ($\lambda = 0.71073$ Å) was performed at 150 K on a STOE IPDS-II diffractometer equipped with an Oxford

Cryosystem open flow cryostat [49]. Absorption correction was partially integrated in the data reduction procedure [50]. The structure was solved by SIR 2004 and refined using full-matrix least-squares on F^2 with the SHELX-97 package [51, 52]. All heavy atoms could be refined anisotropically. Hydrogen atoms were introduced as fixed contributors when a residual electronic density was observed near their expected positions. Diffraction data sets for compounds **1–5** are unfortunately incomplete due to decomposition of the single crystals, resulting in poor data sets and *R*-values for the compounds. However, the isotropic attribution of heavy atoms is unambiguous.

Crystallographic data (excluding structure factors) for the structures in this paper have been deposited with the Cambridge Crystallographic Data Center, 12 Union Road, Cambridge CB21EZ, UK. Copies of the data can be obtained on quoting the depositing numbers CCDC-1527018 (**1**), 1527022 (**2**), 1527023 (**3**), 1527020 (**4**), 1527019 (**5**), and 1527021 (**9**) (Fax: +44-1223-336-033; E-mail: deposit@ccdc.cam.ac.uk). Important crystal data for these compounds are given in the Additional file 1: Table S1.

Other characterizations

For powder XRD measurements, a Stoe IPDS II theta, equipped with monochromated Mo-K_{α1} radiation (0.71073 Å) was used in order to avoid X-ray fluorescence of the cobalt but also a Stoe STADIP, equipped with monochromated Cu-K_{α1} radiation (1.540598 Å) and Mythen detector. TGA was recorded on a Mettler Toledo TGA/SDTA851e in closed aluminium crucibles with a pin hole. Specific surface area was measured on a Micromeritics Gemini V series BET with a pre-treatment

Table 1 The reactants, synthetic conditions and the yields of the compounds **1**, **8–12**

Compound	Formula	Reactants in synthesis	Yields (%)
1	[Co(OPh) ₄ Li ₂ (THF) ₄]	CoCl ₂ (0.1 g, 0.77 mmol) + 4 LiOPh 1 M in THF (3.1 ml, 3.1 mmol)	82
2	[Co(OPh) ₄ Li ₂ (THF) ₄].THF	Idem as 1 , but –24 °C under argon	56
3	[Co(OPh) ₄ Li ₂ (THF) ₂ (H ₂ O)(THF) ₂] ₂	Idem as 1 , but –24 °C in air	<10
4	[Co(OPh) ₄ Li ₂ (TMEDA) ₂]	Idem as 1 , recrystallized from TMEDA	69
5	[Co(OPh) ₄ Li ₂ (dioxane) ₂] _n	Idem as 1 , recrystallized from dioxane	95
6	[Co(OPh) ₄ Li ₂ (DME) ₂]	Idem as 1 , recrystallized from DME	47
7	[Co(OPh) ₄ Li ₂ (Py) ₄]	Idem as 1 , recrystallized from pyridine	39
8	[Co ₂ (O ^t Bu) ₆ Li ₄ (THF) ₂]	CoCl ₂ (585 mg, 4.5 mmol) + 3 LiO ^t Bu 1 M in THF 13.5 ml (13.5 mmol)	87
9	[Co ₂ (O ^t Bu) ₂ (OPh) ₄ Li ₂ (THF) ₄]	CoCl ₂ (500 mg, 3.85 mmol) + LiO ^t Bu (3.9 ml, 3.9 mmol) + LiOPh 1 M in THF (7.7 ml, 7.7 mmol)	85
10	[Co ₂ (O ⁱ Pr) ₆ Li ₂ (THF) ₂]	CoCl ₂ (500 mg, 3.85 mmol) + 3 LiO ⁱ Pr 2 M in THF (5.8 ml, 11.6 mmol)	92
11	[Co ₂ (OEt) ₁₂ Li ₈ (THF) _{8–10}]	CoCl ₂ (500 mg, 3.85 mmol) + 6 LiOEt 2 M in THF (11.6 ml, 23.2 mmol)	89
12	[Co ₂ (OMe) ₆ Li ₂ (THF) ₂ (MeOH) ₂]	CoCl ₂ (500 mg, 3.85 mmol) + 3 LiOMe 2 M in THF (5.3 ml, 11.7 mmol) and MeOH	90

under vacuum at 150 °C for one night. SEM images were recorded on Phenom Desktop SEM and a FEI XL 30 Sirion FEG with Secondary Electron and EDS Energy Dispersive Spectrometer detectors. SEM samples were prepared by spraying them on a carbon tape glued on a SEM holder to reproduce the spraying in the exposure chamber. All images were obtained without sputter coating pretreatment. TEM images were recorded on a FEI/Philips CM-100 Biotwin. Raman spectra were recorded with a confocal micro-Raman spectrometer, HORIBA LabRAM HR800, combined with an optical microscope Olympus BX41, using a red laser at 633 nm for excitation, attenuated with filters in order to avoid thermal degradation of the scotch tape used as sample holder. The Li^+ and $\text{Co}^{2+/3+}$ ion concentrations were determined by inductively coupled plasma optical emission spectroscopy (ICP-OES) using a Perkin Elmer Optima 7000DV.

The muffle furnace used for combustion and tempering is equipped with a eurotherm thermal controller (Tony Güller Naber Industrieofenbau, Zurich, Switzerland).

Metal ion release

A metal ion release test was conducted to assess the amount of potential metal ion dissolution from the tested compounds. 100 mg of each of the micro- and nanoparticles were immersed in 10 ml of deionised water at pH 7 and pH 4.5 for 24 h. The concentrations of the metal ions were then determined using ICP measurements (Additional file 1).

Statistical and data analysis

The microparticles of LiCoO_2 are represented in black and the nanoparticles in grey bars. Data are the mean \pm the standard error of the mean (SEM) and are absolute values. Values were considered significantly different compared to the negative control with $p < 0.05$ using a one way Anova with a post hoc Tukey test (*nanoparticles, #microparticles).

Electrodes and electrochemical tests

Preparation of the electrodes

0.5 g of the nanoscale- LiCoO_2 and 10 wt% SFG graphite with respect to LiCoO_2 were ball milled in a horizontal set-up (Retch MM 400) for 15 min at a frequency of 30 Hz. The ball milling jar had a volume of 10 ml and contained two stainless steel balls of 10 mm in diameter. The electrode paste was prepared in a glass tube, starting with polyvinylidene fluoride (PVDF) (10 wt% with respect to LiCoO_2) and 0.5 ml of N-methyl-2-pyrrolidone (NMP), which were stirred by a mechanical stirrer for 30 min until PVDF was completely dissolved. 2 wt% of ABG graphite with respect to LiCoO_2 was then added and the mixture was stirred for 15 min. Then, the ball milled composite

powder (0.6 g) of graphite and LiCoO_2 were added to the PVDF/graphite/NMP mix and stirred for a half an hour. The so-obtained paste of PVDF/NMP/graphite/ LiCoO_2 was spread onto an aluminum foil by the doctor-blade method and dried overnight at 120 °C. The overall weight ratio of the composite made of nano- LiCoO_2 (active material), carbon and binder was around 78:12:10.

Cell assembly

All compounds used were dried to avoid HF formation in the electrolyte and were assembled in a glove box under argon (MBraun, Germany) having <0.1 ppm of water and oxygen. Typically, the LiCoO_2 electrode was assembled in a coin cell using lithium metal as anode, a few drops of an ethyl carbonate (EC) and diethylene carbonate (DEC) mixture in a 1:1 volume ratio with 1 M LiPF_6 and 2 wt% of vinylene carbonate as electrolyte with respect to solvents and LiPF_6 as well as a Celgard separator.

Battery tests

A potentiostat, Princeton Applied Research 273A, and an Arbin battery test instrument (version 4.27) were used to examine the electrochemical properties of the carbon-nano- LiCoO_2 composite electrodes. Charge and discharge capacities of coin cells were measured by an Arbin 2000 battery test instrument at different current densities of C/20, C/10, C/5, C/2 and 1C. The voltage window was set between 2.6 and 4.4 V vs. Li^+/Li . The current densities between C/20 and 1C were based on the practical capacity of 140 mAh/g.

Li-ion diffusion coefficients were evaluated by cyclic voltammetry at a sweep rate of 1, 0.7, 0.5, 0.2 and 0.1 mV/s between 3.5 and 4.4 V vs. Li^+/Li .

The discharge kinetic of LiCoO_2 electrodes was investigated at various current densities between 20C and C/20. The LiCoO_2 coin cells were re-charged until 4.4 V vs. Li^+/Li at 20C current density and then rested for 3 min. The electrode was discharged at the same current density of 20C until 2.6 V. This procedure was repeated at various lower current densities until C/20 (so-called deep discharge). By this procedure, the capacity vs. the discharge current can be determined directly. The sum of all capacities, obtained at different discharge currents is the maximum discharge capacity of the battery:

$$C_{\text{max}} = I_1 \cdot t_1 + I_2 \cdot t_2 + \dots + I_n \cdot t_n.$$

The equilibrium potentials of LiCoO_2 electrodes were measured with the pulsed cycle method (3 min with applied current, followed by 3 min rest) in the range of potentials between 2.6 and 4.2 V vs. Li^+/Li . The equilibrium charge/discharge current was C/10 (15 mA/g). These procedures were described in detail by Spodaryk et al. [53].

The exchange current densities were calculated from the Tafel plot, i.e. dependence of current vs. overpotential. Currents ($\pm i$), starting from the smallest to the highest, were alternatively applied and the potentials during the current flow were measured. From the overpotential (the difference between measured potential with the applied current and equilibrium potential, i.e. the potential which the electrode reaches during rest time), the exchange current densities were calculated. The detailed method is described by Chartouni et al. [54].

Electrochemical impedance spectroscopy (EIS) data were obtained using a potentiostat/galvanostat PGSTAT302N with FRA module (Metrohm Autolab). Impedance spectra of the Li-ion batteries were measured in the range of working frequencies from 10 mHz to 100 kHz. The range was built using a logarithmic distribution. The voltage modulation amplitude was 10 mV. The EIS spectra were analysed using fitting procedure in NOVA 1.4 software from Metrohm Autolab. The accuracy of the potentials measurements is ± 2 mV, of the current $\pm 2\%$ and of the capacity $\pm 2\%$.

The values of the elements from the equivalent circuit model (Additional file 1: Figure S10) were obtained by the following formulas:

$$Z_{Ri} = R_i$$

where R_i is contact resistance or charge transfer resistance, Ohm, Constant phase element (CPE), which models the behavior of an imperfect capacitor or of a double layer, calculated by:

$$Z_Q = \frac{1}{Y_0(j\omega)^n}$$

where Y_0 is admittance of an ideal capacitance, siemens S; n is an empirical constant, $0 < n < 1$ (n is frequency independent and in the case $n = 1$ formula describes an ideal capacitor, $n = 0$ —resistor, $n = 0.5$ —Warburg impedance); j is imaginary part of impedance; ω is angular frequency, rad/s, $\omega = 2\pi f$; f is frequency, Hz.

The Warburg impedance is provided by:

$$Z_W = \frac{1}{Y_0\sqrt{j\omega}}$$

Lung cell cultures

All in vitro exposure experiments in this study were conducted with a 3D triple cell co-culture model of the human epithelial tissue barrier cultured at the ALI. This system has previously been described in detail [39, 55]. Briefly, the model consists of a layer of human alveolar type II-like epithelial cells (A549, derived from the American Type Culture Collection) with human monocyte-derived macrophages (MDM) on the apical side (upper chamber) and monocyte-derived dendritic cells (MDDC)

on the basolateral side (lower chamber). A549 epithelial cells were cultured at a density of 0.5×10^6 cells/ml in cell culture medium RPMI 1640 (supplemented), on BD Falcon cell culture inserts (high pore density PET membranes, 4.2 cm^2 growth area, $3.0 \text{ }\mu\text{m}$ pore size; *Beckton Dickinson AG, Switzerland*). The cell culture densities of MDM and MDDC were 5×10^4 and 25×10^4 cells/insert, respectively [56].

Human blood monocytes were isolated from different, individual buffy coats received from the Swiss blood donation service (Bern, Switzerland) (i.e. different donor for each exposure), using CD14⁺ MicroBeads as described previously [57]. Due to this, variations in the background between different sets of cell cultures were expected to occur. Co-cultures were incubated for 24 h under suspension conditions in order to allow cell-cell habituation. Subsequently, cell culture medium was extracted from the apical layer to allow formation of the ALI over a period of 24 h in the incubator prior to particle exposures.

Air-liquid interface cell exposure system

The dry powder insufflator (DP-4, Penn Century, USA) was used to pulverise the LiCoO₂ particles. The particle exposure system consisted of a closed chamber ($15 \times 15 \times 35 \text{ cm}$) coated with aluminium foil and equipped with a quartz crystal microbalance (QCM) for the in situ determination of the amount of material deposited. As the material settles onto the QCM, the frequency of the crystal changes (ΔF). The ΔF value (Hz) calculated from the recorded frequency values before and after deposition of material is converted to deposited mass per area ($\mu\text{g}/\text{cm}^2$) as described in [58].

To avoid electrostatic blocking of the needle, aggregation, asymmetric deposition and low deposition yield, a stainless steel needle without bevel of $2 \text{ mm } \varnothing$ and 7 cm of length was used as pulverization means with a gas expulsion flow of $\sim 120 \text{ ml/s}$ of air in two pulse of $\sim 0.5 \text{ s}$ for each exposure.

Particles exposures

As described for the aerosolisation of dry volcanic ash particles [59] the pulverisation of the dry powder of nanoparticles produces a radial distribution of the particles at the bottom of the chamber. In order to obtain a regular and reproducible distribution of particles on the cells, the 6-well culture plates were placed in such a way that the inserts holding the triple cell co-cultures and the QCM balance were disposed equidistant from the centre in a cross-like pattern as drawn in the scheme below (Fig. 1).

Two inserts/wells were used for each of the three different concentrations of nanoparticles and microparticles. Experiments were repeated 3–4 times for each of the two

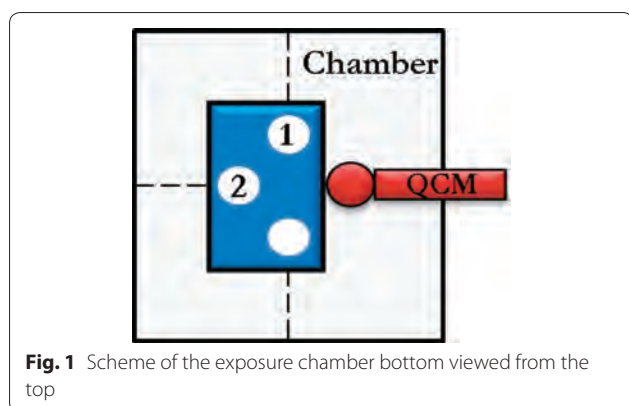


Fig. 1 Scheme of the exposure chamber bottom viewed from the top

particle sizes chosen (micronsize commercial particles and homemade nanoparticles). The pulverisation process took place over a period of about 1 month with each week a different blood donor source.

The samples (wells) were incubated overnight at 37 °C and 5% CO₂. The day after incubation, the supernatant was removed and replaced with 2 ml of culture medium.

Biological assays

Cytokine and chemokine quantification

The pro-inflammatory response of the triple co-culture after exposure to LiCoO₂ particles was quantified using the amount of the pro-inflammatory mediators which are tumor necrosis factor α (TNF-α) and interleukin-8 (IL-8) using commercial ELISA development kit and the related supplier protocol. The positive control for the pro-inflammatory proteins was treated with lipopolysaccharide 1 µg/ml (LPS) for 24 h.

Optical microscopy/LSM microscopy

After the exposure, cells were fixed and labelled as previously described by Lehmann et al. [56]. In short, samples were stained with a 250 µl mix of a 1:50 dilution of phalloidin-rhodamine for cell cytoskeleton and 1:100 dilution of 4',6-diamidino-2-phenylindole (DAPI) for the cell nuclei. Coverslips were then mounted onto microscope slides using Glycergel and imaged by LSM.

Results

1-Solid states structures

Compounds 1–7 were obtained by reacting CoCl₂ with LiOPh in THF, followed by crystallization in THF under different conditions (temperature, presence of water or not, leading to compounds 1–3) or by eliminating the THF solvent and replacing it with other mono- or bidentate ligands, like TMEDA, dioxane, DME, or pyridine (4–7). A general reaction scheme (Scheme 1) resumes the family of compounds obtained. We describe here the



solv = THF, TMEDA, pyridine, DME or dioxane.

Scheme 1 General reaction scheme for obtaining compounds 1–7

single crystal structures of compounds 1–5, on which we base our structural discussion. For compounds 6 and 7, the single crystal structures could not be determined as the single crystal quality was poor; yet, the chemical analyses confirm a chemical composition in analogy to the other five compounds.

Among the compounds, different structure types could be identified depending on the solvent present. For compounds 1–7, the core of the structure is essentially based on one central cobalt ion which is tetrahedrally coordinated by four phenolate entities, bridging pairwise to two lithium ions. The coordination spheres of the lithium cations are completed by coordinating solvent molecules, leading either to molecular entities or a coordination polymer in case of 5. Figure 2 shows as an example of such a core structure the one of compound 1. In compound 3, the terminal ligands of one of the two Li-ions have been formally replaced by two water molecules, which act as bridging ligands between two [Li₂Co(OPh)₄] cores, leading thus to a dimer-type structure. Detailed structure descriptions for 1–5 with distances and angles are given in the Additional file 1: Text 2, while a resume is given in Table 6.

Compounds 8–12

For the compounds 8–12, the aim was to test ligands other than aryloxides, such as alkoxides, and to also mix aryloxides and alkoxides as ligands. The synthesis used is similar to the one for compound 1 (Scheme 2), but replacing the LiOPh with alkoxides or using a mix of both.

Since the precursor compounds 8, 10, 11 and 12 did not afford single crystals, other methods were used to approach their structure. In possible analogy to compound 8, the sodium compound [Na₂Co₂(O^tBu)₆(thf)₂] was described in the literature [60]. Since the sodium ions are coordinated by four ligands, similar to the preferred coordination of Li⁺, and since Co²⁺ tends to a tetrahedral coordination [61], we propose a similar structure for the lithium compound 8 (Fig. 3). The TGA and NMR measurements confirm that there are two THF molecules per three O^tBu ligands and the ICP measurement gives a ratio of one lithium for one cobalt ion.

The compounds 10–12 were also analyzed by TGA and NMR to determine the amount of ligand and solvent remaining in the solid state structure and the ratio between the ligand and the coordinating solvent

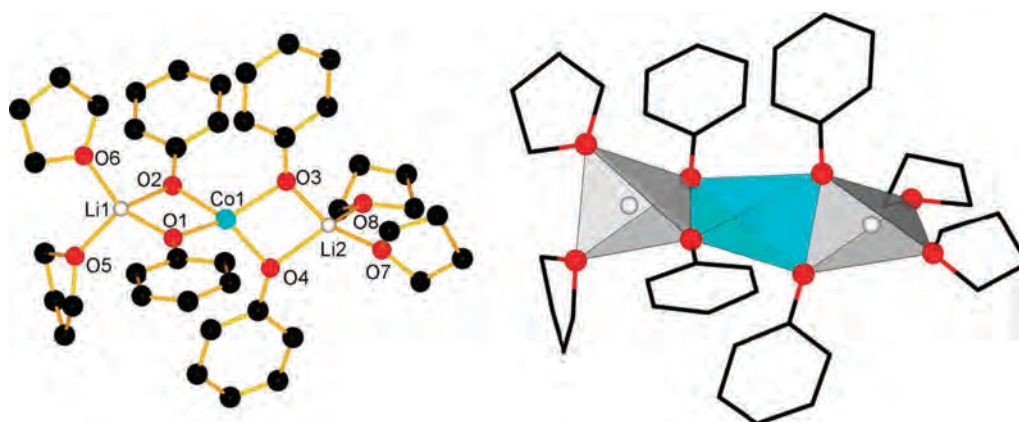
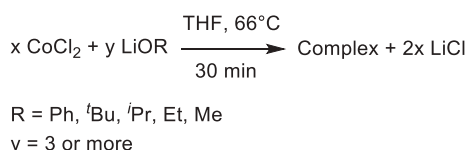


Fig. 2 Labeled view of the molecular structure of **1**, H-atoms are omitted for clarity (left); coordination polyhedra in **1** (right)



Scheme 2 General reaction equation for the synthesis of compound **8–12**

molecules. ICP measurements and argentometric titrations of chloride (Additional file 1: Table S3) were also performed to evaluate the ratio of lithium per cobalt ions and the amount of LiCl remaining in the material. The results are resumed in Table 2.

From the synthesis, we observed that three equivalents of ligand are required to form carbonate-free LiCoO₂ from this precursor **10**. The low amount of impurity of mainly Li₂CO₃ after combustion indicates that there is no excess of unreacted lithium precursor. We also found one Li⁺ for one Co²⁺ ion in the complex as well as two THF molecules. From this data we propose that the OⁱPr-compound possesses a structure similar to the O^tBu-precursor **8** (Fig. 4). Using the same method for the compound **12** and based on the findings shown in Table 2, we can propose a similar structure as for **8** (Fig. 4). The extra methanol molecules are difficult to assess since both methanol and THF have almost the same boiling point. Finally, NMR measurements are not

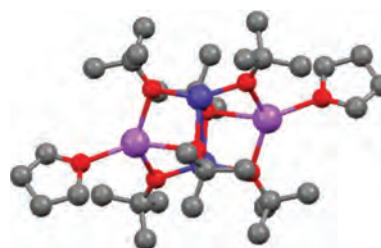
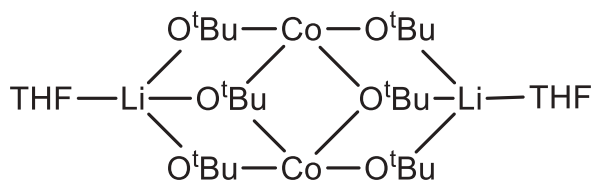


Fig. 3 Proposed structure for **8** (left) based on the [Na₂Co₂(O^tBu)₆(thf)₂] compound (right, dark blue Co, violet Na, red O, grey C; H-atoms omitted described in [60])

Table 2 Combined results from TGA, NMR, ICP and argentometric titration for compounds **8–12**

Compound no—reagent	Ligand eq. vs. Co eq.	Solvent molecules per complex	Free lithium (eq.)	LiCl (eq.)
8 —LiO ^t Bu	3	4 (residual THF)	1 Li per Co	2 Li per Co
9 —LiO ^t Bu + LiOPh	1 + 2 (3)	4	1 Li per Co	2 Li per Co
10 —LiO ⁱ Pr	3	2 THF	1 Li per Co	2 Li per Co
11 —LiOEt	6	4–5 THF	4 Li per Co	2 Li per Co
12 —LiOMe	3	2 THF/2 MeOH	1 Li per Co	2 Li per Co

helpful since the broadening of the signals (due to the paramagnetic influence of the cobalt ion) hides most of the possible peak shifts.

The compound **11** is the only one which does not follow this rule of three ligands per Co^{2+} and requires six ligands per Co^{2+} to form the desired oxide without impurities of Co_3O_4 . An open double heterocubane structure is proposed, as it combines the minimum amount of ligands, the amount of free lithium for coordination, the amount of THF and the preferred coordination of lithium ions (4) and cobalt ions (4,6) as determined by TGA, NMR, ICP and argentometric titration (Fig. 4).

Compound **9** is an interesting mixed ligand compound as it forms molecules of $[(\text{thf})_2\text{Li}(\mu\text{-O}^i\text{Ph})_2\text{Co}(\mu\text{-O}^t\text{Bu})_2]_2$ where the two O^tBu groups act as bridging ligands between two Co^{2+} ions. The O^iPh ligands bridge pairwise

between the cobalt and lithium ions, while two THF molecules complete the coordination of the lithium ions (Fig. 5). A detailed description with distances and angles is given in the Additional file 1: Table S1 and Text 2. The bond valence sums are >2 for both cobalt ions and >1 for both lithium ions, indicating sufficient good coordination of the metal ions by their ligands, as it is also the case for compounds **1–5** (Table 6).

Thermal decomposition to LiCoO_2

Among all compounds, **2** and **3** are difficult to handle as they lose their solvent molecules very quickly. The compounds **4–7** are not well suited for the formation of oxide at low temperature because of their relatively high boiling point, high carbon content and molecular weight. The following investigations for the formation of LiCoO_2

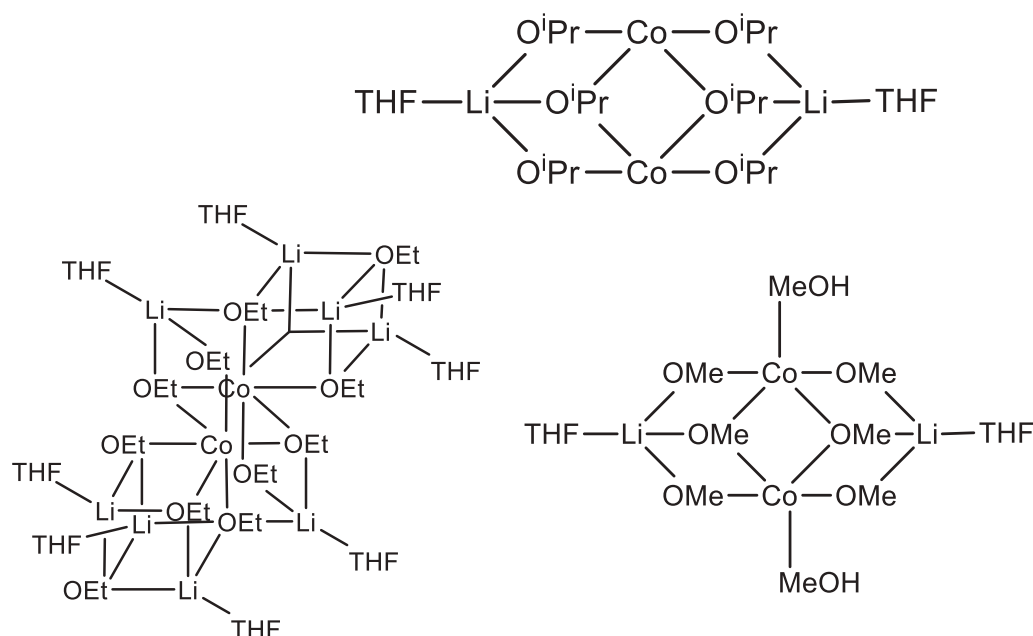


Fig. 4 Proposed structure of compound **10** (top), **11** (left bottom) and **12** (right bottom)

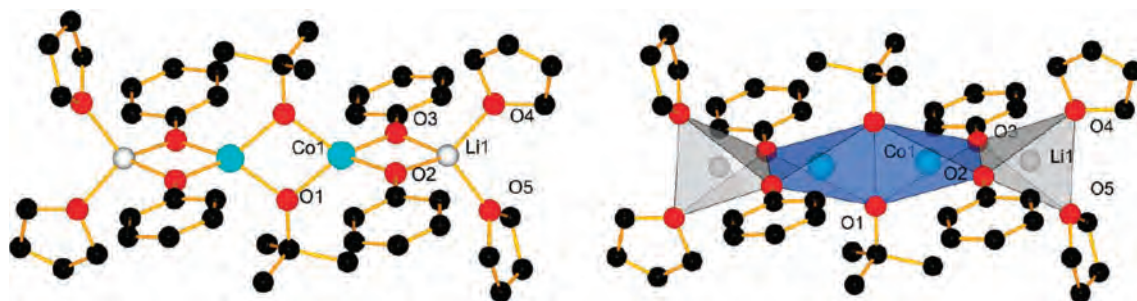


Fig. 5 Molecular view of compound **9** measured by XRD. H-atoms are omitted for clarity

were thus limited to compounds containing THF and the less carbon containing compounds, hence **1** and **8** to **12**.

In order to use these compounds as precursors for the manufacturing of LiCoO_2 , TGA measurements under oxygen atmosphere with open crucible were performed on the chosen compounds (Fig. 6). The general decomposition process of these complexes begins with the loss of the coordinated and residual non-coordinated solvent molecules before 120 °C (THF B.P. 66 °C, MeOH 65 °C). At higher temperature, between ca. 100 and 400 °C depending on the precursor, the combustion process occurs: it consists of an oxidation of the Co^{2+} to Co^{3+} and of the ligand carbon backbone combustion. Above the temperature of 450 °C, the masses remain quasi constant (Fig. 6). The completed combustion temperature and the detail thermal measurement information are described in Additional file 1: Tables S4 and S5.

Based on the minimum temperature of decomposition of the complexes determined by TGA, combustion tests were performed at different temperatures. Heating to the

minimal temperature of decomposition of the precursors of 300 °C for 1 h lead to the formation of the HT-LCO phase with some byproducts (Li_2CO_3) (Fig. 7a). Since Li_2CO_3 is highly soluble in water, it was removed after rinsing. We believe that the formation of HT-LCO at such a low temperature is possible due to the preorganization of metal ions within the heterobimetallic single source precursors. We decided nevertheless to increase the decomposition temperature by 50–100 °C compared to the decomposition temperature of the compounds in order to reduce the amount of byproducts, and for comparison purposes, the temperature was set to 450 °C for 1 h for all compounds.

After indexation of the powder diffractograms obtained after combustion at 450 °C, all of the tested precursors (**1**, **8**–**12**) afforded LiCoO_2 with low amounts of impurities that could not be detected by powder X-ray analysis after washing with water, hence less than 5% (Fig. 7). Heating to the minimal temperature of decomposition of the precursors of 300 °C for 1 h leads to the

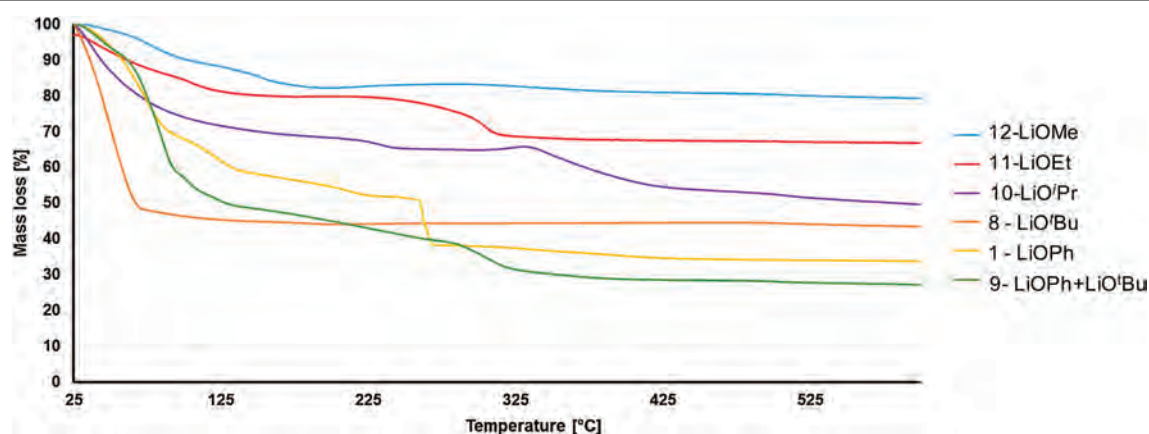


Fig. 6 TGA measurements of complexes **1**, **8**, **9**, **10**, **11**, **12**

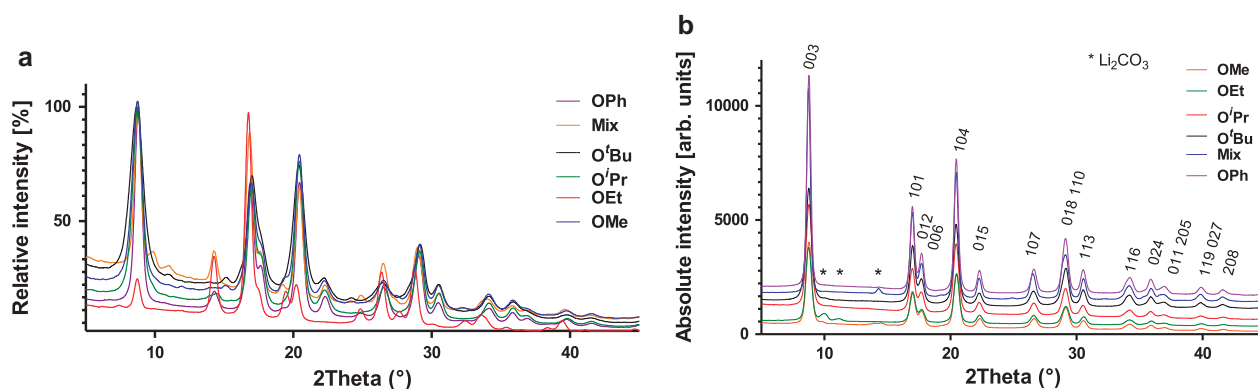


Fig. 7 XRD patterns of the oxides obtained after combustion of the precursors **1**, **8**, **9**, **10**, **11**, and **12** at 300 °C (a) and 450 °C (b) in air

formation of the HT-LCO phase with some byproducts (among which Li_2CO_3). A Rietveld refinement of the different diffractograms, taken on a Mo source, was performed to determine the exact phase of the oxide. The lattice cell parameters from the different precursors correspond to a slightly distorted HT-LCO, with the space group $R\bar{3}m$. This small distortion of the unit cells arises from the fact that this material is composed of nanocrystallites which possess a more strain than standard micro-metric crystallites. The c/a ratio gives also an indication on the general cation ordering of the oxide phase. If the c/a ratio is 4.899 or lower, it means that it is a cation-disordered rock salt structure, also called the LT-LCO with a spinel structure ($Fd\bar{3}m$). Since this ratio c/a is higher than this value in all cases, it indicates that the high temperature phase has been obtained for all precursors (Table 3).

Another method to identify LT and HT phases of LiCoO_2 is to verify the peaks at $2\theta = 65\text{--}67^\circ$ ($\lambda = \text{Cu-K}\alpha_1$). The HT-LCO has two split peaks of the (108) and (110) planes while the LT-LCO has one single peak of the (440) plane at 65° [13, 62]. As shown in Fig. 8 below, all the materials prepared with O^iBu , O^iPr , OMe and OPh show two split peaks corresponding to the HT-LCO phase.

After thermal treatment at 450°C , the morphologies of the materials prepared with different precursors were analyzed using SEM (Fig. 9). All the materials show polyhedral shapes but the materials obtained from LiO^iPr and LiOPh precursors formed rhombohedral and triangle shapes.

Since the detection limit in powder X-ray diffraction is 3–5%, Raman spectroscopy was used to complete the analysis. The HT-LCO possesses only two Raman active modes: A_{1g} (Co-O stretching) ν_1 at 595 cm^{-1} and E_g (O-Co-O bending) ν_2 at 485 cm^{-1} , while LT-LCO has four Raman active modes (A_{1g} , E_g , $2 F_{2g}$) which are respectively at $\nu = 590, 484, 605$ and 449 cm^{-1} and are due to the mixing of cations in the structure [63].

The Raman spectrum of our non-annealed nano-LCO obtained from compound **8** shows a contamination of the

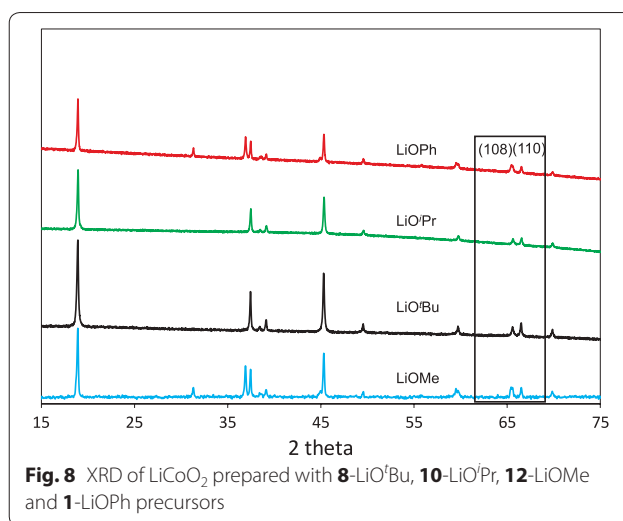


Fig. 8 XRD of LiCoO_2 prepared with **8**- LiO^iBu , **10**- LiO^iPr , **12**- LiOMe and **1**- LiOPh precursors

HT-LCO with the LT phase which can be easily removed by annealing at 600°C for 1 h. No significant improvement can be observed for a 700°C annealing (Fig. 10). In order to avoid particle growth due to coalescence and ripening, the duration and temperature of annealing have to be minimized, hence we used the 600°C annealed nanoparticles for the biological assays described later.

ICP measurements on the nano-LCO obtained from **8** and on commercial micron-sized LCO were carried out and the ratio between Li^+ and Co^{3+} ions was calculated: we found 0.96 ± 0.02 Li^+ ions per Co^{3+} ion for the nano-LCO (Additional file 1: Table S4). Thus the stoichiometry is a little bit lower than the optimal 1:1 stoichiometry ratio. This can be explained at least partly by the washing steps during which part of the Li^+ can be washed away, the mechanical stress induced by ultrasounds and the shear stress of the centrifuge and the annealing in which the Li^+ and Co^{3+} ions can diffuse out of the oxide into the crucible. The ICP measurements of the micro-LCO give a Li^+ content of 1.01 ± 0.02 which is the optimal ratio for the HT-LCO.

Table 3 Cell parameters of the LiCoO_2 formed using different precursors and HT- LiCoO_2 Ref. [61]

Compound	<i>a</i>	<i>c</i>	<i>c/a</i>	Volume (\AA^3)
HT- LiCoO_2 [61]	2.8156(6)	14.0542(6)	4.99	96.49(4)
1 (LiOPh)	2.8193(2)	13.930(3)	4.94	95.88 (3)
8 (LiO^iBu)	2.8179(3)	13.949(3)	4.95	95.93(4)
9 ($\text{LiOPh} + \text{LiO}^i\text{Bu}$)	2.8139(3)	13.970(4)	4.96	95.79(4)
10 (LiO^iPr)	2.8199(1)	13.936(2)	4.94	95.97(2)
11 (LiOEt)	2.8144(2)	13.942(2)	4.95	95.64(2)
12 (LiOMe)	2.8199(2)	13.956(3)	4.95	96.11(3)

Morphologies and determination of the particle and crystallite sizes

The crystallite and particle sizes were assessed via the Scherrer equation (X-ray) and the BET equation (gas adsorption), respectively. The details are described in the Additional file 1: Equation S1 – S5.

Table 4 gives the summary of specific surface area, different sizes of particles and crystallites obtained under identical combustion conditions (temperature, time, speed of heating/cooling and atmosphere composition) depending on the starting complexes.

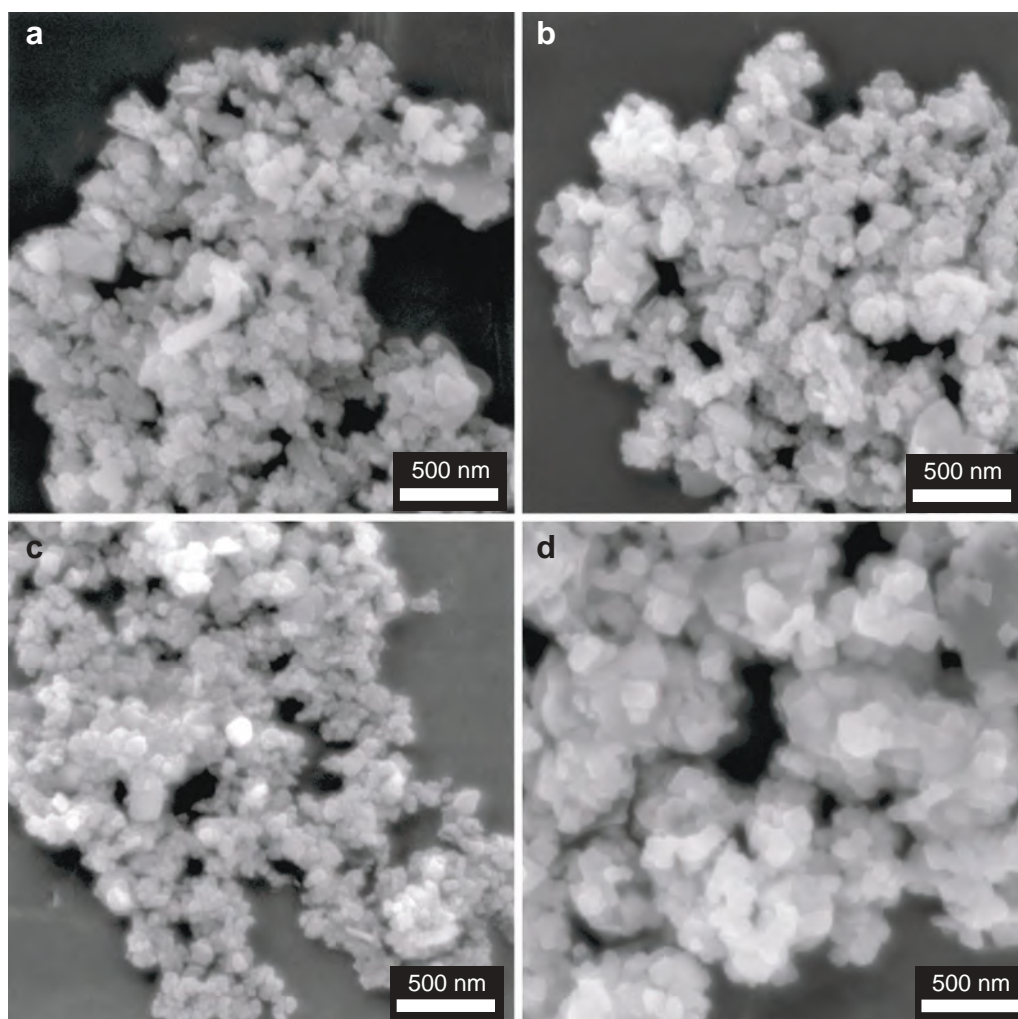


Fig. 9 SEM images of LiCoO_2 prepared with **8**- LiO^tBu (**a**), **10**- LiO^iPr (**b**), **12**- LiOMe (**c**), and **1**- LiOPh (**d**) at 450°C for 1 h

The morphologies of the particles were investigated by SEM images (Fig. 11). The shapes of the particles obtained from the different precursors are similar and submicron. It is also noted that the material always tends to form large aggregates due to its high surface area.

Electrochemistry and Li-ion diffusion

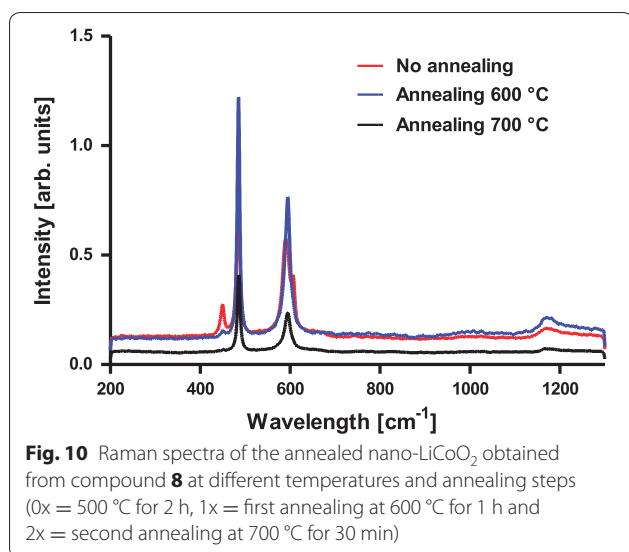
Finally, in order to learn if the size of particles has a direct influence on the Li-ion diffusion, cyclic voltammetry of LiCoO_2 electrodes was performed on two different particles sizes: 40 and 15 nm coming from the precursors **8** and **12**, respectively after a prolonged ball milling of 1 h instead of 15 min.

Figure 12a shows the cyclic voltammograms of LiCoO_2 electrode prepared with LiO^tBu precursor at different scan rates between 0.1 and 1 mV/s.

When Li^+ is extracted from LiCoO_2 , Co^{3+} in LiCoO_2 is oxidized and electron is released ($\text{LiCo}^{3+}\text{O}_2 \rightarrow \text{Li}_{1-x}\text{Co}^{4+/3+}\text{O}_2 + x\text{e}^- + x\text{Li}^+$). On the other hand, oxidized $\text{Li}_{1-x}\text{CoO}_2$ is reduced and electron is uptaken when Li^+ is re-inserted into $\text{Li}_{1-x}\text{CoO}_2$ ($\text{Li}_{1-x}\text{Co}^{4+/3+}\text{O}_2 + x\text{e}^- + x\text{Li}^+ \rightarrow \text{LiCo}^{3+}\text{O}_2$). Therefore, the current increased where the redox reactions of $\text{Co}^{3+}/\text{Co}^{4+}$ occurred above 3.9 V for anodic peaks and between 3.6 and 3.9 V vs. Li^+/Li for cathodic peaks. The CVs and the maximum current peaks of the compound **12** are shown in Additional file 1: Figure S9.

The Li-ion diffusion coefficient can be determined from these cyclic voltammograms by using the Randle–Sevcik equation. The Randles–Sevcik equation [63]:

$$I_p = (2.69 \times 10^5) n^{3/2} A D_{\text{Li}}^{1/2} C v^{1/2} \quad (1)$$



with I_p the peak current; n the number of transfer electrons; A the surface area of the electrode; C the concentration of reactants; and v the scan rate.

The plot of the square root of the scan rate vs. the anodic or cathodic peaks gives the slopes which represent the square root of the Li^+ ion diffusion coefficient value, D_{Li^+} (Fig. 12b).

The Li^+ ion diffusion coefficients (D_{Li^+}) of our nanoparticles were 2.3×10^{-5} and $4.5 \times 10^{-6} \text{ cm}^2 \text{ s}^{-1}$ for **8**-LiO^tBu and **12**-LiOMe, respectively while the one of commercial HT-LCO was $2 \times 10^{-7} \text{ cm}^2 \text{ s}^{-1}$ (Table 5). The values obtained from nanoparticles are 20–100 higher than the standard value for HT-LCO [64]. Thus the kinetics with Li^+ ions are much faster in nanoscale LCO than

in micron-LCO. When we compare the values of diffusion coefficients of 15 and 40 nm of nano-LCO, the larger particle size of 40 nm has even higher diffusion coefficient. It will be explained in the discussion part later.

Electrochemical properties

After D_{Li^+} was determined, the battery properties of our nanoscale LCO materials were investigated. The charge/discharge current is expressed as a C-rate to evaluate battery capacities at various current values. A C-rate is a measure of the rate at which a battery is discharged relative to its maximum capacity. The current density and C-rate are determined by the nominal specific capacity of 150 mAh/g. For example, the current densities are 150 and 7.5 mA/g at 1C (a battery is charged in 1 h) and C/20 (a battery is charged in 20 h), respectively. Figure 13 shows the discharge capacities of LiCoO₂ electrodes prepared by the precursors **1**-LiOPh, **8**-LiO^tBu, **10**-LiO^tPr and **12**-LiOMe. Depending on the precursor used in the synthesis, the specific capacity varies. **10**-LiO^tPr and **1**-LiOPh derived LiCoO₂ electrodes obtained superior capacities to the ones obtained with **8**-LiO^tBu precursors. The mean specific capacity of LiCoO₂ derived from **1**-LiOPh was 210 mAh/g at C/20, which is 77% of the theoretical capacity of 272 mAh/g, while LiCoO₂ from the LiO^tBu precursor had 124 mAh/g (46% of the theoretical value) at the same rate.

After cycling of charge/discharge at different current densities, we disassembled the batteries for all four samples and rinsed the LiCoO₂ electrodes to verify their structures. XRD in Fig. 14 shows that all the cycled LiCoO₂ electrodes have two peaks at (108) and (110) corresponding to the HT-LCO phase, hence the structure is unchanged after cycling.

Table 4 The specific surface area, mean particle size and crystallite size of LiCoO₂ prepared with different precursors

SSA (m²/g)												
Annealed	1-LiOPh		8-LiO ^t Bu		9-(LiOPh + LiO ^t Bu)		10-LiO ^t Pr		12-LiOMe		11-LiOEt	
500 °C	9.46 (0.25)		16.50 (0.2)		9.62 (0.2)		11.50 (0.3)		19.70 (0.12)		not measured	
600 °C	2.59 (0.015)		12.50 (0.14)		0.95 (0.03)		3.65 (0.05)		8.00 (0.07)		0.95 (0.01)	
700 °C	0.50 (0.02)		6.10 (0.17)		0.78 (0.02)		3.04 (0.05)		5.50 (0.05)		0.34 (0.02)	
Particle size (P)* and crystal size(C)** (nm)												
	P(1)	C(1)	P(8)	C(8)	P(9)	C(9)	P(10)	C(10)	P(12)	C(12)	P(11)	C(11)
500 °C	126 (2)	50 (2)	72 (1)	60 (2)	124 (2)	75 (2)	103 (2)	40 (1)	60 (1)	50 (4)	Not measured	Not measured
600 °C	459 (2)	45 (2)	95 (1), 40***	45 (3)	1251 (26)	150 (3)	326 (3)	75 (1)	149 (1), 15***	45 (1)	1251 (9)	110 (3)
700 °C	2376 (60)	90 (2)	195 (4)	55 (2)	1529 (26)	185 (1)	391 (4)	295 (1)	216 (1)	170 (2)	3494 (130)	285 (1)

* The mean particle size was determined by the equation of $d = K/(\rho \times S_{\text{BET}})$, where K is the shape factor, ρ is the density of the material (5.05 g/cc), and S_{BET} is the specific surface area of the material

** Crystal size was determined using Scherrer equation $d = K\lambda/(B \cos\theta)$, where d is the mean crystallite size in volume-weight, λ is the wavelength of the X-rays, B is the width of a peak at a half maximum due to size effects assuming that there is no strain, K is a constant value of 0.89, and θ is the incident angle

*** Particle sizes were obtained after 1 h of ball milling

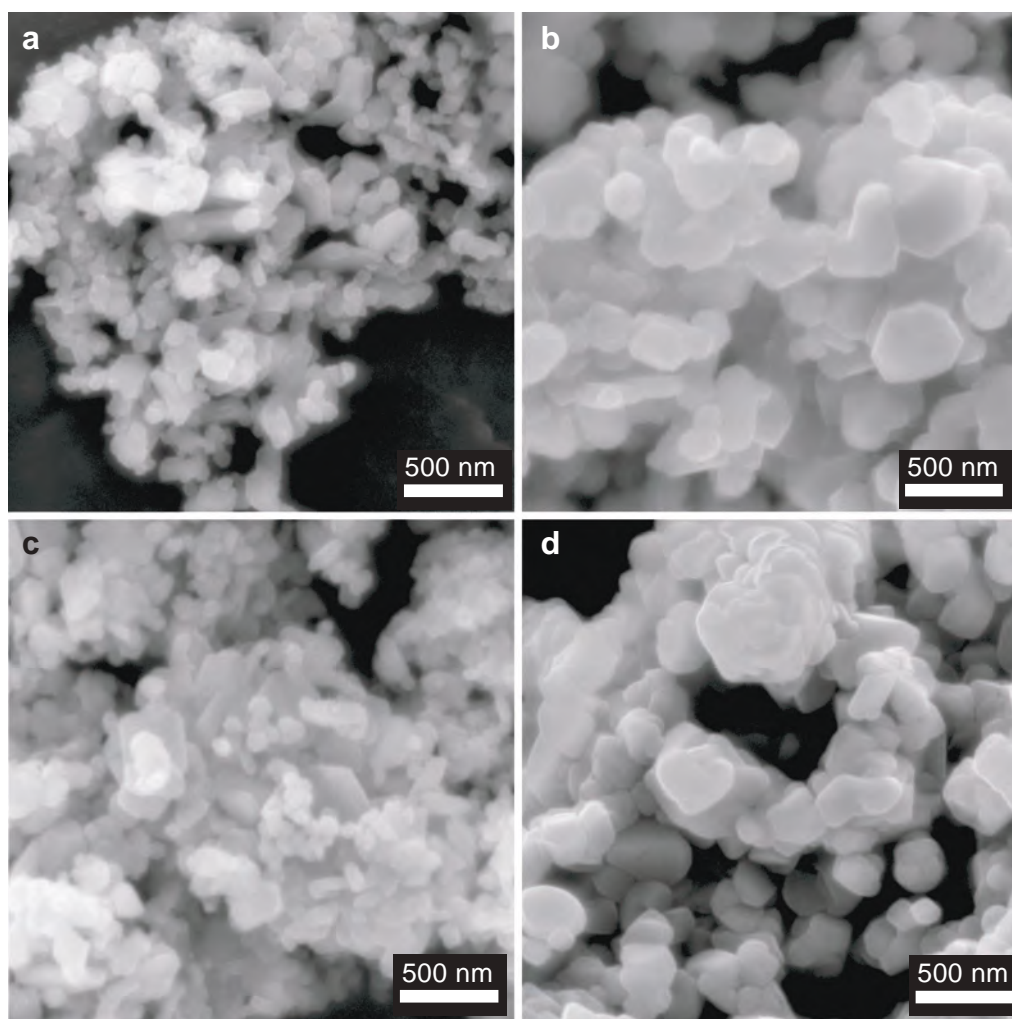


Fig. 11 SEM images of LiCoO₂ materials prepared with LiO^tBu (a), LiOⁱPr (b), LiOMe (c), LiOPh (d) annealed at 600 °C

The equilibrium charge/discharge curves of the LiCoO₂ electrodes obtained from LiOPh, LiO^tBu and LiOMe precursors were investigated as shown in Fig. 15. The markers are measured when the current is not applied to the battery while the dashed lines are recorded when the current is applied. They show the plateau of equilibrium charge curves at 3.9 V and discharge at 3.8 V vs. Li⁺/Li. The coulombic efficiency of the LiCoO₂ electrodes from LiOPh reached >95% with relatively low polarization between charge and discharge process (Fig. 15a). In case of the LiCoO₂ electrode from LiO^tBu (Fig. 15b), the coulombic efficiency reached also >95% but both charge and discharge processes result in half of the capacities compared to these of the electrodes from LiOPh. Moreover, the potentials during charging with the applied current (dashed lines on the graphs) are higher in Fig. 15b compared to these in Fig. 15a, c.

The deep discharge process was evaluated to estimate how fast the battery can reach the maximum discharge capacity of the different LiCoO₂ electrodes. Figure 16 exhibits that the LiCoO₂ electrode from LiOPh precursor, (a), can reach 99% of its maximum capacity (120 mAh/g) within 9 min (at 5.2 C) due to the fast kinetic reaction of Li⁺ ion insertion/extraction. Of course, this maximum capacity remained at any lower current densities, showing the plateau on the right side in Fig. 16a. On the other hand, the electrode from LiOⁱPr precursor, (b), can be discharged to 90% of its maximum capacity (122 mAh/g) at much lower current density of 0.44 C (about 26 min) than (a). (b) can reach 85% (104 mAh/g) of its maximum discharge capacity within 6 min (at 7 C). Thus, this deep discharge measurement supports that the discharge capacities at higher current densities (>C/2) are lower in LiCoO₂ electrode with LiOPh than those in LCO with

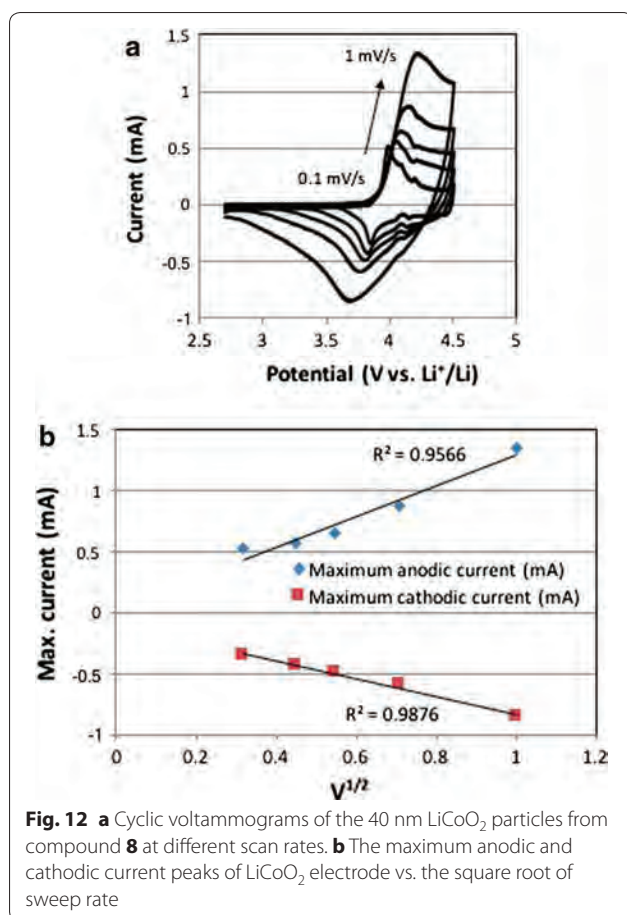


Fig. 12 **a** Cyclic voltammograms of the 40 nm LiCoO_2 particles from compound **8** at different scan rates. **b** The maximum anodic and cathodic current peaks of LiCoO_2 electrode vs. the square root of sweep rate

Table 5 Size and Li-ion diffusion coefficient comparison between two precursors, **8** and **12**, and HT-LCO Ref. [64]

Compounds/precursors	Size	D_{Li} ($\text{cm}^2 \text{s}^{-1}$)
HT-LCO [64]	11 μm	2×10^{-7}
8 — LiO^tBu	40 nm	2.3×10^{-5}
12 — LiOMe	15 nm	4.5×10^{-6}

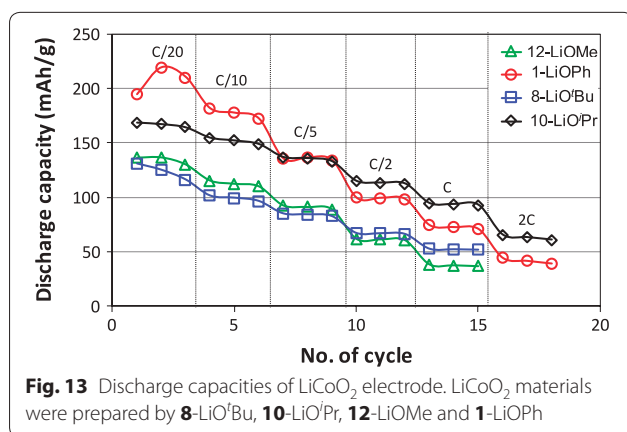


Fig. 13 Discharge capacities of LiCoO_2 electrode. LiCoO_2 materials were prepared by **8**- LiO^tBu , **10**- LiO^iPr , **12**- LiOMe and **1**- LiOPh

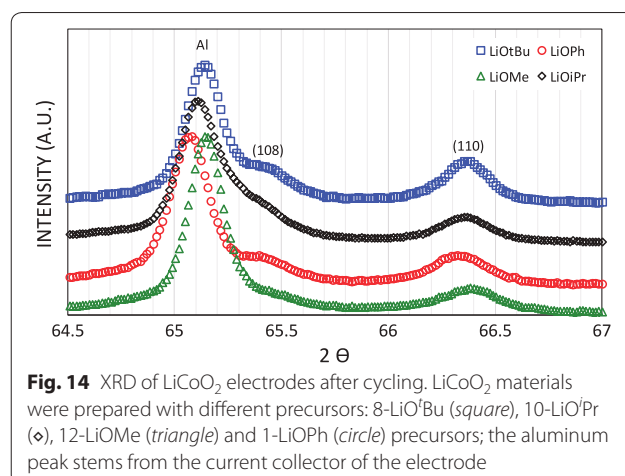


Fig. 14 XRD of LiCoO_2 electrodes after cycling. LiCoO_2 materials were prepared with different precursors: **8**- LiO^tBu (square), **10**- LiO^iPr (\diamond), **12**- LiOMe (triangle) and **1**- LiOPh (circle) precursors; the aluminum peak stems from the current collector of the electrode

LiO^iPr (Fig. 16). Therefore, the kinetics of the electrode (a) obtained from LiO^iPr is an order of magnitude faster than (b) (obtained from LiOPh) at high current densities.

The Nyquist plots presented for electrodes with different precursors were obtained in the frequency range of 100 kHz–0.01 Hz at 25 °C (Fig. 17). The EIS spectra of the electrodes with LiOPh and LiOMe precursors are similar in shape with one semicircle and Warburg branch, while the electrode obtained from LiO^tBu precursor shows hodographs with two semicircles without Warburg impedance. After fitting the EIS data, the equivalent circuit models were proposed (Additional file 1: Figure S11).

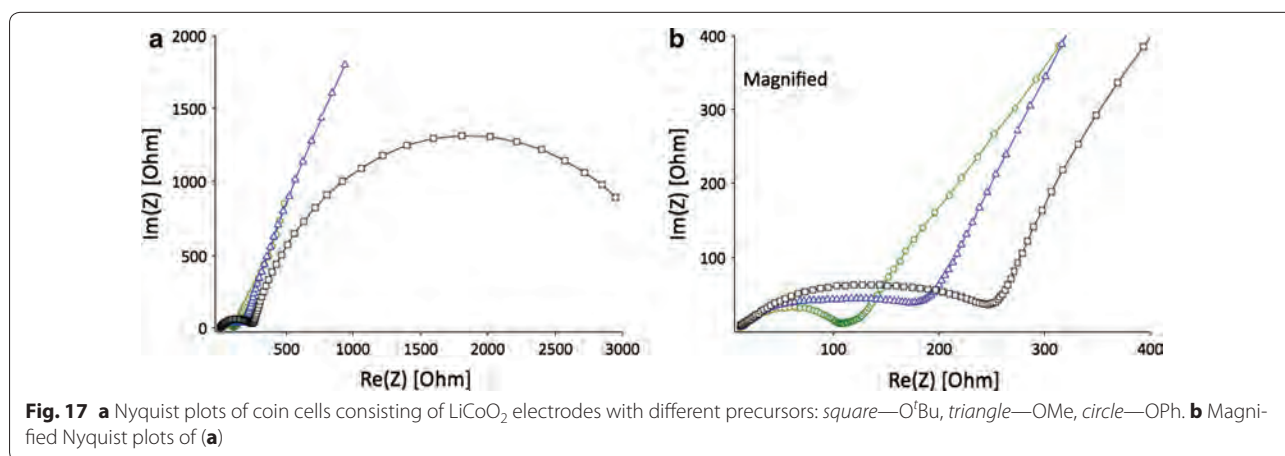
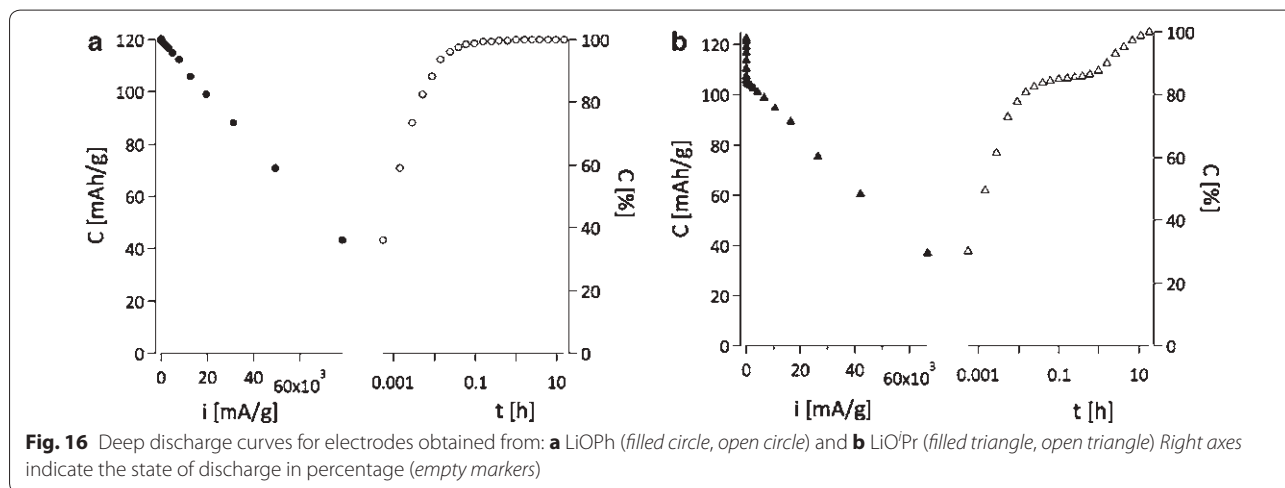
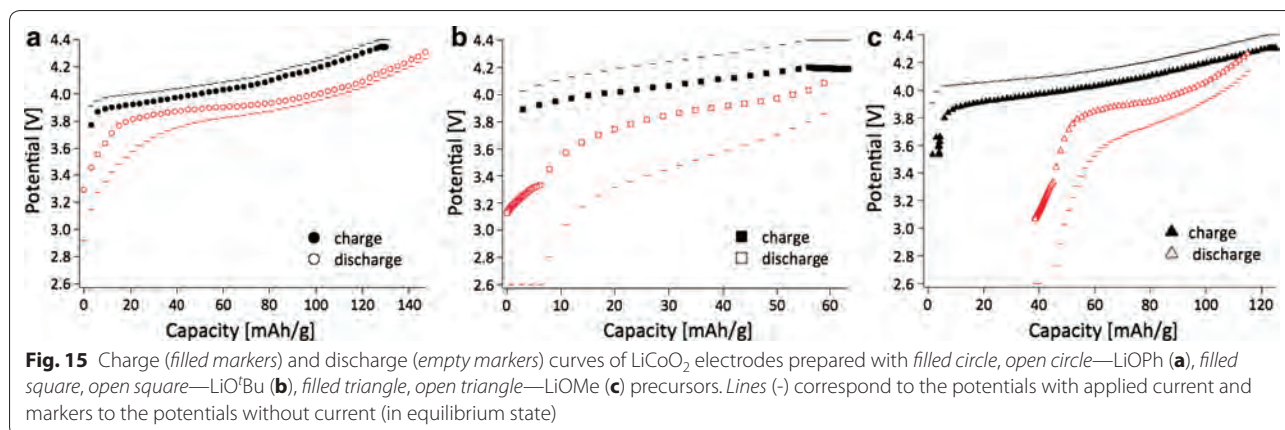
The ion transfer resistance and total impedance of electrodes with different precursors increase in the following sequence: $\text{LiOPh} < \text{LiOMe} < \text{LiO}^t\text{Bu}$, which is in good agreement with the discharge capacities and equilibrium charge/discharge curves.

Hazard assessment of particles

Particle aerosolisation

Nanoparticles obtained from precursor **8**, which was annealed at 600 °C for 1 h, were compared to a commercially obtained, micron-sized LiCoO_2 sample. A dry powder insufflator was used to aerosolise both materials for direct deposition onto the surface of the multicellular epithelial tissue barrier model. Initially, following aerosolisation, the deposition of the two particle types was characterised in terms of their mass deposition, particle size, as well as their distribution and morphology.

The cell-delivered dose was monitored using an integrated quartz crystal microbalance (QCM) and showed a dose-dependent deposition of the both samples, i.e. 0.81 ± 0.2 , 0.55 ± 0.14 and $0.16 \pm 0.05 \mu\text{g}$ for nanoparticles, and 3.92 ± 0.78 , 1.46 ± 0.63 and $0.51 \pm 0.18 \mu\text{g}$ for microparticles. It was, however, not possible to achieve the same range of deposited concentrations for both



nano- and micron-sized particles despite using the same initial feed concentration, as shown in Fig. 18a. Reason for this, apart from the different pulverisation methods, is that the microparticles can be considered to exhibit a higher density, and therefore greater tendency to agglomerate/aggregate leading to a higher surface density compared to the limited agglomeration/aggregation shown by the nanoparticles.

By using TEM it was observed that the pulverized nanoparticles of LCO formed agglomerates/aggregates

ranging from nano-sized to micron-sized (ca. 0.05–50 μm). This could possibly be attributed to the low surface charge of the material (i.e. $\leq \pm 10$ mV). The average size of primary nanoparticles was estimated to be 64 ± 5 nm, as determined by the BET method, while the crystallite size was determined to be 60 ± 5 nm using the Scherrer equation. The micron-sized particles were noted to exhibit a size of 10–12 μm , as previously reported [16–21]. In terms of their morphology, nanoparticles were observed to show rhombohedral/tetrahedral shaped

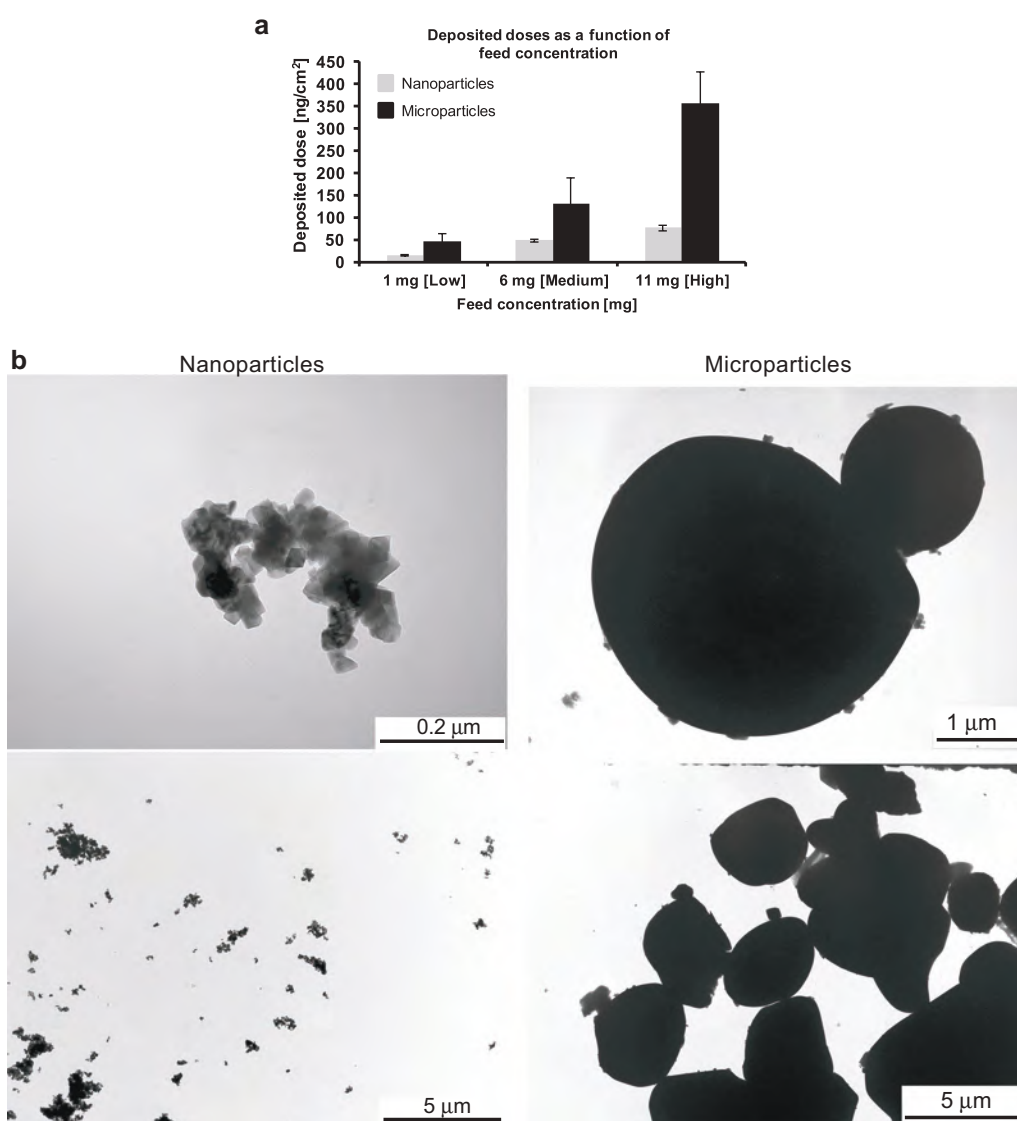


Fig. 18 Deposition characterization of aerosolized nano-sized and micron-sized particles. **a** Average mass deposition (ng/cm^2) of particles quantified using a quartz crystal microbalance (QCM) following nebulisation of low (1 mg), medium (6 mg) and high (11 mg) particle doses using a dry powder insufflator. Data are presented as the mean \pm standard error of the mean. **b** Transmission electron micrographs of aerosolized nano- (left) and microparticles (right), indicating, in a qualitative manner, the heterogeneity of the particle deposition for each particle-size. Images also show a representative overview of the particle morphology following the aerosolisation process

patterns, whereas the commercial microparticles were found to be irregular in shape, with most showing round-ish shapes (Fig. 18b).

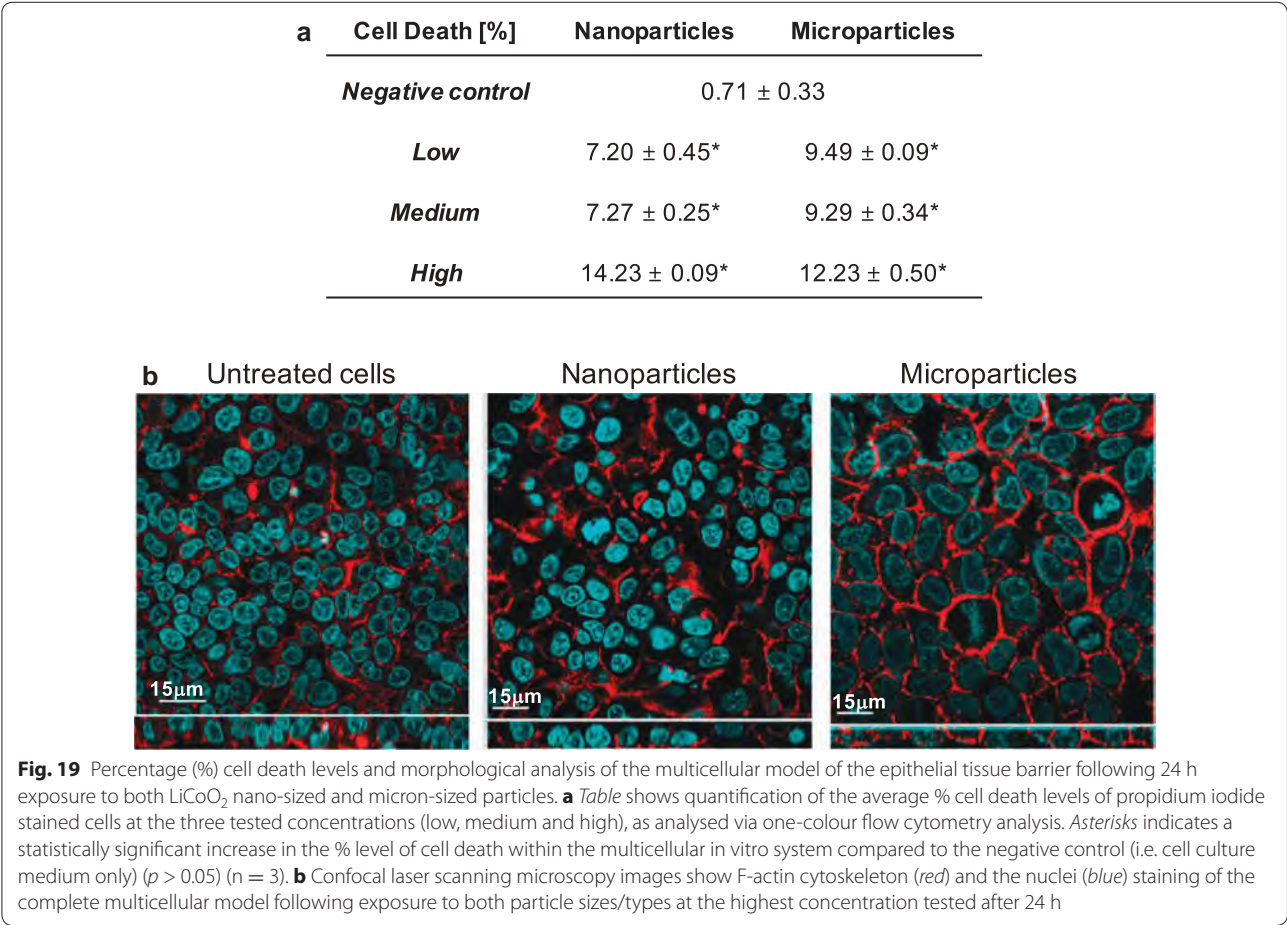
Cell death

After 24 h exposure, LiCoO₂ nanoparticles showed limited ability to cause cell death following their aerosolisation onto the in vitro multicellular epithelial tissue barrier model at each particle concentration tested (Fig. 19a). Both low and medium nanoparticle concentrations showed similar effects, whilst the highest concentration applied increased the level of cell death by 50% compared to the lower concentrations studied. This result can be attributed to an ‘overload’ scenario upon the cells at the highest concentration applied (Fig. 19b) [65]. It is important to note that although these values are significantly different from the negative control (*p* > 0.05) (i.e. cell culture media only), with the highest concentration applied showing a maximum of <15% cell death in the in vitro co-culture system, the findings indicate that the nanoparticles are not causing complete destruction of the cellular system but do induce a limited cytotoxic

effect at these concentrations. Similar results were also evident following micron-sized LiCoO₂ particle exposures at each test concentration (Fig. 19a). In respect to these semi-quantitative results, it is also important to highlight that qualitative assessment, via confocal laser scanning microscopy, showed no morphological changes to the multicellular system following exposure to either particle type at the highest concentration applied for 24 h (Fig. 19b).

(Pro-)inflammatory response

No significant (pro-)inflammatory response (i.e. either TNF-α and IL-8 release) was observed following nanoparticle exposures across all concentrations tested (Fig. 20). Similar results were observed with the micron-sized particles in terms of the TNF-α response from the multicellular system after 24 h exposure. However, microparticle exposures did show a significant increase (*p* > 0.05) in terms of the IL-8 response from the co-culture, in a concentration-dependent manner at this time point (Fig. 20).



Discussion

The general reaction of CoCl_2 and LiOPh for the generation of the precursors **1–7** is based on the LiCl -elimination and the formation of a mixed phenoxide with always the same metal ion ratio of 2:1 for $\text{Li}:\text{Co}$, as found in the core $[\text{Li}_2\text{Co}(\text{OPh})_4]$ of the structures **1–7**. The formation of this type of compound is in our hands independent of the amount of LiOPh added (between 1 and 6 equivalents). The core is always made of a central Co^{2+} ion which is surrounded in a (more or less distorted) tetrahedral way by four phenoxide ligands. Two by two, these O-donors act each as μ -bridging ligands to one Li^+ ion. The coordination sphere of the latter is then completed by either mono- or bidentate donor molecules stemming from the solvent. These coordinated solvent molecules influence the arrangement of the complexes with respect to each other. For instance, 0-dimensional compounds are obtained with monodentate terminal ligands like THF and pyridine or bidentate terminal ligands like DME and TMEDA, whereas bridging ligands such as dioxane lead to polymeric arrangements. In the $[\text{Li}_2\text{Co}(\text{OPh})_4]$ cores (Fig. 21) of all compounds **1–5**, for which the single crystal structures could be determined to satisfaction, the Co–O distances are between 1.938(4) and 1.978(4) Å long, while the angles O1–Co–O2 and O3–Co–O4 are very similar with $86^\circ(\pm 1^\circ)$. The O2–Co–O3 and O1–Co–O4 angles are however more sensitive to the environment of the Li^+ cations (see Table 6), respectively packing effects, and vary between 112 and 127° .

The difference of composition between **1** and **2** originates from the crystallization technique. Indeed, **1** is prepared at room temperature with the addition of heptane

for crystallization, while **2** is crystallized without any co-solvent at -24°C . These two different methods give two different products: one thermodynamic compound **1** and one kinetic compound **2**, which can be considered as solvates to each other [66].

In the structure of the compounds **1** to **7**, an inherent stoichiometric ratio of two Li^+ for one Co^{2+} exists, hence excess of one equivalent Li^+ with respect to the desired LiCoO_2 . During the firing, this excess of Li^+ in the precursor tends to form lithium carbonate either by reaction with the CO_2 in air or with the byproducts of the combustion. The carbonate can clearly be seen in powder X-ray diffractogram of the raw oxide. However, these impurities, as well as the main byproduct LiCl (formation of the precursors), can be easily washed away with water. Successful removal of LiCl was confirmed by powder X-ray diffraction as well as TEM/SEM.

For the compounds **8–12**, except **11**, the stoichiometric ratio is 1:1 for Li^+ to Co^{2+} , thus there is no excess Li^+ and hence almost no formation of lithium carbonate

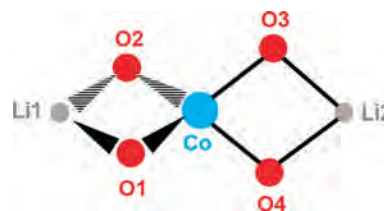


Fig. 21 Schematic representation with numbering of the $\text{Li}_2\text{Co}(\text{OPh})_4$ -core of compounds **1–7**

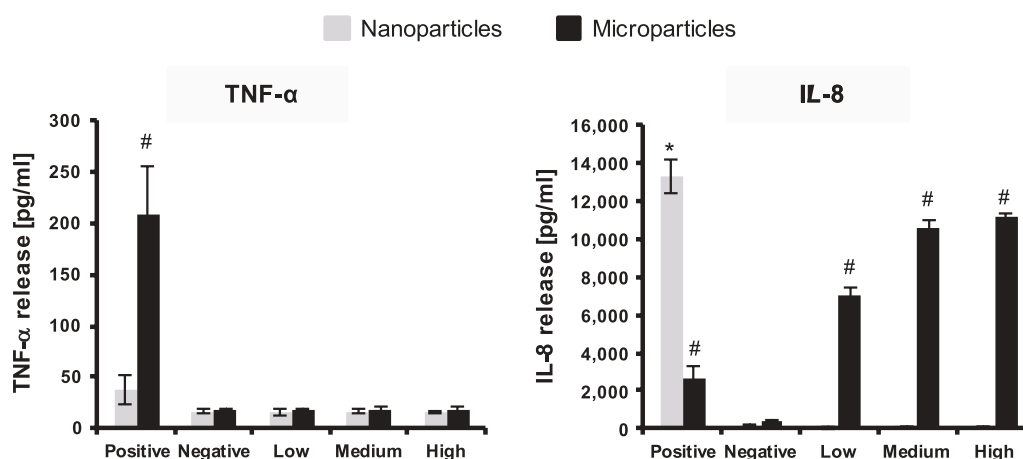


Fig. 20 (Pro-)inflammatory response of the multicellular epithelial tissue barrier following 24 h exposure to nano-sized and micron-sized nanoparticles at the three different test concentrations. Graphs show the results for the specific (pro-)inflammatory mediators chosen; tumor necrosis factor- α (TNF- α) and interleukin-8 (IL-8). Lipopolysaccharide ([100 μl of 1 $\mu\text{g}/\text{ml}$]) served as the positive assay control, whilst the negative control was cell culture medium only. Data is presented as the mean \pm standard error of the mean. * indicates a statistically significant response ($p > 0.05$) compared to the negative control

(Additional file 1). While we produced our nanoscale materials in quite pure form by this washing step, the analysis of the commercial HT-LiCoO₂ shows that it contains some Li₂CO₃ impurities, which is one of the reactants of its synthesis.

The main physical/chemical differences in the final oxides obtained at 450 °C from **1** and **8–12** are the amount of impurities due to stoichiometric reasons and the size of the particles/crystallites obtained. Indeed, the LiOph precursor **1** tends to form more impurities (carbonates, XRD in Additional file 1: Fig. S7) and a larger crystallite size. The amount of impurity is mainly due to the incorrect stoichiometric ratio in the starting structure of 2:1 for Li:Co, but also to a large amount of carbon atoms in the precursor. However, by decreasing the number of carbon atoms using alkoxide and by balancing the ratio between Co and Li to 1:1, better results in terms of size and smaller amounts of byproducts can be achieved. As shown in the Table 4, sizes as low as 60 nm of HT-LCO can be obtained.

We observed different LCO morphologies from the single source precursors. This could be related to the formation of LCO nuclei, which likely depend on the initial structure of the complex precursor. Not only the core structure, but also the arrangement of the molecules with respect to each other may play a role in the formation of different nuclei.

The redox potentials indeed confirm that the obtained nano-LiCoO₂ is in the HT-LCO phase. We also recognized that the oxidation of Co³⁺ to Co⁴⁺ (corresponding

to Li⁺ extraction from Li_{1-x}CoO₂) shows higher current than the reduction of Co⁴⁺ to Co³⁺ (Li⁺ insertion into Li_{1-x}CoO₂). The cyclic voltammograms (CV) of both samples obtained from **12** and **8** show a HT-LCO CV profile with a low polarization and high potential, as expected from the X-ray diffraction pattern.

In terms of the Li⁺ diffusivity, hence the kinetic with respect to Li⁺ ions, we found it to be much faster in nanoscale LCO than in micron-LCO. In other words, the amount of Li⁺ ions available for electrochemistry is larger in nanoscale LCO than that in micron-LCO due to the shorter path length of the Li⁺ ion diffusion. The values obtained are >20 times higher than the standard value for HT-LCO [64]. In the best case measured in our hands, 77%, of all Li⁺ ions were extracted from and re-inserted in the structure of nano-HT-LCO, while for the commercial material, only about 50% of Li⁺ ions (0 < x < 0.5, Li_{1-x}CoO₂) can be used electrochemically in the rhombohedral layered structure of LiCoO₂. Further de-lithiation of commercial, micro-HT-LCO induces a phase transformation to the monoclinic system [17], resulting in irreversible capacity loss upon cycling. Therefore, the phase stability of LiCoO₂ is important during lithiation and de-lithiation in order to obtain high coulombic efficiency and longer cycleability of battery. This is what we could show for the nano-HT-LCO after battery cycling by analyzing the material by XRD. Hence, our LCO materials prepared by heterobimetallic single source precursors are stable upon cycling and provide fast electrochemical reactions with Li⁺ ions due to nanosized particles.

Table 6 Comparison of compounds 1 to 5 and 9

	1	2	3	4		5	9
Tetrahedral volume of Co (Å ³)	3.332	3.384	3.344	3.364		3.339	3.229
Quadratic elongation	1.093	1.088	1.092	1.079		1.100	1.120
Angle variance (° ²)	378.27	360.86	374.83	322.26		401.40	486.42
O1–Co (Å)	1.961 (6)	1.960 (7)	1.95 (1)	1.954 (3)	1.958 (4)	1.954 (4)	1.947 (3) 1.949 (3)
O2–Co (Å)	1.948 (5)	1.957 (6)	1.93 (1)	1.963 (4)	1.955 (3)	1.962 (4)	1.960 (3)
O3–Co (Å)	1.963 (5)	1.946 (6)	1.961 (8)	1.954 (3)	1.966 (3)	1.978 (4)	1.958 (4)
O4–Co (Å)	1.972 (6)	1.960 (6)	1.966 (7)	1.952 (4)	1.961 (4)	1.938 (4)	/
Mean O–Co (Å)	1.961	1.956	1.952	1.956	1.960	1.958	1.953
O1–Co–O2 (°)	84.9 (2)	86.5 (3)	85.7 (1)	86.8 (2)	86.6 (2)	85.6 (2)	80.2 (1)
O3–Co–O4 (°)	86.0 (2)	85.2 (3)	85.1 (4)	87.5 (1)	87.0 (2)	84.8 (2)	83.9 (2)
O1–Co–O4 (°)	122.4 (2)	121.0 (3)	125.6 (4)	118.6 (1)	122.7 (2)	126.5 (2)	124.4 (2)
O2–Co–O3 (°)	118.4 (2)	120.0 (3)	123.0 (4)	117.6 (2)	125.0 (1)	112.4 (2)	125.2 (1)
Mean O–Co–O (°)	85.45 120.4	85.85 120.5	85.4 124.3	86.98 120.98		85.2 119.45	82.0 124.8
BVS on Co	1.93	1.96	1.98	1.96	1.94	1.95	1.97
BVS on Li	1.17 1.14	1.13 1.14	1.13 1.07	1.19 1.17	1.13 1.14	1.19 1.25	1.18

The LCO materials prepared from various complexes showed different specific capacities. This difference may be related to several parameters such as the homogeneity of particle size, ball milling and the shape of LCO particles. Also, when a particle size distribution is broad, the specific capacity can be less good than the one from the narrower size distributed particles. The large size difference can lead to different Li^+ diffusion kinetics. However, the larger particles can be broken during ball milling and the size distribution becomes narrower, improving the kinetics of Li^+ diffusion and finally the specific capacity. The shape of LCO particle can also affect the diffusion of Li^+ because Li^+ diffuses in a specifically oriented layer of the structure.

The smaller particle size provides higher diffusion kinetics with Li^+ because the higher surface area of nano- LiCoO_2 provides more Li^+ ions to be released and uptaken into/from the electrolyte. In addition to the high surface area, there is another parameter governing the diffusion kinetics, which is the orientation of Li^+ diffusion path in the lattice structure of LiCoO_2 . Li^+ is located in one layer of the LiCoO_2 lattice cell, diffusing in one preferred orientation. Thus, the length of Li^+ diffusion path in LiCoO_2 also affects the diffusion kinetics. We reported that the diffusion of Li^+ is not only related to the size of particle but also the shape of particle due to the preferred diffusion direction and its length in the lattice structure [67, 68]. In this regard, the higher diffusion coefficient of 40 nm (compound 8) is probably coming from the shorter diffusion path of Li^+ in a single particle although the compound 12 has a smaller size of 15 nm.

We also found that LiCoO_2 produced from LiO^tBu has a larger overpotential and higher resistance than the one obtained from LiOPh . On the other hand, the LiCoO_2 electrode formed from LiOMe reached >120 mAh/g of charge capacity. However, the discharge capacity was 90 mAh/g with 70% of coulombic efficiency. These differences of equilibrium charge/discharge curves can be explained by different kinetics at equilibrium state.

The deep discharge measurement supports that the discharge capacities at higher current densities (>C/2) are lower in LiCoO_2 electrode with LiOPh than those in LCO with LiO^iPr (Fig. 16). Therefore, the kinetics of the electrode (a) obtained from LiO^iPr is an order of magnitude faster than (b) (obtained from LiOPh) at high current densities.

The electrochemical properties of batteries are influenced by not only the active material but also the composite, consisting of carbon and the active material [69]. The structural morphology and the physicochemical properties of composite affect the electron transfer and

lithium ion diffusion in the electrode [64]. An ongoing follow-up study is hence the optimization of the electrode composites for each nanoscale HT-LCO material as a function of precursor.

In terms of the biological assessment, such studies had never been done on nanoscale LCO and are quite rare for battery materials in general. We found both nano- and micro-LCO to be relatively low toxic in the lung model which we used. The (pro-)inflammatory response upon exposure to nano-LCO was nil across all tested concentrations, while it was dose-dependent for micro-LCO. Neither nanoparticles nor micro-LCO induce a cytotoxic effect at the tested concentrations which leads to more than 15% cell death. In terms of the surface charges of nano and microparticles, we estimate it is low since both particles rather stick together [70].

Conclusions

A series of 12 new precursors containing lithium and cobalt ions in ratios of 2:1 or 1:1 with different aryl- and alkoxide ligands have been prepared and characterized. Their thermal decomposition leads to the formation of nanoscale HT- LiCoO_2 with the size of the so obtained nanoparticles depending on the precursor. Also, precursors with a 1:1 ratio of Li^+ to Co^{2+} lead to quite pure product, while the precursors with a 2:1 ratio gave Li_2CO_3 as byproduct. The use of our precursors allowed lowering the production temperature and time for the generation of HT- LiCoO_2 as a preorganisation of the metal ions takes place in the starting material. The nanomaterials of LiCoO_2 showed a superior Li-ion diffusivity by a factor of 20–100 compared to commercial LiCoO_2 , depending on the precursor used to generate the cathode material. The electrochemical performance was varied depending on the precursors. LiCoO_2 with LiOPh and LiO^iPr provided higher specific capacities while LiCoO_2 with LiOMe and LiOtBu obtained lower specific capacities. Lithium ion diffusion coefficients of our nanoscale LiCoO_2 were >10 times higher than the one of microscale LiCoO_2 due to the shorter path length of lithium ion diffusion in nanomaterial of LiCoO_2 . This means that high surface area of nanoscale LiCoO_2 can release and take Li^+ ions much more than micron LiCoO_2 material at the same condition.

To mimic conditions of recycling of batteries, nanopowders of LiCoO_2 were tested on a lung cell model. During the spraying of the powders, it was shown that the nanopowders tend to aggregate during the process due to a low zeta-potential. Nevertheless, they are slightly more toxic than the micron-scale material, while toxicity remained overall very low.

Additional file

Additional file1: Text 1. Synthesis of bimetallic compounds. **Table S1.** Crystal data. **Text 2.** Single crystal structure descriptions. **Text 3.** Argentometric titration. **Table S2.** Idealistic oxidation reactions of two types of compounds, precursors **1, 5** with 2:1 and precursors **8, 9** with 1:1 stoichiometric ratio between Li⁺ and Co²⁺. **Table S3.** Results of the argentometric titration of chloride and ICP-measurements for lithium. **Table S4.** ICP analysis for Li⁺ and Co³⁺ of LiCoO₂ obtained from different precursors. **Figure S6.** XRD study of commercial LCO, and nano-LCO obtained from LiOtBu before annealing and after annealing at 600°C and 700°C. **Figure S7.** XRD of LiCoO₂ from 9-LiOPh calcined at 450°C before washing. The red line corresponds to HT-LCO and the blue lines are Li₂CO₃. **Table S5.** The combustion temperature and the thermal measurement conditions of the compounds **1, 8–12.** **Table S6.** TGA weight loss in percentage [%] with associated steps of compounds **1, 8–12.** **Equation S1–S5.** Determination of the particle and crystallite sizes. **Figure S8.** Morphologies of LiCoO₂ prepared with different precursors at 450°C. **Figure S9.** (a) Cyclic voltammograms of the 15 nm LCO prepared from the compound 12 at different sweep rates. (b) The maximum anodic and cathodic current peaks of LiCoO₂ electrode versus the square root of sweep rate. **Table S7.** Li⁺ diffusion coefficients determined for HT-LCO obtained from different precursors. **Figure S10.** Nyquist plot for LiCoO₂ electrodes from LiOtBu with fit: filled markers – experimental points, open markers – fit points with error bars a) and corresponding equivalent circuit model b) with fitting report c). **Figure S11.** Nyquist plot obtained for LiCoO₂ electrodes from LiOPh with fit: filled markers – experimental points, open markers – fit points with error bars a) and corresponding equivalent circuit model b) with fitting report c).

Abbreviations

HT-LCO: high temperature LiCoO₂; LT-LCO: low temperature LiCoO₂; THF: tetrahydrofuran; ALI: air-liquid interface; LiOPh: lithium phenoxide; LiO^tBu: lithium *tert*-butoxide; LiOMe: lithium methoxide; LiOEt: lithium ethoxide; LiOⁱPr: lithium *iso*-propoxide; TMEDA: tetramethylethylenediamine; DME: dimethoxyethane; Py: pyridine; IR: infra-red; NMR: nuclear magnetic resonance; XRD: X-ray diffraction; *M*: molecular mass; *a*, *b*, *c*: unit cell dimensions; β : monoclinic angle; *V*: unit cell volume; *Z*: number of independent asymmetric units per unit cell; ρ_{calc} : density; *T*: temperature at which single crystals were measured; Θ : theta angle for single crystal x-ray measurements; *GOOF*: goodness of fit; *R*₁, *wR*₂: quality factors; TGA: thermogravimetric analysis; STDA: simultaneous differential thermal analysis; BET: Brunauer, Emmett and Teller; SEM: scanning electron microscope; FEI: field electron and ion; EDS: energy dispersive X-ray spectroscopy; ICP-OES: inductively coupled plasma optical emission spectrometry; PVDF: polyvinylidene fluoride; NMP: N-methyl-2-pyrrolidone; ABG and SFG: name of graphite provided from the manufacturer; EC: ethylene carbonate; DMC: dimethyl carbonate; DEC: diethylene carbonate; C/20, C/10, C/5, C/2, 1C and 20C: charging for 20 h, 10 h, 5 h, 2 h, 1 h and 3 mins; EIS: electrochemical impedance spectroscopy; FRA: frequency response analyser; RPMI: Roswell Park Memorial Institute; PET: polyethylene terephthalate; CH: cluster of differentiation; DP: dry powder insufflator; ELISA: enzyme-linked immunosorbent assay; BVS: bond-valence-sum.

Authors' contributions

JPB, AC and SM synthesized and characterized the complexes and LCO. BB and MS performed the electrochemistry. AZ proposed the deep discharge analysis. JPB and HB performed the biological assessment with the guidance of MJDC and BRR. NHK guided the characterization, electrochemistry and the manuscript. KMF supervised the project and the manuscript. All authors read and approved the final manuscript.

Author details

¹ Department of Chemistry, University of Fribourg, Chemin du Musée 9, 1700 Fribourg, Switzerland. ² Fribourg Center for Nanomaterials FriMat, University of Fribourg, Chemin du Musée 9, 1700 Fribourg, Switzerland. ³ Adolphe Merkle Institute, University of Fribourg, 1700 Fribourg, Switzerland. ⁴ College of Engineering and Architecture of Fribourg, University of Applied Sciences

of Western Switzerland, Boulevard de Pérolles 80, 1705 Fribourg, Switzerland.

⁵ Laboratory of Materials for Renewable Energy (LMER), ISIC-SB, École Polytechnique Fédérale de Lausanne (EPFL), Valais/Wallis Energypolis, Rue de l'Industrie 17, 1951 Sion, Switzerland.

Acknowledgements

This study was supported by the Swiss National Science Foundation (National Research Program 64), the Swiss Competence Center for Energy Research (SCCER) Heat and Electricity Storage, the FriMat (the Fribourg Center for Nanomaterials), the NCCR "Bioinspired Materials" and the University of Fribourg.

Competing interests

The authors declare that there are no competing interests nor commercial interests.

Ethics and others

Not applicable.

Funding

This work was supported by the National Research Program 64, Project Number 406440_141604 from the Swiss National Science Foundation.

Publisher's Note

Springer Nature remains neutral with regard to jurisdictional claims in published maps and institutional affiliations.

Received: 18 January 2017 Accepted: 31 July 2017

Published online: 22 August 2017

References

- Mizushima K, Jones PC, Wiseman PJ, Goodenough JB. Li_xCoO₂ (0 < x < 1): a new cathode material for batteries of high energy density. *Mater Res Bull.* 1980;15:783–9.
- Reimers JN, Dahn JR. Electrochemical and in situ X-ray diffraction studies of lithium intercalation in Li_xCoO₂. *J Electrochem Soc.* 1992;139:2091–7.
- Ohzuku T, Ueda A. Solid-state redox reactions of LiCoO₂ (R3m) for 4 volt secondary lithium cells. *J Electrochem Soc.* 1994;141:2972–7.
- Ménétrier M, Saadoun I, Levasseur S, Delmas C. The insulator-metal transition upon lithium deintercalation from LiCoO₂: electronic properties and 7Li NMR study. *J Mater Chem.* 1999;9:1135–40.
- Molenda J, Stoklosa A, Bak T. Modification in the electronic structure of cobalt bronze Li_xCoO₂ and the resulting electrochemical properties. *Solid State Ionics.* 1989;36:53–8.
- Van der Ven A, Aydinol MK, Ceder G. First principles evidence for stage ordering in Li_xCoO₂. *J Electrochem Soc.* 1998;145:2149–55.
- Van der Ven A, Aydinol MK, Ceder G, Kresse G, Hafner J. First-principles investigation of phase stability in Li_xCoO₂. *Phys Rev B.* 1998;58:2975–87.
- Amatucci GG, Tarascon JM, Klein LC. CoO₂, the end member of the Li_xCoO₂ solid solution. *J Electrochem Soc.* 1996;143:1114–23.
- Li W, Reimers JN, Dahn JR. Lattice-gas-model approach to understanding the structures of lithium transition-metal oxides LiMO₂. *Phys Rev B.* 1994;49:826.
- Huang W, Frech R. Vibrational spectroscopic and electrochemical studies of the low and high temperature phases of LiCo_{1-x}MxO₂ (M = Ni or Ti). *Solid State Ion.* 1996;86–88:395–400.
- Antolini E. LiCoO₂: formation, structure, lithium and oxygen nonstoichiometry, electrochemical behaviour and transport properties. *Solid State Ion.* 2004;170(3–4):159–71. doi:10.1016/j.ssi.2004.04.003.
- Gummow RJ, Thackeray MM, Wif D, Hull S. Structure and electrochemistry of lithium cobalt oxide synthesised at 400°C. *Mater Res Bull.* 1992;27:327–37.
- Garcia B, Farcy J, Pereira-Ramos JP, Baffier N. Electrochemical properties of low temperature crystallized LiCoO₂. *J Electrochem Soc.* 1997;144:1179–84.
- Rossen E, Reimers JN, Dahn JR. Synthesis and electrochemistry of spinel LT-LiCoO₂. *Solid State Ion.* 1993;62:53–60.

15. Orman HJ, Wiseman PJ. Cobalt(III) lithium oxide, CoLiO_2 : structure refinement by powder neutron diffraction. *Acta Crystallogr C*. 1984;40:12–4.
16. Garcia B, Farcy J, Pereira-Ramos JP, Perichon J, Baffler N. Low-temperature cobalt oxide as rechargeable cathodic material for lithium batteries. *J Power Sources*. 1995;54:373–7.
17. Shao-Horn Y, Croguennec L, Delmas C, Nelson EC, O'Keefe MA. Atomic resolution of lithium ions in LiCoO_2 . *Nat Mater*. 2003;2(7):464–7.
18. Kim J, Fulmer P, Manthiram A, Kim J, Fulmer P, Manthiram A. Synthesis of LiCoO_2 cathodes by an oxidation reaction in solution and their electrochemical properties. *Mater Res Bull*. 1999;34(4):571–9.
19. Myung ST, Kumagai N, Komaba S, Chung HT. Preparation and electrochemical characterization of LiCoO_2 by the emulsion drying method. *J Appl Electrochem*. 2000;30(9):1081–5.
20. Yoshio M, Tanaka H, Tominaga K, Noguchi H. Synthesis of LiCoO_2 from cobalt—organic acid complexes and its electrode behaviour in a lithium secondary battery. *J Power Sources*. 1992;40:347–53.
21. Antolini E. Lithium loss from lithium cobalt oxide: hexagonal $\text{Li}_{0.5}\text{Co}_{0.5}\text{O}$ to cubic $\text{Li}_{0.065}\text{Co}_{0.935}\text{O}$ phase transition. *Int J Inorg Mater*. 2001;3:721–6.
22. Oh IH, Hong SA, Sun YK. Low-temperature preparation of ultrafine LiCoO_2 powders by the sol–gel method. *J Mater Sci*. 1997;32(12):3177–82.
23. Yoon WS, Kim KB. Synthesis of LiCoO_2 using acrylic acid and its electrochemical properties for Li secondary batteries. *J Power Sources*. 1999;81–82:517–23.
24. Peng ZS, Wan CR, Jiang CY. Synthesis by sol–gel process and characterization of LiCoO_2 cathode materials. *J Power Sources*. 1998;72(2):215–20.
25. Sun YK, Oh IH, Hong SA. Synthesis of ultrafine LiCoO_2 powders by the sol–gel method. *J Mater Sci*. 1996;31(14):3617–21.
26. Burukhin A, Brylev O, Hany P, Churagulov BR. Hydrothermal synthesis of LiCoO_2 for lithium rechargeable batteries. *Solid State Ion*. 2002;151:259–63.
27. Fromm KM. Synthesis and crystal structure of $\text{Li}[\{\text{Ca}_7(\text{u}_3\text{-OH})_6(\text{thf})_{12}\}_2(\text{u-l})\}\cdot 3\text{THF}]$, a unique H-bound dimer of a Ca_7 -cluster on the way to sol–gels. *Chem Commun*. 1999;17:1659–60.
28. Fromm KM, Gueneau ED, Goesmann H. Synthesis and crystal structure of $[\text{Ba}(\text{OBut})_4(\text{Li}(\text{thf}))_4(\text{OH})]$: a mixed ligand heterometallic cluster with an unusual low coordination number for barium. *Chem Commun*. 2000;22:2187–8. doi:10.1039/b005638n.
29. Fromm KM, Gueneau ED, Bernardinelli G, Goesmann H, Weber J, Mayor-López MJ, et al. Understanding the formation of new clusters of alkali and alkaline earth metals. *J Am Chem Soc*. 2003;125(12):3593–604.
30. Maudez W, Häussinger D, Fromm KM. A Comparative study of (Poly) ether adducts of alkaline earth iodides—an overview including new compounds. *Z Anorg Allg Chem*. 2006;632(14):2295–8.
31. Maudez W, Meuwly M, Fromm KM. Analogy of the coordination chemistry of alkaline earth metal and lanthanide Ln^{2+} ions: the isostructural zoo of mixed metal cages $[\text{M}(\text{OtBu})_4(\text{Li}(\text{thf}))_4(\text{OH})]$ ($\text{M} = \text{Ca}, \text{Sr}, \text{Ba}, \text{Eu}$), $[\text{MM}'_6(\text{OPh})_6(\text{thf})_6]$ ($\text{M} = \text{Ca}, \text{Sr}, \text{Ba}, \text{Sm}, \text{Eu}, \text{M}' = \text{Li}, \text{Na}$), and their derivatives with 1,2-Dimethoxyethane. *Chem Eur J*. 2007;13:8302–16.
32. Gschwind F, Sereda O, Fromm KM. Multitopic ligand design: a concept for single-source precursors. *Inorg Chem*. 2009;48(22):10535–47. doi:10.1021/ic9009064.
33. Maudez W, Fromm KM. The heterometallic clusters of trivalent rare earth metals of $[\text{Ln}(\text{OPh})_6(\text{Li}(\text{dme}))_3]$, with $\text{Ln}_{1/4}$ Eu and Sm. *Helv Chim Acta*. 2009;92(11):2349–56.
34. Gschwind F, Crochet A, Maudez W, Fromm KM. From alkaline earth ion aggregates via transition metal coordination polymer networks towards heterometallic single source precursors for oxidic materials. *Chimia*. 2010;64(5):299–302. doi:10.2533/chimia.2010.299.
35. Kwon NH, Brog JP, Maharajan S, Crochet A, Fromm KM. Nanomaterials meet Li-ion batteries. *Chimia*. 2015;69(12):734–6. doi:10.2533/chimia.2015.734.
36. Crochet A, Brog J-P, Fromm KM. Mixed metal multinuclear Cr(III) cage compounds and coordination polymers based on unsubstituted phenolate: design, synthesis, mechanism, and properties. *Cryst Growth Des*. 2016;16(1):189–99. doi:10.1021/acs.cgd.5b01084.
37. Buzzee MC, Iqbal AH, Long CM, Millar D, Patel S, Pellow MA, et al. Homoleptic cobalt and copper phenolate $\text{A}_3[\text{M}(\text{OAr})_4]$ compounds: the effect of phenoxide fluorination. *Inorg Chem*. 2004;43:7709–25.
38. Boyle TJ, Rodriguez MA, Ingersoll D, Headley TJ, Bunge SD, Pedrotty DM, et al. A novel family of structurally characterized lithium cobalt double aryloxides and the nanoparticles and thin films generated therefrom. *Chem Mater*. 2003;15:3903–12. doi:10.1021/cm020902u.
39. Rothen-Rutishauser BM, Kiama SG, Gehr P. A three-dimensional cellular model of the human respiratory tract to study the interaction with particles. *Am J Respir Cell Mol Biol*. 2005;32(4):281–9. doi:10.1165/rcmb.2004-0187OC.
40. Gwinn M, Vallyathan V. Nanoparticles: health effects—pros and cons. *Environ Health Perspect*. 2006;114:1818–25.
41. Maynard AD, Robert JA, Butz T, Colvin V, Donaldson K, Oberdorster G, et al. Safe handling of nanotechnology. *Nature*. 2006;444:267–9.
42. Timbrell J. Biomarkers in toxicology. *Toxicology*. 1998;129:1–12.
43. Donaldson K, Stone V, Tran C, Kreyling W, Borm P. Nanotoxicology. *Occup Environ Med*. 2004;61(9):727–8.
44. Li J, Muralikrishnan S, Ng C, Yung L, Bay B. Nanoparticle-induced pulmonary toxicity. *Exp Biol Med (Maywood)*. 2010;235:1025–33.
45. Borm P, Klaessig F, Landry T, Moudgil B, Pauluhn J, Thomas K, et al. Research strategies for safety evaluation of nanomaterials, part V: role of dissolution in biological fate and effects of nanoscale particles. *Toxicol Sci*. 2006;90(1):23–32.
46. Oberdorster G, Stone V, Donaldson K. Toxicology of nanoparticles: a historical perspective. *Nanotoxicology*. 2007;1:2–25.
47. Brog JP, Crochet A, Fromm KM, inventors. Lithium metal aryloxide clusters as starting products for oxide materials patent WO 2012000123 A1; 2011.
48. Shriver DF. The manipulation of air-sensitive Compounds. New York: McGraw-Hill; 1969.
49. Cosier J, Glazer AM. A nitrogen-gas-stream cryostat for general X-ray diffraction studies. *J Appl Crystallogr*. 1986;19:105–7.
50. Blanc E, Schwarzenbach D, Flack HD. The evaluation of transmission factors and their first derivatives with respect to crystal shape parameters. *J Appl Cryst*. 1991;24:1035–41.
51. Burla MC, Calandro R, Camalli M, Carrozzini B, Cascarano GL, Caro LD, et al. SIR2004: an improved tool for crystal structure determination and refinement. *J Appl Cryst*. 2005;38:381–8.
52. Sheldrick GM. A short history of SHELX. *Acta Crystallogr A*. 2008;64(Pt 1):112–22. doi:10.1107/S0108767307043930.
53. Spodaryk M, Shcherbakova L, Sameljuk A, Zakaznova-Herzog V, Braem B, Holzer M, et al. Effect of composition and particle morphology on the electrochemical properties of LaNi 5-based alloy electrodes. *J Alloys Compd*. 2014;607:32–8.
54. Chartouni D, Kuriyama N, Otto A, Güther V, Nützenadel C, Züttel A, et al. Influence of the alloy morphology on the kinetics of AB₅-type metal hydride electrodes. *J Alloys Compd*. 1999;285:292–7.
55. Blank F, Rothen-Rutishauser BM, Schurch S, Gehr P. An optimized in vitro model of the respiratory tract wall to study particle cell interactions. *J Aerosol Med Depos Clear Effects Lung*. 2006;19(3):392–405. doi:10.1089/jam.2006.19.392.
56. Maguire T, Novik E. Methods in bioengineering: alternatives to animal testing. Norwood: Artech House; 2010. p. 239–60. ISBN: 9781608070114.
57. Steiner S, Mueller L, Popovichova OB, Raemy DO, Czerwinski J, Comte P, et al. Cerium dioxide nanoparticles can interfere with the associated cellular mechanistic response to diesel exhaust exposure. *Toxicol Lett*. 2012;214(2):218–25.
58. Lenz AG, Karg E, Lentner B, Dittrich V, Brandenberger C, Rothen-Rutishauser B, et al. A dose-controlled system for air-liquid interface cell exposure and application to zinc oxide nanoparticles. *Part Fibre Toxicol*. 2009;6:32–48. doi:10.1186/1743-8977-6-32.
59. Tomašek I, Horwell CJ, Damby DE, Barošová H, Geers C, Petri-Fink A, et al. Combined exposure of diesel exhaust particles and respirable Soufrière Hills volcanic ash causes a (pro-)inflammatory response in an in vitro multicellular epithelial tissue barrier model. *Part Fibre Toxicol*. 2016;13:67–80. doi:10.1186/s12989-016-0178-9.
60. Anson CE, Klopfer W, Li J-S, L. Ponikiewski, Rothenberger A. A Close Look at Short C-CH₃...Potassium Contacts: synthetic and Theoretical Investigations of $[\text{M}_2\text{Co}_2(\mu_3\text{-OtBu})_2(\mu_2\text{-OtBu})_4(\text{thf})_4]$ ($\text{M} = \text{Na}, \text{K}, \text{Rb}, \text{thf} = \text{tetrahydrofuran}$). *Chem Eur J*. 2006;12(7):2032–8. doi:10.1002/chem.200500603.
61. Akimoto J, Gotoh Y, Oosawa Y. Synthesis and structure refinement of LiCoO_2 single crystals. *J Solid State Chem*. 1998;141(1):298–302.
62. Maiyalagan T, Jarvis KA, Therese S, Ferreira PJ, Manthiram A. Spinel-type lithium cobalt oxide as a bifunctional electrocatalyst for the oxygen evolution and oxygen reduction reactions. *Nat Commun*. 2014;5:1–8. doi:10.1038/ncomms4949.

63. Bard AJ, Faulkner LR. Electrochemical methods: fundamentals and applications. New York: Wiley; 2001.
64. Kwon NH, Yin H, Brodard P, Sugnaux C, Fromm KM. Impact of composite structure and morphology on electronic and ionic conductivity of carbon contained LiCoO₂ cathode. *Electrochim Acta*. 2014;134:215–21.
65. Borm P, Cassee FR, Oberdorster G. Lung particle overload: old school -new insights? *Part Fibre Toxicol*. 2015;12:10–4. doi:10.1186/s12989-015-0086-4.
66. Brog J-P, Chanez C-L, Crochet A, Fromm KM. Polymorphism, what it is and how to identify it: a systematic review. *RSC Adv*. 2013;3(38):16905–31. doi:10.1039/c3ra41559g.
67. Xiao X, Liu X, Wang L, Zhao H, Hu Z, He X, et al. LiCoO₂ nanoplates with exposed (001) planes and high rate capability for lithium-ion batteries. *Nano Res*. 2012;5(6):395–401. doi:10.1007/s12274-012-0220-7.
68. Kwon NH, Yin H, Vavrova T, Lim JHW, Steiner U, Grob  ty B, et al. Nanoparticle shapes of LiMnPO₄, Li⁺ diffusion orientation and diffusion coefficients for high volumetric energy Li⁺ ion cathodes. *J Power Sources*. 2017;342:231–40. doi:10.1016/j.jpowsour.2016.11.111.
69. Kwon NH. The effect of carbon morphology on the LiCoO₂ cathode of lithium ion batteries. *Solid State Sci*. 2013;21:59–65.
70. Lia C-C, Leeb J-T, Loa C-Y, Wu M-S. Effects of PAA-NH₄ addition on the dispersion property of aqueous LiCoO₂ slurries and the cell performance of as-prepared LiCoO₂ cathodes. *Electrochem SolidState Lett*. 2005;8(10):A509–12. doi:10.1149/1.2012287.

Submit your next manuscript to BioMed Central and we will help you at every step:

- We accept pre-submission inquiries
- Our selector tool helps you to find the most relevant journal
- We provide round the clock customer support
- Convenient online submission
- Thorough peer review
- Inclusion in PubMed and all major indexing services
- Maximum visibility for your research

Submit your manuscript at
www.biomedcentral.com/submit



Benefits of publishing in BioMed Central's open access journals



Customer satisfaction

- 89% of authors rated the quality of the overall process as very good
- 90% of authors rated the helpfulness of Editorial staff as very good
- 89% of authors said they would recommend BioMed Central to a colleague



Rapid publication

- Fast and thorough peer review, with an average time to first decision of 6 weeks
- Instant inclusion in all major indexing services including PubMed



High visibility

- Over 25 million page views per month
- Over 7 million user sessions per month
- 1.5 million registered users

"A lot of sincere thanks for your efforts in promoting our paper. The press coverage our article received was unbelievable."
Armen Mulkidjanian



High impact

- Many journals are leaders within their field
- Article-level measures of impact including article accesses and citation tracking
- Over 140 journals with Impact Factors



Innovative publishing solutions

- Innovative publishing tools such as threaded publications and ISRCTN Register facilitate content discovery
- Specialist journals allow integrated publishing solutions of all types of data, e.g. *Trials*, *BMC Research Notes* and *GigaScience*



Online publishing

- No space constraints or color figure charges
- Acceptance of multiple file types and formats, including video content
- All journals free to download as apps



Authors retain copyright

- Articles may be published on multiple websites, blogs, publications, etc.
- Redistribute articles to colleagues, opinion leaders and key decision makers without restriction